Advanced Nondestructive Evaluation II

Proceedings of the International Conference on ANDE 2007

This page intentionally left blank

Advanced Nondestructive Evaluation II

Proceedings of the International Conference on ANDE 2007

Editors

Seung-Seok Lee

Korea Research Institute of Standards & Science, Korea

Joon Hyun Lee • Ik-Keun Park

Pusan National University, Korea

Seoul National University of Technology, Korea

Sung-Jin Song • Man-Yong Choi

Sungkyunkwan University, Korea

Korea Research Institute of Standards & Science, Korea

World Scientific

NEW JERSEY • LONDON • SINGAPORE • BEIJING • SHANGHAI • HONG KONG • TAIPEI • CHENNAI

Published by

World Scientific Publishing Co. Pte. Ltd.

5 Toh Tuck Link, Singapore 596224

USA office: 27 Warren Street, Suite 401-402, Hackensack, NJ 07601

UK office: 57 Shelton Street, Covent Garden, London WC2H 9HE

British Library Cataloguing-in-Publication Data
A catalogue record for this book is available from the British Library.

ADVANCED NONDESTRUCTIVE EVALUATION II
(In Two Volumes, with CD-ROM)
Proceedings of the International Conference on ANDE 2007

Copyright © 2008 by World Scientific Publishing Co. Pte. Ltd.

All rights reserved. This book, or parts thereof, may not be reproduced in any form or by any means, electronic or mechanical, including photocopying, recording or any information storage and retrieval system now known or to be invented, without written permission from the Publisher.

For photocopying of material in this volume, please pay a copying fee through the Copyright Clearance Center, Inc., 222 Rosewood Drive, Danvers, MA 01923, USA. In this case permission to photocopy is not required from the publisher.

ISBN-13 978-981-279-016-3 (Set)
ISBN-10 981-279-016-0

ISBN-13 978-981-279-017-0 (Vol. 1)
ISBN-10 981-279-017-9

ISBN-13 978-981-279-018-7 (Vol. 2)
ISBN-10 981-279-018-7

Printed in Singapore.

COMMITTEES

International Advisory Committee

Jianzhong Shen, *The Chinese Society for Nondestructive Testing (China)*
Teruo Kishi, *National Institute for Materials Science (Japan)*
Chi Hyun Han, *The Korea Society for Nondestructive Testing (Korea)*
Sekyung Lee, *The Korea Research Institute of Standards and Science (Korea)*
Eun Soo Park, *Seoul National University of Technology (Korea)*
Jan D. Achenbach, *Northwestern University (USA)*
Joseph L. Rose, *Pensylvania State University (USA)*
R.Bruce Thompson, *Iowa State University (USA)*

Organizing Committee

Chairman **Seung-Seok Lee,** *Korea Research Institute of Standards and Science (Korea)*
Members **Rong Sheng Geng,** *Beijing Aeronautical Technology Research Centre (China)*
Krishnan Balasubramaniam, *Indian Institute of Technology Madrads (India)*
Masumi Saka, *Tohoku University (Japan)*
Sohichi Hirose, *Tokyo Institute of Technology (Japan)*
Oh-Yang Kwon, *Inha University (Korea)*
Joon Hyun Lee, *Pusan National University (Korea)*
Il-Soon Hwang, *Seoul National University (Korea)*
Ik Keun Park, *Seoul National University of Technology (Korea)*
Sung-Jin Song, *Sungkyunkwan University (Korea)*
Man Yong Choi, *Korea Research Institute of Standards and Science (Korea)*
Tsung-Tsong Wu, *National Taiwan University (Taiwan)*
Sridhar Krishnaswamy, *Northwestern University (USA)*

Local Steering Committee

Chairman **Dong-Jin Yoon,** *Korea Research Institute of Standards and Science (Korea)*
Members **Bongyoung Ahn,** *Korea Research Institute of Standards and Science (Korea)*
Yong-Moo Cheong, *Korea Atomic Energy Research Institute (Korea)*
Yong-Sang Cho, *Korea Electric Power Research Institute (Korea)*
Younho Cho, *Pusan National University (Korea)*
Min Joo Choi, *Cheju National University (Korea)*
Song-Chun Choi, *Korea Gas Safety Corporation (Korea)*
Kyung-Young Jhang, *Hanyang University (Korea)*
Amkee Kim, *Kongju National University (Korea)*
Koung-Seok Kim, *Chosun University (Korea)*
Nohyu Kim, *Korea University of Technology and Education (Korea)*
Kwang-Myong Lee, *Sungkyunkwan University (Korea)*
Young-Sup Lee, *University of Incheon (Korea)*
Seung-Hoon Nahm, *Korea Research Institute of Standards and Science (Korea)*
Won-Joon Song, *Research Institute of Industrial Science & Technology (Korea)*

This page intentionally left blank

PREFACE

This volume includes the papers presented for the 2nd International Conference on Advanced Nondestructive Evaluation (The 2nd ANDE) held in Busan, Korea, 17-19 October, 2007. The aim of the conference is to discuss the current state of nondestructive technologies, which are rapidly progressing by integrating emerging technologies in the various fields.

Of the 583 papers presented at the conference, 240 manuscripts were included in this Volume. We believe that this proceedings volume includes many of the excellent papers presented at the 2nd International Conference on Advanced Nondestructive Evaluation.

Various technical sessions were scheduled that should be noted for both the advances made and the high technical interest shown. There are twenty six organized sessions in Aging and Degradation, Bio and Medical NDE, Composite Materials and Structures, Fatigue and Fracture, Guided Wave, Health Monitoring of Structure, Image Processing, IR Thermography, Materials Properties, Micro Sensor and MEMS, Modeling and Simulation, NDE for Biosytem and Agriculture, NDE in Electronic Industry, NDE in Materials Processing, NDT for Infrastructure, NDT in Nuclear Industry, NDT in Power Plant, Neutron Radiography, New Methods and Devices, Nonlinear Phenomenon, Optical Methods, Railways, Reliability, Signal Processing, Smart Structure and System, and Vibration.

We are grateful to all the members of the committee who have contributed with their invaluable experience and suggestions. We would like to thank all of the sponsoring institutions, organizations and companies which have supported the 2nd ANDE 2007 both financially and otherwise.

Finally, the organizers appreciate the support and contributions of the individuals whose efforts and participation were essential to the successful conference.

This page intentionally left blank

CONTENTS

Committees v
Preface vii

Part 1

SECTION 1 : AGING & DEGRADATION

Stator Insulation Quality Assessment for High Voltage Motors Based on Probability Distributions
H.D. Kim and C.H. Kim 1

Effect of Leakage on Deterioration of Concrete Lining in Conventional Tunnel
H.S. Jung, D.G. Kim, S.T. Lee and S.S. Kim 7

Sulfate Attack of Shotcrete Made with Alkali-Free Accelerator
S.T. Lee, D.K. Kim, H.S. Jung, G.P. Lee, S.S. Kim and K.P. Park 13

Non-Destructive Assessment for Degradation of 9 Cr Steel
J.S. Park, U.B.Baek, W.K. Lee and S.H. Nahm 19

Fretting Wear of Inconel 690 Tubes Tested by Piezo-Actuated Rig
I.S. Chung, M.H. Lee and Y.S. Chai 25

Assessment of Creep Damage on a Pipe Bend of 1/2Cr1/2Mo1/4V Steel
J.S. Hyun, H.S. Choi, W.S. Choi and G.W. Song 31

Detection of Oil-Paper Insulation Aging with Dielectric Spectroscopy in Time and Frequency Domain Measurements
S.H. Lee, J.H. Kim and S.O. Han 37

Temperature Dependence of Return Voltage Characteristics
S.H. Lee, Y.H. Kim, J.H. Joeng, S.G. Han, D.G. Park and S.O. Han 43

Finite Element Analysis to Evaluate Wall Thinned Pipe Using PVDF Comb Transducer
B.M. Song, J.H. Lee and D.H. Lee 49

Properties of Shotcrete Immersed in Various Harmful Solutions
D.G. Kim, H.S. Jung, S.T. Lee and H.S. Shin 55

SECTION 2 : BIO & MEDICAL NDE

A Morphological Study in the Mandibular Second Premolar Using a Micro-CT
K.J. Chun, O.S. Yoo and Y.Y. Won 61

Biomechanical Nondestructive Evaluation of Joint Movements and Muscle Length of Lower Limbs during Hemiplegic Walking
S.J. Hwang, J.S. Son, Y.H. Kim and J.M. Park 67

Fault Diagnosis Based on Voxel Data Obtained from CT
J.C. Han, H.B. Youn and H.K. Kim 73

The Estimation of Knee Varus Torque by an Accelerometer in Osteoarthritis Patients and Healthy Adults
S.H. Hwang, S.B. Park and Y.H. Kim 79

Development of the Health Age Formular and Examination for Women
J.H. Shin 85

Reconstruction of Images of Speed of Sound from Medical Ultrasound Images
M.K. Jeong, S.J. Kwon, M.J. Choi and Andrew J Coleman 91

Measurement and Evaluation of Impulse Force Which Human Body Receives by Contact of Machine and Structure
Y. Itoh, T. Nemoto, S. Yanai, K. Koide, A. Inamori, H. Matsuura and A. Shimamoto 97

Evaluation of Hand Function Recovery in Chronic Hemiparetic Patients Using Electromyographic Responses
K.S. Tae, S.J. Song and Y.H. Kim 103

The Balance Recovery Mechanisms against the Forward Perturbation
S.J. Hwang, H.S. Choi, K.S. Tae and Y.H. Kim 109

EMG Pattern Recognition Using Neural Networks during the Postural Balance Control of Human Body
H.K. Choi, J.H Jeong and W.H. Cho 115

Passive Elastic Characteristics and Musculoskeletal Kinematics of Human Foot for Biomechanical Analysis
H.K. Choi, S.Y. Kim and W.H. Cho 121

EMG Analysis of Muscular Fatigue and Muscle Activity Due to Turtle Neck Syndrome
W.H. Cho, W.Y. Lee, S.H. Yoon, C.H. Jeong and H.K. Choi 127

The Relationship among the Center of Pressure, the Center of Mass and the Horizontal Acceleration of the Body in Postural Sway, Falling and Walking
H.S. Choi and Y.H. Kim 133

Joint Moments and Lumbar Curvatures during Symmetrical Lifting
S.H. Hwang, S.J. Hwang, Y.E. Kim and Y.H. Kim 139

Determination of the Material Property for the Rear Fixation Device of the Vertebrae by FEM
D.J. Oh, S.H. Yoo, J.H. Song, Dhaneshwar Mishra and S.C. Hwang 145

A FES Sensor System Using a Tilt Sensor for Improving Hemiplegic Gait
S.W. Park, J.S. Son, S.J. Kang and Y.H. Kim 151

Homogeneiyt and Ranklet Based Mass-Type Cancer Detection in Dense Mammographic Images
W.H. Kim and S.M. Kim 157

The Evaluation of Usefulness of the FEA and Relationship between Trabecular Microstructural and Biomechanical Properties in Human Femoral Head
M.H. Baek, W.Q. Cui, K.J. Chun, Y.E. Kim, Y.Y. Won and J.H. Hur 163

Evaluation Algorithm Based on Automatic Image Analysis for Malarial Blood Cell Images
C.H. Kim, J.Y. Kim and S.H. Hong 169

A Study on the Performance of 3D Acoustic Field Analysis Method for the Evaluation of Medical Ultrasonic Probe
W.J. Yu, S.C. Noh, H.G. Min, M.K. Park and H.H. Choi 174

Measurement of Shaking for the Sacral-Region Circumference Skin under State of Decubitus
T. Nemoto, Y. Ito, C.C. Lee, Z. Isogai, K. Koide, N. Noda, H. Matsuura, H. Isoe, H. Yamashita, H. Okano and F. Nogata..... 180

Mechanical Properties of the Human Carotid Artery Using Ultrasonography and Presumption of Arteriosclerosis
T. Nemoto, Y. Ito, H. Matsuura, Y. Yokota, Y. Kawamura, M. Maruyama and F. Nogata..... 186

SECTION 3 : COMPOSITE MATERIALS & STRUCTURES

Characterization of Structural Performance in Ceramic Matrix Composites
J.G. Kim and J.H. Lee 192

A Study on Natural Frequency Detection of Vehicle Components; Sensors and Actuators
B.S. Kim, K.C. Shin, J.S. Yoon and H.J. Park 198

A Study on the Fire Resistance Capacity of Asymmetric Slimflor Beam Members
S.H. Han and S.K. Choi 203

A Study on Stress Analysis and Experimental Evaluation for the All Composite Structure of Wig Vehicle
J.D. Han, Y.S. Lee, K.J. Kang and H.K. Jeong 209

An Elastic-Plastic Finite Element Analsys of the Interface with Perpendicular Crack Using the Property Gradient in Fiber Reinforced MMC
J.W. Kang and O.H. Kwon 215

A Study for Load Bearing Capability of Laminates with Embedded Shape Memory Alloy Subjected to Low Velocity Impact
K.W. Kang and J.K. Kim 221

Nondestructive Testing and Strength Prediction of Adhesive Bonded Joints Using the Scan Type Magnetic Camera
H.C. Yoon and J.Y. Lee 227

A Study on the Light-Weight Thin-Walled Member for Optimum Crashworthiness Design
K.S. Lee, H.K. Seo, W.C. Hwang, I.Y. Yang and K.H. Im 233

Influence of Stacking Condition on Axial Compression and Bending Collapse of the Hybrid Hat Shaped Member
J.H. Kim, J.H. Kim, J.W. Park, Y.J. Yang and I.Y. Yang 239

A Study on the Drilling Characteristics According to Drill Diameter of Laminate Composite
S.C. Lee, S.T. Jeong, J.N. Park and G.J. Cho 245

SECTION 4 : FATIGUE & FRACTURE

Effect of Wear to the Fatigue Life of Shaft Based on Product Lifecycle Management
Y.T. Li, Y.B. Wei and M. Song 252

Compressive Fatigue Stength of Al-Alloy Foam with Different Thicknesses
M. Hossain, I.H. Kim, K.W. Shin and A.E. Kim 258

Study of Experimental Examination on Strength Evaluation in the Design of Double Column for
S. Sasaki, K. Hagiwara and T. Ezumi 264

Evaluation of Fracture Toughness of Interfacial Cracks Subjected to Mechanical and Thermal Load Using Finite Element Method
D. Mishra, S.H. Yoo, D.J. Oh, J.H. Song and Y.T. Lee 270

High-Velocity Impact Characteristic of CFRP Composite
R. Kubota, D. Numata, M. Anyouji, A. Shimamoto and K. Takayama 276

Wear Amount Prediction of Automobile Tire by Finite Element Analysis
J.H. Lee, J.R. Cho and J.H. Choi 282

Transformed Solution for Fixed Specimen with Notches by Infinitely Similar Element Method
Y.T. Li, W.Y. Jin and C.F. Yan 288

Stress Analysis on Discontinuous Finite-Width Plate by Hybrid Method
L. Chen and T.H. Baek 294

Fatigue Analysis of the Cervical Plate System Installed in Cervical Spine Using Finite Element Method
I.C. Yang, S.M. Kim and S.Y. Cho 300

Durability Analysis of Rubber Diaphragm for Vehicle Suspension Damper System
S.K. Koh, T.H. Baek and H.Y. Hwang 306

Failure Assessment Analysis to API 5l X65 Pipeline Subjected to Large Plastic Deformation
J.H. Baek, Y.P. Kim, W.S. Kim and C.S. Seok 312

Fatigue Crack Growth Behavior for Welded Joint of X80 Pipeline Steel
Y.P. Kim, C.M. Kim, W.S. Kim and K.S. Shin 318

An Analysis for Fatigue Behavior of the Brazed Joints
H.J. Shim, K.W. Kang and J.K. Kim 324

Evaluation of Fatigue Strength of the Bogie Frame for Electrical Multiple Unit
S.C. Yoon and J.G. Kim 330

An Evaluation of Residual Stress Redistribution Caused by Fatigue Crack Propagation by Finite Element Method
E.J. Park, E.J. Kim and S.H. Yoo 336

Fatigue Strength Analysis of the Web Plate of Wheels Using Critical Plane Approach
J.W. Seo, S.J. Kwon and S.T. Kwon 342

Fatigue Behavior of Inconel Alloys Due to Fretting and High Temperature
S.W. Woo, J.D. Kwon, D.K. Park and C.Y. Lee 348

Influence of the Damaged Blade of a Multiple-Stage Axial Compressor on Turbine Components of the Heavy-Duty Gas Turbine
M.S. Kang, W.N. Yun, K.Y. Kim and J.S. Kim 354

Influence of Stress and Excitation Size on the Velocity of Compression Wavefront in Jointed Rock Masses
M.S. Cha, E.S. Hong, S.H. Baak and G.C. Cho 360

X-Ray Diffraction Analysis on Fatigue Fracture Surface of SG365 Steel
M.B. Lim, W.J. Park, J.D. Son and G.S. Choi 366

The Study of Evaluation Tensile Characteristics and Plane Strain Fracture Toughness in Induction Surface Hardened of the SM53C Steel
H.B. Jeon, S.C. Huh and W.J. Park 375

Fracture Characteristrics of Ceramic Plates Using Shock Tunnel
K.J. Kim, J.H. Kim, Y.S. Lee, J.H. Park, K.H. Song, S.H. Koo and S.I. Moon 382

An Evaluation of Fracture Toughness for Ceramics
K.J. Kim, J.H. Kim, Y.S. Lee, N.S. No, S.H. Koo and S.I. Moon 388

Fatigue Life of Compound Cylinder Combining Autofrettage and Shrink Fit Due to the Firing
Y.S. Lee, J.H. Park, J.H. Kim, Q.M. Yang, K.U. Cha and S.K. Hong 394

Fatigue Life Evaluation of Pipe Welds in Power Plant Using Advanced Nondestructive Methods
S.G. Lee, S.K. Park, K.B. Yoo and D.G. Park 400

A Study on Accelerated Life Test Utilizing Fatigue Damage Theory for Automobile Components
D.H. Jung, Y.W. Choi, B.K. Lim and S.I. Bae 406

Comparison of Fatigue Properties of Al Alloys for Chassis Components
C.Y. Kim, J.H. Park, J.Y. Park, B.I. Choi, H.J. Lee, S.M. Hyun and J.S. Kim..... 412

SECTION 5 : GUIDED WAVE

Acoustic Performance of a Magnetostrictive Strip Sensor for a Torsional Guided Wave
Y.M. Cheong and S. Kim..... 418

A Study on Time Domain Computer Simulation of Ultrasonic Guided Wave Mode Conversion
Y.H. Cho, Y.K. Choi and N.H. Kim 424

Signals of Magnetostrictive Sensors on Artificial Defect Pipes of Carbon and Stainless Steel
D.S. Koo, S. Kim, Y.M. Cheong and C.S. Park 431

Welding Zone Defect Detection Usefulness Estimation of Laser Guided Lamb Wave
K.S. Song and J.Y. Kim 437

A Study of Guided Ultrasonic Wave Application for Heat Exchanger Performance Improvement
Y.H. Cho, J.h. Jung and J.H. Kim 443

Study on Mode Switching Algorithm and Damage Evaluation for Efficient and Precision SHM Using Smart Sensor
Y. Hong, B.H. Han, D.P. Hong and Y.M. Kim 450

Bumper Impact Perception for Pedestrian Protection Using Smart Sensor
Y. Hong, G.P. Wang, H.W. Park, D.P. Hong and Y.M. Kim..... 456

SECTION 6 : HEALTH MONITORING OF STRUCTURE

Wideband Radar Imaging Of Concrete Specimens for NDT
H.C. Rhim and J.W. Oh 462

Health Monitoring of Composite Structures Based on Acoustic Wave Sensing Using Fiber Optic Sensors
B.R. Mattapally, M.R. Bhat and Murthy C.R.L. 467

Application of Genetic Algorithm and Gauss-Newton Method to System Identification
Grace S. Wang and Fu-Kuo Huang 475

A Study on Remote Monitoring and Security of Control System Using IPSEC
H.J. Na, W.K. Lee, S.H. Nahm, D.H. Ryu, S.H. Lee and S.C. Lee 481

Health Monitoring of Steel Crane Girder Using PZT Sensors
K.J. Shin, H.J. Kim, C.W. Jung and W.J. Kim 487

Characterization of Crack Detection Methods Using Strain Mode Shapes on Plates with Various Geometry
B.S. Kim and S.H. Yoo 499

Detection of Various Damage Patterns Using Impedance Measurement and Statistical Post Processing
Y. Hong, S.H. Hwang, D.P. Hong and Y.M. Kim 505

Measurement and Monitoring of Mechanical Loads of Large Slender Structures Using Distributed Fiber Optic Sensor
J.W. Lee, Y.C. Huh, J.H. Park, Y.Y. Nam, G.H. Lee, Y.J. Park, J.Y. Kim, Y.S. Kim and Y. B. Lee 511

Material Characterization of Lock Plate for Gas Turbine Plant
Y.H. Cho, K.S. Jeong, L.J. Jin and C.Y. Lee 517

The Precise Measurement of Steel Cable Tension in Cable Stayed Bridges by Nondestructive Magnetic Sensor
H.W. Park, B.Y. Ahn, S.S. Lee and W.G. Lee 524

SECTION 7 : IMAGE PROCESSING

Visualization of Tooth for Non Destructive Evaluation
H. Gao, M. Julius Hossain, O. Chae and Jim X. Chen 536

Image Processing Based Defect Inspection System for Pharmaceutical Products
H.J. Kim, D.H. Ryu and T.W. Choi 542

Characterization of Self-Assembled Monolayers by Using a Near-Field Microwave Microprobe
H. Melikyan, T. Sargsyan, A. Hovsepyan, A. Babajanyan, S.W. Kim, J.C. Kim, K.J. Lee, B. Friedman and R. Levicky 548

Image Segmentation Based on Fuzzy MFA
K.D. Ban and Y.K. Chung 554

Low Error and Real-Time Stereo Vison Algorithm for 3D Visual Inspection
S.C. Park and H. Jeong 560

Analysis of the Detection of Voids of Construction Joints and Shapes of Inner Cavities in Concrete Using an Ultrasonic Pulse Velocity Method
S.K. Park and D.H. Choi 566

Radial Image Processing in the Discrete Polar Coordinate
W.H. Kim, H.J. Kim and S.M. Kim 572

Nonlinear Diffusion Equation for Image Denoising in Mixed-Gaussian Noise Environment
H.I. Hahn and D.H. Ryu 578

Study on the Fiber Orientation of Weld Line Parts during the Injection Molding of Fiber Reinforced Plastic by Image Processing
J.W. Kim and D.G. Lee 584

Real-Time Face and Hand Discrimination and 3d Position Extraction Using a Stereo Vision Embedded System
Y.K. Kim, H.C. Shin, J.I. Cho and D.H. Hwang 590

Non-Destructive Evaluaion of Cement-Grout by Surface Electrical Resistivty Method
M. Farooq, J.H. Kim, S.G. Park and Y.S. Song 599

Efficient Clustering Based on the Image Context for the Object Recognition
E.J. Koh, P.K. Rhee, J.H. Won and C.S. Bae 605

The Development of Displacement Measurement System by Using CCD Camera
H.S. Jeon, Y.C. Choi, J.C. Lee and J.W. Park 611

Image Restoration by Using a Wiener Filter Designed for Digital X-Ray Imaging Systems
S.Y. Lee, S.I. Choi, H.S. Cho, J.E. Oh, K.Y. Kim, B.S. Lee and S. Kim 617

SECTION 8 : IR THERMOGRAPHY

Current and Future Role of Medical Thermography
J.Y. Park 623

Experimental Design and Evaluation of Thermographic Reference Block
W.T. Kim, J.H. Park and K.S. Kang 629

Detection of Defects in Lumber Using IR Thermography
C.D. Eom, Y.J. Han, K.M. Kim, K.B. Kim, J.J. Lee and H.M. Yeo 635

A Study on Nondestructive Evaluation of Painted Metal by Using IR Thermography
S.H. Chol, K.S. Song and J.Y. Kim 641

Fast and Reliable Detection of Superficial Intracranial Hemorrhage by Hand-Held Device Using Near-Infrared
J.Y. Park, S.D. Kim and D.J. Lim 647

SECTION 9 : MATERIALS PROPERTIES

AE Characteristics of Pre-Cracked Charpy Specimens for the Multi-Passed Weldment for the Pressure Vessel Steel
E.G. Na, H. Kim and S.K. Lee 653

Deformation of Pure Magnesium in Tensile Test Investigated by STFT of AE Signals
Y. Li and M. Enoki 660

Dynamic Characterization on Al-Alloy Foam Damaged By Cyclic Load
I.H. Kim, S.G. Kim, A.K. Kim, S.J. Kim and J.H. Park 666

Glucose Concentration Monitoring Using a Surface Plasmon Polariton
A. Babajanyan, J.C. Kim, K.J. Lee, R. Khachatryan and K. Nerkararyan 672

Stiffness and Energy Loss Characteristics during Saturating-Drying Process in Low Porosity Rock
T.M. Oh, M.S. Cha, G.C. Cho and E.S. Hong 678

Numerical and Experimental Studies on Cooling Patterns of Al-Mg System Alloy Material during the Casting Product Process
Y.K. Oh, H.S. Yoon and H.D. Yang 684

Homogenized Material Properties and Mechanical Behavior of Hybrid Functionally Graded Composites
J.H. Choi and J.R. Cho 690

Glucose Biosensing by Using a Microwave Dielectric Resonator
J.C Kim, A. Babajanyan, S.W. Kim, H.K. Lee, J.Y. Kim and K.J. Lee 696

Influence of Fineness of Limestone Powder on External Sulfate Attack
H.S. Jung, S.T. Lee, K.P. Park and S.S. Kim 702

Enhancement of Detection Efficiency for G-Type Nerve Agent Simulants Based on DBR Porous Silicon
S.H. Jang, J.H. Kim, Y.D. Koh and H.L. Sohn 708

An Analysis for Mechanical Properties of Rubber Granule Layer of Synthetic Surfaced Track
K.W. Kang, H.J. Shim, J.K. Kim and J.B. Park 714

The Measurement of Thermal Diffusivity for Semi-Infinite Solid Using the Photothermal Displacement Method
P. S. Jeon, J. H. Kim, H. J. Kim and J. Yoo 720

A Study on the Bauschinger Effect of Gun Barrel High Strength Steel
W.S. Shim, J.H. Kim, Y.S. Lee, S.K. Hong and G.U. Cha 728

The Effect of Shot Peening on the Improvement of Fatigue Strength and Fatigue Crack Characteristics of the Aluminum Alloys
T.H. Song, M.B. Lim, S.C. Huh and W.J. Park 734

A Study on the X-Ray Diffraction Analysis and the Fatigue Crack Growth Behavior for the Aluminum Alloys
M.B. Lim, J. Jun, S.C. Huh and W.J. Park 743

A Study on Laser Surface Hardening of Tool Steel Using Optical Pyrometry
Y.T. Yoo and H.J. Shin 751

The Effect of Niobium According to Solution Annealing and Age Hardening of High Strength Steel
B.H. Choi, K.C. Jang and B.K. Choi 757

A Study on the Supercooling Characteristics of TMA-Water Clathrate Compound as Low Temperature Latent Heat Storage Material
C.O. Kim, N.K. Chung and J.H. Kim 763

Optical Characterization of Sensory Rhodopsin II Thin Films Using a Near-Field Microwave Microscope
S.H. Kim, Y.W. Yoon, A.R. Choi, K.H. Jung, K.J. Lee, B. Friedman and T. Ishibashi..... 769

SECTION 10 : MICRO SENSOR AND MEMS

Angle Effect of Micro-Scale Crosshatch Grooved Patterns under Lubricated Sliding Contact
Y.H. Chae..... 775

Effect of Micro-Scale Dimple Size on Steel Surface under Lubricated Sliding Contact
Y.H. Chae..... 780

SECTION 11 : MODELING AND SIMULATION

Finite Element Analysis of Laser Stitch Welded High Strength Steels for Automotive
H.S. Bang, H.S. Bang, Y.K. Lee, C.I. Oh and C.S. Ro..... 786

Evaluating the Quality of Soil Grouting by the SASW Method
P.H. Tsai and J. Lai 792

Stress Analysis of Mandibular First Premolar with Finite Element Models
K.J. Chun, O.S. Yoo, K.R. Park and S.H. Yoo 798

Cascaded Linear-Systems Analysis of CMOS Flat-Panel Detectors for Digital Radiography
S.M. Yun, M.K. Cho, C.H. Lim, H.K. Kim, T. Graeve, H.S. Cho and J.M. Kim..... 804

Numerical Analysis on 3-Dimensional Thermal Deformation of Automobile Tire Mold Using Al Alloy 5000 Series Material
Y.K. Oh, Y.S. Kim and H.S. Yoon 810

Modeling of Dielectric Response of Oil-Paper Insulation Systems Using Return Voltage Method
S.H. Lee, D.G. Park and S.O. Han 816

Residual Stress Analysis and Measurement of Fuel Injection Pipe
S.K. Koh and E.G. Na 822

Numerical Analysis and Experimental Studies on Current Shunts for Clamp on Meter
W.W.S. Wijesinghe and Y.T Park 828

System Identification of a Steel Bridge Using Modal Flexibility Matrix
K.Y. Koo, D.K Kim, J. Cui and H.Y. Jung 834

Geometric Calibration in CBCT Using Coordinates-Transformed Sampling
S.K. Heo, M.K. Cho and H.K. Kim 841

Inverse Analysis of Stress-Strain Distribution from Monitored Response of Structures
H.S. Shin, D.G. Kim and S.H. Baek 846

Optimal Design of an Linear Motion Mechanism
J.S. Lee and E.J. Park 852

Effects of Pulse Train Characteristics on the Through Transmission Pulsed Eddy Current Signal
Y.K. Shin and D.M. Choi 858

A Study on the Critical Fracture Pressure on the Al_2O_3 Ceramic Circular Plate under Shock Impact
Y.S. Lee, J.H. Lee, J.H. Kim, J.P. Kong, K.J. Kim, S.H. Koo and S.I. Moon 865

A Study on Evaluation of Shear Strength of Nature-Friendly Costal Environment Block Connection
C.H. Kim 871

Simulation Studies for the Influence of Tomographic Parameters on the Image Quality of Digital X-Ray Tomosynthesis
J.E. Oh, S.I. Choi, M.S. Lee, K.Y. Kim, S.Y. Lee, H.S. Cho, B.S. Lee, and S. Kim .. 877

The Characteristics of Bilge Separation Sensor System for Improving Accuracy
W.S. Che, K.W. Kim and H.S. Kwon 883

A Study on the Evaluation Sliding Behavior of Nature-Friendly Assembled Conduit Connection
C.H. Kim 889

Design and Simulation of Roll Forming Process for Under Rail
S.H. Jeong, S.H. Lee and G.H. Kim 895

Possible Effects of FSW Tool Pin Configuration on Residual Stress Distribution
Y.G. Kweon, Rajesh S.R, H.J. Kim, W.S. Chang, C.K. Chun and S.J. Kim 902

Design and Characterization of MR Damper
H.L. Kim, Y.S. Lee, E.Y. Lee and G.S. Lee 908

Time Reversal Reconstruction of Dispersive Ultrasonic Lamb Waves in Thin Plates
H.J. Jeong 914

SECTION 12 : NDE FOR BIOSYSTEM AND AGRICULTURE

Investigation of Rice Taste Elements at Wide Area, Using Remote Sensing and GIS Technology
T. Ueda, C. Ryu, M. Suguri and M. Umeda 920

Line-Scan Spectral Imaging System for Online Poultry Carcass Inspection
K. Chao, C.C. Yang and M.S. Kim 926

Bending Strength Prediction of Structural Lumber by X-Ray Scanner
J.K. Oh, K.M. Kim, K.B. Shim, J.H. Park, H.M. Yeo and J.J. Lee 932

Field Application of the Ultrasonic CT Technique for Evaluating Deterioration in Ancient Wooden Building
S.J. Lee, K.M. Kim and J.J. Lee 939

Estimation of Optimal Plucking Time of Green-Tea Using Canopy Reflectance
T. Kurimoto, C.S. Ryu, M. Suguri and M. Umeda 945

Sampling and Calibration Requirements for Soil Property Estimation Using NIR Spectroscopy
K.S. Lee, D.H. Lee, Kenneth A. Sudduth and S.O. Chung 951

Detection of Bone and Cartilage of Beef Using Magnetic Resonance Imaging
S.M. Kim, C. Garvey, D. Williams, Y.S. Seo and M. Mccarthy 957

Realtime Monitoring of Tomato Concentrate Processing Using RF Sensors
S.M. Kim, C. Garvey, T. Leary and M. Mccarthy 963

Cataloging of Olive Accessions Using Magnetic Resonance Technique
S.M. Kim, E. Stover, J. Hansen and Michael J. Mccarthy 969

Quantitative Evaluation of Knot in Japanese Larch Lumber Using X-Ray Scanning
J.K. Oh, K.M. Kim, K.B. Shim, H.M Yeo and J.J. Lee 975

Estimation of Nitrogen Content of Rice Using Hypersepcetral Remote Sensing
C.S. Ryu, M. Suguri and M. Umeda 982

Estimation of Quality and Quantaty of Green-Tea by Hyperspectral Image
M. Suguri, C.S. Ryu and M. Umeda 988

Detection of Fecal Residue on Poultry Carcasses by Laser Induced Fluorescence Imaging
B.K. Cho, M.S. Kim, K.L. Chao, Alan M. Lefcourt, K. Lawrence and B.S. Park 994

Detection of Pathogenic Salmonella in Milk by Using an Impedance Biosensor
G.Y. Kim, J.H. Moon, H.J. Kim and A.S. Om 1000

SECTION 13 : NDE IN ELECTRONIC INDUSTRY

Self-Layer Subtractive Digital Tomosynthesis
M.K. Cho, S.K. Heo and H.K. Kim 1006

Study for Blade Ceramic Coating Delamination Detection for Gas Turbine
C.J. Choi, J.Y. Kim, M.Y. Kim and Y.S. Ahn 1011

Tomography Image Nondestructive Measurement for Melt Polymer Morphology
L. Lifu 1017

Nondestructive Characteristics of 1080 and 5083 Aluminum Alloy by ECAP
K.W. Nam, S.K. Kim, S.S. Park and S.H. Ahn 1023

Characteristics of Laser Transformation Hardening for Rod-Shaped Medium Carbon Steel(SM45C) by Gaussian Beam
J.D. Kim, J.S. Oh and W.J. Kang 1029

A Study on the Weldability of Aluminized Steel Sheet by Nd:YAG Laser
J.D. Kim, M.H. Lee and J.H. Lee 1035

Monitoring of CO_2 Hydrate Formation in Sediments Using Compressional Wave Velocity
T.H. Kwon, H.S. Kim, G.C. Cho and J.S. Lee 1041

Formation Mechanisms of Weld Defects and Dynamic Behavior of Keyhole in Galvanized Steel Welding by CO_2 Laser
J.D. Kim and H.J. Park 1047

SECTION 14 : NDT FOR INFRASTRUCTURE

The Development and Application of a New Elastic-Wave-Based Scanning System for Imaging Defects inside Concrete Structures
J.H. Tong, S.T. Liao, C.L. Chiu and W.Y. Juan 1053

Spectral Energy Transmission Method for Crack Depth Estimation in Concrete
J.Y. Min, C.B. Yun, S.W. Shin and J.Y. Zhu 1059

Development of Landslide Early Detection System Using Microwave
H.C. Rhim and L.H. Jin 1065

Feasibility of Evaluating the Compaction Quality of Soils by the Impact Echo Method
J. Lai, C.Y. Chiu and C.C. Cheng 1070

Color Change and Residual Compressive Strength of Concrete Exposed to High Temperature Using Spectrophotometric Method
J.W. Lee, K.H. Choi and K.P. Hong 1076

Identify the Locations of Concrete Cracks with Employing the Improved Active Contour Model to Extract Regional Boundaries from GPR
Y. Huang and S.C. Hsu 1082

Non-Destructive Evaluation of Asphalt Concrete Pavement System Using FWD Tests Considering Modeling Errors
J.H. Yi, Y.S. Kim, J.M. Kim and S.H. Mun 1088

Nondestructive Identification of Fatigue Cracking in a Composite Actuator with a PZT Ceramic during Electromechanical Cyclic Loading
S.C. Woo and N.S. Goo 1095

Estimation of Mechanical Properties of Concrete from the Drilling Resistance Parameters
S.H. Chang, S.W. Choi, G.J. Bae and J.H. Lee 1103

Implementation of Bender Elements for Measuring Stiffness Changes of Concrete Materials Due to Cracking
Z.O. An, W.S. Shin, E.S. Hwang and Y.J. Mok 1109

A Framework for Nondestructive Evaluation Methods Accounting for Uncertainty of Model and Aging Effect of Concrete
K.J. Hong and J.S. Kim 1115

A Study of the Structural Internal Assessment of Concrete Slab Using the Ground Penetrating Radar Exploration
S.U. Hong and Y.S. Cho 1121

SECTION 15 : NDT IN NUCLEAR INDUSTRY

Remote Measurement of Pipe Wall Thinning by Microwaves
Y. Ju 1128

3-Dimensional Quantitative Measurement of a Geometric Anomaly in Steam Generator Tubes Using a Diagnostic Eddy Current Probe (D-Probe)
D.H. Lee, M.S. Choi, D.H. Hur, J.H. Han and M.H. Song 1134

Methodology for Detecting Failed Fuel Assembly in a Liquid Metal Reactor
S.H. Seong, S. Hur, J.C. Park and S.O. Kim 1140

Development of Magnetic Phase Detection Sensor for the Steam Generator Tube in Nuclear Power Plants
D. Son, W.I. Joung, D.G. Park and K.S. Ryu 1146

Study on a Neutron Flux Detection and its Digital Signal Processing for Nuclear Reactors
S. Hur, J.C. Park, B.H. Kim, S.H. Seong and S.J. Lee.....1152

Development of an Underwater UT Inspection System for Reactor Welding Areas
Y.R. Choi and J.C. Lee.....1158

Development of 3D Image Processing Software for UT-NDE of Steam Generator of Nuclear Power Plant
M.W. Nam, Y.S. Lee, C.S. Park and O.Y. Yang 1164

SECTION 16 : NDT IN POWER PLANT

Characteristics of Phased Array UT Crack Evaluation with the Number of Active Element and Scan Angle Changes
Y.S. Cho and J.H. Kim.....1170

Development of Water Absorption Test Equipment for Generator Stator Windings in Power Plant
Y.C. Bae, H.S. Kim and D.Y. Lee 1177

Assessment of Fluid Leak for Power Plant Valve Using Pb-free Acoustic Emission Sensor
S.G. Lee and S.K. Park.....1183

Leak Diagnosis of Control Valves for Power Plants Using Multi-Measuring Methods
S.G. Lee, J.H. Park and Y.B. Kim 1189

Effects of Magnetic Phase on the ECT Signal in the SG Tubes
D.G. Park, K.S. Ryu, D. Son and Y.M. Cheong 1195

SG Eddy Current Issues Updates in Korea
S.J. Kim, K.J. Kwon, J.G. Ko, S.G. Lee and H.S. Do..... 1201

Application of Digital Radiography Inspection for Pipe Weldments in the Power Plants
S.K. Park, B.C. Park, D.S. Gil, Y.S. Ahn and Y.S. Cho..... 1207

Evaluation of Residual Stress for Boiler Welds in Thermal Power Plant by Nondestructive Method
K.B. Yoo and J.H. Kim 1213

Ultrasonic Signal Processing Algorithm for Detecting the Keyway Cracks on Turbine Rotor Disk
S.I. Cho, J.K. Lee, U.H. Seong, W.C. Seo, J.O. Lee, Y.H. Son and S.S. Jung 1219

SECTION 17 : NEUTRON RADIOGRAPHY

Experimental Approach for Water Discharge Characteristics of PEMFC by Using Neutron Imaging Technique at NRF, Hanaro
T.J. Kim, J.R. Kim, M.H. Kim and C.M. Sim 1225

SECTION 18 : NEW METHODS AND DEVICES

Optimal Design of an Ultrasonic Array Sensor for NDE Applications
H.Y. Kim and Y.R. Roh 1231

Design of Special Shoes with a Position Control Device for Water Level Gauging in a Bellows Tube
K.M. Koo, C.H. Song, Y.S. Kim, Y.M. Cheong, I.C. Lim and C.S. Park 1237

A Study on Inhalation Force Improvements of Ventilation Hood to Remove a Harmful Material
H.D. Yang and Y.K. Oh 1243

SECTION 19 : NONLINEAR PHENOMENON

Acoustic Nonlinearity of Zironium Alloy by a Resonant Ultrasound Spectroscopy
Y.M. Cheong and Y.S. Kim 1249

Experimental Study on Nonlinear Acoustic Properties of Contacting Solid Interfaces
J.Y. Kim, A. Baltazar and J.S. Lee 1255

SECTION 20 : OPTICAL METHOD

A Study on the Analysis of O-Ring under Uniform Squeeze Rate and Internal Pressure by Photoelastic Experimental Hybrid Method
O.S. Kwon, J.S. Hawong, J.B. Nam, S.L. Han and S.H. Park 1261

Quantitative Magnetic Imaging Using Magneto-Optical Method
T. Ishibashi and K. Sato 1267

Measurement of Modulation Transfer Function of an Optical System by Using Skew Ray Tracing
T.T. Liao, J.F. Lin and C.H. Lu 1273

Digital Speckle Pattern Interferometer to Measure the Deformation Distributions of a Tensile Specimen
S.K. Park, S.H. Baik, H.K. Cha, Y.S. Kim, Y.M. Cheong and H.K. Jung 1279

Measurement of the Concentration of Glucose by a Circular Polariscope with Electro-Optic Modulation
J.F. Lin, T.T. Liao and C.C. Chang 1285

Fabrication and Characterization of Prismatic Band Filter Gradient Rugate Porous Silicon
J.H. Kim, S.H. Jang, Y.D Koh and H.L Sohn 1291

Analysis of Chemically Induced Residual Stress in Polymeric Thin Film Using Curvature Measurement Method
S.S. Lee, I.W. Jeon and M.H. Yi 1297

SECTION 21 : RAILWAYS

Fatigue Life Evaluation for the Floor System of a Steel Railway Bridge
D.H. Choi, H.Y. Choi, H. Yoo, J.S. Lee and S.K. Park 1303

Stress Intensity Factor Calculation on Critical Points of Railway Bogie Frame
H.K. Jun 1309

A Study on Partial Side Wears for the Brake System of Railway Vehicles
J.H. Song, S.H. Yoo, D.J. Oh, D. Mishra and D.H. Jo 1315

Sensitivity for Internal and Surface Defects of Railway Wheel Using Induced Current Focusing Potential Drop
S.J. Kwon, D.H. Lee and J.W. Seo 1322

The Effect of the Evolution of Contact Surface Profile on Fatigue Crack Nucleation Site in Press-Fitted Shaft
D.H. Lee, S.J. Kwon, J.B Choi and Y.J. Kim 1328

The Influences of the Wheel Profiles on the Wheel Wear and Vibrational Characteristics of the Passenger Cars Running on the Kyeongbu Line
C.W. Lee and J.C. Kim 1334

Evaluation of Strength for Bogie Frame of Railway Freight Car through Finite Element Analysis
Y.S. Ham 1340

Measurement of the Lateral Displacement of the Wheel-Rail Based on the Vision Sensor
M.S. Kim and W.H. You 1346

SECTION 22 : RELIABILITY

Reliability Analysis of Static Bearing Capacity Evaluation of Driven Steel Pipe Piles Using MCS
J.H. Park, J.W. Huh, K.J. Kim, J.H. Lee and K.S. Kwak 1352

Safety Assessment of Subway Rolling Stocks Using Nondestructive Evalaution and Engineering Analysis Techniques
J.G. Kim, J.W. Seo, S.C. Yoon and S.T. Kwon 1358

Failure Analysis of Integrated Circuits Based on Nondestructive Evaluation
H.J. Kim, K.H. Um and S.J. Shin 1364

An Analysis of the Main Effect Factors of Brush Wear for Automotive Blower Motors
W.G. Shin, S.H. Lee and Y.S. Song 1370

Design & Reliability of an Optimal Structure Using Neural Network
J.S. Lee 1376

Comparison of the Mechanical Properties of Laser and Arc Welded 9Cr-1Mo Steel
C.I. Oh, H.S. Bang, H.S. Bang, M.S. Go, S.J. Kim and C.S. Ro 1382

Artificial Neural Network (ANN)-Based Reliability Analysis of a Fiber Reinforced Polymer (FRP) Deck
D.H. Kim, D.K. Kim and J. Cui..... 1388

Mechanical Characteristics of Hybrid Welded Joints of Galvalume Steel
Y.H. Kim, H.S. Bang, S.J. Kim, C.S. Ro and H.S. Bang 1395

Analysis of Round Robin Test for Reliability Evaluation on Ultrasonic Thickness Measurement of Wall Thinned Pipe in Nuclear Power Plant
J.H. Lee, D.H. Lee and S.H. Lee 1401

Boundary Element Analysis of Osmotic Blistering Behavior of Polymeric Coating Film
S.S. Lee..... 1408

SECTION 23 : SIGNAL PROCESSING

Gearbox Condition Monitoring Using Feature Samples and Principal Component Analysis
W. Li, K. Ding and Z. Yang 1414

An Adaptive Filter for the Minimization of Tracking Error in a Non-Minimum Phase Beam with Uncertainty
Y.S. Lee 1420

A Robust Error-Adaptive NLMS Algorithm for Echo Cancellations
M.S. Kim 1426

SECTION 24 : SMART STRUCTURE & SYSTEM

Development of a Lateral Mode Piezoelectric Oscillator Sensor to Detect Damages in a Structure
Y.R. Roh and B.S. Kim..... 1432

Retrofit of Concrete Cylinders by Steel Jackets with Lateral Confining Stress
E.S. Choi, B.S. Cho, Y.S. Chung and S.C. Cho 1438

Piezoelectric Sensor Self Diagnostics Using a Modified Impedance Model
S.H. Park, C.B. Yun, G.H. Park and Charles R. Farrar..... 1444

Smart Particles Containing Multiple Photonic Band Gaps Based on Rugate-Structured Porous Silicon
S.J. Kim, S.H. Jang, Y.D. Koh, J.H. Kim, C.Y. Park, J.H. Park and H.L Sohn 1450

SECTION 25 : VIBRATION

Accurate Vibration Analysis of N-Sided Poplygonal Mindlin Plates with V-Notches or Sharp Cracks
J.W. Kim and H.Y. Jung 1456

Active Structural Control Technique Using Lattice Probabilistic Neural Network Based on Learning Rule
D.H. Kim, D.K. Kim, S.K. Chang, Charito Fe M. Nocete and W.S. Park 1462

Corner Stress Singularity Effects on the Vibration of Skew Plates Having V-Notches or Sharp Cracks
J.W. Kim and H.Y. Jung 1468

Effects of Tip Mass on Stability of Rotating Cantilever Pipe Conveying Fluid with Crack
I.S. Son, H.I. Yoon, S.P. Lee and D.J. Kim 1474

This page intentionally left blank

ANGLE EFFECT OF MICRO-SCALE CROSSHATCH GROOVED PATTERNS UNDER LUBRICATED SLIDING CONTACT*

CHAE YOUNG-HUN

Engineering of Tribology Institute, Kyungpook National University, 1370 Sankyuk-dong, Buk-gu, Daegu 702-701, Republic of Korea

Special surface pattern of tribological applications is an attractive technology of engineered surface. Therefore, reduction friction is considered to be necessary for improved efficiency of machines. The current study investigated the friction property of micro-scale crosshatched grooved pattern on bearing steel flat using pin-on-disk. The samples fabricated by photolithography and electrochemical etching process. We discuss the friction property due to the influence of hatched-angle on contact surface. We demonstrated the lubrication mechanism for a Stribeck curve. It was found that the friction coefficient is changed by an angle of crosshatch on contact surface. It was thus verified that micro-scale crosshatch grooved pattern could affect the friction reduction considerably under mixed and hydrodynamic lubrication conditions. Also the lubrication regime influences the friction coefficient induced by special angle of cross-hatch.

1. Introduction

A number of the applications of surface texturing have been developed with relatively large frictional interfaces, for example mechanical seals [1]. Micro-dimples contribute to function mainly in hydrodynamic lubrication conditions. In the case of flat parallel sliding surfaces, a texture can improve reducing friction [2].

Surface texture for tribological situation are expected to play as reservoirs of lubrication and wear particle trapping, preventing seizure due to insufficient lubrication [3-5]. The contact surface with special pattern has recently been researched the effect of reducing friction [3-7]. In order to fully realize their potential, the friction characteristics of surface texturing need to be well understood.

In this paper attempts to investigate not only the friction property for micro-scale grooved surface pattern but also the effect of angle of crosshatch under mixed and hydraulic lubrication condition. We will discuss the friction behavior

* This work is supported by MOCIE and KOTEF through HRTP for RI.

depend the angle of crosshatch on contact surface. Also we will find an optimum angle of crosshatch in this study.

2. Experimental Procedure

Table 1 show the experiment condition in test. In order to fabricate the surface pattern on the surface of contact area, we carry out photolithography and electrochemical etching process. So, sample can show in Fig. 1.

The test procedure employed was a step-loading procedure at fixed sliding speeds. At each sliding speed, the applied load increased in a step-wise manner. The load steps followed a sequence of 5 N, 10 N, 15 N, 20 N, 30 N and 40 N. The duration of each load step was 1min. The sliding speeds employed were 0.04, 0.08, 0.12, 0.16, 0.20, 0.24, 0.28, and 0.32 ms^{-1}. In all Lubricated tests, fresh paraffin oil was used in each step. In order to avoid initial unstable conditions, each friction test was carried out following a running-in operation with duration of 15 min.

Table 1. Experiment condition for friction test.

Parameters	Condition
Contact type	Pin-on-Disk
Disk material	Bearing steel
Pin material	Bearing steel
Diameter of pin[mm]	6
With of groove for pin[μm]	100
Density of groove for pin[%]	20
Depth of groove for pin[μm]	4
Surface roughness	
- Pin before fabrication[μm]	0.008Ra, 0.016Rq
- Disk [μm]	0.039Ra, 0.052Rq
Diameter of sliding track	40
Pressure range [MPa]	0.5-3.5
Speed range [m/s]	0.02-0.30
Lubricant	Paraffin oil
Temperature	Room temperature

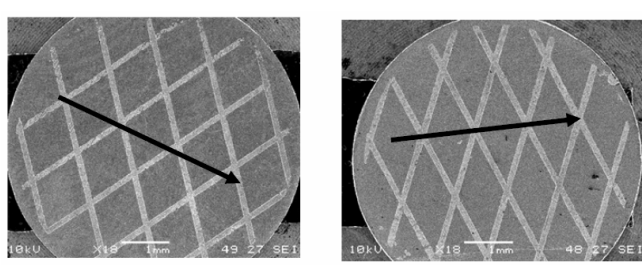

Fig. 1. SEM of sample (Arrow is sliding direction).

3. Results and Discussion

The friction coefficient as a function of velocity and normal pressure is shown in Fig. 2. The important point to notice from this figure is that the curve of groove-150 and groove-140 sample lower reduced friction coefficient than that of other specimen.

To analysis for those results of micro-scale groove under lubrication condition surface texture, we describe lubrication mechanism for a Stribeck curve [8, 9]. It is a relationship between the friction coefficient and a dimensionless parameter for lubrication condition.

Which can be expressed as;

$$S = \frac{\mu VD}{L} \tag{1}$$

Where S is the Lubrication parameter, μ is the dynamic viscosity in Pa-s, v is the sliding velocity in ms^{-1}, D is the diameter of contact in m, L is the normal load in N.

On the generalize Stribeck curve, depend on the geometry, materials, sliding conditions and thickness of the lubrication oil film between the sliding surfaces. The Lubrication parameter S was calculate for this experiment and plotted against friction coefficient in order to generalized Stribeck curve in Fig. 3. Fig. 3 shows the occurrence from the mixed lubrication to hydrodynamic condition. It is convinced to change the friction property according to angle of crosshatch grooved pattern. Also in order to verify angle effect of crosshatch in detail, we carry out fabricate additional samples of angle of 135 and 145 such as groove-135 and groove-145.

Fig. 4 shows the friction property of from groove-130 to groove-150. As regard to the friction property, angle of 135degree of crosshatch grooved pattern indicate better than that of other sample.

We can describe the hydrodynamic lubrication mechanism[8], because the lubrication condition regime has an influence on the friction property induced grooved crosshatch angle from results of this experiment (Figure 3 and 4). A lubrication flow statue in interface between contact surfaces depends on velocity and normal load. It also shows that the friction coefficient is low not only low speed and low pressure but also high pressure and low speed, comparing with other specimens. The crosshatch groove pattern can change from mixed lubricating domain to fluid lubricating domain by setting of angle[10,11]. However, understanding of the density of pattern and the friction property

according to size and depth is necessary to understand the reason and the mechanism.

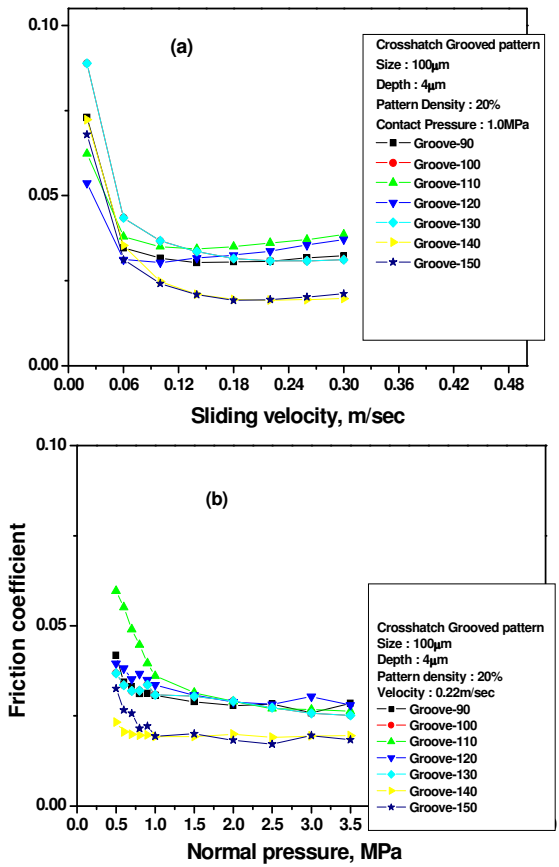

Fig. 2. The friction coefficient as a function of sliding velocity and normal load under variation angle of crosshatch grooved patter.

4. Conclusion

It was verified that angle of crosshatch grooved pattern affect on the friction property considerably under mixed and hydrodynamic lubrication conditions. Lubrication condition regime has an influence on the friction coefficient as the angle of grooved pattern. With regard to improved friction property, angle of 135 degree better in this study.

References

1. N. Nakada, Tribology International, V.27, 3 (1994).
2. Y.K. Gryk and I. Etsion, Tribology Transactions, V. 45, 444 (2002).
3. I.Etsion, Y.Kligerman and G.Halperin, Tribology Transactions, 42, 511 (1999).
4. H. Tian, N.Saka and N.P.Suh, Tribology Transactions, 32, 289 (1989).
5. I. Etsion and L.Burstein, Tribology Transactions, 39, 677 (1996).
6. X. Wang, K.Kato, K.Adachi and K.Aizawa, Tribology International, V. 34, 703 (2001).
7. I. Etson and G. Halperin, Tribology transaction, 45, 430 (2002).
8. X. Wang, K.Kato and K.Adachi, Lubrication Engineering, Aug., 27 (2002).
9. A. Ronen, I.Etsion and Y.Kligerman,TribologyTransaction, 44, 359 (2001).
10. Y.H.Chae and S.S.Kim, Tribology letters, 35 (2000).
11. M. Wakuda, Y.Yamauchi, S.Kanzaki and Y.Yasuda, Wear, 254, 356 (2003).

EFFECT OF MICRO-SCALE DIMPLE SIZE ON STEEL SURFACE UNDER LUBRICATED SLIDING CONTACT*

CHAE YOUNG-HUN

Engineering of Tribology Institute, Kyungpook National University, 1370 Sankyuk-dong, Buk-gu, Daegu 702-701, Republic of Korea

The current study investigated the effect of micro-dimple size on reduction friction to understand the potential of friction reduction through micro-scale dimple to fabricate by photolithography on pin-on-disk test using flat-on-flat contact geometry. It was verified that the friction property with respect to the same pitch influences the size of dimple under lubricated sliding contact. Additionally, it was recognized from Stribeck curve that the friction property has a connection with the size of dimple. This can explain the relationship between the friction coefficient and a dimensionless parameter for lubrication condition. The friction property has an effect on the size of surface texture on reduction friction, not only because of the density of dimple, but also because of the ratio of diameter/pitch. A ratio of approximately 0.5 is recommended under the tested friction condition. It is suggested that the ratio of d/p is an important parameter for surface texture design.

1. Introduction

As is well known, friction loss is about 40 % of total for typical automotive engine power [1]. A considerable number of studies have been conducted on reduction friction and surface finishing which are therefore considered to be necessary requirements for improved efficiency saving fuel [2-4]. The surface texture of reducing friction contributes to function mainly in hydrodynamic and mixed lubrication conditions [6]. Etsion [7] reported that the friction property of a mechanical seal has an influence on the critical pore size and pore ratio. Wang [8] investigated the critical parameters in order to evaluate for aspects of surface texture such as the critical load ratio, the ratio of depth/diameter, and the ratio of pit area. It was emphasized that the effect of surface texture depends on critical parameters in water lubrication. Ronen [9] also reported that the benefit of surface texture on reduction friction has influence on the optimum value of the depth/diameter ratio. In spite of convincing results for the effect of surface texture, its friction properties need to better understand in order to fully realize its mechanism of that.

* This work is supported by MOCIE and KOTEF through HRTP for RI.

The aim of this study was to investigate the effect of micro-dimple size on reduction friction. According to the same pitch or the same density for 50 μm, 80 μm and 110 μm diameter of the dimple, we can verify the friction property for the size effect of dimple. In addition, in order to reveal the relationships between the parameter of surface texture and the friction property, the ratio of diameter/pitch was investigated.

2. Experiment

2.1. *Fabrication for micro-dimple on surface*

Table 1 shows the experimental conditions and parameters of the specimens. The pin and disk were bearing steel material. The diameter of the pin was 5 mm and the disk was 60 mm with a thickness of 5 mm. In order to fabricate micro-dimples on the contact surface for the pin, we carried out photolithography. Fig. 1 shows the size and pattern of the micro-dimple on the surface measure by Wyko NT3300. The dimension of micro-dimple was about 50±5 μm, 80±4 μm and 110±2 μm diameter and those depth was about 4-5 μm. The density of the dimple could be calculated from the real size of dimple as observed by optical profile.

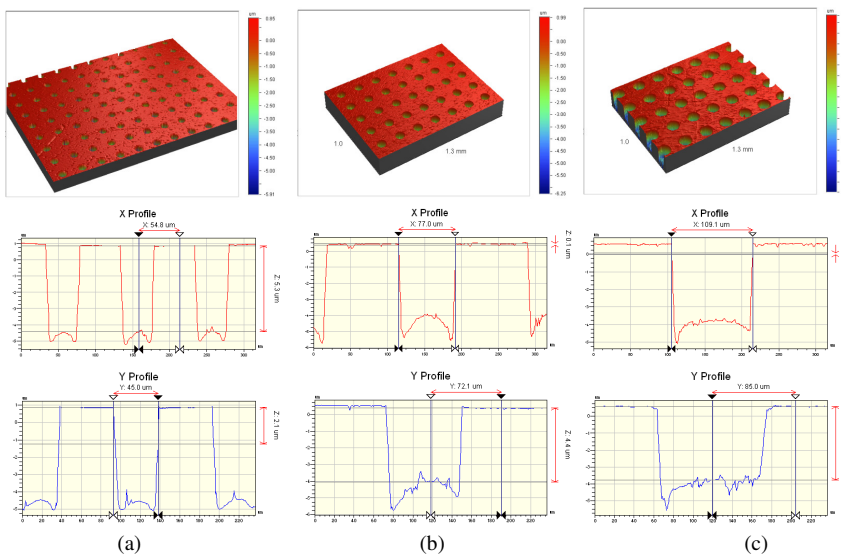

Fig. 1. Surface topography for (a)50 μm, (b)80 μm and (c)110 μm of diameter.

Table 1. Experiment condition for test.

Parameters	*Conditions*
Contact type	Pin-on-Disk
Disk material	Bearing steel
Pin material	Bearing steel
Size of dimple for pin [μm]	50,80,110
Depth of dimple for pin [μm]	4-5
Surface roughness	
- Pin before fabrication [μm]	0.008 R_a, 0.016 R_{max}
- Disk [μm]	0.039 R_a, 0.052R_{max}
Diameter of small disk[mm]	5
Diameter of sliding track[mm]	40
Normal load range [N]	5-40 N
Pressure range [MPa]	0.25-2.05
Speed range [m/s]	0.04-0.32
Lubricant	Paraffin oil(Saybolt number 125/135)
Temperature	Room temperature

Table 2. The size and density of pattern.

Size[μm]	Pitch[μm]	Density[%]
50	95	20
	160	8
80	160	20
110	160	38
	229	20

2.2. *Testing method and test condition*

Friction experiments were conducted on pin-on-disk test using flat-on-flat contact geometry [10]. Prior to testing, the pin and the disk specimens were cleaned in an ultrasonic bath. Afterwards, the specimens were rinsed with de-ionized water, and then blow-dried with dry nitrogen. The test procedure employed was a step-loading procedure at fixed sliding speeds. At each sliding speed, the applied load increased in a step-wise manner.

3. Result and Discussion

3.1. *Influence of the same pitch of dimples*

The variations in the friction coefficient of 50 μm, 80 μm, and 110 μm dimples as a function of sliding velocity under a normal load of 5 N, 15 N, 20 N, and 30 N as shown in Fig. 2. All specimens had 160 μm of pitch between micro-dimples. At a sliding velocity of 0.04 m/s, the friction coefficient for the 50 μm dimple

increased from over the contact pressure of 20 N, whereas the friction coefficient of the 80 μm and 110 μm dimples decreased with increasing the sliding velocity and normal load. It was found that the friction coefficient depended on the sliding velocity and that it increased with sliding velocities under 20 N of the normal load (Figure 2(a)-(c)). In the case of 30 N, the friction coefficient of the 50 μm dimple was higher than that of 80 μm and 100 μm. Let us with examine the size effect of the micro-dimple using these results. It is verified that the friction property with respect to the same pitch influences the size of the dimple under lubricated sliding contact. In order to design the size of micro-dimple on reduction friction, it is necessary to control the pitch. Therefore, the diameter of the dimple plays a significant a role in friction reduction.

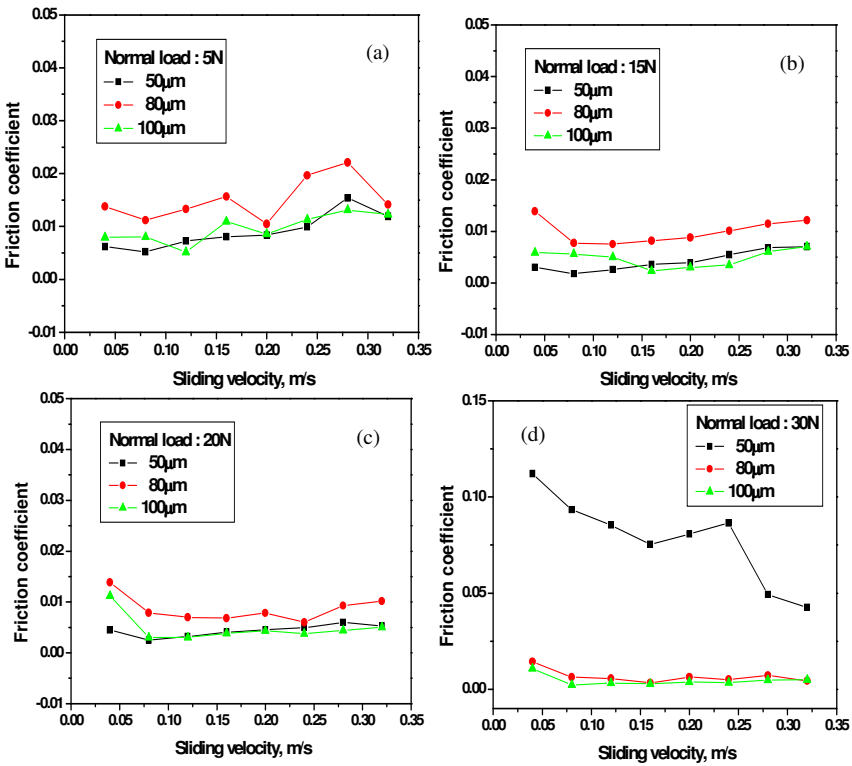

Fig. 2. Friction coefficient as a function of normal load for 160μm of pitch under (a) 5 N, (b) 15 N, (c) 20 N and (d) 30 N.

3.2. *Influence of the same density of dimple*

From Figure 3, we can recognize from the Stribeck curve that the friction property has a connection with the size of dimple. The dimensionless number S was calculated for this experiment and plotted against the friction coefficient in order to obtain the generalized Stribeck curve. This reveals the occurrence from the mixed lubrication to hydrodynamic lubrication condition. From the plots of the Stribeck curves of the specimens, it is clear that the friction coefficient is related on the pitch and density via the size of the dimple. This provides evidence that the size of dimple influences the friction property even at the same pitch. However, the question is whether the density of dimple is increased with the size of dimple without pitch change.

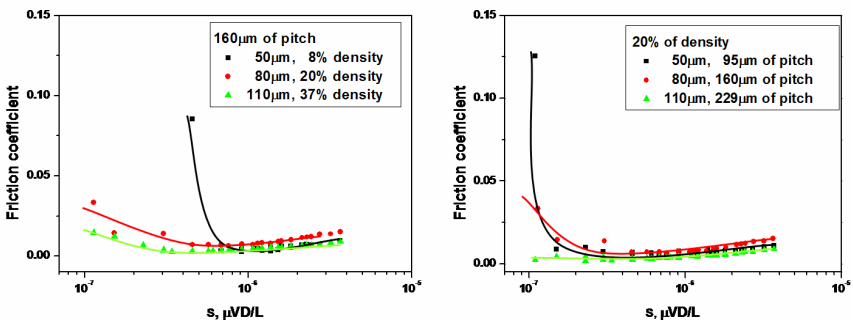

(a) (b)

Fig. 3. Strabec curve for (a)160μm of pitch and (b) 20% of density.

As the second step in our analysis, we examined the size effect for the same density of dimple. We can see the friction coefficient as a function of the dimensionless parameter for 50 μm, 80 μm, and 110 μm in terms of 20 % of density. This may be explained that the friction property depends on the size of the dimple in the same density [11]. It was found that the friction property of the 110 μm dimple was better than other size of dimple. Consequently, this indicated that the friction property is relative to the size of dimple of the same density.

In summary, with respect to the same pitch and density, the friction property depends on the size of dimple. In order to identify the reason, it is necessary to identify the critical parameters of the ratio of d/p as shown in Figure 4. In the case of 50 μm, a friction property of 0.55 of d/p is better than that of 0.31. In addition, a friction property of 0.48 of d/p on 110 μm dimple is improved in comparison with 0.69 of d/p are shown in Fig. 3. We can thus recognize from this figure that the optimum ratio of d/p is approximately 0.5 of the same diameter. It was found that the ratio of d/p influences the friction property. It is clear that the ratio of d/p is an important parameter for surface texture design.

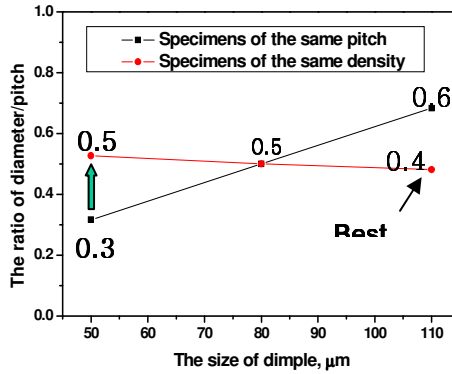

Fig. 4. The ratio of diameter/pitch as a function of the size of dimple.

4. Conclusion

The experimental results and observations from this study have lead to the following conclusions:

(1) It was verified that a friction property of 110 μm dimple is better than that of 50 μm and 80 μm dimples with 160 μm of pitch.

(2) The friction property has an effect on the size of surface texture on reduction friction, not only because of density, but also because of the ratio of diameter/pitch.

(3) A ratio of approximately 0.5 is recommended under the tested friction conditions.

References

1. N. Nakada, *Tribology International*, **27**, 3 (1994).
2. Y.K. Gryk and I. Etsion, *Tribology Transactions*, **45**, 444 (2002).
3. I.Etsion, Y.Kligerman and G.Halperin, *Tribology Transactions*, **42**, 511(1999).
4. H. Tian, N.Saka and N.P.Suh, *Tribology Transactions*, **32**, 289 (1989).
5. I. Etsion and L.Burstein, *Tribology Transactions*, **39**, 677 (1996).
6. X. Wang, K.Kato, K.Adachi and K.Aizawa, *Tribology International*, **34**, 703 (2001).
7. I. Etson and G. Halperin, *Tribology transaction*, **45**, 430 (2002).
8. X. Wang, K.Kato and K.Adachi, *Lubrication Engineering*, **Aug.**, 27 (2002).
9. A. Ronen, I.Etsion and Y.Kligerman, *Tribology Transaction*,**44**, 359 (2001).
10. Y.H.Chae and S.S.Kim, Tribology letters, 35 (2000).
11. M. Wakuda, Y.Yamauchi, S.Kanzaki and Y.Yasuda, *Wear*, **254**, 356 (2003).

FINITE ELEMENT ANALYSIS OF LASER STITCH WELDED HIGH STRENGTH STEELS FOR AUTOMOTIVE[1]

Heeseon BANG*

Department of Naval Architecture & Ocean Engineering, Chosun University, Gwangju, 501-759, Korea

Hansur BANG

Department of Naval Architecture & Ocean Engineering, Chosun University, Gwangju, 501-759, Korea

Yoonki LEE*

Department of Automobile Engineering, Chosun College of Science & Technology, Gwangju, 501-759, Korea

ChongIn OH

Department of Naval Architecture & Ocean Engineering, Chosun University, Gwangju, 501-759, Korea

Chanseung RO

Institute of Joining & Manufacturing, Chosun University, Gwangju, 501-759, Korea

In this study these advantages of the laser welding has been considered for Nd:YAG laser stitch welding(LSW) as a substitute for resistance spot welding(RSW) of lightweight car body plates. First, optimized parameters for Nd:YAG laser stitch welding for automotive high strength steel sheet(SRPC340) have been determined comparing the economical and mechanical characteristics to match with the currently used spot welding characteristics. Second, the mechanical phenomena of thermal elasto-plastic behavior on the Nd:YAG laser stitch welded joints has been clarified by two-dimensional thermal elasto-plastic analysis using F.E.M.

Keywords: Laser stitch welding; High strength steel; Thermal elasto-plastic analysis; Finite element method.

[1] * Corresponding authors. E-mail address: banghs@chosun.ac.kr, lyk9001@mail.chosun-c.ac.kr

1. Introduction

Commercially available Nd:YAG laser welding is increasingly broadening the scope of their industrial application in the automotive industry and enables steel vehicles to achieve significant weight reductions [1].

In this paper, to substitute Nd:YAG LSW for RSW in manufacturing in automotive body industry, numerical analysis and experiment both the welding processes have been carried out. The obtained numerical results are then compared with the experimentally measured values and reviewed. So a two-dimensional thermal elastic-plastic program using F.E.M. has been developed for highly accurate analysis of welding phenomena at any point. From the results analyzed by the developed program, mechanical characteristics and their production mechanism on Nd:YAG laser stitch welded joints have been clarified.

2. Experimental Details

The shape and principal dimension of the specimen is 100mm wide, 300mm long and 1mm thick as shown in Fig. 1. Lap joining is conducted piling up 30mm. The chemical compositions and the welding conditions(LSW, RSW) of the base metal used SRPC340, high strength steel sheet, are given in Table1~3, respectively. Welding parameters such as welding speed, pitch and welding length varies to determine optimized parameters of Nd:YAG LSW. Moreover, in order to optimize the welding length of Nd:YAG laser welded joints, tensile tests of Nd:YAG laser welded joints with different welding length(15 mm, 20 mm) have been performed and compared with that of resistance single spot welded joint.

When Nd:YAG laser welding is applied, the output power(3.0kw) and the focal depth(f_d) are fixed and welding speed varies under the range of 2mm/min ~3mm/min. The laser beam irradiation was perpendicular to the surface of specimen. The surface of each specimen was cleaned using a stainless steel wire brush and degreased by wiping with methyl alcohol.

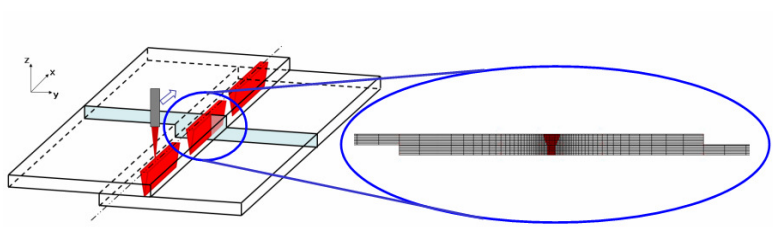

Fig. 1. Schematic illustration of the Nd:YAG Laser welding and mesh division

Table 1. Chemical compositions of base metal (wt%)

Parameter	Value
C	0.0006
Si	0.02
Mn	0.004
P	0.140
S	0.076

Table 2. Laser welding parameters

Parameter	Value
Laser power	3.0kw
Focal depth	+1mm
Welding speed	2.0~3.0m/min
Shielding gas	Argon 15ℓ/min
Pitch	50 mm, 60 mm
Welding length	15mm, 20mm

Table 3. Resistance spot welding parameters

Parameter	Value
Electrode force	180Kg_f
Welding current	9KA
Pitch	60 mm
Squeeze time	30Cycle
Welding time	15Cycle
Holding time	10Cycle

3. F.E Formulation for Thermal Elasto-plastic Analysis

For the thermal-stress problem, the first thing need to be done is to obtain the temperature distribution of un-steady state heat transfer problem for continuance object. Heat transfer problem, which changes with time thermal-strain changes depends on this temperature change treat this as initial strains.

So, in order to do generally analysis of the welding stress, one must also consider temperature independency of material through elastic and plastic region, with isotropic of material in mind.

Also in the plastic region, Von-mises yield-criteria were used as yield point function with linear-isotropic hardening-rule in consideration. The element used is 4 noded iso-parametric element. Strain-stress relation was represented with increment, which is based on plastic-flow theory. F.E formation of elasto-plastic problem is stated belows.

$$\{dF\} = [K]\{dU\} - \{dL\}$$

We obtained F.E formula finally,

$$\sum[K]\{dU\} - \sum\{dL\} = \sum\{dF\} = 0$$

4. Results and Discussions

4.1. *Experimental results*

Fig. 2 shows the bead shape and cross section of Nd:YAG laser welds with welding speed of 2.0~3.0m/min. It is found that the relation between welding speed and width, penetration depth is inversely proportional due to the heat input. This means the penetration depth and the width decreases if welding speed increases.

From the observation of bead surface, cross section, it is concluded that welding speed of 2.5 mm/min is proper for penetration and no welding defects(undercut, porosity and crack). To determine optimized parameters of Nd:YAG laser welding, tensile test results of Nd:YAG laser welded joints with various welding length(15 mm and 20 mm) and pitch length (50 mm and 60) mm are compared with resistance spot welded joints showing in Fig. 3. From the results, reasonable welding parameters(welding length of 20 mm and pitch length of 60 mm) with adequate welding quality can be obtained.

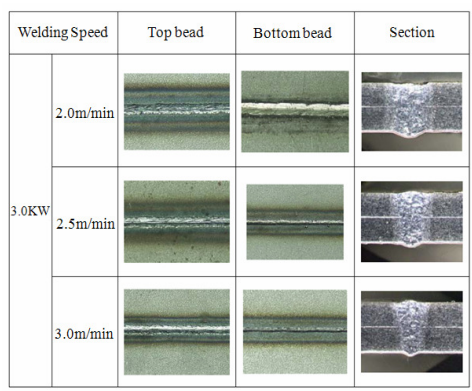

Fig. 2. Bead shape and cross section of Nd:YAG laser welds with various welding speed

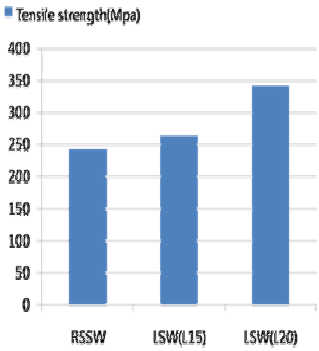

(a) welding length

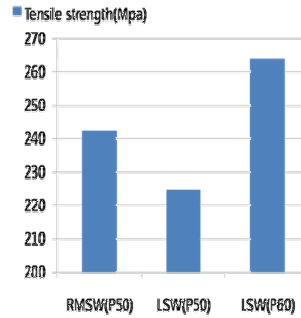

(b) pitch length

Fig. 3. Tensile test results of Nd:YAG laser welded joints with various welding length, pitch length and resistance spot welded joints

4.2. *Characteristics of distribution of welding residual stresses*

The deterioration of material and welding residual stresses are caused by spatial and temporal temperature distribution in regions a short distance from heat source.

In order to predict accurately these properties, therefore, the thermal elasto-plastic analysis is required to examine their history. To grasp heat distribution characteristics of Nd:YAG laser stitch weld zone, unsteady heat conduction analysis is executed using 4-node iso-parametric element optimum welding parameters (welding length of 20 mm and pitch length of 60 mm) from experiments. The thermal conduction into the material and thermal radiation to air are treated as the boundary condition. Convective flow in the weld pool, vaporization in keyhole and radiation heat transfer are not considered.

Fig. 4 shows distribution of temperature in Nd:YAG laser stitch welded joints with time under above optimum welding condition. Maximum temperature of 1900°C has been obtained at the starting point of each stitch. As the welding speed and cooling rate are high, it is confirmed through simulation analysis process that formation width of heat-affected area is very small.

Shown in Fig. 5 is distribution of welding residual stresses of Nd:YAG laser stitch welded joints along the x-axis at the position z=0.1mm. The components of residual stresses, σ_x and σ_y, which are produced in the weld metal and HAZ are tensile.

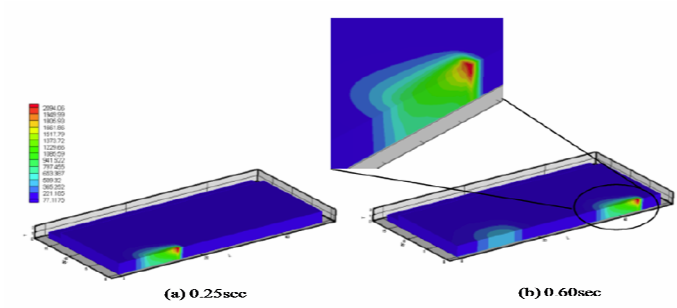

Fig. 4. Distribution of temperature in Nd:YAG laser stitch welded joints with time

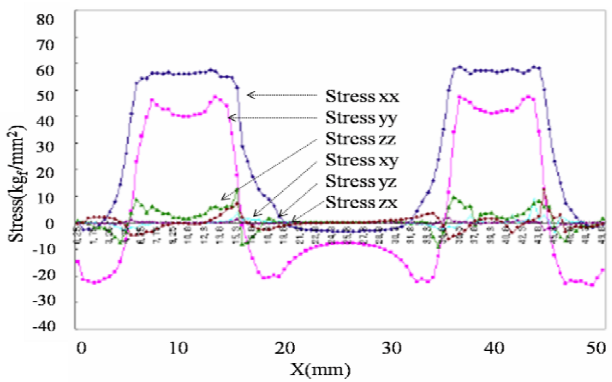

Fig. 5. Distribution of welding residual stress distribution in Nd:YAG laser stitch welded joints

5. Conclusion

From the results of experiment and numerical simulation, we could confirm the possibility of Nd:YAG laser welding to high strength steel sheet (SPRC) and predict the mechanical behavior in welds through thermal elasto-plastic analysis. The effects of pitch and welding length on weldability of Nd:YAG laser stitch welded joints are evaluated, indicating that a pitch of 50mm on welding length of 20mm was advantageous compared to a pitch of 60mm on welding length of 20mm.

References

1. Y.S. Yang and S.H. Lee, Journal of Materials Processing Technology, **94**, 151(1999).

EVALUATING THE QUALITY OF SOIL GROUTING BY THE SASW METHOD

PEI-HSUN TSAI

Department of Construction Engineering, Chaoyang University of Technology
168 Gifeng E. Rd , Wufeng, Taichung County 413, Taiwan

JIUNNREN LAI

Department of Construction Engineering, Chaoyang University of Technology
168 Gifeng E. Rd , Wufeng, Taichung County 413, Taiwan

The primary objective of this study is to assess the applicability of the SASW (Spectral Analysis of Surface Wave) method in determining the extent and degree of improvement after soil grouting, a technique commonly used for ground improvement. Numerical modeling and laboratory testing were performed to obtain the theoretical and experimental dispersion curves. Numerical studies using FEM were undertaken to examine the extent of grouting and the dynamic characteristics of the improved soils through the dispersion curves. Laboratory tests inside a sand box were also performed to confirm the validity of the numerical modeling. Results of this study indicate that the SASW method can detect the extent of soil grouting.

1. Introduction

Soil grouting is a technique commonly used in ground improvement. The quality of grouting is uncertain because the grouting body is embedded in soil and is imperceptible. Therefore, how to access the extent and degree of improvement after soil grouting is very challenging task for practicing engineers. Drilling and sampling are ordinary methods for evaluating the quality and extent of grouting, but it can be troublesome. A fast, effective and economic method is necessary to detect the extent as well as the quality of grouting.

The Spectral Analysis of Surface Wave (SASW) method was introduced for the nondestructive evaluation of stiffness profiles of soil and pavement system in the past. Nazarian and Stokoe [1] proposed the procedures of SASW method to investigate the stratification of soil deposit. Since then, the SASW method has been improved in both the experimental and theoretical aspects. Many researchers use the SASW method to verify the profiles of soil and pavement [2-7] or for the detection of underground obstacles [8-12]. This method can obtain the shear-wave velocities of soil deposit by using common seismic instrument. It

is also very economical because that it does not require drilling bore holes. Therefore, the SASW method, which can obtain the dispersion curve of the strata, is a very promising technique to be used for evaluating the extent and degree of soil grouting. This objective of this study is to assess the applicability of the SASW method in determining the extent and degree of improvement after soil grouting.

2. Numerical Simulation

In numerical simulation, the ABAQUS software was used to simulate stress wave propagation in the soil medium. ABAQUS is a finite element code and it can solve 3 dimension dynamic problems. A concrete block buried in a sand tank was used to simulate soil grouting. A schematic drawing of the configuration is shown in Fig. 1. In the numerical analysis, about 30000 elements in the finite element mesh were used. The materials (sand and concrete) are assumed elastic, and their properties are shown in Table 1.

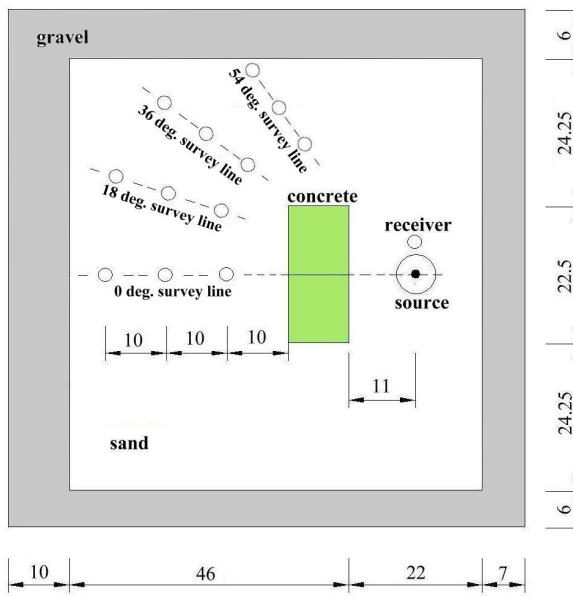

Fig. 1. Schematic drawing of the configuration

Table 1. Material properties of this study

Material	Young's modulus	Poisson's ratio	Density
Soil	1.0×10^{8} Pa	0.20	2200 kg/m^3
Concrete	2.4×10^{10} Pa	0.25	2300 kg/m^3

An impact loading with a magnitude of 10N and duration of 0.05 sec. is applied on one side of bedded concrete block. The velocity responses on other side of concrete block are calculated. The non-reflection boundary condition was assumed around the edge of the element mesh. Then the procedures of fast Fourier transform (FFT) and spectral analysis are performed. Finally, the phase difference between the receivers of the survey lines was obtained as shown in Figure 2. The diagram shown in Figure 3 is dispersion curve of 4 survey lines from numerical results. As Rayleigh waves travel along the 54 degree survey line, the soil despite profile without concrete block will be displayed. But along the other survey lines, the dispersion curve are affected by the embedded concrete block.

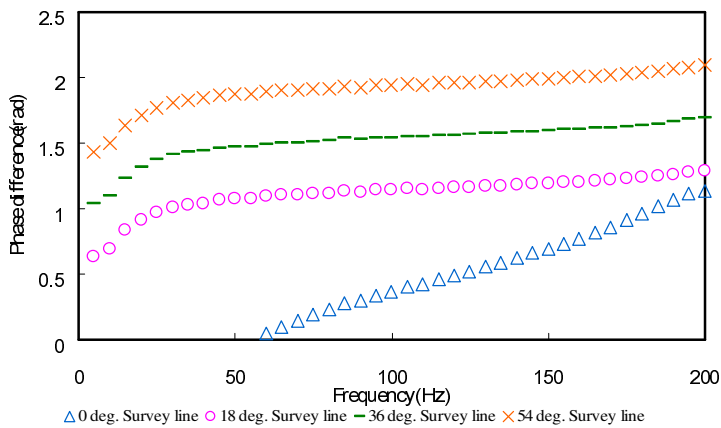

Fig. 2. Phase difference from numerical simulation

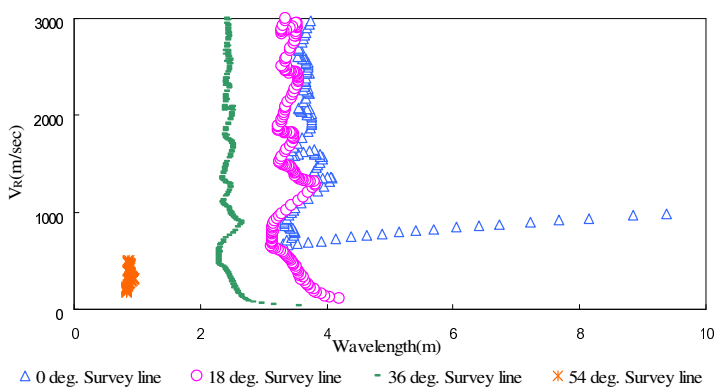

Fig. 3. Dispersion curve from numerical simulation

It should be noted that the dispersion curves shown in Figure 4 only have short wavelength, i.e., near-surface can't be treated, and it could be due to the size of element is small in order to simulate the laboratory test. Therefore, it can't reflect the influence of high frequency waves. However, it still reveals that the dispersion curve of the survey line pass the concrete block is different from that of the others.

3. Laboratory Test

To verify the numerical results, an experimental SASW test was performed in sand box (1m×1m×1m). In order to reduce the effect of wave reflection, it filled thin gravel layer around the sand (Fig. 4). And then a concrete block (10cm×10cm×22.5cm) was embedded 10 cm beneath the surface in the sand box, One side of block on sand surface set an iron chuck, the other side on sand surface installed 3 accelerators to monitor the vibration induced by small hammer beating on the chuck. The spacing between the accelerators was 10 cm.

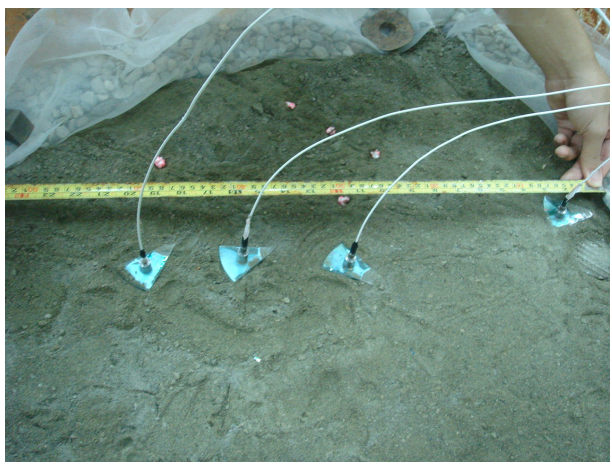

Fig. 4. Photograph of the test chamber

There are 4 survey lines of accelerators, the angles between central line and survey line were 0°, 18°, 36°, and 54°, respectively, as shown in Figure 1. In order to reduce the effect of noise, the representative value should take the average of measured values of 5 times. The time series of recorded signals is recorded and transforms to the frequency domain using the Fourier transform. In the frequency domain, the cross-spectrum for the recorded signal is computed. The phase difference between accelerators as a function of frequency, from the phase difference information of the cross-spectrum and the receiver spacing, a

Rayleigh wave versus wavelength profile for the sand box is generated. Results of SASW testing and analysis are presented in Figure 5. It can be seen from Fig. 5 that the 54° survey line yields the lowest Rayleigh wave velocity value (200m/s) because it does not pass through the concrete block thus only reflect the velocity of soil. The 0° survey line yields the highest Rayleigh wave velocity value (2500m/s), and this value is very close the Rayleigh wave velocity of concrete.

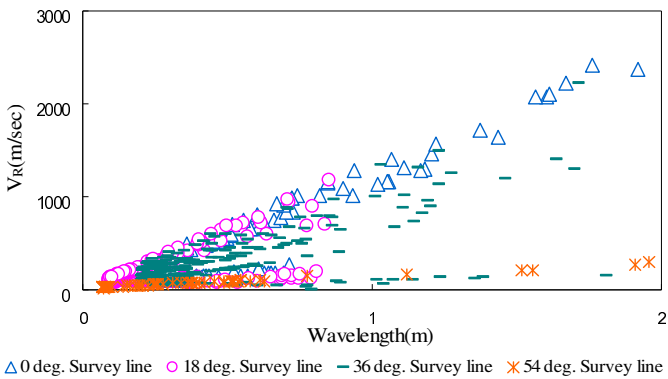

Fig. 5. Dispersion curve of experiment test

4. Conclusions

Due to the existence of the concrete block, the dispersion curve is different from that of normal soil layer. From the results of experiment test and numerical analysis, it can be concluded that the SASW method can predict the dimensions of grout block. Furthermore, the SASW method can provides a valuable tool for evaluating the Rayleigh wave velocity of grouted soil block.

References

1. S. Nazarian and K.H Stokoe II, Report No.256-4, *Center for Transportation Research Record*, *The Univ. of Texas at Austin*, (1982).
2. I. Sanchez-Salinero, J. M. Roesset, K.Y. Shao, K. H. Stokoe II and G.J. Rix, *Transportation research record* **1136**, 86 (1987)
3. N. Gucunski and R.D. Wood, *ASTM* **STP29**, 1 (1991).
4. S. H. Joh. *Ph. D. Dissertation*, *The Univ. of Texas at Austin*, (1996)
5. S. Nazarian, D.Yuan and V. Tandon, *Transportation Research Record*, **No. 1654**, 1 (1999).
6. K.O. Addo, *NRCC* **53**, 53 (2000).

7. C.B. Park, J. Ivanov, R.D. Miller, J. Xia and N. Ryden, *SAGEEP 2001*, RBA-6 (2001).
8. J. C. Sheu, K.H. Stokoe II and J. M. Roesset, *Transportation research record* **1196**, 51 (1988).
9. K.H. Stokoe II, S.G. Wright, J. A. Bay and J.M. Roesset, *ISSMFE* **10**, (1994).
10. N. Gucunski, V. Ganji and M. H. Maher, *Soil Dynamics and Earthquake Engineering* **15**, 223 (1996).
11. V. Ganji, N. Gucunski and M.H. Maher, *Journal of Geotechnical and Geoenvironmental Engineering* **123(3)**, 212 (1997).
12. A. Nasseri-Moghaddam, G. Cascante, C. Phillips and D.J. Hutchinson, *Soil Dynamics and Earthquake Engineering* **27**, 300 (2007).

STRESS ANALYSIS OF MANDIBULAR FIRST PREMOLAR WITH FINITE ELEMENT MODELS

KEYOUNG JIN CHUN

Fusion Tech Center, KITECH, 35-3 Hongcheon Ypjang
Cheonan, Chungnam 330-825, Korea

OUI SIK YOO

Fusion Tech Center, KITECH, 35-3 Hongcheon Ypjang
Cheonan, Chungnam 330-825, Korea

KYUNG RYUL PARK

Fusion Tech Center, KITECH, 35-3 Hongcheon Ypjang
Cheonan, Chungnam 330-825, Korea

SEUNG HYUN YOO

Department of Orthopaedic Surgery, Ajou University, San 5 Wonchun Yeongtong
Suwon, Gyeonggi, 443-749, Korea

The occlusal force of the tooth leads to loss of tooth tissue owing to attrition and abrasion, and may cause abfraction and pathological change of the dentine. Thus, we draw up finite element models, examine them applying ordinary occlusal force and analyze the stress distribution. Specimens used were mandibular first premolars from 15 Korean males and 13 females and were made into finite element models from medical images that were obtained using a micro-CT. We can find the fact that the irregular feature of the tooth is not useful only to masticating and pronouncing as well known, but that it is also suitable for protecting inner tissue by dispersing stress and delivering proper pressure to periodontal tissue to continue a physiological action. Also, image analysis can let us know the factor that is the cause of a disorder due to stress concentration in the cervical line. These results are expected to support the field of dental treatment planning, operating procedure and clinical trial, and the advance of technical expertise to develop implants and dentures.

1. Introduction

Dental interlocking is a key factor for oral health and function of patients to have a physiological maxillomandibular relation and adequate contact to the antagonist tooth. It also has the full implications involved in oral functions such as mastication, articulation, and esthetic dentition. The occlusal force causes

attrition and abrasion, and leads to dental tissue loss. This force also causes abfraction or secondary dentin formation [1].

The irregular feature of the tooth is suitable for protecting inner tissue by dispersing stress and delivering proper pressure to periodontal tissue to continue a physiological action. The dispersion of the occlusal force is essential to occlusal therapy. Thus, we used the finite element model, applied typical occlusal force and then determined the internal stress distribution of the model.

2. Materials and Methods

2.1. *Specimens and Conditions*

Specimens were mandibular first premolars from 15 Korean males and 13 females. Medical images of the cross sections were obtained using SkyScan1072 (Skyscan, Belgium). The spacing between cross sections of the specimen was set to 21.31㎛ and then the specimen photo was taken. In case the tooth length was less than 20mm, about 1000 cross sections were photographed for each tooth. Properties of dental tissue [2, 3] are shown in Table 1. Occlusal force is 205N and the direction is shown as Figure 2 according to Hiroshi Horiuchi [4].

Table 1. Properties of Dental Tissue

	Young's modulus [GPa]	Poisson's Ratio
Enamel	84.1	0.20
Dentin	18.6	0.31
Pulp	2.0	0.45

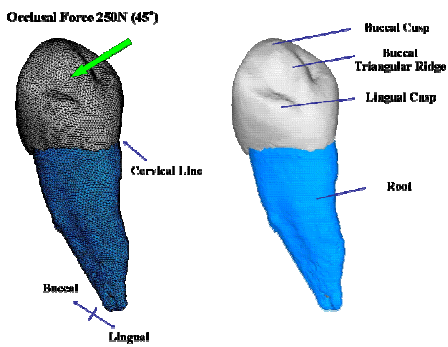

Fig. 1. Occlusal Force Direction

2.2. *Model Generation*

The surface-model from CT-images were obtained using Vworks (Ver. 4.0, CyberMed) of 3D medical imaging software and built the mesh-model using Rapidform (2006, INUS Tech.) and HyperMesh (Ver. 7.0, Altair Eng.). As indicated in Figure 2, the tooth model was created by dental tissue as enamel, dentin, and pulp. We used Nastran (MSC) and ABAQUS (Ver. 6.4) for finite element analysis.

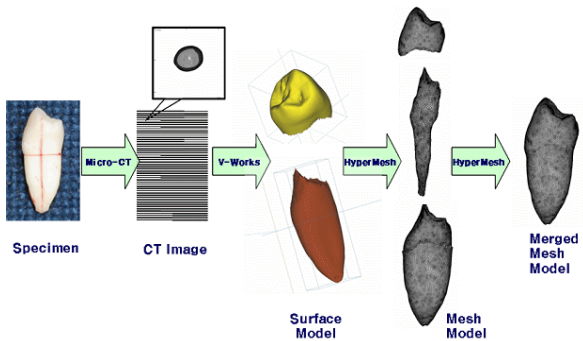

Fig. 2. Model Generation From CT-image

3. Results

Figure 3 shows the internal stress distribution of the mandibular first premolar by the occlusal force. This force loaded on the buccal cusp was dispersed mainly along the enamel, and then the stress of it was concentrated on the CEJ (cement-enamel junction).

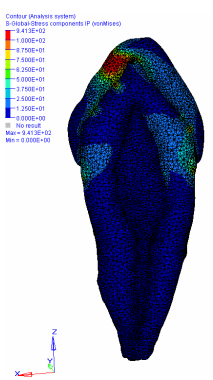

Fig. 3. Internal Stress Distribution of Mandibular First Premolar

The compressive stress acted on the buccal CEJ, and this was larger than the tensile stress on the lingual CEJ. It is noticed from the following figure that the stress on the buccal cusp of the enamel was transferred mainly away from the DEJ (dentine-enamel junction) because of the cone shape and an adequate inclination of dentine of the crown. It was also not transferred to pulp.

As shown in Figure 4, other types of mandibular teeth have some different paths from the mandibular first premolar.

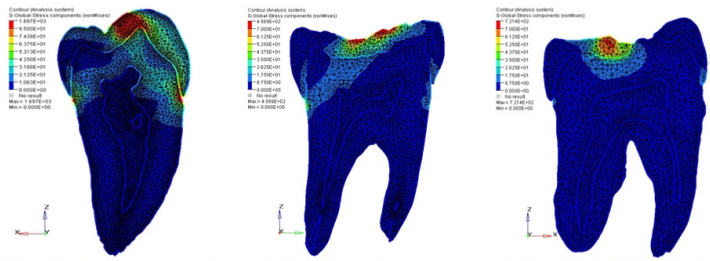

Fig. 4. Internal Stress Distribution of Mandibular Molars

The occlusal force decreased rapidly through dentine of the crown, and scarcely affected the pulp. Figure 5 illustrates this fact. This linear graph was measured along the center line of the cross section at the cervical line in the respect of buccal-lingual dimension and mesial-distal dimension.

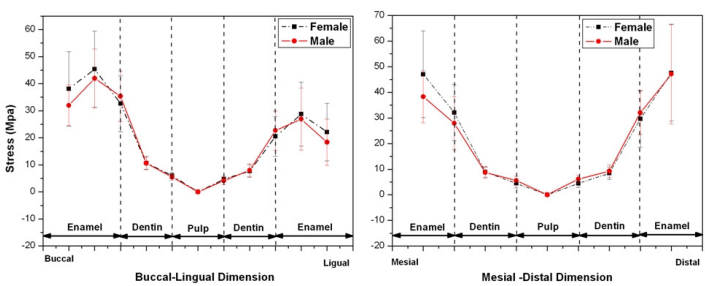

Fig. 5. Stress Distribution at Cross Section of the Case Occluded on Buccal Triangular Ridge (by H.J.Lee [5])

4. Discussion

An occlusion is divided into two contacts, point contact and surface contact. Figure 6 represents the consequence of the occlusal force for the case occluded on the buccal triangular ridge in the direction of 45°. The oblique occlusal force

has the demerit that partial dentine withstands a rapid stress change. Figure 7 demonstrates 3 point contact and the resultant force acts on teeth in the vertical direction.

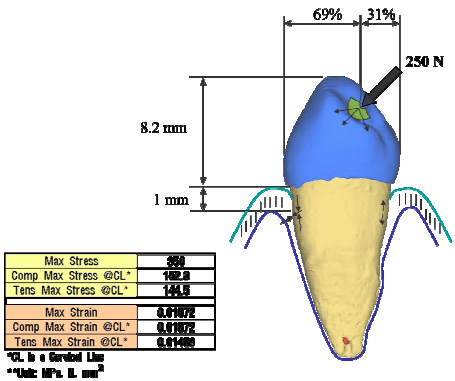

Fig. 6. Effects of Occlusal Force for the Case Occluded on Buccal Triangular Ridge

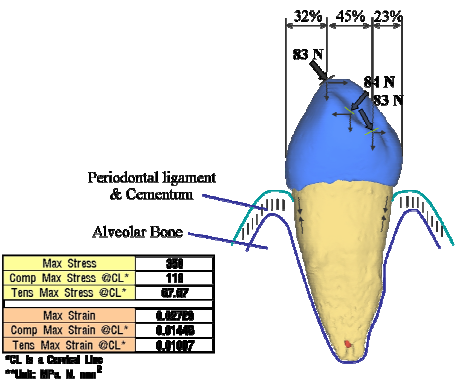

Fig. 7. Effects of Occlusal Force for 3 Point Contact

Three point contact is more stable for the influence of the stress on the cervical line as indicated in Figure 8. The stress region of the Figure 8(a) case of the following figure inclines to one side more than that of the Figure 8(b) case from the center line. Also, the Figure 8(a) case has a wider area and respectively higher stress than Figure 8(b). This is because its stress did not spread into the crown and concentrated on the cervical line.

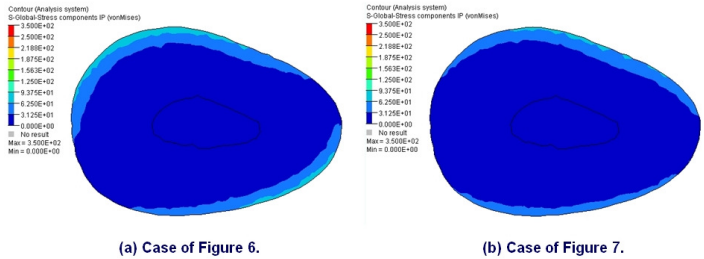

Fig. 8. Stress Distribution at Cross Section of Cervical Line

5. Conclusion

We studied the consequence of the occlusal force on mandibular first premolars. The results indicate that the irregular feature of the tooth is a suitable structure for dispersing the occlusal force and the degree of the stress concentration on the cervical line is according to the stress transfer path. As well, dentine lasts and the stress and pulp aren't affected by it at the cross section of the cervical line.

This study is expected to support the field of dental treatment planning, operating procedure and clinical trial as well as the advance of technical expertise to develop implants and dentures.

Acknowledgments

This study was performed with funding from the Korea Institute of Industrial T echnology (KITECH). The authors would like to thank M. W. Shin (D.D.S) at K angbuk Samsung Hospital and H. J. Lee (MS) at Doosan Engine for their great a ssistance throughout this study.

References

1. H. O. Sohn, et al., *Occlusion and occlusal surface formation,* JiSung publisher (2005).
2. H. E. Lee, et al., *J. Dent.* **30**, 283-290 (2002).
3. C. L. Lin, et al., *Comp. Meth. & Prog. In Biomed.* **59**, 187-195 (1999).
4. H. Horiuchi, et al., *Oral physiology,* Gomoonsa (2003).
5. H. J. Lee, K. J. Chun, et al., *KSPE Conf.,* **I**, 171-172 (2006).

CASCADED LINEAR-SYSTEMS ANALYSIS OF CMOS FLAT-PANEL DETECTORS FOR DIGITAL RADIOGRAPHY*

SEUNG MAN YUN, MIN KOOK CHO, CHANG HWY LIM, HO KYUNG KIM†

School of Mechanical Engineering, Pusan National University, Jangjeon, Geumjeong Busan 609-735, Republic of Korea

THORSTEN GRAEVE

Rad-icon Imaging Corp., Belick Street Santa Clara, CA 95045-2404, USA

HYOSUNG CHO

Department of Radiological Science, Yonsei University, Jangjeon, Geumjeong Wonju 220-710, Republic of Korea

JUNG-MIN KIM

College of Health Science, Korea University, Jeuneung, Seongbuk Seoul 136-703, Republic of Korea

For the better design and usage of CMOS (complementary metal-oxide-semiconductor) flat-panel detectors in digital x-ray radiography, we have theoretically evaluated the spatial-frequency-dependent detective quantum efficiency, DQE(f), by using the cascaded linear-systems theory. In order to validate the developed model, the DQE(f) was experimentally assessed by using the measured modulation-transfer function (MTF) and noise-power spectrum (NPS), and the estimated incident x-ray fluence. With the developed model, we have investigated the DQE(f) with respect to various design parameters of the CMOS photodiode such as quantum efficiency, fill factor and additive electronic noise. This theoretical approach is useful tool for the understanding of a developed imaging system and be helpful for the better design or optimizing a developing system.

1. Introduction

Although the technology in digital radiography detectors has been matured, there is not a universal detector to cover all the imaging tasks. Thus, the optimization

* This work was supported by the Korea Science and Engineering Foundation (KOSEF) grant funded by the Korea government (MOST) (Grant No. R01-2006-000-10233-0).

† Corresponding Author: E-mail: hokyung@pusan.ac.kr

of design parameters in an imaging detector is essential for the pursuing imaging task. One reasonable way for the optimization is to analyze detective quantum efficiency (DQE) as a function of design parameter because the DQE represents the signal to noise transfer efficiency in an image and thus considered as the appropriate metric of detector performance [1].

The CMOS (complementary metal-oxide-semiconductor) photodiode array in conjunction with a scintillator is recently paid attention to the use in digital radiography because it has smaller image lag and larger pixel fill factor, which is defined as the fractional photosensitive area, against to the conventional flat-panel detectors based on amorphous silicon technology [2]. In this study, we have modeled the spatial-frequency-dependent DQE, DQE(f), of CMOS flat-panel detectors by using the cascaded linear-systems transfer theory.

2. Materials and Methods

The detector, in this study, has been constructed with a scintillator for converting incident x rays to light photons and CMOS photodiode arrays for reading out the emitted light photons, that is converting those to electrical charges. As the scintillator, a commercial Gd_2O_2S:Tb screen (Eastman Kodak, Rochester, NY, USA) was used. The CMOS photodiode array (Rad-icon Imaging Corp., CA, USA) has a format of 512 × 1024 pixels with a pitch of 48 μm. Readout electronics is integrated onto the one narrow side of array. Since the CMOS photodiode array can be butted along any other side, large-area imaging is possible.

The DQE is typically assessed from the incident x-ray mean fluence $\overline{q}$, mean system gain $\overline{G}$, modulation-transfer function (MTF), and noise-power spectrum (NPS) of a detector [3]:

$$\mathrm{DQE}(f) = \frac{\overline{q}\overline{G}^2 \mathrm{MTF}^2(f)}{\mathrm{NPS}(f)} = \frac{\overline{q}\overline{G}^2 \mathrm{MTF}^2(f)}{\sum_{n=0}^{\infty} \mathrm{NPS}_{pre}(f \pm \frac{n}{d}) + \mathrm{NPS}_{add}(f)}, \qquad (1)$$

where f is the spatial frequency. NPS_{pre} and NPS_{add} denote the presampling NPS and the additive electronic NPS, respectively. Infinite summation indicates a digital sampling process with a pitch of d.

Figure 1 is a block diagram describing the signal and noise propagation in CMOS flat-panel detectors considered in this study. Neglecting the production and reabsorption processes of characteristic x rays, the cascaded model can be described by several elementary processes for the incident x-ray fluence; interaction in a scintillator with a probability of A_Q (or quantum detection

efficiency), conversion of the detected x-ray photons into light photons with a mean amplification factor of A_M, stochastic light scattering in the scintillator characterized by a transfer function of $T_{scn}(f)$, conversion of the light photons into chargers in the CMOS photodiode with a probability of A_D, and deterministic blurring by the photodiode aperture characterized by a transfer function of $T_{apert}(f)$. The model further employs the digital sampling process, denoted by III as shown in Figure 1, and the addition of electronic noise termed by σ_{add} in Figure 1.

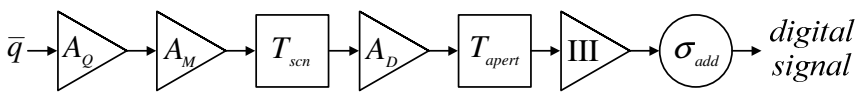

Fig. 1. Block diagram describing the cascaded model to assess the signal and noise transfer in the CMOS photodiode array in conjunction with a scintillator.

This cascaded modeling approach assumes that the response of a detector must be linear and shift invariant. Moreover, the random noise process must be wide-sense stationary, and the detector must be ergodic [3].

For a squared pixel geometry of photodiode having a pitch of d and an aperture of a in one direction, each term in Eq. (1) according to the cascaded linear-systems transfer theory is described as follows [3,4]:

$$\overline{G} = a^2 A_Q A_M A_D , \tag{2}$$

$$\text{MTF}(f) = T_{scn}(f) T_{apert}(f) , \tag{3}$$

$$\text{NPS}_{pre}(f) = \bar{q} a^4 A_Q A_M A_D \left[1 + A_D \left(\frac{A_M}{I} - 1 \right) T_{scn}^2(f) \right] T_{apert}^2(f) , \tag{4}$$

where I is the statistical or Swank factor appeared from the combined effects in amplification process, such as the polychromatic x-ray energy incidence, the distributed energy absorption, and the distributed light pulses. In this study, the additive NPS is treated as a white noise spectrum such that

$$\text{NPS}_{add}(f) = d^2 \sigma_{add}^2 , \tag{5}$$

where σ_{add} is the standard deviation of the additive electronic noise. This approach is reasonable because the electronic noise in one pixel is typically not correlated with the noise in other pixels.

Table 1. Summary of the physical parameters used in the cascaded model analysis. Values were computed for the CMOS photodiode array in conjunction with a Lanex^{TM} Min-R screen for the imaging condition of RQA 5.

Parameters	Description	Values
a	Pixel aperture	0.044721 mm
d	Pixel pitch	0.048 mm
γ	Fill factor	87%
$\overline{q}$	Incident x-ray fluence	4.4×10^5 mm^{-2}
A_Q	Quantum detection efficiency of the scintillator	0.23
A_M	Mean amplification factor of the scintillator	520
A_D	Quantum efficiency of the CMOS photodiode	0.55
I	Swank factor	0.99
$T_{scn}(f)$	MTF of the scintillator	$(1 + 1.0001f^2)^{-1}$
$T_{apert}(f)$	MTF due to the aperture integration	$\lvert\mathrm{sinc}(af)\rvert$
σ_{add}	Additive electronic noise	1100 e^-

The physical parameters describing the signal and noise properties of the Gd_2O_2S:Tb screen and the CMOS photodiode can be estimated using Monte Carlo codes; MCNPX^{TM} (ORNL, USA) and DETECT2000^{TM} (Laval University, Quebec, Canada) for x rays and light photons, respectively. All the values used for the theoretical analysis are given in Table 1 [4].

To validate the developed model, the DQE was experimentally assessed by using the measured MTF and NPS, and the estimated incident x-ray fluence. For a representative radiation quality, RQA 5, suggested by IEC (International Electrotechnical Commission, Report 1267), the presampled MTF was measured using a slanted-slit method to avoid aliasing and the NPS was determined by 2D Fourier analysis of white images. The fluence was estimated using the experimentally measured exposure and half-value layer (HVL), and the computational program for x-ray spectral analysis.

Based on the developed model, we investigated the DQE with respect to various design parameters of the photodiode such as quantum efficiency, fill factor and additive electronic noise.

3. Results and Discussion

Figure 2 shows the comparison between the theoretically estimated and experimentally measured DQEs of the CMOS flat-panel detector. Although the overall tendencies reasonably agree, large discrepancy is observed at the low spatial-frequency band. The discrepancy between the model and the measurement is probably due to the over compensation of the low frequency

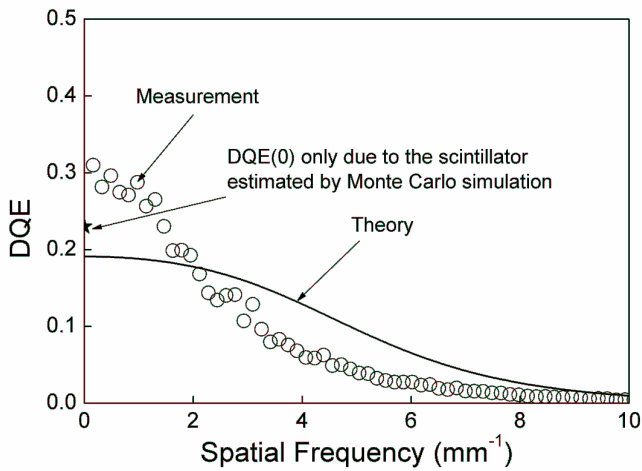

Fig. 2. Comparison between the measured and calculated DQEs. The cascade model shows a reasonable agreement in the overall tendency of DQE.

drift effect in the flat-field corrections [2]. From the cascade model, the DQE at the zero-spatial frequency, DQE(0), is approximately $A_Q \times I$ so that the overlying scintillator mainly governs the imaging performance of the detector. The DQE(0) can be effectively estimated by the Monte Carlo simulation and the simulated result is marked on Fig. 2. The loss of DQE(0) due to the underlying CMOS photodiode array is small.

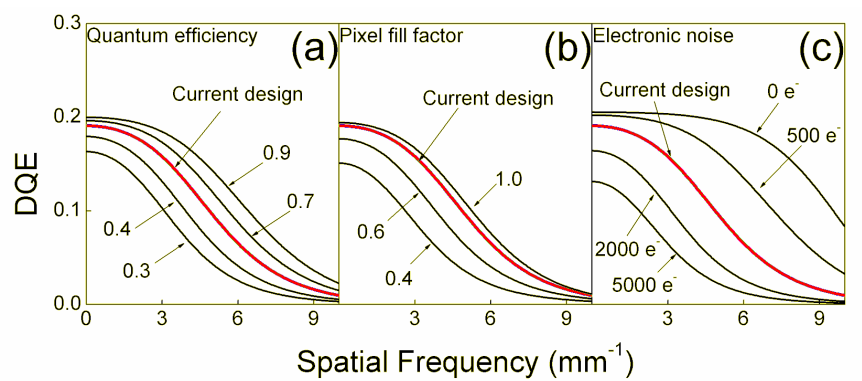

Fig. 3. Cascaded model analysis of DQEs with respect to various design parameters of the CMOS photodiode array such as quantum efficiency, pixel fill factor and additive electronic noise.

Figure 3 summarizes the calculated DQE with respect to various design parameters of the CMOS photodiode array. The DQE is gradually improved as both the quantum efficiency and the fill factor of the photodiode array are enhanced [see Fig. 3(a) and (b)]. The dependence on the quantum efficiency is more prominent than the pixel fill factor. As shown in Fig. 3(c), the DQE is very vulnerable to the magnitude of additive electronic noise because it is independent upon the spatial frequencies.

4. Conclusion

The cascaded linear-systems model can be utilized to describe the signal and noise propagation in the CMOS flat-panel detector and estimate its imaging performance. From the cascaded model analysis, the overall imaging performance or DQE(0) is mainly determined by the overlying scintillator. The DQE(f) can be affected by the performance of the photodiode array. The most significant design parameter in the CMOS photodiode array is the additive electronic noise. The developed model is a useful tool to design the CMOS flat-panel detector for digital radiography as well as other imaging detectors having similar detector structures.

References

1. C. E. Metz, R. F. Wagner, K. Doi, D. G. Brown, R. M. Nishikawa, K. J. Myers, *Med. Phys.* **22**, 1057 (1995).
2. H. K. Kim, S. C. Lee, M. H. Cho, S. Y. Lee, and G. Cho, *IEEE Trans. Nucl. Sci.* **52**, 193 (2005).
3. M. Sattarivand and I. A. Cunningham, *IEEE Trans. Med. Imag.* **24**, 211 (2005).
4. H. K. Kim, *Appl. Phys. Lett.* **89**, 233504 (2006).

NUMERICAL ANALYSIS ON 3-DIMENSIONAL THERMAL DEFORMATION OF AUTOMOBILE TIRE MOLD USING AL ALLOY 5000 SERIES MATERIAL

YOOL-KWON OH

Department of Mechatronics Engineering, Chosun University, 375 Seosuk-dong, Dong-gu, Gwangju, 501-759, South Korea

YOUNG-SUN KIM

Department of Precision Mechanical Engineering, Chosun University, 375 Seosuk-dong, dong-gu, Gwang-ju, 501-759, South Korea

HEE-SUNG YOON

Department of Advanced parts and Materials Engineering, Chosun University, 375 Seosuk-dong, Dong-gu, Gwang-ju, 501-759, South Korea

The present study investigates on 3-dimensional thermal deformation of automobile tire mold using Al alloy 5000 series materials. In this study, the commercial package COMSOL Multiphysics™ which can be analyzed the thermal and structural mechanics is used to predict the thermal deformation inside the Al alloy tire mold. And, thermal-structure analysis is performed that how to happen the temperature variation, displacement and stress distribution inside the Al alloy during the solidification process of it. The results of this study are revealed that temperature variations of the tire mold occurred the rapid solidification process no more than 15 minutes when the metal casting device is used. Also, the results of displacement and stress distributions at the principle parts could be predicted how to happen the thermal deformation in tire mold. Therefore, the numerical results are possible to improve the manufacturing process of mold products as the manufacturing device is to modify and supplement. Also, it will be helped to understand the thermal characteristics of Al alloy series materials during the melting or solidification process.

1. Introduction

The tire mold used during the tire manufacturing process in used for curing process during which the tread pattern is formed. Depending on the separation method during manufacturing, molds are classified into full-type molds and sectional-type molds. Recently, it is use the sectional-type mold because full-type molds, shear force is generated when the tire product is transformed and thus damaged or internally strained. However, it still has a shortcoming that

rubber flush might be made in the sectional part when the tire in formed and thus the mold should be made highly precise and it takes long time to manufacture.

In this study, the thermal deformation inside the automobile tire mold using Al alloy 5000 series material was predicted by numerical analysis.

2. Theoretical analysis

Heat transfer phenomenon by temperature difference defined with Eq. (1) by fourier`s transform [1].

$$q = -\lambda_x \frac{dt}{dx} \tag{1}$$

In each thermal conductivity coefficient defined $\lambda_x = \lambda_y = \lambda$ (Integer) by consideration with isotropic material on material by induction with thermal conductivity coefficient equation on Eq. (1) It will define with next Eq. (2)

$$\rho c \frac{\partial T}{\partial t} - \nabla \cdot (\lambda \nabla T) = Q \tag{2}$$

Apply conduction and convection previous equation,

$$\rho c_p \frac{\partial T}{\partial t} + \nabla \cdot (-\lambda \nabla T + \rho c_p T u) = Q \tag{3}$$

Previous equation, apply thermal convection equation on boundary area of the surface area,

$$q = h(T_\infty - T) \tag{4}$$

Appear as previous equation.

3. Numerical analysis

While the mold product for the automobile tire was manufactured, the numerical analysis was performed based on the finite element method [2-3] in order to estimate the thermal deformation of the 5000 series aluminum alloy material including temperature, displacement and stress. For the numerical analysis, "COMSOL Multiphysics^{TM}," a commercial program for heat transfer analysis and thermal-structural analysis, was used.

In this study, properties of al alloy 5000series is 94.2 ~ 96.8% for the aluminum, 3 ~ 4% for the magnesium and 640°C for the liquidus temperature of

aluminum and 590°C for the solidus temperature of aluminum. The properties appeared with Table 1.

Table 1. Physical properties of Al Alloy 5000 series material

Properties	Unit	Value
Solidus Temperature	°C	590
Liquidus Temperature	°C	640
Thermal Conductivity	W/m·K	140
Young's Modulus	Gpa	70
Poisson's Ratio	-	0.33
Density	Kg/m^3	2670
Specific Heat	KJ/kg·K	0.88
Thermal Expansion Coefficient	-	23.6×10^{-6}

3.1. Numerical analysis method

Figure 1 shows the 3-dimensional analysis model. The analysis model consisted of upper and lower parts of the metal casting device, the core and the mold. The initial temperature condition of each part was pre-determined as 300°C for the metal casting device, 80°C for the core and 640°C for the mold. For this study, the boundary condition was set with the metal casting device; the contact surface between the core and the mold was assumed to be in conduction state; and the inside of the parts other than the contact surface was assumed to be in convection state.

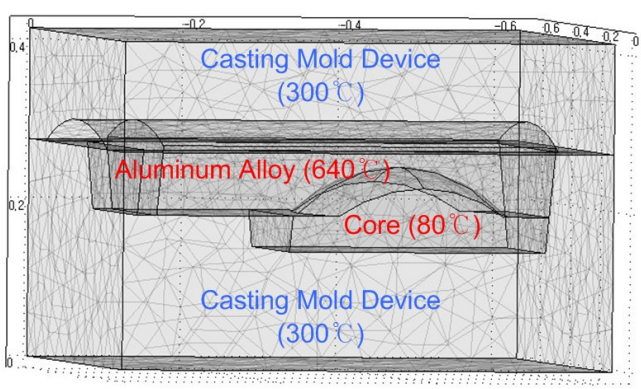

Fig. 1. Schematic diagram of 3D analysis model and initial conditions

The numerical analysis was carried out by calculating the temperature, displacement, and stress of the mold in the metal casting device for 15 minutes from the initial state until it was removed from the metal casting device and that of the mold removed from the metal casting device until it was completely cooled at room temperature, on 9 measurement positions. Also, figure 2 appeared measurement points of numerical analysis.

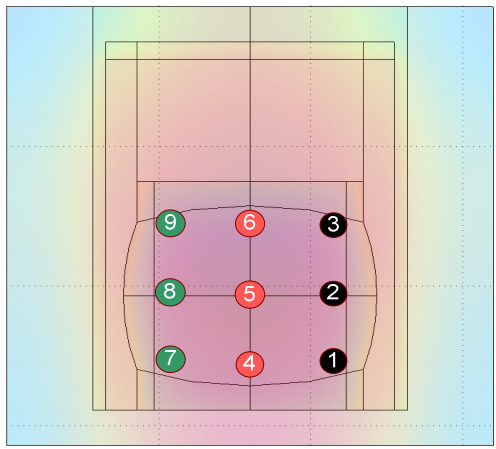

Fig. 2. Schematic diagram of measurement points in tread part

4. Numerical results

Results of numerical analysis, Al alloy most occurred temperature variation during the initial cooling time at 15 minutes in the inside of metal casting device. Especially, because the metal casting device was in contact with the mold surface, sudden heat transfer occurred on both sides of the mold and thus the temperature at these sides appeared to be higher than the temperature at the middle part (measurement points of 4, 5 and 6). This result appeared at figure 3(a). And then, measured from the 15 minutes when the mold was taken out until it was completely cooled at room temperature. The cooling pattern from 15 to 420 minutes on all measurement points appeared to be simulation. This result appeared at figure 3(b).

Displacement and stress are generated by the temperature difference between the surface and inside of the mold material, Al alloy. This temperature difference is closely related to the precision of the mold product and the thermal deformation of the mold material.

Figure 4(a) and figure 4(b) show the displacement inside the mold for 15 minutes from the initial state and the one until it was completely cooled after the 15 minutes when it was removed from the metal casting device, which were calculated by the numerical analysis method. As shown in Figure 4(a), high temperature difference made the displacement at the middle part bigger than the one at both ends of the mold.

Figure 5(a) shows the stress inside the mold for 15 minutes, which was calculated by the numerical analysis method. It appeared to be larger at the middle part than on its sides. The cooling speed at the middle part was slower than the one on its sides because of the flow characteristic of the mold material, and the stress was larger at the middle part because of the shrinkage caused by the cooling speed difference. Figure 5(b) shows the stress calculated until the mold was completely cooled after it was removed from the metal casting device in 15 minutes, which appeared to be larger on the measurement points of 2, 5 and 8 than on other points because of slow cooling speed.

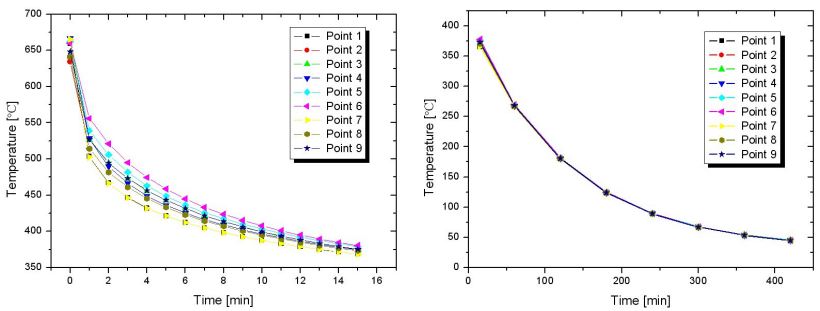

(a) From 0 to 15 minutes (b) From 15 to 420 minutes

Fig. 3. Temperature variations during the cooling time in each point

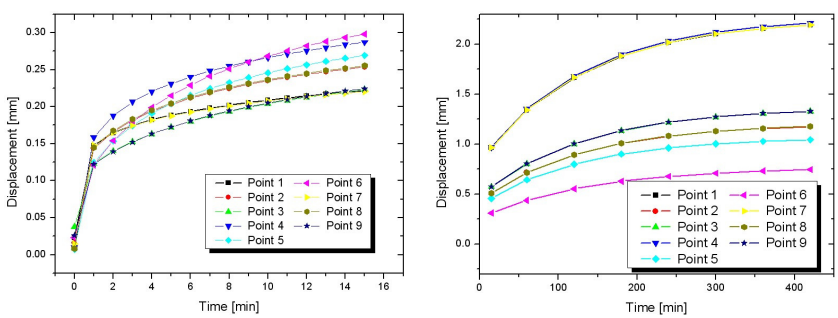

(a) From 0 to 15 minutes (b) From 15 to 420 minutes

Fig. 4. Displacement variations during the cooling time in each point

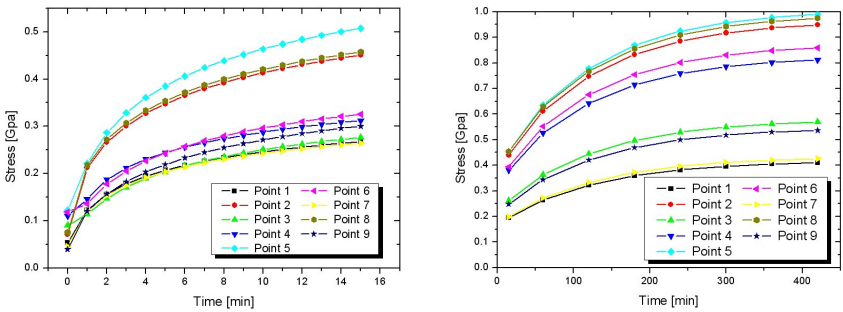

(a) From 0 to 15 minutes (b) From 15 to 420 minutes

Fig. 5. Stress variations during the cooling time in each point

5. Conclusion

This study investigates on 3-dimensional thermal deformation of tire mold using Al alloy 5000series materials and the following conclusion has been reached.

1. Temperature at the sides of mold appeared to be higher than of the middle by rapid temperature difference because metal casting device was in contact with the mold surface for 15 minutes. The cooling pattern from 15 to 420 minutes on all measurement points appeared to be similar.
2. The displacement for 15 minutes in the metal casting device appeared to be larger at the middle part (measurement points of 4, 5 and 6) than on its sides, and the one calculated for the time until it was completely cooled at room temperature after it was removed from the metal casting device appeared to be larger on the measurement positions of 1, 4 and 7 near the atmosphere than on other points.
3. The stress inside the 5000series Al alloy mold appeared to be larger at the middle part because of the cooling speed difference for the cooling process.

References

1. S. K. Park, Y. H. Lee and J. H. Lim, “A Comparative study between Green`s Function Method and Fourier Transform Method in Determining Thermal Wave Characteristics”, J. KSPSE, Vol 4, No 4, pp. 16-24, 2000.
2. C. H. Lee, “Finite Element Method”, J. KSME, Vol 13, No 3, pp. 203-208, 1973.
3. H. M. Si, C. D. Cho, “Analysis of themal stress of casting by means of finite element method”, KSME, pp. 402-407, 1998.

MODELING OF DIELECTRIC RESPONSE OF OIL-PAPER INSULATION SYSTEMS USING RETURN VOLTAGE METHOD

SEI HYUN LEE†

Electrical engineering, Korea Polytechnic collages, 91-2 Gayang-2dong Dong-gu Daejeon, 300-700, Korea

DOO GIE PARK, SANG OK HAN

Material and High voltage laboratory, Chungnam National University, 220 Gung-dong Yuseong-gu, Daejeon, 305-764, Korea

In this paper, the influence of insulation systems inhomogeneity on polarization spectra and the modeling the dielectric absorption in oil-paper insulator were discussed. The model of the dielectric absorption was developed and the trend of its results was coincided in about 10%. In addition, the moisture content in oil-paper insulation determined on the basis of dominant time constant value may be incorrect.

1. Introduction

The condition of oil-paper insulation is the important factor assuring a reliable operation of power transformers. The aging and life expectancy of the insulation depend on operating conditions of transformer − the aging process proceeds faster at higher operating temperature, especially in the presence of water.

The estimation of water content in paper insulation via moisture measured from oil samples is a commonly used standardized method (IEC 60422). However, to determine reliably the moisture level in the paper insulation, the ideal equilibrium between moisture content in oil and paper is required. The equilibrium state will be reached when the transformer will operate at invariable loading, because the concentration of water in oil depends on temperature to a high degree. For majority of transformers it is not possible to reach ideal equilibrium, therefore the moisture content in paper insulation cannot be unequivocally determined on the basis of oil samples analysis [1].

The dielectric response methods for diagnosis of power transformers allow to determine the water content in paper insulation in most direct manner. These

methods are based on analysis of polarization phenomena in time and frequency domain. The most known methods are based on RVM, FDS, PDC etc.

When there is a moisture content inhomogeneity in oil-paper insulation, we discussed the phenomenon of polarization spectra by different water distribution, simulated it by EMTP(Electric Magnetic Transient Program) and analyzed those.

2. Insulation Model for Dielectric Response

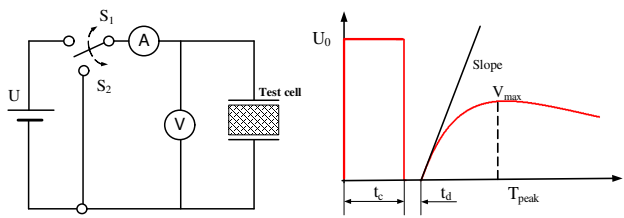

Fig. 1. Return Voltage Circuit and time diagram of return voltage

In Figure 1, if S_1 closed, the cell is charged for charging time. Next, if S_1 opened and S_2 closed, the cell is discharged for discharging time. Ratio of charging time and discharging time is two. That late polarization such as interface polarization, space charge polarization, dipole polarization, orientation polarization etc. doesn't depolarize for discharge time. Therefore, voltage are detected to voltmeter if open S_2. A capacitor consists of two conductive plates separated by a dielectric material, when connected to a voltage source, one conductive plate charges positively and the other one negatively. The capacitor remains charged after being disconnected from the voltage source, and can be discharged by shorting its terminals. The voltage on the capacitor is proportional to the amount of charge on the conductive plates. Because of dielectric absorption, the voltage on the capacitor partially recovers after momentarily shorting its terminals. The magnitude of this recovery is lower if the short is maintained for a longer time. Thus, energy still remains in the capacitor after a momentary short. To fully discharge the capacitor, the short needs to be maintained for a long time. This effect of the dielectric absorption can be modeled. The electric current charges and discharges the energy absorption element at slow rates. Because of these slow rates, a momentary short discharges only partially the energy absorption element [2].

$$i(t) = C\frac{dv}{dt} \quad \text{---------- (1)}$$

where C is the capacitance and is the recovery voltage. The current $t(t)$ is decomposed into a sum of exponential decay terms. Each term represents the current coming from a virtual compartment of the energy absorption element.

Thus, the energy absorption element is divided in compartments characterize by energy storage capacitors and exponential transfer functions, similar to adding multiple or distributed relaxation times in dielectric theory.

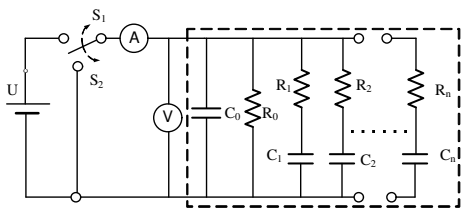

Fig. 2. Electrical equivalent circuit model

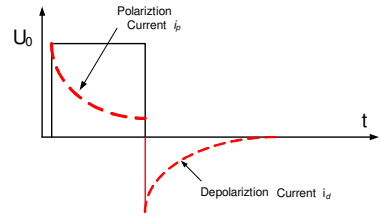

Fig. 3. Polarization and depolarization current curve

The capacitance and time constant of each circuit are calculated from the $i(t)$ decomposition terms. Based on the calculated values, a mathematical model of the dielectric absorption is built. From the mathematical model it is then shown how to calculate the elements of an electrical circuit model of the type shown in Figure 2. The conduction current in the insulation is due to the insulation resistance R_0, C_0 represents the geometric capacitance of the insulation system.

In Figure 3, most of the circuit parameters have been derived from measured polarization and depolarization currents (i_p and i_d). The capacitance C_0 is determined by conventional capacitance measurement techniques at power frequency. The insulation resistance R_0 is calculated from the difference between polarization and depolarization currents at larger values of time. The depolarization current is comprised of summation of various relaxation mechanisms that appear at different locations within the transformer insulation. Various parts of the insulation have their unique relaxation characteristics depending upon the aging and moisture condition. The relaxation currents can thus be modeled as the sum of exponentials of the various relaxation mechanisms. The individual elements $R_i - C_i$ with the corresponding time constants $\tau_i = R_i \cdot C_i$ can then be determined by fitting the depolarization current with the following equation

$$i_d = \sum_{i=1}^{n} \left(A_i \cdot e^{(-t/\tau_i)} \right) \text{ ------ (2)}, \quad \text{Where } A_i = U_0 \cdot \frac{1 - e^{(t_p/\tau_i)}}{R_i} \text{ ------ (3)}$$

The first task in the modeling work is to identify the τ_i and A_i corresponding to different branches. The final part of the depolarization current is used to find out the values of τ_i and A_i corresponding to the largest time constant branch using an exponential curve-fitting technique. Once the

exponential component with the largest time constant is identified, it is then subtracted from the original depolarization current to go to the next level. In this level, like before, the final part of the resultant current curve is influenced by the second largest time constant only, with the next smaller time-constant branches practically going to zero well before that time. Following the same exponential curve-fitting procedure, the values of τ_i and A_i corresponding to the second largest time-constant branch are found out. Proceeding in the same way—all of the other time-constant branches are identified. Once the values of τ_i and A_i corresponding to different time-constant branches are found, the values of R_i and C_i can be easily separated and the equivalent model can be constructed[3].

3. Experimental and Results Analysis

Electrodes were made from copper (92mm×20mm×1.5mm) and closed by cellulose paper(95×190×0.18). It was removed for bubble in oil for 5 hours by vacuum pump. Such made electrode and insulation oil dried during 5 hours at 105°C in vacuum oven. The test cells were the capacitor bundles of oil-paper insulation.

Electrode was covered by the paper that has been in normal temperature state and that dried for 10 minutes at temperature of 45°C in vacuum oven. The moisture content of investigated capacitor bundles, determined from polarization spectra analysis, is shown in Table 1.

Table 1. The moisture content of investigated capacitor bundles

Name	Mositure Content
B_1	4.2%
B_2	5.7%
B_1+B_2	4.3%

RVM meter, Tettex 5462 is used for testing. Charging voltage is 1000 V and charging time is from 0.02 s to 100 s. And for measuring PDC, we used electrometer, Keithley 6514.

Figure 4 presents polarization spectra of capacitor bundles B1 and B2 with qualitatively different insulation and resultant polarization spectrum of bundles B1 and B2 connected in parallel. The polarization spectrum of capacitor bundle B1 has maximum at charging time 0.33 s what corresponds to 4.2 % of moisture content in paper insulation whereas the polarization spectrum of capacitor bundle B2 has maximum at charging time 0.067 s what corresponds to 5.7 % of moisture content. The resultant polarization spectrum received from parallel connection of capacitor bundles B1 and B2 has a maximum at charging time

0.077 s what corresponds to 5.4 % of moisture content in paper insulation. The results show that when is a large difference of moisture content in oil-paper insulation, the resultant polarization spectrum has a character close to insulation of worst quality, however the moisture content determined on the basis of this spectrum is lower than the moisture content in worst insulation.

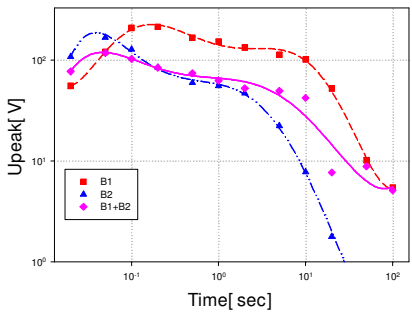

Fig. 4. RVM spectra comparison of test cell

By getting parameters of electrical equivalent circuit from PDC test, the data was expressed to following Table 2.

Table 2. Equivalent Circuit Parameter Values

Branch	B_1		B_2	
	R_i [GΩ]	C_i [nF]	R_i [GΩ]	C_i [nF]
1	0.50	32.3	0.02	2.18
2	1.04	23.2	0.08	2.14
3	1.98	34.5	0.15	3.54
4	3.29	58.5	0.21	4.57
5	4.65	73.7	0.31	4.61
6	5.93	80.8	0.37	4.69

In Figure 5, the model of the dielectric absorption was developed and the trend of its results was coincided in about 10%. The variations in the R_i and C_i values of the smaller time-constant branches shift the dominant central time constants of the RV spectra with affecting the position of the subsidiary peaks. Thus, RV spectra with higher R_i and C_i (better insulation condition) are found to have higher values of dominant central time constants (first peak) as compared to the RV spectra with lower R_i and C_i . This supports the observation that the values of R_i and C_i for the smaller time-constant branches correspond to the condition of the oil, which affects the initial portion of the polarization and depolarization current and only the first dominant peak of the RV spectra. This is a significant finding, which will help to interpret RV results.

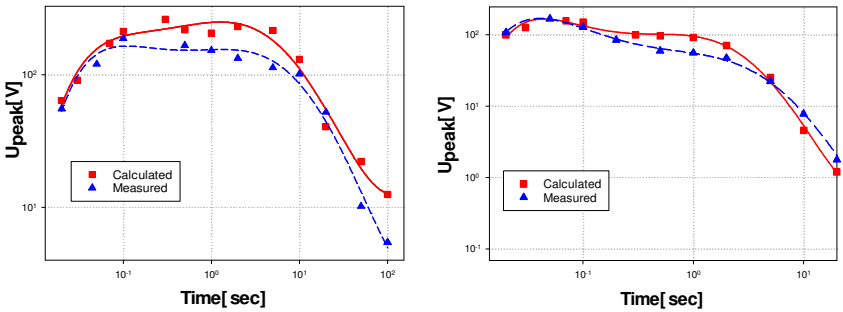

(a) Spectra of few moisture contents (b) Spectra of much moisture contents

Fig. 5. Comparison calculated and measured RVM spectra

4. Conclusion

In order to analyze polarization spectra obtained from return voltage measurements requires many experiences.

Dominant time constant value is important parameter to determine the moisture content in paper insulation, but it may be incorrect, many factors may influence on that situation.

The moisture content determined from return voltage measurements is lower than that in the moistest part under the condition, which is a moisture content inhomogeneity in paper insulation,

Return voltage method may not detected exactly content of the water separately, between the moisture content parts.

In addition, modeling based on measurement was carried. The trend of model's value was much the same, so to analyze and compare the polarization of spectra can be used easily..

References

1. Marek Ossowski, Jaroslaw Gielniak, "Dielectric response of oil-paper insulaton systems of large moisture and temperature inhomogenity", Proceedings of the XIVth international symposium on high voltage engineering, August 25-29 2005
2. Cosmin lorga, "Compartmental analysis of dielectric absorption in capacitors", IEEE Transactions on Dielectrics and Electrical Insulation, Vol. 7, No. 2, April 2000
3. Tapan K. Saha, "Deriving an Equivalent Circuit of Transformers Insulation for Understanding the Dielectric Response Measurements, IEEE Transactions on Power Delivery, Vol. 20, No. 1, January 2005

RESIDUAL STRESS ANALYSIS AND MEASUREMENT OF FUEL INJECTION PIPE

SEUNGKEE KOH

School of Mechanical Engineering, Kunsan National University
Kunsan, Chonbuk, 573-701, Korea

EUIGYUN NA

School of Mechanical Engineering, Kunsan National University
Kunsan, Chonbuk, 573-701, Korea

In order to investigate the optimum condition of the autofrettage process for the diesel engine fuel injection pipe, different levels of autofrettage pressure, pressure rising time, pressure holding time, and repetition of autofrettage were applied. Autofrettage was performed by applying the hydrostatic internal pressures of 604 MPa, 535 MPa and 500 MPa on the fuel injection pipe, corresponding to theoretical overstrain levels of 26%, 14%, and 9%, respectively. The autofrettage residual stresses in the fuel injection pipe were experimentally measured by using X-ray diffractometer. As the overstrain level increased, the magnitude of compressive tangential residual stress at the bore increased. It was found that the rising time to the autofrettage pressure, holding time at the autofrettage pressure, and repeated application of the autofrettage pressure had no significant influence on the residual stress distributions in the pipe.

1. Introduction

For a thick-walled pressure vessel subjected to internal pressure, the largest tensile tangential stress occurs at the inside diameter. If the vessel is subjected to a pulsating internal pressure, then fatigue cracks usually originate at the inside surface and grow rapidly, resulting in final fracture. To prevent the failure of the thick-walled pressure vessel, an autofrettage process that produces favorable compressive tangential residual stresses at the bore of the vessel has been commonly employed [1, 2]. The compressive residual stress counteracts the tensile operating stress caused by the internal pressure, thus increasing the elastic strength of the pressure vessel. Therefore, the estimation of the residual stress distribution in the autofrettaged pressure vessel is very important for the accurate prediction of the elastic and fatigue strengths of the pressure vessel [3].

Recently, a common rail system in diesel engine fuel injection equipment has been developed in order to meet the future stringent emissions requirements and improve the fuel economy. The atomization by the electronic-controlled

fuel injectors promotes combustion at all engine speeds, thus achieves reduced emissions and engine noise, and high fuel economy. Therefore, the common rail system requires maintaining high injection pressure for the fuel piping. In this research, the thick-walled fuel injection pipes in the common rail diesel engine system were autofrettaged with different levels of autofrettage pressure, pressure rising time, and number of repetition. In order to find an optimum autofrettage procedure for the fuel injection pipe, residual stresses in the autofrettaged pipes were measured experimentally and compared to the analytical results.

2. Autofrettage Pressure and Residual Stress Distribution

In order that the fuel injection pipe subjected to the high internal pressure has sufficient elastic and fatigue strengths, the tangential tensile stress at the bore of the thick-walled pipe should be quite lower than the yield strength of the material. This can be attained by inducing the tangential compressive residual stress at the bore, i.e. autofrettage process, since the residual compressive stress compensates for the operating tangential stress. The autofrettage is a metal forming process, applying a hydrostatic pressure high enough to produce the plastic deformation in the pipe. Releasing the pressure generates the non-uniform elastic recovery and thus induces residual stresses through the thickness of the pipe.

A thick-walled pipe considered in this research was developed for the fuel injection piping in the common rail diesel engine system. The pipe was subjected to a pulsating internal pressure of 105 MPa during operation. Inside and outside radii of the pipe were 14 mm and 27 mm, respectively. The pipe was made of SCM440 steel with yield and tensile strengths of 1018 MPa, and 1109 MPa, respectively. The radial and tangential stresses due to internal pressure can be represented by the following Lamé equation [4],

$$\sigma_r = \frac{P_i a^2}{b^2 - a^2}\left[1 - \frac{b^2}{r^2}\right] \qquad \sigma_\theta = \frac{P_i a^2}{b^2 - a^2}\left[1 + \frac{b^2}{r^2}\right] \tag{1}$$

where *a, b* are inner and outer radii of the pipe, respectively. Assuming the elastic-perfectly plastic behavior and von Miese yield criterion for the pipe material, the autofrettaged pressure P_u, for a partially autofrettaged tube as shown in Figure 1 can be obtained as follows [2],

$$P_u = \frac{\sigma_Y}{\sqrt{3}}\left[\left(1 - \frac{\rho^2}{b^2}\right) + 2\ln\frac{\rho}{a}\right] \tag{2}$$

where the radius, ρ corresponds to the elastic-plastic boundary during the autofrettage pressure loading. The level of autofrettage is expressed by the percent overstrain(%OS), representing the ratio of the plastically deformed thickness to the total thickness of the pipe.

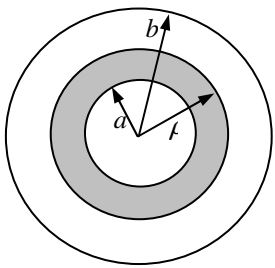

Fig. 1. Autofrettaged thick-walled pipe.

Three different levels of pressure such as 604 MPa, 535 MPa, and 500 MPa were applied to the pipe for autofrettage, which were corresponding to the autofrettage levels of 26%OS, 14%OS, and 9%OS from Eq. (2), respectively. The autofrettage pressure as a function of overstrain level can be shown in Figure 2. From Eq. (2), a theoretical autofrettage pressure of 773 MPa can be obtained for the case of 100%OS.

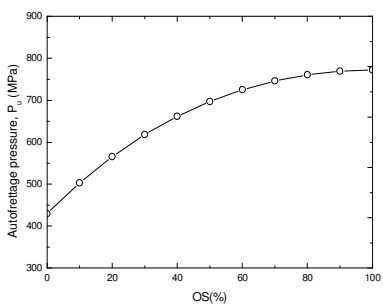

Fig. 2. Autofrettage pressure for different overstrain levels.

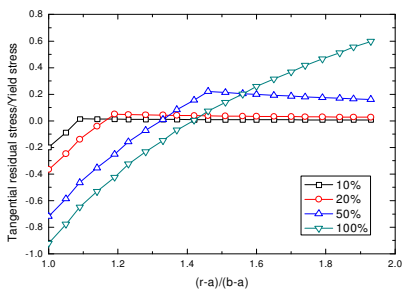

Fig. 3. Theoretical tangential residual stress distributions in an autofrettaged pipes.

Tangential residual stresses in a partially autofrettaged pipe can be calculated by assuming the elastic-perfectly plastic material behavior, plane strain condition, and von Mises yield criterion,

$$\sigma_\theta = \frac{2}{\sqrt{3}}\sigma_Y\left\{\frac{a^2}{b^2-a^2}\left(1+\frac{b^2}{r^2}\right)\left[\frac{c^2-b^2}{2b^2}-\ln\frac{\rho}{a}\right]+\left[\frac{\rho^2+b^2}{2b^2}-\ln\frac{\rho}{r}\right]\right\}, \quad \text{for } a \le r \le \rho$$
$$= \frac{2}{\sqrt{3}}\sigma_Y\left(1+\frac{b^2}{r^2}\right)\left[\frac{\rho^2}{2b^2}+\frac{a^2}{b^2-a^2}\left\{\frac{\rho^2-b^2}{2b^2}-\ln\frac{\rho}{a}\right\}\right], \quad \text{for } \rho \le r \le b \tag{3}$$

Residual stress distributions in an autofrettaged fuel injection pipe with yield strength of 1018 MPa are shown in Figure 3. The magnitude of compressive tangential residual stress at the bore increases as the level of autofrettage increases, approaching the value of yield strength for fully autofrettaged pipe as shown in Figure 4.

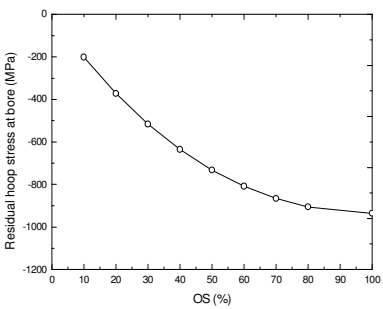

Fig. 4. Tangential residual stress versus overstrain level in autofrettage pipes.

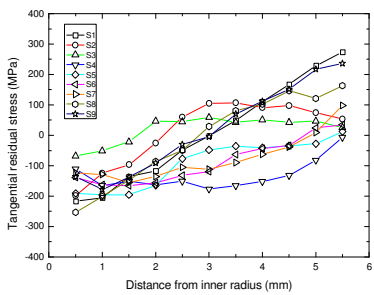

Fig. 5. Measured tangential residual stresses in autofrettaged fuel injection pipes.

3. Residual Stress Measurement of Autofrettaged Pipe

Since the deformation behavior of material depends on the loading rate, the time to reach the autofrettage pressure and the time to hold the pressure can have influence on the residual stress distributions in the autofrettaged pipes. In order to investigate the effects of the autofrettage process variables and to find an optimum procedure in the pipe autofrettage, the several different values of pressure rising and holding times were applied to the autofrettage, including the repetition of autofrettage.

Residual stresses in the pipe induced by the autofrettage were determined experimentally using X-ray diffraction method. Specimens with a ring shape

were cut perpendicular to the longitudinal axis of the autofrettaged pipe and listed in Table 1. The cutting surface was electro-polished and tangential residual stresses along the thickness of the pipe in the radial direction at an interval of 0.5 mm distance. Measured tangential residual stress distributions are shown in Figure 5, indicating that compressive residual stresses ranging from -70 MPa to -260 MPa at the bore and from -100 MPa to 280 MPa at the outside of the pipe.

Table 1. Conditions for injection pipe autofrettage.

Specimen ID	Autofrettage pressure (MPa)	Pressure rising time (min.)	Pressure holding time (min.)	Repetition of autofrettage
S1	604	2	0	1
S2	536	2	0	1
S3	500	2	0	1
S4	604	5	0	1
S5	604	5	0	1
S6	604	2	5	1
S7	604	2	5	1
S8	604	2	0	3
S9	604	2	0	3

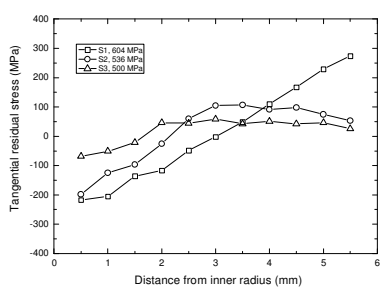

Fig. 6. Tangential residual stresses for different autofrettage pressures in injection pipes.

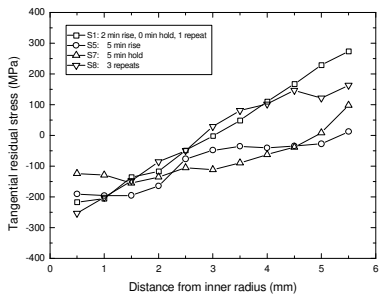

Fig. 7. Tangential residual stresses for different autofrettage processes at a pressure of 604 MPa.

Residual stress distributions in pipes with different autofrettage pressures of 604 MPa, 535 MPa, and 500 MPa are shown in Figure 6. The higher the level of autofrettage pressure, the larger the magnitude of the compressive residual stresses near the bore. Since the residual stress at the inside surface could not be measured, the value at the bore was determined by extrapolation. Theoretical and measured residual stresses at the bore are listed in Table 2. It

was found that the measured values were lower than the theoretical values, and the difference was attributed to the Bauschinger effects by reverse yielding. The measured compressive residual stress at the bore for the pressure of 535 MPa was 250 MPa, which was larger than the tangential stress of 182 MPa due to operating pressure of 105 MPa in the fuel injection pipe, implying the improved elastic strengths of the pipe due to autofrettage. Effects of the pressure rising time, holding time, and repetition on the residual stress distributions are shown in Figure 7 for the autofrettage pressure of 640 MPa. No significant effect was observed.

Table 2. Comparison of theoretical and experimental residual stresses at the bore of the autofrettaged injection pipes.

Autofrettage pressure (MPa)	OS (%)	Tangential residual stresses (MPa)	
		Theory	Experiment
604	26	-462	-380
535	14	-276	-250
500	9	-180	-120

4. Conclusions

To ensure the elastic strength of the high pressure fuel injection pipe used for common rail diesel engine system, optimum conditions of autofrettage process were investigated. As the overstrain level increased, the magnitude of compressive tangential residual stress at the bore increased, resulting in the tangential compressive autofrettage residual stress which compensated for the tangential stress due to operating pressure. It was found that the rising time to the autofrettage pressure, holding time at the autofrettage pressure, and repeated application of the autofrettage pressure had no significant influence on the residual stress distributions in the pipe.

5. References

1. I. L. Spain and J. Paauwe, *High Pressure Technology,* Van Nostrand Reinhold (1977)
2. D. W. A. Rees, *Int. J. Mech. Sci*. 46, 1675 (2004)
3. S. I. Lee and S. K. Koh, *Int. J. Pressure Vessels & Piping*, 79, 119 (2002)
4. S. P. Timoshenko and J. N. Goodier, *Theory of Elasticity*, McGraw-Hill (1970)

NUMERICAL ANALYSIS AND EXPERIMENTAL STUDIES ON CURRENT SHUNTS FOR CLAMP ON METER

W.W.S. WIJESINGHE
Korea Research Institute of Standards and Science, Korea

YOUNG TAE PARK
Korea Research Institute of Standards and Science, Korea

A comparison of numerical analysis and experimental studies on ac/dc resistive shunts is presented. The comparison was performed for the recently developed low resistance current shunts, which are very useful to measure the ac current very precisely in clamp on meter. In this paper, more attention has been given for non destructive phase angle analysis of resistive shunt in both ways since most of the authors concerned with especially the amplitude of impedance of ac/dc resistors. The numerical analysis revealed that the major contribution is given by inductance rather than capacitance of the resistors and structure of shunt to produce phase angle difference between current and voltage. Furthermore, the analysis shows that the ac/dc ratio error is very small and agreed with experimental result with the level of ±1 ppm. Base on the experimental results of phase angle error is higher than the theoretical value and agreed within the level of ±5 ppm at 50 Hz.

1. Introduction

A precision clamp on meter can be used nondestructive analysis of ac and dc low current in a automobile Electrical system. Currents measurement instruments are need to be calibrated very precisely to obtain accurate results. Current shunts are commonly used to calibrate both AC and DC current measurement instrument in order to measure current very precisely at metrological level. However, when current is converted into ac voltage a phase shift occurs between current and voltage influence of imaginary component which is caused by inductance and capacitance of the resistive shunt. This phase angle difference between current and voltage causes of an error in ac current measurement. Recently, in ac current and power measurement fields the special attention has been given to calculable ac/dc resistors and publications on theoretical and experimental analysis about the shunt resistors have been published [1]-[2]. However, most of the reports gave more attention to the real

part of the total impedance and presented ac/dc difference of the shunt. But, the imaginary component mainly depend on time constant τ of the ac resistance is given more contribution to the phase angle difference between current and voltage. Therefore analyzing time constant τ of the shunt resistor is given clear idea of the phase angle. Moreover determining time constant very precisely, the realization of the standard of shunt resistor is possible. In this paper, the phase angle of the low ohm shunt resistors has been analyzed.

2. Impedance of Resistive Shunt

The standards representation of a resistor can be considered as a series circuit consisting of a resistance R and an inductive L, across self-capacitance C. The impedance **Z** of such arrangement can be written as

$$Z = \frac{R + j\omega[L(1-\omega^2 CL) - CR^2}{(1-\omega^2 CL)^2 + \omega^2 C^2 R^2} \tag{1}$$

The in phase resistance or amplitude of the equivalent impedance R_w with the angular frequency ω rad/s and the imaginary or series reactance part of the equivalent impedance L_e are given in following equations

$$R_\omega = \frac{R}{(1-\omega^2 LC)^2 + \omega^2 C^2 R^2} \approx R[1 + \omega^2 C(2L - CR)] \tag{2}$$

$$L_e = \frac{\omega[L(1-\omega^2 CL) - CR^2]}{(1-\omega^2 LC)^2 + \omega^2 C^2 R^2} \approx \omega(L - CR^2) \tag{3}$$

and the Phase displacement (Φ) between the voltage and current is

$$\Phi = \omega\left(\frac{L}{R} - CR\right) \tag{4}$$

and time constant τ

$$\tau = \frac{L}{R} - CR \tag{5}$$

The equation (4) shows that the phase angle mainly depend on the time constant for fixed angular frequency ω while equation (5) reveals that the time constant τ be determined by dc resistance values of shunt and its residual capacitance and inductance. Furthermore, equation (5) shows that low value resistors have larger time constant relatively higher value resistors. Therefore, the residual capacitance and inductance of the low value resistors should be minimized as possible to reduce the value of time constant. The resistive shunts can make using bifilar coil or parallel resisters. In general, the capacitance of the both type of resistors is in the order of 10^{-11} to 10^{-12} farad. The residual induction of the well design bifilar type resistive coil is around 1x 10^{-7} Henry and the phase angle difference of the current and voltage is more than 200 parts in 10^{-6}. Therefore, to reduce the self-induction of the resistive shunt many parallel resisters have to be used.

3. Structure of the Shunt

The designed current shunts are similar to the JEMIC design [3] and two shunts were developed with nominal current values of 1 A and 5 A having resistance 1 Ω and 0.2 Ω respectively. The output voltage for each shunt is one volt. The 1 Ω ac/dc resistive shunt, rated 1 A, consist of twenty five 25 Ω Vishay type metal foil resistors connected in parallel while 0.2 Ω shunt having fifty 100 Ω resistors connected in parallel. The structure of the shunt includes three double-sided printed circuit board plates connected by twenty-five ribs as shown in Figure 1. The input plate is separated by ribs from the output plates to minimize the inductive coupling between input and output of the circuit.

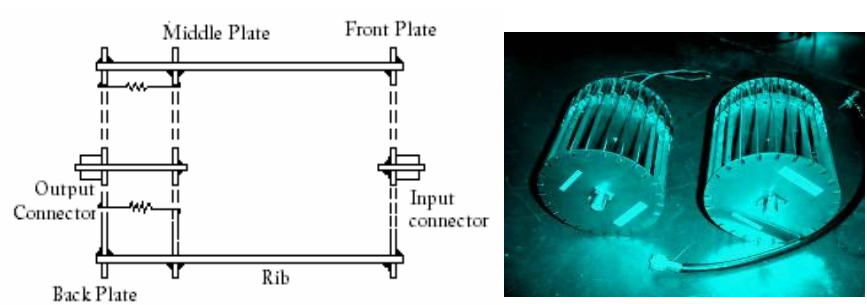

Fig. 1. Structure of the shunt and designed 1 A and 5 A resistive shunts

The model is consisting of several identical components as shown in Figure 1. The input current goes one side of the rib through resistor and returns other side of the rib. Therefore, each rib can consider as (R+L-C-R+L) network and the resistor as (R+L) with parallel C in series with the T network [2]. Both input and output plates can be considered as R-C-R network. Figure 2 shows that the simplified theoretical model for the shunt.

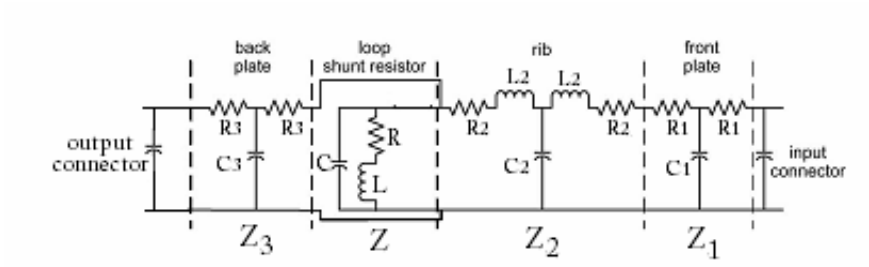

Fig. 2. Simplified equivalent circuit

Let the impedance of loop shunt resistors can be written as follows.

$$Z = R[1 + \omega^2 C(2L - CR^2) + j\omega(L - CR^2) \quad (6)$$

The equivalent circuit and total impedance of each component mentioned above are very useful to select mechanical dimensions of the resistive shunt. Although longer ribs reduce the coupling effect between input and output, it may increase the capacitance and inductance of the shunt. Therefore, optimum length of ribs compensates both effects. Since the power rating of the resistors are very small, number of resistors were connected in parallel increasing number of ribs, thus increasing the internal capacitance of the shunt. Therefore, two or four resistors can be connected together in small plate to reduce the number of ribs and impedance Z_2 as well. However, smaller dimension increases the working temperature of the shunt. In fact, we need optimum dimension to design the resistive shunt. However, it is very important to calculate the inductance and capacitance of the structure contribute to the loop shunt resistors.

4. Numerical and Experimental Analysis

As mention above the structure of the developed current shunts are consist of rectangle PCB ribs and circular input and out put plates. The self-inductance of the rectangle plate can be written as

$$L = 4\left\{(b+l)A_{11} - bA_{12} - lA_{13} + 2\left(b^2+l^2\right)^{\frac{1}{2}} + \frac{a}{2} - \frac{3}{4}(b+l) - \frac{1}{2}\left((b+l)^2 4 + a^2\right)^{\frac{1}{2}}\right\} \times 10^{-9}\, H \qquad (7)$$

Where $A_{11} = \ln\left[\dfrac{\left(4(b+l)^2 + a^2\right)^{\frac{1}{2}} + a}{a}\right]$, $A_{12} = \ln\left[\dfrac{\left(b^2+l^2\right)^{\frac{1}{2}} + b}{l}\right]$ and

$$A_{13} \ln\left[\frac{\left(b^2+l^2\right)^{\frac{1}{2}} + l}{b}\right]$$

and the *l*, b and a are the length, wide and copper thickness of the each ribs in meter respectively. The thickness of the PCB plate is 1 mm. While the dimension of the each rib is 12.5 cm x 1 cm and the radius of the circular input and output plates is 7 cm. The calculated self-induction of the each rib is 3 nH and the self capacitance is approximately 20 pF. The capacitance of the input and output PCB plates are 400pF. According to manufactures specification the self-capacitance and induction of the resisters used are 10pF and 80nH. Therefore, the self-induction is prominent compare to capacitance effect. The calculated ratio error and phase angle error are presented in Table 1.

The designed resistive shunts were calibrated in National Research Council of Canada (NRC) and Korea Research Institute of Standards and Science (KRISS). The calibration system is based on current comparator including amplitude and phase control amplifiers, signal source, current Tranconductance amplifier and lead compensation circuit. In this shunt calibration system the transconductance amplifier supplies the relevant (1 A or 5 A) current signal to the test shunt and voltage across the shunt compare with the voltage at the 1 kΩ standard resistor through the buffer. The calibration results from both KRISS and NRC are presented in Table 1.

Table 1. Comparison results of the shunt resisters at 50 Hz

Shunt	Experimental Results		Theoretical results
	KRISS Results	NRC Results	
1 ohm (1 A)	5 + j2.5	1 + j4	1>>r + j1
0.2 ohm (5 A)	6 + j3.3	1 + j5	1>>r + j1

The equations (6) shows that the real part of the impedance of the resistive shunt is frequency dependant. The term of ω^2LC is contributing the ratio error of the shunt. According to numerical analysis those reactance (L and C) are very small and the order of values are 10^{-9} and 10^{-11} respectively. Therefore, the term ω^2LC is less than 1 ppm when the angular frequency value is up to 10^4 and it means that the ratio error should be less than 1 ppm theoretically. The NRC results are complying within the 1ppm with theoretical value. However, the KRISS results are higher than the expected theoretical value due to the higher system uncertainty. The comparison of numerical and experimental results shows that the phase angle error of the resistive shunt is agreed within the leval of 5ppm at 50 Hz. According to nondestructive analysis, the resistive shunts can be used for the calibration of high accuracy clamp on meters for precise ac/dc current and power measurement.

Conclusion

The numerical and experimental analysis of the resistive shunt revealed that the major contribution is given by inductance of the resistors and structure of shunt to produce phase angle difference between current and voltage. Furthermore, the analysis shows that the ac/dc ratio error is very small and the phase angle error is higher than the theoretical value.

References

1. Piotr S. Filipski, AC-DC current shunts and system for extended current and frequency ranges. *IEEE . Vol., 55, No. 4, 2006.*
2. Takuhiro Tsuchiyama and Takuya Tadokoro, Development of a high precision AC standard shunt for AC power measurement. *Conference on Precision Electromagnetic Measurements ,Canada, 2002.*
3. Takuhiro Tsuchiyama and Takuya Tadokoro, Development of a high precision AC standard shunt for AC power measurement. *Conference on Precision Electromagnetic Measurements ,Canada, 2002.*

SYSTEM IDENTIFICATION OF A STEEL BRIDGE USING MODAL FLEXIBILITY MATRIX

KI YOUNG KOO

Department of Civil and Environmental Engineering, Korea Advanced Institute of Science and Technology,335 Gwahangno,Yuseong-gu Daejeon,305-701 Republic of Korea

DOO KIE KIM AND JINTAO CUI

Department of Civil Engineering, Kunsan National University Miryong, Kunsan, Jeonbuk, 573-701, Republic of Korea

HIE YOUNG JUNG

Department of Civil Engineering, University of Seoul Dongdaemun-gu, Seoul 130-743, Republic of Korea

This paper represents a new FEM model updating method for bridges using deflections obtained by modal flexibility matrix from dynamic structural response measurements. Generally, natural frequencies and mode shapes have been widely used in FEM model updating procedures instead of deflections or strains since these static measurements are hard to be obtained in practical situations. In this study, a new FEM model updating method is proposed based on static deflections obtained by dynamic measurements via modal flexibility. The proposed model updating method is easy in implementation and fast in computation since only static analysis is needed during optimization avoiding eigen-analysis. Experimental verification was carried out on a steel-box girder bridge model and it was found that the proposed method reasonably fits the estimated deflection.

1. Introduction

Recently, the modal flexibility has become one of the promising damage detection features owing to its high sensitivity to damage. Through numerical studies for a spring-mass system with five degrees of freedom, the modal flexibility is shown to be a more sensitive tool for damage detection than the natural frequencies and mode shapes (Zhao and DeWolf 1999 [1]). During the past three decades, vibration-based SHM methods have been extensively studied and developed utilizing the various vibration characteristics such as natural frequencies, mode shapes, modal curvatures, and modal flexibility. An excellent review can be found (Doebling et al. 1996 [2]).

The identification of mathematical models of physical structures based on experimental measurements is a problem that has been receiving increasing attention recently. Numerous publications and methods are available on the subject of system identification of structures [3-5]. The use of system identification approaches for damage detection has been expanded in recent years owing to the improvement of structural modeling techniques incorporating response measurements and the advancements in signal analysis and information processing capabilities [6]. M.Q. Feng and D.K. Kim *et al.* [7] proposed a method to build baseline models for bridge performance monitoring using neural networks. P. Gupta and N.K. Sinha [8] proposed an improved approach for nonlinear system identification using neural networks. Pepijn W.J. van de Ven [9] proposed a neural network augmented identification of underwater vehicle models that use several neural networks to identify different parts of the model separately. In other aspects, A. Pavic and Z. Miskovic [10] proposed a combined experimental and analytical approach to investigate modal properties of a lively open-plan office floor based on state-of-the-art finite-element (FE) modeling, FRF-based shaker modal testing, FE model correlation, manual model tuning, and sensitivity-based automatic model updating of a detailed FE model of this composite floor structure.

In this paper, a method to estimate deflection by modal flexibility is presented to simplify the system identification into static analysis. The modal flexibility is defined as a product of dynamic modal parameters, i.e., natural frequencies and mode shapes. The objective is to build a baseline model of a steel bridge based on experimental dynamic response data. To meet it, the optimization process is employed by defining a cost function based on the computation of deflections.

2. Theory

2.1. *Deflection estimation by modal flexibility*

The flexibility **G** defined as an inverse of the stiffness matrix **K** satisfies the equation as follows and can be used to estimate a deflection under an arbitrary load **f**.

$$\mathbf{u} = \mathbf{G}\mathbf{f} \tag{1}$$

where **u** is a deflection vector and **f** is a load vector.

The modal flexibility matrix $\mathbf{G}_m$ is defined as an expansion of the flexibility matrix using modal parameters as follows.

$$\mathbf{G}_m = \mathbf{\Phi}_m \mathbf{\Lambda}_m^{-1} \mathbf{\Phi}_m^T \tag{2}$$

where $\mathbf{\Lambda}_m$=[\ ω_i^2 \], ω_i is the i-th natural frequency, i=1,…, m; $\mathbf{\Phi}_m$=[ϕ_1 … ϕ_m], ϕ_i is the mass-normalized i-th mode shape, and m is the total number of modes estimated from a experiment.

In Eq. (2), the influence of the i-th mode on the flexibility matrix decreases with ω_i^{-2}. The advantage of utilizing the flexibility matrix for system identification is that it can be established accurately by using only a few lower modes, which may be accurately evaluated from the conventional vibration (acceleration)-based test on real structures. When the modal flexibility matrix is evaluated using Eq. (2) based on the natural frequencies and mode shapes, any deflection profile under an arbitrary load **f** can be estimated by a simple matrix multiplication as Eq. (1).

2.2. *Positive bending inspection loads*

In this study, PBILs (Positive Bending Inspection Loads) are used to obtain deflections using Eq. (1). A PBIL which is defined as a load or a system of loads which guarantee positive bending moments in the inspection region, makes deflection change sensitive to structural changes so that the optimization can be carried out rapidly. Examples of PBILs are shown in Table 1 for a two span continuous beam used in the experimental study.

Table 1. Examples of PBILs for various inspection regions.

Beam Types	Inspection Regions Ω	PBILs	Definitions of Inspection Loads
2-Span Continuous Beam			(f^1)
	1st span-region	f^1	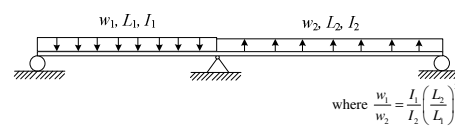
	2nd span-region	$-f^1$	
			(f^2)
	Intermediate support-region**)	$f^{2*)}$	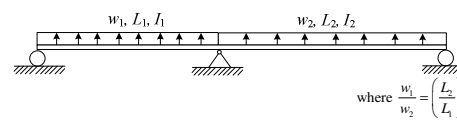

*) f^1 and f^2: Span-region inspection load and intermediate support-region inspection load.

**) Intermediate support-region may cover 1/4 of the span regions on both sides of the support.

2.3. *FEM model updating by deflections under PBILs*

To update a FEM model, the following cost function can be used based on deflections obtained by modal flexibility.

$$C(EI_i) = \sum_{j=1}^{2} \frac{\left\| d_j^{NS}(EI_i) - d_j^{EXP} \right\|}{\left\| d_j^{EXP} \right\|} \tag{3}$$

where $C(EI_i)$ is the cost function and E is Young's modulus and I_i is bending rigidity at the i-th beam element; d_1^{EXP}, d_2^{EXP} are experimental deflections under two PBILs (f^1 and f^2) obtained by modal flexibility; $d_1^{NS}(EI_i)$, $d_2^{NS}(EI_i)$ are corresponding deflections from the FEM model.

3. Experimental Study

3.1. *Experimental setup*

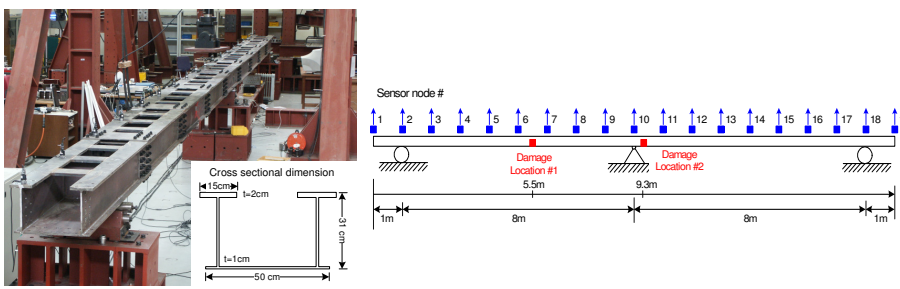

(a) Overview of test set-up (b) Accelerometer layout and damage locations

Fig. 1. Laboratory test on a steel-box girder bridge model

Experimental study was carried out on a bridge model as shown in Figure 1. The test bridge is an 18-meter long, two-span continuous box-girder bridge model composed of 9 segmental boxes connected by bolts. Detailed dimensions of the test bridge are given in Figure 1-(a). Nineteen accelerometers were evenly placed along one side on the upper surface of the box-girder as shown in Figure 1-(b). Small damages of narrow cuts were imposed at two locations on the bottom flange by the saw cuts as described in Tables 2 and 3. Vibration responses were induced by successive impact loads at 4-minute interval and the acceleration responses were measured with 200 Hz sampling rate. The acceleration measurements were repeated 18 times for the intact. The experiments were performed for about 6 hours while the temperature remained nearly steady to make temperature effects negligible.

3.2. *FEM model updating results*

A FEM model using 18 beam elements was used to perform the model updating as shown in Figure 2. Point spring support was employed to imitate the rubber pad inserted under three support points.

Fig. 2. FEM model of the steel bridge

Figure 4 shows the comparison of the deflections before and after identification and the experimental deflections. One can note that the numerical deflections agree well with the experimental results. This demonstrates that the identification method using deflection estimated by the flexibility matrix is effective and efficient.

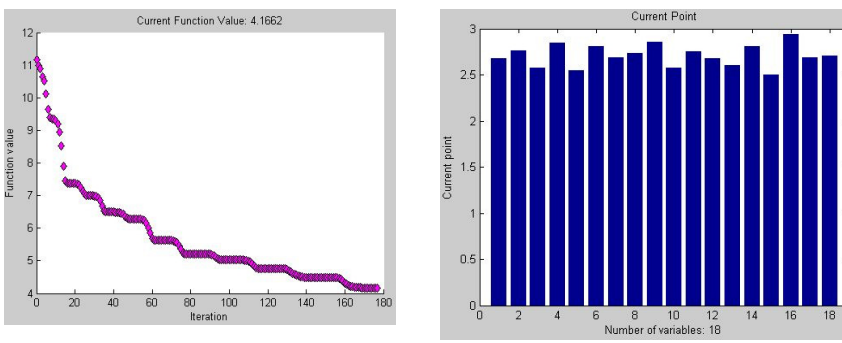

Fig. 3. The cost function values and optimized values during optimization process

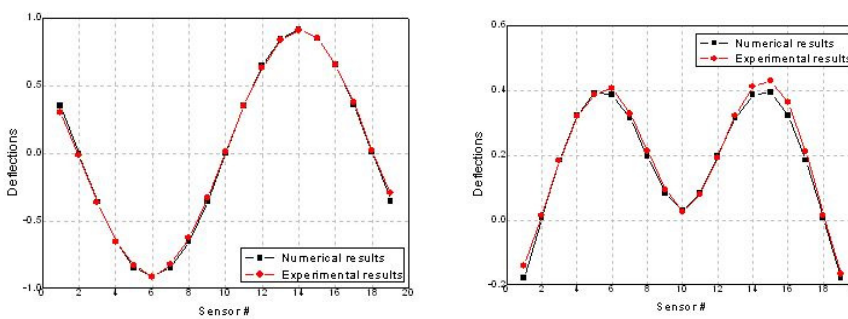

(a) Deflections under f^1 and f^2 before model updating

Fig. 4. Comparison of numerical and experimental deflections under PBILs

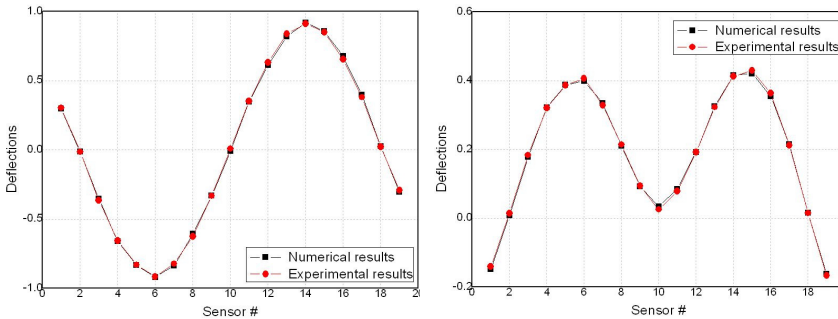

(b) Deflections under f^1 and f^2 after model updating

Fig. 4. *Continued*

4. Conclusion

This paper presented a FEM model updating method utilizing deflection estimated by the modal flexibility matrix for system identification. The modal flexibility matrix can be formed using modal parameters, such as natural frequencies and mode shapes. The following concluding remarks are drawn:

1. The advantage of utilizing a deflection obtained by modal flexibility matrix for system identification is that it can be established accurately by using only a few lower modes, which may be accurately evaluated from the conventional vibration (acceleration)-based test on real structures.
2. The identification results show a good convergence between numerical and experimental deflections (which were transformed using the flexibility matrix estimated from experimental modal parameters). It demonstrates that the presented method is effective and efficient on system identification of the structures based on experimental dynamic response data.

Acknowledgments

This work was supported by grant No.R01-2006-000-10610-0(2006) from the Basic Research Program of the Korea Science and Engineering Foundation (KOSEF) and Korea Research Institute of Standards and Science (KRISS). The authors wish to express their gratitude for the financial support.

References

1. Zhao, J. and DeWolf, J. T. Sensitivity study for vibrational parameters used in damage detection, Journal of Structural Engineering-ASCE 125(4):410-416, (1999).
2. Doebling, S. W., Farrar, C. R., Prime, M. B. and Shevitz, D. W. Damage Identification and Health Monitoring of Structural and Mechanical Systems from changes in their Vibration Characteristics: A Literature Review. Los Alamos National Laboratory Report LA-13070-MS, (1996).
3. K.J. Astrom and P. Eykoff., System identification – a survey, Automatica, (1971).
4. L. Ljung. System Identification: Theory for the User, Prentice-Hall, Englewood Cliffs, NJ, (1987).
5. S.A. Billings., Identification of nonlinear systems--a survey, IEE Proc, (1980).
6. J.J. Lee, J.W. Lee, J.H. Yi, C.B. Yun, H.Y. Jung., Neural networks-based damage detection for bridges considering errors in baseline finite element models, Journal of Sound and Vibration 280 555-578, (2005).
7. M.Q. Feng, D.K. Kim, J.H. Yi and Y. Chen., Baseline models for bridge performance monitoring. Journal of Engineering Mechanics, DOI: 10.1061/ (ASCE) 0733-9399(2004)130:5(562), (2004).
8. P. Gupta and N.K. Sinha., An improved approach for nonlinear system identification using neural networks, Journal of The Franklin Institute 336 721-734, (1999).
9. P. van de Vena, T. A. Johansenb, A. J. Sørensenc,C. Flanagana, and D. Toala., "Neural network augmented identification of underwater vehicle models", Control Engineering Practice 15 715–725, (2007).
10. A. Pavic, Z. Miskovic, and P. Reynolds., Modal Testing and Finite-Element Model Updating of a Lively Open-Plan Composite Building Floor, DOI: 10.1061/(ASCE)0733-9445(2007)133:4(550), (2007).
11. Matlab user's guide, Release 7.1. The MathWorks, Inc. June, (2005).

GEOMETRIC CALIBRATION IN CBCT USING COORDINATES-TRANSFORMED SAMPLING*

SUNG KYN HEO, MIN KOOK CHO, HO KYUNG KIM†

School of Mechanical Engineering, Pusan National University, Jangjeon, Geumjeong Busan 609-735, Republic of Korea

Cone-beam computed tomography (CBCT) is very vulnerable to misalignment in the source, object and detector geometries especially when CBCT employs a large-area flat-panel imager as an x-ray imaging detector. We present geometric calibration methodologies when the detector is misaligned in the CBCT geometry, which is basically based on the coordinates-transformed sampling. The efficacy of the proposed method is assessed by the numerical phantom simulation and its experimental application is demonstrated.

1. Introduction

X-ray computed tomography (CT) is now an essential imaging modality in industrial quality control and nondestructive evaluation [1]. Recent cone-beam computed tomography (CBCT), enabling three dimensional (3D) scanning almost in real time, further pushes up the necessity in industry [2]. However, the CBCT suffers from artifacts, which come from not only the underlying physics (*e.g.*, the x-ray scattering effect) but also the geometric misalignment, and much vulnerable to them than the fan-beam CT [3]. To reduce these artifacts, a large amount of effort has been invested since the CBCT was introduced.

In ideal CBCT geometry, the x-ray focal spot, the center of axis-of-rotation (AOR) and the center of imaging detector should be in line, but the mechanical displacement and skewness are unavoidable in the practical systems [4]. Even small amount of variance in geometry can cause large distortion in the reconstructed images. In this study, we demonstrate the effects of various types of geometric misalignment on the image quality of reconstructed images by using the numerical phantom experiments. In order to restore the distortion artifacts caused from the geometric misalignment, we propose simple coordinates-transformed sampling method.

* This research was performed for the Nuclear R&D Programs funded by the Ministry of Science & Technology (MOST) of Korea (Grant No. M20609000107-06B0900-10710).

† Corresponding Author: E-mail: hokyung@pusan.ac.kr

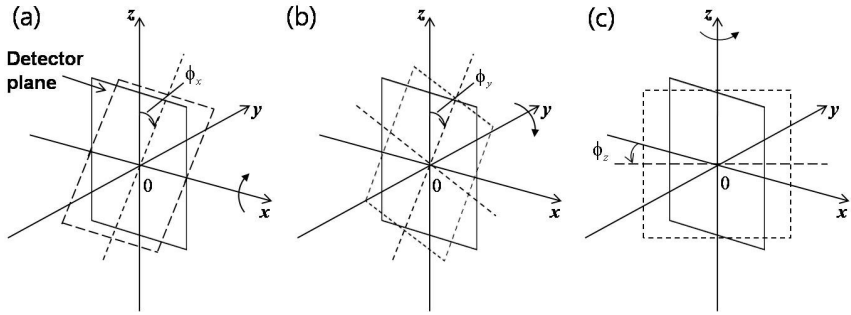

Fig. 1. Definition of detector misalignments around *x*-axis (a), *y*-axis (b), and *z*-axis (c).

2. Materials and Methods

Among various CBCT reconstruction methods, we use the Feldkamp's method in this study [5]. The Feldkamp algorithm is a simple extended version of the conventional filtered backprojection (FBP) method, typically used in fan-beam CT, in longitudinal direction by weighting the cone angles. Thus, the Feldkamp algorithm is approximate and may cause large distortions when the cone angle is wide [6]. When small parts are, however, inspected, this method is powerful because it is very fast and easily applicable.

In the Feldkamp method, a tomogram in slice is evaluated by superimposing the filtered line data, which are sampled from a filtered two-dimensional (2D) projection data at a given projection angle, over the scan angle. Thus, if the projection data are obtained in the misaligned geometry, the reconstructed image will be seriously distorted.

Combinational misalignments among the focal spot, the AOR and the detector can be simply expressed as a function of only the misalignment of detector. As depicted in Figure 1, misalignments at the detector plane are summarized as follows.

- Tilting in *y*-*z* plane: The detector is tilted around *x*-axis and the magnitude of tilting is described by ϕ_x.
- Tilting in *x*-*z* plane: The detector is tilted around *y*-axis and the magnitude of tilting is described by ϕ_y.
- Rotating along *z*-axis: The detector is rotated around *z*-axis and the magnitude of rotation is described by ϕ_z.

The degree of combinational misalignments can be expressed by the transformation matrix:

$$\mathbf{T}=\begin{bmatrix}1 & 0 & 0\\ 0 & \cos\phi_x & -\sin\phi_x\\ 0 & \sin\phi_x & \cos\phi_x\end{bmatrix}\begin{bmatrix}\cos\phi_y & 0 & \sin\phi_y\\ 0 & 1 & 0\\ -\sin\phi_y & 0 & \cos\phi_y\end{bmatrix}\begin{bmatrix}\cos\phi_z & -\sin\phi_z & 0\\ \sin\phi_z & \cos\phi_z & 0\\ 0 & 0 & 1\end{bmatrix}. \quad (1)$$

For the misaligned sampling coordinates $[x \quad y \quad z]$, the corrected sampling coordinates $[x' \quad y' \quad z']$ can be estimated by

$$[x' \quad y' \quad z']^T = \mathbf{T}^{-1}[x \quad y \quad z]^T + [\Delta x \quad \Delta y \quad \Delta z]^T, \quad (2)$$

where $[\Delta x \quad \Delta y \quad \Delta z]$ is a translation vector describing how much the detector center position is shifted in *x*, *y*, and *z* directions. It should be noted that the misalignment in ϕ_x and ϕ_z causes a displacement in *y*-axis direction. This displacement can be easily corrected by considering magnification factor:

$$M = \frac{d_{SO}}{d_{SD} - y}, \quad (3)$$

where d_{SO} and d_{SD} denote the source-to-object and source-to-detector distances, respectively.

In order to demonstrate the effects of geometric misalignments on the image quality of reconstructed images, we performed numerical phantom simulation. We used the Defrise phantom [7], which consists of seven ovals arranged through *z*-axis. Figure 2 shows simulated projection views of the Defrise phantom for the well-aligned case and misaligned cases along each axis by 10°. The performance of restoration of image distortions based on Eqs. (2) and (3) was also evaluated.

The proposed method was also performed with the experimentally measured data, which were obtained from the laboratory miniaturized CBCT system [2]. The system consists of an x-ray source with small focal spot of 35 μm, a rotational stage with a minimum step of 0.036°, and an x-ray imaging detector with a pixel pitch of 48 μm and an active area of 50 × 50 mm^2. The detector was intentionally disturbed by $\phi_y = 0.8^o$ and Δx =0.559 mm.

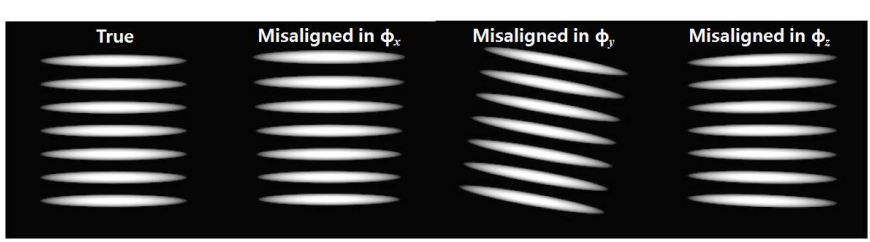

Fig. 2. Various projection images of the Defrise phantom for the defined misalignments.

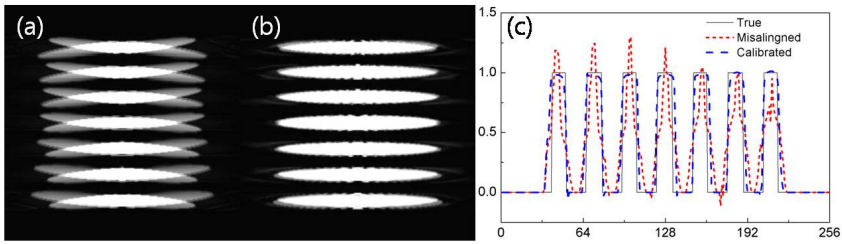

Fig. 3. Longitudinal cross-section views of the reconstructed Defrise phantom for (a) before and (b) after correction procedure. Profiles along the vertical direction for the true Defrise phantom, (a), and (b) are shown in (c).

3. Results and Discussion

Figure 3(a) shows a reconstructed, longitudinal cross-section view of the Defrise phantom when compositely misaligned for every axis by 10°, and Figure 3(b) shows the corrected by the proposed transformed sampling. The profiles of the views in vertical direction are plotted in Figure 3(c). The correction is as good as reasonably.

The experimental results are shown in Figure 4. Figure 4(a) and (c), respectively, show a 3D-rendered and axial cross-sectional view of the capacitor reconstructed when the misalignment was given. Corrected images are correspondingly shown in Figure 4(b) and (d). Correction process is very effective in tomography.

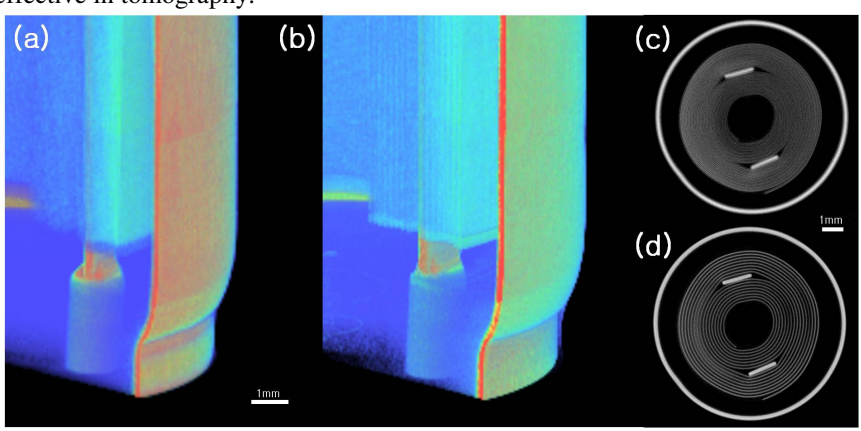

Fig. 4. 3D-redered and axial cross-sectional views of a capacitor: (a) and (c) are before, (b) and (d) are after correction procedures.

It should be noted that the restoration of image distortions in tomography due to the misalignment of a detector in CBCT geometry was carried out

assuming that we had already known the quantity of misalignment. However, it is not easy to measure precisely, and, hence, quantify the geometric misalignments. Ways and means for a precise quantitative measurement of misalignment is challenging, and which is essential for the high-resolution tomography, such as micro- or nano-tomography, typically achieved in highly magnified geometry vulnerable to misalignment.

4. Conclusion

In this study, we evaluated the artifacts caused by geometric misalignments in the reconstructed tomography. In order to remove or reduce the artifacts, we proposed a calibration method based on coordinates-transformed sampling. The performance of the method was verified by numerical and experimental simulations. If we can exactly identify the quantity of misalignments, the proposed method will be very useful in high-resolution tomography applications.

References

1. A. V. Bronnikov, *Opt. Eng.* **38**(2), 381-386 (1999).
2. M. K. Cho, H. K. Kim, T. Graeve, and J.–M. Kim, *Key Eng. Mater.* **321-323**, 1052 (2006).
3. A. C. Kak, M. Slaney, *Principles of computerized tomographic imaging*, IEEE Press (1988).
4. Y. Sun, Y. Hou, F. Zhao, J. Hu, *NDT&E International* **39**, 499-513 (2006)
5. L. A. Feldkamp, L. C. Davis and J. W. Kress, *J. Opt. Soc. Am. A* **1**, 612 (1984).
6. X. Yan and R. M. Leahy, *IEEE Trans. Med. Imag.* **10**(3), 462-472 (1991)
7. H. Kudo, T. Saito, *IEEE Trans. Med. Imaging* **13**(1), 196-211 (1994)

INVERSE ANALYSIS OF STRESS-STRAIN DISTRIBUTION FROM MONITORED RESPONSE OF STRUCTURES

HYU-SOUNG SHIN, DONG-GYOU KIM†

Underground Structure Div., Korea Institute of Construction Technology (KICT)
Ilsan, Kyunggi, 411-712, South Korea

SEUNG-HAN BAEK

Water Purification Div., Mine Reclamation Corp., Seoul, South Korea

This paper is concerned with an inverse problem to capture a variety of stress paths taking place on a structure undergoing a loading, which involves a number of monitoring points. The problem can be taken into consideration by a couple of inverse algorithms based on finite element method: conversional Park's formulation (PF) & proposed FE based displacement controlled formulation (DF). It is, then, focused on to investigate sensitivity on the number and location of monitoring points involved in a structural test for obtaining better stress-strain distribution by the inverse analyses. As a result, the DF shows better results than the PF but the both seem to be sensitive to the monitoring points involved. An optimum monitoring scheme is given for the problem of concern in this study. However, it is important to confirm a well arranged monitoring scheme prior to operating any inverse methodologies

1. Introduction

A loading structure is stressed in complex stress paths. A number of sensors are, as usual, used for measuring the stress levels at certain points in order to monitor safety of the structure with allowable stress levels (strengths). It is economically consumable task although it is necessary for maintaining a structure. Therefore, an inverse analysis should be useful if it can extract stress or strain levels inside the structure from a limit number of displacements easily obtained because it is easier and relatively cheaper to measure displacements rather than stress level.

Motivated by this, an inverse procedure (DF) proposed in this study is compared with the inverse algorithm (PF) formulated by Park et al. [1]. To date, there have been various inverse algorithms, each of which has its own particular purpose. However, most of the inverse algorithms deal with some kinds of parameter identification from either structural tests or field measurements [2,3].

† Corresponding Author: dgkim2004@kict.re.kr

Apart from the various publications, Hisatake's [4] and Park's [1] approaches are closest to the inverse procedure required here. In both, the displacements at certain monitoring points are known and stresses and strains are targets of the inverse procedure. Especially, since the recent work by Hisatake [5] and Hisatake et al. [6], the limitation of the original formulation in terms of the number of monitoring points has been overcome. It becomes much more flexible to apply. Park et al. [1] gave a formulation different from [4,5,6]. However, it leads to the same results as the most recent version of Hisatake's algorithm.

In this section, Park's formulation (PF) based on Hisatake's inverse algorithm [5], as implemented in this study, is applied to back-analyzed stress and strain distributions from the assumed displacements at the monitoring points set up *a priori*. Then, wide-ranging comparative investigations are made between both the strain distributions resulting from the PF and the proposed DF proposed here.

2. Inverse FE procedure from monitored displacements

Based on the FE framework, a stiffness equation can be expressed as follows:

$$\begin{Bmatrix} \boldsymbol{f}_* \\ \boldsymbol{f}_i \\ \boldsymbol{f}_0 \\ \boldsymbol{f}_c \end{Bmatrix} = \begin{bmatrix} \boldsymbol{k}_{11} & \boldsymbol{k}_{12} & \boldsymbol{k}_{13} & \boldsymbol{k}_{14} \\ \boldsymbol{k}_{21} & \boldsymbol{k}_{22} & \boldsymbol{k}_{23} & \boldsymbol{k}_{24} \\ \boldsymbol{k}_{31} & \boldsymbol{k}_{32} & \boldsymbol{k}_{33} & \boldsymbol{k}_{34} \\ \boldsymbol{k}_{41} & \boldsymbol{k}_{42} & \boldsymbol{k}_{43} & \boldsymbol{k}_{44} \end{bmatrix} \begin{Bmatrix} \boldsymbol{u}_* \\ \boldsymbol{u}_i \\ \boldsymbol{u}_0 \\ \boldsymbol{u}_c \end{Bmatrix} \tag{1}$$

where $\{\boldsymbol{f}\}$, $\{\boldsymbol{u}\}$ and $\{\boldsymbol{k}\}$ are a nodal force vector, a nodal displacement vector and a stiffness matrix, respectively, in which $\boldsymbol{f}_\mathrm{i}$, $\boldsymbol{u}_\mathrm{i}$ and $\boldsymbol{k}_\mathrm{ij}$ are the sub vectors/matrices. Subscripts *, *i*, *0* and *c* denote that; *: nodes at which displacements are monitored and nodal forces are zero ($\boldsymbol{u}_*$: known, $\boldsymbol{f}_* = 0$), *i*: nodes at which nodal forces do not act and displacements are unknown, ($\boldsymbol{u}_i$: unknown, $\boldsymbol{f}_i = 0$), *0*: nodes at which external forces act but their values are unknown ($\boldsymbol{u}_0$: unknown, $\boldsymbol{f}_0$: unknown), *c*: nodes at which displacements are prescribed ($\boldsymbol{u}_c$: known, $\boldsymbol{f}_0$: unknown). Eliminating the last row of Eq. (1) lead to:

$$\begin{Bmatrix} \boldsymbol{f}_* - \boldsymbol{k}_{14}\boldsymbol{u}_c \\ \boldsymbol{f}_i - \boldsymbol{k}_{24}\boldsymbol{u}_c \\ \boldsymbol{f}_0 - \boldsymbol{k}_{34}\boldsymbol{u}_c \end{Bmatrix} = \begin{bmatrix} \boldsymbol{k}_{11} & \boldsymbol{k}_{12} & \boldsymbol{k}_{13} \\ \boldsymbol{k}_{21} & \boldsymbol{k}_{22} & \boldsymbol{k}_{23} \\ \boldsymbol{k}_{31} & \boldsymbol{k}_{32} & \boldsymbol{k}_{33} \end{bmatrix} \begin{Bmatrix} \boldsymbol{u}_* \\ \boldsymbol{u}_i \\ \boldsymbol{u}_0 \end{Bmatrix}. \tag{2}$$

Eq. (2) can be rearranged to obtain an explicit expression for the displacement vector as follows:

$$\begin{Bmatrix} \boldsymbol{u}_* \\ \boldsymbol{u}_i \\ \boldsymbol{u}_0 \end{Bmatrix} = \begin{bmatrix} \boldsymbol{L}_{11} & \boldsymbol{L}_{12} & \boldsymbol{L}_{13} \\ \boldsymbol{L}_{21} & \boldsymbol{L}_{22} & \boldsymbol{L}_{23} \\ \boldsymbol{L}_{31} & \boldsymbol{L}_{32} & \boldsymbol{L}_{33} \end{bmatrix} \begin{Bmatrix} \boldsymbol{f}_* \\ \boldsymbol{f}_i \\ \boldsymbol{f}_0 \end{Bmatrix} - \begin{bmatrix} \boldsymbol{L}_{11} & \boldsymbol{L}_{12} & \boldsymbol{L}_{13} \\ \boldsymbol{L}_{21} & \boldsymbol{L}_{22} & \boldsymbol{L}_{23} \\ \boldsymbol{L}_{31} & \boldsymbol{L}_{32} & \boldsymbol{L}_{33} \end{bmatrix} \begin{Bmatrix} \boldsymbol{k}_{14}\boldsymbol{u}_c \\ \boldsymbol{k}_{24}\boldsymbol{u}_c \\ \boldsymbol{k}_{34}\boldsymbol{u}_c \end{Bmatrix} \tag{3}$$

where $\{\boldsymbol{L}\}$ is the inverse matrix of $\{\boldsymbol{k}\}$. Appling the conditions $\boldsymbol{f}_* = 0$ and $\boldsymbol{f}_i = 0$ to Eq. (3) leads to;

$$\begin{aligned} \boldsymbol{u}_* &= \boldsymbol{L}_{13}\boldsymbol{f}_0 - \boldsymbol{U}_* \\ \boldsymbol{u}_i &= \boldsymbol{L}_{23}\boldsymbol{f}_0 - \boldsymbol{U}_i \\ \boldsymbol{u}_0 &= \boldsymbol{L}_{33}\boldsymbol{f}_0 - \boldsymbol{U}_0 \end{aligned} \tag{4}$$

where

$$\begin{aligned} \boldsymbol{U}_* &= \left(\boldsymbol{L}_{11}\boldsymbol{k}_{14} + \boldsymbol{L}_{12}\boldsymbol{k}_{24} + \boldsymbol{L}_{13}\boldsymbol{k}_{34}\right)\boldsymbol{u}_c \\ \boldsymbol{U}_i &= \left(\boldsymbol{L}_{21}\boldsymbol{k}_{14} + \boldsymbol{L}_{22}\boldsymbol{k}_{24} + \boldsymbol{L}_{23}\boldsymbol{k}_{34}\right)\boldsymbol{u}_c \\ \boldsymbol{U}_0 &= \left(\boldsymbol{L}_{31}\boldsymbol{k}_{14} + \boldsymbol{L}_{32}\boldsymbol{k}_{24} + \boldsymbol{L}_{33}\boldsymbol{k}_{34}\right)\boldsymbol{u}_c. \end{aligned} \tag{5}$$

In order to determine a set of $\boldsymbol{f}_0$ which satisfies Eq. (4) a necessary condition of minimising the sum of square of the external forces is employed. A set of Lagrange multipliers represented by the vector $\boldsymbol{\lambda}$ is introduced. Applying this to the first of Eq. (4) leads to;

$$P = \boldsymbol{f}_0^T \boldsymbol{f}_0 - \boldsymbol{\lambda}^T \left(\boldsymbol{L}_{13}\boldsymbol{f}_0 - \boldsymbol{U}_* - \boldsymbol{u}_*\right) \tag{6}$$

in which *P* is the function to be minimised. Then, differentiation of Eq. (6) with respect to $\boldsymbol{f}_0$ and $\boldsymbol{\lambda}$ in turn gives;

$$\begin{aligned} 2\boldsymbol{f}_0 \quad - \boldsymbol{L}_{13}^T\boldsymbol{\lambda} \quad &= 0 \\ -\boldsymbol{L}_{13}\boldsymbol{f}_0 + \boldsymbol{U}_* \quad + \boldsymbol{u}_* \quad &= 0. \end{aligned} \tag{7}$$

By solving the system of Eq. (7), the $\boldsymbol{f}_0$ can be obtained as follows:

$$\begin{aligned} \boldsymbol{\lambda} &= \quad 2\left(\boldsymbol{L}_{13}\boldsymbol{L}_{13}^T\right)^{-1}\left(\boldsymbol{U}_* + \boldsymbol{u}_*\right) \\ \boldsymbol{f}_0 &= \boldsymbol{L}_{13}^T\left(\boldsymbol{L}_{13}\boldsymbol{L}_{13}^T\right)^{-1}\left(\boldsymbol{U}_* + \boldsymbol{u}_*\right). \end{aligned} \tag{8}$$

Substituting $\boldsymbol{f}_0$ in Eq. (4), the unknown displacements at all the nodes can also be determined. From the back-analysed displacements, strains and stresses can be computed at all the gauss points by using the strain matrix $\boldsymbol{B}$ and elastic constitutive matrix $\boldsymbol{D}$. It is obvious that the formulation described here is available only for linear elastic materials. However, if the $\boldsymbol{D}$ matrix is replaced by elastoplastic matrix $\boldsymbol{D}_{ep}$ the formulation having been made so far may also be applicable to inverse analysis of non-linear material behaviour. For this it is necessary to calculate the $\boldsymbol{D}_{ep}$ at any strain state given. However, only an elastic case will be considered in this study.

3. Comparative studies on various monitoring schemes

A two-dimensional plane stress panel set up as shown in Figure 1 is subjected to an in-plane load (=3.5 kN) applied through a stiff plate to a part of the top boundary. On account of the symmetry of the structure only half the panel is modelled. The material of the panel is assumed isotropic and linear elastic. The FE analysis of the panel is first carried out using a standard FE code with 72 iso-parametric elements, each of which has four integration points. The elastic properties used for the panel are; Young's modulus E = 5.0 GPa and Poisson's ratio ν = 0.35. The displacements at the monitoring points in Figure 1 are assembled and subsequently used as input data for each inverse analysis. This is called the 'forward analysis'. The principal strain distribution obtained from the forward analysis provides the target for each inverse analysis.

Four monitoring points ($p_1 - p_4$) are assumed as shown in Figure 1. Two inverse analyses (DF and PF) are carried out using various numbers and combinations of the monitoring points.

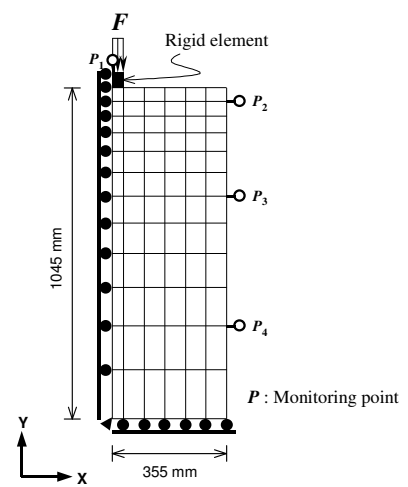

Fig. 1. The plane stress panel used for the forward and the inverse analyses.

3.1. *A single vertical monitoring point (p_1)*

A single monitoring point p_1, which is located at the same position as the applied load and measures movement in the same direction (i.e. vertical), is considered first. In both DF and PF, the geometrical model and elastic properties required are the same as the ones used in the forward analysis. The

vertical displacement at the monitoring point p_1 that was obtained from the forward analysis is applied.

As can be seen in Figure 2 all the results from both inverse schemes show–good agreement with the targets (i.e. the major and minor principal strains obtained in the forward analysis) despite the fact that there was no monitoring of horizontal displacements. This is obviously due to the fact that same ν as the one used in the forward analysis was used in both the inverse analyses. As a result, with a single monitoring point p_1 at which the load was applied in the forward analysis, the strain distribution was properly estimated from the monitored displacement.

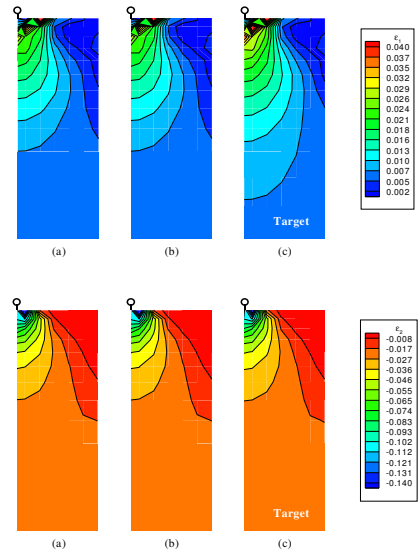

Fig. 2. Comparison of the principal strain distributions from (a) DF, (b) PF, (c) forward analysis - A single vertical monitoring point.

3.2. *A vertical and a horizontal monitoring points (p_1+p_3)*

As shown in Figure 3, both analyses lead to good estimations of the strain distribution. However, part of the major principal strains resulting from the PF was slightly overestimated.

3.3. *One vertical and three horizontal monitoring points (p_1+ p_2+ p_3+ p_4)*

Figure 4 shows that the strain distribution from the DF was estimated reasonably. However, the result from the PF was severely overestimated and erratic, especially around monitoring points. From the results in Figure 4, it is viewed that if the monitoring points

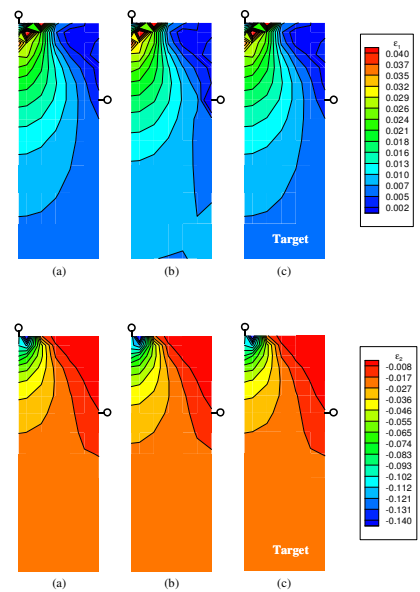

Fig. 3. Comparison of the principal strain distributions from (a) DF, (b) PF, (c) forward analysis - One vertical and one horizontal monitoring points.

are chosen including the loading points in the forward analysis, the results from the DF are acceptable regardless of the position of the other monitoring points. On the other hand, the PF is highly sensitive or even leads to very erratic results depending on the number as well as the position of monitoring points.

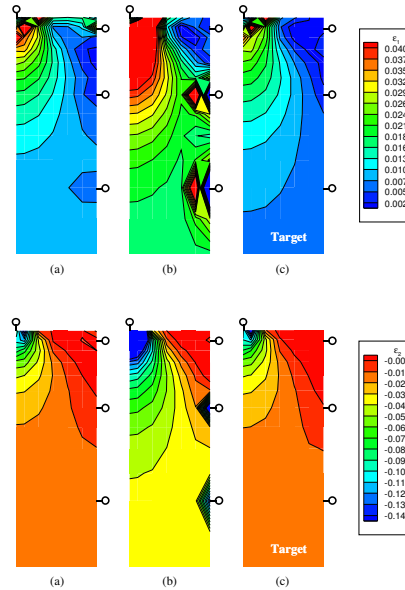

Fig. 4. Comparison of the principal strain distributions from (a) DF, (b) PF, (c) forward analysis - One vertical and three horizontal monitoring points.

4. Conclusion

For inferring stresses or strains in a structure from some monitored displacements, two different approaches have been compared on a plane stress panel with various monitoring schemes. From the comparative studies, it is concluded that the DF has better performance than the PF, provided some of monitoring points are located at the same position as loading points.

By using the inverse algorithm proposed here, it becomes possible to obtain rich stress and strain information from a few numbers of monitored displacements which are relatively cheap to be obtained in engineering.

References

1. 1.Park, C. H., Kim, C. Y. and Lee, H. K., *J. of Korean Society for Rock Mechanics*, **9**, 296-305 (1999).
2. Augello, A. J., Bray, J. D., Abrahamson, N. A. and Seed, R. B., *J. of Geotechnical and Geoenvironmental. Eng.* **124(3)**, 211-1998 1998).
3. Ohkami, T. and Swoboda, G., *Comp. & Geotech.* **24**, 279-295 (1999).
4. Hisatake, M., *Proceeding of International Symposium on Field Measurements in Geomechanics*, 1047-1056 (1983).
5. Hisatake, M., *Proceeding of Computer Methods and Advances in Geomechanics*, 1479-1484 (1991).
6. Hisatake, M., Murakami, J. and Toki, T., *Proceeding of Tunnelling and Ground Conditions*, 493-500 (1994).

OPTIMAL DESIGN OF AN LINEAR MOTION MECHANISM

JONG-SHIN, LEE

Dept. of Computer Aided Mechanical Eng., Juseong College, San 4, Deokam-Ri, Naesu-Ep, Cheongwon-Gun, Chungbuk, Korea

EUNG-JOON, PARK

College of Mechanical Engineering, Ajou Univ. San 5, Wonchun-Dong, Yeongtong-Gu, Suwon, Korea

This study is concerned about the optimization design of supporting parts which takes an important role in appliances with mechanical structure of moving vertically. Firstly, major factors, which influence stress and strain of supporting parts, were identified by factor test. Optimization of design was carried out through response surface methodology, using the major factors which were identified in the factor test. Also the feasibility of design optimization was confirmed by comparison with the results by FEM analysis.

1. Introduction

There are a lot of mechanisms having mechanical structure which operates in an up and down motion. Such a mechanical structure is used in various types of products and automation mechanisms that are used in the production line. The parts supporting the mechanisms which operate in an up and down in a linear motion are very important and require detailed and sensitive design. When there is a problem with a stress or a strain in those parts, the operational system will be seriously affected on the quality such as a noise, and a reduction in the life. Normally, the procedure of developing the product includes a concept and planning phase, a design and development phase, and a production and manufacturing phase. According to the investigation by RAC [1], in order to satisfy the performance and a reliability that are required for the product, 95% of the total expense for the development is spent during the concept and planning phase and the design and development phase from among all 3 of phases of the development. Thus, more effective and prudent development should be conducted during the concept and planning phase and the design and development phase. Moreover, 70~80% of the reliability of the product is determined during these phases, the optimized design having consideration of the reliability should be done from this stage of the phase. It is possible to spend

less time on design and secure the reliability by understanding the important design parts in the mechanisms and determining the optimal design parameter for the part. Also, it is possible to quickly manage to response to a situation when the setting is changed. Thus, the study explains the methods of ensuring the quality and durability by conducting the optimal design which is suitable for a load in the parts of the mechanisms operating in an up and down motion. In order to carry out the study, a factorial design, a response surface analysis, and a finite element method were applied in the part design which is suitable for a load [2][3][4].

2. Model Design and Optimization

2.1. *Model Design*

Figure 1. illustrates a supporting part of the mechanism which operates in an up and down motion of a linear movement. The model for the structure of the linear movement used was a structure that is actually used in the medical instruments. The material of the supporting part used for the study was SS440, under consideration of the manufacturing expense and the productivity. There are 3 supporting parts installed with corresponding bolts predetermined distance away from each other on the body, and underneath of each supporting part has a bearing installed. Each bearing does a rolling contact with a processed flat layer, which creates a structure where the driving shaft can operate in an up and down motion.

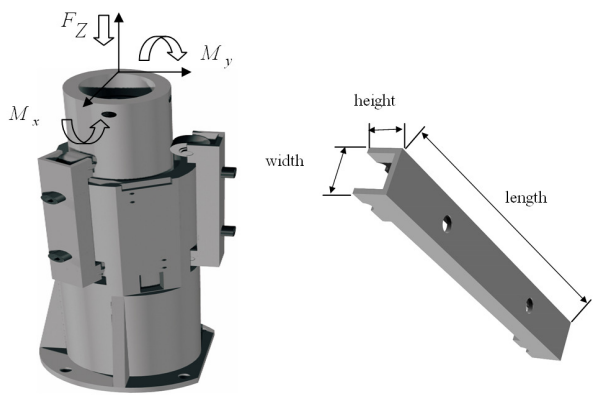

Fig. 1. Model for Optimization.

2.2. *Factorial Design*

The factorial design is effective on estimating a main effect and an interaction of all factors. In this study, the factorial design was conducted in order to search for a main factor which affects the stress and strain in the supporting part. The width (w), length (ℓ), and height (h) which are determined to be important influences on the shape of the supporting part were selected as factors to conduct the experiment. The main effect and the interaction of each factor were estimated through a factorial design, which were used as design factors for optimizing the response surface analysis.

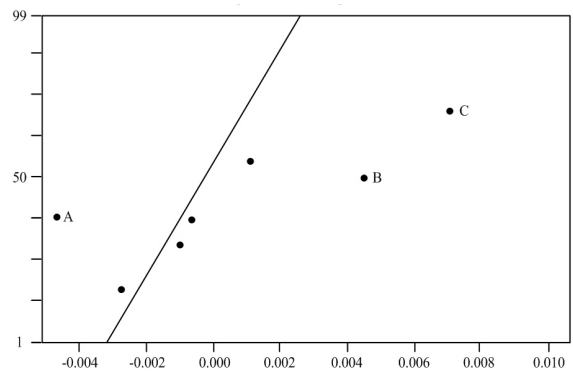

Fig. 2. Normal probability of the standard effects (response is stress, Alpha = .10).

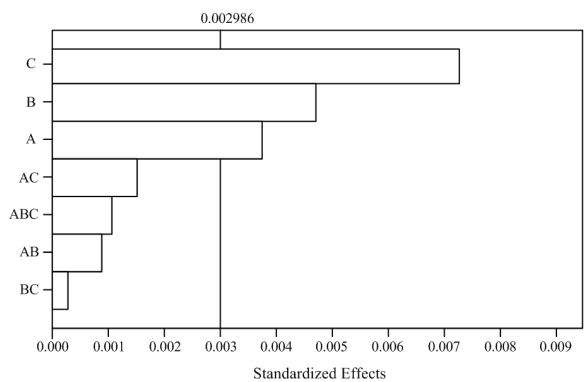

Fig. 3. Pareto chart of the standardized effects (response is stress, Alpha = .10).

There are 3 factors in the study, and the levels of all factors were set to 2. Here, it is to find the important factor rather than strictly dividing them, and therefore the alpha of the level of significance was set as 0.1. Figure 2. shows

that the effect which is not significant is gathered near the straight line, which means that further it goes, it is likely to be significant. Figure 3. also shows that each factor A, B, and C are significant. Here, A represents the width, B represents the length, and C represents the height. Also, the interaction between each factor is not significant. Therefore, 3 factors were determined as important factors affecting the stress and the strain, and thus the optimal design was carried out.

2.3. *Response Surface Methodology*

The response surface analysis is a method which analyzes the outcome value of the input variable and which equation the input variable has when the optimal condition is found through ANOVA or factorial design. If there is a curvature in the response variable, the response surface deign is used. The response surface design can be designed to be close to the optimal response value. In this study, the design variable was divided into 3 types such as a width (w), a length (ℓ), or a height (h). "w" that is used in the response surface analysis used 2 levels such as 195mm, and 205mm, and "h" used 2 levels such as 19mm, and 24mm. The result obtained from the response surface analysis is shown in Figure 4..

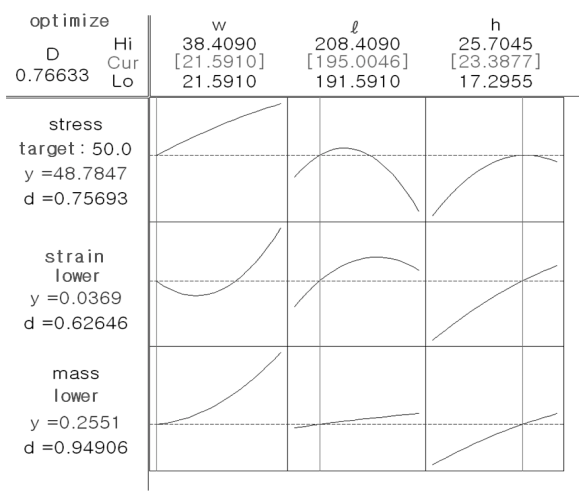

Fig. 4. Optimized values.

As a result of the ANOVA, the linear term and the square term were significant for the stress, whereas the interaction was not significant. Also, the square term was significant for the strain, whereas the linear term and the interaction were not significant. Therefore, the interaction was excluded in the response surface analysis, since it is not significant.

The changes of the response value for all levels of the factors were investigated by using a contour plot. The values were obtained according to changes of w, l, and h. It was found out that the response values such as the stress, the strain, and quantity can be varied according to changes of 3 factors. The optimization is possible since there is a curvature in the response surface. The response value that is to be optimized was set to 50MPa as a maximum stress in consideration of the safety factor. Also, the minimum values of the strain and the quantity were used for optimization. As a result of the analysis by using the response surface analysis, the optimization was achieved at w=21.59mm, ℓ =195mm, h=23.39mm. Fig. 4 shows the optimized result by the response surface.

3. Finite Element Analysis

The finite element analysis on the supporting part was conducted in this study. The actual load used in the medical instrument was ser as an external load, which is 22,500 Nm of the y-axis torque, 5,000 Nm of the x-axis torque, and 150N of z-axis load. In order to calculate the stress and the strain of the supporting part, ANSYS DesignSpace was used. The interpretation was conducted based on the closest value of the optimal condition obtained by the response surface analysis, which is w=22mm, ℓ =195mm, h=23mm. Figure 5. shows the interpretation result of the strain, and Figure 6. shows the interpretation result of the stress.

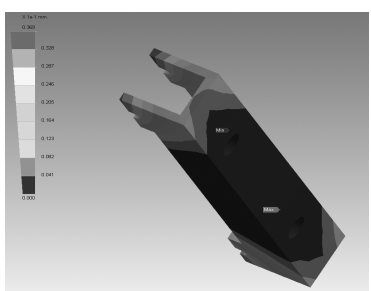

Fig. 5. Strain Contour.

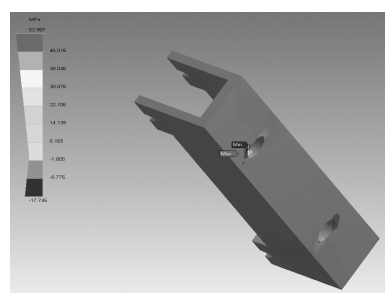

Fig. 6. Stress Contour.

As a result of the interpretation, the maximum stress was 52.8MPa, and strain was 0.0369mm. According to these values, there are differences of 5.6% and 5.4%, which shows that the optimization was satisfactorily performed, when comparing with the optimal requirement condition, the maximum stress of 50MPa, and the strain of 0.035m. It is determined that the error is calculated from the values approximated for the optimization and the errors occurred during the optimization.

4. Results

In this study, the optimal design of the part supporting the mechanism which operated in an up and down motion in a linear movement. The supporting part in the structure having the up and down motion is very important. The factorial design and the response surface analysis were used as methods for optimization. The main factor which affects the stress and the strain was selected by using the factorial design, and the optimal value of the main factor was calculated by using the response surface method. Also, the optimal value was compared with the above-mentioned value by using the finite element analysis. In the case of the model used in the study, the width, the length, and the height were used as main factors. As a result of performing the optimization, the closest optimal condition can be obtained at the condition where w=22mm, ℓ =195mm, and h=23mm. Also, it is confirmed that the result is very satisfactory since there is around 5% of an error in the interpretation result obtained by using the optimal result and the finite element analysis.

References

1. RAC, *Blueprints for Product Reliability*, (1996).
2. Jasbir S. Arora, *Introduction To Optimum Design*, Mcgraw-Hill International Editions, (1994).
3. R. H. Myers, and D. C. Montgomery, *Response Surface Methodology: Process and Product Optimization Using Designed Experiment*, Jon Wiley & son, (1995).
4. S.S. Rao, *Reliability-Based Design*, McGraw Hill Inc (1992).

EFFECTS OF PULSE TRAIN CHARACTERISTICS ON THE THROUGH TRANSMISSION PULSED EDDY CURRENT SIGNAL

YOUNG-KIL SHIN, DONG-MYUNG CHOI

School of Electronic and Information Engineering, Kunsan National University, San 68, Miryong-Dong, Kunsan, Chonbuk, 573-701, Korea

Effects of pulse width and period on pulsed eddy current (PEC) signal are investigated by using a combination of two numerical methods. Through transmission type PEC testing is modeled and signal responses due to varying thickness are studied. The time taken to reach the peak amplitude of step response is first examined and those from maximum and minimum thickness are used as the pulse width. Results show that the peak amplitude of PEC signal gets reduced, but the time to peak amplitude is increased as the thickness increases. Results also indicate that the pulse width needs to be shorter if the peak amplitude is used to evaluate the thickness, but when the time to peak is used to evaluate it, the longer pulse width is more useful. Experiment with period variation shows that the period of pulse should be more than 12 times the pulse width so as the PEC signal to die out. Otherwise, peak value of signal reduces and converges to a value that is always lower than the peak value obtainable from the period mentioned above.

1. Introduction

Pulsed eddy current (PEC) testing differs from sinusoidal eddy current testing in that a pulse of current is induced in the test object [1]. As an input to PEC test, it is usual to use a train of pulses instead of a single pulse. Pulse train consists of series of *on* and *off* time of input current. A period includes one *on* and one *off* time. The *on* time is called the pulse width. In this paper, effects of pulse width and period variations on PEC signal are investigated. Through transmission type PEC testing is modeled by a combination of finite element method and backward difference method and PEC signals from aluminum and inconel plates are considered.

The time taken to reach the peak amplitude of a step response is first sought to yield the biggest peak value of PEC signal and those from maximum and minimum thickness are used as the pulse width in the numerical modeling. PEC signals from various thicknesses are calculated and signal features such as peak amplitude and the time taken to reach the peak value are examined to find a

better way to evaluate the plate thickness. Also, four different periods of pulse are tested to find the proper *off* time before the next pulse.

2. Numerical Methods

Pulse input current induces pulse eddy currents in a test plate so that magnetic fields change with time. Therefore, a transient analysis is applied to predict PEC signal behavior. In this paper, the finite element method is used for spatial modeling and the backward difference method is used for temporal analysis [2,3].

The governing equation for PEC testing is

$$\nabla\times\left(\frac{1}{\mu}\nabla\times\overline{A}\right)=\overline{J_S}-\sigma\frac{\partial\overline{A}}{\partial t} \tag{1}$$

where μ, σ, $\overline{J_s}$, $\overline{A}$ are permeability, conductivity, pulse current density vector, and magnetic vector potential, respectively. In this work, Eq. (1) is written using a cylindrical coordinate system. Applying the finite element formulation and the backward difference method for space and time respectively, the following recurrence relationship is obtained and the magnetic potential at any time can be calculated step by step.

$$\left[\frac{1}{\Delta t}[C]+[S]\right]\{A\}^{n+1}=\{Q\}^{n+1}+\frac{1}{\Delta t}[C]\{A\}^{n} \tag{2}$$

The signal in PEC testing is the electromotive force induced in the sensor coil so that it can be calculated as follows.

$$V_{emf}=\frac{\{A\}^{n+1}-\{A\}^{n}}{\Delta t}2\pi r_c \tag{3}$$

where r_c is the centroidal radius of a coil element.

Analysis model of through transmission PEC probe is shown in Figure 1. Exciter and sensor coils are located at either side of the test plate. Ferrite core is used in the sensor.

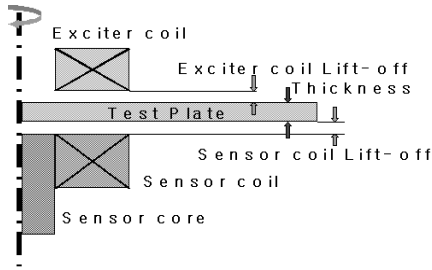

Fig. 1. Through transmission pulsed eddy current probe.

3. Effects of Pulse Width

PEC signals due to thickness variation of aluminum and inconel plates are investigated. To yield the biggest peak value of PEC signal, the step response is first investigated as shown in Figure 2 (a) and Figure 4 (a) and the time taken to reach the peak amplitude is monitored. Since the time to peak value increases with thickness, those from maximum and minimum thickness are selected and used as the pulse width. Resulting signals from aluminum and inconel plates are shown in Figure 2 (b), (c) and Figure 4 (b), (c), respectively. When the pulse width is too short, the peak amplitude is less than that of step response. If the pulse width is long enough, signal passes the peak point and reduces somewhat before the steep drop, which is caused by the pulse-off. Peak amplitude and the time to peak value are monitored and their behaviors due to varying thickness are drawn in Figure 3 and 5. These figures indicate that the pulse width needs to be shorter if the peak value is used to evaluate the thickness, but when the time to peak value is used to evaluate it, the longer pulse width would be more useful.

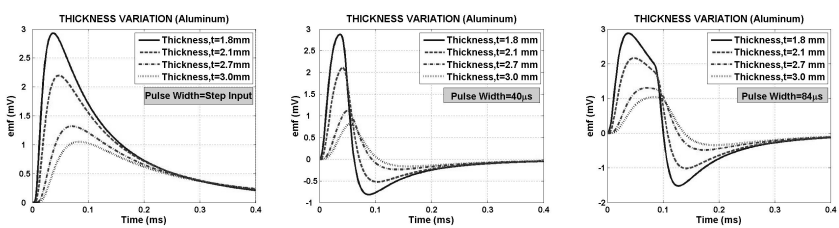

(a) Step response (b) Pulse width = 40 μS (c) Pulse width = 84 μS

Fig. 2. Step response and PEC signals from aluminum plates with different pulse width and thickness.

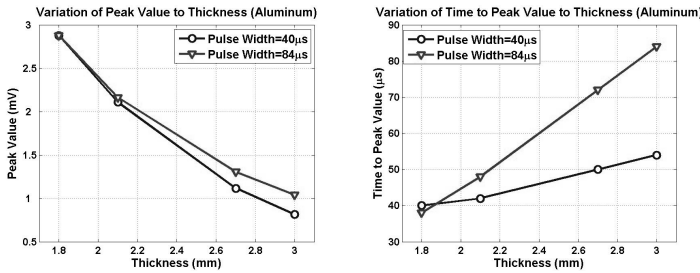

(a) Peak value (b) Time to peak value

Fig. 3. Behavior of peak value and the time to peak value due to varying thickness obtained from aluminum plate with two different pulse widths.

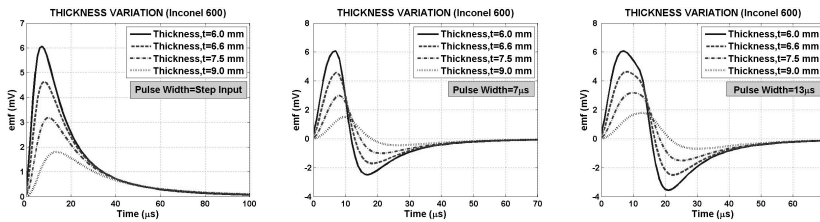

(a) Step response (b) Pulse width = 7 μS (c) Pulse width = 13 μS

Fig. 4. Step response and PEC signals from inconel plates with different pulse width and thickness.

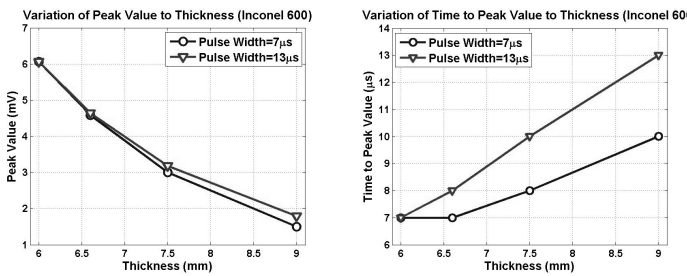

(a) Peak value (b) Time to peak value

Fig. 5. Behavior of peak value and the time to peak value due to varying thickness obtained from inconel plate with two different pulse widths.

4. Effects of Period of Pulse

The pulse width that yields the biggest peak value of PEC signal can be decided by using the time to peak amplitude of the step response. Then, when will be

good to start a next pulse in the pulse train input? To answer this question, 4 periods indicated in Figure 6 are tested for both aluminum and inconel plates.

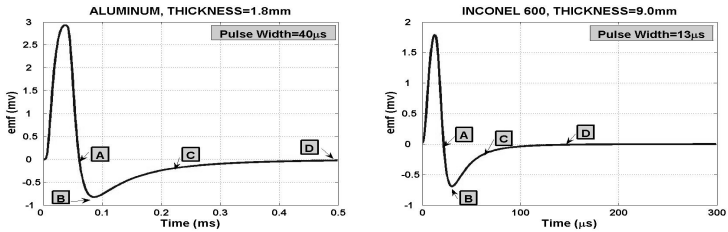

(a) Aluminum (b) Inconel

Fig. 6. Four periods used for experiments are indicated in PEC signals from aluminum and inconel plates.

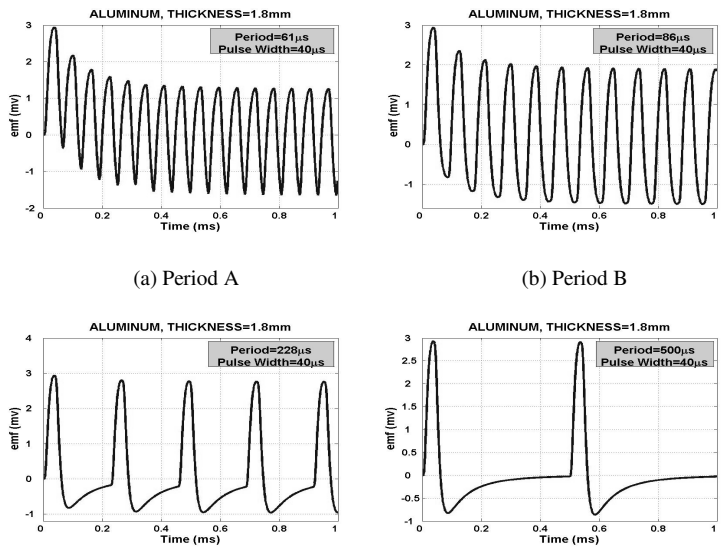

(a) Period A (b) Period B

(c) Period C (d) Period D

Fig. 7. Pulse train PEC signals from aluminum plate with four different pulse periods.

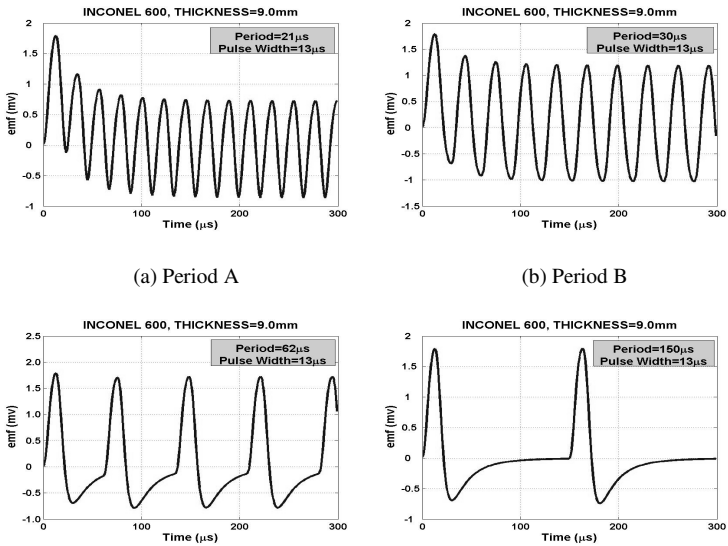

(a) Period A (b) Period B

(c) Period C (d) Period D

Fig. 8. Pulse train PEC signals from inconel plate with four different pulse periods.

Figures 7 and 8 show pulse train PEC signals by using different pulse periods and they are from a 1.8 mm thick aluminum plate and a 9 mm thick inconel 600 plate. If the period is not long enough, the peak value of pulse train PEC signal continuously reduces and it takes a while to be stabilized. The converged peak value is always lower than that obtained by using the longer pulse period. These results suggest that the period of pulse needs to be more than 12 times the pulse width so that the PEC signal dies out completely.

5. Conclusion

Numerical modeling of the through transmission type PEC testing is performed and effects of pulse train characteristics are investigated in this paper. To get the biggest signal, the time to peak value of step response is used as the pulse width. Results of pulse width variation study suggest that the shorter pulse width is desired if the peak value is used to evaluate the thickness, while the longer pulse width is needed if the time to peak value is used to evaluate it. Study of period variation shows that the period of pulse should be long enough for a single cycle PEC signal to die out completely before the next pulse starts. Approximately, the period of pulse needs to be more than 12 times the pulse width.

References

1. C. J. Renken, *Materials Evaluation* **3**, 356 (2001).
2. B. Allen, N. Ida and W. Lord, *IEEE Trans. Mag.* **21**, 2250 (1985).
3. R. Ludwig and X. W. Dai, *IEEE Trans. Mag.* **26**, 299 (1990).

A STUDY ON THE CRITICAL FRACTURE PRESSURE ON THE AL_2O_3 CERAMIC CIRCULAR PLATE UNDER SHOCK IMPACT

YOUNG-SHIN LEE*

Director of BK21 Mechatronics Group. Dept of Mechanical Design Engineering, Chungnam National Univ., 220 Gung-dong Yuseong-gu, Daejeon, 306-764, Korea

JUNG-HEE LEE, JAE-HOON KIM, JEONG PYO KONG, KYOUNG JOO KIM

BK21 Mechatronics Group. Dept. of Mechanical Design Engineering, Chungnam National University, 220 Gung-dong Yuseong-gu, Daejeon, 306-764, Korea

SONG-HOE KOO, SOON-IL MOON

Agency for Defense Development, Daejeon, Korea

This paper investigated critical fracture pressure on the Al_2O_3 (Aluminum Oxide, Alumina) ceramic circular plate under shock impact. The diameter of ceramic circular plate is 70 mm. A computational technique for the modeling of ceramic circular plate is presented using an explicit finite element solver. In numerical analysis, the plate models with solid elements are applied. For validation, experimental investigations have been done by the shock tube device. The critical fracture pressure has been measured in this test and is compared with the numerical results. The critical fracture pressure of experimental result is existed between $\mapsto = 75^\circ$ and $\mapsto = 90^\circ$: $\mapsto$ is quarter angle of simply supported portion in numerical analysis.

1. Introduction

Ceramic has many good characteristics such as high strength, high melting, wear resistance, corrosion resistance and so on. Recently, with the improvement of the technology about the production of ceramic, the ceramic materials are being developed. The Al_2O_3 ceramic has a similar characteristic with MACOR class ceramic that the compressive strength is bigger than tensile strength. And the glass ceramic can endure well at a high temperature circumstance and when it is burning, there is no gas. Dome port, having these glass ceramic material properties, exist between the air transport duct and solid rocket booster. When the ramjet is working, from the outer pressure changes, it must destructed by

* Corresponding author. Tel: +82-42-821-6644; Fax: +82-42-821-8894; e-mail: leeys@cnu.ac.kr

itself and removed quickly[1]. But MACOR glass ceramic is expensive then the other ceramic material. So Al_2O_3 ceramic is selected and evaluated the critical fracture pressure.

The dome port cover is fractured by inlet pressure[2]. The concept of this operation is similar to an apparatus of shock tube. Shock tube is an experimental apparatus used for compression wave and expansion wave.

In this paper, the critical fracture pressure on the ceramic circular plate under shock impact is studied. Dynamic analysis with finite element method is performed to predict the critical fracture pressure. For validation, experimental investigations have been done by the shock tube device. The critical fracture pressure has been measured in this test and is compared with the numerical results.

2. Theoretical background

2.1. *Theory of uniformly loaded circular plate*

Consider the case of a circular plate of radius a under a uniformly distributed load P_0. The stresses in plate with clamped edge are expressed by Eq. (1,2)

$$\sigma_r = \frac{3p_0 z}{4t^3}[(1+\nu)a^2 - (3+\nu)r^2] \tag{1}$$

$$\sigma_\theta = \frac{3p_0 z}{4t^3}[(1+\nu)a^2 - (1+3\nu)r^2] \tag{2}$$

And the stresses in plate with simply supported edge are expressed by Eq.(3,4)

$$\sigma_r = \frac{3p_0 z}{4t^3}(3+\nu)(a^2 - r^2) \tag{3}$$

$$\sigma_\theta = \frac{3p_0 z}{4t^3}[(3+\nu)a^2 - (1+3\nu)r^2] \tag{4}$$

Where r is θ and z are component in cylindrical coordinate. ν is Poisson's ratio.

2.2. *Theory of pressure in the shock tube*

Mach number of incident wave is determined by P_4/P_1 of pressure ratio, k of specific heat ratio. This relation is given in Eq. (5).

$$\frac{P_4}{P_1} = \left[\frac{2kM_s^2 - (k-1)}{k+1}\right] \times \left[1 - \frac{a_1(k-1)}{a_4(k+1)}\left(M_s - \frac{1}{M_s}\right)\right]^{-\frac{2k}{k-1}} \tag{5}$$

The pressure ratio of the driven gas pressure behind reflected shock wave (P_5) and driven gas pressure before expansion (P_1) is given in Eq. (6)[4].

$$\frac{P_5}{P_1} = \left[\frac{2kM_s^2 - (k-1)}{k+1}\right] \cdot \left[\frac{(3k-1)M_s^2 - 2(k-1)}{(k-1)M_s^2 + 2}\right] \tag{6}$$

The schematic diagram of shock tunnel is displayed in Fig. 1. Index number 1 is driver gas before expansion, 2 is driven gas behind contact surface, 3 is driver gas after contact surface, 4 is driver gas before expansion and 5 is reflected wave (fractured pressure).

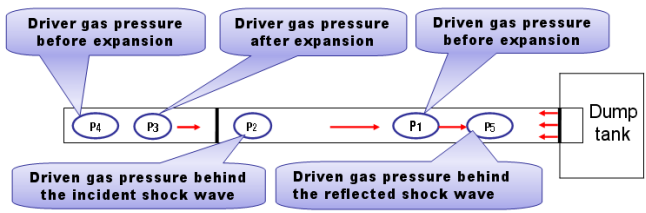

Fig. 1. Schematic diagram of shock tunnel

3. Experimental procedures

The experiments were carried out in the shock tube device. The rupture of the diaphragm in the driver's section generates a shock wave which travels downstream toward the end tunnel. The plates used in this investigation were inserted in the last flange before the dump tank. The circular plates were clamped between the female and male parts of the flange. Air is used for test gas and driving gas in this test.

The materials used is Al_2O_3 (Duckseung Works) ceramics. The chemical composition and mechanical properties of Al_2O_3 ceramics are given in Table 1 [5]. Dimension of the plate is 98 mm in diameter. Thickness is 2.2, 3.2, 4.2 and 5.0 mm.

Table 1. Chemical composition and mechanical properties of Al_2O_3 (960A) [5]

Composition	Approximate weight (%)	Mechanical properties	Value
Aluminum, Al_2O_3	95	Density	3.8 g/cc
Silicon, SiO_2	2.6	Young's modulus, 25℃	371 GPa
Calcium, CaO	0.3	Poisson's ratio	0.22
Magnesium, MgO	0.7	Tensile strength	266.7 MPa
Chromium, Cr_2O_3	1.4	Hardness, Rockwell A (H_{RC})	77.14

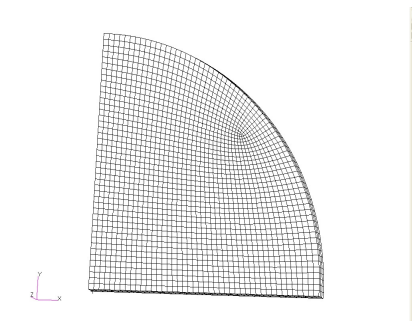

Fig. 2. Finite element model

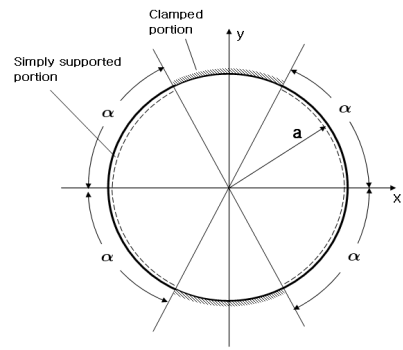

Fig. 3. Configuration of circular plate with partially clamped and simply supported condition:
↦ is quarter angle of simply supported portion

4. Finite element analysis method

The fracture simulation of ceramic circular plate under shock pressure is performed by the finite element method with nonlinear code LS-DYNA. Fig. 2 shows the finite element model on the 1/4 circular plate. Symmetric boundary conditions were used at x and y direction. Boundary conditions, the clamped and simply supported boundary condition, were applied plate circumstance, as shown in Fig. 3. This ↦ presents quarter angle of simply supported portion. The elements used at the analysis were the 8-node solid elements. The totals of 11,096 elements and 44,384 nodes points were applied to describe the finite element model. The element size is less than 0.8 mm and pressure is acted inside face of plate. The whole impulse time was 1 ms and the analysis time was 3 ms in F.E.M.. To analysis the fracture behavior another finite element mode had been modeled. These elements did not share nodes and every element had 2~8 different nodes in the same location. These were necessary to express the

fracture when the damage was break out. The adjacent nodes are constrained tied condition. When the element has tensile strength, tied condition is untied. The fracture-strain is 0.001. Here variation 0.001 was used through the tensile experiment[6].

5. Results and discussion

This section presents the prediction of critical fracture pressure by using the finite element method compared with experimental test results. The circular plate used experimental test assumed to be not perfectly clamped with flange. So the numerical analysis method was performed with various boundary condition which has quarter angle ↦ (0°~90°) of simply supported edge. The numerical results of the critical fracture pressure according to the thickness of ceramic circular plate and partial clamped angle are given in Fig. 4. The critical fractured pressure in test is 10 bar at 3.2 mm and 16.5 bar at 5 mm for Al_2O_3 ceramic circular plate. As the thickness of circular plate increases, the critical fracture pressure gradually increases in test.

When ↦ = 0°, the plate is fully clamped edge condition, the critical fracture pressure of numerical analysis has 3 times over than experimental fracture pressure. When ↦ = 90°, the fully simply supported edge condition, the critical fracture pressure of numerical analysis is lower than experimental fracture pressure. As the thickness of circular plate increases, the difference between fracture pressure of experiment test and fracture pressure of numerical analysis increases at ↦ = 0°, clamped condition.

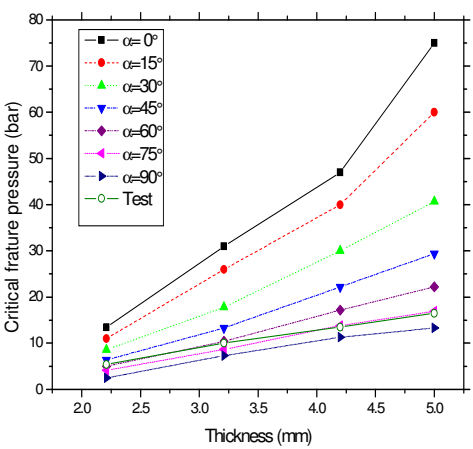

Fig. 4. Comparison of critical fracture pressure according to quarter angle ↦ of simply supported edge on the circular plate.

Table 2. Critical fracture pressure of circular plate according to the thickness and angle of simply support edge in numerical analysis

↦	2.21 mm	3.21 mm	4.20 mm	5.00 mm
0°	13.5	31.1	47.5	75.3
15°	13.0	26.2	44.1	64.3
30°	8.5	17.8	30.1	40.7
45°	6.3	13.3	22.2	29.4
60°	5.1	10.4	17.2	22.2
75°	4.1	8.6	13.8	16.9
90°	2.5	7.3	11.3	13.3
Test	5.4	10	13.5	16.5

At 2.21 mm and 3.21 mm thickness, the critical fracture pressures of experimental results are existed between ↦ = 60° and ↦ = 75°. At 4.20 mm and 5.00 mm thickness, the critical fracture pressures of experimental results are existed between ↦ = 75° and ↦ = 90°.

6. Conclusions

In this study, the critical fracture pressure has been measured in this test and is compared with the numerical results by changing thickness and quarter angle ↦ of simply supported portion. The conclusions of this study are as follows:

1. When ↦ = 0°, the plate is fully clamped edge condition, the critical fracture pressure of numerical analysis has 3 times over than experimental fracture pressure. When ↦ = 90°, the fully simply supported edge condition, the critical fracture pressure of numerical analysis is lower than experimental fracture pressure.
2. The critical fracture pressures of experimental results are existed between ↦ = 60° and ↦ = 90°:↦ is quarter angle of simply supported portion.

Acknowledgments

This work was supported by Defense Acquisition Program Administration and Agency for Defense Development under the contract UD060012AD.

References

1. P. R. Scannell, N. R. Milich and E. O. Kalil, *Advanced Integral Roket Ramjet Port Cover Development,* AIAA, No. 1980-1279(1980).
2. F. F. Webster, *Liquid Fueled Integral Rocket/Ramjet Technology Review*, AIAA, pp. 1978-1108(1978).
3. G. Briassulis, J. H. Aqui, J. Andreopoulos and C. B. Watkins, *A Shock Tube Research Facility for High-Resolution Measurements of Compressible Turbulence*, Experimental Thermal and Fluid Science, Vol. 13, pp. 430-446(1996).
4. D. R. Smith and A. J. Smits, *The Effects of Steamline Curvatrue and Pressure Gradient on the Behavior of Turbulent Boundary layers in Supersonic Flow*, AIAA, pp. 94-2227(1994).
5. E. Soppa, S. Schmauder, G. Fischer, J. Brollo and U. Weber, *Deformation and damage in Al/Al_2O_3*, Computational Materials Science, Vol. 28, pp. 574-586(2003).
6. D. H. Kim, J. H. Kim, Y. S. Lee, N. S. Rho, C. K. Park, K. S. Lee, and S. I. Moon, *Study on Dynamic Fracture Characteristic and Application to the Structure of Advanced Glass Ceramic*, International Journal of Modern Physics B, Vol.20, No.25-27, pp. 3908-3913, (2006).

A STUDY ON EVALUATION OF SHEAR STRENGTH OF NATURE-FRIENDLY COSTAL ENVIRONMENT BLOCK CONNECTION

CHUN HO KIM

Department of Civil Engineering, Joong Bu University, Chubu-myeon ,Geumsan-gun, Chungcheongnam-do, Korea, 312-702, The Republic of Korea

As ships moor in a quay wall or a lighter's warf, reflected wave caused by advancing wave into the port or port wave creates resonance to heighten wave height in a harbor, which makes difficult to keep appropriate level of temperature, impedes for ships to moor and load or unload, and increase damage rate of small ships by collision. Therefore a lot of studies have been done about wave absorbing blocks. Wave absorbing blocks are assembled on site so to require shear strength evaluation of connection. Thus the study hear is intended to evaluate share strength by getting sliding load and fracture strength of the C.E block connection through a non-linear boundary FEM analysis and a shear test on the connection and to develop a method to evaluate shear strength of connection only with a FEM analysis through computer simulation but without a further test. The test showed that the non-linear boundary analysis of the nature-friendly C.E. block connection can be a model to evaluate shear strength of the connection.

1. Introduction

Recent sea-level rising by global warming is expected to give a lot of damage to Korea of which three sides face the ocean. Installation of previous simple shapes and artificial concrete structure as a protection and lack of a capacity to prevent beach erosion are causing other damages.

In addition, the resonance caused by reflected wave, which results from harbor advancing wave or harbor wave in a quay wall or a lighter's warf where ships moor, heightens wave height in a harbor that makes difficult to keep appropriate temperature and impedes mooring or load/unload of ships. As a damage rate by collision of small ships is high, many studies are under proceeding about various wave absorbing blocks.

Since wave absorbing block is for assembling construction on site, evaluation on shear strength of connection is required. Therefore the study is intended to evaluate shear strength by getting sliding load and fracture strength of the C.E. block connection through a non-linear boundary FEM analysis and a shear test on the connection and to develop a method to evaluate shear strength

of connection only with a FEM analysis through computer simulation but without a further test.

2. Nature-friendly C.E. Block

Nature-friendly C.E blocks supplement environmental problems and improve constructability and applicability. Also they can use areas neighboring the see level so that water-friendly environment can be built. Thus, they are effective to obtain space and provide habitants for ocean organism and fry by an inner porous part of the block installed on the bottom. The following shows Figure 1 composition of the nature-friendly C.E. block, of which section shape is like Figure 2 and unit is mm.

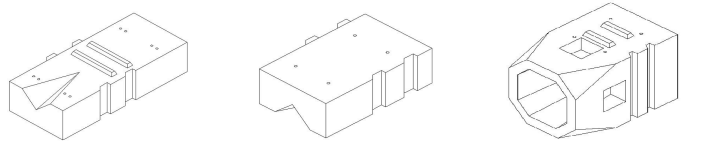

Base block Top block C.E block

Fig. 1.

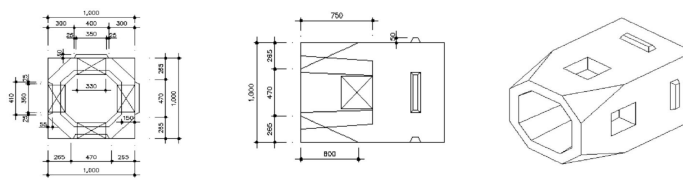

Front view Side view Perspective view

Fig. 2.

Main materials of the nature-friendly C.E. blocks include concrete and steel reinforcement. Concrete has design strength (f_{ck}) of 33MPa, a temperature expansion efficient (E_c) of 25,851MPa, a temperature expansion coefficient (α) of 1.0×10^{-5}/°C, and a poisson's ratio of 0.17.

3. Shear Test of Nature-friendly C.E. Block Connection

3.1. *Test Method*

When soil pressures work on the back of the nature-friendly C.E. block or by collision between ships, it is necessary to evaluate shear strength of the shear key that creates shear resistance of the block. Thus, a shear test was conducted to the nature-friendly C.E. block connection in order to measure sliding load and

fracture strength of the connection. A specimen shear key was manufactured copying that of a real block like the connection specimen.

After A specimen was located in the following frame, male and female specimen were piled up each other Figure 3. The installation of various strain gauges, displacement system and introductory accumulator is like below. A load cell among them is manufactured by CAS with the maximum capacity of 980kN.

In the shear test of the connection, A specimen of which design strength(f_{ck}) is 33MPa had vertical prestress of 9.8kN×4, 19kN×4 and 29kN×4 while each of them was positioned in a load cell of 980kN capacity. Then, the load was increased from 0 to 980kN. The applied axial force and load position are like followings Figure 4.

Fig. 3. Specimen deferment

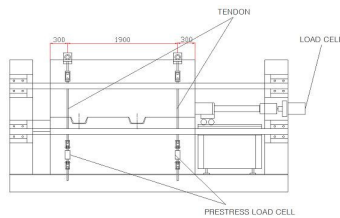

Fig. 4. The introductory axial force and load position

3.2. *Test Result and Implication*

The shear test on the nature-friendly C.E. block connection was conducted to measure sliding load and fracture strength of the connection. Results are as follow.

Specimen 1 with the applied axial force of 9.8kN×4 had sliding with 58kN load Figure 5. Specimen 2 with 19kN×4 of the applied axial force had sliding with 107kN load Figure 6. Specimen 3 under 29kN×4 had sliding with 117kN load Figure 7. The Specimen 4 under 9.8kN×4 had sliding with 78kN load Figure 8. And there was elastic behavior after contacting the shear key. The shear key was not fractured even when load was increased up to 980kN which is the limit of load cell capacity. Thus, it is verified that primarily it resists to some shearing forces with friction against existing load but resists with shear strength of the shear key once the shear key is contacted. Since the fracture strength suggested by Concrete Structure Design Standard is, it was not destroyed under the load bigger than. Thus, it is verified that the shear key satisfies shear strength.

Fracture strength is Concrete has design strength (f_{ck}), effective height(d), width(b_w) given by: $v_c = 1/6\sqrt{f_{ck}}\, b_w d = 1/6\sqrt{33}\times 1100\times 300 = 316kN$ and there are two shear keys 316kN × 2 = 632kN.

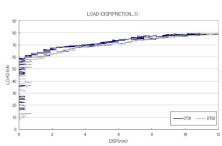

Fig. 5. Specimen 1

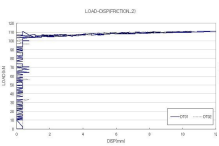

Fig. 6. Specimen 2

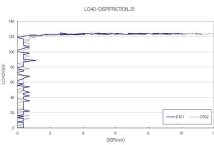

Fig. 7. Specimen 3

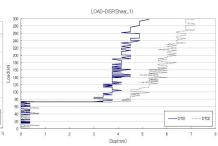

Fig. 8. Specimen 4

A shear test on the nature-friendly C.E. block connection was conducted to measure shear strength of the connection. The result is like followings. First of all, the more the applied axial force, the bigger the sliding load as shown at table 1. The friction coefficient was move than 0.6.

Table 1. Sliding load and Friction Coefficient by Applied axial force.

	Applied axial force	Sliding load	The coefficient friction
A specimen 1	9.8kN × 4 = 39kN	58 kN	0.67
A specimen 2	19kN × 4 = 78kN	107 kN	0.73
A specimen 3	29kN × 4 = 118kN	117 kN	0.99
A specimen 4	9.8kN × 4 = 39kN	78 kN	0.5

4. Non-linear Boundary Analysis of Nature-friendly C.E. Block Connection

4.1. *Interpretation Method*

To develop a system to evaluation shear strength of the nature-friendly C.E. block connection only with a FEM analysis through computer simulation without a test upon evaluation, a non-linear boundary FEM analysis was conducted to the connection using a FEM program, LUSAS. In the non-linear boundary analysis of the connection, a shear key was considered to draw on stress and sliding load of the connection. The materials with test is same. The non-linear boundary FEM analysis of the nature-friendly C.E. block connection was conducted in a 2-dimensional X-Y plane. The load combination includes dead load(automatically calculated by the program) and load horizontally provided from 0 to 980kN. The boundary condition is composed figure 9 of a hinge support that limits translation displacement of x and y axis, a roller support that limits translation displacement of the x axis, and a slide line that considers contact friction figure 9. The friction coefficient of a contact surface was applied as 0.6 by using a safety ratio(S) of 1.2 based on the test result.

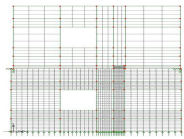

Fig. 8. Boundary condition

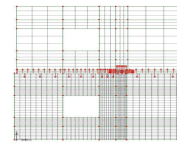

Fig. 9. Slide line

4.2. *Interpretation Result and Implication*

To evaluate shear strength of the nature-friendly C.E. block connection only with a FEM analysis through computer simulation without a test upon evaluation, a non-linear boundary analysis was conducted by applying a friction coefficient of 0.6 obtained from the shear test of the connection. The results are like followings.

It is verified that stress is concentrated on the shear key when load of 0.98kN is applied figure 10. When load is 98kN figure 11, separated shear keys are contact each other like below. Under load of 196kN figure 12, the shear keys are contact and the stress distribution range around the shear keys increases.

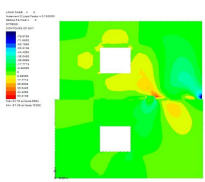

Fig. 10. Shear stress
(load 0.98kN)

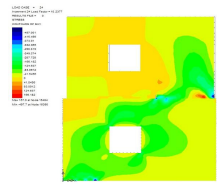

Fig. 11. Shear stress
(load 98kN)

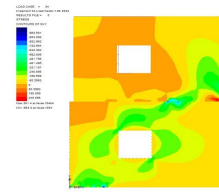

Fig. 12. Shear stress
(load 196kN)

Then, sliding occurs with load of 51kN figure 13 and contacts with a shear key when displacement reaches to 10mm. Load increases again and the elasticity transforms. As shown figure 14 below, sliding occurred with load of 51kN to reduce stress, and there were load increase and elasticity transformation. In addition, stress is concentrated on a shear key so to require appropriate reinforcement in design.

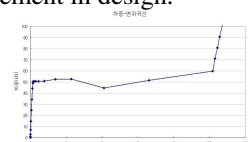

Fig 13. Non-linear boundary condition
F.E.M Analysis result load-displacement curve

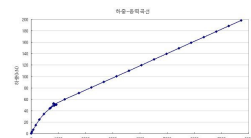

Fig 14. Non-linear boundary condition
F.E.M Analysis result load-displacement curve

5. Conclusion

Although a variety of tests should be conducted to evaluate design and construction status of the nature-friendly C.E. block connection, a non-linear boundary FEM analysis and a shear test were conducted to the connection in order to develop a method to evaluate shear strength of the connection only with a FEM analysis through computer simulation without a further test upon evaluation. The test results are like followings.

1. The shear test of the connection showed that sliding load is 58kN and a friction coefficient is 0.67 when an applied axial force is 39kN. Under 78kN, the sliding load is 107kN and the friction coefficient is 0.73. Under 118kN of applied axial force, the sliding load is 117kN and the friction coefficient is 0.99. It is verified that the more the applied axial force, the bigger the sliding load.
2. The shear test showed that sliding occurs with 78kN load but the connection shear key is not destroyed even the load is increased up to 980kN, which is the limit capacity of a load cell. Thus, under shear force, it primarily resists with friction force on the contact and the shear key secondarily resist after sliding. Since it is not destroyed under the load bigger than fracture strength (632kN) by concrete structure design standard, the shear key satisfies shear strength.
3. Sliding load was estimated as 51kN from the non-linear boundary analysis on the connection where a friction coefficient of 0.6 is used with a safety rate(S) of 1.2 based on the test result. As the shear test of the connection shows the sliding load is 58kN, the non-linear boundary analysis of the connection can be a good model to evaluate shear strength of the connection.
4. For a future non-linear boundary analysis of concrete block and block contact connection, a friction coefficient should be applied as 0.6 when considering a safety rate as 1.2 or as 0.5 when considering a safety rate as 1.5.
5. The study result shows that the non-linear boundary FEM analysis can be used to evaluate shear strength of the nature-friendly C.E. block connection without a test upon shear strength evaluation of the connection.

References

1. Michale. E. M., Ocean Engineering Wave Mechanics, John Wiley & Sons(1972).
2. Chu-Kia Wang, “Reinforced Concrete Design”, Wang Salmon(1983).
3. Ho, S. K. and Rowe, R.K. “Finite Element Analysis of Geosynthetics Reinforced Soil Walls”, Geosynthetics(1993).
4. Jhon, B. H. Handbook of coastal Engineering, McGraw-Hill(2000).

SIMULATION STUDIES FOR THE INFLUENCE OF TOMOGRAPHIC PARAMETERS ON THE IMAGE QUALITY OF DIGITAL X-RAY TOMOSYNTHESIS

J. E. OH

Department of Radiological Science, Yonsei University, Wonju, 220-710, Korea

S. I. CHOI[1], M. S. LEE[1], K. Y. KIM[1], S. Y. LEE[1], H. S. CHO[1, *], B. S. LEE[2], S. KIM[3]

[1]*Department of Radiological Science, Yonsei University, Wonju, 220-710, Korea*
[2]*School of Biomedical Engineering, Konkuk University, Chungju, 380-701, Korea*
[3]*Department of Nuclear Engineering, Cheju National University, Cheju, 690-756, Korea*

In this study, by using the MATLAB® 7.0 program, we investigated the influence of tomographic parameters such as the tomographic angle (θ) and the angle increment between each projection (Δθ) on the DXTS image quality. A simple image reconstruction algorithm, the so-called the modified shift-and-add (MSAA), was studied in order to reduce effectively the blurring artifact that typically occurred in the conventional reconstruction algorithm of shift-and-add (SAA). We evaluated the image quality of the reconstructed images based upon the SAA and MSAA algorithms in terms of the signal-to-noise ratio (SNR), the image uniformity, etc., as a function of tomographic parameters. According to our simulation results, the image quality enhances as the tomographic angle is larger and the angle increment smaller. In addition, the MSAA algorithm seems to be effective for the reduction of the blurring effect. We expect that the simulation results will be useful for the optimal design of a DXTS system for our ongoing application of nondestructive testings.

1. Introduction

The principle of tomosynthesis is not new, but recently digital X-ray tomosynthesis (DXTS) has gained popularity in many areas of medical and industrial applications owing to the recent digital revolution in imaging [1-3]. The DXTS is a 3D imaging technique that has the ability to address shortcomings of conventional X-ray imaging modalities in which all structures in the imaged volume become superimposed onto a 2D radiograph. It refers to a limited-angle technique of 3D image reconstruction with a low X-ray exposure, in which a set of projection data acquired within a limited-tomographic angle are subsequently used to synthesize the whole imaged object, basically by using the

[*] Corresponding author: hscho1@yonsei.ac.kr, +82-33-760-2428 (phone), +82-33-760-2815 (fax)

image reconstruction algorithm of the shift-and-add (SAA). Figure 1 shows (a) a schematic illustration of the DXTS principle and (b) the geometrical structure used in the simulation. Here a sequence of projections within a limited angle are acquired by moving the X-ray tube and the detector oppositely in a linear fashion around a fulcrum on a specific plane, and then all the projection data are properly shifted-and-added such that only the specific plane is focused (i.e., tomographic plane) and others are blurred out. The shift length for the projection acquired at the tomographic angle θ can be calculated as the following equation:

$$Shift(\theta) = \frac{H \cdot \Delta h \cdot \tan\theta}{h} \tag{1}$$

where H is the source-to-detector distance, h is the distance from the source plane to the tomographic plane, and Δh is the distance between the fulcrum plane and tomographic plane.

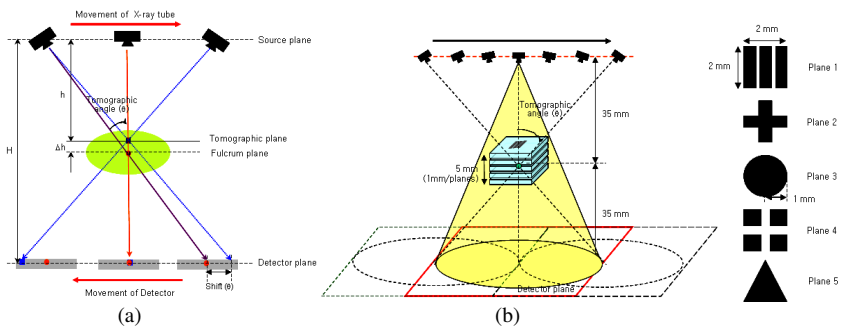

Fig. 1. (a) Schematic illustration of the principle of the DXTS and (b) the geometrical structure used in the simulation.

In this study, by using the MATLAB® 7.0 program, we investigated the fundamental principle of the DXTS and the influence of tomographic parameters, such as the tomographic angle and the angle increment between each projection, on the DXTS image quality. A simple image reconstruction algorithm, the so-called the modified shift-and-add (MSAA), was studied in order to reduce effectively the blurring artifact that typically occurred in the conventional reconstruction algorithm of shift-and-add (SAA).

2. Materials and Methods

2.1. *Simulation Geometry*

As shown in Figure 1 (b), the simulation geometry consists of 5 separate planes with different patterns. All patterns have a size of 2 mm x 2 mm and were set arbitrarily to have a linear attenuation coefficient of unity. The X-ray tube and the detector moved oppositely in a linear fashion and were synchronized for each other. The detector was placed 70 mm below from the X-ray source and the fulcrum plane was located in the middle of the source and detector. We first acquired several projections at the tomographic angles of $\pm 10^o$, $\pm 20^o$, $\pm 30^o$, $\pm 40^o$, $\pm 50^o$, $\pm 60^o$ and the angle increments of 1^o , 2^o , 5^o , 10^o , 20^o and then reconstructed DXTS images from the projection data by using the SAA and MSAA algorithms. The image quality of the final DXTS images was evaluated and compared with each other in terms of the signal-to-noise ratio (SNR), the image uniformity, and so on.

2.2. *Modified Shift-and-Add (MSAA)*

We studied a simple image reconstruction algorithm, MSAA, to reduce the blurring artifact effectively. The MSAA is fundamentally based upon the SAA but has a correction procedure by extracting the blurring artifact from the firstly-reconstructed image data for the whole planes of interest (POIs) and then subtracting it from the firstly-reconstructed image data of the POI to be focused. Here the first step of the correction procedure is performed just by replacing the original image data for the specific POI with zeros. Figure 2 shows the resultant images for each plane of interest reconstructed by using (a) the SAA and (b) the MSAA algorithms at the tomographic angle of $\pm 40^o$ and the angle increment of 5^o.

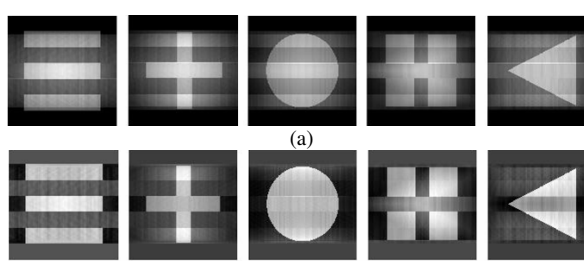

Fig. 2. The resultant images for each plane of interest reconstructed by using (a) the SAA and (b) the MSAA algorithms at the tomographic angle of $\pm 40^o$ and the angle increment of 5^o.

3. Simulation Results

3.1. *Image Quality vs. Angle Increment ($\Delta\theta$)*

Figure 3 shows (a) the resultant images of the plane 3 reconstructed at the angle increments of 1°, 5°, and 10° at a fixed tomographic angle of ± 40° and (b) the grayscale distributions measured in the horizontal direction and in the vertical direction in the middle of the images.

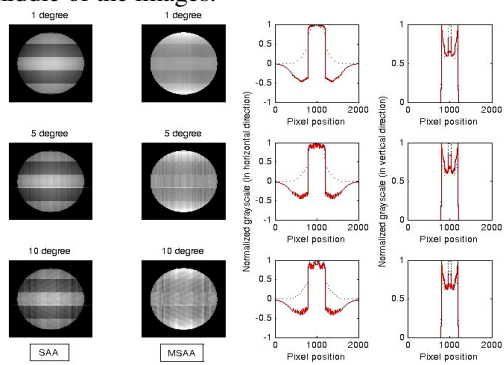

(a) (b)

Fig. 3. (a) Resultant images of the plane 3 reconstructed at the angle increments of 1°, 5°, and 10° at a fixed tomographic angle of ± 40° and (b) the grayscale distribution.

Figure 4 shows the measured SNR (a) in the horizontal direction and (b) in the vertical direction, which is defined as the following equation:

$$SNR = \frac{\overline{\mu_{object}} - \overline{\mu_{BG}}}{\sigma_{object}} \tag{2}$$

where $\overline{\mu_{object}}$ is the mean pixel intensity of the object, $\overline{\mu_{BG}}$ is the mean pixel intensity of the image background, and σ_{object} is the standard deviation of the object.

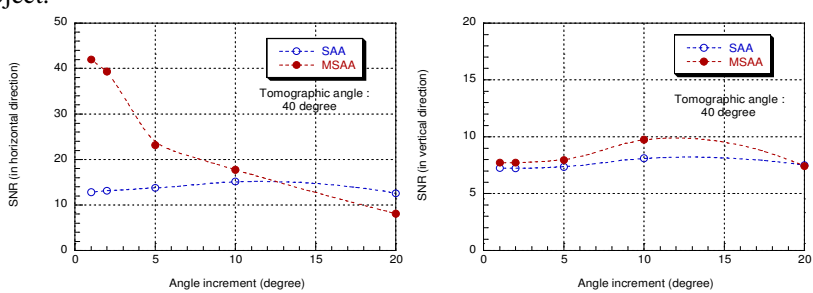

(a) (b)

Fig. 4. Measured SNR (a) in the horizontal direction and (b) in the vertical direction as a function of the angle increment.

As indicated in Figure 4 (b), the measured SNR in the vertical direction was not seriously dependent of the angle increment for both SAA and MSAA algorithms, while in the horizontal direction the SNR improved significantly for the MSAA, as shown in Figure 4 (a), possible due to the parallax effect of the tomography in the scanning direction. The image uniformity with the MSAA was much better than with SAA (see Figure 3).

3.2. *Image Quality vs. Tomographic Angle (θ)*

Figure 5 shows (a) the reconstructed images of the plane 3 with tomographic angles of ± 20°, ± 40°, and ± 60° at a fixed angle increment of 5° and (b) the grayscale distributions measured in the horizontal direction and in the vertical direction in the middle of the images. Figure 6 shows the measured SNR (a) in the horizontal direction and (b) in the vertical direction as a function of the tomographic angle. As indicated in Figure 5 and 6, the measured SNR in both directions was noticeably dependent of the tomographic angle for both SAA and MSAA algorithms, and the image uniformity was better for the MSAA than for SAA and for larger tomographic angle.

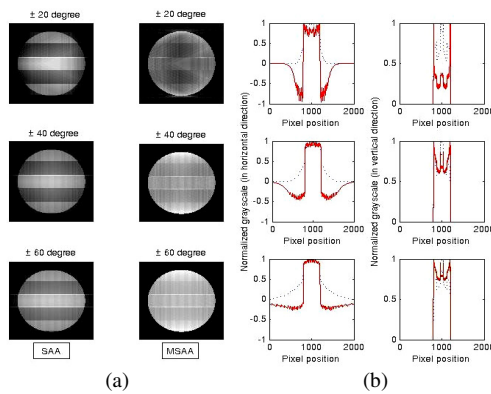

(a) (b)

Fig. 5. (a) Reconstructed images of the plane 3 with tomographic angles of ± 20°, ± 40°, and ± 60° at a fixed angle increment of 5° and (b) the grayscale distributions.

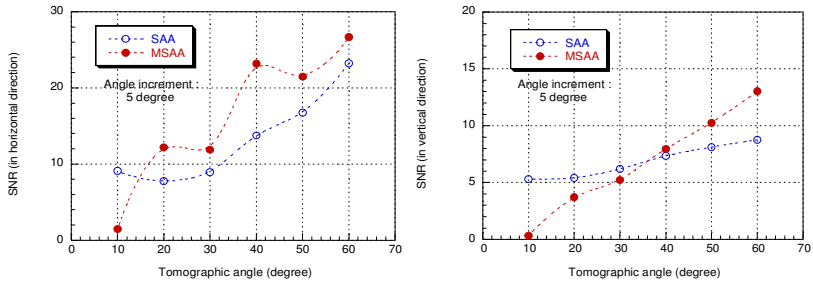

(a) (b)

Fig. 6. Measured SNR (a) in the horizontal direction and (b) in the vertical direction as a function of tomographic angle.

4. Conclusions

For the optimal design of a digital X-ray tomosynthesis system in our ongoing application of nondestruction testings, we evaluated the influence of tomographic parameters such as the tomographic angle and the angle increment on the image quality in term of the signal-to-noise ratio (SNR), the image uniformity, and so on. A simple reconstructed algorithm, MSAA, was also studied and found to be effective for the reduction of the blurring artifact. The image quality of the DXTS improved as the tomographic angle increased and the angle increment decreased. More detail evaluation of the influence of the tomographic parameters on the image quality are being performed.

Acknowledgments

This work was supported by the Basic Atomic Energy Research Institute (BAERI) program of the Ministry of Science and Technology (MOST) under contract No. M2-0376-03-0000.

References

1. J. Dobbins III and D. Godfrey, *Phys. Med. Biol.*, **48**, 65 (2003).
2. J. Liu, D. Nishimura, and A. Macovski, *IEEE Trans. Med. Imaging.*, **8 (2),** 168 (1989).
3. L. T. Niklason, *Radiology*, 205, 399 (1997).
4. R. J. Warp, D. J. Godfrey, and J. Dobbins III, *Proc. SPIE*, **3977**, 376 (2000).
5. J. Duryea, J. Dobbins III, and J.A. Lynch, *Med. Phys.,* **30**, 325 (2003).
6. Christian Bernhardsson, *Medical Radiation Physics Clinical Sciences, Lund University*(2006).

THE CHARACTERISTICS OF BILGE SEPARATION SENSOR SYSTEM FOR IMPROVING ACCURACY

WOO-SEONG CHE* KYONG-WOO KIM*

**Dept. of Mechatronics Engineering, Tongmyong University*

HYU-SANG KWON†

Fluid Flow/Acoustics & Vibration Engineering, Korea Research Institute of Standards and Science(KRISS), 1 Doryong-dong Yuseong-gu, Daejeon, 305-340, Korea

Up to date bilge separation sensor has to be extremely accurate and highly reliable. To design and build such a bilge separator, a precise oily water separation level sensor that distinguishes oil from water is critical. Three dimensional simulations have been carried out to figure out the characteristics of capacitive level sensors, which grounds the finding of the parameters required to design the sensors. By parallel positioning of level sensors as well as digital implementation of the operation circuit, the parasitic capacitance problem which is inherent to capacitive level sensors has been taken care of. It has been shown that proposed system is immune to environmental noise. This paper concludes with the future research direction that can be pursued with the newly defined parameters of the capacitive level sensors.

1. Introduction

Strict regulations have been being made to combat the increasing threat of global environment pollution. One of the severe environmental contamination stems from the oily sewage, chemicals and harmful substances produced by marine vessels. In particular, Marine Environment Protection Committee (MPEC) enforces the use of Bilge Separator in every vessel [1]. Those requirements are described in the annex of MARPOL (The International Conventions for the Prevention of Pollution from Ships). Bilge separator put in force has to be able to screen the bilge by no more than 15 PPM resolution and is shown in Figure1 [2]. Bilge separator separates the oil and water by sensing the difference between specific gravities. Level detecting sensors are used to measure the height of oily substances and capacitive type sensors are most widely accepted [3].

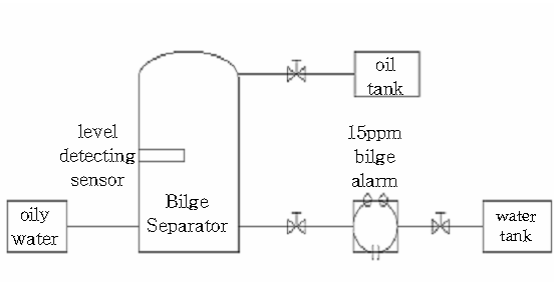

Fig. 1. Block diagram of bilge separator

In this paper, three dimensional simulations have been carried out to figure out the characteristics of capacitive level sensors, which grounds the finding of the parameters required to design the sensors. Digital circuits are constructed to facilitate to explore the way of coping with the parasitic capacitance problem.

2. Level sensor operation principle

Electrostatic capacitive level sensor is measuring the capacitance generated onto a specific dielectric. Measured quantity of capacitance tells the nature of capacitive substance based on the relation that capacitance increases with the area of electrode and inversely proportional to the electrode gap. Substance-specific dielectric constant finally determines [4] the capacitance of materials such as oil and water. It is expected that the capacitance of a hybrid dielectric changes as the mixture ratio varies.

3. Computer simulations

Prior to oil and water separation, generally, bilge separator is filled up with the solution which consists of two layers - oil and water. If we can find the relation between capacitance value and the height of water layer, measured quantity of the capacitance enables us to grab the number of the height of both water and oil layer. Geometric structure of the bilge separator is a hindrance to analytic finding of the capacitance value of the target substance. Computer simulations using MAXWELL, therefore, have been performed. Figure 2 shows the structure of the model bilge separator upon which our simulation was carried. Simulations focused on the transition of the capacitance value due to the variation of parameters such as height of water layer($l_{\mathbf{w}}$), height of oil layer($l_{\mathbf{o}}$), the length of bilge separator($L_{\mathbf{b}}$), Diameter of bilge separator ($D_{\mathbf{b}}$), the length of sensor probe ($l_{\mathbf{s}}$), and the diameter of sensor probe ($d_{\mathbf{s}}$).

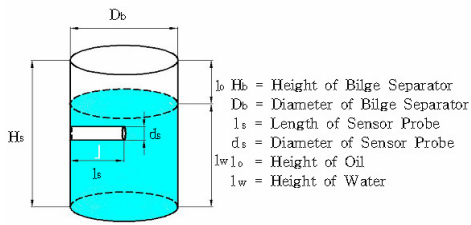

Fig. 2. Bilge separator structure

In order to determine the parameters of prototype bilge separator, the capacitances were measured for four scenarios of which the parameters are shown in Table 1.

Table 1.

	l_s(cm)	d_s(cm)
Case 1	17.5	1
Case 2	17.5	2
Case 3	35	1
Case 4	35	2

The results are also shown in Figure 3.

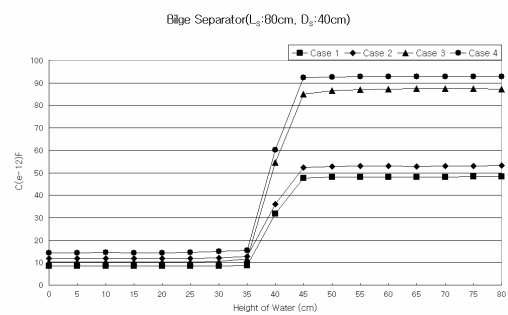

Fig. 3. Capacitance values for various sensor parameters

Data of Figure 3 are obtained for the separator that has 80 cm and 40 cm as L_b and D_b, respectively. Simulation results say that the length of sensor probe (l_s) is a dominant factor affecting the capacitance value while the diameter (d_s) is not. We, based on this finding, set the diameter of sensor probe to 1 cm.

To find the dependence of capacitance value on the physical size of the 160 cm and 80 cm as L_b and D_b, respectively. Parameters of probe sensor are same as those in Table 1. In Fig. 4 the results for larger tank is shown.

It is clear from two figures 3 and 4 that the capacitance value of bilge separator is independent of how large the tank is. We furthered the learning of the capacitance dependence on the sensor probe length (l_s) by simulations under finer variations of l_s.

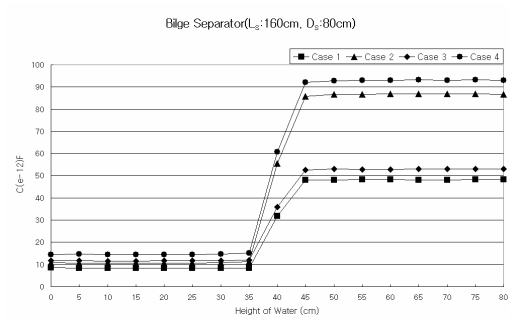

Fig. 4. Capacitance values for larger tank

We note as expected that the measured capacitance changes as the length of probe sensor varies from 10 cm to 32.5 cm by 2.5 cm incremental steps. Figure 5 helps us to choose 17.5 cm as the number of l_s, which produces 50 pF of capacitance. Note that 50 pF is ten times of the noise capacitance. It is noteworthy that the only parameter affecting the separator capacitance is probe sensor length. We also pay attention to the probe sensor location. Sudden capacitance change occurs when the probe is sitting in the border line between oil and water.

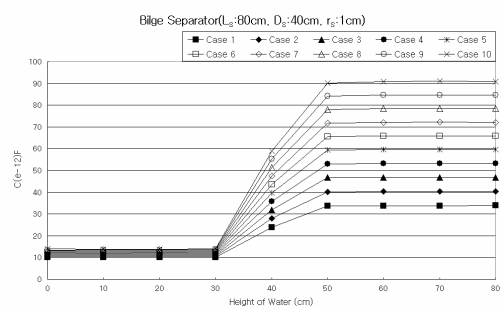

Fig. 5. Capacitance values for various sensor lengths

4. Implementation of prototype and Experiments

A prototype bilge separator has been built based on preset parameters, i.e. cylindrical container size of 80 cm (L_b) x 40 cm (D_b) and probe sensor size of 17.5 cm (l_s) x 1 cm (d_s). Two main parts, namely, fixture segment and signal processing segment constitutes the level sensor. The probe surface has been Teflon coated to keep the liquid from adhering. The residual liquid adhered to sensor electrode may cause false detection [5].

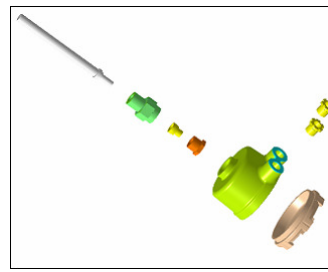

Fig. 6. Fixture segment structure

One of the most important issues in building the signal processing segment is how to cure the parasitic capacitance inherent to all the level sensors [6, 7, 8, and 9].

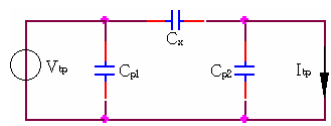

Fig. 7. Two-port measurement

The parasitic capacitances exist in various forms, connection cable capacitance to name one. In Figure 7, the parasitic capacitance is depicted by C_{p1} and C_{p2} while the sensor capacitance is indicated by C_x. The only way to eliminate the effects of both parasitic capacitances is to force a voltage V_{tp} on the transmitting electrode and to sense the current I_{tp}. The current I_{tp} depends only on V_{tp} and C_x. Fig.8 shows a circuit which eliminates the parasitic capacitance.

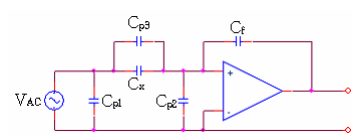

Fig. 8. Parasitic capacitance elimination circuit

Here, C_{p1} represents the parasitic capacitance from the electrode E_1 and C_{p2} from electrode E_2 and C_{p3} from imperfect shielding, respectively. V_{ac} applied to sensor capacitor C_x generates a current which eliminates C_{p1} and C_{p2}. C_{p3} can be eliminated by performing an offset measurement [11].

The Experimental capacitance values obtained through the prototype bilge separator is shown in Fig. 9. The measured values nicely agree with the computer simulation results. When the length of water layer is in the vicinity of 40 cm, in other words, the probe sensor is put in the border line, the capacitance value suddenly changes.

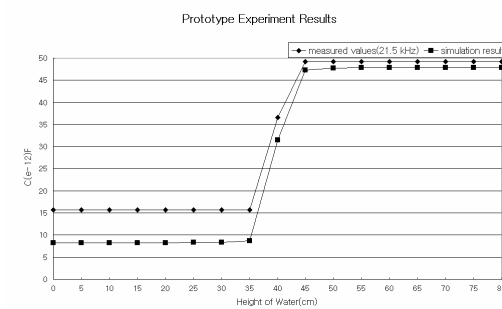

Fig. 9. Prototype experiment results

5. Conclusion

Computer simulations show that the capacitance of level sensor is independent of tank size and sensor probe diameter. The sensor probe length, however, does affect the capacitance value. Based on the preset parameters that are recommended from the computer simulations, a prototype bilge separator has been built. It has been found that the capacitance value changes from 15 pF to 50 pF with the mixture ratio variation. Efforts for the elimination of the parasitic capacitance have been made during the design of signal processing circuit. When we get 50 pF as the sensor capacitance our separator turned out to have 10 dB SNR since the noise and parasitic capacitance rendered themselves to be 5 pF.

References

1. Dj.M. Maric, P.F. Meier and S.K. Estreicher, *Mater. Sci.,* Forum Vol. 83-87 , 119 (1992).
2. M.A. Green *High Efficiency Silicon Solar Cells,* Trans Tech Publications, Switzerland (1987).
3. A J jaworski and T Dyakowski, *Diffusion Processes in Advanced Technological Materials*, edtied by D. Gupta Noyes Publications/William Andrew Publising, Norwich, NY in press (2004).
4. G. Henkelman, G.Johannesson and H. Jónsson, *Theoretical Methods in Condencsed Phase Chemistry*, edited by S.D. Schwartz, volume 5 of Progress in Theoretical Chemistry and Physics, chapter, 10, Kluwer Academic Publishers (2000).
5. R.J. Ong, J.T. Dawley and P.G. Clem, *submitted to Journal of Materials Research* (2003).
6. P.G. Clem, M. Rodriguez, J.A. Voigt and C.S. Ashley, *U.S. Patent 6,231,666* (2001).

A STUDY ON THE EVALUATION SLIDING BEHAVIOR OF NATURE-FRIENDLY ASSEMBLED CONDUIT CONNECTION

CHUN-HO KIM

Civil Engineering, Joongbu University, Chubu-myeon ,Geumsan-gun, Chungcheongnam-do, 312-702, Korea

Blocks as main materials of an assembled conduit need to take different behaviors according to a shape or connection. Thus it is required to assess sliding behavior of connection of an assembled conduit for vegetation. Here the study is intended to implement a FEM analysis in non-linear boundary condition and a contact friction test of assembled conduit connection and develop a system to evaluate sliding behavior of connections only with FEM analysis using a computer simulation. The study result shows that a non-linear boundary analysis of nature-friendly assembled conduit connection is a helpful model to understand sliding behavior of the connection.

1. Introduction

Recently the environmental problems, maintenance of agricultural waterways has recently begun to add a variety of public-interested plural functions of local resources to an original transportation function of waterways to improve renaturation on environment. Unlike previous waterways, the assembled conduit for vegetation manufactured for solving environmental problems is designed to conserve and harmonize with the natural environment by obtaining space for vegetation. Byeong-wan Lee verified safety of the nature-friendly assembled conduit for vegetation in his study. However most of the previous studies have focused on utilization of water by waterways. As the main material of the assembled conduit, blocks need to take different behaviors by shape or by connection, the above should be considered to evaluate sliding behavior of connections of nature-friendly assembled conduit. Therefore the study is intended to implement a FEM analysis in a non-linear boundary condition and a contact friction test of the assembled conduit connection and thereby develop a system to evaluate sliding behavior of the connection only with the FEM analysis without a further test.

2. Nature-Friendly Assembled Conduit

The assembled conduit for vegetation provides habitants to various vegetables by forming a space on the axial part which is installed as assembled put into a jagged part on the bottom as shown at Figure 1. On the bottom plate a vegetation space is prepared for gastropoda, amphibia and earthworms. Also, the nature-friendly assembled conduit is very stable against a tractive force. The conduit is composed of an assembled block for vegetation and a waterway bottom like Figure 2. Figure 3 presents vegetation after a test construction of the nature-friendly assembled conduit.

Fig. 1. Prefabricated conduit

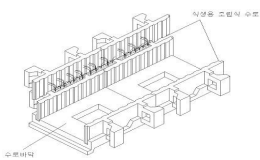

Fig. 2. Composed conduit

Fig. 3. Test construction of conduit

The nature-friendly assembled conduit is composed of concrete and steel reinforcement; compression strength of concrete is above 29MPa and its bending strength (f) is 235MPa. The section of the conduit is shown at Figure 4 in unit of mm.

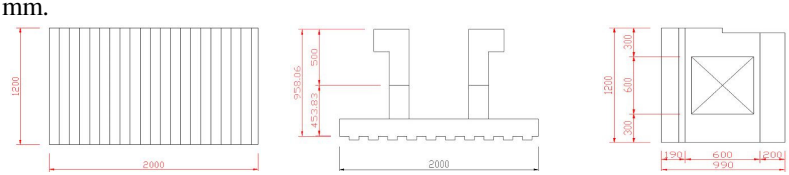

Front view Plane view Side view

Fig. 4. A plan of prefabricated conduit

3. Friction Test of Connection

3.1. *Test Method*

When soil pressure works on the back of the assembled conduit, the connection of the conduit has sliding and resistance and then a shear key has shear resistance. Thus a specimen of assembled conduit connection was manufactured for a test. The purpose is to measure and evaluate sliding load and a friction coefficient of the assembled conduit connection.

Main materials of the assembled conduit include concrete and steel reinforcement. Design strength of concrete (f_{ck}) is 29MPa and its unit weight is

25kN/m^3. Steel reinforcement is SD30 (f_y = 235MPa). An elasticity coefficient of steel reinforcement (E_c) is 2.0×10^5 MPa, a temperature expansion coefficient (α) is 1.0 X 10^{-5}/°C, and the poison ratio is 0.18. The specimen used in the study is manufactured copying the shear key of the assembled conduit. The size of the shear key is same with a real shear key. The specimen is left with piled up as Figure 5 after positioning at a frame. An applied axial force is measured with prestress load cell attached to 4 points. To check sliding of a specimen, it was installed to the both axial sides into the axial direction of the specimen. In the test of connection of an assembled conduit, prestress of 9.8kN×4, 19kN×4 and 29kN×4 was laden on the specimen of which design strength, fck is 29MPa and positioned in a load cell of 980kN. Then, load from 0 to 980kN was laden for the test. The applied axial force and the loading position are like Figure 6.

Fig. 5. Positioned of specimen

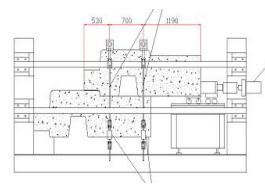

Fig. 6. Loading position

3.2. *Test Result and Consideration*

To measure sliding load and a friction coefficient of the assembled conduit connection, a wave absorbing block connection test was conducted with the following results.

For the specimen 1 with an applied axial force of 9.8kN×4, sliding occurs with 35kN load. For the specimen 2 with an applied axial force of 19kN×4, sliding occurs with 59kN load. Finally, for the specimen 3 with an applied axial force of 20kN×4, sliding occurs with 88kN load(see Figure 7, Figure 8, Figure 9).

Fig. 7. Specimen 1

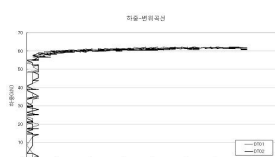

Fig. 8. Specimen 2

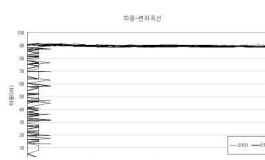

Fig. 9. Specimen 3

To measure sliding load and a friction coefficient of the assembled conduit connection, a test was conducted with the following results. Table 1. shows that the more applied axial fore the bigger sliding load according to the friction test

and that the friction coefficient of the specimen 1 was 0.9, that of the specimen 2 0.75, and that of the specimen 3 0.75.

Table 1. Result of friction test

	Applied axial force	Sliding load	Coefficient of friction
Specimen 1	9.8 kN ×4	35 kN	0.9
Specimen 2	19 kN ×4	59 kN	0.75
Specimen 3	29 kN ×4	88 kN	0.75

4. Non-linear Boundary Analysis of Connection

4.1. *Analysis method*

In order to develop a system to evaluate sliding behavior of connection only with FEM analysis without a test upon evaluation, a FEM analysis in a non-linear boundary condition was conducted to the connection of the nature-friendly assembled conduit using LUSAS, which is a FEM program. The non-linear boundary analysis of the connection considered a shear key to draw on stress and sliding load of the connection.

Materials of the FEM analysis in a non-linear boundary condition for the nature-friendly assembled conduit connection uses from analysis with the material which it uses form friction test is same. The non-linear boundary FEM analysis for the nature-friendly assembled conduit connection was conducted in a three-dimensional X-Y-Z plane. Figure 10 is modeling with a 3-dimensional solid continuum element while load was combined with dead load(automatically calculated in the program) and load horizontally supplied from 0 to 980kN. The boundary condition is composed of a hinge support that limits translation displacement of x and y axes (see Figure 11), a roller support that limits translation displacement of the x axis only, and a slide line that considers friction of a contact surface (see Figure 12). A friction coefficient of the slide line was applied as 0.6 by using safety factor of 1.2(S=1.2) based on the test result[5].

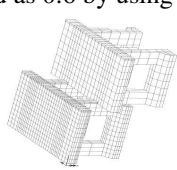

Fig. 10. 3D modeling

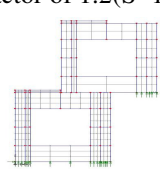

Fig. 11. Boundray condition

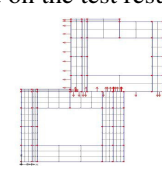

Fig. 12. Slideline

4.2. *Analysis Result and Consideration*

In order to develop a system to evaluate sliding behavior of connection only with a FEM analysis of computer simulation without a test upon evaluation of the connection, a friction coefficient of 0.6 was used for a non-linear boundary analysis with the following results.

Under 0.98kN load, the shear stress of the lower block is concentrated like Figure 13. Under 42kN load, the shear stress concentrated on the lower block reaches to the upper block (see Figure 14). Under 98kN load, a contact area has stress concentration and the upper block has sliding to contact with the upper block (see Figure 15). In addition, as shown at Table 2, the bigger the load the higher the displacement and shear stress. Sliding also occurs under 42kN load (see Figure 16). The non-linear boundary analysis of connection using computer simulation shows that it can be a good model to understand sliding behavior of the nature-friendly assembled conduit connection

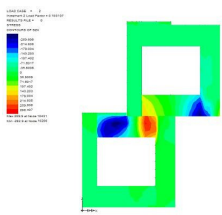

Fig. 13. Shear stress (load : 0.98kN)

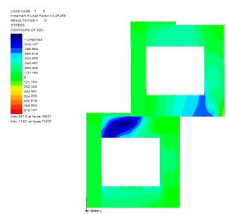

Fig. 14. Shear stress (load : 42kN)

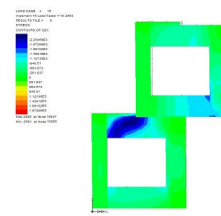

Fig. 15. Shear stress (load : 98kN)

Table 2. Result of nonlinear boundrary condition analysis

LOAD(kN)	Shear stress(MPa)	Displacement(mm)	Sliding
0.98	1.78	0.77	Non sliding
42	8.68	36.83	**Sliding**
98	23.55	160.99	**Sliding**

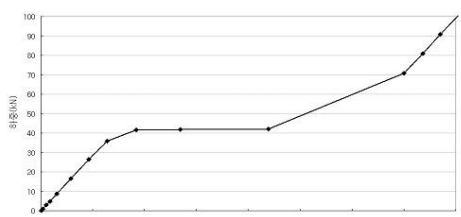

Fig. 16. Result of analysis(load-displacement curve)

5. Conclusion

A variety of tests should be conducted to evaluate design and construction status of an assembled conduit. However, to develop a system to evaluate sliding behavior of connection only with a FEM analysis through computer simulation without a test upon the evaluation, a non-linear boundary FEM analysis on the connection and a contact friction test of the conduit were implemented to get the following results.

1. A friction test on the assembled conduit connection showed that the more the applied axial force the bigger the sliding load. A friction coefficient of the specimen 1 is 0.9; and that of the specimen 2 and the specimen 3 0.75 for each.
2. Applying a friction coefficient of 0.6 considering a safety factor of 1.2 based on the test result, a non-linear boundary analysis was conducted to get sliding load. The sliding load ratio against an applied axial force is 0.80 on average in the test and 0.87 by analysis. Thus, the analysis can be a good model to understand sliding behavior of the nature-friendly assembled conduit connection.
3. For any future non-linear boundary analysis of concrete blocks and a block-contact connection, the friction coefficient is calculated as 0.5 for a safety factor of 1.5 and as 0.6 for a safety factor of 1.2.
4. The study showed that the sliding behavior of the assembled conduit connection for vegetation can be evaluate only with a non-linear boundary FEM analysis without a test.

References

1. Chu-Kia Wang, Reinforced Concrete Design, Wang Salmon (1983).
2. Gray, D. H and Ohshi, H., Mechanics of Fiber Reinforcement in Sand, Journal of the Geotechnical Engineering Division, ASCE (1983).
3. Ho, S. K. and Rowe, R.K., Finite Element Analysis of Geosynthetics Reinforced Soil Walls, Geosynthetics (1993).
4. Timoshenko, Mechanics of Materials, PWS Publishing (1997).
5. FEA Ltd, LUSAS Powerfull FE technology for specialist applications, LUSAS Modeller User Manual (1999).
6. James G. Macgregor, Reinforced Concrete Mechanics and Design, Prentice Hall (1999).

DESIGN AND SIMULATION OF ROLL FORMING PROCESS FOR UNDER RAIL

SANGHWA JEONG

Dept. of Mechanical Eng, Chosun Univ, 375 Seosuk-dong, Gwangju, 501-759, Korea
shjeong@chosun.ac.kr (Corresponding Author)

SANGHEE LEE, GWANGHO KIM

Dept. of Mechanical Eng, Chosun Univ Graduate School, 375 Seosuk-dong, Gwangju, 501-759, Korea
yuhua79@paran.com, *mudol78@paran.com*

Cold-roll-forming (CRF) is a well known process used to manufacture long sheet metal products with a constant cross section. It can manufacture products of the uniform cross section on a large scale as a continuous processing. However, process analysis is very difficult because of the inherent complexity. Therefore, time is consuming and analysis much money are needed for manufacturing goods. In order to overcome this difficulty, a new computational method based on the rigid-plastic finite element method is developed for the analysis of roll forming process and the optimal design.
In this paper, to manufacture the upper member at under rail composed of three members, the design of roll forming process and the simulation are performed. Tensile test is performed about SCP-1 to obtain material properties and curve fitting is executed to set up the flow stress equation. The flower pattern of the upper member in the under rail is designed. The final shape is predicted after simulation. The longitudinal strain is estimated on the basis of simulation results. In addition, the numerical magnitude of bow and camber are predicted from the results of the simulation.

Keywords: Slide Rail; Roll Forming Process; Rigid-Plastic Finite Element Method; Longitudinal Strain; Camber; Bow; Flow Stress Equation.

1. Introductions

The under rail used in this research is composed of three members as one kind of the double slide rail. The slide rail is generally formed by the press process, but it is formed by the roll forming process for the products that have intricate shapes or require precision. Cold roll forming can be described basically as a process where a metal sheet is continuously formed in the transverse direction

into a product with a desired cross-sectional profile by passing a series of pairs of forming rolls. The roll forming shows both compression and tension and the residual strain remains in the final shape of the strip, which go through several passes. Also buckling take place in the finished products. It is difficult to predict it precisely because buckling is influenced by many factors. It is difficult to predict the shape in each pass due to this kind of effect. M. Kiuchi [1,2] from Tokyo University in Japan formulated the roll forming process, computed the longitudinal strain, and suggested the optimal algorithm of the roll forming process. Jimma and Ona [3,4]developed an empirical equation to determine the number of passes necessary for designing the rolls through combining the angle of bending of the flange, which is made by the bending of the strip, and the number of passes. As the analysis of plastic deformation is difficult, however, the slide rail products are still manufactured based on experiences or trial error.

In this paper, the roll forming process of the under rail using rigid-plastic finite element method is simulated. We designed the upper member at the under rail composed of three members is developed. The upper member is designed by the constant radius method and the constant arc length forming method. From the tensile test of SCP-1, the flow stress equation required in rigid-plastic FEA is elicited. To lay out good forming rolls of the upper member, two types of the flower pattern are designed and the final shape is estimated after simulation of roll forming process. SHAPE-RF software [5], which interprets the roll forming processes in the basis of Rigid-Plastic Finite Element Method, is used. The residual strains the last pass of two types are predicted in order to determine the formability of products. Also, magnitude of the bow and the camber is compared to estimate buckling phenomenon.

2. Design of roll forming process

In plastic deformation after yield, material constant equivalent to continuous yield stress is described as flow stress, instead of as yield stress. The method of describing the increase phenomenon of the flow stress by work hardening numerically is like the below [6].

- Square n hardening equation, $\sigma_f = K\bar{\varepsilon}^n$ (1)
- Ludwick equation, $\sigma_f = Y + K\bar{\varepsilon}^n$ (2)
- Swift equation $\sigma_f = K(\bar{\varepsilon}_0 + \bar{\varepsilon})^n$ (3)

where, K = stiffness coefficient;

$\overline{\varepsilon_0}$ = initial strain;

n = work-hardening exponent.

In this paper, the swift formula of Eq. (3) is used in order to get the optimum flow stress equation by using the numerical analysis method. rigid plastic-work hardening curve is fitted using the power curve, and a flow stress equation as shown in Eq. (4) is computed.

$$\sigma_f = 1840(0.00254 + \bar{\varepsilon})^{0.39657} \tag{4}$$

The appearance of the upper member at the under rail is shown in Figure 1. In considering of the capacity of the roll forming mill possibly to be manufactured currently, the horizontal distance is set as 330mm for 1-6 pass and as 660mm for 7-9 pass to reduce elongation because much strain is predicted. The big change of forming angles in designing the flower patter is called "Jump" phenomenon and this phenomenon becomes a cause of buckling through causing high stress to products. Therefore, in this paper, the bending angle is same for the passes that have the same leg height, and decrease it for the passes that have a long leg height (I: 15° increase, II: 10° increase, III: 30° increase). The upper member at the under rail is nonsymmetrical. The non-symmetrical cross section causes serious torsion in product when the orientation of section could not be put in a proper position. The cross-section of Figure 1 is rotated to minimize the flexural rigidity coefficient of the cross-section as shown in Figure 2. The flower pattern is set as 9 pass and Two types of the flower pattern the upper member are designed. One is the constant arc length forming method (TYPE-A) and the other is the constant radius forming method (TYPE-B) [7]. For TYPE-A, its increases the bending angle with changing the bending radius of the curved element. In case of TYPE-B, the adjacent straight element varies, because the bent element should be bent gradually as the bending radius is constant when the bending angle of the bent element varies.

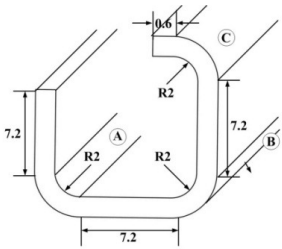

Fig. 1. Cross-section of the upper member

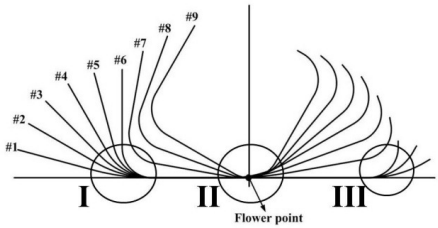

Fig. 2. Flower diagram of upper member

3. Finite element analysis of roll forming process

The input conditions for roll forming process analysis are listed Table 1. We set up the rpm ratio of the top roll and the bottom roll is set up as 1:1 to prevent the increase of the interior stress caused by the difference of the rotation velocity of the rolls by setting up the two rolls as driving rolls. Other friction factors is excluded by setting the forming rolls as rigid bodies and setting up the friction coefficient as 0.1 in this paper.

Table 1. Input conditions for FEA

Horizontal distance to the previous roll stand(mm)	330, 660	Number of elements in rolling direction	20
Number of elements in width direction	53	Number of elements in thickness direction	3
Width	35	Thickness(mm)	1.6
Friction condition(μ)	0.1	Specify self-contact penalty constant	10^8
Young's modulus(GPa)	210	Ultimate tensile stress(MPa)	480.40
Yield strength(MPa)	158.12	Poisson's ratio	0.3

In order to determine the formability of the two types (TYPE A: the constant arc length forming method, TYPE B: the constant radius forming method), the longitudinal strain and the numerical magnitude of the camber and the bow is estimated. In the roll forming process, the residual strain can be described like the following Eq. (5) [8].

$$\varepsilon^{residual} = \varepsilon^{\max} - \varepsilon^{exit} \tag{5}$$

Where, $\varepsilon^{residual}$ = Residual strain in strip

$\varepsilon^{\max}$ = Maximum value of longitudinal strain
ε^{exit} = Longitudinal strain in roll exit

The camber is the deviation of the strip edge from a straight line in the

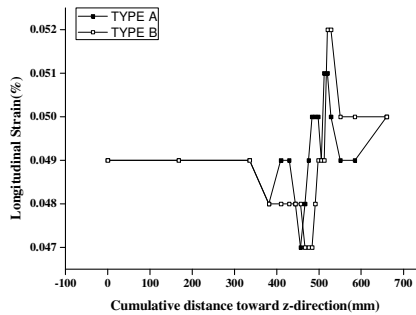

Fig. 3. Longitudinal strain in last pass

horizontal plane. The bow is a degree of a formed product's being deflected from a straight line on the vertical plane. Figure 3 describes the longitudinal strain from the entry roll to the exit roll of the section passing the last roll predicted by the results of simulation. It is estimated that the residual strain of TYPE A is 0.001% and the residual strain of TYPE B is 0.002%. It means that more residual strain would remain in the strip in TYPE B than in TYPE A. Because the residual strain causes wavy during the process or buckling after the completion of all processes, it is predicted that camber and bow will appear bigger in TYPE B than in TYPE A. the numerical magnitudes of camber and bow simulated by the two types of the flower pattern are compared. Figure 4(a) describes the numerical magnitude of camber in the two types. The numerical magnitude of camber appears as 11.416mm in TYPE A, and in TYPE, it appears higher as 20.713mm. Figure 4(b) shows the numerical magnitude of bow in the two types. The numerical magnitude of bow also shows a trend similar to that of the numerical magnitude of camber, and it is 19.828mm for TYPE A and 22.759 for TYPE B, so that it is predicted that the numerical magnitude of bow would be bigger in TYPE B than in TYPE A. From the above results, it is estimated that the upper member at the under rail will be formed better by the constant arc length forming method (TYPE A) than by the constant radius forming method (TYPE B).

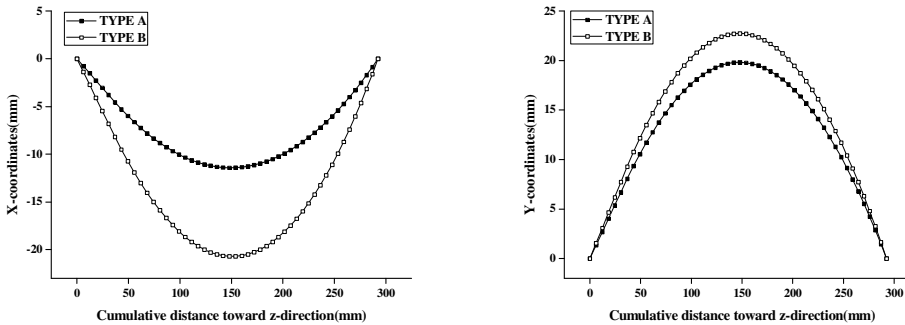

(a) camber (b) bow

Fig. 4. Comparison of camber and bow between two types

4. Conclusion

In this paper, the under-rail is designed, and the roll-forming process of upper member is simulated using SHAPE-RF, the roll forming analysis program using rigid-plastic finite element method. The material used for the finite element analysis is a cold rolled carbon steel sheet, and its material property is investigated through a tensile test. For the numerical analysis on SCP-1, a flow stress equation is obtained by using a swift formula. The number of pass is set up the total 9 in the basis of the capacity of the roll forming mill and the empirical equation. The bending angle is uniformly designed for minimizing the generation of "Jump" phenomenon. Also, for the flower pattern, the bow and camber caused in forming is decreased by establishing the orientation of flower pattern of the upper member at the curved element. Two types of the flower pattern are designed. One is the constant arc length forming method (TYPE-A) and the other one is the constant radius forming method (TYPE-B). The finite element analysis is conducted for the two types in order to find out how to design the curved element the most suitable for the upper member. The residual strain at the entry roll and the exit roll of the last roll is estimated in order to discriminate the formability of the upper member. According to the results of estimating each residual strain, it is estimated that TYPE A has 0.001% and TYPE B has 0.002%. It is predicted that TYPE B would have a higher probability of the generation of buckling than TYPE A. The results of estimating the camber and bow is agree the same with those of estimating residual strain. For the numerical magnitude of camber, it is predicted that TYPE A would show

11.416mm and TYPE B 20.713mm, for the numerical magnitude of bow, it is predicted that TYPE A would show 19.828mm and TYPE B 22.759mm, so that TYPE B would show higher numerical magnitude for both camber and bow. Based on the above analysis results, it is expected that appearance can form better of a product forming roll of the upper member at under rail is designed by the constant arc length forming method (TYPE A) than by the radius forming method (TYPE B).

References

1. M. Kiuchi, "Analytical study on cold roll forming process," Report of the Inst. Of Ind. Sco., Univ of Tokyo, 1973.
2. M. Kiuchi and T. Koudobashi, "Automated design system of optimum roll profiles for cold roll forming," 3rd Int Conf. on Rotary Metal Working Process, 1984.
3. H. Ona and T. Jimma, "Experiments into the cold roll forming of straight asymmetrical channels," Journal of Mechanical Working Technology, 1983.
4. H. Ona, T. Jimma and H. Kozono, "A computer aided design system for cold roll forming," Advanced Technology of Plasticity, 1984.
5. S. M. Hong, D. S. Kim, D. S. Kim, H. J. Yun and N. S. Kim, "Development of roll forming simulation program," Society of CAD/CAM Engineers, 2000.
6. T. J. Kim, "A determination of material properties of tube in hydroforming using inverse engineering and tube bulge test," M.Sc. Thesis, Univ. of Sogang, Seoul, 2002.
7. G. T. Halmos, *Roll Forming Handbook* (CRC Taylor & Francis, New York, 2005).
8. Y. Y. Kim, "Buckling Analysis and Buckling Limit of Strain on Roll Forming Process," M.Sc. Thesis, Univ. of Sogang, Seoul, 2002.

POSSIBLE EFFECTS OF FSW TOOL PIN CONFIGURATION ON RESIDUAL STRESS DISTRIBUTION

YOUNG-GAK KWEON †

Facility and Automation Research Center, RIST, Pohang 790-600, Korea

RAJESH S.R, HEUNG-JU KIM, WOONG-SEONG CHANG, CHANG-KEUN CHUN

Welding research center, RIST, Pohang, 790-330, Korea

SEONG JOO KIM

Survey Team, Korean Register of Shipping, Korea

The mechanical properties of a friction-stir weld depend in detail on the tool design, the rotation and translation speeds, the applied pressure and the characteristics of the material being joined. In this present paper the micro-structural and residual stress distribution in FS Welded al6061 has been studied for different tool pin configuration. In order to numerically determine the residual stress, finite element heat source model has been developed on the basis of experiment results. For the stimulation, four models with different tool pin configuration such as cylindrical shaped threaded and non-treaded pin, frustum shaped threaded and non-treaded pin were used. The thermal histories obtained from the heat transfer analysis were used to determine the residual stress distribution. The maximum calculated residual stress value are in the order of Cylindrical pin > Frustum pin > Threaded Cylindrical pin > Threaded Frustum pin.

1. Introduction

Al-alloys have superior property of hot and cold working and corrosion-resistances. However welding of these alloys with the existing fusion process needs an extreme expertise to prevent defect. Recently Friction Stir Welding (FSW) is being applied in various industrial fields for welding Al-alloys, as the defects are comparatively less than that of fusion welding process. The success of FSW process for Al6061-T6 alloy would increase its applications for various structural components manufacturing, particularly in the aerospace industry due to its lightweight and high strength.

† Corresponding author: ygkweon@rist.re.kr

In FSW the work-piece are butt welded together by plunging the rotating tool in to the weld line till the shoulder offers the required compressive pressure while moving along the joint line. During this process the axis of the tool (top end) is tilted backward 2.5^0 within the plane defined by the normal axis of plate and welding line. In friction stir welding the heat is mainly generated from friction and plastic deformation and this temperature does not exceed the melting temperature, for optimum welding parameters.
The four types of tool pin configurations such as cylindrical shaped threaded and non-treaded pin, frustum shaped threaded and non-threaded pin were modeled to compare the variation in residual stress distribution based on tool pin configuration.
In the present study, two-dimensional nonlinear thermal elastic-plastic simulations of FSW process for various tool pin configuration has been carried out based on the experimentally determined stir zone dimensions.

2. Background Literatures

The earliest literature many of the authors have specified that the maximum temperature in the optimized FSW process does not exceed 80% of the melting point temperature of the material being welded.[1] Some authors have assumed that 100 % of this heat is generated by friction between tool shoulder and the material matrix. They also assumed that the downward pressure P applied on the tool shoulder surface is uniform and correlated heat generation rate with downward pressure using the friction coefficient. They predicted temperature field due to moving heat source using Rosenthal equation and correlated the heat input equation with the friction process of the shoulder [2, 3].
According to Askari et al. [4] the heat generation due to plastic work is the dominating term during the steady state FSW process.
Rajesh et al.[5,6] presented that the heat generation due to plastic work is the dominating term during the steady state friction stir welding (FSW) process. Based on this phenomenon they developed a 3D-analytical model of the stir zone around the FSW tool pin. In their model, the heat generated from the pin due to friction force during steady state FSW process has been neglected as the material in this zone is plasticized and it has undergone plastic deformation rather than inducing friction to the tool pin boundary.
Buffa et al.[7] presented the fundamental role of the tool geometry on the micro structural variation in the weld and heat affected zone. A 3D FE model for FSW based on thermo-mechanically coupled rigid-visco-plasticity has been developed. They also predicted material flow patterns in the welded joint at varying pin angle and advancing speed.
Considering all the above literature, in this work the heat generation in FSW process has been divided into two components such as heat generation due to plastic deformation and heat generation due to friction. Also approximate

percentage of heat generated from shoulder and pin has been determined based on the experimental and numerical studies. Based on the thermal histories obtained the residual stress distributions are numerically determined and experimentally validated.

3. Experimental Procedures

The aluminum alloy has been butt welded with tool profiles as shown in the Figure 1. The plates are 4mm thick 50mm wide and 200 mm long. The shoulder diameter and the pin length have been kept constant; 18mm and 3.6 mm respectively. All the simulation and experiments were performed using the same procedure and process parameters such as shoulder sinking in to the plate of 0.1 mm, rotation speed of 1000 r.p.m, travel speed of 200 mm/min and tilting angle of 2.5^{o}. To experimentally validate the numerically determined residual stress both x-ray diffractometer and strain gauges sectioning method has been employed.

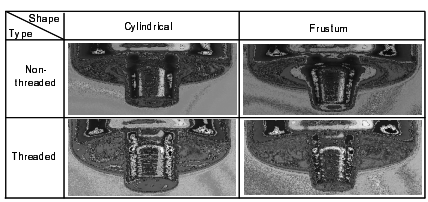

Fig. 1. FSW tool type used for the experiment

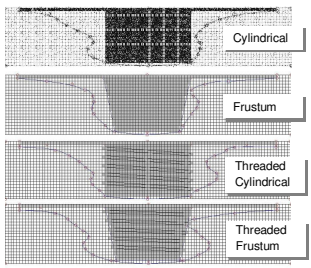

Fig. 2. FE Mesh marked with the stir zone boundary for various tool pin configuration. (left is advancing side and right retreating side)

4. FEM based residual stress modeling

Simulation is used to explain and distinguish the residual stress distribution for various pin configurations in FSW process. Residual stress modeling is performed using an in-house solver developed by the author. The in-house solver has been successfully used and validated by the author for various other welding methods.

The four noded iso-parametric elements have been used for modeling. The total number of nodes and elements are 4263 and 4040, respectively. A sufficiently fine mesh at the stir zone, thermo-mechanically affected zone and heat-affected zone was generated to obtain more accurate results. The boundary conditions of the FE model were same as those of the experimental condition. The temperature dependent material properties of Al6061-T6 have been used for FE analysis.

The heat flux is given to the element with in the stir zone boundary. The coordinate of the stir zone boundary line on the transverse plane normal to the

welding direction is determined using optical microscopy. These x and y coordinate are used to sketch the stir zone boundary on the finite element mesh of each tool pin types as shown in Figure 2. The elements having more than 0.75 of its area with in the stir zone are taken as the heat source zone.

For the heat input calculations the heat generated in the FSW process has been assumed to be a combination of friction heat from the tool-work-piece interface and the heat generated due to plastic deformation in the vicinity of the tool pin. The elements at the tool-work piece interface has been given the heat input value calculated based on friction and remaining elements with in the stir zone boundary, with value based on plastic deformation.

Friction is the force that opposes the relative motion or tendency of such motion of two surfaces in contact. It is not, however, a fundamental force, as it originates from the electromagnetic forces and exchange force between atoms. In situations where the surfaces in contact are moving relative to each other, the friction between the two objects converts kinetic energy into heat. In FSW process the heat flux due to friction along the contact interface of tool and metal matrix in the advancing side and retreating side are calculated by the equation.

Advancing side: $q_{fa} = \frac{(V_f + V_t)F}{A_a}$, Retreating side: $q_{fr} = \frac{(V_f - V_t)F}{A_r}$ (1)

Where V_f: Forward travel speed, V_t : tool tangential velocity = $2R\omega$, R: radial distance of the tool surface from tool axis, ω: Angular velocity, F: Frictional force, A_a, A_r: are the surface areas of the tool in contact with metal matrix along advancing and retreating side respectively.

The heat generation rate due to plastic deformation is calculated as the product of flow stress and plastic strain. So the heat fluxes due to plastic deformation in the advancing and retreating side are

Advancing Side: $q_{pa} = 0.9 \times \sigma \times \dot{\varepsilon}_{pa}$, Retreating Side: $q_{pr} = 0.9 \times \sigma \times \dot{\varepsilon}_{pr}$ (2)

Where 0.9 is the fraction of plastic deformation energy transformed in to heat.

The flow stress is calculated based on the Johnson-cook Model [8]. In the JC model, the Von Mises flow stress, σ is expressed as

$$\sigma = (A + B\varepsilon^n)(1 + C\ln\dot{\varepsilon}^*)(1 - T^{*m}) \quad (3)$$

Where ε is the equivalent plastic strain,

$$\dot{\varepsilon}^* = \dot{\varepsilon}/\dot{\varepsilon}_0 \quad (4)$$

is the dimensional less strain rate and

$$T^* = \frac{T - T_r}{T_m - T_r} \quad (5)$$

Where T_r is a reference Temperature and T_m is the melting temperature of the material, T should be larger than T_r. The five material constants A, B, n, C and m are solved based on the steps followed by Akhtar and Liang [9]

According to Boothroyd [10] the strain rate in the plastic deformed region varies linearly from the tool surface to stir zone boundary. Based on this

Advancing side: $\dot{\varepsilon}_{pa} = \frac{(V_f + V_t)}{W_a}$, Retreating side: $\dot{\varepsilon}_{pr} = \frac{(V_f - V_t)}{W_r}$ (6)

Where $\dot{\varepsilon}_{pa}$ and $\dot{\varepsilon}_{pr}$ are the strain rate in the plastic deformed regions of advancing and retreating side and W_a and W_r are the width of the stir zone in the advancing and retreating side.

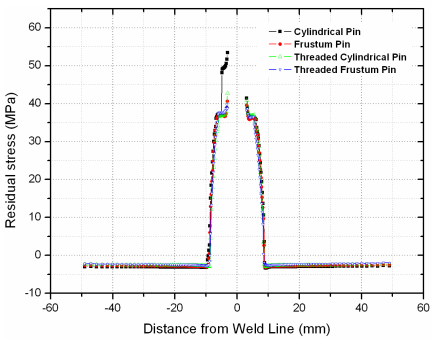

Fig. 3. Simulation result of longitudinal residual stress (left is advancing side and right retreating side)

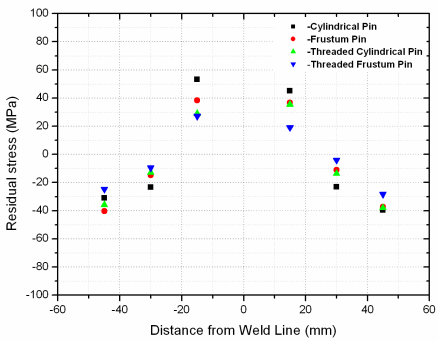

Fig. 4. Experimental result of longitudinal residual stress (left is advancing side and right retreating side)

5. Result and Discussion

The numerical simulations of the residual stress distributions in Friction stir Welded Al6061-T6 alloys using finite element heat source model has been developed. In the case of non-threaded pin the maximum temperature has been concentrated near the base metal surface in contact with the tool shoulder of advancing side, which indicates the frictional heat generated between tool shoulder and base metal surface was the most significant heat source in the FSW process with non-threaded pin. Where as, in the case of threaded pin, threads drag down softened work-piece material. When discharged at the bottom it is then forced upward. This motion is repeated around the pin during friction stir welding with threaded pins. In such regions the material offers less resistance to the pin boundary. Also this region rotates in the same direction as the tool, forming a complex 3D material deformation profile. In this region the heat is generated by plastic deformation more than friction. So in the simulated results it's been noticed that the maximum residual stress got distributed downward toward the pin. Also the maximum residual stress as in figure 3 and figure 4 in the case of the threaded pins are comparatively less than that of the non-threaded pin. This is because, for threaded pin the percentage of heat generated due to

plastic deformation is higher than friction component and the rate of heat generated by friction is greater than that due to plastic deformation.

6. Conclusions

A simple two-dimensional thermo-elastic plastic analysis has been implemented to simulate the residual stresses for various type of tool pin used in Friction stir welding. Experimental results confirmed the dependability of the program. From the result of this study, the maximum residual stress follows the order of Cylindrical pin (53 MPa) > Frustum pin (38 MPa) > Threaded Cylindrical pin (35 MPa) > Threaded Frustum pin (22 MPa). From the simulation and experimental results, the Threaded frustum pin case is advantages from the point of view of weld efficiency and process stability. Also maximum temperature is less compare to other pins.

References

1. McClure, J C., Tang, W., Guo, X., Murr, L E., Nunes, A., J. Mater Process Manuf Sci., 7,163 (1998)
2. Feng, Z., Gould, J E., J. Mater Process Manuf Sci. 7, 185(1998)
3. Feng, Z.,Gould, J E,.Lienert,T.J., Hot deformation of Aluminum alloys-II, TMS, 149 (1998)
4. A. Askari, S. Silling, B. London, M. Mahoney, TMS Publication, 43 (2001)
5. Rajesh S.R., Bang H.S., Kim H.J., Bang H.S., Adv Mater Research, 15, 339 (2007)
6. Rajesh S.R., Bang H.S., Kim H.J.,W.S Chang., J. Mater Process Technol. 187, 224 (2007)
7. Buffa G., Hua J., Shivpuri R., Fratini L., Mater Sci Eng A, 419,389 (2006)
8. Johnson,G.R., Cook, W.H., Proceedings of the seventh International symposium on ballistic, 541 (1983)
9. Akhtar S.K., Liang R., Inter. J. Plasticity, 15,1089 (1999)
10. Boothroyd G., Scripta Book Company, ISBN 0-07-006498-9, (1975)

DESIGN AND CHARACTERIZATION OF MR DAMPER

HAE LAN KIM[*]

Dept. of Mechanical Design Engineering, BK21 Mechanical Group, Chungnam National University, 220 Gung-dong, Yuseong-gu, Dajeon, 305-764, Korea

YOUNG SHIN LEE [†]

Corresponding Author, Director of BK21 Mechanical Group, Dept. of Mechanical Design Engineering, Chungnam National University,Daejeon, 305-764, Korea[§]

EUN YUP LEE [**]

Dept. of Mechanical Design Engineering, BK21 Mechanical Group, Chungnam National University, 220 Gung-dong, Yuseong-gu, Dajeon,305-764, Korea

GYU SEOP LEE [***]

Dept. of Mechanical Design Engineering, BK21 Mechanical Group, Chungnam National University, 220 Gung-dong, Yuseong-gu, Dajeon, 305-764, Korea

Three kinds of MR damper, such as valve mode type, direct-shear mode type and squeeze mode type are applied in engineering field. In this paper, a valve mode type MR prototype damper was designed and fabricated for experimental study. The circuit design of MR damper consisted with the bobbin, retainer and outer cylinder. The magnetic analysis with finite element method was performed to define these parameters such as the bobbin length, inner cylinder width, MR fluid gap. Damper characterization was performed on universal material test system (MTS) 810. The vibration frequency, displacement and current were considered as input factors, and the damping force was measured as the output factor. Force versus displacement diagrams and force versus velocity diagrams have been plotted with these factor levels. Further, the damper can be used for building and automotive damper with 1 Hz ~ 5 Hz range.

1. Introduction

Magnetorheological fluid(referred to as "MR"fluid) is discovered by Rabinow[1] and suspension of magnetically polarizable particles in an inert fluid medium like silicone oil. When applied magnetic field, the particles get

[†] leeys@cnu.ac.kr

[§] Corresponding Author Dept. of Mechanical Design Engineering, Chungnam National University,Daejeon,305-764, Korea

polarized and align along the flux lines, forming chain-like structures[2]. The formation of such chain-like structures would induce additional flow resistance, which directly depends on the magnetic field strength. When there is no magnetic field, the particles have a tendency to settle down due to gravity. So it is turnable transition from a free-flowing state to a semi-solid state upon the application of external magnetic field. Magnetorheological dampers are semi-active control devices that use MR fluids to produce controllable dampers[3],[4],[5]. Because of their mechanical simplicity, high dynamic range, low power requirements, large force capacity, and robustness, this class of devices are regarded as one of most promising devices for vibration reduction MR dampers divided into three groups of operational modes, valve mode, direct shear mode, and squeeze mode[6]. In this paper, circular design was done and used FEM to verify whether it is possible. (Initially the parameters were defined by Ampere's law and flux equation and they didn't name in this paper.) Here used small size of parameters to define whether this kind of structure damper can work normally. Then the testing was done to verify the properties.

2. Design of MR damper

Figure 1 (a) shows the circular designed dimension of MR damper. Here b is length of bobbin, r is fluid gap and a is width of retainer. A1 is rod section area, A2 is bobbin area, A3 is coil A4 is MR fluid gap and A5 is outer cylinder. Then used ANSYS 8.0 to perform the magnetic analysis. At the analysis used 2-D magnetic element plane 13 and the MR fluid used MRF-132LD which come from Lord company. The coil diameter is 0.4mm and cross section is 0.032 mm. Consider the gravity of damper here choose a smaller then 8 mm and b smaller then 30 mm. A1 used S45C as material while A2 used pure steel as material which have high permeability(4000 Tesla), A3 resistance is $6.75\ I * 10^{-6}$ (I is electric current), A4 is full of MR fluid and A5 is retainer section and used S45C as material. Figure 1 (b), Figure 1 (c) show the analytical results on the flux and magnetic density with 1 ampere current applied. The result of this design is very high magnetic flux around the rear of the bobbin but row flux levels through the active areas. And the maximum magnetic density occurs at bobbin grand with the value 1.284 tesla. The high permeability(4000 tesla) materials always occurred saturation when magnetic density is 1.3 tesla. So from the result the current shouldn't higher than one ampere. And the results can prove that this kind of circular design was possible. So used this kind of circular configuration to design the MR damper is possible and initially designed as Figure 2 shows.

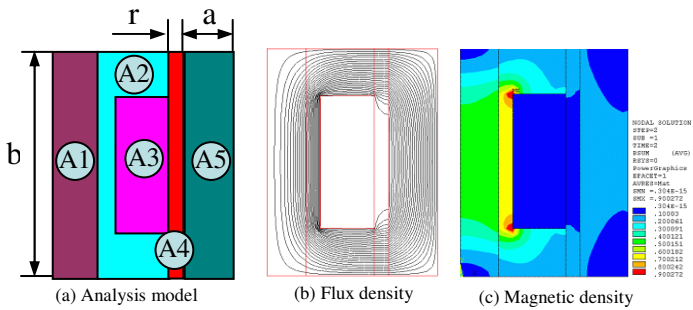

Fig. 1. Magnetic analysis model and results for flux and magnetic density

The piston rides in an outer cylinder and forces fluid through the cylinder chamber into MR fluid gap between retainer and bobbin then into the anther side of cylinder chamber. The flow must then return through the chamber into the MR fluid gap back into the initial cylinder chamber. Here continuous bows express the path of the fluid and divide bows show the path of the magnetic flux. Then produced a damper used the configuration of Figure 2 shows.

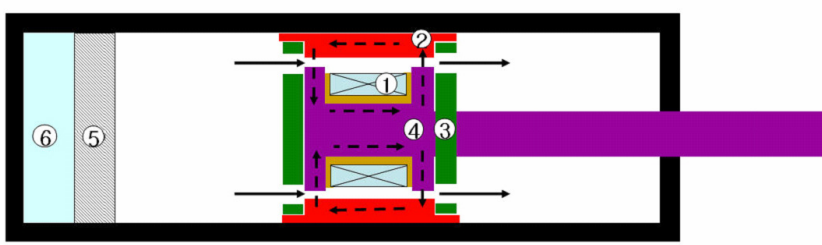

No.	Part Name	No.	Part Name
1	Coil	4	Piston
2	Retainer	5	Floating piston
3	Flux ring	6	N_2 gas

Path of Magnetic flux
Path of MR fluid

Fig. 2. Cross sectional view of the damper design showing paths of magnetic flux and MR fluid

3. Experiment and Damper Characterization

Damper characterization was performed on a hydraulically powered MTS 810 materials testing system load frame. Figure 3 (a) shows the damper mounted in the load frame for testing. The computer controlled servo-actuator was able to reliably drive the damper up to 5 Hz. The characterization tests were run at 1, 3 and 5 Hz with applied currents of 0, 0.2, 0.4, 0.6, 0.8 and 1 ampere respectively. A script for the servo-actuator control software was written that would automatically run each frequency for 5 cycles and save that data to a file. After the script had finished and all frequencies had been cycled through, a new current value would be set and the script would be run again. An example of raw data (displacement versus time and force versus time) from such a test point is shown in Figure 3 (b) and Figure 3 (c). Figure 4 (a-d) presents the force and damper displacement results at four applied current levels with different frequencies at each plot. From these diagrams it can be observed that, as the frequency increases from 1 to 5 Hz, the damping nature changes from small coulomb to a little bigger coulomb. As the current increases from 0 ampere (Figure 4 (a)) to 1 ampere (Figure 4 (d)) the force become bigger and bigger. applied 0.6 (Figure 4 (c)) ampere current the slope began and when applied 1 ampere current the slope began to get serious. Figure 5 presents the force and damper velocity results at two frequencies with different current at each plot. The force-velocity loop as shown in Figure 5 indicates that a nonlinear relationship exists between the force and velocity. And the higher the frequency, the larger the non-linearity. Further from the plots, we also observed that the force-displacement (Figure 3 (b)) and force-velocity (Figure 3 (c)) plots have loops, which increased in size with current input. From Figure 5, we observed also that the hysteresis loop becomes a straight line after a certain velocity value. The gradient of this line represents the post-yield damping of the fluid. This understanding is very important when designing MR dampers for different applications like structural (around 0.1-1 Hz), automotive (around 0.1-10 Hz) or machine vibration isolation applications (around 0.1-10000 Hz)[9].

4. Conclusions

In this paper the design and characterization testing of a MR damper was presented. The conclusions of this paper are as follows:

(1) FEM analysis was done with applied current 1 A. The maximum magnetic density was 1.284 tesla and happened at the bobbin parts. The saturation happened when the magnetic density was 1.3 Tesla, so the current must be

(a) Damper mounted in MTS

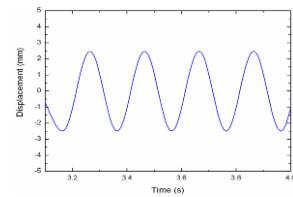

(b) Time and displacement relationship

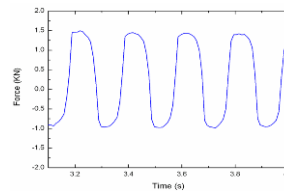

(c) Time and displacement relationship

Fig. 3. Test damper mounted in MTS and the result for time history displacement and force data from MTS machine at 5 Hz and 1 ampere current.

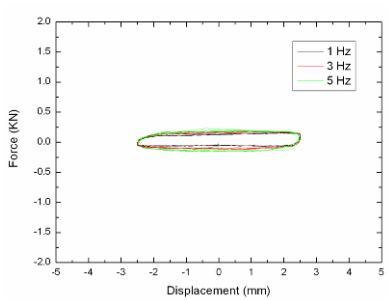

(a) 0.0 ampere current applied

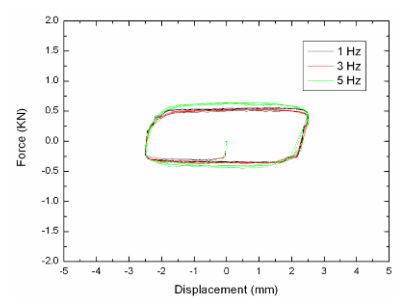

(b) 0.2 ampere current applied

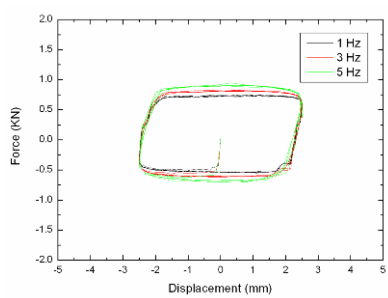

(c) 0.6 ampere current applied

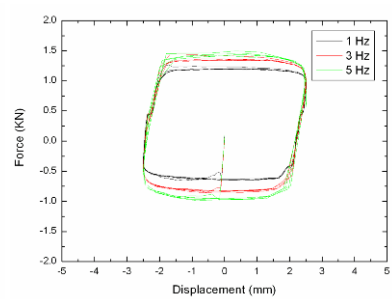

(d) 1.0 ampere current applied

Fig. 4. MTS force and displacement results for a sinusoidal input under different currents condition

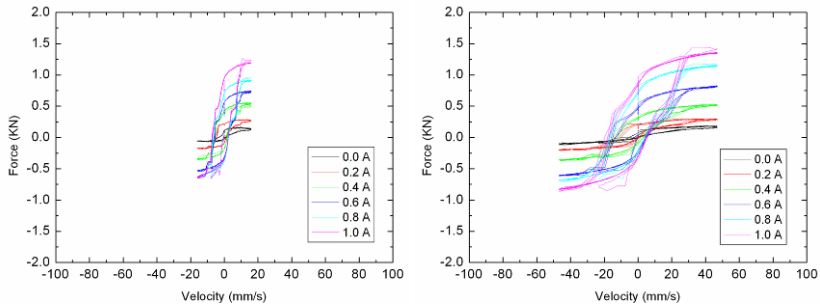

(a) 1 Hz frequency applied (b) 3 Hz frequency applied

Fig. 5. MTS force and velocity results for a sinusoidal input under different frequencies condition

smaller than one ampere. FEM analysis proves that the design was possible.
(2) The force-displacement relationship and the force-velocity relationship of the MR damper are obtained.
(3) The experimental verification indicates the effectiveness of the magnetic saturation EFM analysis on the MR damper circuit part.
(4) The damper can be used by structural (around 1-5 Hz) and automotive (around 1-5 Hz).
(5) The developed MR device has been successfully applied to model bigger MR damper that can be used for absorbing vibration.

References

1. M. R. Jolly, J. W. Bender, and J. D. Carlson, *SPIE 5th Annual Symposium on Smart Structures and Materials.* CA, ?, (1998).
2. S. A. Mazlan, N. B. Ekreem and A. G. Olabi, *Smart Mater. Struct*, 16, 1678-1682, (2007).
3. S. Guo, S. Yang, and C. Pan, *Intelligent Material Systems and Structures.* 17, 3-14, (2006).
4. M. Borowiec, G. Litak, and M. I. Friswell, *Applied Mechanics and Materials*. 5-6, 277-284, (2006).
5. F. Yi, S. J. Dyke, J. M. Caicedo and J. D. Carlson, *J. Eng. Mech.* 127, 1152-1164, (2001).
6. G. Kamath, N. M Wereley, and M. Jolly, *Mechanics and Mechanisms of Material Damping*. ? , 1325-1335, (1997).
7. R. A. Snyder, and N. M. Wereley, *Smart Structures and Integrated Systems*. 3668, 507-519, (1999).
8. Xiaojie Wang, F. Gordaninejad, *Damping and Isolation*, 3989, 232-243, (2000).
9. A. C. Shivaram and K. V. Gangadharan, *Smart Mater. Struct*, 16, 1310-1314, (2007).

TIME REVERSAL RECONSTRUCTION OF DISPERSIVE ULTRASONIC LAMB WAVES IN THIN PLATES

HYUNJO JEONG

Div of Mechanical and Automobile Eng, Wonkwang University, 344-2 Sinyong-dong Iksan, Jeonbuk 570-749, Korea

Time reversal (TR) of nondispersive body waves has been used in many applications including ultrasonic NDE. However, the study of the TR method for Lamb waves on thin structures is not well established. In this paper, the full reconstruction of the input signal is investigated for dispersive Lamb waves by introducing a time reversal operator based on the Mindlin plate theory. A broadband and a narrowband input waveform are employed to reconstruct the A_0 mode of Lamb wave propagations. Due to the frequency dependence of the TR process of Lamb waves, different frequency components of the broadband excitation are scaled differently during the time reversal process and the original input signal cannot be fully restored. This is the primary reason for using a narrowband excitation to enhance the flaw detectability.

1. Introduction

The origin of the time reversal (TR) concept traces back to time reversal acoustics [1-3]. In time reversal acoustics, an input body wave can be exactly reconstructed at the source location if a response signal measured at a distinct location is time-reversed and reemitted to the original excitation location. This phenomenon is referred to as TR of body waves and has been used in many applications including ultrasonic nondestructive evaluation and underwater communications.

While the TR method for nondispersive body waves in fluids has been well established, the study of the TR method for Lamb waves on plates is relatively new [4-6]. The effect of dispersion on the time reversal analysis of Lamb waves in a homogeneous plate was first studied by Wang et al. [7] by introducing the time reversal operator into the Lamb wave equation based on the Mindlin plate theory [8].

Due to the frequency dependence of the time reversal process of Lamb waves, different frequency components of the broadband excitation are scaled differently during the time reversal process and the original input signal cannot be fully restored.

In this paper, the full reconstruction of the input signal is attempted for Lamb waves. The TR of the A_0 mode Lamb wave is investigated by introducing a time reversal operator in a frequency domain using the Mindlin plate theory.

To achieve this goal, a narrowband input waveform is employed to enhance the TR of Lamb waves. The complete reconstruction of the input signal can be achieved when a narrowband excitation is employed for Lamb wave propagations.

2. TR of A_0 mode Lamb Wave in a Thin Plate

The time reversibility of waves is based on the spatial reciprocity and time reversal invariance of linear wave equations. In the time reversal method, an input signal can be reconstructed at an excitation point (point A) if an output signal recorded at another point (point B) is reemitted to the original source point (point A) after being reversed in a time domain as illustrated in Fig. 1.

When a sensor A is used as an actuator and another sensor B is used as a receiver (Fig. 1), the received voltage at sensor B can be written as

$$V_B(r,\omega) = I_A(\omega)K_a(\omega)G(r,\omega)K_s(\omega) \tag{1}$$

where r is the wave propagation distance from the sensors, K_a and K_s the mechanical-electro efficiency factor of sensor A and B, G the frequency response function of sensor B as a result of the input at sensor A. The frequency response function G for the A_0 mode Lamb wave is obtained by applying appropriate transformation techniques in the spatial and time domain to the wave equation based on the Mindlin plate theory [7]

$$G(r,\omega) = -\frac{i\pi h^2}{2D}\frac{\gamma_1 k_1^3 a J_1(k_1 a)H_0^{(1)}(k_1 r)}{k_1^2 - k_2^2} \tag{2}$$

where D, γ_1, a, $J_1(\cdot)$ and $H_0^1(\cdot)$ are the flexural stiffness of the plate, the amplitude ratio of dilatational to shear wave potentials at the wave number k_1, radius of sensor A, the first order Bessel function and the zeroth order Hankel function of the first kind, respectively. The wave numbers k_1 and k_2 are determined at the A_0 and A_1 modes of the Lamb waves, respectively.

Once a response signal is measured at sensor B, the reconstructed input signal at sensor A can be obtained by reemitting the time-reversed response signal at sensor B. The time reversal operation of a signal in the time domain is equivalent to taking the complex conjugate of the Fourier Transform of the signal in the frequency domain. Therefore, the reconstructed signal at sensor A from the reemitted signal at sensor B can be written in a similar fashion to Eq. (1) as

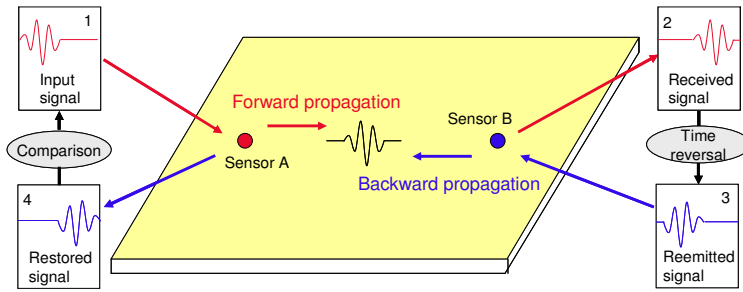

Fig. 1. Time reversal process of A_0 mode Lamb wave in a thin plate

$$V_A(r,\omega) = V_B^*(r,\omega)K_a(\omega)G(r,\omega)K_s(\omega) \tag{3}$$

where a superscript * denotes a complex conjugate. By using Eq. (1), the signal received at sensor A is rewritten as

$$V_A(r,\omega) = I_A^*(\omega)K_a^*(\omega)K_s^*(\omega)K_a(\omega)K_s(\omega)G(r,\omega)G^*(r,\omega) \tag{4}$$

Performing an inverse Fourier transform, the reconstructed input signal V_A at sensor A is

$$V_A(t) = \frac{1}{2\pi}\int_{-\infty}^{\infty} I_A^*(\omega)K_{as}^*(\omega)K_{as}(\omega)G^*(r,\omega)G(r,\omega)e^{-iwt}d\omega \tag{5}$$

where K_{as} denotes the product between K_a and K_s. If the TR of waves is satisfied, the reconstructed signal $V_A(t)$ in Eq. (5) would be identical to the time-reversed original signal $I_A(T-t)$ where *T* represents the total time duration of the signal. To directly compare with the original input signal $I_A(t)$ at sensor A, Eq. (5) should be time reversed, thus

$$V_A(T-t) = \frac{1}{2\pi}\int I_A(\omega)K_{TR}(\omega)G_{TR}(r,\omega)e^{-i\omega(T-t)}d\omega \tag{6}$$

where

$$K_{TR}(\omega) = K_{as}(\omega)K_{as}^*(\omega), \qquad G_{TR}(\omega) = G(r,\omega)G^*(r,\omega) \tag{7}$$

Here, K_{TR} is a factor determined by the electro-mechanical efficiency of the sensor, and G_{TR} is referred to as a time reversal operator of A_0 mode Lamb wave determined by the Mindlin plate theory. In Eq. (6), assuming K_{TR} is

constant, the TR is achieved only if G_{TR} is independent of the angular frequency ω. However, because the impulse response function $G(r,\omega)$ of a plate structure is frequency dependent, the time reversal operator G_{TR} varies with respect to the frequency. This indicates that the wave components are non-uniformly scaled depending on the frequency. Therefore, the original input signal cannot be reconstructed if a broadband input signal is used.

3. Numerical Examples

To justify the use of a narrowband excitation for the time reversal process, a numerical example of the time reversal process is provided here. In particular, a broadband Gaussian pulse as shown in Eq. (8) and Figs. 2(a), (b) and a narrowband 100 kHz toneburst as shown in Eq. (9) and Figs. 3(a), (b) are used as input signals in a numerical simulation of the time reversal process.

For the broadband simulation, the following Gaussian pulse is employed to derive the sensor A:

$$y(t) = Ae^{-(t-\mu)^2/2\sigma^2} \tag{8}$$

where μ=20 μs and σ=2 μs. For the narrowband toneburst signal, the following input function is used.

$$y(t) = \begin{cases} A[1-\cos(2\pi ft/N)]\cos(2\pi ft) & (0 < t < N/F) \\ 0 & \text{otherwise} \end{cases} \tag{9}$$

where the frequency f=100 kHz and the number of cycles N=5. An aluminum plate (E=73 GPa, ν=0.3, ρ=2770 kg/m^3, h=1.02 mm) is used with sensor diameter a= 3.175 mm and propagation distance r=152.4 mm.

The time domain input signals are shown in Figs. 2(a) and 3(a) for broadband and narrowband cases, respectively. Their frequency spectra are also shown in Figs. 2(b) and 3(b). The response signal received at sensor B is shown in Figs. 2(c) and 3(c). The broadband input signal causes a velocity dispersion on the A_0 mode propagation even at a short distance of 152.4 mm. On the contrary, the narrowband input signal remains its shape throughout the propagation.

When the response signal is reversed in time and reemitted to the input sensor, the velocity dispersion of Lamb waves is compensated as shown in Figs. 2(d) and 3(d). However, the shape of the original pulse is not fully recovered

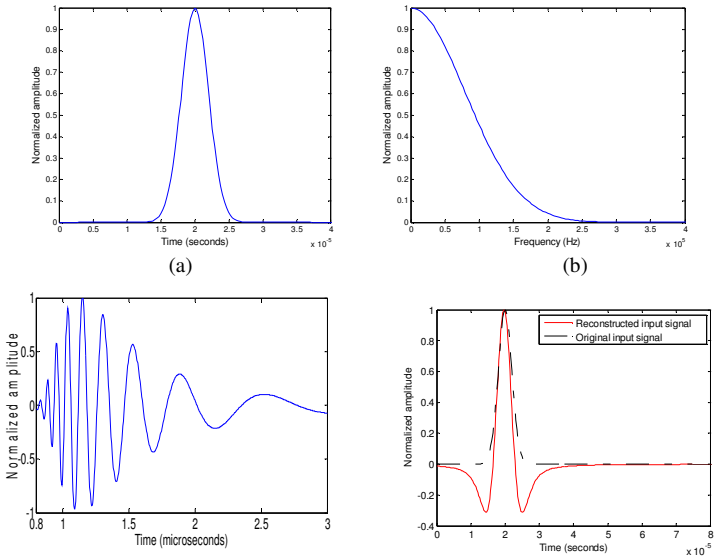

Fig. 2. Time reversal process of a broadband Gaussian pulse. (a) Time domain input signal (b) Its magnitude spectrum, (c) Response signal of sensor B at the propagation distance r=152.4 mm, and (d) Reconstructed TR signal compared with the original input signal.

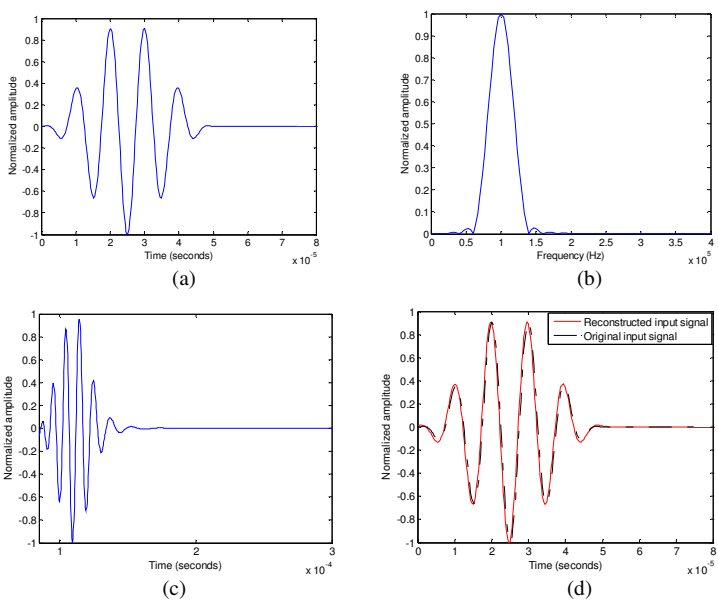

Fig. 3. Time reversal process of a narrowband toneburst waveform. (a) Time domain input signal (b) Its magnitude spectrum, (c) Response signal of sensor B at the propagation distance r=152.4 mm, and (d) Reconstructed TR signal compared with the original input signal.

when the Gaussian input is used as illustrated in Fig. 2(d). This is because the various frequency components of the Gaussian input are differently scaled and superimposed during the time reversal process. On the other hand, as shown in Fig. 3(d), the shape of reconstructed toneburst waveform is practically identical to that of the original input because the amplification of the time reversal operator is almost uniform in this limited frequency band.

4. Conclusions

The full reconstruction of the known excitation signal at the original input location is attempted through the time reversal process of dispersive Lamb waves. The TR of the A_0 mode Lamb wave is investigated by introducing a time reversal operator in a frequency domain using the Mindlin plate theory. The complete reconstruction of the input signal cannot be achieved when a broadband excitation is employed for Lamb wave propagations. Due to the frequency dependence of the time reversal process of Lamb waves, different frequency components of the broadband excitation are scaled differently during the time reversal process and the original input signal cannot be fully restored. The use of narrowband input waveform fully restores the original input signal in the time reversal process of dispersive Lamb wave propagations. This is the primary reason for using a narrowband toneburst excitation in most experiments. The ultimate goal of future work is to enhance the flaw detectability in thin-walled structures through spatial ad temporal focusing due to the TR of Lamb waves.

References

1. M. Fink, *Scientific American* **281**, 91 (1999)
2. M. Fink and C. Prada, *Inverse Problems* **17**, R1 (2001)
3. C. Draeger, D. Cassereau and M. Fink, *J. Acoust. Soc. Am.* **102(3)**, 1289 (1997)
4. R. K. Ing and M. Fink, *IEEE Ultrasonics Symposium* **1**, 659 (1996)
5. R. K. Ing and M. Fink, *IEEE UFFC* **45**, 1032 (1998)
6. H. W. Park, H. Sohn, K. H. Law and C. R. Farrar, *J. Sound and Vib.* **302**, 50 (2007).
7. C. H. Wang, J. T. Rose and F.-K. Chang, *Proc.SPIE* **5046**, 48 (2003).
8. L. R. F. Rose and C. H. Wang, *J. Acoust. Soc. Am* **116(1)**, 154 (2004).

INVESTIGATION OF RICE TASTE ELEMENTS AT WIDE AREA, USING REMOTE SENSING AND GIS TECHNOLOGY

TETSUYA UEDA, CHANSEOK RYU, MASHIKO SUGURI, MIKIO UMEDA †

Environmental Science and Technology, Graduate School of Agriculture Kyoto University, Kitashirakawa Oiwake-cho,Kyoto, 606-8502, Japan

In this research, about 20ha paddy fields (15% of same variety field) were investigated in 400ha. Protein content was predicted by GreenNDVI (r=0.62). The sampling fields were divided into two groups depending on the growing term in order to analyze more precisely, using GIS function. In the group of long growing term, it is possible improve protein content prediction model (r=0.76). In the group 1, the factors that have a very high quality in protein content were investigated using GIS database function. Protein content was affected by top dressing application date and harvesting date (5% at a significant level by T-test). Using remote sensing and GIS, it is possible to suggest effective management on the difference of cultivation condition.

1. Introduction

Recently, the Japanese government tries to decrease the cultivation area of rice paddy because of the surplus of rice. Therefore, the quality of rice is focused on the farmer. However, it is difficult to control the quality of rice, because there is several factors influence the rice quality, such as protein and amylose contents. It is necessary to investigate the factors for rice quality including management date, amount of fertilizer, soil property and growth stage and so on.

Remote sensing technology is useful tool for detecting the rice growth information. Previous research, it was possible to predict protein and amylose content by GreenNDVI (Terada et al., 2005). It was possible to predict protein contents using multi spectral remote sensing (R^2=0.786) and hyperspctral remote sensing (R^2=0.848) (Ryu et al., 2005). Using remote sensing, growth information and spatial variability in wide area can be investigated. However, it is difficult to establish the prediction model in wide area, because each field has a different condition such as variety, management of fertilizer and soil property. On the other hand, it is important to construct the database for management in order to organize and supply information to farmers. Also, it is important to analyze management information to supply the good quality to consumers.

† Work partially supported by grant Subsidy Project for Creation of Biomass Circle.

GIS software is a useful tool in terms of constructing the database and analyzing field information geographically. At Wakayama prefecture in Japan, GIS database system for mandarin orange was constructed. Furthermore, sugar content of mandarin orange was investigated and predicted geographically (Miyamoto et al., 2004). Therefore, using remote sensing and GIS technology, it is possible to establish the prediction model and to provide the effective management.

The aims of this work are to predict protein content and to investigate the factor that causes the difference in protein content or GreenNDVI from airborne image, using remote sensing and GIS.

2. Materials and Methods

2.1. *Test area*

The test area was located in Yagi-town, Nantan-city, Kyoto prefecture in Japan. The tested species was *Oryza sativa L.*, and variety was *KINU-HIKARI*. *KINU-HIKARI* is the middle growing variety and common variety in this region. In this region, *KINU-HIKARI* is cultivated at 121ha (30%) within 400ha paddy field. In this research, 67 fields (18ha, 15% of *KINU-HIKARI* fields) were investigated. Each field had the information about fertilizer amount, yield and management (planting, fertilizer application, sampling, harvesting), respectively.

2.2. *Remotely sensed data*

The images were taken by ADS 40 sensor (Spectral Imaging, Airborne Digital Sensor 40). The bands are blue, green, red, and NIR, and ground resolution was 0.25m. RGB raster image was used as a base map. GreenNDVI was calculated by following equation. GreenNDVI image was converted from floating data (-1 to 1) to byte type data (0 to 255) in order to analyze it by GIS. This image was separated by the district level because the volume of image was too large to transform from raster to vector file.

$$GreenNDVI = (DN_{NIR} - DN_{Green}) / (DN_{NIR} + DN_{Green}) \quad (1)$$

Where,

DN_{NIR}: The digital number of NIR

DN_{Green}: The digital number of Green

2.3. *Sampling of rice taste elements*

8 stocks of rice plants were sampled about 1 week before harvesting at each field. These were threshed and dried to about 15% of moisture content.

And then husked to brown rice and sorted by the mesh of #1.90. Rice taste elements were measured by the NIR detector (Satake, RCTA11A).

2.4. *Construction of the GIS database*

A series of thematic layers and tables were organized by GIS software, geographically (ArcView9.1, ESRI). There are many types of data in GIS layers, such as raster, and shape file (vector file) and information table data. Figure1 shows the district shape file. Field shape file, district shape file and GreenNDVI shape file were constructed. Figure 2 shows the field shape file and GreenNDVI shape file. The averages of GreenNDVI value in each field was calculated by overlaying field and GreenNDVI shape files. Furthermore, the table in field shape file was given an ID number and field information in order to analyze the effective factors for protein content.

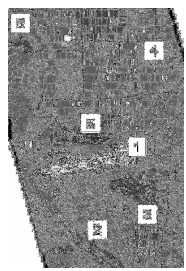

Fig. 1. District shape file.

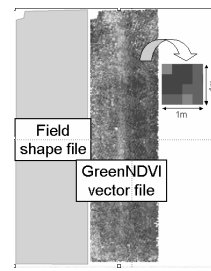

Fig. 2. Field shape file and GreenNDVI shape file.

3. Results and Discussion

3.1. *Prediction model of protein content*

Table 1. Correlation between GreenNDVI and protein content divided by district.

District No.	The area of sampling field (The number of fields)	Protein content		Coefficient of correlation
		Mean	S.D.	
District 1	4.0ha (14)	7.46	0.27	0.52
District 2	1.5ha (15)	7.68	0.26	0.49
District 3	2.5ha (9)	7.68	0.29	0.79
District 4	4.8ha (14)	7.65	0.34	0.82
District 5	2.2ha (9)	7.77	0.31	0.65
District 6	2.5ha (7)	7.86	0.29	0.87
Total	18ha (67)	7.66	0.31	0.62

Table 1 shows the coefficient of correlation between GreenNDVI and protein content divided by district. The values of protein content and *r* have different

tendency in each district. It is possible to predict protein content with GreenNDVI (r=0.62).

3.2. *Analysis of protein content prediction model using GIS*

The field management, such as date, applied of fertilizer, soil property and growth stage, might be important factors for protein content and GreenNDVI, because each field has different management condition. Therefore, sampling fields were divided by management information, which were extracted from GIS database. With respect to the amount of top dressing, sampling fields were divided into two groups. There was no significant difference at two groups by GreenNDVI and protein content. With respect to growing term, sampling fields were divided by two groups depending on the days from transplanting to image acquiring. Figure 3 shows the coefficient of correlation classified by the growing term. Sampling fields were divided into two groups (over 102 and under 98), because r drastically changes from 98 days. Table 2 shows the number of fields divided as two groups in each district. Except district 1, two groups are depending on the district. It seems that growing term is one of important factors to predict protein content more precisely using remote sensing. Figure 4 shows the prediction model divided by growing term. It is possible to improve the protein content prediction model using GIS function. However, in the case of group 2, it is necessary to identify the reason shown in figure 3 and 4. Figure 5 shows the distribution of group 2 by each district. Though there is no significant difference in growing term and amount of fertilizer between three districts (T-test), GreenNDVI of district 2 was lower than that of district 3 and 5.

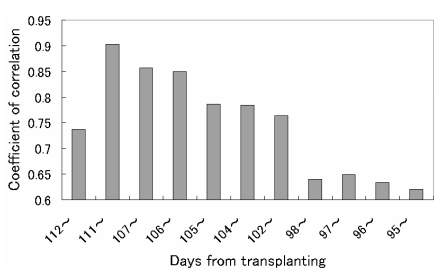

Fig. 3. Coefficient of correlation classified by the days from transplanting.

Table 2. The number of fields in each group.

District No.	The number of field	
	Group 1 (102 ~)	Group 2 (~ 98)
District 1	11	3
District 2	0	15
District 3	0	8
District 4	14	0
District 5	0	9
District 6	7	0
Total	32	35

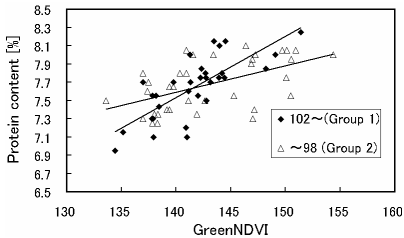

Fig. 4. Correlation divided by the growth stage.

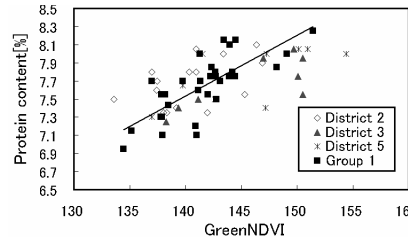

Fig. 5. Correlation divided by three districts.

It is considered that soil property of district 2 is sandy, because the fields in district 2 are close to the river as compared with other districts. Therefore, nitrogen might be easy to leak through the soil.

3.3. *Analysis of protein content improvement using GIS*

It is necessary to improve the protein content as low as possible in the group 1, when farmer want to raise their rice quality. Therefore, the factors that have a very high quality in protein content were investigated using GIS database function. 35 fields were divided into two sections, such as low and high protein content, and five management factors were considered as effective factor for protein content. Table 3 shows the management factors and results of T-test. There was a significant difference in top dressing application date and harvesting date at a level of 5%. Especially for harvesting date, there was also a significant difference in GreenNDVI.

Table 3. Management factors and significant difference by T-test.

Management factor	Significant difference T-test (protein content)	Significant difference T-test (GreenNDVI)
Factor 1 Basal dressing application date	No	No
Factor 2 Basal dressing amount	No	No
Factor 3 Top dressing application date	5%	No
Factor 4 Top dressing amount	No	No
Factor 5 Harvesting date	5%	5%

Figure 6 and Figure 7 show the histogram of top dressing application date and harvesting date divided by protein content. It is possible to find the factors, which is able to improve protein content, using GIS function.

It is known that protein content is affected by top dressing amount (Ryu et al., 2007). Coefficient of determination between top dressing amount and protein content was 0.75. In that case, top dressing was applied only once in order to

investigate the influence of the amount of fertilizer. However, in this research, it is complicated to consider several parameters because top dressing was applied in two installments. Therefore, the influence of the valance of fertilizer amount in each time should be investigated in order to identify the effect of nitrogen amount.

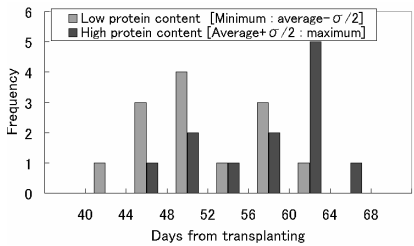

Fig. 6. Histogram of topdressing application date.

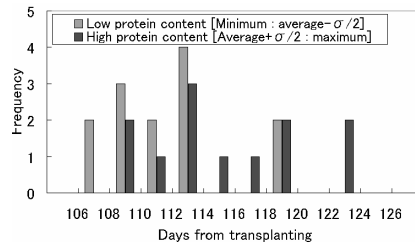

Fig. 7. Histogram of harvesting date.

4. Conclusion

In this research, about 20ha paddy fields (15% of same variety field) were investigated in 400ha. Protein content was predicted by GreenNDVI (r=0.62). Sampling fields were divided by two groups depending on the growing term in order to analyze more precisely, using GIS function. In the group of long growing term, it was possible to improve protein content prediction model (r=0.76). In district 3 and 5, GreenNDVI was higher than group 1 because of the shortness of growth term. It is considered that soil property of district 2 is sandy, because the fields in district 2 are close to the river as compared with other districts. In the group 1, the factors that have a very high quality in protein content were investigated using GIS database function. Protein content was affected by top dressing application date and harvesting date (5% at a significant level by T-test). Using remote sensing and GIS, it is possible to suggest effective management way on the difference of cultivation condition.

References

1. Ryu, C., Terada, C., Ueda, T., Suguri, M., Umeda, M., Journal of JSAM Kansai Branch 100, 130 (2006)
2. Ryu, C., Suguri, M., Umeda, M., In proc. 1st ACPA, 53 (2005).
3. Miyamoto, K. Hort. Res. 3 (3), 245 (2004)
4. ArcGIS tutorial, ESRI.
5. Y. Shao, X. Fan, H. Lin, J. Xiao, S. Ross, B. Brisco, R. Brown, G. Staples., Remote Sensing of Environment 76, 310 (2001)
6. Ryu, C., Suguri, M., Iida, M., Umeda, M., Journal of JSAM 69(1), 55 (2007)

LINE-SCAN SPECTRAL IMAGING SYSTEM FOR ONLINE POULTRY CARCASS INSPECTION

KUANGLIN CHAO, CHUN-CHIEH YANG, MOON S. KIM

Food Safety Laboratory, Animal and Natural Resources Institute, Agricultural Research Service, U.S. Department of Agriculture, Powder Mill Rd. Bldg 303, BARC-East, Beltsville, MD 20705, U.S.A.

An online line-scan imaging system capable of both hyperspectral and multispectral visible/near-infrared reflectance was developed to inspect freshly slaughtered chickens on a processing line for wholesomeness. Hyperspectral images were acquired using the line-scan imaging system for 5549 wholesome chicken carcasses and 93 unwholesome chicken carcasses on a commercial processing line, for analysis to optimize ROI size and location and to determine the key intensity waveband and ratio wavebands to be used for online inspection. Multispectral imaging algorithms were developed for multispectral inspection of over 100,000 chickens on a 140 bpm processing line during two 8-hour shifts at a commercial poultry plant. In-plant testing results indicated that the imaging inspection system can perform successfully on a commercial poultry processing line.

1. Introduction

With the 1996 final rule on Pathogen Reduction and Hazard Analysis and Critical Control Point (HACCP) systems,[1] FSIS implemented the HACCP and Pathogen Reduction programs in meat and poultry processing plants throughout the country to ensure food safety for consumers. More recently, FSIS has also been testing the HACCP-Based Inspection Models Project (HIMP) in a small number of volunteer plants.[2] HIMP requirements include zero tolerance for unwholesome chickens exhibiting symptoms of "septox" – a condition of either septicemia or toxemia. USDA inspectors remove these unwholesome birds from the processing lines during their bird-by-bird inspections, which can, by law, be conducted at a maximum speed of 35 birds per minute (bpm) for an individual inspector. The inspection process is subject to human variability, and the inspection speed restricts the maximum possible output for the processing plants while also making inspectors prone to fatigue and repetitive injury problems. This limit on production throughput, combined with increases in chicken consumption and demand over the past 2 decades, places additional pressure on both chicken production and safety inspection system.

U.S. poultry plants now process over 8.8 billion broilers annually. Commercial poultry processing lines in the U.S. currently are operated at speeds up to 140 bpm; however, such processing lines require up to four inspection stations, each with an FSIS inspector to conduct bird-by-bird inspection at the 35 bpm speed limit. Thus there remains a need to develop rapid, nondestructive, and accurate inspection systems that can inspect chickens for wholesomeness on commercial processing lines.

The objective of this study were to provide an online line-scan imaging system capable of both hyperspectral and multispectral visible/near-infrared reflectance, and a method of using the system to inspect freshly slaughtered chickens on a processing line for wholesomeness and unwholesomeness.

2. Materials and Methods

2.1. *Hyperspectral/Multispectral Line-Scan Imaging System*

The imaging system consisted of a Electron-Multiplying Charge-Coupled-Device (EMCCD) camera (PhotonMAX 512b, Roper Scientific, Inc., Trenton, NJ), an ImSpector V10 imaging spectrograph (Spectral Imaging Ltd., Oulu, Finland), and a pair of high power, broad-spectrum white light-emitting-diode (LED) line lights (LL6212, Advanced Illumination, Inc., Rochester, VT). The camera operates with a 10 MHz, 16-bit digitizer for high-speed image acquisition. The spectrograph aperture slit of 50 μm limits the instantaneous field of view (IFOV) of the imaging system to a thin line. Light from the linear IFOV is dispersed by a prism-grating-prism line-scan spectrograph and projected onto the EMCCD camera. The spectrograph creates a two-dimensional image for each line-scan, with the spatial dimension along the horizontal axis and the spectral dimension along the vertical axis of the EMCCD Imaging Device.

2.2. *Chicken Imaging Acquisition*

The hyperspectral/multispectral line-scan imaging system (HMLIS)[3] was used to acquire images of chickens hung on a commercial processing line moving at 140 bpm, as shown in Figure 1. The system was positioned such that the distance between the lens and IFOV target area was 914 mm, with the LED line lights illuminating the IFOV target area from a distance of 214 mm. The IFOV spanned 177.8 mm, which translated into 512

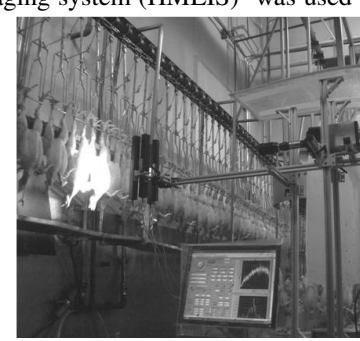

Fig. 1. HMLIS on a processing line.

spatial pixels, with each pixel representing an area of 0.12 mm^2.

2.3. *Procedures*

Following spectral and spatial calibration of the imaging system, acquisition of hyperspectral line-scan images (512 spatial pixels by 55 spectral channels) was conducted on the chicken processing line for 5549 wholesome and 93 unwholesome birds. These images were analyzed for Region of Interest (ROI) optimization and selection of a key wavelength and ratio wavebands based on average spectral differences between wholesome and unwholesome birds. Random track mode on the imaging system was implemented for multispectral inspection using only the key wavelength and ratio wavebands. LabView software (National Instruments Corp., Austin, TX) was used to develop software modules for detecting the starting point (SP) and ending point (EP) of each bird, and for implementing classification algorithms based on fuzzy logic. During two 8-hour shifts, the imaging system conducted multispectral inspection for over 100,000 birds. A veterinary medical officer identified bird conditions during several 30-40 minute periods for verification of system performance.

3. Results and Discussion

Figure 2 shows example images, at four bands, of chickens on the processing line, including one unwholesome chicken (fifth from the left) among the series in the image.

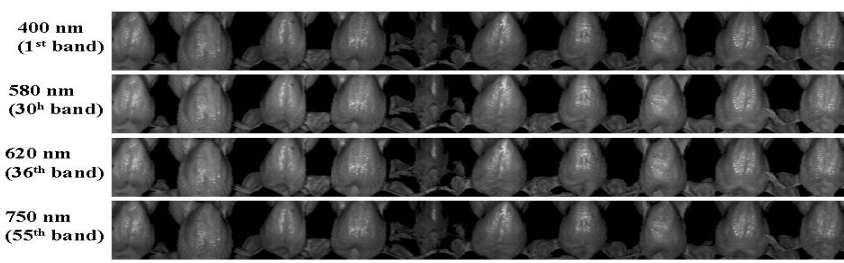

Fig. 2. Chicken carcass images at four spectral wavebands, acquired during hyperspectral line-scan imaging on the chicken processing line.

The hyperspectral images were analyzed to optimize the ROI size and location and the key wavebands for differentiation by reflectance intensity and by waveband ratio. Figure 3 shows two contour images of chicken carcasses with the SP and EP marked and connected by a line.

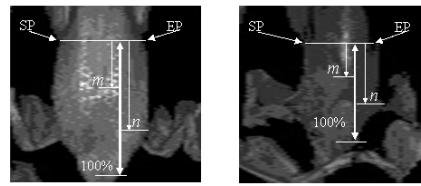

Fig. 3. SP, EP, *m*, and *n* parameters marked on two example chicken images.

The possible size and location of the ROI is described by parameters *m* and *n*, which extend below the SP-EP line. The values of *m* and *n* indicate, by percentage of the pixel length between the SP-EP line and the furthest non-background pixel below the SP-EP line, the location of the upper and lower ROI borders.

The difference between the average wholesome and average unwholesome value at each of the 55 bands was calculated and the range of these differences for possible ROIs is shown in Figure 4. Because the 40%-60% ROI showed the range with the greatest difference values between the average wholesome and unwholesome spectra, this ROI was considered the optimized ROI to be used for multispectral inspection.

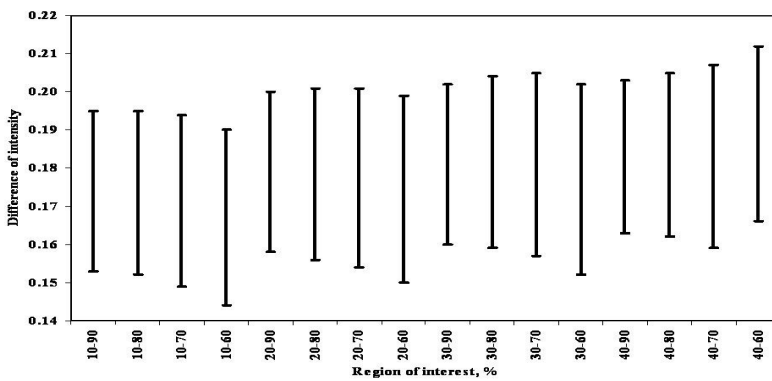

Fig. 4. The range, for possible ROIs, of difference values between average wholesome and average unwholesome chicken spectra, for optimizing the ROI to be used for inspection of chickens.

The 30th band showed the greatest difference between the average wholesome and the average unwholesome spectra from among all 55 bands for the optimized ROI; this band, corresponding to 580 nm, was selected as the key waveband to be used for intensity-based differentiation of wholesome and unwholesome chicken carcasses. Figure 5 shows the averaged wholesome and unwholesome chicken spectra, marked with the wavebands that were investigated for differentiation of wholesome and unwholesome chicken carcasses by a two-waveband ratio. The difference in average ratio values were

calculated for ($W_{440}/W_{460} - U_{440}/U_{460}$), ($W_{500}/W_{540} - U_{500}/U_{540}$), and ($W_{580}/W_{620} - U_{580}/U_{620}$). The last ratio, using the 580 nm and 620 nm wavebands, showed the greatest difference between the averaged wholesome and unwholesome chicken spectra and was thus selected for use in differentiation by two-waveband ratio.

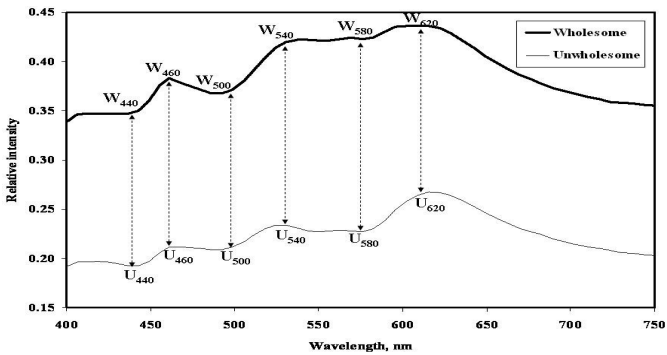

Fig. 5. The averaged wholesome and unwholesome chicken spectra, for possible key wavebands that can be used for two-waveband ratio differentiation of wholesome and unwholesome chickens.

The optimized ROI and key wavebands determined were used for multispectral inspection of over 100,000 chickens on a 140 bpm processing line during two 8-hour shifts at a commercial poultry plant. For multispectral classification, fuzzy logic membership functions[4] were built based on the mean and standard deviation values for the 580 nm key waveband from the hyperspectral analysis data subset, and on the mean and standard deviation values for the 580 nm and 620 nm two-waveband ratio.

The total numbers of wholesome and unwholesome chickens identified by the system are shown in Table 1 below, compared with numbers drawn from FSIS tally sheets created by three inspection stations on the same processing line during those two inspection shifts.

Table 1. Wholesome (W) and unwholesome (U) birds identified during inspection shifts by processing line inspectors and by the imaging inspection system.

	Line inspectors			Imaging inspection system		
	W	U	Total	W	U	Total
Shift 1	53563 (99.84%)	84 (0.16%)	53647 (100%)	45305 (99.37%)	288 (0.63%)	45593 (100%)
Shift 2	64972 (99.89%)	71 (0.11%)	65043 (100%)	60922 (99.84%)	98 (0.16%)	61020 (100%)

A veterinarian also conducted several periods of system verification, each lasting approximately 30 to 40 minutes. The veterinarian conducted bird-by-bird observation of chicken carcasses immediately before they entered the IFOV of the imaging system. The imaging system output was observed for agreement with the veterinarian's identifications. The veterinarian observed 16,174 wholesome birds and 43 unwholesome birds over 4 verification periods during inspection shift 1. Of these birds, the imaging system incorrectly identified only 118 wholesome birds (99.27% correct) and 2 unwholesome birds (95.35% correct). The veterinarian observed 27,626 wholesome birds and 35 unwholesome birds over 6 verification periods during inspection shift 2. Of these birds, the imaging system incorrectly identified only 46 wholesome birds (99.83% correct) and 1 unwholesome bird (97.14% correct). These results, with the percentages listed in Table 1, suggest that the imaging inspection system can perform successfully on a commercial poultry processing line.

4. Conclusion

The hyperspectral/multispectral line-scan imaging system can be used for online inspection of chicken carcasses for the detection of unwholesome birds on high-speed processing lines. The imaging system inspected over 100,000 chickens on a commercial 140 bpm kill line during continuous operation and achieved over 99% accuracy in identifying wholesome chickens and over 96% accuracy in identifying unwholesome diseased chickens. Use of the line-scan imaging system will help poultry processing plants to improve food safety and production efficiency and satisfy increasing consumer demand for poultry products.

References

1. U.S. Department of Agriculture, Food Safety and Inspection Service, *Fed. Regist*. **61**: 38805 (1996).
2. U.S. Department of Agriculture, Food Safety and Inspection Service, *Fed. Regist*. **62**: 31553 (1997).
3. K. Chao, C. C. Yang, Y. R. Chen, M. S. Kim, and D. E. Chan, *Sens. & Instrumen. Food Quality and Safety*. **1**, 62 (2007).
4. C. C. Yang, K. Chao, Y. R. Chen M. S. Kim, and D. E. Chan, *Biosystems Engr.* **95**, 483 (2006).

BENDING STRENGTH PREDICTION OF STRUCTURAL LUMBER BY X-RAY SCANNER

JUNG KWON OH

Department of Forest Sciences, Seoul National University, #200 R.M.6218 San 56-1 Sillim-9-dong, Gwanak-gu, Seoul, 151-921, Korea

KWANG-MO KIM

Department of Forest Products, Division of Wood Engineering, 207 Cheongyangni-2-dong Dongdaemun-gu, Seoul, 130-712, Korea

KUGBO SHIM

Department of Forest Products, Division of Wood Engineering, 207 Cheongyangni-2-dong Dongdaemun-gu, Seoul, 130-712, Korea

JUNG-HWAN PARK

Department of Forest Products, Division of Wood Engineering, 207 Cheongyangni-2-dong Dongdaemun-gu, Seoul, 130-712, Korea

HWANMYEONG YEO

Department of Forest Products, Division of Wood Engineering, 207 Cheongyangni-2-dong Dongdaemun-gu, Seoul, 130-712, Korea

JUN-JAE LEE

Department of Forest Sciences, Seoul National University, #200 R.M.6218 San 56-1 Sillim-9-dong, Gwanak-gu, Seoul, 151-921, Korea

Wood is a natural material with physical and mechanical characteristics that vary over a wide range. The prediction of lumber strength is very important to guarantee the safety of the building. In this study, we intend to predict the bending strength of structural lumbers by x-ray and the knot ratio based I_k/I_g model was proposed. Experimental result verified the proposed model. The predictive model could improve the predictive accuracy of bending strength of lumber, from 0.36 to 0.42 of R^2.

1. Introduction

Wood is a natural material with physical and mechanical characteristics that vary over a wide range. For structural use, lumber with similar mechanical properties

should be placed in the categories called stress grades. There are two methods to grade lumber, which are visual grading and machine grading.

The current visual grading is based on the established empirical rules for wood defects by the grader's observation of the appearance of the lumber. However, Madsen [3] concluded that the present visual grading rules do not perform as expected. Most current automated machine grading work based on the stiffness. This method is based on the observation that the stronger lumber pieces tend to have higher bending stiffness. In practice, the relationship between lumber strength and bending stiffness is not well-defined [4]. The strength of the lumber mainly depends on defects such as knots, but this grading machine is not very sensitive for detecting defects [3].

Knots are almost always present in large numbers in a piece of the lumber. It is well-known that knots are the most serious defect as they can greatly reduce the strength of the lumber. Denzler *et al.*[8] reported that the coefficient of determinant between the strength of lumber and knot information is from 0.15 to 0.35 in their review paper and combining knot information with modulus of elasticity and density can improve the predictive accuracy of lumber strength. In order to estimate the strength of lumber above the acceptable level in practical use, it is required to improve the accuracy of the lumber strength prediction with only knot information at first. Oh *et al.*[6] proposed a knot ratio evaluation method. In this study, this knot ratio evaluation was also tried to be applied to the bending strength estimation of the lumber.

The objectives of this study are to predict the bending failure location and bending strength, and it intended to improve the accuracy of the bending strength prediction with only knot information extracted from x-ray image.

2. Materials and Methods

2.1. *Specimens*

The 461 pieces of *Japanese Larch* lumber with dimensions of 38mm x 140mm x 3.6 m were sampled from commercial mills. They were kiln-dried to an average equilibrium moisture content of approximately 18%.

2.2. *X-ray measurement*

In this study, an image intensifier was used for the x-ray detector, (Thales Image Intensifier TH9429). This equipment doesn't need developing the film and printing. And an x-ray digital image can be taken at once. X-ray image was taken with x-ray passing through 38mm thick of 38 x 140mm lumber. We took x-ray

images and calculated the density of specimens along the full length and width of each lumber by using Beer's law [5].

2.3. *Measurement of bending strength*

After x-ray measurement, the static bending test was performed on the same specimens with 3-point loading, following ASTM D 198. The test span was 2.4m and speed of test was set at 1mm/min. The specimens were loaded in the edgewise direction and the lateral supports were installed. The selection of the tension face of the bending specimen can have a significant effect on the bending strength of a specimen. In this study, the tension face of the specimen was chosen at random. After the failure of the lumber, the maximum load and the location of the failure were recorded on the sheet.

2.4. *Predicting of failure location and the strength*

The failure location prediction interpreted the knot x-ray image which has only knot information. Knot x-ray image was extracted from x-ray image for full length and width of the lumber by knot detection algorithm [6]. And the knot x-ray image was converted into knot ratio information as Figure 2.B shows [6]. Considering a specific cross section, 1-dimension array of knot ratio for a cross section can be expressed, as in Figure 1. Knot ratio evaluation method can give more detailed information than knot detecting method as Figure 1 shows. With the two types of knot information, the moment of inertia of the knot, I_k, was calculated respectively. I_k was calculated for every cross section in this manner, and the moment of inertia of the full cross section was calculated using the lumber dimension. Figure 3.C shows I_k/I_g values along the lumber length.

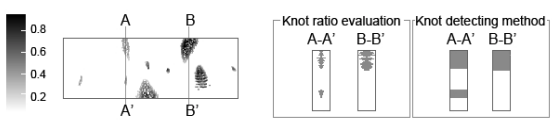

Fig. 1. Comparison between knot ratio evaluation and knot detecting method

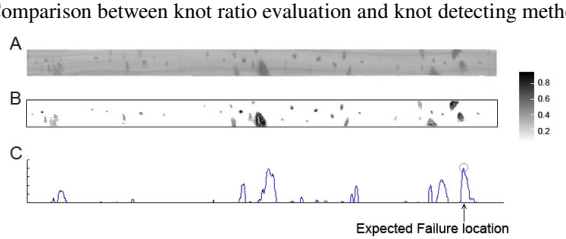

Fig. 2. Basic idea of predicting failure location and lumber bending strength
(A : Raw x-ray image, B : Knot ratio information, C : Knot ratio information B : I_k/I_g)

The basic idea of predicting failure location and lumber bending strength is that the cross section with maximum I_k/I_g value is the critical cross section of the lumber and this maximum I_k/I_g value is expected to be related to the lumber strength (Figure 2.).

It is well-known that closely-spaced knots have more effects than well-spaced knots on the strength of the lumber. In the current visual grading rule, knots within about 150 mm are regarded as a knot cluster, and the sum of knot diameters was used to determine the grade of the lumber [7]. In this study, the knot cluster was also defined as two or more knots within 150 mm. To consider the spacing between knots, the knot information of the cross sections within 150mm was multiplied by the reducing factor that is linearly reduced along the distance from the target cross section. And this modified knot information was projected to a single target cross section (Figure 3.). Every cross section was reconstructed in this manner. I_k/I_g was calculated with these reconstructed cross sections, and the expected failure location was found.

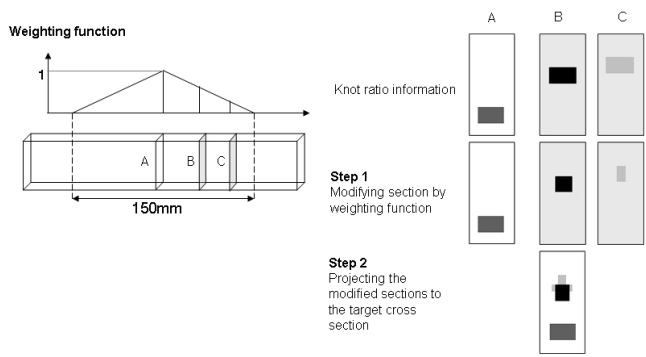

Fig. 3. An example of knot cluster evaluating method.

In the bending test, the tension side was chosen randomly. However, it is well-known that most lumbers fail at tension side by tension stress. Therefore, we prepared two x-ray images for tension side and full cross section.

In order to verify the improvement of predictive accuracy by knot ratio evaluation that was newly applied in this study, the failure location and lumber strength were predicted by the two methods respectively, which are knot ratio evaluation method and knot detecting method.

3. Results and Discussions

In order to verify the proposed lumber strength predicting model, 3-point bending test was carried out. Because the stress is different along the location of

the lumber length under the 3 point loading as moment diagram (Figure 4.B) shows, a bit of modification of the proposed model was required. I_k/I_g value can be easily converted into I_c/I_g value as following equation (Figure 4D).

$$I_c/I_g = (1-I_k)/I_g \quad (1)$$

Where I_c is the moment of inertia for clear part. And then I_c/I_g was divided by *Moment* (Figure 4.E). The cross section with minimum $(I_c/I_g)/Moment$ was defined to be the critical cross section at which the lumber is expected to fail.

Instead of bending strength, the bending stress at the expected failure location was calculated. The regression analysis between the I_k/I_g value at the expected failure location and bending stress at the expected failure location was carried out.

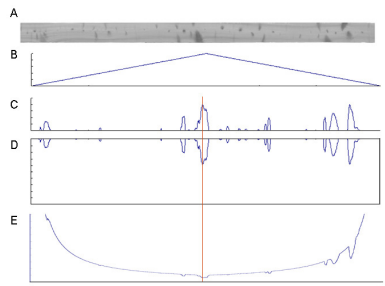

Fig. 4. Prediction of failure location under 3-point loading.
(A: Raw x-ray image, B: Moment diagram C: I_k/I_g, D:I_c/I_g, E: $(I_c/I_g)/Moment$)

In order to optimize the predicting model, the 4 cases of analysis were carried out (Table 1). Table 1 shows the results of predictive accuracy of failure location and lumber strength.

Table 1. Comparison of predictive accuracy of failure location and lumber strength for four cases

Case			Prediction of failure location (%)	Prediction of lumber strength (R^2)
No.	Knot evaluation method	X-ray image		
1	Knot ratio evaluation	Full cross section	70.1	0.42
2	Knot ratio evaluation	Tension side	80.4	0.42
3	Knot detection	Full cross section	66.5	0.38
4	Knot detection	Tension side	77.3	0.36

From comparison between case 1, 2 and case 3, 4, it was found that the knot ratio evaluation method improved the accuracy of failure location prediction and lumber strength prediction. And the accuracy of the failure location prediction with the tension side x-ray image was much higher than with the full cross section x-ray image. However coefficient of determinant for the prediction of lumber strength did not show large differences between the tension side x-ray image and the full cross section x-ray image

From these results, it could be concluded that more detailed knot information acquired by knot ratio evaluation could improve the predictive accuracy of the failure location from 77.3% to 80.4% and the bending strength of lumbers from 0.36 to 0.42 of R^2. From the results of failure location prediction, it was found that the tension side knots are fatal defects to lead the lumber to the bending failure. But, the regression analysis with tension side x-ray image did not give the improved answer. Although the tension side knot mainly causes the reduction of bending strength, it is thought that the compression side knot also bring to additional reductions of the lumber strength. Because the analysis with the tension side x-ray image did not consider the additional strength reductions by compression side knot, the predictive accuracy of strength wasn't improved. Further studies on the additional strength reductions by compression side knot are required.

4. Conclusions

This study was intended to estimate the bending strength of the lumber, using only knot information measured by an x-ray scanner and to improve its accuracy. By the knot ratio based I_k/I_g method, the bending failure location could be predicted with a good accuracy (80.4%). The predictive accuracy of bending strength could be improved from 0.36 to 0.42 of R^2 by the newly applied the knot ratio evaluation method.

References

1. Anil K. Jain, Fundamentals of Digital Image Processing, Prentice Hall. pp. 384-389 (2003).
2. American Society for Testing and Materials, 2005, Standard Test Methods of Static Tests of Lumber in Structural Sizes, ASTM D 198-05a (2005).
3. Borg Madsen, Structural behaviour of timber, Timber Engineering LTD. pp. 307-338 (1992).
4. Gary S. Schajer, Lumber strength grading using x-ray scanning, Forest Prod. J. 51(1): 43-50 (2000).
5. Institute of Isotopes of the Hungarian Academy of Sciences, Industrial Application of Radioisotopes, ELSEVIER. pp. 232-239 (1986).
6. Jung-Kwon Oh, Kwang-Mo Kim, Kugbo Shim, Hwanmyeong Yeo, Jun-Jae Lee, Quantitative Evaluation of Knot in Japanese Larch Lumber using X-ray Scanning, The 2nd international conference on Advanced Nondestructive Evaluation Submitted (2007).
7. Western Wood Products Association, Western Lumber Grading Rule (2005).

8. Denzler J.K., Diebold R., Glos P., Machine strength grading –commercially used grading machines – Current development, 14th international symposium on nondestructive testing of wood, pp. 11-16 (2005).

FIELD APPLICATION OF THE ULTRASONIC CT TECHNIQUE FOR EVALUATING DETERIORATION IN ANCIENT WOODEN BUILDING

SANG JOON LEE

Department of Forest Sciences, Seoul National University,
#200 room 6218, San 56-1, Shillim 9-dong, Gwanak-gu, Seoul, 151-921, Korea

KWANG MO KIM

Department of Forest Products, Korea Forest Research Institute,
207, Cheongyangni 2-dong, Dongdaemun-gu, Seoul, 130-712, Korea

JUN JAE LEE

Department of Forest Sciences, Seoul National University,
#200 room 6218, San 56-1, Shillim 9-dong, Gwanak-gu, Seoul, 151-921, Korea

The possibility of field application of the ultrasonic test based on the CT image reconstruction was found out with application to the Korean Confucian shrine. Ultrasonic CT images of all columns were possibly reconstructed with high accuracy even there are some lack of the data caused by the buried part by walls of the building. Most of the columns were severely deteriorated by the termite attack and the weathering effect.

1. Introduction

In Korea, there are many magnificent ancient buildings with great cultural significance [1]. Major structural members of the buildings have been normally constructed with wood because of its convenience of acquirement and manufacturing. However, wood can be deteriorated by various biological causes as well as the weathering effect.

In this study, ultrasonic test was performed for CT (Computed Tomography) image reconstruction for the quantitative detection of the inner deterioration which is very important for the structural safety of the building. The CT concept was developed about one-hundred years ago, and has been strikingly expanded mainly with the medical sciences. Unlike the preexisting approach with using indoor facility, simple and portable equipment must be used for the field application [2]. This aspect can make it hard to derive accurate results, and

moreover there are technical problems for getting data on the buried members by the wall and/or the floor. So, reliable ultrasonic CT image reconstruction was considered in this study with the reduced number and lack of the test data.

2. Materials and Methods

2.1. *Confucian shrine in Korea*

One Confucian shrine which is located at the middle-west of South Korea (*Yeasan-ri, Iksan city, Jeollabukdo*) was chosen for this research. And this building has been administrated by Cultural Properties Administration in Korea by being designated as the significant cultural shrine. All fourteen columns of this building were tested.

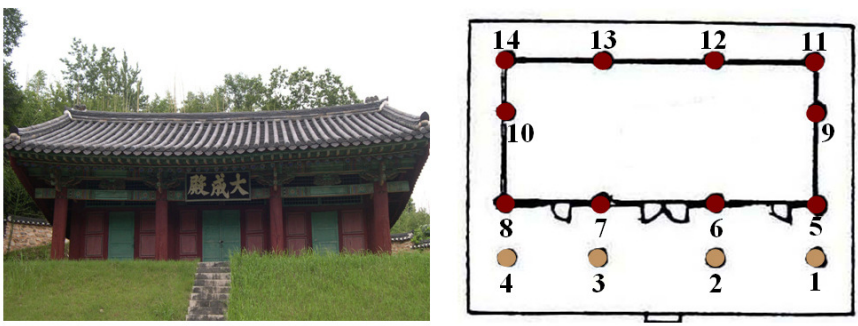

Fig. 1. Photograph and ground plan of the Confucian shrine.

2.2. *Methods*

2.2.1. *Measurement of the cross-sectional shape*

For reconstructing reliable ultrasonic CT image which is based on the real shape of the member, the cross-sectional shape was measured with the 3-D Tracker (ISOTRAK II). Table 1 shows the mean diameter of the columns which were calculated from the thirty six coordinates of measured cross-sectional shape.

Table 1. Mean diameter of columns and percentage of acquired ultrasonic TOF data.

Column No.	1	2	3	4	5	6	7	8	9	10	11	12	13	14
Diameter (cm)	48	40	42	46	43	51	48	36	42	49	39	40	40	42
Acquisition (%)	51	25	78	13	38	13	30	41	7	12	21	38	20	64

2.2.2. *Ultrasonic TOF measurements and data assumptions*

Two hundred seventy ultrasonic TOF data were measured for reconstructing one ultrasonic CT image. Ultrasonic signals were acquired from forty to one hundred eight degree with every twenty degrees.

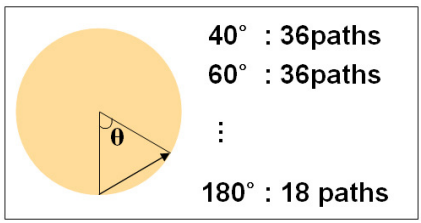

Fig. 2. Measurement of ultrasonic signals.

Rate of acquired ultrasonic data from two hundred seventy required data was calculated for considering the reliability of reconstructed CT images (Table 1). Ultrasonic signals were not able to be acquired in two cases; 1) Not-measurable data due to the buried parts by walls, 2) Not-measured data due to the severely damaged surface or inner parts. In the case of the Not-measurable ultrasonic TOF data, these data were assumed to have the average value of data for certain tested angle. After assuming the Not-measurable data, Not-measured ultrasonic TOF data were assumed to have the infinite value for regarding these parts as deteriorated parts.

2.2.3. *Verification with the drilling resistance test*

Drilling resistance test was performed for verify the ultrasonic test results and find out the real internal condition of tested columns. Line distributions of the drilling resistance value and pixel value of the ultrasonic CT image were compared. And based on eight line distributions of drilling resistance values, image of specific gravity distribution was composed for effective visualization.

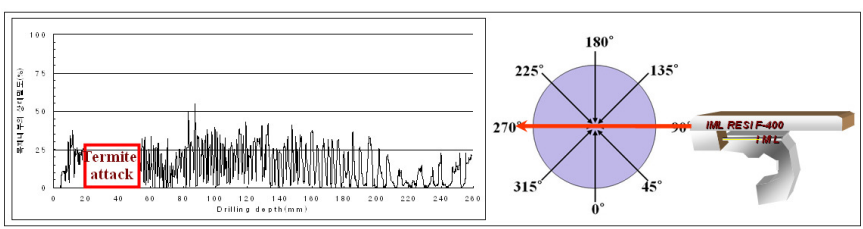

Fig. 3. Example of line distribution from the drilling resistance test.

3. Results and Discussion

3.1. *Rate of ultrasonic TOF acquisition for CT reconstruction*

In the case of column No.6, only 13% data was acquired and Not-measured data was 65% and it's the highest value from total columns. This high value is considered to be caused by the surface condition and inner empty hole due to the rough conservation work, and reconstructed CT image reflects this. Only very small area of the outside was visualized and image was severely distorted. From the tested angles, rate of acquired TOF data tends to decrease as the angle increase, so in many cases, only outside of the member was visualized such as the column No.6. CT image shows very severe damage of this column however it's not possible to confirm the real inner status.

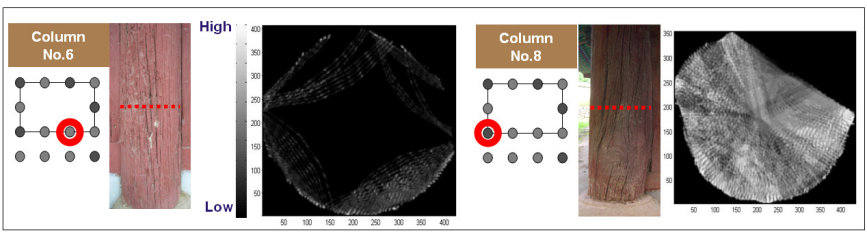

Fig. 4. Ultrasonic CT image of the column No.6 and No.8.

In contrast, relatively reliable image was reconstructed for the column No.8. In the case of this column, Not-measurable data was 56% which is the highest value from total columns which is due to the additional facility in the building however Not-measured data was only 3%. In spite of the very large portion of the buried parts which makes it hard to acquire the data, reliable image was reconstructed only with the tested results.

3.2. *Verification of the ultrasonic test results*

3.2.1. *Comparison of the line distributions and images*

Technically, the most reliable data for estimating the internal state of tested column is considered to be the line distribution of the drilling resistance test because drill directly scans the density of wood. Even the annual ring distribution due to the alternative existence of the earlywood and the late wood was able to be confirmed (figure 5). And empty hole where the resistance value is zero was also well confirmed. This defect is considered to be the termite attack because termite attacks and makes empty holes along the annual ring.

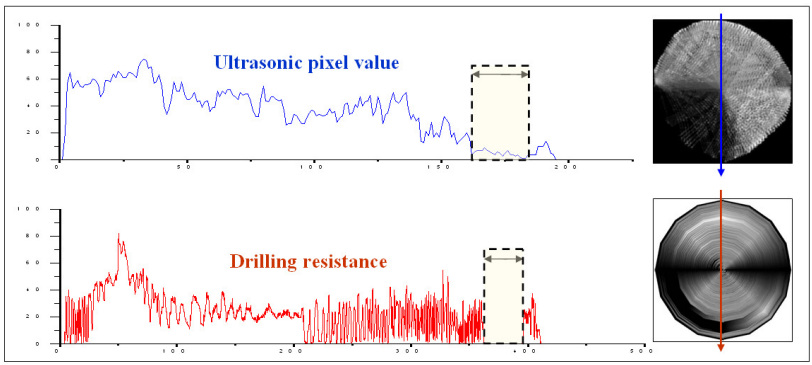

Fig. 5. Comparison of the ultrasonic and drilling resistance results – Column No.12.

From the line distribution of the ultrasonic pixel value, this defect is rather exaggerated and pixel values were not exactly zero. Originally, ultrasound is hard to penetrate through the air and this result is considered to be reflection of this nature of ultrasound.

3.2.2. *Effect of the surface and internal deterioration*

In the case of the outer exposed four columns, only Not-measured data can be existed from the two causes of lack of test data. And the rate of acquired TOF data of the column No.1 was 51% which is relatively high value. From the figure 6, specific gravity distribution derived from the drilling resistance test shows slight surface deterioration from around 0° to 90°. However, this defect is rather exaggerated in the ultrasonic CT image, and this aspect is due to the one difficulty of ultrasonic test which is largely affected by the surface condition of the tested member. About a fourth area were detected as defects.

Internal damages were also well reflected to the ultrasonic CT image, and column No.4 shows one example. Large area along the annual ring was deteriorated from the result of the drilling resistance test, and this is considered to be the termite attack. Ultrasonic CT image shows very severe damage of the column because of this defect.

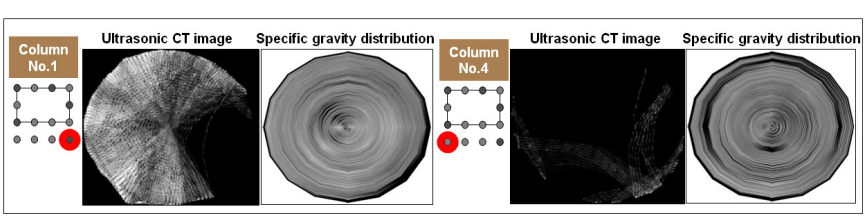

Fig. 6. Comparison of ultrasonic CT image and specific gravity distribution – Column No.1 & 4.

3.2.3. *Visualization of columns*

Figure 7 shows the total results of the ultrasonic test derived from above-mentioned criterion. Severe damages make it hard to analyze the real internal state of the column No. 2, 4, 6, 9, 10 and 11, and most of the columns were considered to be damaged by the termite attack and the weathering effect.

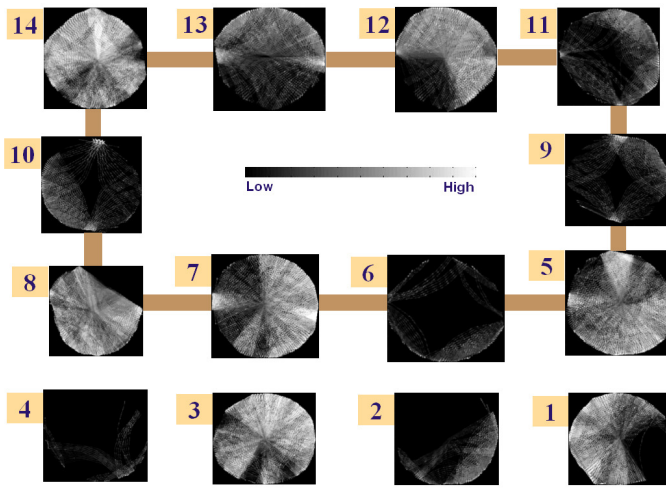

Fig. 7. Ultrasonic CT images of total columns in tested building.

4. Conclusion

One Korean Confucian shrine was tested for finding out the possibility of the on-site measurement with ultrasonic test. Reconstructed ultrasonic CT images of column members of the building were well reflects the internal and surface conditions and well agreed with the drilling resistance test result which says its high reliability.

Acknowledgments

This work was supported by the Korea Science and Engineering Foundation grant funded by the Korea government (No. F01-2005-000-10135-0)

References

1. S. J. Lee, K. M. Kim and J. J. Lee, Key Engineering Materials, Vol. 321-323: 1172-1176 (2006).
2. H. Yanagida, Y. Tamura, K. M. Kim and J. J. Lee, Japanese Journal of Applied Physics, 46(8A): 5321-5325 (2007).

ESTIMATION OF OPTIMAL PLUCKING TIME OF GREEN-TEA USING CANOPY REFLECTANCE

TEPPEI KURIMOTO, CHANSEOK RYU, MASAHIKO SUGURI, MIKIO UMEDA

**Environmental Science and Technology, Graduate School of Agriculture Kyoto University, Kitashirakawa Oiwake-cho, Kyoto, 606-8502, Japan*

While tea shoots are growing, these lose quality. Thus, it is important to determine the optimal plucking time when the yield and the quality are well-balanced. In order to offer farmers a practical method to decide the optimal plucking time, we used a portable crop growth information measurement apparatus and tried to estimate the yield and the quality in 2005, 2006 and 2007. NDVI was correlated with dry mass and nitrogen concentration at 0.1% or 1% significant level and changed similarly but shifted in each year. sNDVI was proposed to remove the fluctuation of NDVI. sNDVI at the optimal plucking time predicted by the changes of dry mass and nitrogen concentration was 0.04 to 0.06. The value of sNDVI possibly helps tea farmers to determine the plucking time.

1. Introduction

The Japan's production of tea is 90,000t/year and it is 7th largest in the world. Tea drinking is traditionally enjoyed. Recently, it is getting attention because of its good effect for health. In vitro and animal studies provide strong evidence that polyphenols derived from tea may possess the bioactivity to affect the pathogenesis of several chronic diseases. Among all tea polyphenols, epigallocatechin-3-gallate has been shown to be responsible for much of the health promoting ability of green tea (Khan et al., 2007). The nitrogen concentration and crude fiber concentration are known as indices of the quality of tea (Goto et al., 1990). Nitrogen concentration decreases and crude fiber concentration increases as the tea shoots get deteriorated. While tea shoots are growing, these lose quality. And the deterioration progresses quickly after the shoots become banjhi shoots. Thus, it is important to evaluate the tea yield and quality, and determine the optimal plucking time when the yield and the quality are well-balanced.

Rate of banjhi shoots is recommended as one of the indicator of optimal plucking time. The time when the rate is from 50% to 80% is said to be the optimal plucking time by guideline index of tea product in Shizuoka. But it is

laborious and time-consuming to count it and most farmers are determining the plucking time by their intuition. The availability of Near-infrared spectroscopy to estimate the nitrogen (Goto et al., 1986), total polyphenols and caffeine (Chen et al., 2006) concentration of tea was verified. However, this method wants samples to be dried, ground and sieved. When the concentrations are clarified, those of tea leaves in the field must be changed. As a non-destructive measurement, satellite's image was used for tea field remote sensing (Samarasinghe, 2003 and Ryu et al., 2006). However, it was difficult to estimate the tea growth of each field.

In this study, multi spectral sensor which is portable and easy to measure was used to measure the canopy reflectance of tea. The purpose is to evaluate tea growth and predict the optimal plucking time.

2. Materials and methods

2.1. *Test field and period*

This study was carried out at a tea field of Sugimoto Tea Factory at Wazuka-cho Souraku-gun Kyoto, Japan. The cultivar of the tea was *Camellia sinensis L., Yabukita*. Experimental period was 1st crop season, from April 19 to May 7 in 2005, from April 28 to May 15 in 2006 and from April 20 to May 16 in 2007. The tea plant was covered with butter muslin and shaded on May 9 in 2006 and on May 7 in 2007. Dates when tea shoots were plucked by farmers were May 7 in 2005, May 16 in 2006 and May 11 in 2007. In 2007, plucking time was delayed at 2 points for our study.

2.2. *Portable crop growth information measuring apparatus*

A portable crop growth information measuring apparatus (PCGIMA), which was developed by Bio-oriented technology research advancement institution of Japan, was used to measure the reflectance of tea plants. The sensor of this apparatus consists of three sets of two silicon photodiodes covered with spectral filters. The central wavelengths of those filters are 550nm for green, 650nm for red, and 880nm for near infrared and the half bandwidth are 50nm. One silicon photodiode of a set is set vertical upward and another is set vertical downward. The upward photodiodes measure incoming light intensity and downward ones measure reflected one, and reflectance is calculated for each band. From 255mm height, the apparatus can measure the reflectance in a circle (d = 300mm) on the canopy of a tea plant.

2.3. *Measurements*

The measurements were carried out once in two or three days. Sampling points were set at 15 points in 2005, at 15 points before the tea plants were shaded and at 6 points after that in 2006, and at 5 points before plucked and at 2 points after that in 2007. These points were slightly shifted after sampled. In 2007 before shaded, 7 fixed points were set only for measuring reflectance to be compared with sampling point.

The canopy reflectance was measured by PCGIMA. A circular flame (d=300mm) was set on the canopy during the measurement to mark test area in 2005. In 2006, the reflectance was measured with and without the flame at a point. In both situations, only a little data shift was found and the data without the flame is used in this paper in order that measuring situation become closer to practical use. And in 2007, the flame wasn't used for reflectance measurement.

After measuring the reflectance, shoots which were inside the circular flame and had more than 2 opening leaves were plucked. And they were counted dividing into banjhi shoots and non-banjhi shoots. The plucked shoots were primary-parched with microwave oven and dried with circulation drier at 60 degree centigrade for 24hours. Dried tea samples were weighted and finely ground with pulverizing mill and nitrogen concentration were measured by NC-900 (Sumica Chemical Analysis Service, Ltd) in 2005 and 2006, and by NC-22 (Sumica Chemical Analysis Service, Ltd) in 2007.

3. Results and discussion

Table 1 shows the correlation coefficients of NDVI vs. dry mass and NDVI vs. nitrogen concentration. NDVI was positively correlated with dry mass and negatively correlated with nitrogen concentration. All of the correlations without that of NDVI vs. nitrogen concentration in 2007 were correlated at 0.1% significant level. The correlation between NDVI and nitrogen concentration in 2007 was significant at 1% level. NDVI can be an indicator of yield and quality of green-tea.

In 2005 and 2006, the relations of NDVI vs. dry mass and NDVI vs. nitrogen concentration showed similar trend (Fig. 1). The value of NDVI in 2007 was smaller than in 2005 and 2006. NDVI were seemed to be influenced not only by dry mass and nitrogen concentration but also by other factors. From 2006, shading-cultivation was started in the test field. It is known that tea plants lose their vigor by shading (Sakai, 1987). Thus, the leaves grown at previous tea season which had less vigor presumably made the NDVI smaller in 2007.

Table 1. Correlation coefficients of NDVI vs. dry mass and nitrogen concentration.

	n	Dry mass	Nitrogen concentration
2005	130	0.87***	-0.77***
2006	94	0.91***	-0.70***
2007	41	0.91***	-0.45**

** : 1% significant level *** : 0.1% significant level

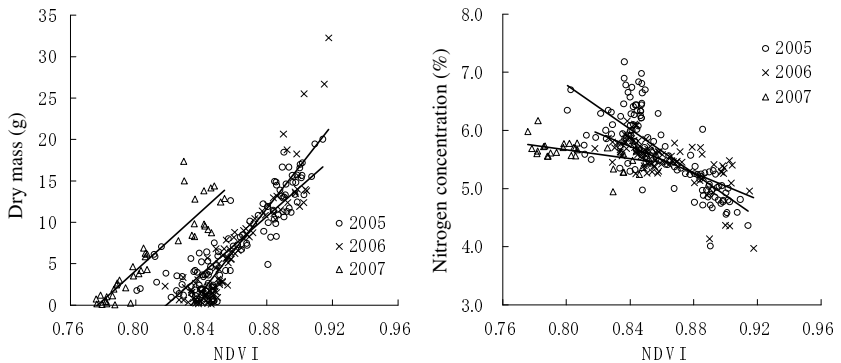

(a) NDVI vs. Dry mass (b) NDVI vs. Nitrogen concentration

Fig. 1. Relation of NDVI vs. Dry mass and NDVI vs. Nitrogen concentration.

Figure 2 shows the changes of dry mass and nitrogen concentration. Dry mass increased and the increase got less around the plucking time. Nitrogen concentration decreased constantly in 2005. In 2006 and 2007, it decreased, got constant and decreased again. Suppose it is the optimal plucking time before an acute negative change, e.g. smaller increase of dry mass or larger decrease of nitrogen concentration. On the basis of this supposition, around May 4 in 2005, May 12 in 2006 and May 7 or 14 in 2007 are assumed to be the time. On May 7 in 2007, the rate of banjhi shoots was 26.2% and on May 14, it was 75.2. Considering the rate of banjhi shoots, on May 14 in 2007 are seemed to be the optimal plucking time.

Figure 3 (a) shows the changes of NDVI. When the banjhi shoots appeared, NDVI started to increase. And around the plucking date, the increase got less or stopped. The year-on-year shift to the left or right depends on the earlier or later growth period which may be due to the temperature, precipitation and so on. The upward or downward shift might be caused by the influence of old leaves. On the canopy of tea plants at the early stage of shoots growth, there is little new shoots and the reflectance is mostly influenced by the old leaves. Thus, the stagnancy of

NDVI at the early stage can be regarded as the base NDVI of new shoots growth. In order to remove the base NDVI shift, shifted-NDVI (sNDVI) was calculated using the following equation.

$$sNDVI = NDVI - (\text{average of initial 3 } NDVI) \quad (1)$$

Figure 3 (b) shows sNDVI of three years. sNDVI at the presumed optimal plucking time is 0.04 to 0.06 in each year. The value of sNDVI can be a help for farmers to determine the plucking time.

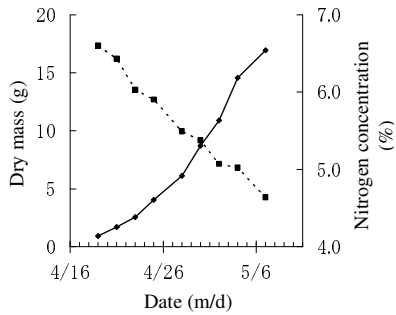

(a) 2005

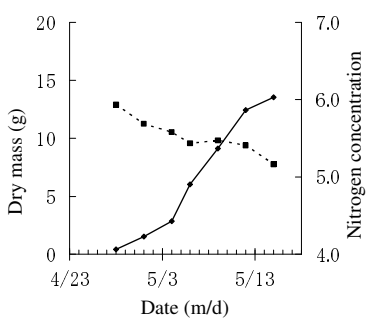

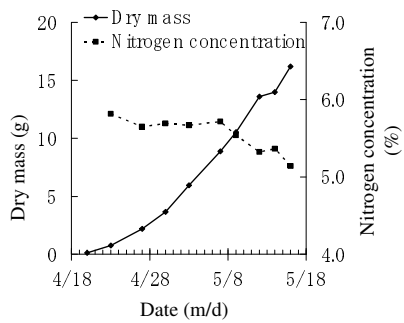

(b) 2006 (c) 2007

Fig. 2. Changes of dry mass and nitrogen concentration.

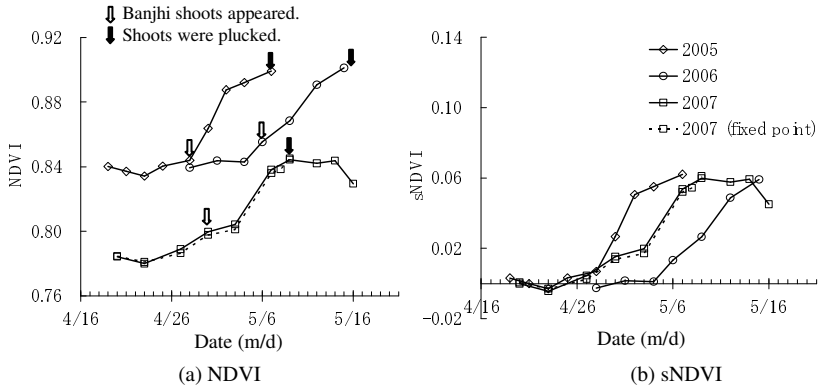

Fig. 3. Changes of NDVI and sNDVI.

4. Conclusion

The easy measuring apparatus with multi-spectral sensors (PCGMA) was used to measure the reflectance of tea canopy. NDVI was positively correlated with dry mass and negatively with nitrogen concentration at 0.1% or 1% significant level. NDVI can be an indicator of yield and quality of green-tea. In each year, NDVI changes similarly but shifted. The leaves grown at previous tea season are assumed to be the cause of the shift and sNDVI was proposed. sNDVI at the optimal plucking time predicted by the change of dry mass and nitrogen concentration was 0.04 to 0.06. The value of sNDVI possibly helps tea farmers to determine the plucking time. The cause of NDVI shift isn't exactly proved in this study. It should be proved in future study.

References

1. N. Khan and H. Mukhtar, Life Sciences 81, 519 (2007)
2. T. Goto, T. Shibata and Y. Yamaguchi, Bull. Shizuoka Tea Exp. Stn. 15, 43 (1990)
3. T. Goto, J. Uozumi and T. Suzuki, Bull. Shizuoka Tea Exp. Stn. 12, 61 (1986)
4. Q. Chen, J. Zhao, X. Huang, H. Zhang and M. Liu, Microchemical Journal 83, 42 (2006)
5. G.B. Samarasinghe, Agricultural Water Management 58, 145 (2003)
6. C. Ryu, Y. Makino, H. Ishida, C. Terada and M. Umeda, Report of JSAM Kansai branch 100, 132 (2006)
7. S. Sakai, Report of tea experiment station 22, 19 (1987)

SAMPLING AND CALIBRATION REQUIREMENTS FOR SOIL PROPERTY ESTIMATION USING NIR SPECTROSCOPY

KYOU SEUNG LEE, DONG HOON LEE

Dept. of Bio-Mechatronics Engineering, Sungkyunkwan University, Suwon, Republic of Korea

KENNETH A. SUDDUTH

Cropping Systems & Water Quality Research Unit, USDA Agricultural Research Service, Columbia, Missouri, 65211, USA

SUN-OK CHUNG

Dept. of Bioindustrial Machinery Engineering, Chungnam National University, Daejeon, 305-764, Republic of Korea

Soil physical and chemical properties are important in crop production since they control the availability of plant water and nutrients. Optical diffuse reflectance sensing is a potential approach for rapid and reliable on-site estimation of soil properties. One issue with this sensing approach is whether additional calibration is necessary when the sensor is applied under conditions (e.g., soil types or ambient conditions) different from those used to generate an initial calibration, and if so how many sample points are required in this additional calibration. In this study, these issues were addressed using data from 10 fields from 5 states in the north-central USA, selected to represent ranges in climate, soil, and landscape characteristics. Results showed that data from soil regions and horizons with variations spanning those expected in sensor use should be included in the initial calibration of a sensor. Otherwise, modification of the initial sensor calibration with a minimum of 8 to 12 sample points for each new soil region and horizon would be needed. These results will provide useful guidelines for calibration and field application of an optical diffuse reflectance sensor to estimate soil properties.

1. Introduction

Precision agriculture is a management system where application of agricultural chemicals such as fertilizers, pesticides, and herbicides is matched to actual needs point-by-point within fields. This approach can provide economic benefits to farmers and protection of the soil environment from excessive applications of chemicals. For successful implementation of precision agriculture, site-specific quantification of soil physical and chemical properties affecting soil quality and crop production is important.

Many investigators have successfully estimated soil physical and chemical properties with visible (VIS), near-infrared (NIR), and mid-infrared (MIR) spectroscopy [1, 2, 3, 4]. Lee *et al.* [1] combined VIS and NIR reflectance sensing with partial least squares (PLS) regression to estimate surface and subsurface soil properties, and to identify wavelength bands important for estimating soil properties. This wavelength selection and model development process was an important first step toward fabrication and field application of an optical soil property sensor.

One important question with a VIS-NIR soil sensor is how many calibration samples are required to provide a prediction model sufficient for field application of the sensor, and how closely the characteristics of those samples must be related to the characteristics of the soils to be analyzed. Therefore, the objectives of this study were to investigate 1) whether additional calibration between optical reflectance and laboratory-determined soil properties would be necessary for application of a sensor under conditions different from those included in its initial calibration, and 2) if so, how many additional within-field sample points would be required to improve the calibration sufficiently.

2. Materials and Methods

2.1. *Soil and Spectral Data Acquisition*

Soils used in this study were obtained from 10 fields managed in a corn-soybean rotation, 2 each in Missouri (MO), Illinois (IL), Michigan (MI), South Dakota (SD), and Iowa (IA), as described by Sudduth *et al.* [5]. These fields were selected in part due to the degree of within-field soil and production variability, and to represent ranges of climate, soil, and landscape characteristics typical of the north-central USA. Soils were sampled from 12 to 20 sites in each field. Soil texture (clay, silt, and sand fractions, %), cation exchange capacity (CEC), Ca, and Mg (cmol kg^{-1}), organic C (%), total N (%), and pH were determined by laboratory analysis [5].

Soil spectral reflectance data were obtained in the laboratory using an ASD FieldSpec Pro FR[a] spectrometer (Analytical Spectral Devices, Boulder, Colo.). Spectra of air dried and 2-mm-sieved soil were recorded between 350 and 2500 nm at 1.4- to 2-nm intervals. Each soil spectrum was obtained as the mean of 10 scans. The spectrometer data collection software automatically adjusted the data

[a] Mention of trade names or commercial products is solely for the purpose of providing specific information and does not imply recommendation or endorsement by the US Department of Agriculture or its cooperators.

for dark current variations, using dark current scans obtained at the beginning of each data collection session, and at least once every 30 minutes thereafter. A Spectralon (Labsphere Inc., North Sutton, N.H.) reflectance standard was scanned after every 10 soils and used to convert the raw spectral data to decimal reflectance. More detailed information on soil and spectral data acquisition was given by Lee *et al.* [1].

2.2. *Analytical Procedures*

Partial least squares (PLS) regression, implemented in Unscrambler version 9.1 (CAMO Inc., Oslo, Norway), was used to develop calibrations between soil properties and reflectance spectra. Several observations identified as outliers by visual inspection, or with missing data values, were removed. Then, data were transformed from reflectance to absorbance, normalized, and smoothed with an 8-point moving average [1].

Two sets of PLS models were developed, one including samples from all soil horizons, and the other including only samples from the surface soil horizon. Model evaluation was based on RPD, the ratio of standard deviation to RMSEP.

$$RMSEP = \sqrt{\sum_{i=1}^{m} \frac{(\hat{\gamma}_i - \gamma_i)^2}{m}} \tag{1}$$

where: m = number of samples used for prediction and $\hat{\gamma}_i$, γ_i = predicted value and measured value of soil property, respectively.

RPD is a useful measure of fit when comparing results from datasets containing different degrees of variability, with a higher RPD indicating a more accurate prediction. Saeys *et al.* [6] stated that RPD values less than 1.5 generally indicated a model was not useful, while discrimination between high and low values, approximate quantitative prediction, and good prediction would be possible using models with RPD values of 1.5 to 2.0, 2.0 to 2.5, and 2.5 to 3.0, respectively.

For analysis, data from the two fields in each of MO, IL, IA, and MI were pooled. The two SD fields, which were geographically separated and had considerably different soils, were kept separate, resulting in six datasets: MO, IL, IA, MI, SD#1 and SD#2. Three different calibration methods were used for the analysis as follows:

- *Method 1: Full Information Calibration.* This method used data from all six datasets in development of the initial calibration equation. The calibration equation was then used to get separate prediction statistics for each of the six datasets.

- *Method 2: Calibration Without Field-Specific Information.* This method simulated use of a "factory-calibrated" sensor under conditions different from those used to develop the initial calibration. A calibration was developed using 5 of the 6 datasets and prediction statistics were calculated for the remaining, "leave-out" dataset. This process was repeated six times to obtain prediction statistics for all datasets.
- *Method 3: Hybrid Calibration.* This method was intermediate between methods 1 and 2, simulating the addition of a small number of field-specific calibration points to an initial general calibration. Calibrations were developed as in method 2, but with a number of additional calibration points from the "leave-out" dataset included. The number of additional points was iteratively increased from zero (equivalent to method 2) to the maximum number of points in the dataset (equivalent to method 1). Prediction statistics were calculated as for method 2.

3. Results and Discussion

Table 1 shows that differences in RPD values between calibration methods 1 and 2 were positive, indicating that method 1 was more predictive than method 2 in all cases. In the analysis for all soil horizons, differences in RPD were greater than 0.4 for most of the soil properties in the MO, IL, IA, and MI datasets. Increases in RPD were greater for some fields and properties than for other fields and properties. For example, RPD for clay fraction, Mg, and CEC increased in MO fields more than in IA fields, and organic C increased more than any other property in all fields except for SD#1. Soil property models for the two SD fields did not improve by as much as for most other fields, with the exception of organic C estimation in SD #2, where RPD changed by 0.77.

These results showed VIS-NIR soil property estimations would be considerably degraded if calibrations did not include data from samples similar to those encountered in the analysis. The pooled datasets used in this analysis suggested that samples may not need to be from the exact fields under study, but at least should come from fields with similar soils and management histories. For the SD fields, method 1 all-horizon results were not much better than those for method 2. This may indicate that the conditions in the SD fields were not different enough from those in the other fields to require complete calibration, or it may have been because the SD datasets were kept separate for analysis, and therefore contained fewer calibration data points than the other datasets.

When only surface soil data were considered, increases in RPD were also observed for many fields and properties, although total N did not improve markedly, nor did soil properties for dataset SD#1. Overall, we concluded that it is necessary to include, in the calibration stage, data from horizons and soils in

which a sensor is expected to operate. If these data are not included in an initial calibration, then they should be part of a new or additional field-specific calibration step.

Table 1. Differences in RPD values between calibration methods 1 and 2 using data from (top) all soil horizons and (bottom) surface soil horizon. Positive numbers indicate a higher RPD (more accurate prediction) for method 1 compared to method 2.

Using all soil horizons

Leave out	Clay	Silt	Sand	Ca	Mg	CEC	Organic C	pH	Total N
MO	0.786*	0.773	0.262	0.493	1.072	0.838	1.347	0.469	0.516
IL	0.662	0.270	0.379	0.601	0.162	0.563	1.513	0.467	0.962
IA	0.665	1.074	1.149	0.130	0.191	0.547	1.775	0.185	1.412
MI	0.315	0.431	0.406	0.406	0.678	0.507	0.850	0.422	0.655
SD#1	0.071	0.188	0.203	0.382	0.271	0.097	0.278	0.371	0.338
SD#2	0.213	0.378	0.305	0.288	0.110	0.155	0.771	0.145	0.077

Using surface soil horizon

Leave out	Clay	Silt	Sand	Ca	Mg	CEC	Organic C	pH	Total N
MO	1.070	0.984	0.293	1.075	0.756	1.128	0.841	0.998	0.048
IL	0.694	0.606	0.142	0.278	0.447	0.176	0.804	0.363	0.066
IA	0.730	1.242	0.890	0.376	0.505	0.162	0.416	0.644	0.059
MI	0.277	0.277	0.288	0.316	0.496	0.203	0.517	0.413	0.251
SD#1	0.201	0.352	0.177	0.399	0.148	0.206	0.183	0.861	0.065
SD#2	0.392	0.772	0.521	0.390	0.098	0.303	0.722	1.414	0.063

* Values are shaded when RPD differences are greater than 0.4

With method 3, RPD increased as the number of test field sample points added to the calibration model increased, but degree of the increase was different for different sites and soil properties. Figure 1 shows examples of RPD vs. number of sample points for CEC (left) and organic C (right) in the all-horizon dataset. Overall, RPD values increased more rapidly as the number of added points increased up to certain number (e.g., about 8 for CEC and 12 for organic C for MO fields). Afterward, the rate of RPD increase was less, or in some cases went to approximately zero. In many cases, the rate of RPD increase at lower numbers of added points was lower for soil properties with less difference between calibration methods 1 and 2 (e.g., CEC) than for those with more difference (e.g., organic C). Based on these results, we concluded that addition of a few within-field calibration points could improve results for a VIS-NIR soil property sensor, and that a large portion of the potential improvement could be obtained by adding 8 to 12 points, depending on soil properties to be estimated.

These results provided preliminary guidance on sampling and calibration requirements for VIS-NIR soil property estimation. Additional data collection, further investigation using additional model selection criteria, interpretation of model improvement in terms of ranges of and NIR reflectance responses to each soil property, and automation of these procedures are subjects for future study.

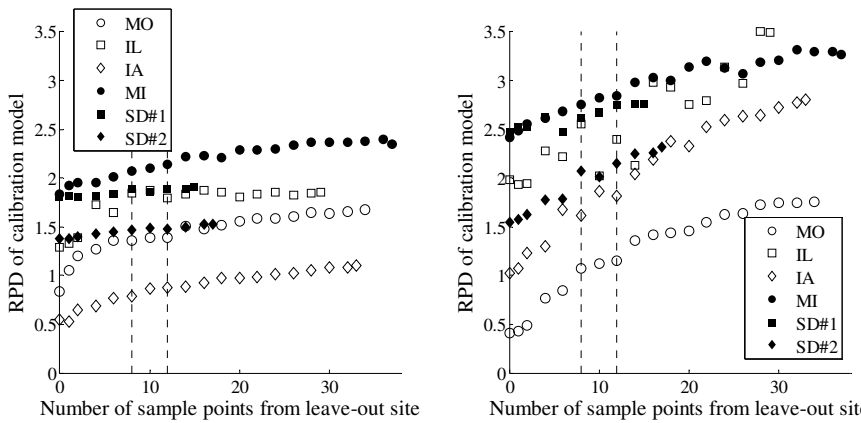

Fig. 1. Example plots of RPD of calibration model vs. number of sample points included from the "leave-out" site for CEC (left) and organic C (right) using data from all soil horizons.

4. Conclusions

The need for field-specific calibration of a VIS-NIR soil property sensor was investigated using data from 10 fields, representing ranges in soil characteristics typical to the north-central USA. Major findings were:

- Improved calibrations were obtained when including data from the field(s) where the sensor was to be used, indicating that soil data from various soil regions and horizons with variations spanning those expected in sensor use should be included in the initial calibration of a sensor.
- Otherwise, modification of the initial sensor calibration with 8 to 12 sample points for each new soil region and horizon would be needed.

References

1. K. S. Lee, D. H. Lee, K. A. Sudduth, S. O. Chung and S. T. Drummond, ASABE Conference Paper 031028 (ASABE, St. Joseph, Mich., 2007).
2. A. M. Mouazen, J. DeBaerdemaeker and H. Ramon, *Soil Tillage Res.* **80**, 171 (2005).
3. K. A. Sudduth and J. W. Hummel, Trans. ASAE 34, 1900 (1991).
4. R. A. Viscarra Rossel, D. J. J. Waloort, A.B. McBratney, L. J. Janik and J. O. Skjemstad, *Geordema*. **131**, 59 (2006).
5. K. A. Sudduth, N. R. Kitchen, W.J. Wiebold, W.D. Batchelor, G.A. Bollero, D.G. Bullock, D.E. Clay, H.L. Palm, F.J. Pierce, R.T. Schuler and K.D. Thelen, *Comp. Elec. Agric.* **46**, 263 (2005).
6. W. Saeys, A. M. Mouazen and H. Ramon, *Biosystems Eng*. **91**, 393 (2005).

DETECTION OF BONE AND CARTILAGE OF BEEF USING MAGNETIC RESONANCE IMAGING

SEONG MIN KIM

Division of Bioresource Systems Engineering, Chonbuk National University, Jeonju, Chonbuk 561-756, Republic of Korea

CASEY GARVEY

Quality & Innovation, ConAgra Foods, Inc., 6-475 Six ConAgra Drive Omaha, NE 68102, USA

DON WILLIAMS

Quality & Innovation, ConAgra Foods, Inc., 6-475 Six ConAgra Drive Omaha, NE 68102, USA

YOUNG SEOB SEO

Department of Biomedical Engineering, University of California, One Shields Ave. Davis, CA 95616, USA

MICHAEL MCCARTHY

Department of Food Science & Technology, University of California, One Shields Ave. Davis, CA 95616, USA

Magnetic resonance imaging (MRI) was used to detect foreign inclusions such as bone, cartilage, and ligament in beef meat. A superconducting 7 T magnet was used to acquire the image data. The spatial resolution of the images was 397 μm. MRI parameters suitable to discriminate meat parts including meat, fat and sap, and foreign inclusions, fragments of cartilage, bone and ligament, were found. A method was developed to detect foreign inclusions in beef meat.

1. Introduction

Fragments of foreign inclusions such as bone, cartilage, ligament in meat are a problem for the processed meat industry. These fragments may occur due to misaligned cutting blades shaving pieces from the skeleton, or they may be due to bones which were already broken before or during slaughter [1]. Meat

products must not contain any fragments of bone, cartilage, and foreign materials according to USDA regulations.

Currently, the most widely used foreign material detection method in the food industry is X-ray [2]. Tao and Ibarra studied detecting bone fragments in deboned poultry using X-ray imaging [3]. Magnetic resonance imaging (MRI) due to its nondestructive nature is widely used in medical fields. Chen *et al.* demonstrated that MRI can be used for evaluation of various internal quality factors of fresh fruits and vegetables [4]. MRI is not harmful to products and does not damage product quality, and can be used in examining food stability and structure, moisture migration, rheology, phase changes, *etc.* [5].

The objective of this study was to find a feasible method to detect foreign inclusions such as fragments of bone, cartilage, and ligaments in beef meat using MRI.

2. Materials and Methods

Beef samples and foreign inclusions such as bone and cartilage were purchased at local market in Davis, CA. Beef samples with about 15 mm thickness were prepared to fit into a plastic sample container 38 mm in diameter and 40 mm in height. The defects were cut into different size fragments from 2 to 18 mm. For MR imaging, the defect fragments were placed in the middle of two thick slices of beef meat (refer Figure 1).

MRI was performed on a 7.05T Bruker Biospec MRI system operating at a proton frequency of 300 MHz. The sample container was held by a sample holder made of Plexiglas mounted in the center of a 72 mm inner diameter imaging probe. A sample holder was used to place a sample in the middle of the NMR coil consistently. A Multi Slice Multi Echo (MSME) imaging pulse sequence with 8.5 ms echo time (TE) and 1723 ms repetition time (TR) was used to acquire multi slice images. MSME was used to map spin-spin relaxation time constant (T_2) of slices of a sample with 16 different TEs, which were set to 8.53, 17.04, 25.58, 34.11, 42.64, 51.16, 59.69, 68.22, 76.74, 85.27, 93.80, 102.32, 110.85, 119.38, 127.9, and 136.43 ms, and TR was 1534 ms. Also, MSME was used to map spin-lattice relaxation time constant (T_1) of slices of a sample with 8 different TRs, which were set to 250.85, 358.62, 539.02, 759.28, 1042.17, 1438.13, 2103.29, and 5000 ms, and TE was 14.26 ms. Image slice thickness was 1 mm and field of view (FOV) was 50.8 mm. The image pixel size was set to 128 x 128, so the spatial in-plane resolution of a voxel is 397 μm.

The acquired MR images were processed with commercial software (MATRLAB R2006b, Mathworks, USA). The estimated spin-lattice relaxation time constant (T_1) and spin-spin relaxation time constant (T_2) were fitted by following exponential curve fitting according to Eq. (1) and Eq. (2), respectively.

$$M_{ij} = M_0 \left[1 - \exp\left(-\frac{TR}{T_1} \right) \right] \tag{1}$$

$$M_{ij} = M_0 \exp\left(-\frac{TE}{T_2} \right) + M_\infty \tag{2}$$

where M_{ij} is the intensity at a particular pixel *ij*th in a MR image, M_∞ is estimate of the average noise in a image, and M_0, T_1 and T_2 are the estimates required.

3. Results and Discussion

Magnetic resonance characteristics of various materials such as meat, fat bone, cartilage, ligament *etc.* were examined. Figure 1 shows various foreign materials in a plastic container for MRI. Table 1 shows average magnetic resonance estimates for proton density and relaxation times, which were calculated using Eq. (1) and Eq. (2). Figure 2 shows T_1 fitting of the data for various materials. Signal intensity approaches a steady state value after 1 sec except for ligament tissue, which is gradually increasing. Fat regions generate the strongest signal and foreign inclusions such as cartilage, ligament, and bone generate less signal intensity than meat sections, which includes meat, fat, and sap. However, air and bone fragment parts generate similar signal intensity, which makes it difficult to discriminate them. Figure 3 shows T_2 fitting data of various materials. Fat parts generate the strongest signal before about 40 ms and thereafter signal intensity of sap parts is bigger than fat parts. Foreign inclusions such as bone and ligament generate less signal intensity than meat part. However, cartilage fragments generate stronger signal compared to meat sections.

Table 1. Average magnetic resonance estimates of various materials.

	meat	fat	bone	cartilage	ligament	sap	air
M_0	$3.98\text{x}10^8$	$5.27\text{x}10^8$	$4.72\text{x}10^7$	$2.12\text{x}10^8$	$1.01\text{x}10^8$	$4.59\text{x}10^8$	$3.50\text{x}10^7$
T_1	123.9	103.3	-	134.4	375.8	139.4	-
M_0	$1.13\text{x}10^4$	$2.78\text{x}10^4$	$6.04\text{x}10^3$	$1.33\text{x}10^4$	$2.87\text{x}10^3$	$2.15\text{x}10^4$	$8.28\text{x}10^2$
T_2	42.92	68.28	-	55.18	45.66	86.16	-

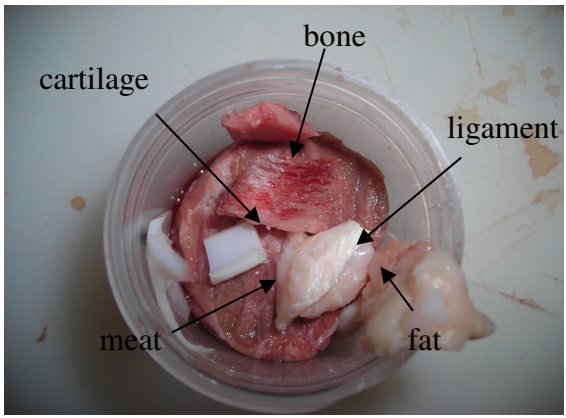

Fig. 1. Various defects in a plastic container. Arrows indicate where calculations made.

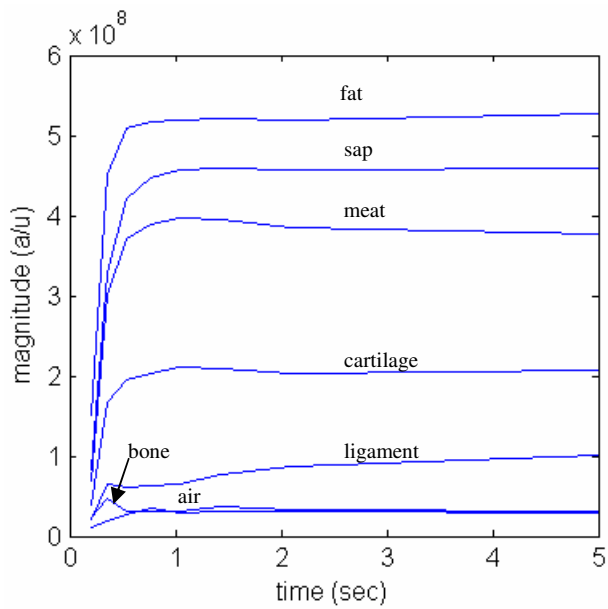

Fig. 2. Intensity variation of various material according to different TRs with TE=14.3 ms.

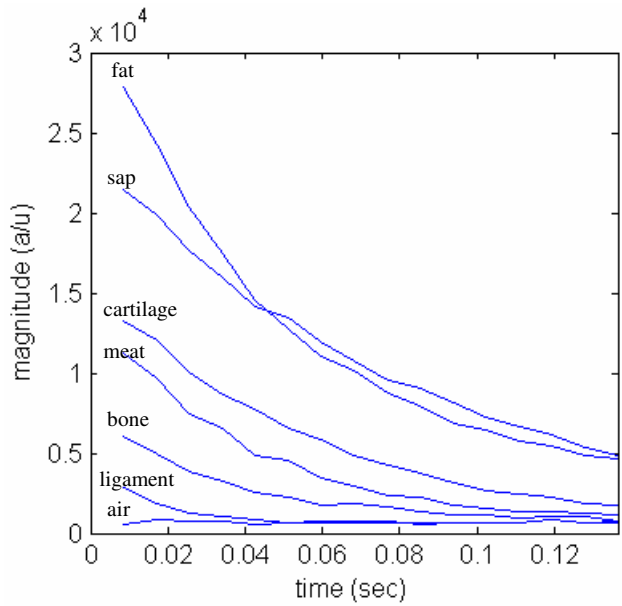

Fig. 3. Intensity variation of various material according to different TEs with TR=1534 ms.

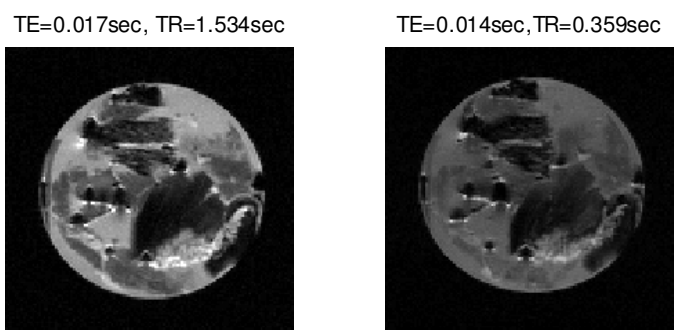

Fig. 4. Magnetic resonance images of sample in Figure 1 showing good contrast between meat parts and foreign inclusions.

Table 2. Image intensity ratio based on fat of various materials.

	fat	meat	sap	bone	cartilage	ligament	air
M11_r	1.000	0.437	0.516	0.140	0.311	0.141	0.077
M12_r	1.000	0.670	0.734	0.105	0.460	0.152	0.033
M13_r	1.000	0.743	0.841	0.064	0.494	0.129	0.052
M21_r	1.000	0.406	0.773	0.217	0.477	0.103	0.021
M22_r	1.000	0.398	0.819	0.202	0.496	0.077	0.034
M23_r	1.000	0.365	0.866	0.190	0.495	0.059	0.036

Table 2 shows image intensity ratio based on fat of various materials. M11_r, M12_r, and M13_r were calculated from magnetic resonance images acquired with TE=14.3 ms and different TRs, TR=250.85, 358.62, and 539.02 ms, respectively. When TR=250.85 ms, the ratios of meat parts including meat, fat, and sap, is usually larger than foreign inclusions. The difference in the ratio between meat and cartilage is about 12%. However, when TR=358.62 ms, the difference of ratio between meat and cartilage is about 21%, which makes it easier to discriminate between them. When TR=539.02 ms, the difference of ratio between bone and air is about 1.2%, which makes it hard to discriminate them if there are air pockets inside meat. So, MRI parameters with TE=14.3 ms and TR= 358.62 are suitable to discriminate meat parts and foreign inclusions. M21_r, M22_r, and M23_r were calculated from magnetic resonance images acquired with TR=1534 ms different and TEs, TE=8.53, 17.04, and 25.58 ms, respectively. When TE=8.53 ms, the ratios of meat parts including meat, fat, and sap, usually larger than foreign inclusions except cartilage. Cartilage generates stronger signal than meat and the difference in the ratio is about 7%. However, when TE=17.04 ms, the difference of ratio between cartilage and meat is about 10%, which makes it easier to discriminate them. When TE=25.58 ms, the difference of ratio between cartilage and meat is about 13%. From analysis of the result, MRI parameters with TE=14.3 ms and TR= 358.62 ms are suitable to discriminate meat parts and foreign inclusions. Figure 4 shows magnetic resonance images showing good contrast between meat parts and foreign inclusions.

4. Conclusions

MRI was used to detect fragments of bone, cartilage, and ligament in beef meat. MRI parameters suitable to discriminate meat parts including meat, fat and sap, and foreign inclusions, fragments of cartilage, bone and ligament, were found. MRI suggests that it is highly feasible for detecting foreign inclusions such as fragments of bone, cartilage, and ligaments in beef meat.

References

1. USDA ERS, **41** (1996).
2. A.D. Dearden, *Food Science and Technology Today.* **10(1)**, 87-90 (1996).
3. Y. Tao and J.G. Ibarra, *Trans. ASAE.* **43(2)**, 453-459 (2000).
4. P. Chen, M.J. McCarthy and R Kauten, *Trans. ASAE.* **32(5)** 1747-1753 (1989).
5. M.J. McCarthy, *Magnetic Resonance Imaging in Foods*. (1994).

REALTIME MONITORING OF TOMATO CONCENTRATE PROCESSING USING RF SENSORS

SEONG MIN KIM

Division of Bioresource Systems Engineering, Chonbuk National University, Jeonju, Chonbuk 561-756, Republic of Korea

CASEY GARVEY

Quality & Innovation, ConAgra Foods, Inc., 6-475 Six ConAgra Drive Omaha, NE 68102, USA

THOMAS LEARY

Department of Chemical Engineering, University of California, One Shields Ave., Davis, CA 95616, USA

MICHAEL MCCARTHY

Department of Food Science & Technology, University of California, One Shields Ave., Davis, CA 95616, USA

Realtime monitoring of fresh tomato concentrate processing was done using two kinds of radio frequency (RF) sensors resonant at different frequencies. Fresh tomato concentrate with soluble solid content of about 5 °Brix was evaporated up to 23 °Brix with a pilot scale evaporator. The RF sensors were installed in a processing pipe. The pastes at a specific °Brix level were sampled and analyzed for physical properties such as soluble solid content and viscosity. The relationships between sensor outputs and measured physical properties were analyzed. Analysis results indicated RF Sensor B operating at 85 MHz showed more consistent output.

1. Introduction

In the tomato processing industry, most process monitoring is done by offline testing, which can be time consuming, labor intensive, and inaccurate. Due to the nature of batch production processes, the operator can't delay packing a batch to verify the state of product during offline testing. The tomato product, sauces and pastes manufactured from fresh tomatoes are sold according to their consistency as measured by a Bostwick index. Paste samples must be taken from the processing line and Bostwick measurements are performed. In addition to the Bostwick index for consistency, tomato products are quantified according to

their soluble sugars concentration, measured in the food industry as degrees Brix. To achieve maximum accuracy, Brix values should be measured on the serum from tomato concentrates using a refractometer.

Another issue that precludes the use of a correlation between Brix value and tomato paste consistency is the effect of enzymatic activity on the size and conformation of pectic substances in the tomato concentrate. Pectins are a type of polysaccharide found in the cell walls of tomatoes that exist in both water-soluble and water-insoluble forms. Both forms contribute significantly to the rheological behavior of tomato concentrates [1]. Traditional rheological instruments, such as rotational and tube viscometers, suffer from fouling issues, and the presence of particles creates wall slip problems in tube viscometers [2]. Optical methods have shown a strong correlation between water-insoluble solids content and Bostwick value for dilute tomato concentrates, but the correlation is weaker for concentrated tomato pastes [3]. Recent work on this subject has examined the feasibility of an ultrasonic Doppler velocimetry technique to monitor tomato concentrate properties during evaporation [4].

The objective of this study was to test the feasibility of in-line RF resonance sensors for measuring viscosity and soluble solid content of tomato concentrate during processing.

2. Materials and Methods

2.1. *Sample preparation and experimental setup*

A high viscosity paste type processing tomato variety, H9780, harvested beginning of September and October, 2006, was used. Fresh, mature tomato fruits were ground into juice, and then processed through a 'hot break', during which it undergoes a rapid heat treatment at 104°C to inactivate enzymes. After seeds and skin were screened out, the tomato juice was then placed under a vacuum of roughly 26.7 kPa for 30 seconds to remove air bubbles before being stored at 4°C until loaded into the evaporator.

Batch evaporation of the tomato concentrate was done in a single stage tube and shell pilot-scale Rossi-type evaporator, which can produce commercial quality paste. The progress of the evaporation was monitored via an on-line refractometer (UR-20, Maselli Measurements, Stockton, CA) to determine the Brix value of the concentrate for sampling points. The evaporation continued until the circulator pump began to cavitate due to the high viscosity of the tomato paste.

During the evaporation process, tomato concentrate was sampled at predetermined Brix values to perform the off-line physical property testing. Six

Brix values were selected: the initial Brix value of the tomato juice, 7, 14, 16, 20, and the final maximum Brix value of the tomato concentrate. Once the final sample was taken, the tomato concentrate in the evaporator was gradually diluted back to its initial Brix value with deionized water, with sampling for off-line testing at the about same Brix values as during evaporation. Ultimately, each complete concentration and re-dilution trial provided 11 sampling points for off-line physical property measurements. Two experiments were performed with sensor A and B. One experiment was utilized tomatoes harvested on September and RF sensor A, and the other was done with tomatoes harvested on October and RF sensor B. Each experiment takes about 12 hours for loading sample, processing, and cleaning evaporator.

2.2. *Dielectric response measurement*

Measurements of the dielectric response of the tomato concentrate were performed in-line using two types of reflection resonance probes (Aspect Magnet Technologies Ltd., Ben Shemen, Israel) operating at different resonance frequencies , sensor A (110 MHz) and sensor B (85 MHz), connected to a network analyzer (Model 8753C 300 kHz – 3 GHz, Hewlett Packard, Palo Alto, CA) and a laptop computer. The probe was mounted on the return line of the evaporator circulator pump, above the tube-and-shell heat exchanger and below the sampling port. LabVIEW software (National Instruments, Austin, TX) controlled the probe via the network analyzer. The computer logged data files containing two reflection coefficient readings for each of the discrete frequencies at 46 second intervals. The resolutions of sensor A and B are 0.15 MHz and 0.1 MHz, respectively. Analysis of the reflection coefficient data was performed using MATLAB (R2006b, MathWorks Inc., Natick, MA). A MATLAB m-file was used to calculate the resonance frequency f_r and the normalized impedance magnitude Z, defined as:

$$f_r = \frac{1}{2\pi\sqrt{LC}} \tag{1}$$

$$Z = \left| \frac{Z_L}{Z_0} \right| \tag{2}$$

where Z_L and f_r are the load impedance and resonance frequency of RF sensor and Z_0 is the characteristic impedance of the cable transmitting the electric current to the resonance probe. Impedance magnitude sum, which was derived

from summing normalized impedance magnitude at the 4.5 MHz (Sensor A) and 3 MHz (Sensor B) swept frequency range around resonance frequency, was calculated and used it for analysis.

2.3. *Physical property measurement*

2.3.1. *Soluble solids*

Soluble solids measurements were performed using a refractometer (RFM 320, Bellingham & Stanley Ltd., Tunbridge Wells, Kent, UK) to analyze the Brix of serum of the tomato concentrate.

2.1.2.*Paste viscosity*

The apparent viscosity of the tomato concentrate samples was measured directly by a rotational viscometer (Viscotester VT24, Haake, Saddle Brook, NJ) using the infinite cup geometry. The tests were performed at approximately process temperature (50°C). This measurement was performed twice and averaged.

3. Results and Discussion

3.1. *Correlation of dielectric response to physical properties*

3.3.1. *Resonance frequency*

The resonance frequency and magnitude of impedance, calculated from reflection coefficient data, of RF sensors were the two parameters with which correlations to physical properties were made. Because the probes were specifically designed for the tomato evaporation process, its resonant frequency was located approximately in the middle of the 30 MHz and 20 MHz swept frequency range for RF sensor A and B, respectively. The left side of Figure 1 and Figure 2 show the plots related to resonance frequency changes of RF sensor A and B during tomato concentrate processing, respectively. Although the resonance frequency clearly decreases as the evaporation proceeds, the resolution of the probe is insufficient to distinguish between tomato concentrates at Brix values higher than 14 °Brix. Sensor A shows frequency upward shift in 0.15 ppm during dilution process and Sensor B doesn't show any frequency shift during evaporation and dilution process.

At the highest Brix values, resonance frequency remains constant. This means no significant change in the mean state of the associated water is observed during this part of the evaporation process.

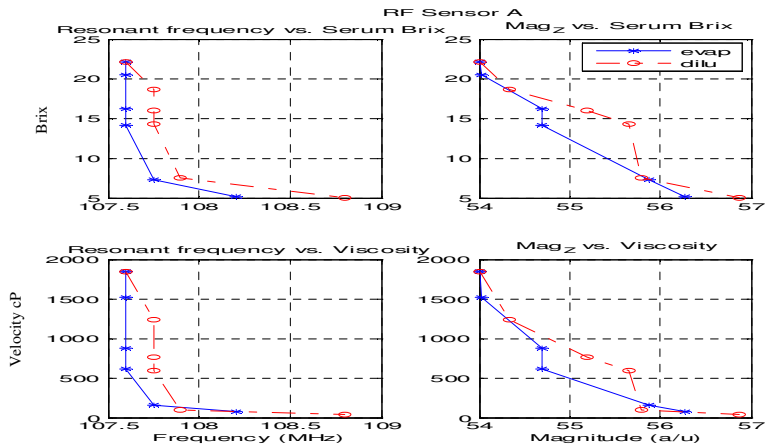

Fig. 1. Analysis plots for Sensor A. evap=evaporation, dilu=dilution.

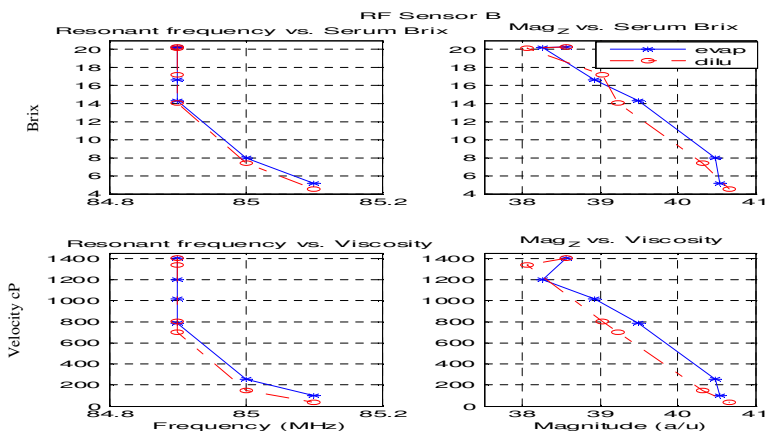

Fig. 2. Analysis plots for Sensor B. evap=evaporation, dilu=dilution.

3.3.2. *Impedance*

The right side of Figure 1 and Figure 2 show the plots related to impedance changes of RF sensor A and B during tomato concentrate processing, respectively. Sensor A shows more changes in impedance magnitude sum than Sensor B. As the evaporation proceeded, the magnitude sums of sensor impedance usually decreased. It could be due to an increase in the material's dielectric loss factor as the ionic species present are concentrated during the evaporation.

3.3.3. *Viscosity and soluble solid content*

Figure 3 shows a plot between viscosity and serum Brix of sampled concentrate of two experiments. The sample used for testing Sensor A is more homogeneous than one used for Sensor B. The important physical properties of the tomato concentrate are its viscosity and soluble solid content expressed as serum Brix. The ultimate goal of this project was to establish a meaningful correlation between these off-line measurements and the dielectric response of the tomato concentrate as measured by one or more parameters via in-line RF sensor. The resonance frequency ceased to change in response to the increasing viscosity of the tomato concentrate after 14 °Brix. However, the impedance magnitude sum decreased as the concentrate viscosity increased. Sensor B responds more linearly in about same range than Sensor A.

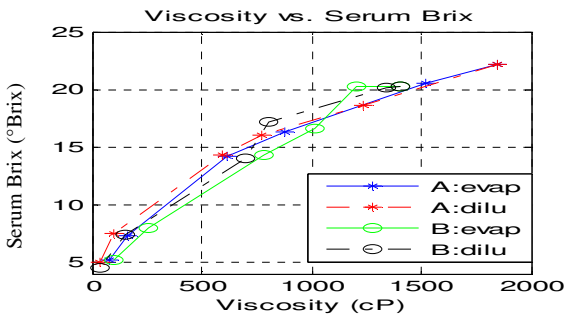

Fig. 3. Relation between viscosity and serum Brix of sampled concentrate of two experiments. A=harvested on September, B= harvested on October.

4. Conclusion

Realtime monitoring of fresh tomato concentrate processing was done using two kinds of radio frequency (RF) sensors resonant at 85 and 110 MHz. Fresh tomato juice with soluble solid content of about 5 °Brix was evaporated up to 23 °Brix with a pilot scale evaporator. The RF sensors were installed in a processing pipe. The relationships between sensor outputs and measured physical properties demonstrate the potential for using a dielectric sensor for process control.

References

1. T.D. Chou and J.L. Kokini, *J. Food. Sci.* ***52***, 1658-1664 (1987).
2. P.J. Cullen, A.P. Duffy, C.P. O'Donnell and D.J. O'Callaghan, *Trends Food Sci. Tech*. **11**, 451-457 (2000).
3. T.A. Haley and R.S. Smith, *Lebensm.-Wiss. U.-Technol.* **36,** 159-164 (2003).
4. Y.J. Choi, R.R. Milczarek, C.E. Fleck, T.C. Garvey, K.L. McCarthy and M.J. McCarthy, *J. Food Proc. Eng*. **29**, 615-632 (2006)

CATALOGING OF OLIVE ACCESSIONS USING MAGNETIC RESONANCE TECHNIQUES

SEONG MIN KIM

Bioresource Systems Engineering, Chonbuk National University, 664-14 Deokjin-dong Jeonju, Chonbuk 561-756, Republic of Korea

ED STOVER

National Clonal Germplasm Repository, USDA, One Shields Ave., Davis, CA 95616, USA

JENNY HANSEN

National Clonal Germplasm Repository, USDA, One Shields Ave., Davis, CA 95616, USA

MICHAEL J. MCCARTHY

Department of Food Science & Technology, University of California, One Shields Ave., Davis, CA 95616, USA

Cataloging of olive accessions was performed using magnetic resonance techniques. CPMG pulse sequence was used to acquire signal in time domain and T_2 was calculated using a bi-exponential curve fitting method. Inversion recovery pulse sequence was used to acquire spectroscopic data and T_1 were calculated for water and oil absorption from proton spectra. The relaxation time constants are useful for examining olive accessions.

1. Introduction

In 2004, the US produced olive on 13,000 Ha producing 94,000 metric tons of fruit, of which only 8% was crushed [1] to produce 383,000 gallons of oil [2]. Globally, oil production dominates, with olive grown on 7,455,049 ha producing 14 million metric tons in 2005 and providing 460 million gallons of oil [2]. Due to reported health benefits of olive oil, both US and global demand are on the rise [3]. The National Clonal Germplasm Repository (NCGR) in Davis, California is home to ~150 olive accessions including 133 that are mature, bearing trees in the Wolfskill Experimental Orchard. The missions of the NCGR are to acquire, maintain, characterize, and distribute plant genetic diversity. Characterization of the olive collection will greatly facilitate

stakeholder utilization of this important collection. Since oil content varies widely in olive accessions [4] and oil production is the most important use of olives worldwide, characterization of oil content is critical data for the NCGR olive collection. Oil and moisture content will be measured using a proton spectra and integrating this to obtain total signal intensity from the oil and moisture [5].

2. Materials and Methods

2.1. *Samples*

Olive samples were collected at different harvest dates for each olive accession. Harvest date was based on date at which 90% of fruit on each tree achieved mature color, with harvests one month before ~90% color, one at ~90% color, and the final harvest one month after achieving ~90% color. Total of 146 harvest samples from 91 olive accessions in the National Clonal Germplasm Repository (NCGR) in Davis, California, were examined. About 30 olives for each harvest from each tree (olive accession) were delivered and some (20 samples were selected for 2 harvest, and then 10 samples were selected for other harvests) of them were selected for NMR measurements. After measuring the weight of each sample to obtain both volume percent oil and weight percent oil content, NMR measurements were performed. And three olives out of the selected olives of each harvest (subset) for NMR measurements were used to measure moisture in a vacuum oven with 24 0.25 In• Hg @ 80℃ for 24 hours.

2.2. *NMR measurements*

The NMR measurements were performed on a 0.6T Oxford superconducting magnet operating at a proton frequency of 25.9 MHz and spectrometer installed in the Department of Food Science and Technology, University of California at Davis. A birdcage-type NMR coil with inner diameter of 75 mm was used to acquire NMR signals. A sample holder was used to place a sample in the middle of the NMR coil consistently. Spin-lattice and spin-spin time constants of each intact whole olive sample were measured. Inversion recovery pulse sequence was used to measure spin-lattice time constant (T_1). The inversion times were set to 20, 50, 100, 200, 500, 800, 1300, 2000, 3000, and 5000 ms. Carr-Purcell-Meiboom-Gill (CPMG) pulse sequence was used to measure spin-spin time constant (T_2).

2.3. *Data analysis*

The calculated spin-lattice relaxation time constant was fitted using Eq. (1). The calculated factors from the inversion recovery signals are relaxation time constants, signal magnitudes, and spectrum peak heights for water and oil components. Peak height ratio (Rpow) of oil (right) to water (left) highest spectrum peaks was calculated from that spectrum. Also, peak area ratio (Rmot) of oil to total (water and oil) peak area and peak area ratio (Rmow) of oil to water peak area were calculated from that spectrum. The calculated factors out of the CPMG signals are relaxation time constants and signal magnitudes for water and oil components. The calculated spin-spin relaxation time constant was fitted by bi-exponential decay curve according to the Eq. (2).

$$M(t) = M_0 \left[1 - 2 \exp\left(- \frac{t}{T_1} \right) \right] + M_\infty \tag{1}$$

Where M_0 is the magnitude of the exponential, T_1 is the characteristic spin-lattice relaxation time constant and M_∞ is the residual noise.

$$M(t) = \sum_i M_{0,i} \exp\left(- \frac{t}{T_{2,i}} \right) + M_\infty \tag{2}$$

Where $M_{0,i}$ is the magnitude of the *i*th exponential, $T_{2,i}$ is the characteristic spin-spin relaxation time constant for the *i*th exponential and M_∞ is the residual noise. The acquired NMR signals were processed with commercial programming software (MATRLAB R2006b, Mathworks, Natick, MA, USA).

3. Results and Discussion

Three accessions harvested on three different dates were tested. Table 1 shows Harvest dates and physical properties of three cultivars. Figure 1 shows variations of measured values of 3 accessions with different harvest dates. The variation in sample weight is similar to the variations of T_1w, T_2w, and T_2o. The average values of those factors are highest at a mature stage (set #2 or second harvest). The pattern of dry weight variation is similar with variations of T_1o, Rpow, Rmow and Rmot. The average values of those factors gradually increase and are highest at the over mature stage (set #3 or third harvest).

Table 2 shows statistics of a linear regression model, f(x)=Ax+B, between dry weight (DW) and selected variables.

Table 1. Harvest dates and physical properties of three cultivars.

Cultivar	ID	Set	Harvest date	Weight (g)	DW (%)
Sevillano	A	#1	2006.10.30	10.169	37.2
		#2	2006.11.25	14.258	35.4
		#3	2007.01.05	8.796	44.3
Picholine DuLa nguedoc	B	#1	2006.11.17	4.473	40.7
		#2	2006.11.25	4.844	42.4
		#3	2007.01.05	4.231	55.2
Vassilika	C	#1	2006.11.17	6.768	38.8
		#2	2006.12.11	6.958	43.5
		#3	2007.01.12	4.489	57.5

※ where, #1: first harvest, #2: second harvest, and #3: final harvest.

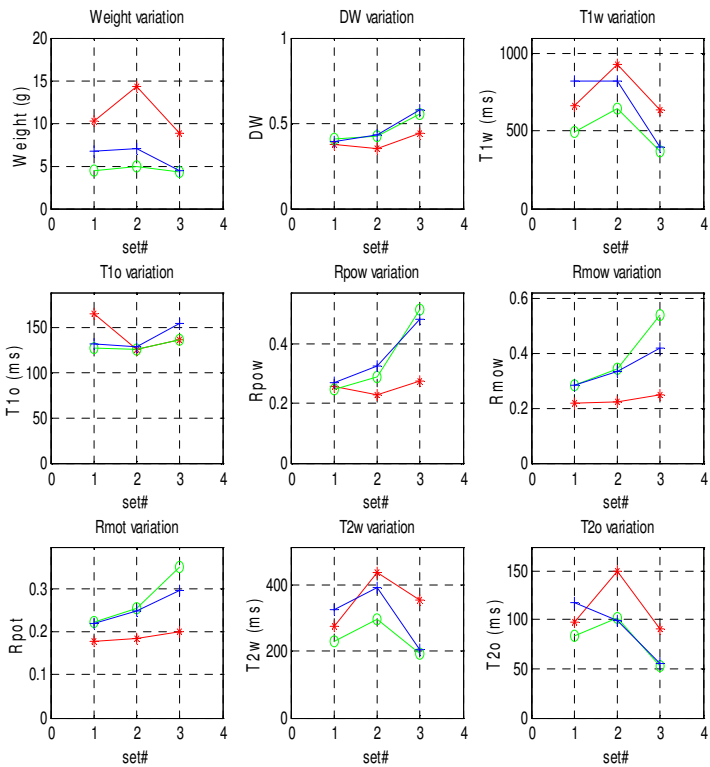

Fig. 1. Variations of measured values of 3 cultivars (ID: A, B, and C) with different harvest dates. set #1: first harvest, set #2: second harvest, and set #3: final harvest. A: -*, B: -+, C: -o

Figure 2 shows linear relationship between dry weight and peak height ratio, Rpow, of all sample data. The relationship shows better R-square value compare to the result using all samples. Figure 3 shows linear relationship between dry weight and inverse of T_2 of oil part, $1/T_{2o}$. The relationship shows less R-square value compare to the result using Rpow values calculated from T_1 measurement data. This implies that T_2 measurement experiment, which usually takes less time than T_1 measurement, is a comparable method for obtaining physical properties of olives.

Table 2. Statistics of linear regression model, DW=Ax+B, between DW and selected variables.

x	A	B	SSE	R^2
$1/T_{1w}$	0.0007	-0.0013	4.362×10^{-6}	0.62
Rpow	0.0131	-0.2538	0.02621	0.91
Rmow	0.0119	-0.2013	0.06693	0.76
Rmot	0.0065	-0.0452	0.01941	0.76
T_{2o}	-3.253	237	6901	0.70
$1/T_{2o}$	0.0005	-0.0096	7.079×10^{-5}	0.83

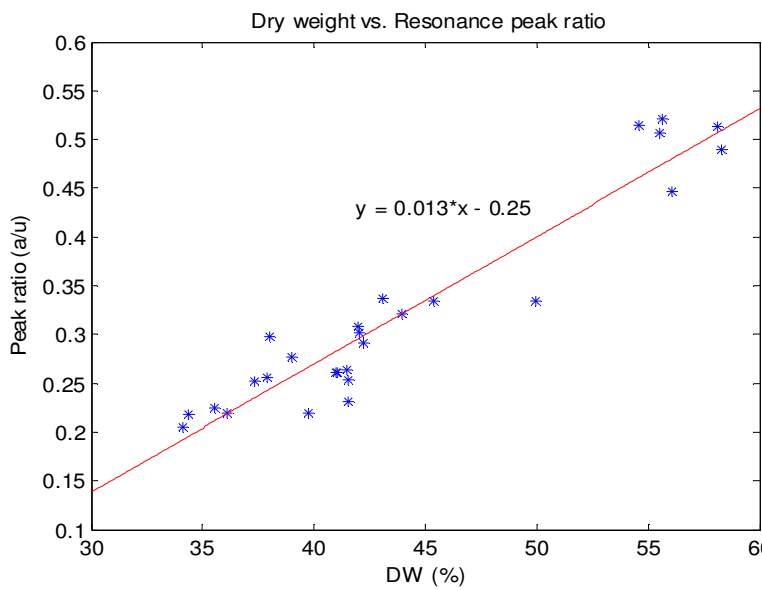

Fig. 2. Linear relationship between dry weight, DW, and peak height ratio, Rpow.

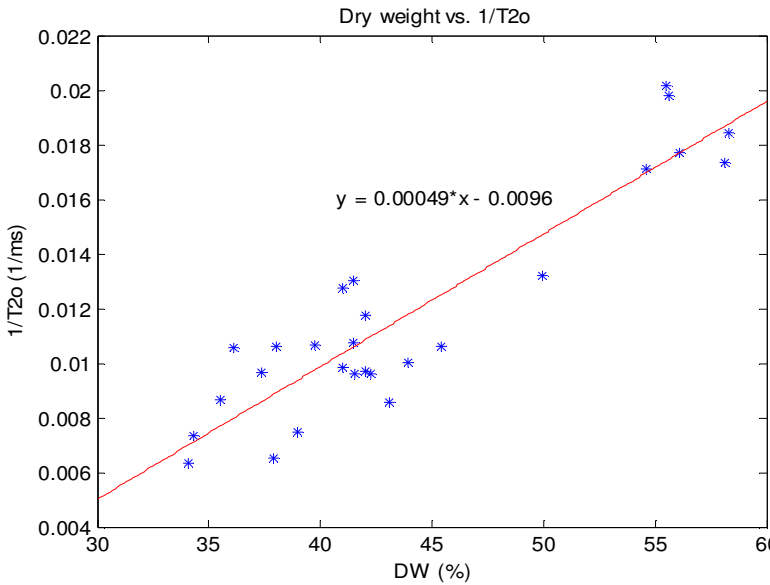

Fig. 3. Linear relationship between dry weight, DW, and inverse of T_2 of oil component, $1/T_{2o}$.

4. Conclusion

Magnetic resonance techniques were used to examine intact whole olive fruits harvested at different maturity stages. CPMG pulse sequence was used to acquire signal in time domain and T_2 was calculated using a bi-exponential curve fitting method. Inversion recovery pulse sequence was used to acquire spectroscopic data and T_1 were calculated for water and oil absorption from proton spectra. The relaxation time constants are useful indexes for examining the state of olive accessions.

References

1. USDA/ERS, *http://usda.mannlib.cornell.edu/usda/usd* (2005).
2. Olive Oil Source, *http://www.oliveoilsource.com/statistics.htm* (2005).
3. CRB, *http://www.crbtrader.com/fund/articles/oliveoil.asp* (2005).
4. J. Tous, A. Romero, J. Plana and J.F. Hermoso, *Acta-Horticulturae*. **586**,113-116 (2002).
5. M.J. McCarthy, P. Chen, S.M. Kim and B. Zion, Instrumentacao Agropecuaria 2000, EMBRAPA-CNPDIAJ. 3-10 (2000).

QUANTITATIVE EVALUATION OF KNOT IN JAPANESE LARCH LUMBER USING X-RAY SCANNING

JUNG KWON OH

Department of Forest Sciences, Seoul National University, #200 R.M.6218 San 56-1 Sillim-9-dong, Gwanak-gu, Seoul, 151-921, Korea

KWANG-MO KIM

Department of Forest Products, Division of Wood Engineering, 207 Cheongyangni-2-dong Dongdaemun-gu, Seoul, 130-712, Korea

KUGBO SHIM

Department of Forest Products, Division of Wood Engineering, 207 Cheongyangni-2-dong Dongdaemun-gu, Seoul, 130-712, Korea

HWANMYEONG YEO

Department of Forest Products, Division of Wood Engineering, 207 Cheongyangni-2-dong Dongdaemun-gu, Seoul, 130-712, Korea

JUN-JAE LEE

Department of Forest Sciences, Seoul National University, #200 R.M.6218 San 56-1 Sillim-9-dong, Gwanak-gu, Seoul, 151-921, Korea

It is well known that knot is a major defect of structural lumbers as regards their ultimate strength capacity. This study is focused on evaluation of knot with x-ray images more accurately. The objectives of this study is the development of quantitative evaluation method of knot with a single x-ray radiation

The simple method to evaluate the ratio of knot in lumber thickness ratio using a single x-ray radiation is proposed in this paper. To verify this knot ratio evaluating method, x-ray equipment measured the density of 38mm thickness lumbers. The lumber was cut at the cross section which has knots and practical knot ratio in x-ray path was measured with a mesh. Because the density of the transit zone is similar to knot density, the estimated knot ratio has a meaning to be the ratio of the knot and transit zone in lumber thickness. The knot ratio could be evaluated quantitatively by the proposed model with 0.13 of RMSE. The proposed knot ratio evaluation method could give the more detailed information of knot with merely a single x-ray radiation.

1. Introduction

The strength of the lumber is reduced by various kinds of defect, such as knots, slope of grain, decay, wane etc. Most of all knots are almost always present in large numbers in a piece of the lumber. It is well-known that knots are the most serious defect as they can greatly reduce the strength of the lumber. Therefore, the detection and evaluation of knot is very important. There are various nondestructive evaluation methods applicable to knot detection. J. S. Machado et al.[1] detected knots with acousto-ultrasonic scanning. E. Baradit et al.[2] tried to detect knots in wood using microwaves.

It is well-known that the knot can be detected by x-ray radiation, because the knot density is higher than the clear wood part, and the intensity of x-ray beam passing through an absorbent material depends on its density. The localized density for a pixel of x-ray image can be calculated by using the attenuation equation of Beer's law [3].

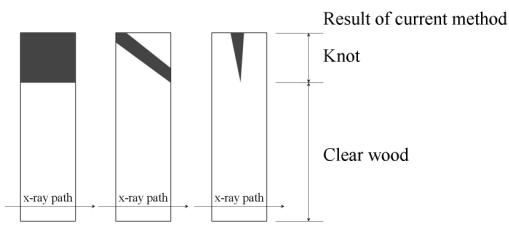

Fig. 1. The results of different shape of knot by current knot detection method

Figure 1 shows three lumbers with different shape of knot. X-ray can detect all of these knots in each lumber. However current knot detecting method can not distinguish them. It is sure that computer tomography (CT) can distinguish these knots of lumbers. However, in case of CT, it takes too much time to use for lumber grading.

In this study, we intended to develop the quantitative evaluation method of knot with a single x-ray radiation.

2. Materials and Methods

2.1. *Specimens*

Japanese Larch lumbers with dimensions of 38mm x 140mm x 3.6 m long were sampled from commercial mills. These test specimens were kiln-dried to an average equilibrium moisture content of approximately 18%.

2.2. *Image analysis for knot detecting*

In this study, an image intensifier was used for x-ray detector (Thales Image Intensifier TH9429). X-ray image for the full length and width of the lumber was taken with x-ray passing through 38mm thick of the specimen.

To detect knots, knots were classified by the presence of high density areas. The 1.2 times average density of the lumber was used for the threshold value, and it was experimentally determined for knot detection. Because the density of the latewood is similar to knot density, the latewood was often misclassified. As Figure 2.B shows, the shape of the misclassified latewood is generally the long horizontal lines with less than 2 mm thickness. The misclassified latewood can be separated from the detected area by this morphological characteristic. After removing the latewood, many noises still remained to be removed. Finally, an x-ray image with only knot information could be obtained, after removing noise.

Fig. 2. Knot detecting work flow
(A : Raw x-ray Image, B : Binary image after applying threshold, C : Removing latewood by mophological characteristics, D : Removing noises, E : Final result).

2.3. *Knot ratio evaluation*

Knot ratio(R_{knot}) was defined to be the ratio of knot in lumber thickness in this study. Although the density of clear wood and knot has a large variation over a wide range, it was assumed that the density of them is uniform.

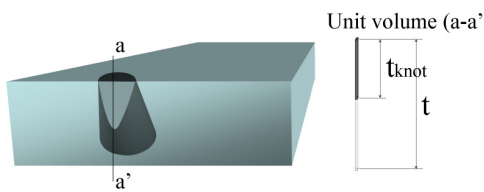

Fig. 3. Schematic diagram of knot ratio

In Figure 3, average density of unit volume, which has 1pixel x 1pixel and thickness of the specimen, can be expressed as the following Eq(1).

$$R_{x,knot} = \frac{\rho - \rho_c}{\rho_k - \rho_c} \quad (1) \qquad \text{Where, } R_{x,knot} = \frac{t_{knot}}{t}$$

Where average density of unit volume, ρ, is the localized density for a pixel of x-ray, clear part density, ρ_c, can be calculated by extracting from x-ray image of the lumber and knot density, ρ_k, could be experimentally measured.

To measure knot density which is input variable for knot ratio evaluation, 10mm thick *Japanese larch* specimens with knot were prepared with knot being at right angle with the wide face (Figure 4.). X-ray images of the same specimens were taken with x-ray passing through 10mm thickness. The boundary of knot was identified by observation of fiber direction with a magnifying camera. The specimen was divided into three zones, which are clear zone, transit zone, knot zone. The x-ray image for each zone was extracted from x-ray image for the specimen. And then, the density for each zone was calculated by Beer's law.

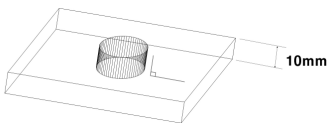

Fig. 4. Preparation for measurement of knot density.

2.4. *Measurement of practical knot ratio*

To verify the proposed knot ratio evaluation model, the cross section which has knots was cut. The boundary of knot was identified by the observation of the cross section using magnifying camera. Using the mesh, the number of cell of mesh matrix which belongs to knot was counted. And the practical knot ratio, $R_{p,knot}$, was calculated by dividing the number of cell for knot by the number of cell for lumber thickness.

3. Results and Discussions

3.1. *Knot density for Japanese larch*

In order to determine the input variable for knot ratio evaluation, the density of knot zone and transit zone for two type of knot, which are tight knot and encased knot, was calculated by Beer's law. The x-ray image for transit zone of the encased knot could not be extracted, because the width of transit zone is smaller than x-ray image resolution of 0.4mm. The average density of knot was 0.95. Therefore it was used for the input variable of knot density for the knot ratio evaluation.

Table 1. The results of knot density measurement

	Tight knot			Encased knot		
	Avg.	St. dev	C.O.V.	Avg.	St. dev	C.O.V.
Knot	0.96	0.069	0.072	0.96	0.063	0.066
Transit zone	0.93	0.073	0.079			

3.2. *Comparison between the knot ratio estimated by x-ray and the practical knot ratio*

Figure 5. shows the relationship between knot ratio estimated by x-ray and the practical knot ratio. The coefficient of determinant was 0.65 and root mean square error (RMSE) was 0.20. The most of lower than 0.5 knot ratio was overestimated. It was thought that the lower knot ratio zone have a relatively larger transit zone, of which density is the similar to knot, and the dense transit zone make knot ratio overestimated (Figure 5. B, Figure 7. B).

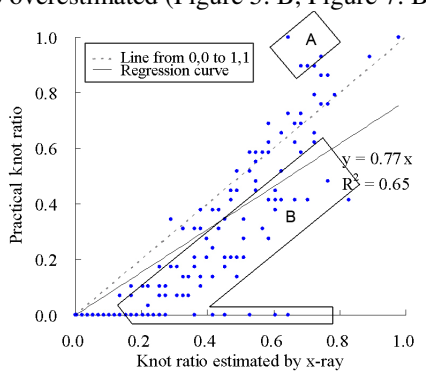

Fig. 5. The relationship between the estimated knot ratio and the practical ratio of knot in lumber thickness.

In the higher knot ratio zone, the direction of most knots is the almost same with the x-ray path (Figure 7.A). It has a relatively small transit zone in the x-ray path or does not have. In general, the big knot has cracks in knot. The direction of the crack is almost the same of x-ray path (Figure 7.A). The reduction of x-ray attenuation makes the almost 100% knot ratio zone underestimated (Figure 5.A).

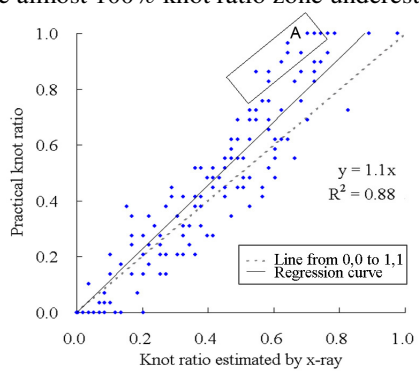

Fig. 6. The relationship between the estimated knot ratio and the practical ratio of knot and transit zone in lumber thickness.

Because the cause of error is dense transit zone, the cross section was divided into the two zones which are the clear zone and the knot & transit zone. And the number of cell of mesh for the knot & transit zone was counted again. Figure 6 shows the relationship between the knot ratio estimated by x-ray and the practical ratio of the knot & transit zone in lumber thickness. It showed stronger relationship of 0.88 of R^2. And RMSE was reduced from 0.20 to 0.13 and the slope of regression curve was closer to 1. However, the effect of crack in knot still remained (Figure 6.A) and the further studies on the effect of crack in knot are required.

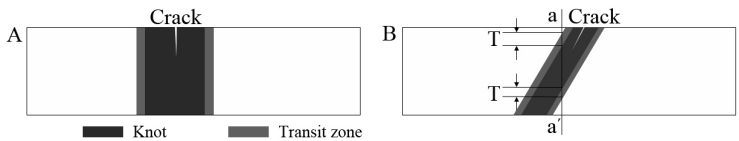

Fig. 7. The effect of transit zone on knot ratio evaluation

From these results, it was found that x-ray can evaluate knot ratio and the knot ratio estimated by the proposed model has meaning to be the ratio of knot and transit zone in lumber thickness. As Figure 8 shows, the knot ratio evaluation method can give the simplified 3-dimensional information of knot. This method is expected to improve the accuracy of the strength estimation, such as compression strength, bending strength etc.

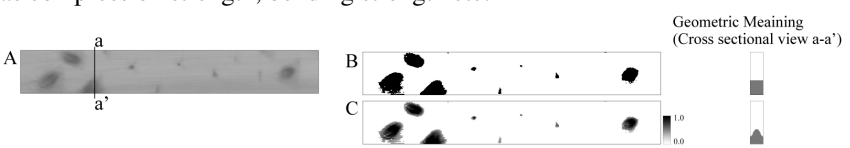

Fig. 8. Comparison between knot detecting method and knot ratio evaluation method (A : Raw x-ray image, B : Result by knot detecting method, C : Result by knot ratio evaluation method).

4. Conclusions

Knot could be detected by x-ray image analysis. The amount of knot could be evaluated quantitatively by the proposed model with 0.13 of RMSE. Because the density of the transit zone is similar to knot density, the estimated knot ratio has a meaning to be the ratio of the knot and transit zone in lumber thickness. Knot ratio evaluation could give the more detailed information of knot with a single x-ray radiation. However, the underestimation problem by the crack in knot still remained and further study on this problem is required.

References

1. J.S. Machado, R. A. Sardinha and H. P. Crus, Feasibility of automatic detection of knots in maritime pine timber by acousto-ultrasonic scanning, Wood Sci Technol 38:277-284(2007).
2. E. Baradit, R.Aedo and J. Correa, Knots detection in wood using microwaves, Wood Sci Technol 40:118-123 (2006)
3. Institute of Isotopes of the Hungarian Academy of Sciences, Industrial Application of Radioisotopes, ELSEVIER. 232-239(1986)

ESTIMATION OF NITROGEN CONTENT OF RICE USING HYPERSEPCETRAL REMOTE SENSING

CHANSEOK RYU, MASHIKO SUGURI, MIKIO UMEDA

Environmental Science and Technology, Graduate School of Agriculture Kyoto University, Kitashirakawa Oiwake-cho,Kyoto, 606-8502, Japan

In this research, hyperspectral remote sensing was applied to analyze the nitrogen contents of rice plants at panicle initiation stage during 3 years. It is possible to estimate the annual nitrogen contents estimation models using the MLR and PLSR analysis. Nevertheless nitrogen contents were variable for 3 years, it is also possible to establish the general nitrogen estimation model by MLR and PLSR analysis using the data of 3 years. It means that the general nitrogen contents estimation model for panicle initiation stage is useful for variable conditions.

1. Introduction

It is necessary to estimate the nitrogen contents of rice plants at panicle initiation stage to decide the amount of nitrogen fertilizer at topdressing. The amount of nitrogen fertilizer at topdressing is an important factor to control nitrogen contents at heading stage, which is depended on the grain quality and quantity. However, it is difficult to estimate nitrogen contents because it is very fluctuant parameter during vegetation growth (Ryu et al., 2004). Remote sensing has great potential for several applications because it enables wide-area, nondestructive and real-time acquisition of information about plant ecophysiological conditions (Inoue, 2003). Remotely sensed data, obtained either by satellite or aircraft, can provide a set of detailed, spatially distributed data on plant growth and development (Plant et al., 1999). Multispectral airborne images was estimated for the use of several ways, such as variable growing condition and yield (Yang et al., 2001), leaf area index and nitrogen concentration (Eva et al., 2002).

Recently, the research using hyperspectral remote sensing is increased. The combined model has developed by evaluation in terms of quantitative predictive capability using hyperspectral data to integrate advantages of indices minimizing soil background effect and indices that are sensitive to chlorophyll concentration (Driss et al., 2002). The potential of airborne hyperspectral remote sensing in crop monitoring and estimation of various biophysical parameters was examined.

Thus postulating hyperspectral sensors onboard an aircraft would result in better relationships between remote sensing data and crop parameters (Goel et al., 2003). However, there is not enough nitrogen contents estimation model at each vegetation stage.

In this study, hyperspectral remote sensing was applied to analyze the nitrogen contents of rice plant at panicle initiation stage for 3 years. The objectives of this research are 1) to analyze hyperspectral images annually by the MLR and PLSR analysis and 2) to establish the general nitrogen contents estimation model at panicle initiation stage using the hyperspectral reflectance.

2. Materials and methods

2.1. *Test field*

The experimental farm of Kyoto University is located in Takatsuki city, Osaka prefecture. The soil of field is classified as *Gray Lowland* soil. The species of tested crop is *Oryza sativa L., cv. HINO-HIKARI*. The experimental field (0.5 ha) was virtually divided 100 sampling plots (5m×10m). The amount of nitrogen fertilizer at basal dressing were applied from 0 kgN/ha to 65 kgN/ha. Figure 1 shows the virtual image of test field at Takatsuki experimental farm of Kyoto University.

2.2. *hyperspectral remote sensing*

The images of field were taken by the hyperspectral remote sensor (AISA+, Spectral Imaging) at panicle initiation stage for 3 years. There are 68 bands from 400nm to 1000nm and ground resolution is about 1m. The standard-reflectors were set on the side of field in order to calibrate the incoming sunlight. Hyperspectral image was analyzed by Environment for Visualizing Images software (Research Systems, ENVI version 3.6) and statistics analysis was done by SPSS software (SPSS Inc, SPSS version 11) and Unscrambler software (CAMO, Unscrambler version 9.6). Each plot was virtually divided. The reflectance of inner parts at each plot was measured.

2.3. *Measurements of ground truths*

The main ground truth is nitrogen contents of rice plants at panicle initiation stage. The sampling plots were 28 plots in 2003, 40 plots in 2004 and 2005. At each plot, there were 2 sampling points and each sampling points was consist of 4 stocks of rice plants.

After taking hyperspectral images, the rice plants were sampled and separated in leaves and steams. And then they were weighted and finely grounded with pulverizing mill. The nitrogen concentration was measured by NC-900 (Sumica Chemical Analysis Service, Ltd). Nitrogen contents were calculated as the products of nitrogen concentration and dry mass per unit area.

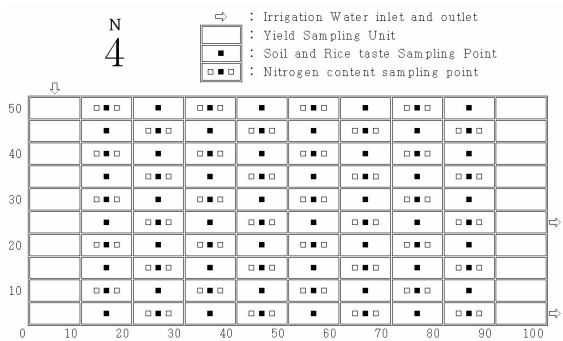

Fig. 1. Virtual image of test field.

3. Results and discussion

Ground truths at panicle initiation stage were investigated for 3 years. Table 1 shows the descriptive statistics of rice plants at panicle initiation stage. There was significant difference in all kind of ground truths between the year 2003 and other years, except nitrogen concentrations. Ground truths in 2003 were almost two third of the others. Dry mass of leaves, leaves and total nitrogen contents in 2005 are almost the twice, comparing with those in 2003. It might be affected by the weather and other conditions, except the field management.

Table 1. Descriptive statistics for ground truths of rice plant at panicle initiation stage.

		DM Leaf[*2]	DM Stem	NC Leaf[*3]	NC Stem	N Leaf[*4]	N Stem	Total N
2003	Mean	140.48	202.71	2.18	0.76	3.07	1.53	4.60
	SD[*1]	18.23	30.58	0.13	0.06	0.44	0.24	0.66
2004	Mean	225.91	363.76	2.06	0.74	4.69	2.70	7.39
	SD	35.01	39.52	0.14	0.07	1.04	0.46	1.47
2005	Mean	272.16	309.45	2.30	0.77	6.26	2.36	8.63
	SD	25.94	33.11	0.18	0.11	0.87	0.34	1.13

([*1] : Standard deviation, [*2] : dry mass, [*3] : nitrogen concentration, [*4] : nitrogen contents)

Table 2 shows the managements and weather conditions of field in 3 years. There was less volume of plants in 2003, in spite of twice amount of nitrogen fertilizer comparing with 2005.
However, the cumulate temperature in 2003 was two third of it in 2004 and 2005. Furthermore, the cumulate daily radiation in 2003 was almost half of 2004 and one third of 2005. Therefore, the volume of plants might be largely affected by the weather conditions.

Table 2. Managements and weather condition of field in 3 years.

	2003	2004	2005
Basal dressing	June 7	June 4	May 27
Amount of basal dressing[*1]	39.6 kgN/ha	25.2 kgN/ha	17.8 kgN/ha
Transplanting	June 12	June 14	June 15
Sampling	August 1	August 3	August 5
Cumulate temperature[*21]	472.60	633.18	610.7
Cumulate daily radiation	366.42	766.39	500.5
Cumulate vegetation day[*3]	51 days	51 days	52 days

([*1] : average amount of nitrogen fertilizer at sampling plots, [*2] : average temperature minus 15 , [*3] : cumulate day from transplanting to sampling)

Figure 2 shows the hyperspectral reflectance in 3 years. In the case of hyperspectral reflectance in 2003, it is completely different, comparing with other years. It is impossible to solve the reason why the difference of reflectance between year 2003 and other years. The statistical analysis were operated by the SPSS for multi linear regression (hereinafter, MLR) with stepwise method and the Unscrambler for partial least square regression (hereinafter, PLSR) with full cross validation.

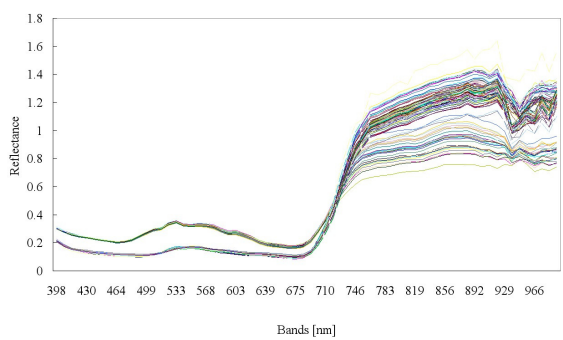

Fig. 2. Hyperspectral reflectance in 3 years.

Table 3 shows the results of MLR analysis with stepwise method for 3 years. It was possible to estimate nitrogen contents at panicle initiation stage of rice plants by MLR analysis. However, the accuracy of nitrogen contents estimation model in 2005 is not so good, comparing with the other years. It was also possible to establish the general nitrogen contents estimation model, regardless the difference of vegetation condition and hyperspectral reflectance.

Table 3. Results of MLR analysis with stepwise method for 3 years.

		2003 (n=27)	2004 (n=40)	2005 (n=40)	Total (n=107)
Variables		R_{965}	R_{737}, R_{993}, R_{892}	R_{576}	R_{701}, R_{692}, R_{892}
R		0.825	0.942	0.541	0.933
R^2		0.681	0.888	0.292	0.870
Adjusted R^2		0.668	0.879	0.274	0.866
SEC		0.382	0.512	0.961	0.721
Coefficients	Constant	-3.993	-1.926	31.534	-1.715
	Variables	10.574	-67.623 7.352 36.677	-157.656	-180.692 203.036 15.048

Table 4 shows the results of PLSR analysis with full cross validation method for 3 years. It was also possible to estimate nitrogen contents at panicle initiation stage of rice plant using PLSR analysis. Figure 3 shows the measured and estimated nitrogen contents using hyperspectral reflectance by PLSR analysis. The results of PLSR analysis might be similar to those of MLR analysis, such as R and SEC. Nevertheless nitrogen contents, estimation model of it were variable, it is possible to establish general nitrogen estimation model. It means that general nitrogen contents estimation model is useful for variable conditions.

Table 4. Results of PLSR analysis with full cross validation for 3 years.

	2003 (n=27)		2004 (n=40)		2005 (n=40)		Total (n=107)	
	Cal.	Val	Cal.	Val	Cal.	Val	Cal.	Val
PCs	1		3		1		5	
Slope	0.627	0.602	0.868	0.795	0.257	0.225	0.879	0.856
Offset	1.715	1.826	0.978	1.547	6.406	6.687	0.865	1.031
R	0.792	0.758	0.932	0.847	0.507	0.443	0.938	0.919
RMSEC[*1]	0.397	0.424	0.528	0.786	0.959	1.001	0.682	0.771
SEC[*2]	0.405	0.433	0.535	0.793	0.972	1.013	0.685	0.774
Bias	$-4.415e^{-08}$	-0.003	5.960^{-08}	0.035	$-1.192e^{-08}$	$1.575e^{-05}$	$9.470e^{-07}$	$-4.010e^{-04}$

([*1] : in the case of validation RMSEP, [*2] : in the case of validation SEP)

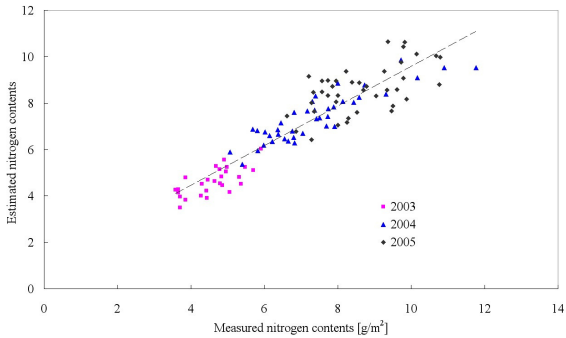

Fig. 3. Measured and estimated nitrogen contents for 3 years by PLSR analysis.

However, the reason of the difference of hyperspectral reflectance between year and year should be solved in order to improve the models. Furthermore, it is also necessary to confirm the extensiveness of the general nitrogen contents estimation model for panicle initiation stage and establish the general nitrogen contents estimation models for other vegetation stages of rice plants.

4. Conclusion

In this research, hyperspectral remote sensing was applied to analyze the nitrogen contents of rice plants at panicle initiation stage during 3 years. It is possible to estimate the annual nitrogen contents estimation models using the MLR and PLSR analysis. Nevertheless nitrogen contents were variable for 3 years, it is also possible to establish the general nitrogen estimation model by MLR and PLSR analysis using the data of 3 years. It means that the general nitrogen contents estimation model for panicle initiation stage is useful for variable conditions.

References

1. P.K. Goel, S.O. Prasher, J.A. Landry, R.M. Patel, A.A. Viau and J.R. Miller, *Trans. ASAE*, *46(4)*, 1235 (2003).
2. H. Driss, J.R. Miller, T. Nicolas, J.T. Pablo and D. Louise, *Remote Sens. of Environ*, *81*, 416 (2002).
3. C. Ryu, M. Suguri and M. Umeda, *In pro. of ATOE*, 113 (2004).
4. C. Yang, J.M. Bradford and C.L. Wiegand, *Trans. of ASAE*, *44(6)*, 1983 (2001).
5. Y. Inoue, *Plant Prod. Sci*., *6(1)*, 3 (2003).
6. E. Goegh, H. Soegaard, N. Broge, C.B. Hasager, N.O. Jensen, K. Schelde and A. Thomsen, *Remote Sens. of Environ*, *81*, 179 (2002).

ESTIMATION OF QUALTY AND QUANTATY OF GREEN-TEA BY HYPERSPECTRAL IMAGE

MASHIKO SUGURI, CHANSEOK RYU, MIKIO UMEDA†

Environmental Science and Technology, Graduate School of Agriculture Kyoto University, Kitashirakawa Oiwake-cho, Kyoto, 606-8502, Japan

Hyperspectral remote sensing was applied to estimate the number of shoots, dry mass and nitrogen concentration of tea plants. It is possible to estimate the number of shoots and dry mass of 1st crop using PLS regression. However, the nitrogen concentration estimation model with full cross validation had less performance than other factors. It might be caused by low variation of nitrogen concentration in 1st crop. By adding data of 2nd crop, the variation of nitrogen concentration was increased and estimation model was improved. In respect of regression coefficients, there were several peaks, which are more sensitive bands to estimate the nitrogen concentration.

1. Introduction

The Japan's production of tea is 90,000t/year and it is 7th largest in the world. Generally, the quality of green tea depends on several parameters and it is laborious and destructive to measure quality parameters with chemical analysis. Therefore, the NIR spectrophotometric analysis was applied to measure the quality parameters, such as the amount of nitrogen concentration (Goto et al., 1986), amino acids (Horie et al., 1993), crude fiber (Smiechowska et al., 2006), caffeine, theanine and tannin (Ikegaya et al., 1988) and so on.

Previous researches have proved that NIR spectrophotometic analysis is one of useful methods to measure the quality parameters. However, most of them put their focus on not tea as plants but tea as product. There are several researches for measuring vegetation growth of tea fields (Samarasinghe et al., 2003 and Ryu et al., 2006). It is hard to improve their quality after harvesting. Therefore, it is important to investigate the nitrogen concentration of tea plants in order to control the quality of tea products (Ryu et al., 2007). It is possible to estimate the number of shoots, dry mass and nitrogen concentration of tea plants using multispectral sensor (Suguri et al., 2006). However, it is necessary to analyze more clearly their parameters.

In this study, hyperspectral remote sensing was applied to estimate quality and quantity parameters, such as the number of shoots, dry mass and nitrogen concentration of tea plants more accurately.

2. Materials and methods

2.1. *Test field and period*

This study was carried out at the tea field of Sugimoto Tea Factory at Wazuka-cho Souraku-gun Kyoto prefecture, Japan. The cultivar of tea was *Camellia sinensis L., Yabukita*, which is most common in Japan. The 1st crop was investigated 7 times from April 28 to May 15 and the 2nd crop was also investigated 6 times from June 19 to July 3 in 2006. In each crop cultivation, the tea plants were shaded from sunlight for a period of time before harvesting in order to increase the quality of the tea. The shading terms of 1st crop was from May 12 to harvest and it of 2nd crop was from June 29 to harvest.

2.2. *Hyperspectral remote sensing*

Spectral Camera QE-V10E (Specim) was used to acquire hyper spectral images. It captures hyper spectral reflectance (400-1000 nm/1024 pixels) of a line (1344pixels), and it was rotated by an electric motor around the axis, fixed horizontally on the top of the vertical bar at the height of 2m. The image was constructed as accumulation of lines. It measured the reflectance of tea plants in the circle (d = 300mm), where tea shoots were sampled as the ground truths. Furthermore, the markers/standard-reflectors were set on the side of the circle while capturing the hyperspectral images in order to calibrate the incoming light and to find where to be captured.

2.3. *Measurements of ground truths*

The measurements of ground truths and capturing hyperspectral images were carried out once in two or three days. Sampling points were set at 15 points and after shading, 6 points for the 1st crop, and 7 points after shading for the 2nd crop. Just after capturing hyperspectral images, the young shoots which have more than 2 opening leaves inside the circular frame, were plucked manually and counted. The plucked shoots were primary-parched with microwave oven and dried with circulation drier at 60 ℃ for 24hours. Dried tea samples were weighted and finely ground with pulverizing mill and nitrogen content were measured by NC-900 (Sumica Chemical Analysis Service, Ltd).

2.4. *Extraction of young leaves in the image*

The captured hyperspectral images were analyzed to extract the young leaves inside the circular frame for the young and old leaves coexisted on the canopy. The nitrogen concentrations of young and old leaves differ and those can be estimated by NDVI and GreenNDVI. Therefore, the difference of NDVI and GreenNDVI was utilized to extract the young leaves inside the circular frame and hyper spectral analyses were applied only on that segment. Figure 1 shows the original image and the segmented image

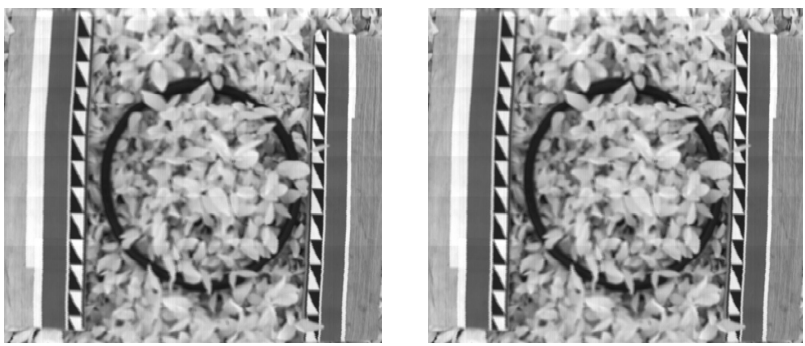

(a) Original hyperspectral image (b) Segment image (NDVI-GreenNDVI)

Fig. 1. Original image and segmented image using NDVI – GreenNDVI

3. Results and discussion

Table 1 shows the descriptive statistics for ground truth of tea plant during 1st crop vegetation growth.

Table 1. Descriptive statistics for ground truth of 1st crop.

1st Crop	No. of shoots			Dry mass			Nitrogen concentration		
	Mean	SD	CV	Mean	SD	CV	Mean	SD	CV
28 April[*1]	12.43	6.30	50.66	0.43	0.22	51.24	5.93[*2]	0.13[*2]	2.19[*2]
1 May[*3]	40.27	9.23	22.92	1.54	0.46	29.88	5.69	0.10	1.74
4 May[*3]	58.53	11.81	20.17	2.86	0.75	26.25	5.58	0.13	2.31
6 May[*3]	109.93	10.42	9.47	6.05	0.75	12.36	5.44	0.13	2.48
9 May[*3]	135.53	21.57	15.91	9.12	1.53	16.76	5.47	0.17	3.13
12 May[*4]	163.67	13.59	8.30	12.43	1.46	11.74	5.41	0.20	3.74
15 May[*4]	171.00	17.44	10.20	13.53	1.32	9.72	5.16	0.41	7.96

([*1] : 14 samples, [*2] : 13 samples, [*3] : 15 samples, [*4] : 6 samples because of shading)

There are less than 5% of coefficient variations for nitrogen concentration in spatial variability during 1st crop, except just before harvesting (15 May). And temporal variability was also small.

Table 2 shows the results of PLS regression with full cross validation for 1st crop. It was possible to estimate the number of shoot, dry mass and nitrogen concentration using hyperspectral remote sensing. However, the calibration and validation of coefficient correlation for nitrogen concentration are 0.632 and 0.494, respectively. It might be affected by low variation of nitrogen concentration at 1st crop. During vegetation growth term of 1st crop, there are less than 1% of nitrogen concentration difference.

Table 2. PLS regression with full cross validation for 1st crop.

1st crop (55 samples)	No. of shoots		Dry mass		Nitrogen concentration	
	Calibration	Validation	Calibration	Validation	Calibration	Validation
PCs	3		3		3	
Slope	0.854	0.821	0.940	0.921	0.399	0.313
Offset	16.759	21.213	0.447	0.621	3.276	3.744
Correlation	0.924	0.896	0.970	0.960	0.632	0.494
RMSEC (RMSEP)	15.566	18.120	0.924	1.053	0.166	0.189
SEC (SEP)	15.710	18.277	0.932	1.062	0.168	0.191
Bias	$-3.260e^{-06}$	0.583	$-4.118e^{-08}$	0.031	$-8.670e^{-08}$	-0.001

Therefore, the data of 2nd crop were included in the analysis. Table 3 shows the descriptive statistics for ground truth of 2nd crop. There was not significant difference at the number of shoots and dry mass between 1st and 2nd crops. However, the nitrogen concentrations differed between 1st and 2nd crops as from 5.16 % to 5.93 % at 1st crop and from 5.01 % to 4.58 % at 2nd crop.

Table 3. descriptive statistics for ground truth of 2nd crop.

2nd Crop	No. of shoots			Dry mass			Nitrogen concentration		
	Mean	SD	CV	Mean	SD	CV	Mean	SD	CV
19 June[*1]	17.33	14.14	81.55	0.61	0.55	89.58	4.82[*2]	0.33[*2]	6.89[*2]
21 June[*1]	43.73	14.75	33.72	1.62	0.65	40.34	5.01	0.19	3.88
24 June[*1]	69.67	29.70	42.63	3.13	1.88	60.15	4.89	0.21	4.31
27 June[*1]	137.33	35.32	25.72	6.63	2.96	44.60	4.69	0.33	7.13
29 June[*3]	172.71	16.32	9.45	9.62	1.00	10.35	4.62	0.17	3.69
3 July[*3]	165.14	40.22	24.35	11.42	3.73	32.63	4.58	0.15	3.36

([*1] : 15 samples, [*2] : 14 samples, [*3] : 7 samples because of shading)

Table 4 shows the PLS regression with full cross validation for 1st and 2nd crops, hereinafter 1st + 2nd crop. It was also possible to estimate the number of

shoots, dry mass and nitrogen concentration. Especially, in respect of nitrogen concentration, the coefficient correlations were increased from 0.632 to 0.848 at calibration and from 0.494 to 0.729 at Validation. It might be affected by the variation of nitrogen concentration, which is increased by including of 2nd crop. In spite of increasing coefficient correlation of nitrogen concentration of 1st + 2nd crops, the numbers of PCs, RMSEC (RMSEP) and SEC (SEP) of the number of shoots and dry mass were increased comparing with 1st crop.

Table 4. PLS regression with full cross validation for 1st + 2nd crops.

1st & 2nd crop (125 samples)	No. of shoots		Dry mass		Nitrogen concentration	
	Calibration	Validation	Calibration	Validation	Calibration	Validation
PCs	7		8		6	
Slope	0.807	0.715	0.882	0.787	0.720	0.604
Offset	19.486	28.964	0.692	1.343	1.425	2.016
Correlation	0.898	0.817	0.939	0.852	0.848	0.729
RMSEC (RMSEP)	24.255	31.968	1.449	2.228	0.219	0.287
SEC (SEP)	24.352	32.096	1.455	2.235	0.220	0.288
Bias	$-1.266e^{-05}$	0.282	-1.090^{-05}	0.092	$2.289e^{-05}$	0.003

Figure 2 shows the regression coefficients of nitrogen concentration between 1st and 1st + 2nd crop. With respect of 1st crop regression coefficients, there are not sensitive region for estimating the nitrogen concentration. As increasing of nitrogen concentration variation, there are several peaks, which are more sensitive regions in order to estimate nitrogen concentration, in all bands. It is possible to improve the accuracy of the nitrogen concentration estimation model. However, there are the fluctuations of regression coefficients from the band number 500. It might be affected from image processing, such as extraction, compensation of reflectance using standard-reflector and there is room for improvement for image processing and analysis.

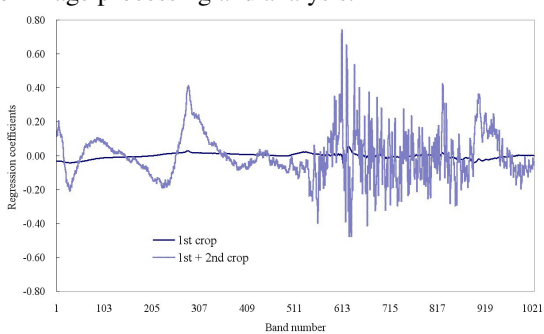

Fig. 2. Regression coefficients difference of nitrogen concentration.

In this study the number of shoot, dry mass and nitrogen concentration were estimated, but the fiber concentration is also important factor for the tea quality, and thus it should also be studied in further works.

4. Conclusion

Hyperspectral remote sensing was applied to estimate the number of shoots, dry mass and nitrogen concentration of tea plants. It is possible to estimate the number of shoots and dry mass of 1st crop using PLS regression. However, the nitrogen concentration estimation model with full cross validation was not seemed to have enough performance, that was less than 0.5 in coefficient correlation. It might be affected by low variation of nitrogen concentration in 1st crop. By including the data of 2nd crop, variation of nitrogen concentration was increased and nitrogen concentration estimation model was improved. In respect of regression coefficients, there were several peaks, which were more sensitive bands to estimate the nitrogen concentration in 1st + 2nd crop than 1st crop.

References

1. G.B. Samarasinghe, Growth and yields of Sri Lanka's major crops interpreted from public domain satellites, Agricultural Water Management 58 (2003) 145-157.
2. Chanseok Ryu, Youhei Makino, Hiroyuki Ishida, Chiyo Terada and Mikio Umeda, Application of remote sensing in tea production, Report of JSAM Kansai branch, 100 (2006) 132-133.
3. Goto, T., J. Uozumi and T. Suzuki. 1986. Near infrared spectoroscopic analysis of total nitrogen content in tea "Sen-cha". Bull. Shizuoka Tea Exp. Stn. 12:61-68. (in Japanese with English summary).
4. M. Smiechowska and P. Dmowski, "Curde fibre as a parameter in the quality evaluation of tea" Food chemistry 94, 2006, pp. 366-368.
5. H. Horie, S.Fukatsu, T. Mukai, T. Goto, M. Kawanaka and T. Shimohara, "Quality evaluation on green tea", Sensors and Actuators B 13-14, 1993, pp. 451-454.
6. K. Ikegaya, H. Takayanagi, T. Anan, M. Iwamoto, J. Unzumi, K. Hishinari and R. Cho, "Determination of the content of total nitrogen, caffeine, total free amino acids, theanine and tannin of Sencha and Maccha by near infrared reflectance spectroscopy", Bull. Vegetable & Tea Exp. B(Kanetani), 1988, pp. 47-90.
7. C.S. Ryu, M. Suguri, T. Kurimoto and M. umeda, "Application of Precision Agriculture to Green Tea Mmanagement" Proceedings of the 2nd Asian Conference on Precision Agriculture (ACPA) 2-4 August 2007, Pyeongtaek, Korea.
8. M. Suguri, C.S. Ryu, A. Asai, T. Kurimoto and M. Umeda, "Estimation of green-tea quality and optimum plucking time using multi and hyperspectral remote sensing", Proceedings of the 3rd International Symposium on Machinery and Mechatronics for Agriculture and Biosystems Engineering (ISMAB) 23-25 November 2006, Seoul, Korea.

DETECTION OF FECAL RESIDUE ON POULTRY CARCASSES BY LASER INDUCED FLUORESCENCE IMAGING*

BYOUNG-KWAN CHO[1], MOON SUNG KIM[2], KUANGLIN CHAO[2], ALAN M. LEFCOURT[2], KURT LAWRENCE[3], BOSOON PARK[3]

[1]*Bioindustrial Machinery Engineering Department, Chungnam National University, 220 Gung-dong, Yusung-gu, Daejeon, 305-764, Republic of Korea*

[2]*Food Safety Laboratory, Animal and Natural Resources Institute, Agricultural Research Service, U.S. Department of Agriculture, Powder Mill Rd. Bldg 303, BARC-East, Beltsville, MD 20705, U.S.A.*

[3]*Quality and Safety Assessment Unit, Richard B. Russell Agricultural Research Center, Agricultural Research Service, U.S. Department of Agriculture, 950 College Station Rd., Athens, GA 30605, U.S.A.*

Feasibility of fluorescence imaging technique for the detection of diluted fecal matters from various parts of the digestive tract, including colon, ceca, small intestine, and duodenum, on chicken carcasses was investigated. One of the challenges for using fluorescence imaging for inspection of agricultural material is the low fluorescence yield in that fluorescence can be masked by ambient light. A laser-induced fluorescence imaging system (LIFIS) developed by our group allowed acquisition of fluorescence from feces-contaminated poultry carcasses in ambient light. Fluorescence emission images at 630 nm were captured with 415 nm laser excitation. Image processing algorithms including threshold and image erosion were used to identify fecal spots diluted up to 1:10 by weight with double distilled water. Feces spots on the carcasses, without dilution and up to 1:5 dilutions, could be detected with 100% accuracy regardless of feces type. Detection accuracy for fecal matters diluted up to 1:10 was 96.6%. Results demonstrated good potential of the LIFIS for detection of diluted poultry fecal matter, which can harbor pathogens, on poultry carcasses.

1. Introduction

Ensuring safety of food commodities is a current issue of major importance in the meat industry. Consumption of poultry contaminated with feces can cause serious human illness.[1, 2] Thus inspection regulations of the Food Safety and Inspection Service (FSIS) of the U.S. Department of Agriculture (USDA)

* This study was carried out with partial support of "Specific Joint Agricultural Research-promoting Projects (Project No. 20070301033004)", RDA, Republic of Korea.

include a zero tolerance policy for visible fecal contaminants on poultry products.[3]

Common routes of poultry skin contamination are ruptures of the digestive tract during evisceration process that can expel internal content. Even though a human expert inspects the wholesomeness of carcasses on the processing line, trace or dilute fecal contaminants may not be easily discernable from water and skin by human eye. Previous researches have shown good potential of multispectral reflectance imaging techniques for detection of fecal matters on poultry carcasses.[4, 5] However, efforts still need to be made to improve the detection sensitivity for the diluted fecal contaminants to comply with zero tolerance standards for contaminant-free production.

Recent researches have exhibited that fluorescence is very sensitive in detecting animal feces on agricultural commodities.[6, 7] In order to accomplish fluorescence imaging under ambient lighting conditions, we developed a gated system capable of ns scale time-resolved fluorescence imaging utilizing a tunable pulsed laser to provide proper excitation.

In this study, the feasibility of a laser-induced fluorescence imaging technique is explored for the detection of diluted poultry feces on poultry carcasses. Optimal discrimination parameters, such as gate-delay time, threshold of fluorescence intensity, and image processing algorithm were suggested.

2. Materials and Methods

2.1. *Sample Materials*

The carcasses and digestive tracts of fifteen chickens, which were grown on soybean protein meal until slaughter at the age of 7 weeks, were obtained from a poultry processing plant. Fecal matters from four different parts of the digestive tracts, colon, ceca, small intestine, and duodenum were extracted and diluted 1:5, 1:10, and 1:50 by weight with double distilled (DD) water. Undiluted and diluted fecal samples were applied in 50μl drops to the surface of the poultry carcasses.

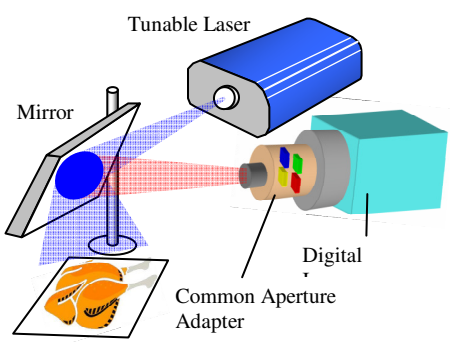

Fig. 1. Schematic of the LIFIS

2.2. *Laser Induced Fluorescence Imaging System (LIFIS)*

A schematic diagram of the LIFIS is shown in figure 1. It consists of a tunable laser, a beam expander, a C-mount zoom lens, a common aperture adapter, and a fast-gated intensified CCD camera. The excitation laser is a frequency tripled, Nd:YAG laser (10 Hz, 6 ns pulse width) with high pulse energy (50 mJ) emitting from 410 to 690 nm (Vibrant VIS, Opotek, CA, USA). The 6 mm diameter laser beam was expanded using a pair of divergent lenses to illuminate whole chicken carcasses under investigation at a distance of c. a. 150 cm from the laser. A fast nanosecond-scale gated-intensified CCD camera (Istar, Andor Technology, MA, USA) coupled to a C-mount 25 mm lens (Rainbow, CA, USA) and a common aperture multispectral adapter (MSAI-04, Optical Insights, AZ, USA) was used to collect fluorescence emission. The adapter uses prisms to convert the incoming image into four equally-sized images in separate quadrants of the focal plane of the camera. Four 25 mm interference filters can be inserted into the aperture for multispectral imaging.

2.3. *Selection of Excitation and Emission Bands*

Three-dimensional fluorescence excitation and emission contour plots for poultry skin and feces were constructed using a spectrofluorometer (Fluorolog III, Horiba Industries, Edison, NJ, USA) as shown in figure 2. The most dominant fluorescence feature of the poultry feces was an emission peak in the red region of the spectrum at about 635 nm with excitation in the blue region (410 to 420 nm) while no apparent emission peak was found in the red region for the poultry skin. Excitation at 415 nm and emission band at 635 nm were considered for this investigation, and narrow interference filter (10 nm FWHM) centered at 630 nm were selected for LIFIS.

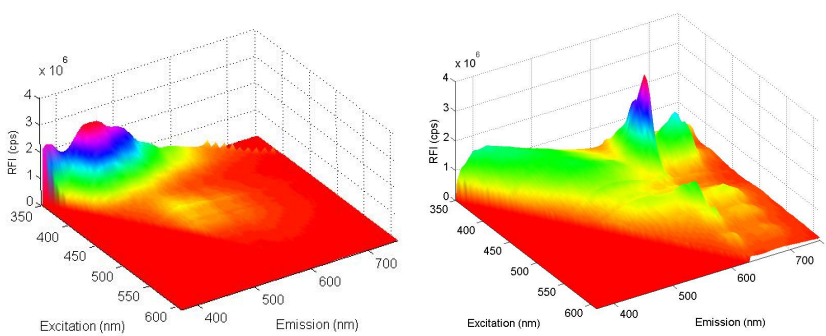

Fig. 2. Representative fluorescence excitation and emission characteristics of poultry skin (a) and fecal matter from the ceca (b).

2.4. *Image Acquisition and Processing*

Visual Basic software (version 6.0, Microsoft, Seattle, WA, USA) operating in a MS Windows environment was used to control the imaging system and to acquire image data (512 × 512 pixel). Fifty time-resolved images spanning 50 ns with approximately 1 ns gate width were acquired for each sample.

Image processing was performed for the acquired image data using Matlab software (version 7.0.4, The Mathworks, Natick, MA, USA). Selection of optimal gate-delay time was based on F values of ANOVA for relative fluorescence intensity (RFI) values of respective gate-delay time between skin and fecal groups. The optimal threshold value of RFI at which the classification accuracy was highest was determined by investigating iterative threshold increments of 0.1% RFI.

3. Results and Discussion

Representative ns-scale time-resolved fluorescence emission spectra of poultry feces and skin are shown in figure 3. In general, fluorescence responses of untreated feces were greater than responses for skin and diluted fecal matters. However, some scattered spots in the areas for skin showed high fluorescence responses which were greater than responses of diluted fecal matters. A possible explanation for the high fluorescence response of the spots may be the presence of feather roots remaining in skin pores.

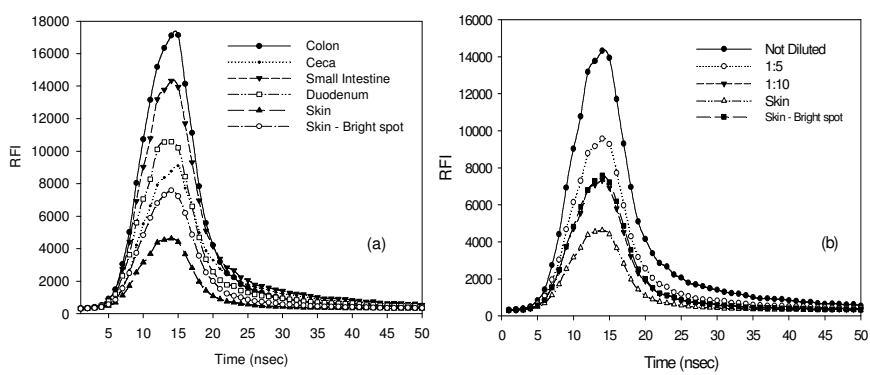

Fig. 3. Representative time-resolved fluorescence emission spectra of poultry skin, and (a) undiluted and (b) diluted fecal matters.

F values of ANOVA for RFI values of feces and skin across the gate-delay time were calculated and shown in figure 4a. The result indicates that the mean

of the two groups were most significantly separated by a delay-gate time at 22 ns. To find an optimal threshold value for separating feces from skin, classification accuracies were calculated for values across the RFI values. Results illustrated that the highest accuracy (96.6%) was obtained by using a threshold of 1120 RFI value (figure 4b). As shown in the frequency histogram, the skin parts, the relatively low intensities, are largely grouped together in contrast to the wide spread of a higher intensities for the fecal matters.

On the basis of the discrimination analysis, undiluted and 1:5 diluted fecal matters could be detected with 100% accuracy regardless of feces types. Classification accuracy for 1:10 diluted feces was 89.9%. Detection accuracies for ceca and colon (100% for both) were higher than those for small intestine and duodenum (90.8% and 95.8%, respectively). The fluorescence response of 1:50 diluted fecal matters could not be discriminated from skin; hence these were excluded from the analysis.

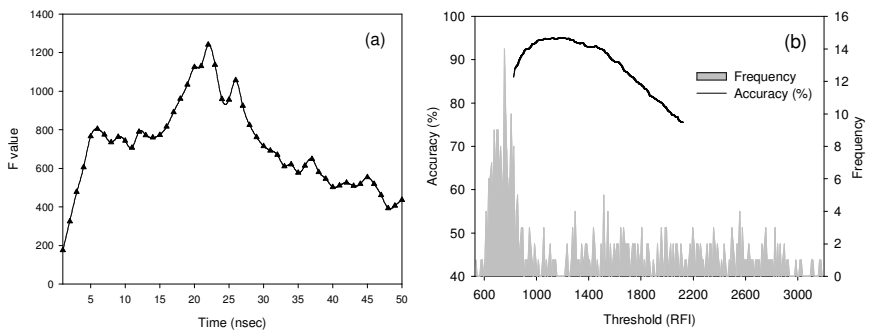

Fig. 4. Gate-delay time and threshold value selection. (a) F values by delay-gate time used for classification, and (b) detection accuracy as a function of RFI threshold with frequency histogram for RFI values of feces and skin.

Figure 5 shows a sequence of processed images beginning with a photo of fecal matters placed on poultry skin. The fecal matters are arranged from top to bottom with no dilution in row 1, and with dilutions of 1:5, 1:10, and 1:50 in rows 2-4. The samples shown in columns 1-4 (from left to right) are fecal matters from the duodenum, small intestine, ceca, and colon, respectively. As shown in the figure 5a, the diluted fecal matters are not easily discernible by naked eye, except for those from ceca. Figure 5b is the image obtained from using a 22 ns gate-delay time after 5×5 binning. Scattered spots which have high fluorescence intensities were observed in the areas for skin. The binary-classification image was obtained by applying the 1120 RFI threshold value to the 22 ns gate-delay time image (figure 5c). Portions of the highly diluted feces

spots are missing, and a few false positives were observed in the sample areas for skin. To eliminate the false positives, a 2×1 erosion algorithm was applied. The resultant binary image showed the successful detection of fecal matters diluted up to 1:5 along with partial detection of 1:10 diluted fecal matters without false positive (figure 5d).

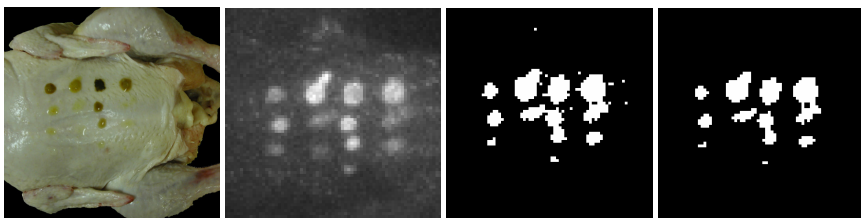

(a) (b) (c) (d)

Fig. 5. (a) Photo of contaminant on a poultry skin; illustration of the image processing sequence: (b) 5×5 binned image at 22 ns gate-delay time, (c) binary image from a threshold of 1120 RFI, and (d) binary image with 2×1 image erosion.

4. Conclusion

In this study the optimization of imaging parameters of a LIFIS was investigated for the detection of diluted fecal matters applied to poultry skin. Fecal matters at dilutions as high as 1:10 could be detected with an accuracy of 96.6% using fluorescence emissions captured with the use of a 415 nm excitation source and a 22 ns gate-delay time with an optimal threshold (e.g., RFI 1120). Results demonstrate that the LIFIS has good potential for the detection of diluted feces on poultry carcasses and could be an alternative to the current human inspection method in automated poultry processing plants.

References

1. S. H. Cody, M. K. Glynn, J. A. Farrar, K. L. Cairns, P. M. Griffin, J. Kobayashi, M. Fyfe, R. Hoffman, A. S. King, J. H. Lewis, B. Swanminathan, R. G. Bryant and D. J. Vugia, *Ann. Intern. Med.* **130,** 202 (1999).
2. P. S. Mead, L. Slutsker, V. Dietz, L. F. McCaig, J. S. Bresee, C. Shapiro, P. M. Griffin, R.V. Tauxe, *Emerging Infectious Diseases.* **5,** 607 (1999).
3. Food Safety and Inspection Service (FSIS), *FSIS Directive* **6420.2,** 1 (2004).
4. B. Park, K. C. Lawrence, W. R. Windham and R. J. Buhr, *Trans. of ASAE.* **45,** 2017 (2002).
5. B. Park, K. C. Lawrence, W. R. Windham and D. P. Smith, *Appl. Engr. Agric.* **21,** 627 (2005)
6. M. S. Kim, A. M. Lefcourt and Y. Chen, *Appl. Optics.* **42**, 3927 (2003).
7. M. S. Kim, Y. Chen, B. Cho, K. Chao, C. Yang, A. M. Lefcourt and D. Chan, *Sens. & Instrumen. Food Qual.* **1**, 151 (2007).

DETECTION OF PATHOGENIC SALMONELLA IN MILK BY USING AN IMPEDANCE BIOSENSOR

GIYOUNG KIM

Safety Evaluation Lab., National Institute of Agricultural Engineering, 249 Seodun-dong, Suwon, 441-100, Republic of Korea

JI HEA MOON

Department of Food and Nutrition, Hanyang University, 17 Haengdang-dong, Seoul, 133-791, Republic of Korea

HAK-JIN KIM

Safety Evaluation Lab., National Institute of Agricultural Engineering, 249 Seodun-dong, Suwon, 441-100, Republic of Korea

AE SON OM

Department of Food and Nutrition, Hanyang University, 17 Haengdang-dong, Seoul, 133-791, Republic of Korea

It is required to develop rapid methods to identify pathogenic *Salmonella* in food products for protecting and maintaining safety of the public health from Salmonellosis. The objective of the present study was to explore feasibility of the interdigitated microelectrode (IME) impedance sensor to detect pathogenic *Salmonella* directly in Milk. Specificity and sensitivity of the IME impedance biosensor to detect *Salmonella* typhimurium in milk were evaluated. For selective detection of *Salmonella*, anti-*Salmonella* polycolonal antibody was immobilized on gold surface of the biosensor. Then sample was introduced onto the sensor surface. Impedance response of the sensor was measured at input frequency of 100 Hz. The impedance signal starts to increase with the samples in which higher concentration of the cells were contained. The sensitivity of the sensor was between 10^3 and 1.5×10^4 CFU/mL *Salmonella* spiked in PBS and in milk.

1. Introduction

Salmonella typhimurium is one of the major foodborne pathogens of concern. The pathogen is usually associated with raw or undercooked eggs and poultry. *S.* typhimurium outbreaks continue to occur, and *S*. typhimurium related outbreaks from various food sources have increased public awareness of this pathogen.

Conventional methods for *Salmonella* detection and identification involve prolonged multiple enrichment steps. Some rapid immunological assays are available with sensitivity comparable to those of the conventional methods. One common rapid detection method is based on impedance characteristics of electrodes in a medium where bacteria reside. Most research conducted with conventional impedimetric methods has focused on the changes in electrical impedance of a medium resulting from the bacterial growth[1,2,3]. Even though the impedimetric method reduces the time for the detection of bacteria in food, it still requires hours of incubation time to detect low number of bacteria.

Recently, biosensors have shown great potential for rapid detection of foodborne pathogens. They are capable of directly monitoring the receptor-analyte reactions in real time. Among the biosensors, impedimetric biosensors have been widely adapted as an analysis tool for the study of various biological binding reactions because of their high sensitivity and reagentless operation. The impedimetric biosensor, which was devised to increase the selectivity and the sensitivity by incorporating a biologically functionalized detection layer on the surface of the electrode, usually measures electrode or interface impedance. The impedimetric biosensor enables qualitative and quantitative monitoring of bacteria by measuring the changes in the electrical impedance due to the presence of bound molecules.

A variety of impedimetric biosensors have been constructed to monitor various biological reactions at the surface of electrodes by immobilizing biomolecules such as enzymes, antibodies, nucleic acids, cells, and microorganisms[4]. In fact, some impedimetric biosensors have been used to detect pathogenic microorganisms including E. coli O157:H7[5]. However, more research is needed to improve the performance of *Salmonella* detection in food.

In this study, an impedimetric biosensor for rapid detection of pathogenic *Salmonella* in food was developed. The impedimetric biosensor was evaluated by performing *S.* typhimurium detection in PBS and milk samples.

2. Materials and Methods

2.1. *Interdigitated Microelectrode (IME) Sensor*

The IME sensor was fabricated from a glass wafer with a 50 nm Cr layer as an adhesive layer. A 100 nm thick interdigitated gold electrode was deposited over the Cr layer using photolithographic processing methods to form an active sensing area. Each sensor had a 3 mm^2 active sensing area and the gap size

between electrode fingers was 5 μm. Each electrode finger had a length of 990 μm and a fixed width of 10 μm. Total number of electrode fingers was 200.

2.2. *Sensor Surface Preparation*

The impedimetric biosensor was fabricated by immobilizing biological binding ligands on the IME sensor. Before the immobilization process, the IME sensor surface was cleaned with acetone, a solution of 0.1 M NaOH and 1% Triton X-100, 100% ethyl alcohol, and deionized water in sequence. The biosensor was prepared to have active binding sites for *S*. typhimurium by using chemical cross-linking method. To attach antibodies onto a gold surface, dithiobis(succinimidyl propionate) was used as a cross-linker. After the linkage was formed between DSP and the gold surface, primary amine groups in the antibodies reacted to the active NHS groups on either end of DSP. Finally, the IME was incubated with 1 mg/ml BSA at room temperature to block non-specific binding sites. Between each step, the IME was rinsed with PBS to remove unbound reagents.

Most reagents including BSA, PBS, Triton-X 100, acetone, NaOH, and ethyl alcohol were purchased from Sigma (St. Louis, MO, USA). DSP was purchased from Pierce (Rockford, IL, USA). Anti-*Salmonella* polyclonal antibody was purchased from KPL (Gaithersburg, MD, USA).

2.3. *Sample Preparation*

Salmonella enterica serotype typhimurium ATCC 14028 was used for the experiments. Fresh cultures of *S*. typhimurium were prepared by incubating stored slant cultures on brain heart infusion (BHI) agar (1.5%) in 5 ml of BHI broth at 37°C. Cell containing buffer was changed to 20 mM phosphate-buffered saline (PBS, pH 7.2) by the following procedure: one ml of the enriched cell suspensions were centrifuged for 10 min at 5000g and the supernatant was discarded. The collected cell pellet was resuspended in 1 ml of PBS and washed two more times with the same procedure. The cells were diluted to appropriate numbers (10^8 – 10^1 CFU/mL) with PBS, and used for the experiment. Enumeration of the enriched *S*. typhimurium was performed using the standard plate count (SPC) method.

Milk samples were prepared by inoculating 100 μl of the cell suspension into the milk. The cells were also diluted to appropriate numbers (1.5×10^9 – 1.5×10^4 CFU/mL) with milk. For negative control, PBS or plain milk, which did not contain *Salmonella* cells, was used. For the sample preparation, packs of milk were purchased from a local grocery store.

2.4. *Impedance Measurements*

Impedance measurements were performed using a Bode 100 impedance analyzer (Omicron electronics, Houston, TX, USA). The impedance magnitude of the biosensor was measured at frequencies ranging between 100 Hz to 1 MHz with a 50 mV (amplitude) excitation voltage. To measure only the impedance of the biosensor, impedance calibration for the wiring and probes was done before the measurements. Measured impedance signal was sent to the data processing computer via a USB connection.

When the impedimetric biosensor and the sample sets were ready, a background signal was measured first using PBS as a sample. With the same biosensor, consecutive measurements were performed using serially diluted bacteria samples in PBS or milk. To allow the antibody-antigen reaction, the biosensor was incubated with the sample for 5 min before the signal measurement. Between measurements, the biosensor was rinsed three times with PBS-Triton (0.02 M phosphate buffered saline (PBS) containing 0.05 % Triton X-100) followed by PBS.

For each sample set, three replicate measurements were performed for statistical analysis. For each experiment, the standard deviation of the mean (SEM) signals from 3 replications with same sample sets was calculated. The error bars on each graph designate ± SEM.

3. Results and Discussion

Sensitivity of the IME impedance biosensor to detect *S.* typhimurium was evaluated with PBS samples. *S.* typhimurium was detected by reading impedance changes caused by the attachment of the cells to the anti-*Salmonella* antibodies immobilized on interdigitated gold electrodes. The background impedance signal was stable at the beginning.

Behavior of real impedance electrodes can be represented by an equivalent circuit model. Equivalent circuit models of electrodes are well documented in the literatures[6,7]. In the low frequency range lower than 100 kHz, double layer capacitance determines the signal. At this region, cell attachment on the biosensor surface greatly influences the signal. To measure the signal that is most sensitive to the attachment of *S*. typhimurium to the antibodies on the biosensor surface, impedance signals at 100 Hz were used for data analysis.

The impedance change of the impedance biosensor to increasing concentrations of *S*. typhimurium spiked into PBS is shown in Figure 1. The impedance change over the background of the biosensor increased with the number of bacteria in the sample. Since, a sample with high cell concentrations

tends to have more cells being attached to antibodies immobilized on the sensor surface, higher concentration of cells in the sample generally increased responses. Because the cells attached onto the surface of the biosensor act as resistors, the attached cells resulted in increased impedance.

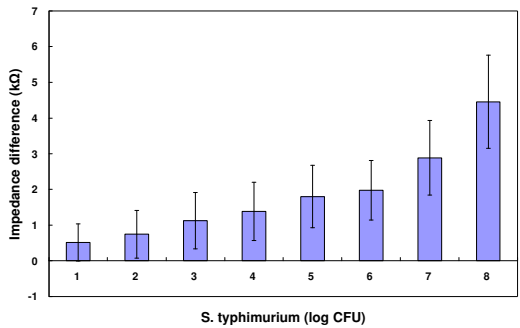

Fig. 1. Impedance change of biosensor for different concentrations of *S*. typhimurium in PBS.

To calculate the detection limit, four background signals were taken before sample readings. The limit of detection was designated as three times the standard deviation of the three background signals minus background signal. A change in signal above the last background signal for all samples tested was considered a positive result if the change was higher than the limit of detection. Detection limit of the impedance biosensor to the PBS sample was 10^3 CFU/mL.

Selectivity of the impedance biosensor to detect *S.* typhimurium was evaluated with milk samples containing 10^8 CFU/mL of *E.coli* cells. Figure 2 shows impedance changes of the biosensor for milk samples.

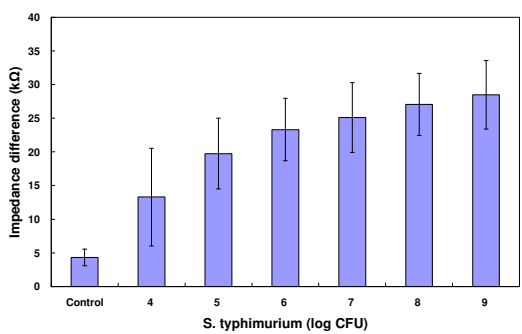

Fig. 2. Impedance change of biosensor for different concentrations of *S*. typhimurium in milk containing 10^8 CFU/mL of *E.coli* cells.

The impedance signal of control sample, which is plain milk with no *Salmonella* cells, was higher than that of PBS due to interference from milk or *E.coli* in the sample. Impedance change of the biosensor for the spiked milk samples also shows increased responses to the increased cell concentration of the sample. The impedance biosensor could detect 1.5×10^4 CFU/mL concentrations of *S.* typhimurium in milk samples.

The impedimetric biosensor developed in this research could detect 1.5×10^4 CFU/mL concentrations of *S.* typhimurium in milk samples in less than 10 min. The majority of the published papers on the detection of bacteria using macro impedance electrode have focused on the electrical characteristic changes of the culture medium. The culture medium method requires relatively long incubation time (5~10 hrs) for detectable medium resistance changes occurres from cell metabolism. However, the impedimetric biosensor developed in this research maximizes the impedance change at the surface of the interdigitized electrodes. Utilizing the impedance signal near the vicinity of the electrode surface may reduces the interference of food particulates in bulk solutions and reduces the detection time.

Acknowledgments

This study was supported by Rural Development Administration of Korea, and by Technology Development Program for Agriculture and Forestry, Ministry of Agriculture and Forestry, Republic of Korea.

References

1. M. C. Easter and D. M. Gilbson, *J. Hygiene* **94**, 245 (1985).
2. D. Gibson, *J. Appl. Bact.* **63**, 299 (1987).
3. L. Yang, C. Ruan and Y. Li, *Biosensors and Bioelectronics* **19**, 495 (2003).
4. J. G. Guan, Y. Q. Miao and Q. J. Zhang, *J. of Biosci. and Bioengr.* **97(4)**, 219 (2004).
5. S. M. Radke and E. C. Alocilja, *Biosensors and Bioelectronics* **20**, 1662 (2005).
6. V. Gerwen, P. Laureyn and W. Layreys, *Sensors and Actuators B* **49**, 73 (1998).
7. R. Gómez, R. Bashir and A. K. Bhunia, *Sensors and Actuators B* **86**, 198 (2002).

SELF-LAYER SUBTRACTIVE DIGITAL TOMOSYNTHESIS*

MIN KOOK CHO, SUNG KYN HEO, HO KYUNG KIM†

School of Mechanical Engineering, Pusan National University, Jangjeon, Geumjeong Busan 609-735, Republic of Korea

We propose a simple method to reduce the blur artifact, frequently claimed in the conventional digital tomosynthesis based on shift-and-add algorithm, and thus restore the image sharpness. The proposed method is basically based on shift-and-add method, but has a correction procedure by finding blur artifacts from the additional forward- and back-projection for the firstly obtained back-projection data. The procedures are: (1) reconstructing volume data with the projection data, (2) replacing the original data at the POI (plane-of-interest) by zeros, (3) performing the additional reconstruction procedure for the manipulated volume data and finding blur artifacts at the POI, and finally (4) subtracting the blur artifacts from the original POI. The proposed method has been compared with the shift-and-add method using the experimental measurements for the PCB phantom. The comparison showed a much enhancement of sharpness in the images obtained from the proposed method.

1. Introduction

Leaner and lighter trends in electric, electronic, and mechanical parts, for example, multi-layer printed circuit boards (PCBs) and ball-grid-array (BGA) packages, highly demand precise defect-detecting techniques [1]. In line with this, x-ray digital tomosynthesis is recently paid attention for the industrial non-destructive testing and evaluation for quality control. Tomosynthesis is traditional geometric tomography to produce an interesting planar cross-section view or laminar image of an object using geometric blurring method. Recent developments both in microfocus x-ray sources and large-area flat-panel detectors have further made tomosynthesis being widely revisited.

Tomosynthesis can allow retrospective reconstruction of an arbitrary number of planes from a single acquisition sequence by moving an x-ray source and a detector in opposite directions across an object [2]. The plane-of-interest (POI) of the object is simply reconstructed by shifting and adding the constituent projection images to bring structures of the POI into registration. POI at an

* This work was supported by the Korea Science and Engineering Foundation (KOSEF) grant funded by the Korea government (MOST) (Grant No. R01-2006-000-10233-0).

† Corresponding Author: E-mail: hokyung@pusan.ac.kr

arbitrary depth can be determined and reconstructed by controlling the amount of shifting. Although this traditional shift-and-add (SAA) tomosynthesis is simple and computationally effective, it, however, suffers from significant blurring artifact due to the superposition of objects from other planes on the POI [2].

We have devised an intuitive simple method to reduce the blur artifact based on an iterative approach, that is a repeated forward and backward projection to determine blurs affecting on the POI and subtract them from the POI [3]. We call it, *self-layer subtractive digital tomosynthesis* (SSDT). In this study, we compare the developed method with the traditional SAA algorithm for the experimental measurements of the designed PCB phantom.

2. Materials and Methods

SSDT basically employs the SAA algorithm. It is noted that the SAA algorithm is equivalent to simple unfiltered backprojection. Main idea of SSDT is as follows. For the given reconstructed volume data, which consist of an arbitrary number of planes, by backprojecting the sequential projection images, a POI is replaced by zeros instead of the original data. Accounting for the acquisition geometry, this manipulated volume data is virtually projected on the detector plane and then backprojected again. The POI in this secondly reconstructed volume data would contain only blurs caused from the out-of-plane objects. Hence, we may obtain a POI with much reduced blurs $\tilde{f}(x, y; z)$ by subtracting the secondly obtained POI from the firstly obtained POI:

$$\tilde{f}(x, y; z) = f_{BP,measured}(x, y; z) - f_{BP,POI=0}(x, y; z), \quad (1)$$

where $f_{BP,measured}(x, y; z)$ describes firstly reconstructed or backprojected POI with the measured data. $f_{BP,POI=0}(x, y; z)$ describes secondly backprojected POI after virtually projecting the firstly reconstructed volume data with $f_{BP,measured}(x, y; z) = \mathbf{Z}$, where $\mathbf{Z}$ is the two-dimensional (2D) image matrix consisting of zero-valued elements.

It should be noted that SSDT is not perfect. After the first backprojection operation, not only the POI but also other planes are contaminated by blurs from planes other than the self-layer, and these blurs contribute to signals in virtual projection images, and which gives rise to additional blurs in the POI through the second backprojection operation. After subtraction, therefore, negative image signals could be produced.

For the feasibility test of the developed method, we carried out a simple experiment. The experimental setup mainly consists of an x-ray source, a jig holding an object to be scanned, and an imaging detector. X-ray tube operated at

variable ranges of 40 – 90 kVp and 2 – 10 mA was used as an x-ray source. As an imaging detector, Gd_2O_2S:Tb phosphor screen coupled to CMOS photodiode array was employed. The field-of-view of the detector is 50 × 100 mm^2 and the pixel pitch is 96 μm. The image readout speed is 17 frames per second. The distance between the source and detector is 583.73 mm. The distance of the source to the jig is 376.6 mm.

As a sample to be scanned, we have manufactured a PCB phantom. The PCB phantom has four layers, and each layer contains various copper line patterns. A sketch describing the cross-sectional view of the phantom is shown in Fig. 1. A photograph of the phantom is also shown in Fig. 1.

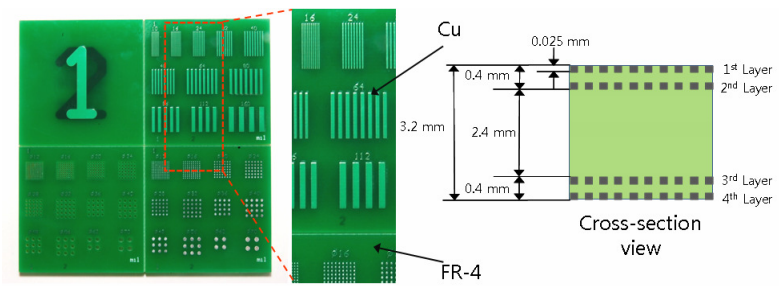

Fig. 1. A photograph depicting a PCB phantom manufactured in this study for the feasibility test of SSDT. The magnified view was covered in the detector. Cross-sectional view and dimensions are also shown.

For the feasibility test of the developed method, projection images of the PCB phantom were obtained with imaging conditions of 85 kVp and 7 mA. Total 11 projection images were acquired for a limited scanning angle of 54°.

The developed method was compared with other conventional methods such as SAA [or unfiltered backprojection (BP)] and the filtered backprojection (FBP) method. For the implementation of filtered backprojection, we simply utilized the Feldkamp's algorithm [4].

3. Results and Discussion

Figure 2 compares the tomograms reconstructed with various methods. The obtained images correspond to the second layer as described in Fig. 1. The arrows shown in Fig. 2 designate makers, intentionally embedded to identify each layer, so that these layers are the second layers. As shown in Fig. 2(a), the tomogram reconstructed from the conventional BP method is very turbid because of the blur artifact coming from other planes. On the contrary, the FBP gives a

tomogram having greater sharpness as shown in Fig. 2(b). However, there exist blurs in scanning direction, which may provide ambiguity in real inspection situation. Moreover, the image is noisy. These phenomena probably due to the filtering process because the FBP method employs high-pass filter and it is very vulnerable to high-frequency noise. Figure 3(c) shows a tomogram obtained with the developed method in this study. Edges of patterns are less sharpened than those obtained with the FBP method, but the overall image sharpness is much enhanced compared with the BP method. Moreover, the blurs in scanning direction due to the filtering process are much suppressed.

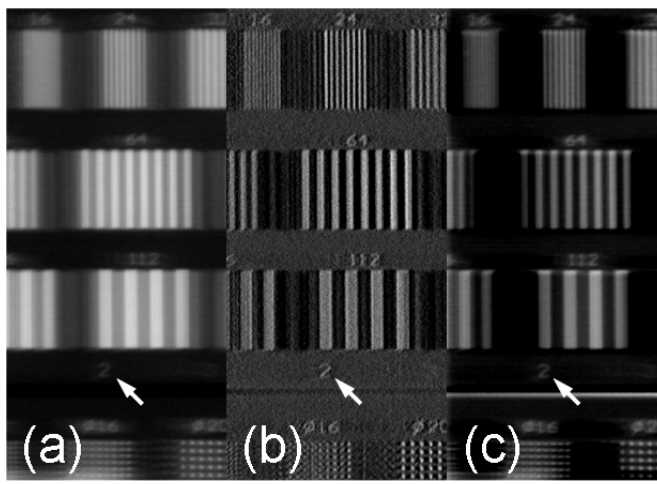

Fig. 2. Tomograms obtained from various digital tomosynthesis methods. (a) Shift-and-add, (b), filtered backprojection, and (c) self-layer subtractive methods.

With regard to computational effort, the developed method is definitely ineffective because it is an iterative approach. Since, however, the tomosynthesis is usually performed with tens of projections and the computation speed with computers is rapidly growing, the computation cost with the developed method is as high as reasonable. Hardware-based computing, for example, utilizing a graphic processing unit (GPU) is another chance of reducing the computation cost.

4. Conclusion

We have developed an iterative digital tomosynthesis technique to restore image sharpness. The image sharpness is much improved compared with the traditional

SAA method. Without any filtering process, the blurs originating from the filtering operation are largely suppressed. The developed method will be useful for industrial x-ray inspection system.

References

1. H. K. Kim, J. K. Ahn and G. Cho, *Nucl. Intr. Meth. A* **545**, 210 (2005).
2. J. T. Dobbins III and D. J. Godfrey, *Phys. Med. Biol.* **48**, R65 (2003).
3. C.–S. Shon, M. K. Cho, C. H. Lim, M. H. Cheong, H. K. Kim, and S. S. Kim, *J. KSNT* **27**, 8 (2007).
4. L. A. Feldkamp, L. C. Davis and J. W. Kress, *J. Opt. Soc. Am. A* **1**, 612 (1984).

STUDY FOR BLADE CERAMIC COATING DELAMINATION DETECTION FOR GAS TURBINE

CHOUL-JUN CHOI[†]

Evaluation & Analysis Team/Researcher, KPS Gas Turbine Technology Service Center, 247 Kyungseo-Dong Seo-Gu, Incheon, 404-718, KOREA

JAE-YEOL KIM*

*Department of Mechatronics Engineering, Chosun University, 375 Seosuk-Dong Dong-Gu, Gwangju, 501-759, KOREA (*Co-Author)*

MOON-YOUNG KIM

GM/Evaluation & Analysis Team, KPS Gas Turbine Technology Service Center, 247 Kyungseo-Dong Seo-Gu, Incheon, 404-718, KOREA

YEON-SHIK AHN

Power Generation Technology, Korea Electric Power Research Institute, 103-169 Moonji-Dong Yuseong-Gu, Daejon, 305-380, KOREA

The component of the hot gas path in gas turbines can survive to very high temperatures because they are protected by ceramic Thermal Barrier Coating (TBC); the failure of such coating can dramatically reduce the component life. A reliable assessment of the Coating integrity and/or an Incipient TBC Damage Detection can help both in optimizing the inspection intervals and in finding the appropriate remedial actions. This study gives the TBC integrity; so other methods are required, like thermography to obtain indications of TBC delamination. Pulsed thermography detects coating detachments and interface defects, with a large area of view but a spatial resolution of few mm. The mentioned techniques as a whole constitute a powerful tool for the life assessment of thermal barrier coating.

1. Instructions

Since such gas turbines for generation are operated under high temperature, high pressure and corrosive environment for a long time, oxidization there of causes serious damages. In particular, since damages to the turbine blade may cause unexpected stop, it is very important to find measures for preventing accidents. Therefore, it is required to regularly diagnose, inspect, maintain or replace hot

[†] This study was supported by research funds from Chosun University, 2005

parts in a gas turbine in order to keep wholesomeness during operation. For this purpose, a life cycle test technique for predicting a maintenance and replacement cycle is needed.

In special, thermal barrier coating is applied to protect the material of blade. However, physical changes in coating and defects on coating layer happen during the cycle of use, causing difficulties in operating a gas turbine. This study is intended to examine the possibility of non destructive testing for delamination and defects on coating layer.

Usually, thermal barrier coating consists of both ceramic top coating of ZrO_2-(6-8wt.%)Y_2O_3 that is excellent for thermal barrier effect and bond coating of MCrAlY (M=Ni and/or Co) that is applied between the material of the blade and top coating, and has reportedly been most excellent in durability.

Ceramic top coating is usually done by porous structure in order to reduce the damages from heat stress. Therefore, oxygen is input through porous ceramic layer at higher temperature and the gas combines with Al on MCrAlY bond coating layer, making up TGO of AL_2O_3. The TGO layer acts as barrier which prevents defective layer from interface oxidization. However, when the layer propagates too rapidly and densely, so reducing cohesion and increasing interface stress between layers, it suffers cracks or delamination. Many studies have been conducted to decrease these defects and to preserve coating layer as longest as possible.

Conventional inspection methods used for such regular maintenance times require much expenses and time and reliable inspection is not applied. To solve such problems, new inspection methods have been presented. One of them is to use an infrared thermography camera. Therefore, in this study, it is described to construct reference data for applying this method to testing wholesomeness of the coating layer of a gas turbine blade.

2. Configuring Test Equipment

2.1. *Infrared Thermography Camera*

An infrared thermography camera is a measuring machine for detecting an infrared wavelength reflected from a measured object from an external light source. With an equation of temperature and a wavelength by the Stefan-Boltzmann Law(1), the infrared wavelength detected from the infrared detector is represented as a function of temperature to show high or low temperatures by graphic images.

As shown in Figure 1, a total standard radiant energy can be represented according to Equation (1). The first term is a radiation emitted by the object. The second term is a radiation emitted by the surroundings and reflected in the object. The third term is a radiation emitted by the atmosphere. The infrared thermography camera used in the test is Thermo-vision 900 SW/TE available from AGEMA. The cooling method of the infrared thermography camera is thermal electric (TE). The detection showed two splits, serial scanning, 2 to 5.4 micron spectrum response. The temperature ranged from -10°C to 500°C (up to 2000°C can be detected when using a high temperature filter is used). Sensitivity was 0.1°C at 30°C, and spatial resolution was 104elements/line (50% modulation). The IR line frequency was 3.5 KHz. Figure 2 shows Research Package 900 that allows the Thermo-vision 900 system operated in X-Windows OS(operation system) to be connected to a Microsoft windows OS based laptop computer.

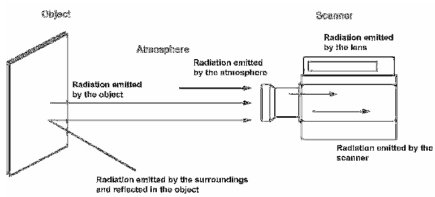

Fig. 1. Measurement situation of IR camera

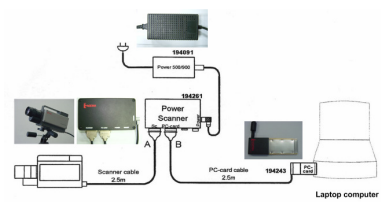

Fig. 2. Infrared thermography camera

$$I_m = I(T_{abj}) \cdot \tau \cdot \varepsilon + \tau(1-\varepsilon) \cdot I(T_{amb}) + (1-\tau) \cdot I(T_{atm}) \quad (1)$$

2.2. *Pulsed Thermography*

Pulsed thermography is one of the most popular thermal stimulation methods in thermography. One reason for this popularity is the quickness of the test relying on a short thermal stimulation pulse, with duration going from about 3 ms for high conductivity material testing(such as metal parts) to about 4s for high conductivity specimens(such as plastics and graphite epoxy laminates). Such quick thermal stimulation allows direct deployment on the plant floor with convenient heating sources, Moreover, the brief heating (generally a few degrees above initial component temperature) prevents damage to the component and pulse duration varies from about 3 ms to 2s.

2.3. *Lockin Thermography*

One approach is lockin thermography where the laser is replaced by a modulated lamp, which generates a low frequency thermal wave simultaneously on the whole surface of the inspected component. Also the infrared detector monitoring just one spot is replaced a continuously recording thermography camera that monitors many spots in the illuminated area. (See Figure 4).

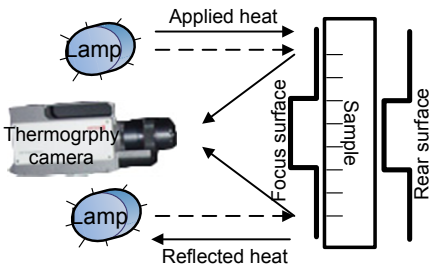

Fig. 3. Principle of Pulse Thermography

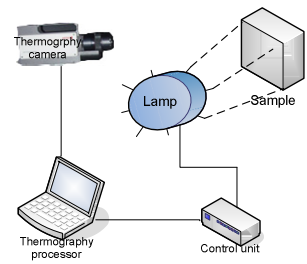

Fig. 4. Principle of lockin thermography

3. Method and Result of the Test

3.1. *Produce Specimens*

For a sample for testing, a one layered used blade of GE's 7FA gas turbine was used. To analyze defects caused by dual coating layers, this was done by making artificial defects between blade and bond coating, between bond coating and top coating. To obtain exact test data, a heat source was applied to cooling holes in the sample, with the testing conducted in a dark room. The test device was configured as shown in figure 6.

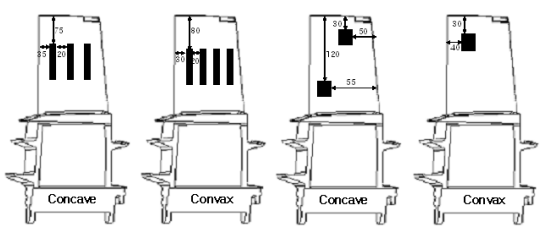

a. material + bond masking b. bond + top masking

Fig. 5. Artificial defect Samples.

Fig. 6. Experiment device.

3.2. *Detection of Aritificial Defect*

Tests were done with a new blade, a used one, and a defected sample under the same conditions and spot temperature data were obtained and analyzed. For a new blade, it had the best coating layer, emitting heat very well and recording the highest temperature. For a defected sample, heat conductivity was not well done in artificial air layer between the blade and coating layer, recording lower temperature. This was found in a testing with other kinds of defected samples.

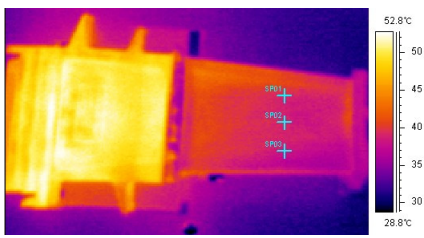

Fig. 7. IR image of Heating system (Convax)

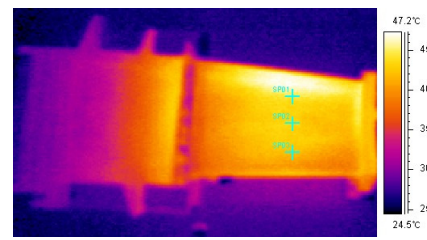

Fig. 8. IR image of Heating system (Concave)

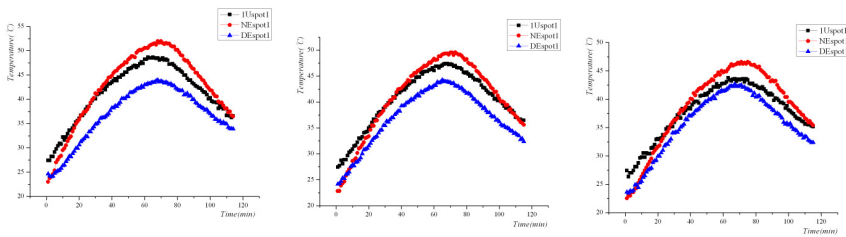

a. Temperature of spot 1 b. Temperature of spot 2 c. Temperature of spot 3

Fig. 9. Temperature of each spot of IR image

3.3. *Detection Delamination on Coating*

While the blade is in operation, delamination often happens on coating layer. The testing methods were done with naked eyes. Tests were conducted to devise how to find defects. Delamination on coating layer could be enough seen with naked eyes. Thermal barrier effect against delamination was also tested through IR device. Defects were found at the ends of the blade as shown in figure 11. The coating layer was delaminated and the exposed blade was found to have higher temperature than those on coating layers as shown in figure 12. For electric appliances parts in relation with IR image, when the difference in temperature shows 4~5°C, they turn out to have defects and are recommended to be repaired or replaced with new ones.

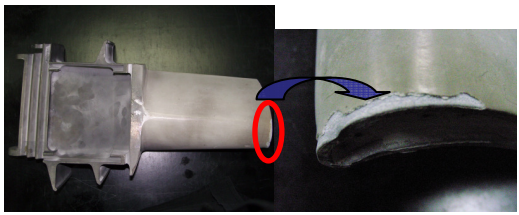

Fig. 10. 7FA(+e)Blade

Fig. 11. Image of defect

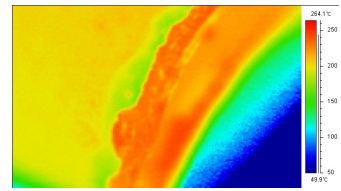

Fig. 12. IR image of defect

4. Conclusion

The test was conducted by examining coating delamination and interface defects on GE 7FA(+e) with IR thermography camera and concluded as follows:

1. An examination was made on whether IR device could be used for non destructive testing of interface defects on coating layer and showed a possibility.
2. Thermal load by coating delamination on the blade could be seen, and objective data was presented to identify whether maintenance should be required or not.
3. Through IR device, any novice could determine whether gas turbine should undergo maintenance test or not.

Acknowledgments

This study was supported by research funds from Chosun University, 2005

References

1. D.J. Yang, C.J. Choi, J.Y. Kim, *Int. J. Modern Physics B*, Vol 20, 4329 (2006).
2. C.J. Choi, J.Y Kim, D.J. Yang, K.S. Song, Y.S Ahn, *Key Engineering Materials*, Vol 340, 483 (2007).
3. Chan K.S, Cheruvu N.S, Leverant G.R, *J. of Engineering for Gas Turbine and Power*, (1998).
4. Antonelli G, Tirone G, *Power Generation Europe*, (2004).
5. Marinetti S, Vavilov V, Bison P.G., Grinzato E., Cernuschi F., *Mater. Eval*, (2003).
6. Gell M, Sridharan S, Wen M, *Int. J. Appl. Ceramic Technology*, (2004).
7. Chen X.,Newaz G., Han X., *Int. Mech. Engineering*, (2001).

TOMOGRAPHY IMAGE NONDESTRUCTIVE MEASUREMENT FOR MELT POLYMER MORPHOLOGY*

LI LIFU

College of Automobile Engineering, South China University of Technology, Guangzhou 510640, China

In this paper, we aim to research an online and nondestructive measurement of melt polymer morphology in the extruder of high pressure and medium temperature by computed tomography image. Firstly, the tomography image of polymer and extruder is obtained by computed tomography measurement system. The size of tomography image is 1024×1024 pixels and its grey level is 256. Then, the object extraction and object image preprocessing are done for melt polymers. The object feature structure extraction is a key technology, which is carried out by the procedure to make the object feature structure have the typical high-order structure of polymer based on maximum a posteriori, such as overlap chain and interpenetration chain. As a result, the tomography chain structure that has submicroscopic geometry is obtained. Finally, experimental result will be reported.

1. Introduction

As the performance of polymer product is determined by its structure formed through polymer processing, it is feasible to improve the quality and performance of polymer product by controlling its structure to meet engineering requirements during polymer processing [1]. However, the polymer processing is in the enclosed space of high pressure and moderate temperature, which has the characteristic of invisible, dynamic and three-dimension, so it is difficult to obtain the polymer configuration with general methods. For this reason, the tomography image measurement has been proposed, by which the tomography image of melt polymer (object) and processing equipments (background) can be gained [2].

Because there is a great contrast between processing equipment and polymer material, it results in the number of object image pixels is few and the dynamic scope of object image grey level is narrow [3]. The object extraction and object image preprocessing are done by image segment, image enhancement and sub-

* This work is supported by grant 29874015 and 50373012 of the Nation Natural Science Foundation of China.

pixel interpolation for the sake of the problem [4], which increases the amount of object information and enlarge its dynamic range.

To extract the object feature structure from the object image, the procedure to make the object feature structure have the typical high-order structure of polymer is put forward based on maximum a posteriori. Then, the feature recognition and measurement of object feature structure are implemented by means of polymer absorption coefficient and its image gray. Therefore, the tomography feature image measurement has offered a novel method to apply computed tomography to engineering measurement for materials science.

2. Feature Image Measurement Principle

The tomography image measurement is consist of image acquisition, object extraction, object image preprocessing, object feature structure extraction, object feature structure recognition and measurement. Fig. 1 is the schematic of tomography image measurement for melt polymer morphology.

When photon stream formed by energy source (gamma rays or X rays) penetrates through enclosed equipment and melt polymer, the effect of photoemission, Compton and electron pair is generated.

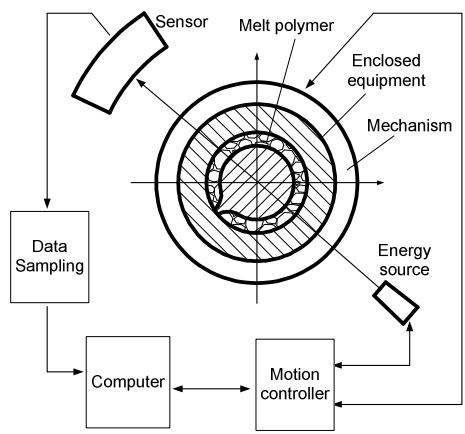

Fig. 1. Schematic of tomography image measurement for melt polymer

Expression (1) indicates the expression of the effect section $\sigma_{\gamma}(x_i, y_i, z_i)$ of random point $i(x_i, y_i, z_i)$,

$$\sigma_{\gamma}(x_i, y_i, z_i) = -\frac{1}{I_i N(x_i, y_i, z_i)} \frac{dI}{dt} \tag{1}$$

where dI is the increment of photon stream intensity I_i when penetrating the polymer with length dt and $N(x_i, y_i, z_i)$ is the atomicity per unit volume for polymer.

The signal of these effects is acquired by photoelectric sensor. And it is transformed into digital signal and inputted to computer. Then, the tomography image Y0 is reconstructed by digital image processing and image reconstruction, which includes the enclosed processing equipment and melt polymer [5]. To increase the amount of object image information, object extraction and object image preprocessing for the tomography image are carried out. As a result, the object feature image X is formed.

According to the image processing theory, the various feature structure S of melt polymer, such as interpenetrate chain, overlap chain, is in the object feature image X. If the number of structure is m, S can be described as expression [6],

$$S = (S_1, S_2, \cdots S_m) \tag{2}$$

To extract the structure S of melt polymer from the object feature image X, the object feature structure extraction based on maximum a posteriori is developed. Firstly, we assume hypotheses $H_j, j = 1 \cdots m$, which is to decide whether the structure S_j is present (hypothesis H_j) or not in the object feature image X. The expression for H_j is

$$H_j : x_k = s_j + n_k \ (k = 1, 2, \cdots, N, \ j = 1, 2, \ldots m) \tag{3}$$

Where S_j is the feature structure image of class j, n_k represents the non-feature structure image of class j; x_k is the object feature image of class k. Then, C_i is defined as a conditional cost, which comes from the decision that hypothesis H_i is chosen as true in the extraction of object feature image X. When the conditional cost C_i in hypothesis H_j takes the minimum, the average risk $C_{i\min}$ of the decision will be minimized according to Bays criterion. It is expressed as:

$$C_{i\min} = \min C_i = \min \sum_{j=1}^{m} C_{ij} P(H_j \mid X) \tag{4}$$

Where C_{ij} is the cost for the decision that H_i is chosen when H_j is true, $P(H_j)$ is a priori probability of H_j. $P(H_j \mid X)$ is the posterior probability of H_j, given the object feature image X. Thus, the $C_{i\min}$ detection will lead to the maximum a posteriori probability test. that is to say, when the polymer

structure S_j of object feature image x_k in hypothesis H_j has the typical high-order structure of polymer, such as overlap chain and interpenetration chain [7], and the amount of S_j information is large, it is taken that H_j is true, the S_j can be confirmed as the object feature structure image of class j. The parameter of hypothesis H_j may be polymer absorption coefficient and its image gray level.

3. Experiment

The experiment target is an extruder and the melt polymer of high pressure and moderate temperature. The extruder is mainly composed of a 20mm diameter single screw and metal barrel. Gamma ray of 1.17 Mev is chosen. The relative resolution of measurement system is 1%, and the spatial resolution can be achieved from 0.02 to 0.08 mm by sub-pixel interpolation. The size of tomography images is 1024 × 1024 pixels and the gray level of image is 256. Polymer chooses low-density polyethylene, and the controlling temperature of solid transportation part, melt part, melt delivery part and die part are set at 150 °C, 160 °C ,180 °C and 210 °C.

Fig. 2 shows the tomography image Y0 of extruder and melt polymer through image acquisition.

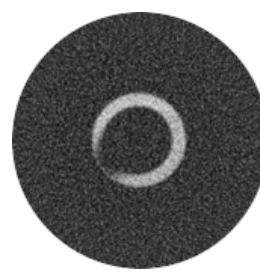

Fig. 2. Tomography image Y0 of extruder and of melt polymer

To improve the object information of image Y0, object extraction is firstly taken by image segment. Then object image preprocessing is done by image enhancement and sub-pixel interpolation. As a result, object feature image X is gotten. Next, the feature structure images S with tomography chain structure are gained by object feature structure extraction based maximum a posteriori from image X. Fig. 3 (a), (b) and (c) are these object feature structure images that the parameter of hypothesis H_j are 110, 140 and 160 in the melt part respectively.

It has been discovered that the feature structure images cannot only exhibit the object feature structure of polymer aggregation, but also indicates its distributions along with time and space. What is more, we can obtain the flow behavior of melt polymer in the affection of external force and heat, the relation between polymer feature structure and its performance during polymer processing by feature structure images recognition and its measurement, which are done by size measurement, shape analysis and texture analysis according to the rule of polymer absorption coefficient and object feature image gray.

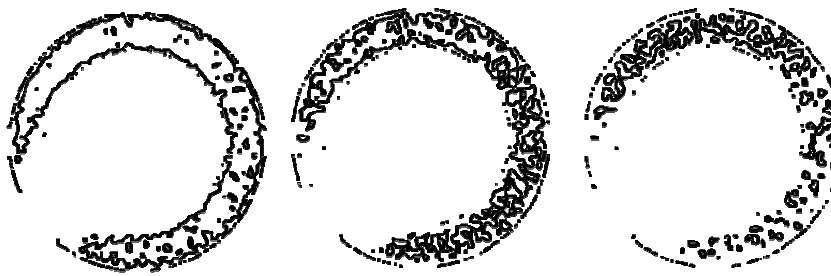

(a) (b) (c)

Fig. 3. Object feature structure images of melt polymer

4. Conclusion

Compared with the general morphological structure measurement of melt polymer, such as visual study, streaming birefringence, laser Doppler anemometry and visualization, tomography feature image extraction and measurement based on maximum a posteriori can not only solve the problem how to obtain melt polymer configuration nondestructively in the enclosed space of high pressure and moderate temperature, but also measure the tomography morphological structure of melt polymer. Therefore, it is useful method to study the processing mechanism of engineering material, such as polymer, in the online and nondestructive mode.

Acknowledgment

The authors thank the support from Nation Natural Science Foundation of China Grant 29874015 and 50373012.

References

1. Qu Jinping and Hu Hanjie, *Principle and Technology of Polymer Processing* (Chemistry Industry Press, Beijng, 2001).
2. Li Lifu and Zhou Nanqiao, *Journal of South China University of Technology (Natural Science Edition)*. **27**, 1 (1999).
3. R. C. Gonzalez and R. E. Woods, *Digital image processing* (Publishing House of Electronics Industry, Beijing 2004).
4. W. K. Pratt, *Digital image processing* (China Machine Press, Beijing 2005).
5. Wu Shifa, *Modern imaging technique and image processing* (Publishing House of National Defense Industry, Beijing 1997).
6. Zhao Shujie and Zhao Jianxun, *The theory of signal detection and estimation* (Tsinghua University Press, Beijing 2005).
7. Gennes, Pierre G de, *Scaling concepts in polymer physics* (Chemical Industry Press, Beijing 2002).

NONDESTRUCTIVE CHARACTERISTICS OF 1080 AND 5083 ALUMINUM ALLOY BY ECAP

KI WOO NAM

Division of Materials Science and Engineering, Pukyong National University, Busan, 608-739, Korea

SUNG KWANG KIM

Defence Agency for Technology and Quality, Changwon Branch, 641-716, Korea

SO SOON PARK

National Institute for Disaster Prevention, Seoul, 121-719, Korea

SEOK HWAN AHN*

School of MechanicalEngineering, Pukyong National University, Busan, 608-739, Korea

The grain size of aluminum alloy was refined to the submicrometer level by using equal-channel angular pressing (ECAP). The effect of grain size refinement was evaluated by the microstructure observations and ultrasonic test. The ultrasonic velocity was faster after equal-channel angular pressed, and the high frequency range appeared. The results of the ultrasonic velocity and the frequency range were expected to be basic data that can prove the grain size refinement.

1. Introduction

The grain refinement is one of very efficient methods for increasing mechanical properties of metallic materials such as strength, toughness and etc. The equal-channel angular pressing (ECAP) technique was suggested by Segal et al [1]. This method can be achieved the grain refinement due to accumulate of high deformation energy in a material because of not accompany reduction of the cross-section of the bulk sample nevertheless increasing of working quantities by continuously repetitive deformation. Because the grain size obtained by ECAP has as refinement as a submicrometer or nanometer one, ECAP method can be obtained additional properties such as super plasticity and etc. The application of nondestructive evaluation method possesses the advantage of time and economy

* Corresponding author shahn@pknu.ac.kr, +82-51-620-1640

because the special process to the manufacture of specimens can be omitted, as full evaluation of microstructures for the production process or product becomes possible [2].

This study was investigated the nondestructive characteristics of the grain refinement of aluminum alloy by ECAP. The microstructure, ultrasonic velocity and frequency analysis have been studied with 1080 Al alloy and 5083 Al alloy.

2. Experimental materials and procedure

2.1. Materials

The materials were the extruded rod of 1080 Al alloy and 5083 Al alloy with a diameter of 20 mm. The chemical compositions and the mechanical properties of specimens are shown Table 1 and 2, respectively.

Table 1 Chemical compositions of specimens [wt%]

	Si	Fe	Cu	Mn	Mg	Cr	Zn	Ti	Al
1080 Al	.053	.086	–	–	–	–	–	–	bal.
5083 Al	.132	.181	.014	.489	4.13	.104	.016	.019	bal.

Table 2 Mechanical properties of specimens

	$\sigma_{0.2}$ (MPa)	σ_U (MPa)	E (%)	Hv
1080 Al	45	57	46	28
5083 Al	167	337	22	76

2.2. ECA pressing

In order to ECA pressing of Al alloys with the diameter of 20 mm, those were made with the diameter of 12.9 mm after machining by the lathe, and then were cut to the length of 100 mm. During the ECAP, two angles (Φ and Ψ) that determine the strain of material have Φ=90° and Ψ=45°, respectively. In addition to, the conditions of ECAP are shown Table 3 [3, 4].

Table 3 Conditions of equal-channel angular pressing

	Using die	Temperature (K)	Pressing speed (mm/sec)
1080 Al	SKD11	room	1.5
5083 Al	SKD61	473	2.5

2.3. Nondestructive test methods

The ultrasonic test was carried out on Al alloys before ECAP and after four passes of ECAP cutting by the thickness of 10 mm. The schematic illustration of measurement systems of the ultrasonic test is shown Fig. 1. In the ultrasonic test,

we analyzed the ultrasonic velocity and the frequency after attenuation using the ultrasonic tester (USD15), the ultrasonic probe of which the broadband transducer with 5 MHz of the main frequency and the personal computer.

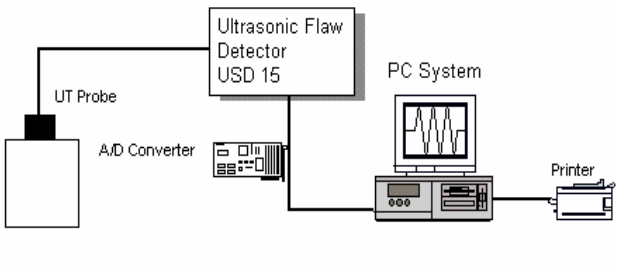

Fig. 1. Measurement system of ultrasonic test

3. Test Results and Discussion

3.1. Microstructures by ECAP

Fig. 2 (a) and (b) are shown optical micrographs of 1080 Al and 5083 Al before ECAP. Fig. 2(c) and (d) are shown TEM micrographs of 1080 Al and 5083 Al after single pass of ECAP. Fig. 2(e) and (f) are shown TEM micrographs of 1080 Al and 5083 Al after four passes of ECAP, respectively.

The average of grain size of 1080 Al before ECAP was about 108 μm, but it reduced quite to about 900 nm after single pass of ECAP. Also, the elongated subgrain band structures with about 2.33 μm of the average length and about 440 nm of the width that not showed before ECAP were observed. These subgrain bends were composed of the low angle boundaries. There is a little difference in these grain structures. But the increase the number of pressing, the grain boundary with the high an azimuthally error was developed. After four passes of ECAP, it was composed of an equal axis grains that have obvious grain boundaries compared with a sample of single pass of ECAP. Also, the elongated subgrain bends that were found from a sample of single pass of ECAP did not almost remained, and the measured grain size was about 360-510 nm. The grain refinement had developed more compared with single pass of ECAP. This does agree about the researched results that applying a worked route rotating in a 90-degree arc to the equal direction the material per pass induces the uniform shear deformation in the material, and then, after single pass of ECAP, the grain size that the material has before ECAP is collapsed to the subgrain bends that have low angle boundaries by shear deformation, and the subgrain that has low angle

boundary causes the grain refinement developing gradually to the equal axis grain that has high angle boundary according to increasing the number of pressing [5, 6].

The average of grain size of 5083 Al before ECAP was about 37 μm, but it reduced to about 156 nm of the average of width and about 523 nm of the average of length after single pass of ECAP. In a sample of four passes of ECAP, the fibrous structures parallel to the extrusion direction were observed. These were similar to the shear bend structures observed in the cold-rolled materials. By four passes of ECAP, the average of grain size was about 233 nm. However, in a sample of four passes of ECAP, the subgrain structure with bend shape did not observed.

Fig. 2(g) and (h) show TEM micrographs annealed for one hour at 573 K after four passes of ECAP of 1080 Al and 5083 Al, respectively.

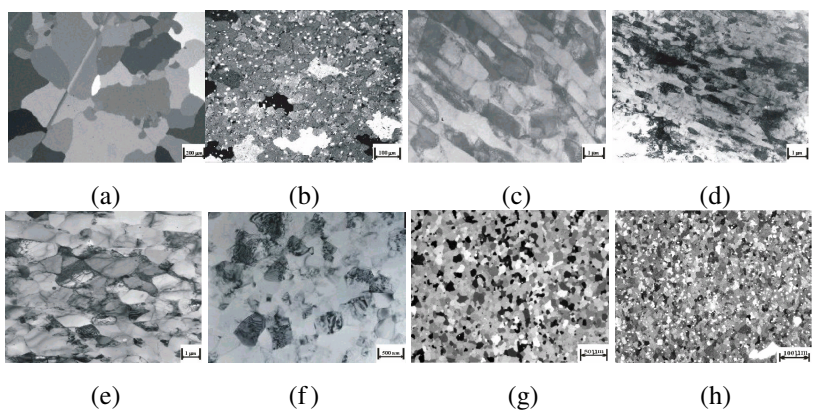

Fig. 2. Optical and TEM photographic of aluminum alloy; (a) 1080 Al before ECAP, (b) 5083 Al before ECAP, (c) 1080 Al after 1 pass, (d) 5083 Al after 1 pass, (e) 1080 Al after 4 passes, (f) 5083 Al after 4 passes, (g) 1080 Al annealed at 573K after 4 passes and (h) 5083 Al annealed at 573K after 4 passes

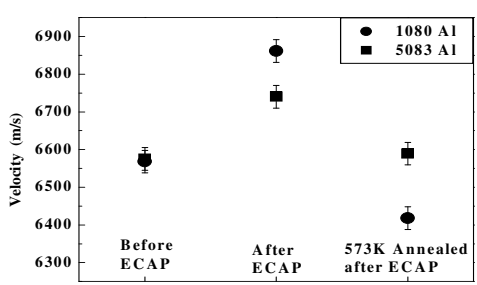

Fig. 3. Ultrasonic velocity of aluminum alloy

3.2. Ultrasonic characteristics

Fig. 3 shows the ultrasonic velocity of aluminum alloys before ECAP, after four passes of ECAP and annealed on 573 K after four passes of ECAP. The ultrasonic velocity of 1080 and 5083 Al after ECAP showed higher than that before ECAP and of the annealed aluminum alloy after ECAP. This ultrasonic

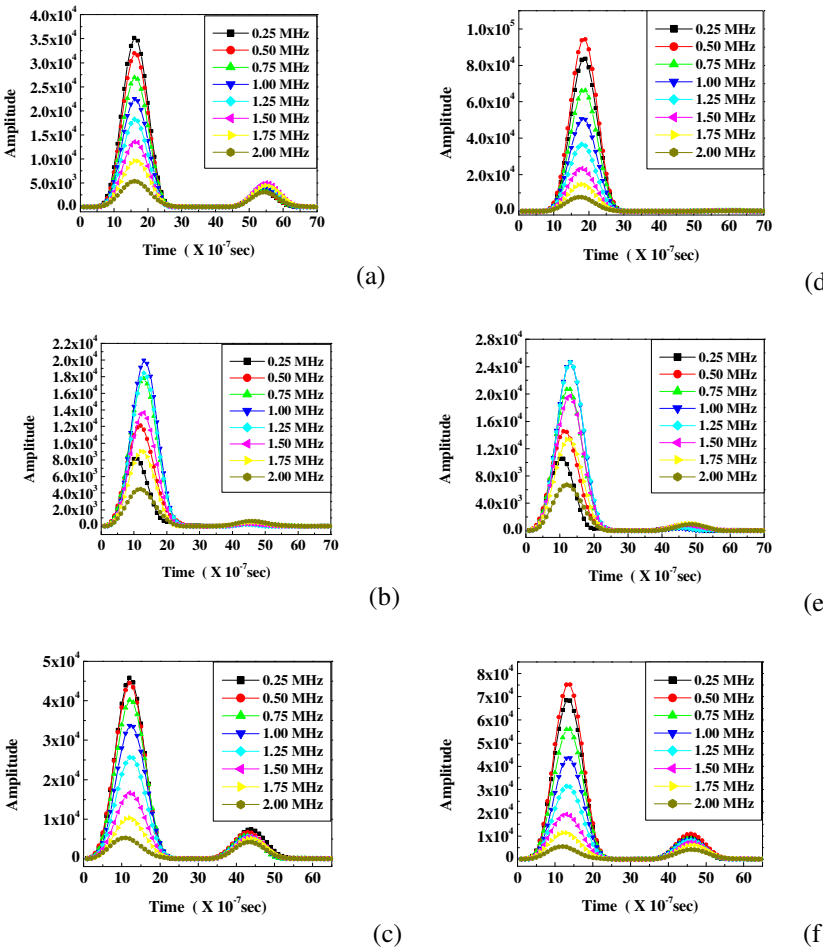

Fig. 4. Time-frequency analysis of aluminum alloy according to ECAP and heat treatment; (a) 1080Al before ECAP, (b) 1080Al after 4 passed, (c) 1080 Al with heat treatment after 4 passed, (d) 5083Al before ECAP, (e) 5083Al after 4 passed and (f) 5083 Al with heat treatment after 4 passed

velocity depends on Young's modulus, density and Poisson's ratio. The reason why the ultrasonic velocity showed highly after ECAP is interpreted that due to increase of Young's modulus by the grain refinement. Also, the decrease in velocity by annealing is interpreted that due to recrystallization and grain growth.

The time-frequency analysis of aluminum alloys before ECAP, after four passes of ECAP and annealed on 573 K after four passes of ECAP is shown in Fig. 4. The main frequency of 1080 Al and 5083 Al indicated 0.25 MHz and 0.5 MHz before ECAP, and indicated 1 MHz and 1.25 MHz after ECAP, respectively. The main frequency after annealing also indicated 0.25 MHz and 0.5 MHz. As mentioned above, the reason why the high frequency range after ECAP shows much than that before ECAP is interpreted that the coarse grain before ECAP attenuated the high frequency range of short wavelength, but the high frequency range is attenuated small by the grain refinement after ECAP, and it shows higher than the low frequency range. Also, the reason why the low frequency of long wavelength not showed to the main frequency is low in the received sensitivity on 0.25-0.5 MHz band width of the broadband transducer with 5 MHz of the main frequency. The main frequency by heat treatment showed the similar main frequency band width as compared with before ECAP due to the recrystallization and the grain growth [2, 7].

4. Conclusion

Ultrasonic velocity after ECAP was higher than that before ECAP. This indicates that the grain refinement pressed by ECAP could be expressed with ultrasonic velocity. From the result of time-frequency analysis for ultrasonic signals, the frequency band width was mainly indicated as 0.25 MHz (1080 Al) and 0.5 MHz (5083 Al) before ECAP, whereas it was obtained as 1 MHz (1080 Al) and 1.25 MHz (5083 Al) by the grain refinement after ECAP. The grain refinement pressed by ECAP could be expressed through the frequency band width of ultrasonic signals.

References

1. V. M. Segal, *Mater. Sci. Eng.(A)*, 197, 157(1995)
2. S. T. Hong et al, *J. Kor. Inst. Met & Mater.*, 37, 754(1999)
3. S. H. Jin et al, *J. Kor. Inst. Met & Mater.*, 38, 1600(2000)
4. H. G. Kang et al, *J. Kor. Inst. Met & Mater.*, 39, 553(2001)
5. K. Nakashima et al, *Acta Metall. et Mater.*, 46, 1598(1998)
6. Y. Iwahashi et al, *Acta metall. et Mater.*, 46, 3317(1998)
7. K. W. Nam et al, *LiMAT-2001*, Ⅱ, 701(2001)

CHARACTERISTICS OF LASER TRANSFORMATION HARDENING FOR ROD-SHAPED MEDIUM CARBON STEEL(SM45C) BY GAUSSIAN BEAM

JONG-DO KIM†

Division of Marine Engineering System, Korea Marine University, Busan, 606-791, Korea

JIN-SEOK OH

Division of Mechatronics Engineering, Korea Marine University, Busan, 606-791, Korea

WOON-JU KANG

Graduated school, Korea Marine University, Busan, 606-791, Korea

LTH(Laser Transformation Hardening) is one area of the laser surface modification techniques. This paper deals with the surface hardening of a rod-shaped carbon steel by a lathe-based laser composite processor with the Gaussian beam optical head and examines LTH characteristics by dominant process parameters, longitudinal and depth-directional hardness distributions and behaviors of the phase transformation in the hardened zone. Especially, in this study, two concepts of the circumferential speed and theoretical overlap rate were applied to experiments as a beam proceeds over a rotating rod. Experimental results such as a hardening depth and width significantly depended on the heat input as the laser power and circumferential speed, and longitudinal hardness distribution was particularly shown to have the periodicity of repetitive increase and decrease, which resulted from tempering effect by an overlap between hardened tracks.

1. Introduction

The results of the LTH(Laser Transformation Hardening) process are affected by thermal conductivity, shape and mass of material as well as power intensity distribution of the laser heat source. Generally, conventional researches on the LTH process have been carried out limitedly on the plain specimen by using the beam with the uniform power distribution and particular shape like a rectangular [1~3]. This study focuses on surface hardening of a rod-shaped SM45C and uses Nd:YAG laser, which has relatively higher metallic absorptivity than CO_2 laser

† Corresponding author : jdkim@hhu.ac.kr

as a heat source. This study's objectives are to examine LTH characteristics by dominant process parameters, longitudinal and depth directional hardness distributions and behaviors of the phase transformation in the hardened zone, and ultimately to investigate the feasibility of LTH process by using the circular Gaussian beam.

2. Experimental method

SM45C, medium carbon steel was used as a workpiece, and its carbon content was 0.45% wt. Experimental setup is composed of a 4kW class CW Nd:YAG laser, 6-axis control robot and small size lathe. A scheme of the experimental setup is illustrated in **Figure 1**. A beam moved on the specimen rotated by a lathe and at the same time the shield gas was sprayed onto the treated surface at a specific angle and distance from a beam-proceeding direction. In this experiment, the optical head with Gaussian circular beam was applied and laser power, beam traveling speed and rotating counts(rpm) were proposed as dominant process parameters. Additionally, as the process used a lathe as a rotating device, the concepts of circumferential speed and theoretical overlap rate were applied to set parameters. Its concepts can be expressed as **Eq. (1)** and **(2)** respectively.

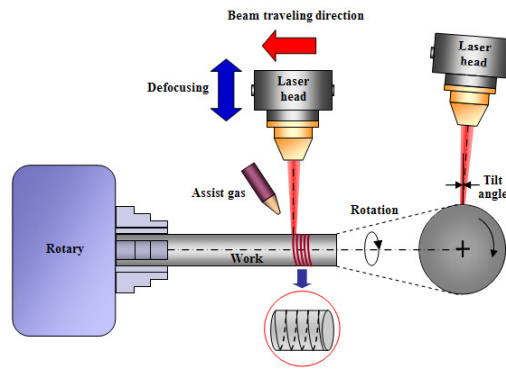

Fig. 1. Schematic illustration of experimental set up

$$v_{circ.}(mm/\min) = N \cdot \sqrt{(3.14 D_r)^2 + (\frac{l_b}{N})^2} \quad \textbf{(1)}$$

$$R_t(\%) = \frac{D_b - \frac{l_b}{N}}{D_b} \times 100 \quad \textbf{(2)}$$

Where, $v_{circ.}$: circumferential speed, R_t : theoretical overlap rate, D_r : rod diameter, D_b : beam diameter, N : rotating counts(rpm), l_b : beam traveling distance per min.

3. Experimental results and discussion

3.1. *Characteristics of the heat treatment as the dominant process meters*

Heat input irradiated on the material is affected by the beam diameter(D_b), laser power(P_L), rpm(N) and beam traveling speed(v_b). **Figures 2, 3** and **4** show the surface and cross sectional pictures of the hardened zone by changes of each parameter. As laser power increases and circumferential speed decreases, heat input increases; thus, the surface hardening depth gradually increases. However, of three parameters, little change in the hardening depth is found especially by change of the beam traveling speed because a processing speed as a variation of beam traveling speed is almost consistent, which also makes heat input almost constant(see **Figure 3**). When the output is 2.0kW or higher(see **Figure 2**) and rotating speed is 10rpm or lower(see **Figure 3**), the surface melting caused by overheating is observed. Especially, the rotating count(rpm) and beam traveling speed have correlation with the overlap rate, which means that as the rotating speed increases and beam traveling speed decreases, the overlap rate increases. Moreover, hardening depth and width in each specimen increase gradually as the number of hardened track increases, because heat is more likely to accumulate inside a steel rod and it is oriented from characteristic of beam proceeding on the rotating workpiece in the air.

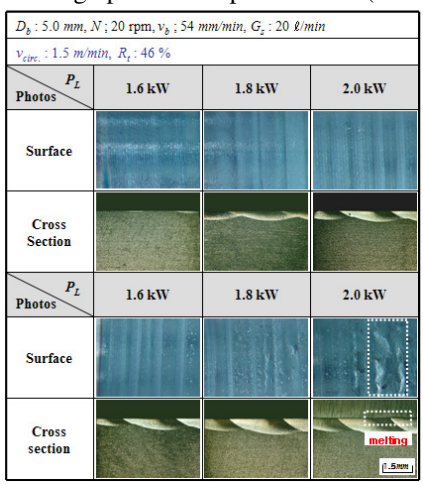

Fig. 2. Characteristics with laser power

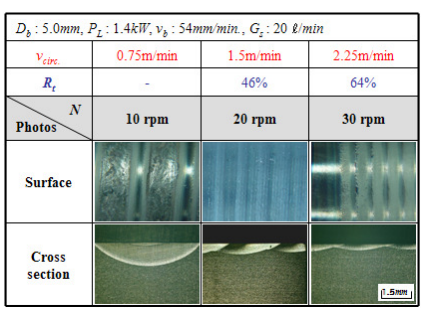

Fig. 3. Characteristics with rpm of specimen

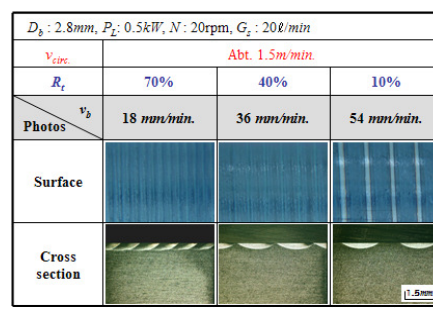

Fig. 4. Characteristics with beam trav. speed

3.2. *Hardness distribution of the hardened zone*

Longitudinal and depth directional hardness distributions in the hardened zone were measured at intervals of 300 and 150 ㎛ respectively by using micro Vickers hardness tester. As shown in **Figure 5(b)**, the longitudinal hardness distribution indicates the periodicity that the hardness repeatedly rise and fall, and this is resulted from tempering by overlap. Especially, the depth-directional hardness was measured at two points(see **Figure 5(a)**), that is, the highest and lowest points of the longitudinal hardness distribution. The depth-directional hardness at the highest point shows a typical tendency that it gradually decreased, as the depth became deeper. On the contrary, the hardness in the lowest point slightly increased and then decreased again(see **Figure 5(c)**). This phenomenon at the lowest point was caused by difference of the tempering effect as a distance from the overlap interface. In other words, it can be explained by the fact that if the distance from the overlap interface is to be far as the depth is deeper, the back tempering effect diminishes and the hardness slightly increase up to the specified point(depth : about 0.6mm in **Figure 5(c)**).

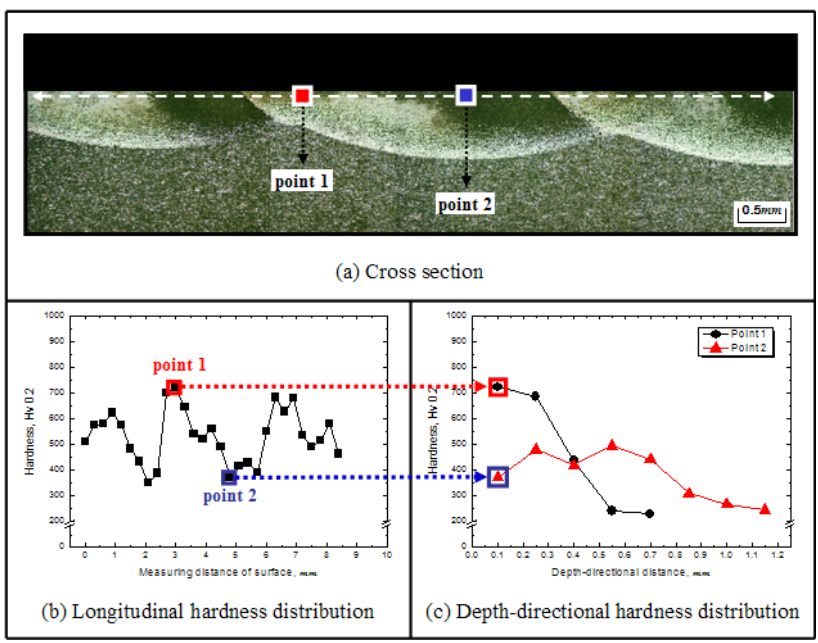

Fig. 5. Hardness distribution in hardened zone

3.3. *Characteristics of the phase transformation*

Phase transformation depended on the temperature gradient and varied by depth and distance from the overlap interface, and this is caused by the difference in thermal cycles. Photos of the regional micro structure in the hardened zone are shown in **Figure 6**. The matrix is SM45C, hypoeutectoid steel with 0.45% wt. of carbon content, and its base structure is composed of pearlite and ferrite in the approximate ratio of 6:4 as shown in **Figure 6(b)**-④. In the vicinity of a surface, most of the matrix is transformed into the martensite phase(①). As a depth is deeper, the rate of the retained austenite in the martensite phase increases(②), and this contributes a gradual degradation of the hardness by a depth. The structure mixed with austenite and ferrite was observed in the interface between the hardened zone and matrix(③) [3,4]. The martensite phase in the region of ⑤ is especially transformed into troostite or sorbite(fine pearlite) phase by the diffusion of supersaturated carbon within the martensite structure, which is resulted from the tempering effect. As shown from Photo ⑥, a tempering zone and an adjacent hardened zone are separated by the overlapped interface. It is expected that the structure of this region would be more complex due to relatively slow thermal cycle.

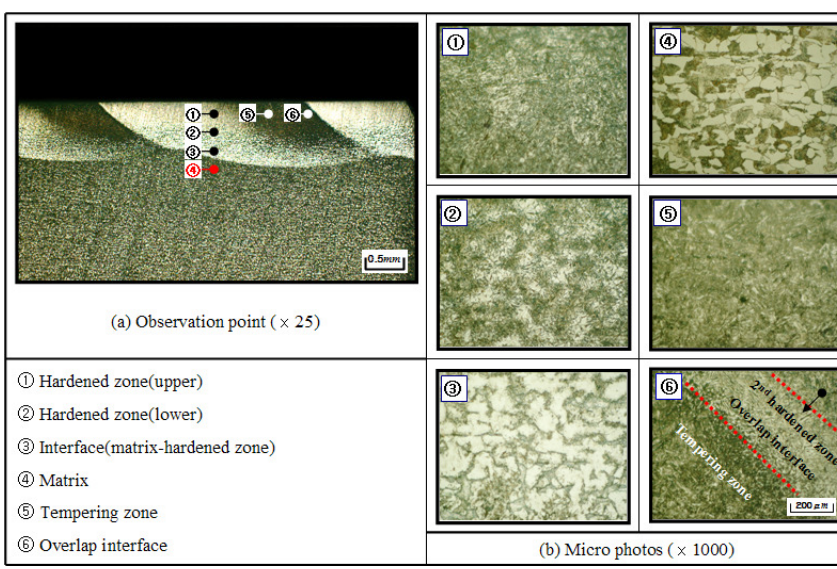

Fig. 6. Regional micro structure in hardened zone

4. Conclusion

This paper discussed several issues including LTH mechanism, hardening characteristics as the dominant process parameters, hardness distribution and phase transformation of the hardened zone. Hardening characteristics such as depth and width was related to heat input that was applied to the workpiece surface, and this depended on the laser power, rotating count of the rod and beam traveling speed. The hardness distribution was measured with longitudinal and depth-directional on cross-section of the hardened zone. The longitudinal distribution indicated a periodicity, which was resulted from the back tempering effect by overlap. The depth-directional distribution expressed different tendencies at the highest and lowest point of the longitudinal hardness distribution. Several phases on the hardened zone were observed through an optical microscope, and these were attributed to the difference in the thermal cycle caused by temperature gradient. Finally, with series of experiments, the feasibility of the surface transformation hardening was verified by using the beam with the Gaussian intensity distribution.

Acknowledgments

This study was supported by the Regional Technology Innovation Program of the MOCIE(Ministry Of Commerce, Industry and Energy, Republic of korea).

References

1. John F. Ready, *Laser Institute of America.* **LIA Handbook of Laser Material Processing**, 223 (2001).
2. Kimihiro Shibata, *Journal of the Japan Welding Society, Vol.64, No.* **Practical Introduction of Laser Transformation Hardening**, 10 (1995).
3. Hiroshi Maruo, Isamu Miyamoto, Takashi Ishide and Yoshiaki Arata, *Journal of the Japan Welding Society, Vol. 50, No.2.* **Investigation of Laser Hardening -Analysis of Hardening Condition in Carbon Steel**, 82 (1981).
4. Zhiyue Xu, Claude B. Reed, Keng H. Leong, Boyd V. Hunter, *ICALEO, section-F.* **Pulsed Laser Surface Hardening of Ferrous Alloys**, 32 (2001).

A STUDY ON THE WELDABILITY OF ALUMINIZED STEEL SHEET BY ND:YAG LASER

JONG-DO KIM†

Division of Marine Engineering System, Korea Marine University, Busan, 606-791, Korea

MYEONG-HOON LEE

Division of Marine Engineering System, Korea Marine University, Busan, 606-791, Korea

JUNG-HAN LEE

Graduated school, Korea Marine University, Busan, 606-791, Korea

Along with the increased interest in environmental problems, aluminized steel sheets have been currently used in a variety of sectors. This study is on the laser weldability of aluminized steel sheets and is to evaluate the effects of aluminum intermixed to the weld on the weld strength. As the result from this study, there is an Al-rich zone in the weld, which has the weld strength decreased due to the structure coarsened by mixing with aluminum and due to the intermetallic compounds in the Al-rich zone.

1. Introduction

What is now used mostly as a surface treated steel sheet is galvanized steel sheet, and aluminized steel sheet is being used for the places requiring high-degree of corrosion resistance. That is to say, the galvanized steel sheet is easier to be manufactured and much lower-priced than the aluminized steel sheet is, and yet the galvanized steel sheet has difficulty in being used under high temperature because of the low melting point of zinc(approximately 419°C) and shows a relatively lower corrosion resistance than the aluminized one does. Aluminized steel sheets, thus, are being used competitively in the sectors requiring heat resistance as well as corrosion resistance[1-3].

There have been problems of the very low weldability of the surface-treated steels, compared to cold rolled steels. Although a lot of studies on the problems

† Corresponding author: jdkim@hhu.ac.kr

have been conducted, they have kept the focus on the galvanized steel sheet and relatively little attention has been paid to the aluminized steel sheet [4-6].

This study, thus, is to examine the weldability of aluminized steel sheets by Nd:YAG laser according to coating conditions of the steel sheets and to understand the phenomena happening while aluminum in the coating layer flows to the weld.

2. Experimental method

The aluminized steel sheets of this study are 0.4mm, 0.6mm, 1.2mm and 1.5mm in thickness(t) and their coating weights(W_c) are 80g/m^2, 120g/m^2 and 160g/m^2 in both sides, and **Table 1** shows the chemical composition of the specimen with the thickness of 0.6mm.

The specimens were welded by 2kW CW Nd:YAG laser at the focal distance, without a gap on the lap joint under the condition of full penetration, and the main parameters of the welding process were restricted to the laser power(1.5 to 2kW) and the welding speed(0.6 to 6m/min). As for the shielding gas, Ar gas(15ℓ /min) was used.

Tensile test was conducted to evaluate the weld strength, and quantitative analyses for the aluminum within the weld were carried out and then, the findings from the analyses were used for the comparative analysis with the weld strength. As a way to understand the weldability according to locations of coating layers, the coating layer was removed per location, and the aluminum intermixed in the weld was observed for its structural examination.

Table 1. Chemical composition of aluminized steel

Thickness (mm)	Al coating Weight (g/m^2)	Chemical composition (wt%)					
		C	Si	Mn	P	S	Fe
0.6	80	0.0024	0.001	0.090	0.120	0.007	bal.
	120	0.002	0.000	0.090	0.015	0.007	bal.
	160	0.0016	0.002	0.080	0.012	0.005	bal.

3. Experimental results and discussion

3.1. *Effects of coating weight on the weld strength*

Figure 1 shows the change of the weld strength according to the thicknesses of the specimens. The weld strength had a tendency of the increase range decreased from the point corresponding to 1.2mm thickness, and it is considered to be related with the fracture position of the tensile specimen. As a result from the tensile test, the specimens with 0.4mm and 0.6mm in thickness had fracture

at the heat affected zone (HAZ) and the ones with 1.2mm and 1.5mm in thickness had fracture at the weld. The weld strength is, thus, thought to be influenced by the width of the weld most greatly as related with fracture and to be influenced additionally by the amount of aluminum intermixed from the coating layer.

The aluminum within the weld was analyzed quantitatively to figure out the effects of the intermixed aluminum on the weld strength. “The area of the aluminum coating layer per unit area of the weld” was theoretically examined on the assumption that the coating layer consists of aluminum only and all the aluminum flows to the weld, and then the ICP(Inductively Coupled Plasma) analysis was carried out for comparing and verifying the results of the examination. As a result, there was no significant difference between 2 values. Figure 2 shows the relation between the quantitative values of aluminum in the weld as calculated by formulas and the weld strength, and, as shown in the figure, the more increases aluminum in the weld, the more decreases the weld strength.

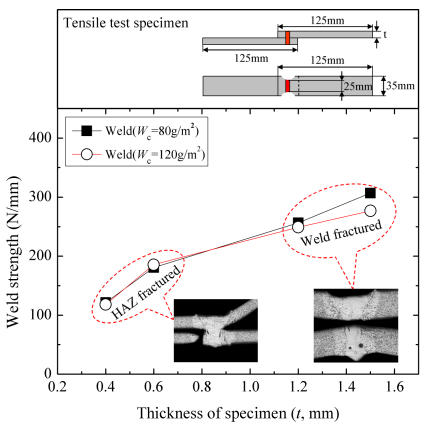

Fig. 1. Variation of weld strength with thickness of specimen

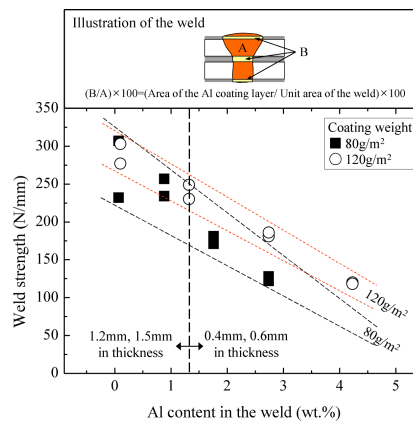

Fig. 2. Variation of weld strength on Al content in the weld

3.2. *Change in the weld according to location of coating layers*

Figure 3 shows the structure of the weld cross-sections according to the locations of the coating layers. As shown in the figure, there was no significant difference of the macro structures between the test specimens having both-layer coating, having the upper layer coating removed and having the lap layer coating removed, but the specimen having both-layer coating removed showed a significant difference. In other words, the steel sheet with aluminum coating had coarse structure and distinct boundary of the heat affected zone (HAZ), whereas

the steel sheet having both-layer coating removed had fine weld structure and showed vague boundary of welding. It is, thus, considered that the aluminum in the coating layer causes coarsening of the weld structure.

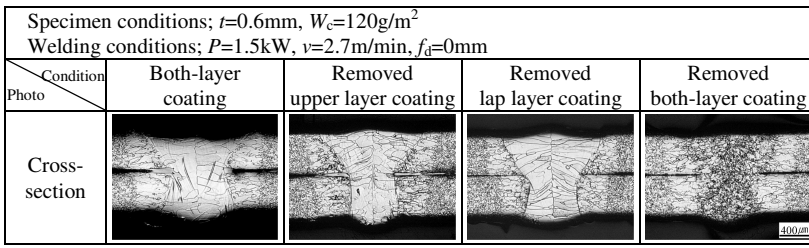

Fig. 3. Weld cross-section of surface pre-treated specimens

3.3. *Behavior of aluminum in the weld*

Figure 4 shows the weld cross-section photographs per coating weight. In the weld, the area having seemed to be an aluminum zone, as insufficiently fused to the base metal, was observed, and the zone was shown particularly near the bonded interface.

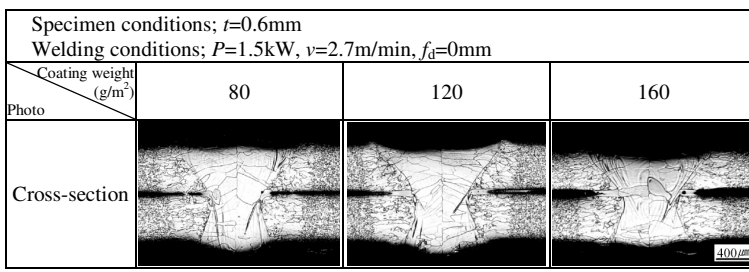

Fig. 4. Weld cross-section of aluminized steel sheet

Figure 5 shows the results of the EPMA analysis for the weld. A small amount of aluminum spread out evenly through the weld, and Al-rich zones were observed partially. It is considered that the aluminum intermixed from the joint part of specimens has difficulty in mixing with the molten metal owing to the

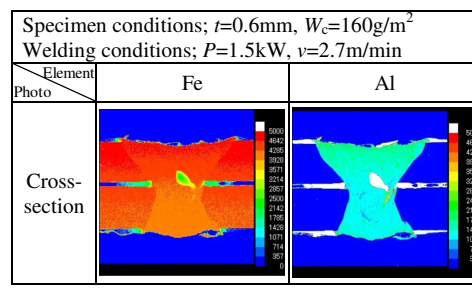

Fig. 5. EPMA analysis results showing Al-rich zone at the weld

characteristics of the laser processes such as rapid heating and cooling, and as the result, Al-rich zones come to be formed partially near the joint part.

Figure 6 shows the result from the micro-hardness test (100gf) to find out the effects of Al-rich zones on the weld strength. The hardness of the Al-rich zones reaches from 318Hv to 1,290Hv, having a tendency of higher values than the average hardness of the weld, approximately 172Hv. The tendency is thought to be caused by the hard compounds made by Fe and Al.

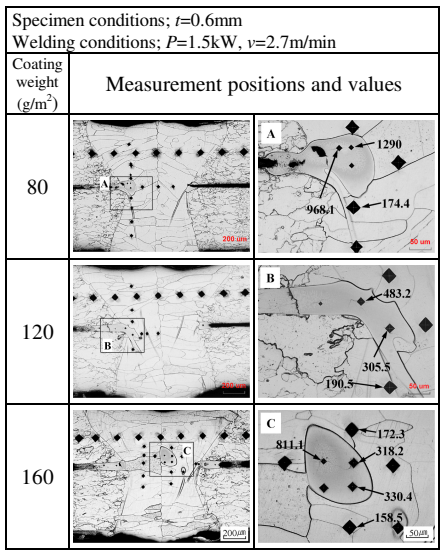

Fig. 6. Micro-hardness results of weld and Al-rich zone

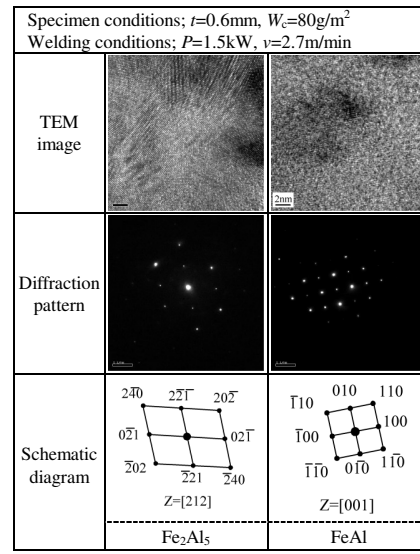

Fig. 7. TEM result of Al-rich zone

Figure 7 shows the result from the TEM analysis for the Al-rich zones. The Al-rich zones were observed to have intermetallic compounds, Fe_2Al_5 and FeAl, as a finding from the analysis on the diffraction pattern. In addition, other intermetallic compounds than the compounds observed in this study are judged to be existent as shown **Table 2** on the micro-hardness values of intermetallic compounds in Fe-Al system. Considering the Al-rich zones spread out near the joint parts, the intermetallic compounds having relatively higher brittleness deteriorate the weld, thereby having adverse impacts on securing the weld strength. Consequently, the reason of the weld strength decreased gradually according to the increased aluminum intermixed to the weld is thought it to be because of the coarsened structure and those intermetallic compounds generated by the aluminum intermixed.

Table 2 Micro-hardness of intermetallic compounds in the Fe-Al system

Phase	Al content		Micro hardness (Hv)
	According to phase diagram	Chemical analysis	
Fe_3Al	13.87	14.04	350
FeAl	32.57	33.64	640
$FeAl_2$	49.13	49.32	1,030
Fe_2Al_5	54,71	54.92	820
$FeAl_3$	59.18	59.40	990
Fe_2Al_7	62.93	63.32	1,080

4. Conclusion

1) As a result of the tensile test, what affects most greatly the weld strength is the width of the weld, and the aluminum intermixed from the coating layer has an additional impact on the strength.
2) From the quantitative analysis on the aluminum within the weld, the more increases the aluminum intermixed, the more decreases the weld strength.
3) When comparing the weld of the specimens having removed coating layers per location with the steel sheet having coating layers in both sides, it is found out that the aluminum in the weld causes the coarsening of the weld structure.
4) The aluminum flowed to the weld during the process of laser welding has difficulty in fusing into the molten metal and forms Al-rich zones, spreading out mostly near the bonded interface.
5) The Al-rich zone has higher values of hardness, compared to those of the neighboring weld.
6) Intermetallic compounds of Fe-Al system are observed in the Al-rich zones, and the reason that weld strength decreases gradually according to the increased aluminum intermixed to the weld is because of the coarsened structure and those intermetallic compounds having strong brittleness, generated due to the aluminum intermixed.

References

1. Susumu Fujiwara and Toshihiro Kondo, Nisshin Steel Technical Report, No.**83**, 13 (2002).
2. Hirofumi Taketsu, Yukihiro Morita, Sigeyasu Morikawa and Shin-ichi Kamoshida, Nisshin Steel Technical Report, No.**83**, 47 (2002).
3. LI YAJIANG, WANG JUAN, ZHANG YONGLAN and X HOLLY, Bull. Mater. Sci., Vol.25, No.7, 635 (2002).
4. MATSUDA Hiroshi and ONO Moriaki, Journal of the Japan Welding Society, 32 (2004).
5. Hongping Gu, Section C-ICALEO, 1 (2000).
6. Claus BAGGER, Isamu MIYAMOTO, Flemming OLSEN and H. MARUO, Proceedings of LAMP, 553 (1992).

MONITORING OF CO_2 HYDRATE FORMATION IN SEDIMENTS USING COMPRESSIONAL WAVE VELOCITY

TAE-HYUK KWON

Department of Civil and Environmental Engineering, KAIST, 373-1 Guseong-dong Yuseong-gu, Daejeon, 305-701, Korea

HAKSUNG KIM

Department of Civil and Environmental Engineering, KAIST, 373-1 Guseong-dong Yuseong-gu, Daejeon, 305-701, Korea

GYE-CHUN CHO

Department of Civil and Environmental Engineering, KAIST, 373-1 Guseong-dong Yuseong-gu, Daejeon, 305-701, Korea

JONG-SUB LEE

Department of Civil and Environmental Engineering, Korea University, 1 5-Ka Anam-dong Sungbuk-gu, Seoul, 136-701, Korea

While CO_2 sequestration is considered a potential methodology for methane recovery and mitigation of global warming, understanding on the CO_2 hydrate and CO_2 hydrate-containing sediments is still limited. In this paper, a laboratory procedure is newly developed to explore hydrate formation in sediments and obtain reliable data on the acoustic wave velocity of hydrate-bearing sediments. The pressure, temperature, and compressional wave velocity are measured during CO_2 hydrate formation from the dissolved gas in sediments. The experimental results show an apparent increase of the compressional wave velocity of sediments after hydrate nucleation. As hydrate crystals grow and fill pore spaces, the acoustic velocity evolves to ~2700 m/s. It is found that higher gas hydrate saturation leads to faster sediment acoustic velocity. The measurements are analyzed by a modified asymptotic Gassmann equation to predict hydrate saturation. The results reveal that the sediments are saturated with almost 91% of the hydrate. Given that in-situ techniques to measure P-waves, such as seismic exploration and well-logging, are well established for the exploration of deep oceans, the measurements presented in this paper are potentially of particular significance for the monitoring of the long-term behavior of CO_2 reservoirs after sequestration in deep oceans.

1. Introduction

Gas hydrates are ice-like crystalline compounds containing gas molecules, and are stable both at low temperature and high pressure. Gas hydrates, including naturally occurring methane hydrate in particular, have driven the rigorous researches in relation to marine science, new energy resources, global climate concerns, and safety issues. Attaining better understanding of CO_2 hydrate and CO_2 hydrate-containing sediments is especially important, as they are expected to form as a by-product of CO_2 sequestration into deep oceanic sediments.

Acoustic wave-based techniques such as seismic surveys are the most promising means of providing valuable information on the long-term behavior of CO_2 sequestrated sediments and can also be employed for the evaluation of methane hydrate quantities in reservoirs. Interpretation of seismic data requires information about material properties and pore-scale processes in sediments. These can be obtained from well-controlled synthetic hydrate-containing sediment samples with known constraints. However, reliable data on the acoustic wave velocity of hydrate-bearing sediments for comparison with previously published models is scarce.

This study focuses on the acoustic measurements of gas hydrate-bearing sediments. Nucleation and accumulation of gas hydrate in sediments are monitored during hydrate formation. Then, by analyzing the wave velocity of hydrate-containing sediments, the saturation of CO_2 hydrate (or hydrate fractional quantity) in pores is estimated and compared to prior published analyses.

2. Experimental Study

2.1. *Experiment Set-up – Specimen Preparation and Measurements*

Experiments were designed to investigate the formation and destabilization of gas hydrate-bearing sediments. All the experiments were conducted in a cylindrical cell (i.e., volume 3.17 cm^3; internal diameter 6.35 mm; height 100 mm), instrumented to measure temperature, pressure, and P-wave velocity (refer to Figure 1). A T-type thermocouple was mounted in the reaction cell to measure the specimen temperature, and the pressure was monitored by a pressure transducer. Pinducers (Valey Fisher, VP1093) were used for P-wave measurements. The frequency content varies from 5 kHz to 1 MHz depending on the sediment stiffness. The cell was submerged in a bath, the temperature of which was controlled between 20 °C and -10 °C by circulating coolant from a cooler.

The fine-grained sands (Ottawa F110 sand; uniform grain size; mean diameter = 120 μm grain size) were compacted in the reaction cell at a porosity $\phi = 0.397$ and no effective stress was applied.

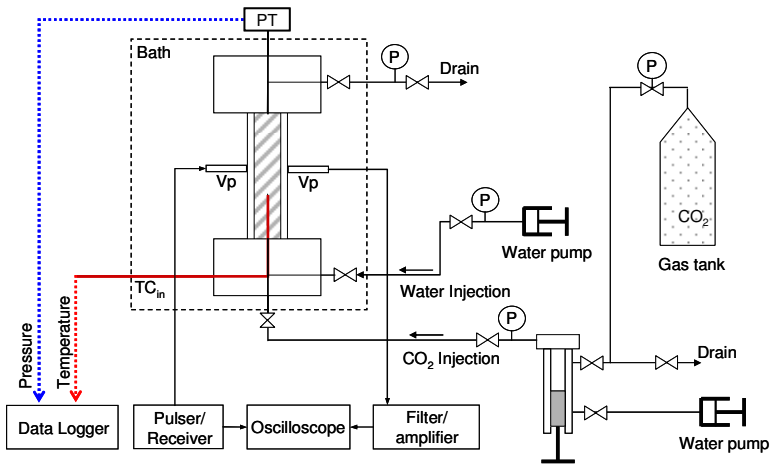

Fig. 1. Experimental setup for the formation and destabilization of CO_2 hydrate-bearing sediments. Vp: p-wave transducers; PT: pressure transducer; P: pressure gauge; TC_{in}: thermocouple inserted in hydrate-bearing sediments.

2.2. *Hydrate Formation and Accumulation in Sediments*

First, the sediment specimen was fully saturated with water and pressurized to 4 MPa. Liquefied CO_2 was injected with approximate 5 MPa of pressure, and pore water in the specimen was saturated with dissolved CO_2 molecules chemically diffused from one end of the specimen. After several days, CO_2 dissolution terminated, as determined by monitoring pressure, and the sediment sample in the reaction cell was thereafter stabilized for 24 hours.

Before commencing the experiments, an isochoric condition was established by closing the valves around the reaction cell. Under an initial pressure of 4.7 MPa, sediments were cooled to 0.5 °C. Temperature and pressure inside the system were monitored during the formation process. P-wave velocity was periodically measured.

3. Results and Discussion

3.1. *Hydrate Nucleation Monitoring with P-wave Velocity*

Figure 2(a) and (b) show the evolution of temperature and pressure inside the sediment specimen during cooling. Phase transformation (hydrate nucleation)

began at approximately 2 °C, showing an temperature jump due to release of heat by exothermic reaction and a sudden drop of pressure at roughly 230 min after the start of cooling. The pore water in the sediments underwent several degrees of supercooling (~ 8 °C) while hydrate is expected to have formed at approximately 10 °C [1].

Figure 2(c) presents the evolution of V_P during cooling. V_P is given by a function of the small-strain bulk modulus K, the shear modulus G, and the density ρ of the medium ($V_P = \sqrt{(K + 4G/3)/\rho}$). V_P of the sediments remains almost constant until solid hydrate crystals nucleate. As soon as the hydrates started to form in pores, an apparent increase of V_P (from ~1650 m/s to ~1740 m/s, as shown in Figure 2c) was noted, as the bulk modulus of the hydrate crystals is higher than that of the pore water. In addition, as the hydrate crystal growth proceeded by diffusion of dissolved CO_2 and pore spaces were filled with solid hydrate (hydrate accumulation), V_P continued increasing up to almost 2700 m/s.

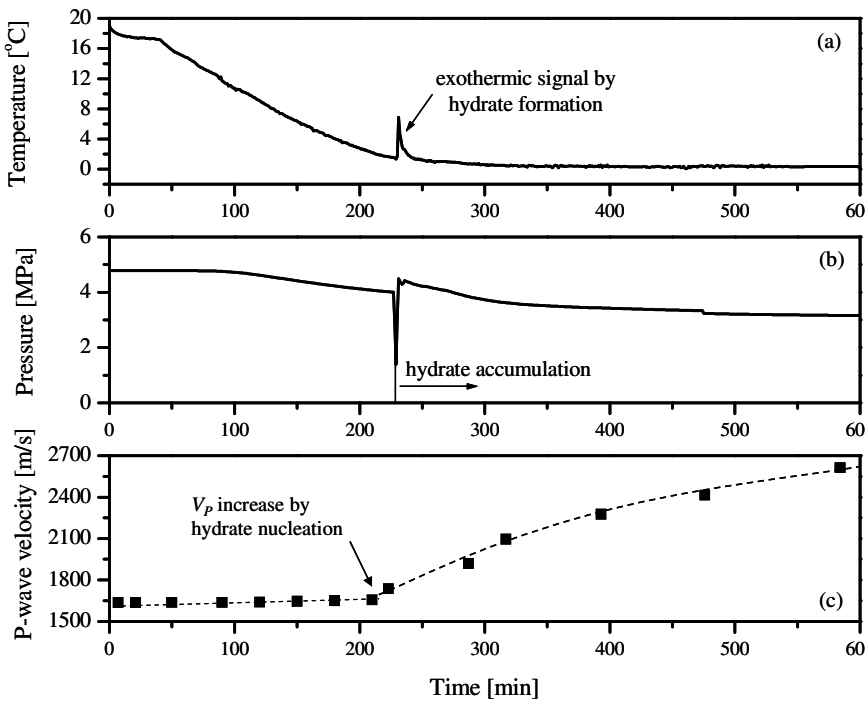

Fig. 2. The evolution of (a) temperature, (b) pressure, and (c) P-wave velocity during hydrate formation in a fine-grained sand specimen.

3.2. *Hydrate saturation estimate with P-wave velocity*

Several field and laboratory test results with synthetic hydrates support the pore filling hypothesis for the hydrate growth habit [2-4]. In turn, compressional wave is more sensitive to capture the hydrate formation rather than shear wave, since an increase in bulk stiffness of pore fluids occurs prior to the shear stiffness of the skeleton during the formation of a small fraction of hydrate in pores [5]. Figure 3 demonstrates the evolution of V_P with hydrate saturation S_h as hydrates fill pores. In this study, S_h is estimated with measured V_P using modified asymptotic Gassmann equation [6,7]:

$$V_P = \sqrt{\frac{M_{sk} + \left[\phi\left(\frac{1-S_h}{K_w} + \frac{S_h}{K_h}\right) + \frac{1-\phi}{K_g}\right]^{-1}}{\phi\left[(1-S_h)\rho_w + S_h\rho_h\right] + (1-\phi)\rho_g}} \tag{1}$$

It is found that the sediment specimen was saturated almost 91% with the hydrate. Lower and upper bounds shown in Figure 3 are calculated using a modified Biot-Gassmann asymptotic solution [7-10]. The lower boundary from the Biot-Gassmann model represents V_P at the low frequency limit and the upper boundary is calculated for the high frequencies with a tortuosity α of 2. The experimental measurements are within the boundaries. This implies that S_h can be estimated with the measured V_P using the asymptotic Gassmann equation (refer to Eq. (1)). Parameters used in this study are listed in Table 1.

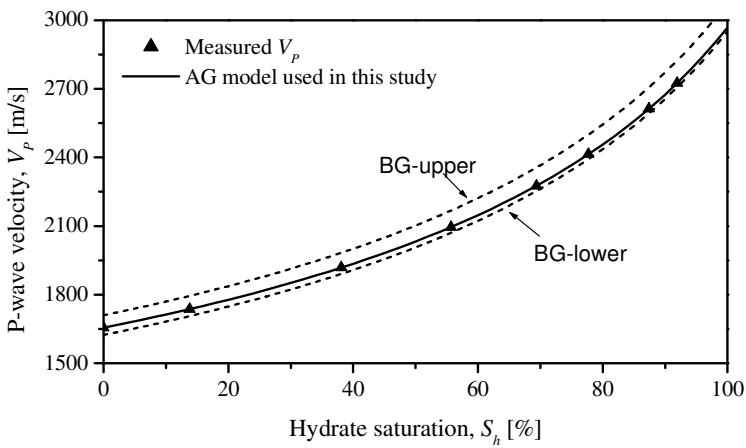

Fig. 3. P-wave velocity with estimated hydrate saturation. (Note: The constraint modulus of the dry skeleton M_{sk} is calculated from V_P of the saturated sediments without hydrates i.e., M_{sk} = 211 MPa. BG-lower and BG-upper: lower and upper bounds of modified Biot-Gassmann model.)

Table 1. Parameters used in calculation of models

Parameters	Mineral grain	CO_2 hydrate	Pore water
Bulk modulus, K [GPa]	36 [a]	10.0*	2.29 [a]
Density, ρ [kg/m^3]	2650	1100 [b]	1000

Data: [a] Lee [11], [b] Aya et al. [12] *The bulk modulus of CO_2 hydrate is computed with V_P = 3780 m/s and V_S = 1962 m/s given in Helgerud et al. [13] for structure I type hydrate.

4. Concluding Remarks

In this study, hydrate formation from dissolved gas in sediments is monitored by evaluation of compressional wave velocity. Measurements of V_P capture the nucleation of gas hydrate in sediment pores and provide a means of monitoring the increase of hydrate saturation. The asymptotic Gassmann equation can be used to predict S_h from measured V_P values. The measurements presented confirm that geophysical exploration using P-wave is promising for the long-term monitoring of CO_2 reservoirs after sequestration in deep oceans.

Acknowledgments

This research was supported by grant No. R01-2006-000-10727-0 from the Basic Research Program of the Korea Science & Engineering Foundation.

References

1. E.D. Sloan, *Clathrate Hydrates of Natural Gases.* (1998).
2. R.L. Kleinberg, C. Flaum, D.D. Griffin, P.G. Brewer, G.E. Malby, E.T. Peltzer, and J.P. Yesinowski, *J. Geophys. Res.*, **108,** B10 (2003).
3. W.F. Waite, W.J. Winters, and D.H. Mason, *Am. Mineral.*, **89,** 1202 (2004).
4. W.J. Winters, I.A. Pecher, W.F. Waite, and D.H. Mason, *Am. Mineral.*, **89,** 1221 (2004).
5. T.S. Yun, F.M. Francisca, J.C. Santamarina, and C. Ruppel, *Geophys. Res. Lett.*, **32,** L10609 (2005).
6. C. Ecker, J. Dvorkin, and A. Nur, *Geophysics*, **63,** 1659-1669 (1998).
7. J.C. Santamarina, K.A. Klein, and M.A. Fam, *Soils and Waves.* (2001).
8. M.A. Biot, *J. Acoust. Soc. Am.,* **28,** 168 (1956).
9. M.A. Biot, *J. Acoust. Soc. Am.,* **28,** 179 (1956).
10. R.D. Stoll, *Geophysics*, **42,** 715 (1977).
11. M.W. Lee, *Geophysics*, **67,** 1711 (2002).
12. I. Aya, K. Yamane, and H. Nariai, *Energy*, **22,** 263 (1997).
13. M.B. Helgerud, W.F. Waite, S.H. Kirby, and A. Nur, *Can. J. Phys.*, **81,** 47 (2003).

FORMATION MECHANISMS OF WELD DEFECTS AND DYNAMIC BEHAVIOR OF KEYHOLE IN GALVANIZED STEEL WELDING BY CO_2 LASER

JONG-DO KIM †

Division of Marine System Engineering, Korea Maritime University, Dongsam-dong 1, Yeongdo-gu, Busan 606-791, Korea

HYUN-JOON PARK

Technical Institute, Sungwoo Hitech, Busan, 940-15, Korea

When the laser welding technology is applied to galvanized steel, good quality weld beads are not easily obtained. Because the galvanized layer caused the spatter, humping bead and porosity which are main part of the welding defect attributed to the powerful vaporizing pressure of zinc. So we performed experiment with objectives of understanding spatter and porosity formation mechanism and producing sound weld beads by giving a reasonable gap clearance in galvanized steels using CO_2 CW laser. And the keyhole behaviors were observed by high speed video camera and X-ray transmission system to investigate the relation with formation of weld defects.

1. Introduction

Laser welding of surface-coating steel could cause a number of weld defects such as spatter and porosity due to a lower boiling point of coating material and there are many difficulties in controlling the weldability because of material and laser welding characteristics.

This study introduces the fundamental alternatives to weld defects by studying the formation mechanism of spatter phenomena with keyhole and porosity from the high speed observation and materialized analyses of laser-induced plasma during the CO_2 laser welding of AH36 galvanized steel. Because the behavior of keyhole and plasma well reflects the behavior of alloying elements vaporizing from the base metal, the results of analysis of laser induced plasma induced plasma can be used to study the behavior of Zn affecting the fusion characteristics of weld metal.

† Corresponding author : jdkim@hhu.ac.kr.

2. Experimental Procedures

2.1. *Material*

In the experiment, 6mm^t galvanized steel for shipbuilding, AH36 is used as a laser welding material and its chemical composition is shown on table 1. Two kinds of galvanizing surfaces are used with the thickness of 15 ㎛ and 30 ㎛. To compare and examine how surface coating condition effects the characteristics of laser welding in lap welding, removal of Zn coated from the surface and variations in Zn coating thickness on the lap position are applied. Table 2 compares the physical constant of Fe and Zn, which are main elements of AH36 and primer coating layer.

Table 1 Chemical compositions of galvanized steels

Element / Material	C	Si	Mn	P	S	Fe
AH36(6mm^t)	0.16	0.40	1.44	0.023	0.005	Bal.

Table 2 Physical properties of Fe and Zn

Physical constant / Element	Density (kg/m^2)	**Melting point (K)**	**Boiling point (K)**	Thermal conductivity J/(m·K)[473K]	Reflectivity (%) R[1.06㎛]
Fe	7,870	**1,808**	**3,027**	61.74	65
Zn	7,130	**692**	**1,176**	105	49

2.2. *CO_2 Laser Welding System and Procedure*

The laser welding energy used in the experiment is a CO_2 laser which has a maximum output of 6kW and RF (exited type) and fast axial flow. The weld zone was shielded by coaxial shield gas nozzle with He of 15ℓ /min.

2.3. *Observation on Behavior of Keyhole and Porosity*

The behavior of keyhole and porosity formed inside of the material was observed through the X-ray transmission imaging system. This system consists of X-ray tube, image intensifier, image processing device, CCD camera, high speed video camera and movable table. The laser welding machine used in this experiment is CO_2 laser of 3-axis transverse flow type with the maximum output of 50kW, the ring mode and the focal point of 381mm.

3. Experimental Results

3.1. *The weldability as function of welding speed and surface coating condition in lap welding*

Figure 1 shows the variation of bead shape such as transverse, longitudinal and bead appearance as function of weld speed and primer coated thickness with no gap clearance (G_c=O) applied to the lap position. The equation on the diagram, t_{pr}(㎛) =S(15)+L(30), means that 15 ㎛ and 30 ㎛ of primer are coated each of the surface and lap position. The right side of figure 1 is the enlarged version of area A and indicates a typical example of porosity created around lap position.

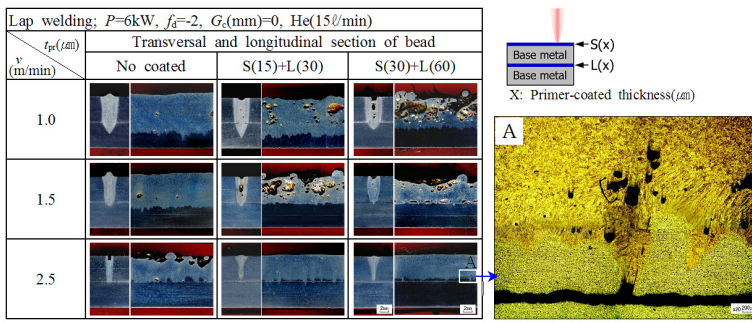

Fig. 1 Variation of bead shape by weld speed and coated thickness.

From the experiment results, it's been learned that the penetration depth gets shallow and bead width gets narrow as welding speed increases. It is important to notice that a large amount of spatter and significant humping bead were created at the limited welding speed of which penetration reaches the lap position. It can be observed that a lot of porosity are formed over the lap position and this phenomena can be frequently occurred on the coated steel because the element of Zn has a low boiling point and can easily be evaporated.

3.2. *Effects of gap clearance and surface coating condition to weldability in lap welding*

This experiment was taken in purpose of minimizing its effect to weld metal by giving a gap clearance so that the vaporizing pressure of the galvanized component can escape.

Figure 2 shows the comparison between sound welding results of lap welding and occurrence of defects within the condition of 15 ㎛ and 30 ㎛ primer coating condition with macro-structure. In the case of a gap clearance is

zero, more significant porosity and spatter are shown on 15 ㎛ and 30 ㎛ primer coated steel compare to those are not coated. But sound welding bead, which has clean bead appearance, no porosity and spatter, is observed if the reasonable gap clearance is applied as function of coated thickness.

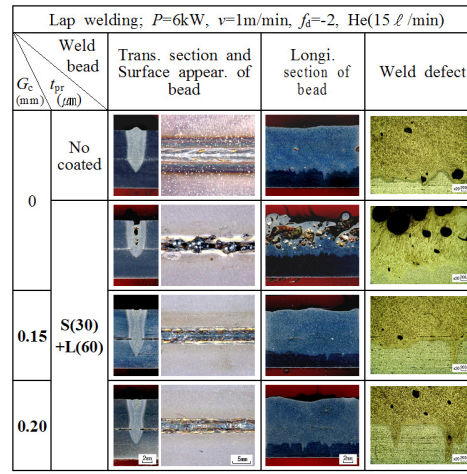

Fig. 2 Effect of gap clearance and t_{pr}(㎛)= S(30)+L(60) coated condition in lap welding.

3.3. *Metallurgical analysis on the vaporizing behavior of the Zn*

Figure 3 shows the SEM photos and EDX analysis for inner surface of fractured porosity from the lap position. From the experiment result, A number of porosity was formed around the lap position and it showed just like inflated-shape from the heat affected zone. Also, from analysis of porosity formation, the major alloyed element of AH36, Fe, was found from the inner surface and the Zn which is the main element of the coating layer was observed. Especially, the inclusion inside of the porosity composes 85%-Zn. but no Zn was found from the dimple structure fractured at the weld metal.

3.4. *Formation mechanism of keyhole and porosity in lap welding*

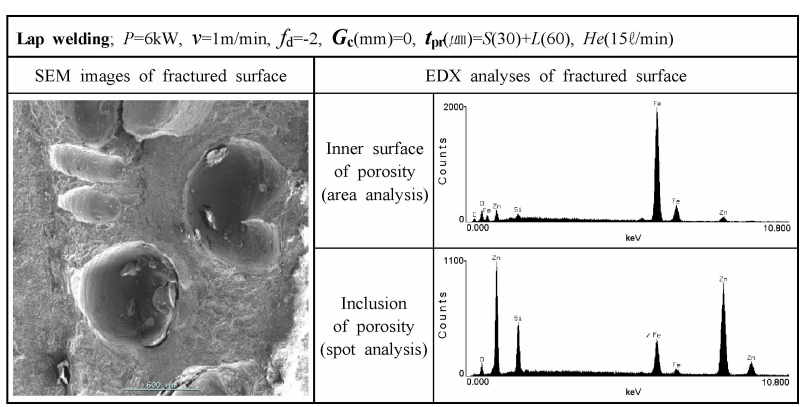

Fig. 3 Photographs of SEM and results EDX analyses in porosity.

This study will directly observe the keyhole behavior by X-ray transmission images and clearly explained about porosity formation mechanism. Figure 4 shows the X-ray transmission images of keyhole and bubbles or porosity during lap welding of galvanized steel and the schematic image was added to help understanding. The keyhole filled out by the vaporized zinc from the lap welding shows very unstable behavior and an abnormal behavior which continuously oversize the porosity by the vaporization from the remaining heat even after the laser beam energy has passed.

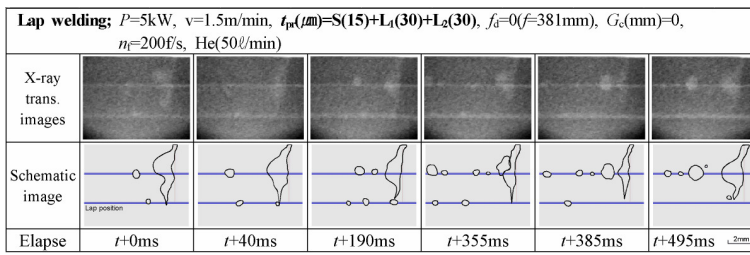

Fig. 4 X-ray transmission images of kyehole and bubbles or porosity during CW CO_2 laser lap welding of galvanized steel.

Figure 5 shows the porosity formation mechanism is lap welding of galvanized steel. The bottom picture is the longitudinal section of the keyhole welding state and the upper one is the surface view of the bottom picture which is intended to help to see porosity formation mechanism from many angles. When the keyhole forms in the material and moves forward, the zinc vaporized from the lap position in front of keyhole is flowed in keyhole. This vaporized zinc is vanished through the keyhole or accelerates unstable behavior by expanding the keyhole. During this process, bubble separated from the keyhole was trapped in the solidification boundary and porosity was formed. Also, even remaining heat after the laser beam energy passes can cause zinc vaporizing which accelerate growth of porosity. The growth direction of porosity is laser beam axis which is the highest temperature and the easiest growth.

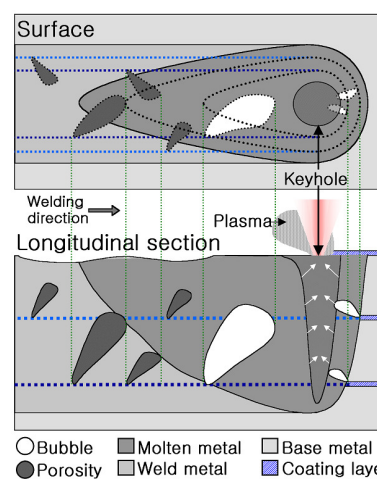

Fig. 6 Porosity formation mechanism in lap welding of galvanized steel

4. Summary

(1) The result of applying lap welding to the steel with uncoated surface and coated surface while giving variation to welding speed shows shallow welding depth and a decrease of bead width when welding velocity increases.
(2) While lap welding with the variation of coated position and coated thickness, more spatter and porosity were created with amount of zinc increases on the lap position than the surface. It got worse with both side coated with zinc.
(3) In lap welding, sound weld bead was obtained by giving the gap clearance of 0.08 to 0.10 ㎜ at the coated thickness S(15)+L(30) and the gap clearance of 0.15 to 0.20 ㎜ at the coated thickness S(30)+L(60). This is the result of applying the reasonable gap clearance as function of coated thickness and the gap clearance helped the pressure of the vaporized zinc to escape instead of inflowing to the weld pool.
(4) By observing the composition of porosity, Zn and Fe, were collected and especially much of Zn element were collected from the inclusion in porosity. Also, because porosity around the heat effected area shapes like a balloon, the major cause of the porosity is the vaporization of the zinc.
(5) The porosity formation mechanism confirmed by X-ray transmission image shows how vaporized zinc from the lap position accelerates the key hole behavior along with the bubble separated from the key hole trapping and remaining as porosity, when key hole is formed and processed inside of the welding material. At the time, even remaining heat after the laser beam energy passes can cause Zn element continues to vapor.

References

1. Hongping Gu: A new method of laser lap welding of zinc-coated steel, ICALEO(2000), p. 1-6.
2. R. Akhter, M.M.Gualini: Mathematical Modeling of the Laser Spot Weling of Zinc Coated Steel in Lap Configuration, ICALEO(1998), p. 207-216.
3. J. Heyden, K. Nilsson and C. Magnusson: Laser welding of zinc coated steel, Proc. 6th Int. Conf. Lasers in Manufacturing(1989), p. 93-104.
4. Y. MASUHIRO, Y. INABA and T. OHJI: Proceedings of LAMP 1992, Nagaoka(1992), p. 381.
5. Takuomi MAIWA. Isamu MIYAMOTO and Kiyokazu MORI: Laser Institute of America (1995), p. 708.
6. D. A. V. Clucas, W. Steen: ICALEO '98 Section F(1998), p. 123.

THE DEVELOPMENT AND APPLICATION OF A NEW ELASTIC-WAVE-BASED SCANNING SYSTEM FOR IMAGING DEFECTS INSIDE CONCRETE STRUCTURES*

JIAN-HUA TONG

Department of Computer Science and Information Engineering, Hungkuang University, No.34, Chung-Chie Rd., Shalu Township, Taichung County, 433, TAIWAN

SHU-TAO LIAO, CHIN-LUNG CHIU, WEN-YEN JUAN

Department of Civil Engineering and Engineering Informatics, Chung Hua University, 707, Sec.2, WuFu Rd., HsinChu, 300, TAIWAN

In this paper, a new elastic-wave-based NDT system was developed and then applied to reveal the defects inside the concrete specimen by imaging method. It integrates the point-source/point-receiver scheme with the SAFT method to achieve the effect like scanning with a phase array system; hence it is equipped with large functioning depth because of the high-energy feature that transient elastic wave method possessed over traditional ultrasonic method. To evaluate the feasibility of this system on NDT of concrete structures, a concrete slab with artificial void inside were built for experiment. 2D plane stress FEM numerical simulations were performed for further comparison. Experimental result shows good agreement with the numerical result not only on the B-scan diagram but also on the processed scanning image. The elastic-wave-based scanning system proposed in this paper exhibits high potential in inspecting the defects of in-situ concrete structures by imaging for civil engineering applications.

1. Introduction

Among the present civil NDT technologies, the elastic-wave-based application always plays a very important role. The point-source/point-receiver scheme is especially suitable for the inspection of on-site civil infrastructures [1-4]. It overcomes the limitation of transmission distance caused by the nature of the traditional ultrasonic probing, which is featured by low output power. However, when it is applied to detect the defects inside the tested concrete structures, especially with complex boundary conditions or multiple inclusions, successful results are usually hard to obtain with analyzing a single batch of response signals. For metallic materials the synthetic aperture focusing technique (SAFT)

* This work was supported by the National Science Council of ROC under Grants NSC 94-2211-E-241-017.

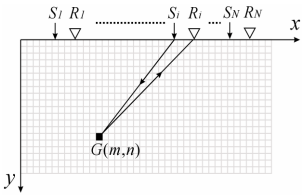

Fig. 1. Schematic of operations and meshing of specimen for image processing.

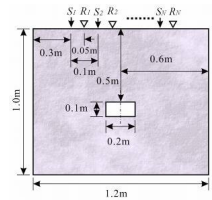

Fig. 2. Dimensions of concrete specimen with rectangular void bar.

is often used as a signal processing strategy in ultrasonic testing as a NDT method, good results of high S/N ratio can be obtained as those obtained with the phase array system [5,6]. In 2007, Tong et al. proposed a new NDT method, which combines the point-source/point-receiver scheme and SAFT method, to image the defects inside the concrete structure [7]. It could be a practical and effective NDT method for defect inspection on civil infrastructures. However, it is indispensable to develop a new NDT system for in-situ applications basing on the new method. In this paper, a new elastic-wave-based scanning system was developed for this imaging method. The experimental result shows that it can expose the defects embedded inside a real concrete structure by imaging method.

2. Principle of Imaging

The measurement of this method is completed with a point-source/point-receiver set with certain space. As shown in Fig. 1, a series of impact-and-receive operations is performed on the free surface of the specimen. Let S_i and R_i represent the locations of a set of the source and receiver for the *i-th* measurement. Furthermore let $T_i(t)$ be the magnitude of the response signal recorded at R_i for this measurement. The domain of the specimen is then divided into mesh grids. An image intensity $I(m,n)$ can be assigned to each grid based on the following calculation:

$$I(m,n) = \frac{1}{N}\sum_{i=1}^{N} T_i(t_i), \qquad t_i = \frac{\left|\overrightarrow{S_iG(m,n)}\right| + \left|\overrightarrow{G(m,n)R_i}\right|}{C_P} \tag{1}$$

Where $G(m, n)$ is the the *m-th* row and *n-th* column grid in the domain, N is the total number of the measurements and C_P is the propagating velocity of the longitudinal wave. In this process, it extracts the information not just from one signal but from all the received signals to form the image. With this process, the intensity will be summed up evidently when an interface exists right at the grid point and it will appear as a bright point. In contrast, it will be canceled out and represented as a dark point in the image.

Consider a concrete slab with a rectangular void inside as shown in Fig. 2. A plan stress FEM program was used for numerical simulation of the inspected signals. Shown in Fig. 3 is the B-scan diagram of the 13 displacement signals in the vertical direction. The fluctuations which are marked with “R”, “B”, “D” and

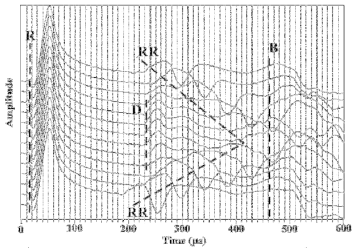

Fig. 3. B-scan diagram of specimen with single rectangular void bar.

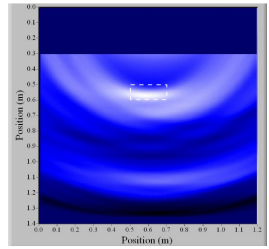

Fig. 4. SAFT image of concrete specimen with single rectangular void bar.

"RR" are associated with the arrival of Rayleigh waves, the reflections from the bottom boundary, the reflections from the defect and the Rayleigh waves reflected from the side boundaries respectively. A scan-like image processed with this method can be obtained as shown in Fig. 4. In this figure, a bright strip in the center indicates that there exists a defect. From the figure, not only the location but also the width of the defect can be observed. To enhance the contrast of the image by reducing the dynamic range which may enlarge by the Rayleigh wave, the image region of a horizontal strip with a certain thickness below the free surface is then erased to a dark area.

3. Composition of System

As shown in Fig. 5, the system is mainly composed of an impact source generator, a vertical displacement transducer, a signal capturing unit and an operation software. The transient elastic wave is first generated by a point impact on the surface of the specimen, and then propagates inside the material. The transducer converts the surface response into an electrical signal. The signal capturing unit amplifies the small signal and converts the analog signal into digital data for further process. The operation software controls all the measurement procedure and finally develops the resultant image.

3.1. *Impact Source Generator*

The source generator is made of a steel bar with a steel ball weld on the end. To generate the elastic wave, the steel bar is bent and then released to hit the surface of the specimen. The force-time function of impact is almost in the form of half cycle $sin^{3/2}t$ function. Derived from Hertz contact theory, the contact time T_C could be expressed as:

$$T_C = 8.034\left[\frac{\rho_1(\delta_1+\delta_2)}{v_0^{1/2}}\right]^{2/5} R \tag{2}$$

While

$$\delta_1 = \frac{1-\nu_1^2}{\pi E_1} \qquad \delta_2 = \frac{1-\nu_2^2}{\pi E_2} \tag{3}$$

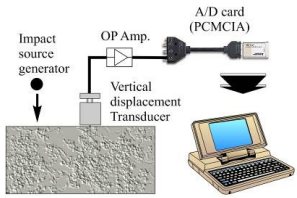

Fig. 5. Composition of the elastic-wave-based scanning system.

Table 1. Wavelength of elastic wave generated by different-sized steel ball impact.

	Experimental result		Hertz theory			
D(mm)	f_c(kHz)	□(mm)	Tc(□s)	f_c(kHz)	□(mm)	□ error
2	44.8	50	9.87	47.5	47	-5.7%
3	34.2	66	14.81	33.1	68	3.3%
4	24.0	94	19.75	26.4	85	-9.1%
5	15.6	144	24.68	19.0	119	-17.9%
6	13.4	168	29.62	15.9	142	-15.7%
7	11.2	201	34.56	13.6	166	-17.6%
8	10.4	217	39.49	11.9	189	-12.6%

Where ν is Poisson's ratio, E is Young's modulus, v_0 is the impact velocity. The subscript 1 and 2 represent the character of the steel ball and that of the half-space respectively. R denotes the radius of the steel ball. Table 1 presents the theoretical value and experimental value of wavelength while elastic wave is generated by specific size steel ball impact. The result shows high capability of Eq. 2 to be the guidance for the selection of steel ball when making the trade-off between resolution and detectable depth.

3.2. *Vertical Displacement Transducer*

The vertical displacement transducer converts the mechanical displacement signal into electrical signal. It is mainly composed of a vertically polarized PZT ceramic cone, backing material and the holding fixture, as shown in Fig. 6. The PZT ceramic cone will produce an electric potential difference between two electrodes when suffered longitudinal deformation. The upper electrode is connected to the backing brass block and then to the BNC connector as the signal source. The lower electrode is connected to the copper film, to the metal holding fixture and finally to the BNC connector as the electrical ground. For perfect contact between the PZT tip and the uneven concrete surface, the lower part of the backing brass is shaped inclined. The backing container holding the backing brass can slide freely along the longitudinal direction of the holding fixture so that PZT tip can reach the measurement position precisely.

3.3. *Signal Capturing Unit*

The signal capturing unit is composed of an amplifying circuit, an A/D converter, and a laptop. The small electric signal proportional to the surface displacement signal is sent to an adjustable amplifying circuit for enhancing the S/N ratio. The output current of the PZT is so small that a voltage follower is adopted as the input buffer of that circuit. In the second stage, a differential voltage amplifier, which has high capability of rejecting environmental random noise, provides a certain voltage gain of the input signal, as shown in Fig. 7. The gain of the amplifier can be adjusted by changing the resistance ratio of R_1 and R_2. The amplified analog signal is digitized by a PCMCIA interfaced A/D converter for further process. The sampling rate of that converter is 20MSPS which is high enough for the elastic wave signal measurement on civil NDT application, whose

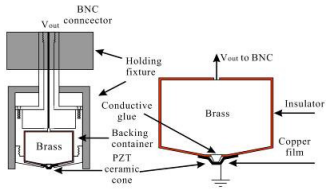

Fig. 6. Scheme of the vertical displacement transducer.

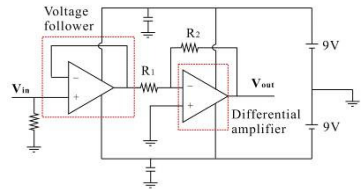

Fig. 7. Scheme of amplifying circuit.

frequency is around 1kHz to 100kHz typically. The laptop can control the signal capturing procedure and process the captured signals further to form the resultant images.

3.4. *Operation Software*

Operation software is essential for coordinating the hardware operation and the data processing when applying the scanning system into the in-situ civil NDT applications. By operating the virtual panel of the software, operator can configure the hardware, input the parameters of measurement and finally get the scanning image. The A/D card should be properly tuned to get higher resolution signal in amplitude axis according to the received signals. Time origin of each received signal is a very important parameter for constructing an image based on the SAFT-imaging method. The software will find the arrival time of Rayleigh wave and then define the time origin of each received signal according to the measurement parameters. To prevent the variant impact force of each measurement on affecting the SAFT process, the received signals will be normalized basing on the amplitude of Rayleigh wave. The normalized B-scan traces will then be processed into a gray-leveled SAFT image.

4. Experimental Results

To evaluate the feasibility of the new system developed in this paper, a defective concrete slab, whose thickness is 3cm, was cased for experiment as shown in Fig. 2. A horizontal void is placed at the center of the block. The experiment was then carried out with a series of impact-and-receive operations on the top surface of the concrete slab. The distance between the impacting source and the receiver is always set to be 5cm and the distance to move from the current impacting point to the next one is 5cm. The first measurement was made at 30cm from the side surface of the block. The B-scan diagram shown in Fig. 8 is the 13 displacement traces recorded when the concrete slab is impacted by a falling steel ball of 8mm in diameter. The reflections from the surface of the void can be found in the B-scan diagram. Using the image processing scheme to process the 13 traces in Fig. 8, a scan-like picture is shown in Fig. 9. It can be seen that a bright zone appears at the place of the void. Another bright strip corresponding to the bottom boundary of the specimen can also be found beneath the defect. As compared to the traditional B-scan diagram, this method can provide better results to identify the number of the defects and their locations, sizes, and front-

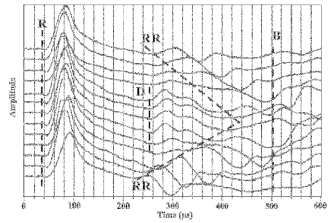

Fig. 8. B-scan displacement diagram of specimen with single rectangular

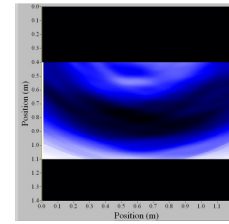

Fig. 9. SAFT image of concrete specimen with single rectangular void bar.

end shapes. The experimental result shows good agreement with numerical simulation shown before.

5. Conclusion

A well developed instrument is indispensible for a new NDT method when it is applied to in-situ concrete structures inspection. The state-of-the-art technologies could provide enough assistance to the development of the instrument on reducing the size and simplifying the operation procedure. In this paper, integrating the point-source/point-receiver scheme with SAFT process, a brand new NDT system for defects imaging was developed. It combines the interdisciplinary technologies, including mechanics, electronics, computer science and so on, to form a portable instrument. This system can expose the defect embedded inside the concrete structures immediately after a series of impact-and-receive operations. The experimental result inspected by this system shows very good agreement with the result simulated by FEM method not only on the B-scan diagram but also on the SAFT image. The location, size, and front-end shape of the defect can be clearly identified from the image. It shows great potential of this new NDT system on detecting the defects of the in-situ concrete infrastructures.

References

1. Wu, T. T., Fang, J. S., and Liu, P. L., *J. Acoust. Soc. Am.*, **97**, 1678-1686 (1995).
2. Wu, T. T., Fang, J. S., Liu, G. Y. and Kuo, M. K., *J. Acoust. Soc. Am.*, **98**, n4, 2142-2148 (1995).
3. J.-H. Tong, T.-T. Wu and C.-K. Lee, *Jpn. J. Appl. Phys.*, **41**, p1, n11A, 6595-6600(2002).
4. Shu-Tao Liao , Jian-Hua Tong , Cheng-Hou Chen , and Tsung-Tsong Wu, *Int. J. Solids Struct.*, **43/ 7-8**, 2279-2298 (2006).
5. Doctor, S. R., Hall, T. E. and Ried, L. D., *NDT E Int.*, **19**, 163-167 (1986).
6. Waszak, J. and Ludwig, R., *IEEE Trans. Instrum. Meas.*, **39**, n2, 441-444 (1990).
7. Jian-Hua Tong, Shu-Tao Liao, Chao-Ching Lin, *IEEE Trans. Ultrason. Ferroelectr. Freq. Control* , **54**, n1, 128-137 (2007).

SPECTRAL ENERGY TRANSMISSION METHOD FOR CARCK DEPTH ESTIMATION IN CONCRETE*

JIYOUNG MIN, CHUNG-BANG YUN

Dept. of Civil & Environmental Engineering, Korea Advanced Institute of Science & Technology
373-1 Guseong-dong, Yuseong-gu, Daejeon, 305-701, Korea

SUNG WOO SHIN

Dept. of Civil and Environmental Engineering, The University of Illinois at Urbana-Champaign
205 N. Mathews Ave., Urbana, IL 61801, USA

JINYING ZHU

Dept. of Civil, Architectural and Environmental Engineering, The University of Texas at Austin
1 University Station C1748, Austin, TX 78712, USA

In this study, the surface wave spectral energy transmission method is proposed for the estimation of crack depth in concrete structures. A calibration curve between the crack depth and the spectral energy transmission ratio has been determined using experimental data on a concrete slab with varying crack depths. The effectiveness of the proposed curve is validated using additional experimental data collected on various concrete specimens with different compositions and different crack depths. The results show that the spectral energy transmission method has excellent potential as a practical and reliable in-situ nondestructive method for in-place crack depth estimation in concrete structures.

1. Introduction

A distinct surface-opening crack in concrete is a critical issue because it affects the durability of concrete and may lead to early failure of concrete structures. Therefore, early detection, accurate measurement and repair of cracks in concrete are important for maintaining structural health.

Over the last ten years, several studies on nondestructive techniques to characterize surface opening crack depth in concrete have been reported [1-10]. Among them, self-calibrating surface wave transmission method [4,5] seems to be a promising nondestructive technique for an in-situ assessment of surface breaking crack in concrete structures. Numerical studies and surface wave

* This work is supported by an ERC program of MOST/KOSEF (Grant No. R11-2002-101-03001-0) and a research project of MOCT/KICTTEP (Grant No. 01-2005-0-049-1-000-01).

transmission measurement on concrete structures demonstrate a great sensitivity to the presence of crack rather than time-of-flight based methods [7]. Especially, the cutting-frequency method [8] is commonly accepted. In this method, the crack depth is estimated by determining the cutting frequency in the transmission function (TRF). However, the experimental determination of the cutting frequency for the crack depth assessment may not be straight-forward because of the significant variation of the measured TRF so the depth evaluation may be erroneous [7-8, 10]. Moreover, since the Rayleigh wave velocity of the test structure should be known in the cutting-frequency method to quantify the crack depth, an additional test is needed.

In this study, the spectral energy transmission method is proposed for the crack depth estimation in concrete, which utilizes the spectral energy transmission ratio of the self-calibrated TRF. The calculated ratio is related with the crack depth by regression analysis. Effectiveness of the proposed relationship is validated by experimental data collected on various concrete specimens.

2. Spectral Energy Transmission Method

Consider a case where two wave sensors, separated by a given distance (D_2), are placed on the surface of a concrete structure as shown in Figure 1. The self-calibrated transmission function can be defined as follows [4,5]:

$$\left|T_{BD}(f)\right| = \sqrt{\frac{V_{AD}(f)V_{EB}(f)}{V_{AB}(f)V_{ED}(f)}} \tag{1}$$

where V_{ij} describes the Fourier transform of the signal which is generated at point i and detected at point j, and T_{BD} is a function of frequency and indicates the ratio of the amplitudes of the surface waves at B and C. Thus, T_{BD} of 1 means complete transmission (no attenuation) of stress waves between two locations, while 0 means no transmission (complete attenuation). Therefore, the values shall be theoretically between 0 and 1.

The spectral energy of the measured surface wave TRF at crack depth d_1 is defined as

$$E(d_1) = \int_{f_L}^{f_U} \left|T_{BD}(f;d_1)\right| df \tag{2}$$

where f_U and f_L is the upper/lower frequency limits for integration, which are very important for a reliable and consistent calculation of the spectral energy. They can be selected using the signal consistency index criterion obtained from five-repeatedly measured TRFs in the crack-free (d_0) condition as follows [5,9]:

$$SC(f) = \frac{\sqrt[5]{\prod_{i=1}^{5} \left| T_{BD_i}(f;d_0) \right|}}{\sum_{i=1}^{5} \left| T_{BD_i}(f;d_0) \right| / 5} \geq 0.95 \tag{3}$$

A calculated spectral energy for a specific crack depth cannot be used for crack depth estimation directly. Since there is no rigorous relation between the amplitude of spectral energy and the crack depth, a relative relation between them must be sought. This can be achieved by the normalization process:

$$R(d) = \frac{E(d)}{E(d_o)} = \frac{\int_{f_L}^{f_U} \left| T_{BD}(f;d) \right| df}{\int_{f_L}^{f_U} \left| T_{BD}(f;d_o) \right| df} \tag{4}$$

Theoretically, the range of the spectral energy transmission ratio is 0 (no transmission) to 1 (complete transmission) similar to the TRF. Therefore, $R(d)$ shall, in principle, decrease as the depth of the surface-breaking crack increases. Once the crack-free spectral energy is obtained, the spectral energy transmission ratio for a specific crack depth can be calculated using Equation 4. Then, the crack depth can be estimated by pre-determined relation between the spectral energy transmission ratio and the crack depth.

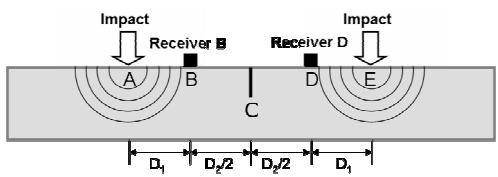

Fig. 1. Experimental setup for self-calibrated transmission function.

3. Experimental Investigation

3.1. *Concrete Slab and Test Setup*

A concrete slab which is nominally 0.25 m thick with lateral dimensions 1.5 m by 2.0 m containing artificial crack was cast. The slab contains an artificial crack (notch) that has a linearly increasing depth from 10 mm to 160 mm across the width of the slab [6]. The test setup consists of two wave sources (steel balls with 8 mm diameter), two accelerometers, a digital oscilloscope, and a laptop computer. Two sensors were located at 15 cm on each side of the crack and the spacing between each wave source and the nearest sensor was also 15 cm.

3.2. *Measured Spectral Energy Transmission Ratio*

Self-calibrated surface wave TRFs were measured on the test structure with various cracking conditions including crack-free and depth-varying cases. The measured TRFs for all 14 cases are shown in Figure 2. The frequency range was determined as 0-32.5 kHz by the signal consistency criterion in the crack-free case shown in Figure 3. The calculated spectral energy transmission ratios versus the crack depths are shown in Figure 4.

The spectral energy transmission ratio decreases dramatically when crack depth is less than 100 mm, therefore, it may be concluded that the spectral transmission energy ratio is a sensitive index for crack depth estimation. The observed relation between the spectral energy transmission ratio and the crack depth suggests a possible approach for the measurement of in-situ crack depth. A calibration formula (curve) can be established based on measured data, and then, for any ratio determined from the self-calibrated TRF, the crack depth can be solved from the pre-established formula.

A four-parameter power model is used to obtain a unique best-fit curve for *R(d)* as

$$R(d) = a_1 \cdot e^{-a_2 \cdot d} + a_3 \cdot e^{-a_4 \cdot d} \tag{5}$$

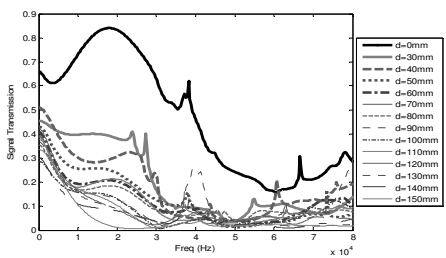

Fig. 2. Surface wave transmission functions for various crack depths.

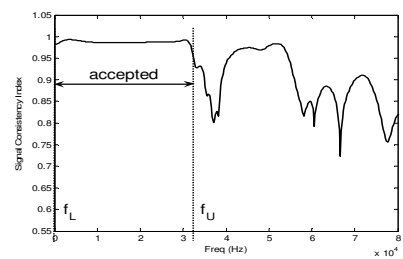

Fig. 3. Determination of frequency range using signal consistency index.

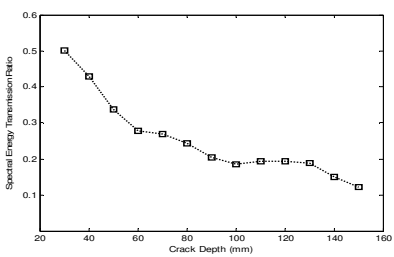

Fig. 4. Spectral energy transmission ratios according to crack depths.

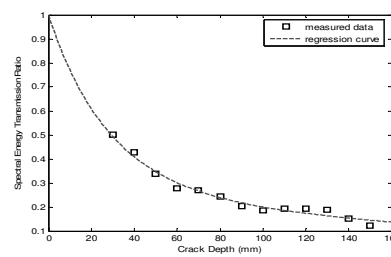

Fig. 5. Proposed curve between spectral energy transmission ratios and crack depths.

where constants a_1, a_2, a_3 and a_4 are empirical parameters to be determined by the least-squares regression. For experimental data shown in Figure 4, the parameters were determined to be 0.7 for a_1, 0.0386 for a_2, 0.3 for a_3, and 0.005 for a_4, giving a fairly high 0.9779 squared correlation coefficient value. As clearly shown in Figure 5, the formula fits very well to experimental data.

3.3. *Validation of Proposed Calibration Curve*

For the proposed method to be more applicable to in-situ structures, it is desirable to have results dependent not on the material property of concrete but on the crack depth. 12 concrete slabs with various compositions and crack depths were prepared as shown in Table 1, which are 15 cm thick with lateral dimensions 40 cm by 40 cm. The experimental setup consists of two accelerometers, an air-gun for applying consistent and repeatable impacts, a signal conditioner, a digital oscilloscope, and a laptop computer. Nominally, the spacing between two sensors is 5 cm and it between each wave source and the nearest sensor is 10 cm.

Estimation errors of the proposed curve are shown in Figure 6. It shows that the experimental data fit well to the proposed calibration curve (Equation 5) and the range of errors is generally less than 10 mm when the designed crack depth is less than 100 mm. It has been found that $R(d)$ does not depend on the composition of concrete, and it mainly depends on the crack depth up to 100 mm. Moreover, considering that the object material is concrete, the proposed curve seems to be very reasonable. When the database is set up with accumulating test results on various concrete structures, more reliable and practical curve can be drawn. Therefore, the effective nondestructive test for crack depth estimation will be possible.

Table 1. Details of concrete slabs.

Test Label	Composition (c:w:fa:ca:sp)	Crack depth (mm)
SP01	1.0:0.3:0.8:1.8:0.015	38
SP02	1.0:0.3:0.8:1.8:0.015	55
SP03	1.0:0.5:2.0:2.0: 0.0	47
SP04	1.0:0.5:2.0:2.0: 0.0	76
SP05	1.0:0.65:2.7:3.6: 0.0	22.5
SP06	1.0:0.65:2.7:3.6: 0.0	70
SP07	1.0:0.65:3.1:3.2:0.0	68
SP08	1.0:0.65:3.1:3.2: 0.0	18
SP09	1.0:0.38:1.55:2.11: 0.0	4
SP10	1.0:0.38:1.55:2.11: 0.0	27.5
SP11	1.0:0.38:1.55:2.11: 0.0	40
SP12	1.0:0.38:1.55:2.11: 0.0	44

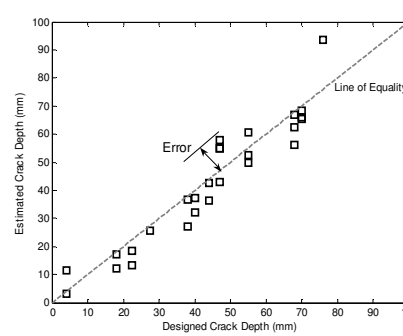

Fig. 6. Errors in crack depth estimation using the proposed method.

4. Conclusion

In this study, the surface wave spectral energy transmission method was proposed for the estimation of crack depth in concrete structures. The spectral energy transmission ratio was introduced and a simple calibration curve between the crack depth and the ratio has been determined using experimental data on a concrete slab with varying crack depths. The effectiveness of the proposed curve was validated using additional experimental data collected on various concrete slabs with different compositions and different crack depths. Finally, it was found that the spectral energy transmission method is not much responsive to the property of concrete but very sensitive to the crack depth, and has excellent potential as a practical and reliable in-situ nondestructive method for in-place crack depth estimation in concrete structures.

Acknowledgments

This work was supported by an ERC (Smart Infrastructure Technology Center) program of MOST/KOSEF (Grant No. R11-2002-101-03001-0) and a research project of MOCT/KICTTEP (Grant No. 01-2005-0-049-1-000-01).

References

1. M.J. Sansalone, J. Lin and W.B. Streett, *ACI Materials Journal*, **95**, 168 (1998).
2. T.T. Wu, J.S. Fang and P.L. Lin, *J. Acoust. Soc. Am.*, **97**(3), 1678 (1995).
3. Y. Lin and W. Su, *ACI Materials Journal*, **93**, 494 (1996).
4. J.S. Popovics, W. Song, M. Ghandehari, K.V. Subramaniam, J.D. Achenbach and S.P. Shah, *ACI Materials Journal*, **97**, 127 (2000).
5. W.J. Song, J.S. Popovics, J.C. Aldrin and S.P. Shah, *J. Acoust. Soc. Am.*, **113**(2), 717 (2003).
6. J. Zhu, *Doctor's dissertation,* Civil and Environmental Engineering, The University of Illinois at Urbana-Champaign (2005).
7. W. Song, J.S. Popovics and J.D. Achenbach, *Federal Aviation Administration Technology Transfer Conference*, Atlantic City, NJ (1999).
8. G. Hevin, O. Abraham, H.A. Petersen and M. Campillo, *NDT&E Internaional*, **31**(4), 289 (1998).
9. J.Y. Min, S.W. Shin, J. Zhu, C.B. Yun and J.S. Popovics, *the 19th KKCNN Symposium on Civil Engineering*, Kyoto, Japan (2006).
10. S.W. Shin, C.B. Yun, H. Furuta and H. Hattori, *the 8th International Conference on Motion and Vibration Control*, Daejeon, Korea (2006).

DEVELOPMENT OF LANDSLIDE EARLY DETECTION SYSTEM USING MICROWAVE

Hong C. RHIM

Department of Architectural Engineering, Yonsei University, Seoul 120-749, Korea

Long Hai JIN

Advanced Structures and Integrated Systems Laboratory Yonsei University, Seoul 120-749 ,Korea

In this research, the development of a microwave method system is proposed for the detection of change in moisture in sloped hillside area. This is for the purpose of early detection of landslide during rainy season. Abrupt landslide results in the loss of properties, casualties, and the block of traffic on the road. The developed system is designed to measure the change in moisture inside hilly area so that any imminent landslide can be warned by setting a threshold value of moisture in its level to cause a failure in the form of landslide. Preliminary experimental work showed a 1 GHz microwave proven to be effective in measuring the change of moisture inside soil.

1. Background

Landslide involves in ground movement, rock falls, and debris flows. One of the causes of the landslide is uprising moisture level inside ground. Especially, during rainy season, rapid buildup of moisture can provide catastrophic result of abrupt landslide. Such landslide results in the loss of properties, casualties, and the block of traffic on the road (Fig 1 and 2).

Fig. 1. Debris flows after landslide

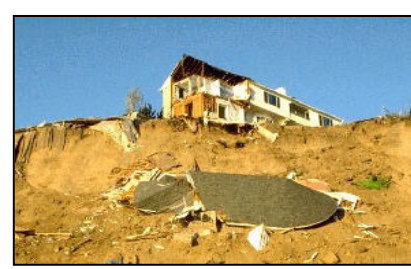

Fig. 2. Landslide in residential area

According to the statistics provided by Korean National Forest Agency, landside consists 22% of total casualties occurred in last 10 years in Korea. Death toll dramatically increases especially when there is a typhoon (Fig. 3).

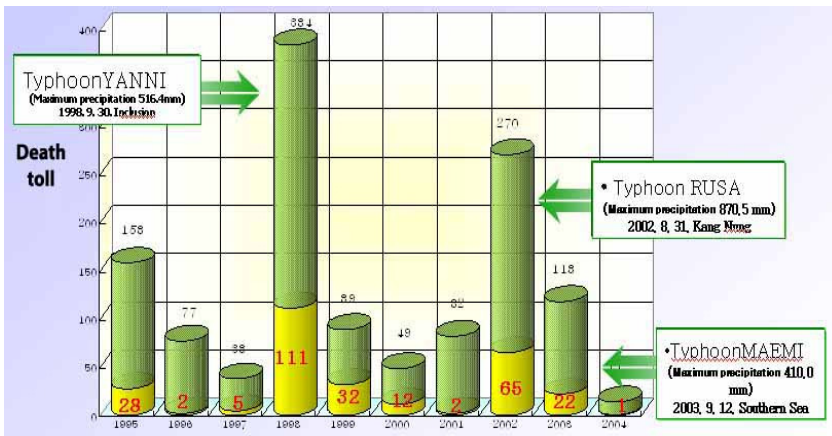

Fig. 3. Number of Death and Typhoon Occurrence in Korea

In this work, a system is designed to measure moisture level inside ground, which is related to the imminent condition of landslide. In order to monitor moisture change, the electromagnetic properties of soil is measured. A set of transmitter and receiver of microwave is placed into the ground to measure the electromagnetic properties of soil. In this paper, the results of preliminary experimental work is provided

2. Electromagnetic Properties of Soil and Moisture Change

Dielectric is a type of material whose dominant charges in atoms and molecules are bound negative and positive charges that are held in place by atomic and molecular forces, and they are not free to travel. However, when external fields are applied, these bound negative and positive charges do not move to the surface of the material, as would be the case of conductors, but their respective centroids can shift slightly in positions relative to each other, thus creating numerous electric dipoles. In general, a dielectric material such as concrete can be characterized by two electromagnetic properties: the permittivity ε and the permeability μ. Most common dielectric materials including FRP and concrete, however, are nonmagnetic, which make the permeability μ very close to the permeability of free-space ($\mu_0 = 4\pi \times 10^{-7} H/m$).

In the dielectric material, the electric flux density $\overline{\mathbf{D}}$ is related to that of in free-space $\overline{\mathbf{D}}_0$ by

$$\overline{\mathbf{D}} = \varepsilon_0 \overline{\mathbf{E}} + \overline{\mathbf{P}} \tag{1}$$

where $\overline{\mathbf{P}}$ is a net electric polarization vector directed along the same direction as the applied field $\overline{\mathbf{E}}$. Therefore, $\overline{\mathbf{P}}$ is also related to $\overline{\mathbf{E}}$ and cab be expressed as

$$\overline{\mathbf{P}} = \varepsilon_0 \chi_e \overline{\mathbf{E}} \tag{2}$$

where χ_e is called the electric susceptibility.

In Fig. 4, the measured dielectric constants of water is shown over the wide frequency range from 100 MHz to 20 GHz. The typical value of highest constant number for water is about 80, which decreases as frequency increases. This trend is evident in concrete with moisture as well in Fig. 5. For the same concrete specimen, as the moisture level inside is increasing, the dielectric constants are quite different as shown.

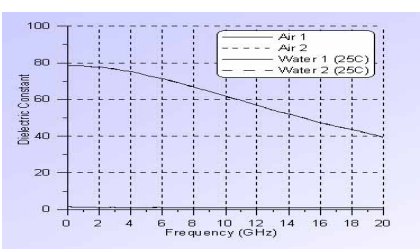

Fig. 4. Dielectric Constant of Water

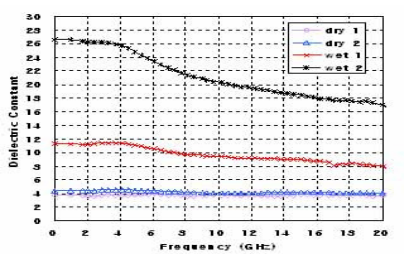

Fig. 5. Moisture Variation and Constants

3. Experimental Results

As a preliminary experiment in the laboratory, a box was made to hold sand (Fig. 6). A 1 GHz ground penetrating radar (GPR) system was used for initial measurements. The antenna was placed on one side of the wooden box and measured the reflected signal from a metal stick. By knowing the exact distance between the source (GPR) and the target (metal stick), the dielectric constant was calculated. The constant was then related to the moisture level of sand compared to pre-existing data base.

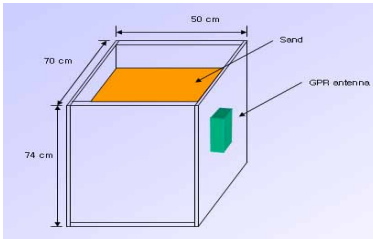

Fig. 6. Sand Box

Fig. 7. GPR system

The results measurements are shown in Fig. 8 and 9. A metal stick is seen at the top of Fig. 8 as a white spot out of reddish background. It is clear that the signal is reflected from the target. Then, in Fig. 9, the reflection is a bit far away compared to the one in Fig. 8, as the target is now 5 cm from the side of the wooden box.

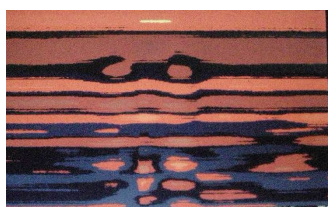

Fig. 8. Stick on Contact

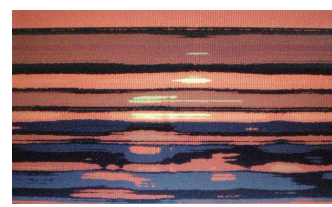

Fig. 9. Stick at 5 cm

4. Conclusion

The microwave method is proposed for the detection of change in moisture in sloped hillside area. Preliminary experiments have shown that the change in the location of the reflected signal helps in determining the dielectric constant of soil. This property can be then related to the moisture level of the ground. This system is for the purpose of early detection of landslide during rainy season. 1 GHz results are proven to be effective in the measurements. Further research will complete the system to be located in the field for practical applications.

Acknowledgments

Authors would like to thank for the financial support provided by the Ministry of Construction & Transportation (MOCT) Korea and Korea Institute of Construction

and Transportation in Technology Evaluation and Planning (KICTTEP) through "Infra-Structure Assessment Research Center (ISARC)" under its Program No. 04 Core Technology C02-02.

References

1. Topp, G.C., Davis, J.L., and Annan, A.P., *Electrimagnetic determination of Soil water content: measurements in coaxial transmission lines* Water Reservoir. Vol. 16, No. 3, pp. 574-582, 1980.
2. K.K.K. Singh, *Ground penetrating radar study for hydrogeological conditions related with mining activity*, Environmental Geology 44: pp. 20-27, 2003.
3. S. Laurens, J.P. Balayssac, J. Rhazi, G. Klysz, G. Arliguie, *Non-destructive evaluation of concrete moisture by GPR: experimental study and direct modeling*, Materials and Structures 38, pp. 827-832, November 2005.
4. L.W. Galagedare, G.W. Parkin, J.D. Redman, *Measuring and Modeling of Direct Ground Wave Depth Penetration Under Transient Soil Moisture Conditions* Subsurface Sensing Technologies and Applications, Vol. 6, No. 2, April 2005.
5. Jürgen Schmalholza, Heiner Stoffregenb, Andreas Kemnac and Ugur Yaramancia, 2004, *Imaging of Water Content Distributions inside a Lysimeter using GPR Tomography*, Vadose Zone Journal 3:1106-1115.
6. Fang Ji, Kawasaki Akiyuki, sadohara satoru, *Development of a Slope Failure Management System Using ArcGIS Server*, ESRI International User Conference 2005.

FEASIBILITY OF EVALUATING THE COMPACTION QUALITY OF SOILS BY THE IMPACT ECHO METHOD

JIUNNREN LAI

Department of Construction Engineering, Chaoyang University of Technology
168 Gifeng E. Rd , Wufeng, Taichung County 413, Taiwan

CHIA-YU CHIU

Central Water Resources Office, Ministry of Economic Affairs
1340-6, Chungcheng Rd., Wufeng, Taichung County 413, Taiwan

CHIA-CHI CHENG

Department of Construction Engineering, Chaoyang University of Technology
168 Gifeng E. Rd , Wufeng, Taichung County 413, Taiwan

The objective of this study is to establish a systematic procedure based on stress wave propagation speeds to evaluate the quality and engineering properties of compacted soils for the quality control of earth works. To achieve this goal, three different materials used in the earth dam of the PaoShan Second Reservoir were collected. Proctor, Impact Echo, as well as California Bearing Ratio (CBR) tests were performed on compacted samples of the three materials. Results of these tests indicate that the shear (S) wave velocity of the samples is proportional to their dry density. The compressive (P) wave velocity of the samples decreases as their moisture content increases. Also, the P-wave and S-wave velocities of the samples are proportional to their CBR values. It is thus concluded that the Impact Echo method is a tool with high potential for the evaluation of compaction quality of soils.

1. Introduction

The construction of highway embankment or earth dam requires compacting the back-fill materials layer-by-layer. In practice, for the purpose of quality control, Proctor tests were performed in the laboratory to obtain the maximum dry density "$\rho_{d,max}$" of the back-fill material. Sand-cone tests were performed to measure the field dry density "$\rho_{d,field}$" of the compacted layer. The relative compaction "R" is defined as the ratio of $\rho_{d,field}$ and $\rho_{d,max}$. For most earth works, a relative compaction of higher than 95% is required. However, the sand-cone test is a destructive test and performing this test is labor intense and time consuming. Furthermore, this test can only obtain the physical properties of the

compacted soil. If the engineer wants to know the engineering properties of the compacted material, additional tests such as the static plate load test or the California Bearing Ratio (CBR) test must be performed. Therefore, several researches have been done to find out an alternative solution.

Starting from the 1980s, the time domain reflectometry (TDR) technique was used to measure the volumetric water content of soils [1-3]. Yu and Drnevich [4] further applied this technique to measure the gravitational water content and dry density of compacted soils. The basic idea of this method is to correlate the density and moisture content of soils to their electrical conductivity. The disadvantage of this method is that it still can not obtain the engineering properties of the compacted material.

In recent years, stress wave propagation theory was used to measure the porosity and moisture content of soils and rocks. Allen [5] found that the primary (P) wave velocity of a saturated granular soil is controlled by its void ratio. Berryman et al. [6] proposed using seismic wave velocity to determine the degree of saturation and porosity of porous rocks. Rix and Stokoe [7] used Spectrum Analysis of Surface Wave (SASW) method to measure the stiffness profile of pavement sub-grades. Kim et al. [8, 9] applied the SASW method and found good correlation between the dry density and shear (S) wave velocity of compacted soils. From the experience of these investigations, it can be conclude that using wave propagation speed to evaluate the compaction quality of soils is very promising.

2. Testing Program

2.1. *Materials Tested*

The objective of this study is to establish a systematic procedure based on stress wave propagation speeds to evaluate the density and water content of compacted soils, which can be used for the quality control of earth works. To achieve this goal, three different materials used in the earth dam of the PaoShan Second Reservoir were collected and tested. Index properties of these materials are shown in Table 1. The shell material, which has the lowest plasticity, is a brown mixture of weathered sand stone and clay shale, and will be placed on the outer shell at downstream of the dam.. The core material is classified as clay of low plasticity (CL) according to the Unify soil Classification system (USCS). It is a weathered mud stone with gray color, and is used as water barrier at the center of the earth dam. The high plasticity special compaction (HPSC) material is red in color. It has the finest particle size and highest plasticity among the three materials, and will be placed between the foundation and the main body of the dam.

Table 1. Index properties of the materials used in this study

Material Type	Sand content (%)	Clay content (%)	Liquid limit (%)	Plastic index (%)	USCS Classification
shell	31.2	68.8	20.8	4.2	CL-ML
core	23.7	76.3	23.4	10.3	CL
HSPC	2.5	97.5	52.1	17.2	MH

2.2. *Testing Methods*

In order to obtain the dry density vs. water content relationship of the tested materials, a series of samples were compacted at different water contents according to the procedures specified in the ASTM D 698 standard. After the weight of the samples was taken, the P-wave and S-wave velocities of each sample were measured using the test setup as illustrated in Figs. 1a and 1b. The CBR of these samples was than measured according to the ASTM D 1883 standard. Finally, these samples were oven dried to obtain their water content.

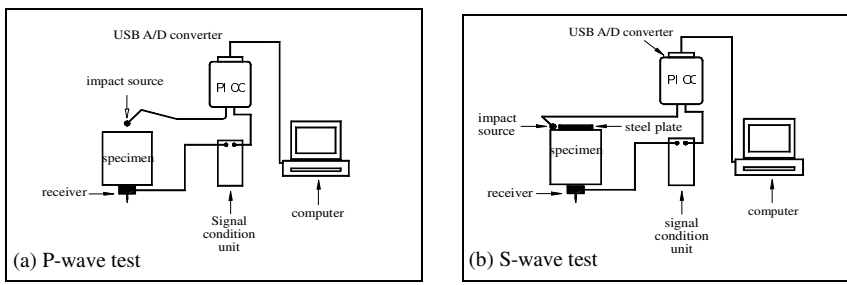

Fig. 1. Schematic diagram of test setup for P-wave and S-wave velocity measurement

3. Test Results

3.1. *Relationship Between Density and Water Content*

Results of the Proctor test are shown in Fig. 2 and summarized in Table 2. All the three materials have the typical compaction cure – the dry density increases as water content increases, reaching a peak value, than decreases as water content further increases (Fig. 2). Also, the maximum dry density ($\gamma_{d,max}$) of a material decreases as its plasticity index (PI) increases, and the optimum water content (ω_{optt}) increases as its PI increases as shown in Table 2.

Table 2. Summary of Proctor test results

Material Type	Plastic index (%)	Maximum dry density (kN/m^3)	Optimum water content (%)
shell	4.2	19.03	8.5
core	10.3	18.05	11.1
HSPC	17.2	14.91	26.3

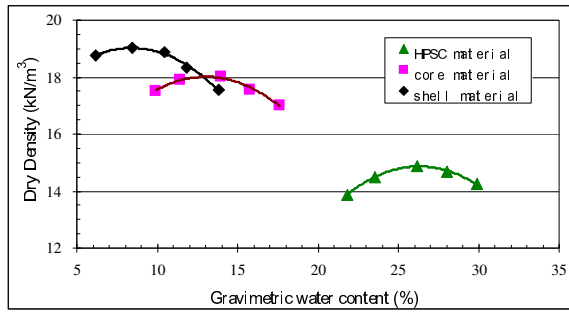

Fig. 2. Results of Proctor tests on the three materials

3.2. *P-wave Velocity vs. Water Content*

The relationship between P-wave velocity and compaction water content for the three materials are shown in Fig. 3. For the two (shell and core) materials with lower plasticity, the P-wave velocity decreases as compaction water content increases, because the sample is weaker at high water contents thus leads to a lower P-wave velocity. But the linear relationship does not exist for the HPSC material. For clays with high plasticity, the strength peaks at compaction water content close to the optimum water content, therefore, we would expect that its P-wave velocity reaching a maximum value at compaction water content around its optimum water content.

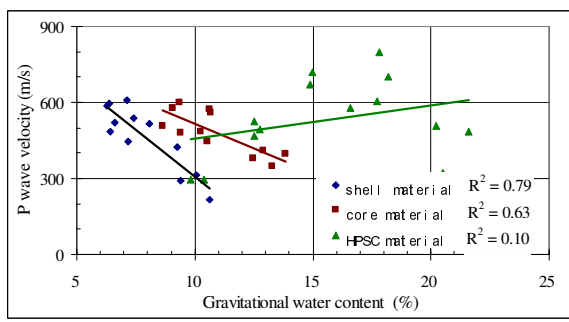

Fig. 3. Relationship between P-wave velocity and compaction water content..

3.3. *S-wave Velocity vs. Dry Density*

The S-wave velocities are plotted against dry densities as shown in Fig. 4a for the shell material and in Fig. 4b for the core material. It can be seen from these two figures, for samples compacted at dry of optimum (i.e., compaction water content less than the optimum water content), the S-wave velocity increases as

dry density increases. For clays compacted at dry of optimum, we would expect their strength to increase proportionally as their dry density increase. Therefore, a linear relationship between the S-wave velocity and dry density can also be expected.

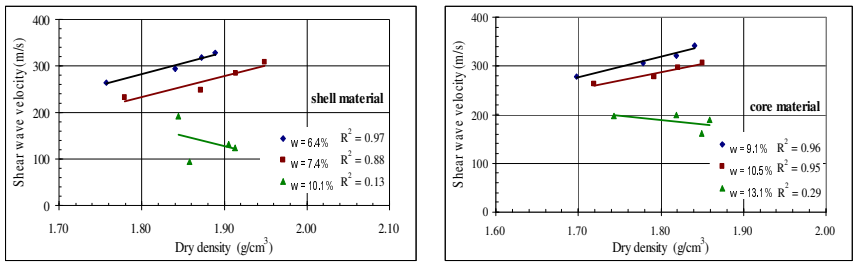

(a) Shell material (b) Core material

Fig. 4. Relationship between S-wave velocity and dry density for the two materials with lower PI

3.4. *P-wave and S-wave Velocities vs. CBR*

The California Bearing Ratio of both materials is plotted against P-wave velocity as shown in Fig. 5a and against S-wave velocity as shown in Fig. 5b. It can be seen from these two figures, both the P-wave and S-wave velocities increase as the CBR increases. We would expect that the California Bearing Ratio of most soils will be proportional to their strength. Therefore, a linear relationship between the wave propagation speeds and the California Bearing Ratio can also be expected.

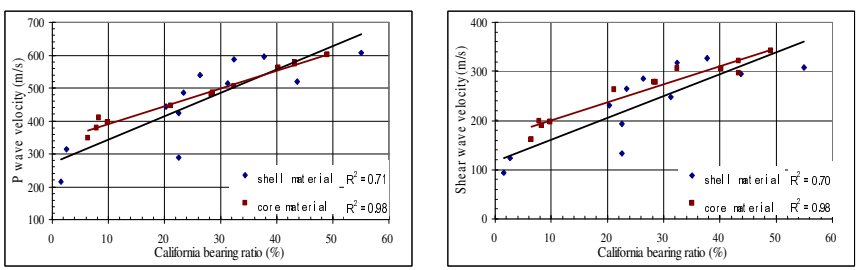

(a) P-wave Velocity (b) S-wave Velocity

Fig. 5. Relationship between body wave velocities and California Bearing Ratio

4. Summary and Conclusions

The objective of this paper is to investigate the feasibility of using Impact Echo NDT technique to evaluate the quality of a compacted soil layer. From the results of this study, the following conclusions can be drawn:

1. The shear (S) wave velocity of the samples is proportional to their dry density.
2. The compressive (P) wave velocity of the samples decreases as their moisture content increases.
3. Both the P-wave and S-wave velocities of the samples are proportional to their CBR values.

From the discussion mentioned above, the stress wave propagation method not only can obtain the physical properties (density and moisture content) of compacted soils, it can also evaluate their engineering properties such as California Bearing Ratio. It is thus concluded that the Impact Echo method is a tool with high potential for the evaluation of compaction quality of soils

Acknowledgments

The work presented in this paper is sponsored by the National Science Council of Taiwan. Their support is deeply appreciated.

References

1. G.C. Topp, J.L. Davis and A.P. Annan, *Water Resource Reservation* **6**(**3**), 574 (1980).
2. C.H. Benson and P.J. Bosscher, *ASTM* **STP1350**, 113 (1999).
3. K. Noborio, *Computational Electronic Agriculture* **31**(**3**), 213 (2001).
4. X. Yu and V.P. Drnevich, *Journal of Geotechnical and Geoenvironmental Engineering* **130**(**9**), 922 (2004).
5. N.F. Allen, F.E. Richart and R.D. Woods, *Journal of the Geotechnical Engineering* **106**(**3**): 235 (1980).
6. J.G. Berryman, P.A. Berge and B.P. Bonner, *Geophysics* **67**(**2**), 391 (2002).
7. Rix, G.J. and K.H. Stokoe II, *Transportation Research Board*, 1 (1989).
8. D.S. Kim and H.C. Park, *Canadian Geotechnical Journal* **36**(**2**), 91 (1999).
9. D.S. Kim, M.N. Shin and H.C. Park, *Soil Dynamics and Earthquake Engineering* **21**, 39 (2001).

COLOR CHANGE AND RESIDUAL COMPRESSIVE STRENGTH OF CONCRETE EXPOSED TO HIGH TEMPERATURE USING SPECTROPHOTOMETRIC METHOD

JOONG-WON LEE

Department of Architecture, Ansan College of Technology, Ansan, 425-792, Korea

KWANG-HO CHOI

Department of Architecture, Namseoul University, Chonan, 138-130, Korea

KAP-PYO HONG

Department of Architectural Engineering, Yonsei University, Seoul, 120-749, Korea

The purpose of this study is to quantify the color changes of concrete exposed to high heat by a spectrophotometric method and to investigate the relation between the color change and residual compressive strength. In order to assess the depth of the damaged core under fire, 12 specimens were prepared for the experiment with variables of concrete strength (20MPa, 40MPa, 60MPa) under experimental setting of 800□ temperature condition for 2 hours. Color change analysis of the split specimen after heating was conducted, and split tensile stress test was performed to find the residual compressive strength in relation to the depth of specimen. The results show that the residual compressive strength of specimens is consistent with the full development of the red color and this proposed method as NDT may be used to evaluate the residual compressive strength and to investigate the exposed temperature at which the strength degradation has occurred.

1. Introduction

When reinforced concrete structure is damaged by fire, its properties such as concrete compressive strength, modulus of elasticity, yield strength of the steel are deteriorated and accompanied by color change.

The concrete exposed to high temperature undergoes a color change by the heat. It is known that it changes to pink/red, whitish grey, buff color at the temperature ranges of 300°C~600°C, 600°C~900°C, and 900°C~1000°C, respectively. Since the color change of the concrete is related to the temperature increase, the degree of the deterioration of the concrete compressive strength can be predicted through the color change [2,3].

The purpose of this research is to analyze the color change of the concrete exposed to high temperature of fire by a spectrophotometer so that the relationship of the concrete compressive strength deterioration to the exposed temperature is delineated. Through this endeavor, the effectiveness of the spectrophotometric method is to be verified for NDT.

2. Experimental Procedure

2.1. *Test Method and Concrete Mix*

The Φ 100x200 cylinder specimen heated on one side was sliced into pieces in order to measure the depth of the damage to the concrete exposed to high temperature [1]. Each sliced test specimen was subjected to color analysis and measurement of its split tensile strength. The result was then compared with an intact (unheated) specimen to evaluate the depth of the damage. The test specimens were prepared under the experimental setting of four specimens for each compressive strength subjected to the heating at 800°C for 2 hours. Thus, a total of 12 specimens were prepared for three compressive strengths of 20MPa, 40MPa, and 60MPa so that the average value from 4 measurements can be obtained for each compressive strength test setting. Additionally, the specimens were sliced into four pieces of 2cm thickness and one piece of 10cm thickness from the heated surface in order to measure the heat damage by the depth.
Table 1 shows the characteristics of the concrete mix.

Table 1. Concrete Mix Table

Strength (MPa)	W/C (%)	s/a (%)	Binder (kg/m^3)	Unit water content (kg/m^3)	Unit mass (kg/m^3)				
					Coarse aggregate	Fine aggregate	Cement	FA	Ad
20	67.8	50.0	255	173	917	910	229	26	1.28
40	43.2	45.9	405	175	919	774	364	41	2.03
60	31.8	42.8	560	178	863	641	482	112	5.60

note) FA : admixture (fly ash), Ad : admixture (AE dehydration agent)

2.2. *Color Measurement* [2,5]

The color change of a concrete structure subjected to a fire damage can be represented and quantified by Hue, Saturation, and Lightness in a color space of Figure 1.

The L*C*h* color space in Figure 2 is presently one of the most popular color space for measuring object color and widely used virtually all fields. In this color space, L* represents lightness and C* is chroma(saturation), and h is the

hue angle. The value of chroma C* is 0 at the center and increases according to the distance from the center. Hue angle h is defined as starting at the +a* axis and is expressed in degrees; 0^o would be +a*(red), 90^o would be +b*(yellow), 180^o would be –a*(green), and 270^o would be –b*(blue).

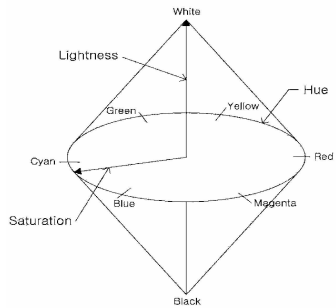

Fig. 1. HSI color space

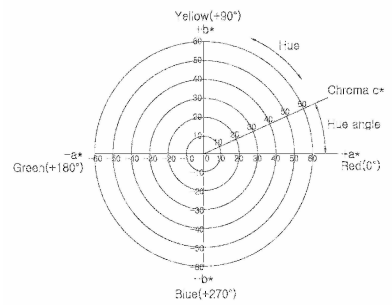

Fig. 2. L*C*h color space

The color analysis of the heated and sliced test specimens was conducted after the one side heating and air cooling of one day. The spectrophotometer used for this color analysis was CM -2500d of Minolta Company of Japan.

3. Experimental Result and Analysis

3.1. *Cracking and Discoloring Status*

Photo 1 shows the cracking and discoloring status at the surface of the concrete test specimen heated with an electric furnace. Although small cracks of 0.15mm and 0.2~0.3mm size were observed around the surface of specimens of 20MPa strength and 40MPa strength, respectively, under the heating condition of 800°C, a relatively large crack of 0.6~0.7mm occurred around the surface of 60MPa strength specimen and propagated into the inside of the specimen.

The result of a visual inspection of the color change at the heated surface indicates that specimens of 20MPa and 40MPa strength changed clearly into red color. However, no apparent change in color of the specimen of 60MPa strength was observed.

Photo 1. Crack Pattern at the Heated Surface of the Test specimen

3.2. *Hue Change in Response to L*C*h* Color Space*

Figure 3 represents the color changes for each strength of the test specimen in L*C*h* color space.

As the depth of the test specimen gets closer to the heated surface, the change in the hue angle for specimens of all strengths approach in the direction of red, i.e. +a axis. Additionally, the hue angles at the heated surface were 76.72 degree, 77.91 degree, and 81.81 degree for the test specimens of 20MPa, 40MPa, and 60MPa strength, respectively. This attests for the fact as observed by a visual inspection that the change in color of the test specimen of 20MPa compressive strength at the heated surface gets closest to red in color among all other specimens.

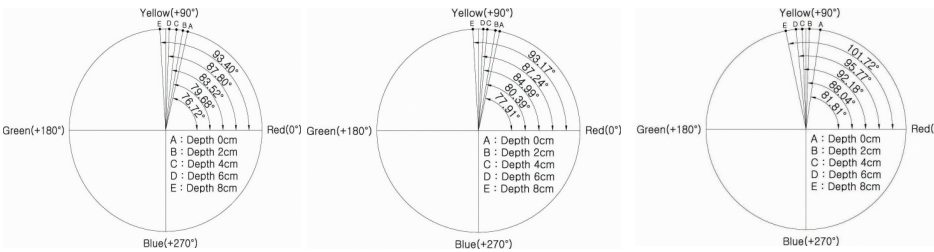

(a) 20MPa (b) 40Mpa (c) 60MPa

Fig. 3. Hue Angle Change in the L*C*h* color space for each strength of the test specimen

3.3. *Relative Hue Change and Residual Compressive Strength Ratio by the Depth of the Test Specimen*

The split tensile strength of the sliced test specimen was used to predict its compressive strength using the relational equation of ACI between the split tensile strength and compressive strength, i.e. $f_{ct}=0.56\sqrt{f'_c}$ [4].

Figure 4 compares the relative hue value ratio of the heated specimen to intact specimen. For specimens of 20MPa, 40MPa, and 60MPa strength, the relative hue value varied between 84%~102%, 85%~101%, and 83%~103%, respectively. Thus, the change in the relative color ratio exhibited a consistently decreasing pattern as the depth from the surface gets larger, and the change in relative hue value was less as the strength of the concrete specimen increased to 60MPa.

Additionally, the residual compressive strength ratio increased with the depth of the specimen while the relative color ratio exhibited a similar pattern of increasing with the depth of the test specimen. This fact points to a possible relationship of residual compressive strength and relative color ratio.

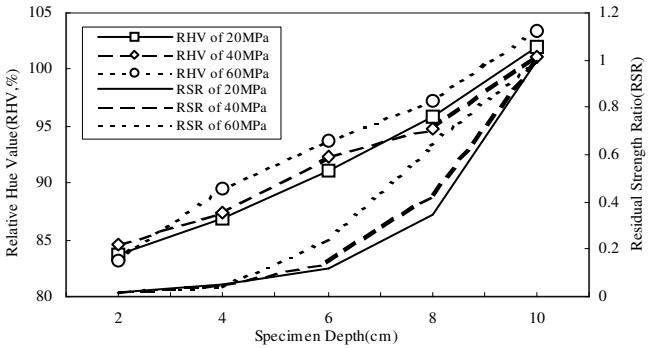

Fig. 4. Relative Hue Value and Residual Compressive Strength Ratio by depth of the specimen

3.4. *Relationship of Relative Hue Change to Residual Compressive Strength Ratio*

Figure 5 shows the relationship of residual compressive strength ratio and relative hue change of the heated specimens of 20MPa and 40MPa, which exhibited a consistent trend of hue change during the heating experiment. Moreover, a 3rd power equation with R^2 value of 0.86 was chosen to increase the reliability of the regression analysis of the relationship.

Examining the relationship of residual compressive strength and relative hue change in the figure, the residual compressive strength ratios were below 10%, 10%~20%, 20%~50%, and 50%~100% when the relative hue changes were below 85%, 85%~90%, 91%~95%, and 96%~100%, respectively. This observation indicates that the residual ratio of the compressive strength decrease as the relative hue change is greater.

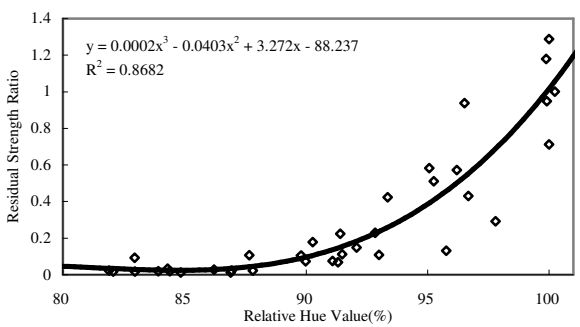

Fig. 5. Relation between Relative Hue Value and Residual Compressive Strength Ratio

4. Conclusion

The following conclusions are derived from the result of comparing and analyzing the color change and residual compressive strength ratio computed from split tensile strength measurement of the specimens heated at one side against intact test specimens.

1. The result of color analysis by the depth of the concrete specimens revealed that the relative hue change exhibited a consistently decreasing pattern as the depth increased.
2. As the relative hue change increased, the residual compressive strength ratio exhibited a decreasing trend. Therefore, the residual compressive strength of specimens is consistent with the full development of the red color change.
3. The spectrophotometric method proposed in this study can be used as a non-destructive method for the evaluation of compressive strength reduction by measuring the color change of the concrete exposed to high temperature such as a fire.

Acknowledgment

This research was supported by Construction Core Technology Development Program (2004 Academic-Industry Cooperative Research Program Task Number C02-02) of Korea Institute of Construction & Transportation Technology Evaluation and Planning under the auspice of the Ministry of Construction and Transportation and the partially by Namseoul University. The authors express their sincere appreciation for the support.

References

1. J. R. dos Santos, F. A. Branco and J. de Brito, “Assessment of concrete structures subjected to fire”, Magazine of concrete research, 54, No.3, June, pp203～208, (2002).
2. N. R. Short, J. A. Purkiss, S. E. Guise, “Assessment of fire damaged concrete using color image analysis”, Construction and building materials, pp9～15, (2001).
3. Nabi Yűzer, Fevziye Akőz, Leyla Dokuzer Őzturk, “Compressive strength-color change relation in mortars at high temperature”, Cement and Concrete Research, pp1～5, (2004).
4. Chu-kia Wang, Charles G. Salmon, “Reinforced concrete design”, Happer & Row, pp12～13, (1985).
5. Konica Minolta, “Precise color communication”, (2004).

IDENTIFY THE LOCATIONS OF CONCRETE CRACKS WITH EMPLOYING THE IMPROVED ACTIVE CONTOUR MODEL TO EXTRACT REGIONAL BOUNDARIES FROM GPR

YISHUO HUANG

Department of Construction Engineering, Chaoyang University of Technology
168 JiFeng E. Rd.
Wufeng, Taichung 41349, Taiwan

SUNG-CHI HSU

Department of Construction Engineering, Chaoyang University of Technology
168 JiFeng E. Rd.
Wufeng, Taichung 41349, Taiwan

To identify the locations of concrete cracks is an important way to evaluate the healthy of an aged reinforced-concrete structure. Ground penetration radar, GPR, has been widely employed to identify concrete cracks with locating discontinuities while the transmitted radar signals pass through different mediums or the weaknesses of concrete. The paper employs the improved active contour model that incorporated the alignment as part of other driving force, together with the geodesic active contour for regularization, and minimal variance criteria. An initial closed curve is chosen. Then, the level set method developed by Osher and Sethian is applied to implement the curve propagation toward its optimal location. In doing so, the regional boundaries are extracted from the given GPR images. With comparing the data distribution in the extracted regions, the weaknesses of concrete are identified. The paper demonstrates it is feasible to locate concrete cracks from the weaknesses of concrete form the GPR imagery with the stable and simple numerical scheme implemented with the improved active contour model.

1. Introduction

Ground penetration radar, GPR, is a remote sensing tool designed for exploring the characteristics of shallow subsurface. The electromagnetic waves used in GPR are sensitive to the physic properties of the scanned materials. With an antenna located in boreholes, the subsurface properties are estimated tomographically, and are record to form a 2D image with high resolutions in horizontal and vertical direction. Recently, GPR has been widely adapted to diagnose the pavement damages in non-destructive evaluation [1]. Cracks in concrete are an important clue to evaluate the health of a reinforced-concrete structure.

GPR data can provide an efficient way to identify the suspicious locations of cracks in concrete. Crack formation in concrete is caused with unbalanced forces acting on those infrastructures made of concrete. Cracks in concrete cause the changes of the dielectric structure of concrete. The study proposes an algorithm to isolate the regional boundaries in GPR data such that elements in each regional boundary have similar dielectric properties. The regional boundaries are extracted the improved active contour model.

Active contour model, also called snake model or deformable model, extracts regional boundaries based on the balance of forces acting on boundaries. In 1988, Kass and Witkin proposed that extracting regional boundaries with the iteration approaches based on minimum energy [3]. The proposed method is called the snake Model or deformable Model. Kichenassamy extracted regional boundaries with partial differential equations, PDEs, and evolving curve [4]. Osher and Sethian proposed the level set method to evolve the specified curve with energy tendencies to divide the whole image into several sub-regions such that in each sub-region, the pixel values are homogeneous [5]. The improved active model employed the minimal variance criterion as the criteria to stop the iterations during extracting the regional boundaries [6].

In this paper, we employ the improved active contour model to extract the regional boundaries from GPR data. The same algorithm is employed on the GPR data collected on the same material but different places. With comparing the differences between two GPR data, the weakness in concrete can be located and identified. Those identified places are the places of cracks in concrete. From the field test, the proposed method demonstrates its capability to identify specious locations of crack in concrete.

2. Theory of improved active model

The snake model is an efficient way to extract the boundary of an object. The snake model is developed by Kass. In his model, the image is composed with different closed sets such that those elements in each closed set are homogeneous. Each closed set is surrounded with a closed curve, and is shown mathematically as follows

$$\Gamma = \bigcup_{i \in I} C_i \tag{1}$$

where C_i is a closed curve with piece-wise continuous property, and is defined as $C = \{c : [a \quad b] \to \Omega, c(a) = c(b), and \quad c \quad is \quad piecewise\}$. The energy, $E(c)$, in the closed curve is supposed to include the internal and external forces acting on the closed curve. The internal forces in the closed curve try to shrink and

push the curve inward. On the other hand, the external forces pull the curve outward. The internal forces and external forces gradually reach the equilibrium with increasing processing time. With the time increasing, the closed curve slowly moves toward the regional boundary. Eventually, the closed curve is stopped while the internal forces are equal to external forces. In the other words, the image energy reaches its minimum. The final shape of the closed curve is located at the object's boundary. The energy is defined as follows

$$E(c) = \left[\int_a^b |c'(q)| dq + \beta \int_a^b |c''(q)| dq \right] + \lambda \int_a^b g^2(|\nabla I(c(q))|) dq \tag{2}$$

where $c(q) = (c_x(q), c_y(q))$, $c'(q) = \left(\frac{dc_x}{dq}, \frac{dc_y}{dq} \right)$ and $|c'(q)| = \sqrt{\left(\frac{dc_x}{dq} \right)^2 + \left(\frac{dc_y}{dq} \right)^2}$.

Similarly, *c*" is the second derivative of the closed curve, *c*. With applying the calculus of variation, the Eq. (2) can be rewritten as Euler-Lagrange equation [7]. The Euler-Lagrange equation can be shown as follows

$$-c'' + \beta c^{(iv)} + \lambda \nabla F_c(c) = 0 \tag{3}$$

where $c^{(iv)}$ is the fourth-order derivative and $F_c(c) = g^2(|\nabla I(c)|)$. Malladi proposed to employ level set approach to implement the snake model [8]. Level set is an approach to consider an initial curve which is moving toward the object's boundary with increasing time during the forces acting on the curve. In general, the initial curve is called the zero level set, and time parameter is set to zero, *t*=0. While the time parameter is cumulated, the curve is moving along its normal direction with the speed function, *F(k)*. For simplicity, the β shown in the equation (2) is set to zero such that Euler-Lagrange equation is written as follows

$$\frac{\partial u}{\partial t} = g(I)|\nabla u| div\left(\frac{\nabla u}{|\nabla u|} \right) + \nabla g \cdot \nabla u = g|\nabla u| \kappa + \nabla g \cdot \nabla u \tag{4}$$

where *I* is the original image data, ∇ operator is defined as the gradient operator, $g(I) = \frac{1}{1 + |\nabla I|^2}$, *u* is the image containing the closed curve with the same size of the original image, $div\left(\frac{\nabla u}{|\nabla u|} \right) = \frac{u_{xx} u_y^2 + u_{yy} u_x^2 - 2 u_x u_y u_{xy}}{(u_x^2 + u_y^2)^{3/2}} = \kappa$ and $\cdot$ operator is defined as the inner product. The level set approach is employed to find the numerical solution of Eq. (4). With increasing the time parameter, the closed

cure is moving toward the object's boundary. In order to avoid over-working, the criterion for stopping processing is needed to be setup first.

Chen and Vese proposed a minimal variance criterion [9]. The criteria is given by

$$E_{MV}(C,c_1,c_2)=\frac{1}{2}\iint_{\Omega_C}(I(x,y)-c_1)^2\,dxdy+\frac{1}{2}\iint_{\Omega\setminus\Omega_C}(I(x,y)-c_2)^2\,dxdy \qquad (5)$$

where *I(x,y)* is an given image; c_1 and c_2 are two constants which are the mean intensities inside and outside the closed curve C, respectively. The boundary is located at the place where the $E_{MC}=0$. Chan and Vese define the arc-length $\int ds$ as a regularization term. With employing the criterion of Eq. (5), the Eq. (4) is rewritten as follows

$$\phi_t=\left(\alpha\mathrm{div}\left(\mathrm{g(x,y)}\frac{\nabla\phi}{|\nabla\phi|}\right)+\eta(\phi,\nabla I)\right)|\phi| \qquad (6)$$

where $\eta(\phi,\nabla I)=\left[sign\left(\langle\nabla\phi,\ \ \nabla I\rangle\right)\Delta I+\alpha div\left(g(x,y)\frac{\nabla\phi}{|\nabla\phi|}\right)+\beta(c_2-c_1)\left(I-\frac{c_1+c_2}{2}\right)\right]|\nabla\phi|$

3. Field data

With the improved active contour model, the regional boundaries in GPR data are extracted. The same instrument is applied on the same material at different places. Cracks in concrete are identified at the positions where the regional boundaries extracted from different GPR data are not located at the same positions. The proposed idea is based on the assumption that the dielectric properties are different at the locations of cracks. The field data was collected on a construction site. The surfaces of concrete were smoothed, and are shown in Fig. 1. The surfaces were carefully drawn several lines to make sure that the GPR data was collected in right positions. During the collecting procedures, each line is measured twice with GPR.

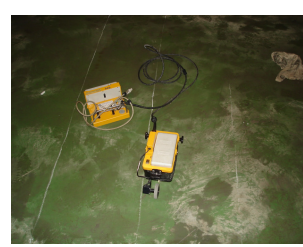

Fig. 1. Collecting GPR data on the smoothed concrete surface.

The GPR data is presented in Fig. 2. In the Fig. 2 (a) and (b) illustrate the collected GPR data on the smoothed concrete surface. Fig. 2 (c) shows the extracted boundaries with the proposed research methodology. Fig. 2 (d) shows that the extracted boundaries from original and rescanned data are similar.

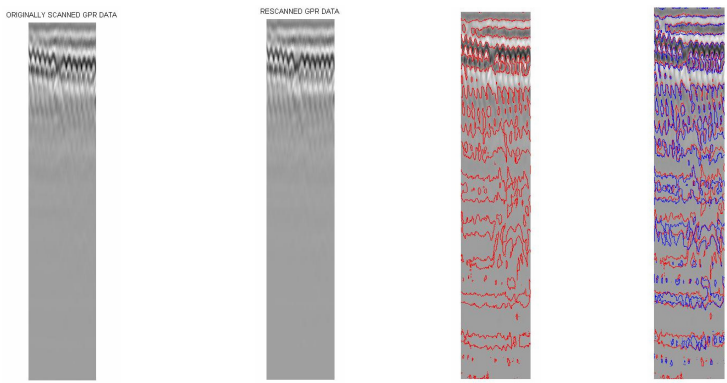

(a) (b) (c) (d)

Fig. 2 (a). Original GPR data. (b). Rescanned GPR data. (c). Extracted boundaries with the proposed method. (d). Overlapping the extracted boundaries.

The same method applied on different GPR data collected at different lines. The experiment results are illustrated in Fig. 3. Fig. 3 (d) shows the intersection results of the extracted boundaries.

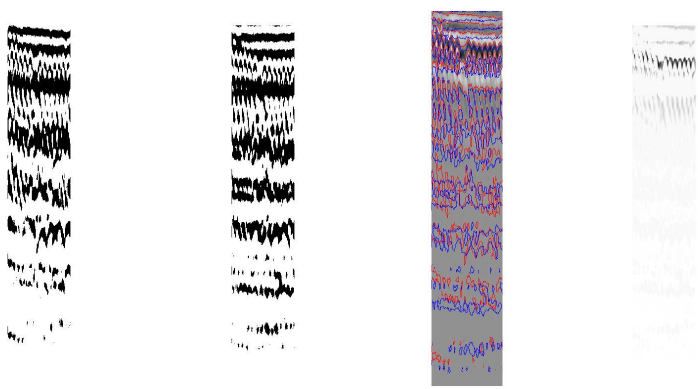

(a) (b) (c) (d)

Fig. 3. (a). Extracted boundaries. (b). Extracted boundaries from another line. (c) Overlapping the extracted boundaries. (d). Intersection results of (a) and (b).

4. Discussions and Conclusion

From the results shown in Fig. 3, the proposed method demonstrates the capabilities to identify the changes of dielectric properties while cracks in concrete occurred. Comparing the intersection part and GPR data collected at different lines, we found out that the information collected under the ground line 80cm is ignored. At the construction work site, there is 80cm thick concrete layer containing pipes and steel rebar. Those cracks in concrete are probably located at the interface between concrete and soil from Fig.3 (d). The proposed method can be used in non-destructive evaluation for large area. The robustness of the proposed algorithm will be discussed in future. Further researches will focus on evaluate the relationship between GPR data and field concrete core-drilled sample.

References

1. A. Benedetto, F. Benedetto, M.R. DeBkasiis and G. Giunta. Reliability of signal processing technique for pavement deamages detection and classification using ground penetration radar, IEEE Sensors Journal, Vol.5, No.3, pp.471-480 (2005).
2. J. Irving and R. Knight. Numerically modeling of ground-penetration radar in 2-D using MATLAB, Computers & Geoscience 32, pp. 1247-1258, (2006).
3. M. Kass, A. Witkin, and D. Terzopoulos, "Snake: Active Contour Model," International Journal of Computer Vision, Vol. 1, pp. 321-331, (1988).
4. S. Kichenassamy *et al.*. "Gradient flows and geometric active contour models," in Proc. 5th International Conference on Computer Vision, Boston, MA., USA., (1995).
5. S. Osher and J. A. Sethian. "Fronts propagating with curvature dependent speed: Algorithms based on Hamilton-Jacobi formulation," Journal of Computational Physcis, Vol. 79, pp.12-49, (1989).
6. R. Kimmel. "Fast Edge Integration," Geometric Level Set Methods in Imaging, Vision, and Graphics, Springer, NY, pp.59-74, (2003).
7. Aubert, G. and Kornprobst, P.. Mathematical Problems in Image Processing: Partial Differential Equations and the Calculus of Variations, Springer, (2001).
8. R. Malladi, J. A. Sethian and B. Vermuri. "Shape Modeling with Front Propagation: A Level Set Approach," IEEE Trans. on PAMI, Vol. 17, No.2, pp.158-175, (1995).
9. Chan, T. F. and Vese, L. A.. "Active Contours without Edges," IEEE Trans. on Image Processing, Vol.10, No.2, pp. 266-277, (2001).

NON-DESTRUCTIVE EVALUATION OF ASPHALT CONCRETE PAVEMENT SYSTEM USING FWD TESTS CONSIDERING MODELING ERRORS

JIN-HAK YI

Korea Ocean Research and Development Institute
Sa-2-dong, Sangnok-gu, Ansan-si, Gyeonggi-do, 426-744, Korea

YOUNG-SANG KIM, JAE-MIN KIM

Chonnam National University
Dundeok-dong, Yeosu-si, Jeonnam, 550-749, Korea

SUNG-HO MUN

Korea Expressway Corporation
Dongtan-myeon, Hwaseong-si, Gyeonggi-do, 445-812, Korea

The structural integrity assessment technique for the asphalt pavement system is studied considering the modeling errors introduced by material uncertainties. To this end, the artificial neural network is utilized to estimate the elastic modulus of soil layers using the measured deflection data from the FWD (Falling Weight Deflectometer) test. A wave analysis program for a multi-layered pavement system is developed based on the spectral element method for more accurate and faster calculation. The developed program is applied for the numerical simulation of the FWD tests, the generation of training and testing patterns for the neural network. The evaluation capability of neural network is investigated when the input data is corrupted by the modeling errors, and it is found that the estimation results can be significantly deviated due to the modeling errors. To reduce the effect of the modeling error, (in other words to improve the robustness of the algorithm), we proposed an alternative scheme to generate the training patterns considering modeling errors, and it is finally concluded that the estimation results can be improved by using the proposed training patterns from extensive numerical simulation study.

1. Introduction

The FWD (Falling Weight Deflectometer) test, which is operated by dropping a certain level of mass and measuring the maximum surface deflections using several sensors by equal spaces, is most widely used to evaluate the structural integrity of asphalt concrete pavement system. And many studies have been carried out to improve the testing method and the evaluation schemes of the conventional FWD test [1-3]. Most commercialized FWD systems are utilizing the regression analysis using a large scale of database and/or the iterative optimization schemes for estimating the elastic modulus of soil layers. In this study, the artificial neural network technique, which is one of the widely used soft computing techniques in civil engineering field, is applied to evaluate the structural integrity of pavement system. In most cases, the modeling errors due to the uncertainties in the material properties such as layer thickness, Poisson ratio, unit weight, and damping ratio were not seriously considered to carry out the inverse analysis using FWD test data. However, it is almost impossible to assign the material properties exactly and therefore it is inevitable to have a certain level of modeling errors. In this point of view, it is very important to investigate the effects of modeling errors considering the uncertainties in the material properties on the maximum deflection data of FWD test. To this end, we carried out the inverse analysis using the artificial neural networks with and without modeling errors utilizing newly developed computer code, WALS (Wave Analysis of Layered System) based on the spectral element method for more accurate and faster calculation. And we proposed an alternative scheme to generate training patterns considering the modeling error to improve the estimation results in the cases where there exists the modeling error.

2. Theoretical backgrounds

2.1. *Spectral element method*

The wave propagation in a multi-layered system can be analyzed using several commercial computer codes such as ABAQUS and ANSYS and also it can be performed using many other specialized codes for wave propagation analysis such as BISAR, CHEVRON, ELSYM5, and WESLEA. Generally, it requires too much computing time to generate a number of training patterns by general-purpose commercial codes. In the contrary, the analysis is carried out inaccurately when we apply the specialized and compact-sized computer codes. Therefore, we developed a new computer code, WALS (Wave Analysis of Layered System), theoretically based on the dynamic stiffness matrix method and

the spectral element method for more accurate and faster calculation [4,5]. The developed software is used to simulate the FWD test, to carry out the reliability analysis, and to generate the training and testing patterns for artificial neural network technique.

2.2. *Artificial neural networks*

In this study, the elastic moduli of soil layers are estimated using a multi-layered perceptron neural network utilizing the maximum deflection data obtained from the FWD test as input data. Error back propagation algorithm is used to train the neural networks and the maximum deflection data and the corresponding elastic moduli are used as input and output (target) data, respectively.

Since theoretical backgrounds of the general training rules for neural networks are referred in many research papers, in this paper, we intended to just introduce the basic concept of noise injection learning algorithm [6], which improves the generalization capability of a neural network by imposing random noise in the input data during training process and is done by a similar scheme with the proposed generation algorithm training patterns considering modeling errors. In the case of the FWD tests, the noise injection learning can be performed by imposing a certain level of random noise (α) to the input data as follows,

$$x_{ij} = f_j^{FWD}(\mathbf{p}_i, \mathbf{h}_i, \mathbf{E}_i, \boldsymbol{\rho}_i, \boldsymbol{\gamma}_i)(1+\alpha) \tag{1}$$

where x_{ij} is the input data, i.e. the maximum deflection at the j-th measuring point of the i-th training pattern, $\mathbf{p}_i$, $\mathbf{h}_i$, $\mathbf{E}_i$, $\boldsymbol{\rho}_i$ and $\boldsymbol{\gamma}_i$ are the amplitude of impact load, layer thickness, elastic modulus, Poisson ratio, and damping ratio of the i-th training pattern, and α is the Gaussian random noise with zero mean and σ standard deviation. In this problem, since we need to estimate the elastic modulus only, the other parameters can be fixed as the representative values, i.e. $\mathbf{p}_i = \mathbf{p}$, $\mathbf{h}_i = \mathbf{h}$, $\boldsymbol{\rho}_i = \boldsymbol{\rho}$, and $\boldsymbol{\gamma}_i = \boldsymbol{\gamma}$. And the function f_j^{FWD} represents the maximum deflection at j-th measuring point by the FWD test. By introducing noise injection learning algorithm to the neural network, the more reliable estimation can be carried out when the measurement data is corrupted by measurement noise. However, the noise injection learning can only reduce the effects of the measurement noise and the noise injection learning is not sufficient to reduce the effects of the modeling errors included in the numerical model. Therefore, we proposed an alternative generation scheme of training patterns considering the modeling errors as follows,

$$x_{ij} = f_j^{FWD}(\mathbf{p}_i(1+\beta_p), \mathbf{h}_i(1+\beta_h), \mathbf{E}_i(1+\beta_E), \boldsymbol{\rho}_i(1+\beta_\rho), \boldsymbol{\gamma}_i(1+\beta_\gamma)) \quad (2)$$

where, β_k is the Gaussian random noise with zero mean and σ_k standard deviation for the k -the material parameter. It can be understood that the equation (1) for the conventional noise injection learning is considering the output errors in the FWD test, while the equation (2) for the proposed generation scheme is considering the input errors in the numerical model.

3. Example analysis

3.1. *Example pavement system*

Four layer pavement system with AC surface, subbase, and subgrade layers, and infinite soil media is considered as an example pavement system as shown in Figure 1. The representative material properties are shown in Table 1. On the other hand, the ranges of the elastic moduli are shown in the parenthesis. Four (4) structural integrity conditions (Table 2) are considered to investigate the evaluation capability of neural network as an inverse analysis tool.

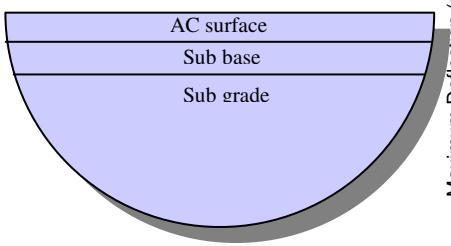

Fig. 1. Example Pavement System

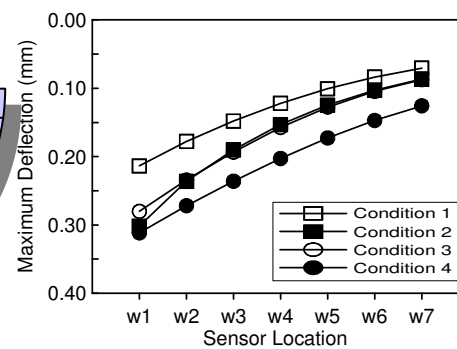

Fig. 2. Comparison of maximum deflection curves for condition I, II, III and IV

Table 1. Modeling Parameters for Pavement System

Parameters	AC Surface	Subbase	Subgrade	Bedrock
Unit weight(kg/m3)	2350	2100	1900	2400
Thickness, H(m)	0.30	0.40	4.30	∞
Elastic modulus, E(MPa)	3500 (150-21000)	350 (150-750)	100 (35-210)	23040
Poisson ratio	0.35	0.40	0.45	0.20
Damping ratio	0.05	0.02	0.05	0.05

Table 2. Elastic modulus for integrity conditions

Conditions	Elastic modulus, E (MPa)			Description
	AC Surface(E1)	Subbase(E2)	Subgrade(E3)	
I	10000	500	150	Healthy condition
II	5000	450	120	Poor surface
III	8000	250	120	Poor subbase
IV	8000	450	50	Poor subgrade

3.2. *Inverse analysis using neural networks*

The neural network consists of four layers, i.e. input layer, two hidden layers, and output layer, and each layer consists of 7, 15, 10 and 3 neurons, respectively. The maximum deflection values for the seven measuring points and the elastic moduli for three (3) pavement layers are utilized as the information for input layer and output layer. Therefore each training pattern consists of seven input values (maximum deflections) and the three target values (elastic moduli). The minimum number of training patterns is decided as 1000, which is recommended by [7,8] as about two times of the number of total synaptic weights. Table 3 show the estimation results for the structural integrity conditions I, II, III and IV by using the numerical simulation data without modeling error. These results are obtained for the ideal cases, i.e. no modeling error exists, and it can be easily found that the estimation is very successfully carried out with very small estimation errors, i.e. maximum 6.3% for AC surface layer, maximum 26.5% for sub-base layer, and maximum 5.14% for the base layer. It can be concluded that the neural network can be a useful tool for inverse analysis using FWD test data when no modeling error exists.

Table 3. Estimation results by neural network without modeling error

	Conditions	I	II	III	IV
AC Surface	$E_{estimated}$ (MPa)	9337	5214.4	7940	8078.9
	E_{target} (MPa)	10000.00	5000.00	8000.00	8000.00
	Error (%)	6.63	-4.288	0.75	-0.986
Subbase	$E_{estimated}$ (MPa)	459.75	492.13	316.25	462.23
	E_{target} (MPa)	500.00	450.00	250	450.00
	Error (%)	8.05	-9.362	-26.5	-2.72
Subgrade	$E_{estimated}$ (MPa)	142.29	114.5	114.59	49.447
	E_{target} (MPa)	150.00	120.00	120.00	50.00
	Error (%)	5.14	4.583	4.508	1.106

Figure 3 shows the comparison of the estimation results by the conventional neural networks which is used for obtaining the results in Table 3 (denoted as NN-A, herein) and by the neural network trained using the training patterns newly proposed to consider the material uncertainties (see Eq. 2) (denoted as NN-B) when the testing patterns are simulated with modeling error. In the case of AC surface layer, the estimation errors are up to in the range of 5-12% by using conventional neural network (i.e. NN-A), and the estimation error is reduced to under 4% by adopting NN-B. In the cases of subbase and subgrade layers the estimation errors are also slightly reduced. It can be concluded that (1) the estimation error can be increased significantly when modeling error exists and (2) the proposed generation scheme of training patterns can handle the modeling error very effectively.

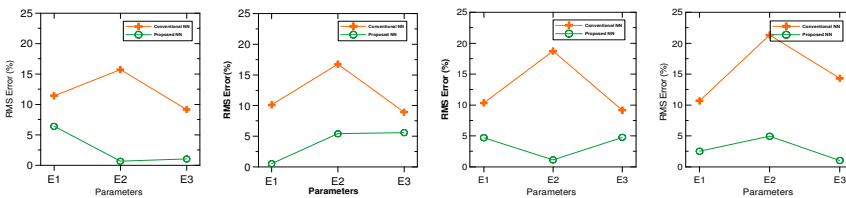

(a) Condition I (b) Condition II (c) Condition III (d) Condition IV

Fig. 3. Estimation results by neural network

Figure 4 shows the estimation results by NN-A and NN-B for each integrity conditions with and without noises. It can be found that the elastic modulus can be under estimated up to 20%. However, the estimation errors can be reduced for all layers by introducing the generation scheme of training patterns accounting for the uncertainties in material properties.

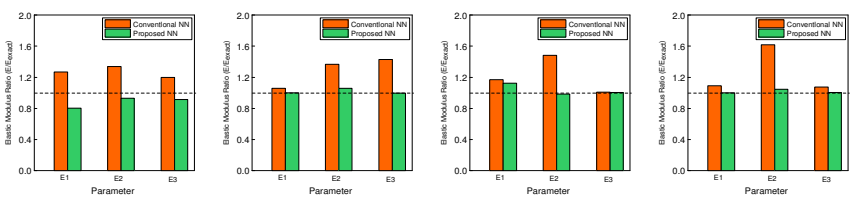

(a) Condition I (b) Condition II (c) Condition III (d) Condition IV

Fig. 4. Example of estimation results for conditions I, II, III, and IV with modeling errors of 5%

4. Concluding remarks

In this study, we proposed the alternative generation scheme of training patterns by extending the conventional noise-injection learning algorithm to consider the

material uncertainties for improving the robustness of the neural network technique as an inverse analysis tool for the FWD test. It was found that the modeling error can increase the estimation error significantly, and the proposed scheme could handle the modeling error very effectively.

Acknowledgment

This study is financially supported from Korea Expressway Corporation, and the authors would like to express our sincere appreciation to the supports.

References

1. R.Y. Liang, J.X. Zhu, Dynamic analysis of infinite beam on modified Vlasov subgrade, J. of Transportation Engineering, ASCE, 121(5), 434-442, 1995.
2. Y.G. Kim, Y.R. Kim, Layer moduli prediction of asphalt concrete pavements using artificial neural network, KSCE Journal of Civil Engineering, 2(4), 467-479, 1998.
3. R. Al-Khoury, A. Scarpas, C. Kasbergen, and J. Blassuwendraad, Spectral element technique for efficient parameter identification of layered media, Part II: Inverse calculation, Int. J. of Solids and Structures, 38, 8753-8772, 2001.
4. C.B. Yun, J.M. Kim, C.H. Hyun, Axisymmetric elastodynamic infinite elements for multi-layered half-space, Int. J. Num. Meth. Eng., 38, 3723-3743, 1995.
5. R. Al-Khoury, A. Scarpas, C. Kasbergen, and J. Blassuwendraad, Spectral element technique for efficient parameter identification of layered media, Part I: Forward calculation, Int. J. of Solids and Structures, 38, 1605-1623, 2001.
6. K. Matsuoka, Noise injection into inputs in back-propagation learning, IEEE Trans. Systems, Man, and Cybernetics, 22(3), 436-440, 1992.
7. V.N. Vapnik, A.Ya. Chervonenkis, On the uniform convergence of relative frequencies of events to their probabilities, Theory of probability and its applications, 16(2), 264-280, 1971.
8. C.B. Yun, E.Y. Bahng, Substructural identification using neural networks, Computers & Structures, 77(1), 41-52, 2000.

NONDESTRUCTIVE IDENTIFICATION OF FATIGUE CRACKING IN A COMPOSITE ACTUATOR WITH A PZT CERAMIC DURING ELECTROMECHANICAL CYCLIC LOADING

Sung-Choong Woo[†]

Artificial Muscle Research Center, Konkuk University, 1 Hwayang-dong, Gwangjin-gu, Seoul 143-701, Republic of Korea
lilsuzy@hanyang.ac.kr

Nam Seo Goo

Intelligent Microsystem Program, Department of Advanced Technology Fusion, Konkuk University, 1 Hwayang-dong, Gwangjin-gu, Seoul 143-701, Republic of Korea
nsgoo@konkuk.ac.kr

Information on the onset and evolution of damage within materials is essential for guaranteeing the integrity of actuator systems. This work describes an investigation into the feasibility of using an acoustic emission (AE) technique to evaluate the integrity of a composite actuator with a PZT ceramic under electromechanical cyclic loading. The detected AE signals during the cyclic tests have been analyzed in terms of the behavior of the AE count rate and waveform in association with the performance degradation of the composite actuator. After the test, fatigue damages were observed with the aid of a scanning electron microscope. The results show that the fatigue cracking of the composite actuator with a PZT ceramic occurred in the PZT ceramic layer, and that the performance degradation caused by the fatigue damage varied immensely depending on the existence of a protecting composite bottom layer. The results also confirm that the evolution of fatigue damage in the composite actuator with a PZT ceramic can be nondestructively identified via in situ AE monitoring and microscopic observations.

Keywords: Fatigue cracking; piezoelectric composite actuator; acoustic emission; waveform.

1. Introduction

Due to their outstanding displacement performance and high load capability, piezoelectric actuators are widely used in the tail wing of micro air-vehicles,

[†]Corresponding author.

micro-pumps for drug delivery systems and synthetic jet actuators, as well as in other fields of biomimetic fish robots. The performance of piezoelectric composite actuators, in particular, can be manipulated and maximized by controlling the stacking sequence during their hand layup procedures or by controlling drive frequencies and applied electric fields during the actuation process. However, the constituent PZT ceramic is susceptible to fracturing or cracking on account of the inborn high brittleness. The accumulation of fatigue cracking in piezoelectric composite actuators results in a significant reduction in performance, ultimately leading to failure. Piezoelectric actuators are usually subjected to a prolonged out-of-plane cyclic condition. Thus, an experimental investigation of the initiation and evolution of fatigue cracks is necessary for gaining a better understanding of the safety and integrity of piezoelectric actuators. In previous studies, we have successfully used an acoustic emission (AE) technique to elucidate the fracture process of plate-type piezoelectric composite actuators under a mechanical bending load [1,2].

We now present an AE-based nondestructive evaluation technique to obtain information on the initiation and propagation of electromechanically induced fatigue cracks in composite actuators with a PZT ceramic [3]. In this experiment, no artificial pre-notches are introduced. After the fatigue tests, we identified the fatigue failure mechanisms by analyzing the characteristics of the AE count rate and signal waveforms.

2. Experimental

2.1. *Preparation of samples*

As illustrated in Fig. 1, two different layup sequences were used to fabricate the actuating samples. Sp#1 consists of four layers without a bottom layer, whereas sp#2 consists of five layers with a glass-epoxy bottom layer that protects the PZT ceramic. The samples were manufactured with woven fabric carbon-epoxy prepregs (WSN1K-B), woven fabric glass-epoxy prepregs (GEP108), and a PZT ceramic (3203HD). Details of the material properties and the actuating mechanism can be found in [4] and [5]. Samples laminated in a hand layup procedure were co-cured at a temperature of 177 °C in an autoclave in accordance with the curing cycle for three hours.

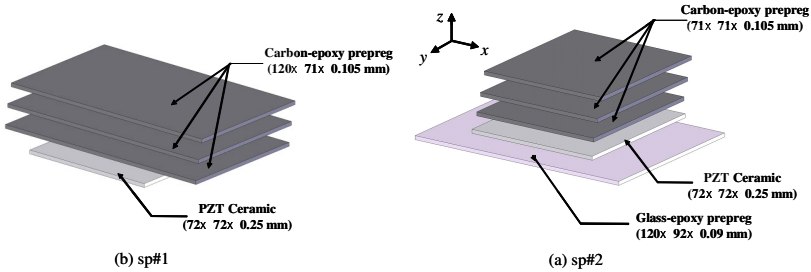

Fig. 1. Schematic of actuating samples used in fatigue tests.

2.2. *Fatigue Tests*

As illustrated in Fig. 2, we placed the samples on two supporting jigs separated by a distance of 72 mm. We then performed fatigue tests until 10^7 cycles by providing an electric field for the embedded PZT ceramic through a high-voltage signal function generator (TD-2 Power Supplier), which was connected to a digitizing oscilloscope (HP 54622A). Next we applied a mechanical loading to the upper surface of the sample by using a weight of 2 N. The samples were excited at their resonance frequencies with an AC input voltage equivalent to a peak-to-peak voltage of 300 V_{pp} in the form of a sinusoidal wave. The resonance frequencies were determined experimentally to be 24 Hz for sp#1 and 13 Hz for sp#2. The mean values of the electric fields were set at zero; thus, an amplitude ratio of $R = E_{min}/E_{max} = -1$ prevails. The flexural actuating displacement was obtained at the center of the samples by using a noncontact laser displacement system (Keyence LK-081). We tested three samples for each actuator type, and the result presented here is a typical one.

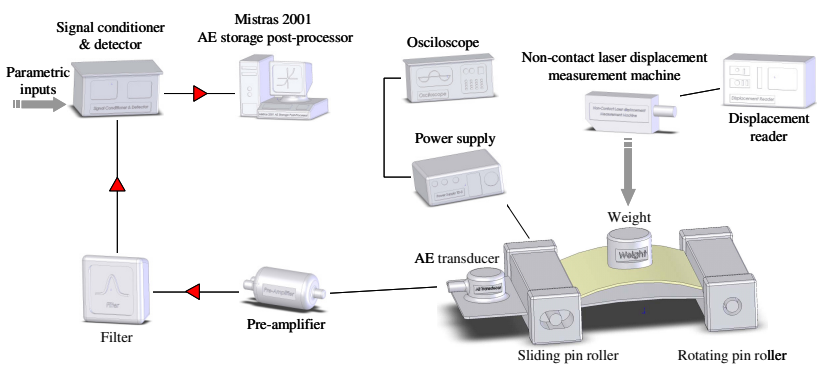

Fig. 2. Schematic of the experimental arrangement for fatigue tests with AE monitoring.

2.2. *In situ AE monitoring and fractography*

In situ monitoring of fatigue damages within the samples was accomplished with the aid of the AE signal acquisition and processing package MISTRAS 2001 of Physical Acoustics Corporation. An AE sensor was attached to one side of the test sample by means of a coupling agent. Pre-amplification of 40 dB and band-pass filtering of 10 kHz to 1200 kHz were performed by a pre-amplifier. For the AE acquisition parameters, we used a threshold level of 45 dB, a sampling rate of 4 MHz, and a hit lockout time of 1 ms. Pencil lead break tests were performed for the calibration of the applied setup. We then monitored the AE signals in real time as the actuating displacement was recorded. The monitoring continued until the number of cycles reached 10^7 or until the sample finally failed. After the tests, we carefully disassembled the samples to avoid any damage and then we inspected the damage in the PZT ceramic layer by means of a scanning electron microscope (SEM).

3. Results and discussion

Fig. 3 shows a typical displacement–cycle curve as well as the behavior of the AE count rate for sp#1 and sp#2. The AE count rate in Fig. 3 is defined as the number of AE event hits every 10^5 cycles. In the case of sp#1, the initial actuating displacement was 4.58 mm. There was no displacement reduction or any AE signals before 3.0×10^5 cycles. However, a high AE count rate occurred together with a 20 % reduction in actuating displacement at 3.0×10^5 cycles, suggesting the initiation of fatigue damage in sp#1. Subsequently, the actuating displacement degradation continued at a much slower rate until 4.3×10^6 cycles and the AE count rate was low. After that, the actuating displacement decreased again immensely at a maximum count rate, indicating the occurrence of critical damage such as cracking. This phenomenon is discussed later. Sp#1 reached the final failure at 5.2×10^5 cycles because of fatigue cracking and short-circuiting in the PZT ceramic layer, which was visible to the naked eye. In the mean time, a relatively intermediate AE count rate was detected after 4.3×10^6 cycles. At the final failure of sp#1, the actuating displacement was 1.84 mm, which was approximately 60 % less than the initial actuating displacement of 4.58 mm. Hence, the use of sp#1 without the bottom protecting layer yields a significantly lower actuating displacement.

In the case of sp#2, as shown in Fig. 3(b), the actuating displacement is almost constant before 1.5×10^6 cycles and there were no detectable AE events, suggesting that no fatigue damage has yet occurred in sp#1. The AE signal became detectable at 1.5×10^6 cycles, where a high AE count rate was observed. At this time, the actuating displacement dropped by 8.14 % below the initial

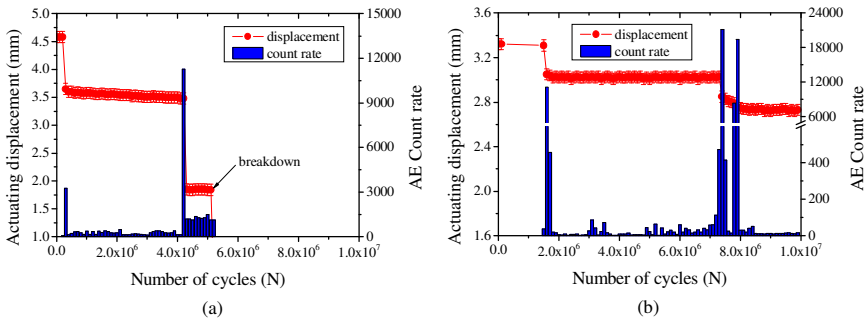

Fig. 3. Actuating displacement versus the AE count rate with an increasing number of cycles for (a) sp#1 and (b) sp#2.

actuating displacement of 3.32 mm. As the number of cycles increased to $7.4\text{x}\ 10^6$ cycles, the drop in displacement was not large and the activity in the AE count rate was not conspicuous but showed only a slight variation. Hence, the initiation and evolution of fatigue damage is not active in sp#2 during the cycles. From $7.4\text{x}\ 10^6$ cycles to 10^7 cycles, the AE count rate is occasionally high and there is reduction in displacement. Even with the passing of 10^7 cycles, sp#2 is well actuated without a significant reduction in the actuating displacement and without any failure. At 10^7 cycles, the measured value of the actuating displacement was 2.73 mm, which is approximately 17.8 % less than the value of the initial actuating displacement of 3.32 mm. It thus appears that the protecting bottom layer delays the growth of fatigue damage or stops cracks from propagating in the PZT ceramic layer.

Fig. 4 shows the SEM observations of sp#1. In Fig. 4(a), we can see the unfatigued surface of sp#1 with its undamaged grains and boundaries. In Fig. 4(b), we can see that when the fatigued surface is loaded up to $1.6\text{x}\ 10^6$ cycles the transgranular micro-damage is dominant. In contrast, Fig. 4(c) shows the propagation of conspicuous intergranular fatigue cracking along the grain boundaries. Additionally, we can see that the surface of the PZT ceramic is melted down by a high electric field on either side of the fatigue cracking, though, aside from the cracking, the transgranular fatigue damage is still extensive in other areas. Thus, the high AE count rate at $4.2\text{x}\ 10^6$ cycles, as shown in Fig. 3(a), may be due to the intergranular cracking on the PZT ceramic layer. Figure 4(d) shows many pits, pores and dimples induced by short-

circuiting in the PZT ceramic layer during the final failure. No superficial damage was observed in the fiber composite layer of either sp#1 or sp#2.

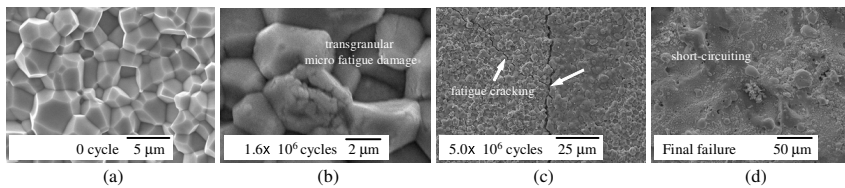

Fig. 4. SEM images for sp#1: (a) the unfatigued surface of PZT ceramic (b) micro-damage in the grain of a PZT layer, (c) fatigue cracking and (d) pores and dimples caused by short-circuiting.

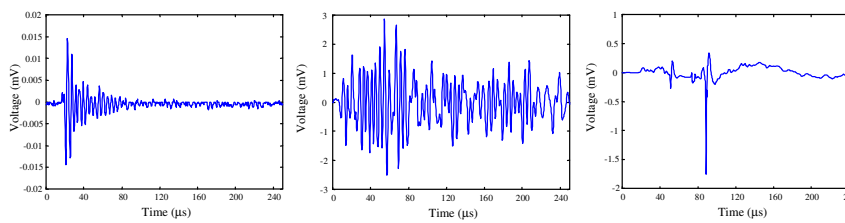

Fig. 5. Typical waveforms corresponding to the fatigue failure modes: (a) transgranular micro-damage, (b) intergranular fatigue crack propagation and (c) breakdown by short-circuiting.

The signals from the specimens are classified into three types on the basis of the waveform and signal voltage, and the typical waveforms are plotted in Fig. 5. As shown in Fig. 5(a), type A, which was detected during the entire cyclic test, is a burst-type signal showing a shortly rising and slowly decaying waveform with a comparably low voltage. In contrast, type B, which was detected only after $4.2\text{x}\ 10^6$ cycles, exhibits a continuous-type signal with a very high voltage. We suggest, therefore, that a waveform such as type A, as displayed in Fig. 4(b), is formed due to the weak emissions that originate from the transgranular micro-damage in the PZT ceramic layer, and that type B is possibly formed, as shown in Fig. 4(c), due to the intergranular cracking along the grain boundary during the fatigue crack propagation. Type C, on the other hand, which was detected only at the breakdown of sp#1 due to short-circuiting, shows a burst and continuous type signal with a high voltage. Note also that sp#2 showed few type

B signals and no type C signals. Hence, as stated already, the lack of intergranular cracking and short-circuiting in sp#2 may be due to the way the glass-epoxy bottom layer restrains the crack propagation.

4. Conclusions

By analyzing the behavior of the AE event rate and the signal waveform, we were able to elucidate the fatigue damage mechanism of a composite actuator with a PZT ceramic under electromechanical cyclic loading. The initial fatigue damage of the composite actuator with a PZT ceramic was caused by the transgranular damage in the PZT ceramic layer; the final failure was caused by the main crack propagation induced by a combination of intergranular damage and short-circuiting. As the number of cycles increased, a noticeable reduction in displacement coincided with a high AE count rate. The transgranular damage is related to a burst-type signal with a low voltage. Continuous-type signals with an intermediate voltage are due to intergranular cracking. The short-circuiting shows the characteristics of a burst-type signal and a continuous type-signal with a high voltage. Our results confirm that the AE technique is applicable to the health monitoring of a composite actuator with a PZT ceramic, particularly when the actuator is subjected to fatigue caused by a combination of external cycling mechanical loading and internal electrical actuation.

Acknowledgments

The present work was supported by the Korea Research Foundation Grant (KRF-2006-005-J03302). The authors appreciate this financial support.

References

1. Woo SC, Goo NS. Analysis of the bending fracture process for piezoelectric composite actuators using dominant frequency bands by acoustic emission. Compos Sci Tech 2007;67(7):1499–1508.
2. Woo SC, Goo NS. Identification of failure mechanisms in a smart composite actuator with a thin sandwiched PZT plate based on waveform and primary frequency analyses. Smart Mater Struct 2007;16(4):1460–1470.
3. Eitzen DG, Wadley HNG. Acoustic emission: establishing the fundamentals. J Res Natl Bureau Stand 1984;89(1):75–100.
4. Woo SC, Goo NS. Prediction of actuating displacement in a piezoelectric composite actuator with a thin sandwiched PZT plate by a finite element simulation. J Mech Sci Tech 2007;21(3):455–464.

5. Woo SC, Park KH, Goo NS. Influences of dome height and stored elastic energy on the actuating performance of a plate-type piezoelectric composite actuator. Sensor Actuat A 2007;137(1):110–119.

ESTIMATION OF MECHANICAL PROPERTIES OF CONCRETE FROM THE DRILLING RESISTANCE PARAMETERS

SOO-HO CHANG, SOON-WOOK CHOI, GYU-JIN BAE

Underground Structure Research Division, Korea Institute of Construction Technology, 2311, Daehwa-dong, Ilasan-gu, Goyang, Gyeonggi, 411-712, Republic of Korea

JUN-HWAN LEE

Department of Civil Engineering, Yonsei University, 134, Sinchon-dong, Seodaemun-gu, Seoul, 120-749, Republic of Korea

For the quick rehabilitation of a damaged concrete structure, it is important to rapidly and thoroughly investigate the damaged zone. This study proposes a new drilling resistance method by which the mechanical properties of concrete materials can be easily and quickly estimated. Especially, it also aims to derive the optimum testing conditions as well as the relationships between drilling parameters and mechanical properties. As a result, the favorable relationships between actual mechanical properties and drilling resistance parameters were successfully obtained. Compared to some conventional non-destructive testing methods, the proposed testing method allows the estimation of the mechanical properties of concrete and mortar materials with higher accuracy.

1. Introduction

Concrete materials can be as severely damaged and deteriorated by the high temperatures during a fire as other artificial materials [1]. In a real fire, the amount of heat transferred from an initial fire-exposed surface to the inner part of a concrete structure is highly dependent on the structure's thermal properties. As a result, the remaining concrete that is far from the initial surface may be sound even though the near-surface areas are severely damaged. This fact prevents the existing non-destructive tests from being applied to fire-damaged concrete. Generally, in order to estimate the extent of a fire-damaged zone and its temperature history, differential thermal analysis, X-ray diffraction analysis, thermogravimetric analysis and neutralization test have been carried out along with mechanical tests just after obtaining core specimens directly from a damaged concrete structure [2]. From the tests, it is possible to quantitatively and reliably evaluate the fire-damaged zone within a structure. However, the time-consuming tests retard the prompt rehabilitation of a damaged structure.

Moreover, the biggest problem is that several core specimens with the diameter of 100 mm are necessary for an accurate diagnosis.

Therefore, the rapid evaluation of a fire-damaged concrete structure may be crucial and important for economic and rapid rehabilitation. Especially, different damage levels in the direction of structural thickness should be continuously evaluated. This study aims to develop a new drilling resistance method by which to quickly and easily obtain continuous results related to damage in a perpendicular direction to the surface of a structure. It also aims to make a portable machine for the drilling resistance test and to determine the optimum testing conditions. Finally, the study intends to derive the relationships between drilling resistance and the mechanical properties of concrete from a series of tests.

2. Proposal for the Drilling Resistance Test

2.1. *Concept*

The drilling resistance of concrete material is highly dependent upon several drilling parameters such as drill penetration rate, rotational speed, thrust, and the type of drill bit used. Therefore, the fundamental procedure is to determine the drilling resistance index with the high sensitivity to the material condition as well as the high compatibility with a small-sized drilling machine. In this study, the drill bit and rotational speed were considered as constant testing conditions for simplicity. When drilling thrust is considered to be constant, the resultant penetration rate can be utilized as a drilling resistance index. However, the testing machine should be provided with a high enough thrust range capability to be compatible with high strength concrete, so it can be concluded that such a testing concept is not suitable for a portable drilling rig. On the other hand, in a testing condition with a constant drill penetration rate, the reaction force normal to the drilling surface and the resultant torque can be easily measured and interpreted only if a high capacity transducer is introduced.

2.2. *Drilling Resistance Testing Machine*

The prototype for the drilling resistance testing machine under a constant penetration rate and rotational speed was newly manufactured to derive the relationships between drilling resistance indices and the mechanical properties of concrete (Fig. 1). The main specifications are summarized in Table 1. During a drilling test, reaction force, torque and bit penetration depth are continuously monitored by load cell, torque cell and LVDT respectively.

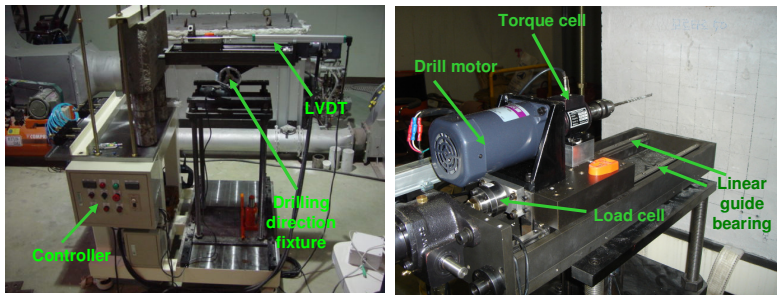

Fig. 1. Drilling resistance testing machine.

Table 1. Specifications of drilling resistance testing machine.

Parts	Main specifications
Load cell	Maximum capacity: 1,962 N
Torque cell	Maximum capacity: 490.5 N·cm
Drill motor	Power: 220 W Maximum RPM: 1,550 rpm
Speed motor (to control penetration rate)	Power: 90 W Maximum RPM: 1,250 rpm
LVDT	Maximum capacity: 30 cm

3. Drilling Resistance tests

3.1. *Testing Conditions*

In this study, a total of sixteen 0.6×0.6×0.4 m rectangular specimens were cured to derive the optimum testing condition as well as the relationships between drilling resistance and the mechanical properties of a cementitious material. For comparisons, the Schmidt hammer test and ultrasonic velocity measurements were performed on each specimen in addition to the drilling resistance tests.

3.2. *Optimum Testing Condition*

To obtain the optimum testing condition, a series of drilling resistance tests were conducted for homogeneous mortar. From the tests, it was revealed that torque with large variations is too sensitive to minute shock or microscopic structures to be utilized as a drilling resistance index (Fig. 2). In this study, only reaction forces were interpreted as drilling resistance by excluding torque from the drilling data. From the measurement of drilling reaction forces at different RPMs, it was shown that the maximum penetration depth proportionally increased as the RPM increased. Considering that the required investigation depth is more than 10 cm in a severe fire and the allowable RPM of the manufactured drilling

machine is 1,550 rpm, the rotational speed in this study was set to 1,300 rpm (Fig. 3).

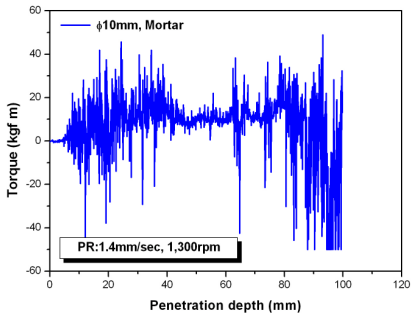

Fig. 2. Torque variations during drilling.

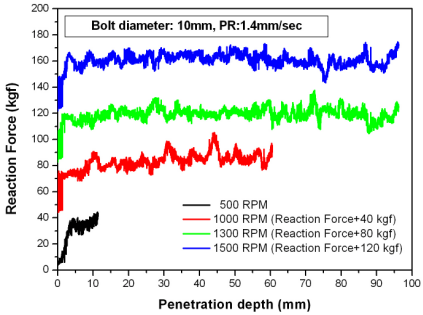

Fig. 3. Effect of RPM on drilling reaction force.

The effects of drill bit diameter and penetration rate on the measured data were investigated under nine testing conditions. The conditions include three-different penetration rate conditions for three kinds of drill bit diameter. When the diameter of the drill bit was 10 mm, the deviation of the measured reaction forces became minimal (Fig. 4). The deviation was also minimal in case of the penetration rate of 1.4 mm/sec for every bit diameter condition (Fig. 4). From the tests, it was confirmed that the most suitable testing conditions are a penetration rate of 1.4 mm/sec, 1,300 RPM, and a bit diameter of 10 mm for a given machine capacity.

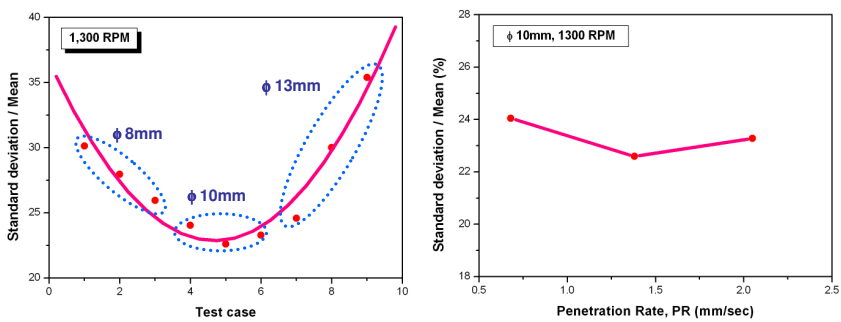

Fig. 4. Effects of bit diameter and drill penetration rate on the deviation of test results.

3.3. *Relationships between the Drilling Resistance and Mechanical Properties of a Cementitious Material*

Although it was almost impossible to derive a clear relationship to estimate the elastic modulus of mortar from the existing non-destructive tests, the definite

linear relationships between drilling reaction force and the mechanical properties of mortar were observed with much higher coefficients of determination over 0.91 from regression analyses (Fig. 5).

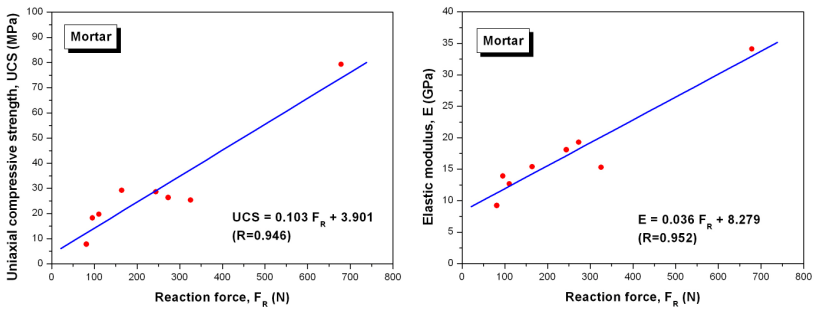

Fig. 5. Derived relationships between reaction force and the mechanical properties of mortar.

The fact that concrete includes randomly distributed coarse aggregates made it impossible to apply the reaction force as a drilling resistance index. The probable reason is that aggregates are produced from a hard rock material, and it takes more energy to drill them than is required by the concrete base matrix. To consider the effect of coarse aggregates on the mechanical properties, a drilling energy concept was introduced to concrete (Fig. 6).

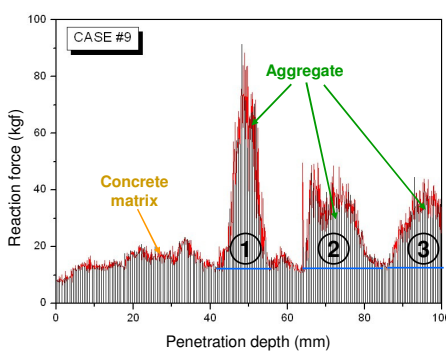

Fig. 6. Drilling energy concept to consider the effect of coarse aggregates within concrete.

First, the total area is calculated by integrating a recorded reaction force graph for the whole penetration depth. Second, the area below the average reaction force for the concrete base matrix without aggregates is separately calculated. Then, the amount of reaction energy contributed to aggregates is determined by subtracting the concrete base area from the total area. The reaction energy solely from aggregates depends on the number of aggregates

encountered while drilling. Therefore, the normalized aggregate reaction energy is calculated by dividing the aggregate reaction energy by the encountered number of aggregates. Finally, the normalized reaction energy for concrete is defined as the sum of the normalized aggregate reaction energy and the concrete base energy (Fig. 6).

When the drilling energy concept was applied, good relationships between the normalized reaction energy and the mechanical properties of concrete were successfully derived (Fig. 7). As was the case with mortar, their correlations were much better than those of other non-destructive tests. These results show the high applicability to estimate mechanical properties of concrete based on drilling energy.

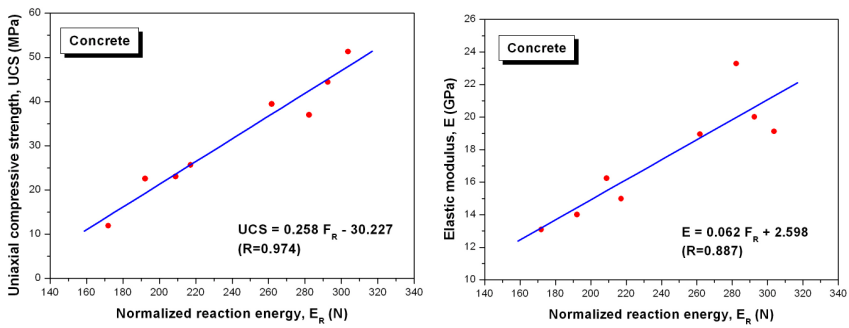

Fig. 7. Relationships between reaction energy and the mechanical properties of concrete.

4. Conclusions

In this study, a drilling resistance testing method was newly proposed to estimate the mechanical properties of concrete in a perpendicular direction to the surface of structure. From a series of tests, it was proven that the proposed method yields a better correlation than the conventional testing methods. It is expected that higher accuracy will be obtained when additional data is introduced.

Acknowledgments

This work was supported by grant no. C03-02 from the Korean Ministry of Construction and Transportation.

References

1. G. A. Khoury, *Tunnels & Tunnelling International.* **November**, 40 (2002).
2. R.M. Faure, V. Pozzi, C. Trasino and G. Hemond, *Proc. of ITA-AITES.* **1**, TS4A4 (2002).

IMPLEMENTATION OF BENDER ELEMENTS FOR MEASURING STIFFNESS CHANGES OF CONCRETE MATERIALS DUE TO CRACKING

ZU-OG AN

Department of Civil Engineering, Kyung Hee University
Seochun-dong, Kiheung-ku, Yongin-si, Gyeonggi-do, 446-701, Korea

WOO-SEOP SHIN

Manager, Civil Division, Samsung Corporation
Bundang-ku, Sungnam-si, Gyeonggi-do, 463-824, Korea

EUI-SEUNG HWANG

Department of Civil Engineering, Kyung Hee University
Seochun-dong, Kiheung-ku, Yongin-si, Gyeonggi-do, 446-701, Korea

YOUNG-JIN MOK

Department of Civil Engineering, Kyung Hee University
Seochun-dong, Kiheung-ku, Yongin-si, Gyeonggi-do, 446-701, Korea

Bender elements, composed of thin piezo-ceramics and elastic shims have been used as miniature actuators and receivers to measure stiffness(p-wave or s-wave velocities) of granular materials. To expand their implementation to as hard a material as concrete, the basic structure of the element would be modified. The most suitable bender elements were developed by adding an extra compressible layer to the element. To verify the applicability to concrete material, three pairs of bender elements were buried at three different locations in a concrete beam before casting of concrete and p-wave measurements were carried out during concrete curing and as cracks developed under load increment. P-wave velocity dropped abruptly at the initiation of cracking and was decreased as gradually as cracks progressed. The results indicate the pattern of the stiffness decrement can be correlated with the geometry of cracks.

1. Introduction

Bender elements, composed of piezo-materials and metal shims, have favorable features for instrumentation such as simple principle of energy conversion, excellent control capability and small physical size. They have been used as miniature actuators and receivers to measure stiffness (p-wave or s-wave

velocities) of geotechnical materials [1]. To expand their implementation to as hard a material as concrete, the basic structure of the element would be modified. To verify their applicability to concrete material, modified elements were installed in concrete test specimen and used to measure stiffness changes of concrete due to cracking.

2. Bender Element

A bender element consists of two piezoceramic sheets sandwiching a central metal shim as shown in Figure 1. Bender elements can be made into various shape, size, and arrangement of piezoceramic sheets and metal shims. They can be optimized with proper shape, thickness and material stiffness depending upon usage purposes. Figure 2 shows the process of manufacturing a bender element by cutting a piezoceramic sheet into proper size, bonding components, connecting electrodes and coating.

The bender element can bend as piezoceramic sheet on one side expands while the other side contracts with an applied voltage. Expanding and contracting of the sheets are reversed as the direction of the voltage is changed. Thus, application of an AC voltage enables the element vibrate and be used as an actuator. On the other hand, if the element is deformed by outside force, it generates voltage and can be used as a receiver.

There are two types of bender elements: series-connected and parallel-connected. With the same voltage applied, the parallel-connected bender element generates twice the tip displacement as the series-connected bender element. On the other hand, series-connected bender elements can generate twice the voltage as parallel bender elements under the same deformation.

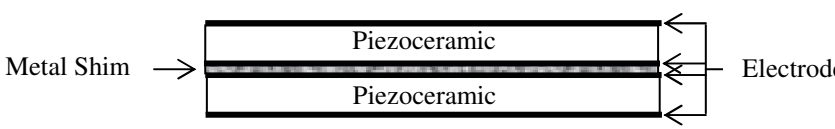

Fig. 1. Structure of a bender element.

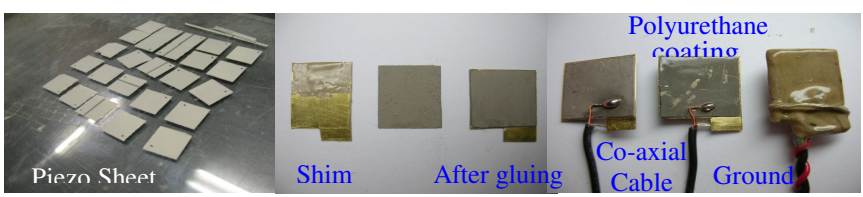

Fig. 2. Manufacturing process of a bender element

Thus, parallel-connected bender elements are used as actuators (source) while series-connected bender elements are better suited as receivers [2].

3. Modification of Bender Element

The bender element has been used to measure the properties of granular materials, whose compressibility allows the element to bend. Concrete is relatively incompressible and the bender element needs a modification so that it can wiggle (flexural action). That is, a compressible layer was added to one side of the element so as to supply a room, as shown Figure 3. The other side of the element would contact intimately with surrounding concrete.

Several different materials, such as polyurethane, wax, shrinkage tube and polyester, were attempted for as a compressible layer. Each element with different type of compressible layer was tested in plaster, which sets quickly and enables to be recovered easily for another use. The signals, as shown Figure 4, are p-waves measured with the elements buried in plaster 10cm apart and exited with the voltage of about 30 volts and the frequency of 30-40 kHz. The polyester turned out to be the best compressible layer. The p-wave arrival times, indicated by an arrow as shown in the figure, are very distinct to identify. P-wave velocity of the plaster was about 3400 m/sec. and Poisson' ratio was 0.25 from the accompanying measurement of shear waves.

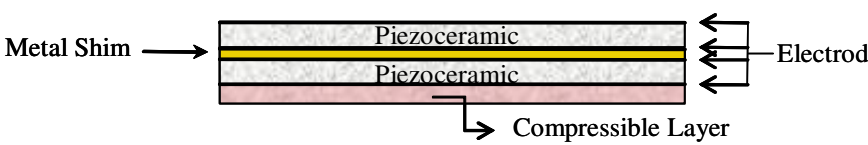

Fig. 3. Structure of modified bender element.

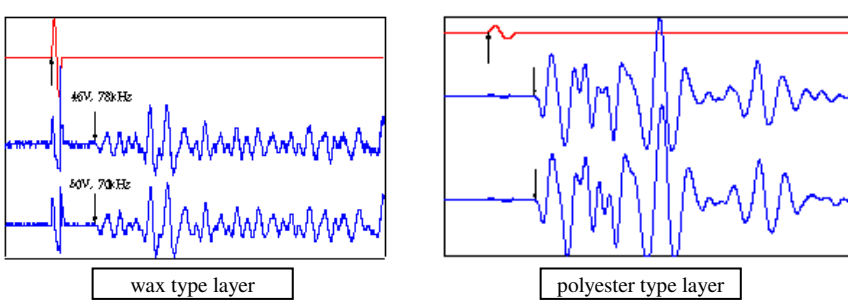

Fig. 4. P-wave signals measured in plaster.

4. Concrete Beam Tests

To verify the applicability of modified bender elements to concrete material, a concrete beam specimen was manufactured and tested. Concrete beam specimen is 2,400mm long, 200mm wide and 350mm deep. Materials used in the specimen are conventional concrete and reinforcing steel.

Three pairs of bender elements were buried at three different locations in a concrete beam as shown in Figure 5. P-wave measurement tests were carried out in two stages. In the first stage, tests were done during concrete curing to find out the status of concrete hardening. After fully hardened, in the second stage, tests were done as the crack developed under the loading.

Figure 6 shows the variation of p-wave velocity during concrete curing. It shows dramatic changes of velocity during the first 24 hours of curing and gradual increase after. These results are well agreed with the result in the reference [3]. It can be concluded that the bender elements can be applied to concrete material and measured wave velocities are sufficiently accurate.

After fully cured, the concrete specimen was loaded for the crack to be developed. To initiate the crack between the actuators and receivers, wooden

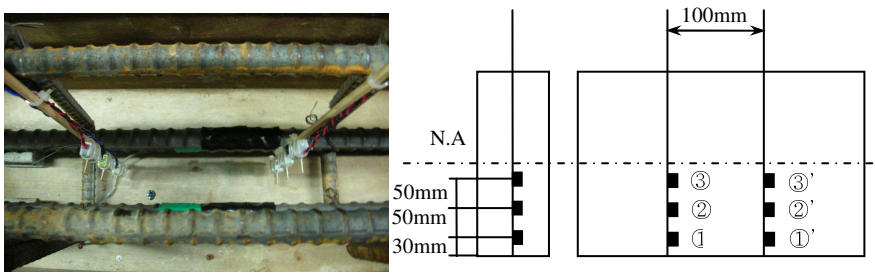

Fig. 5. Installation of bender elements

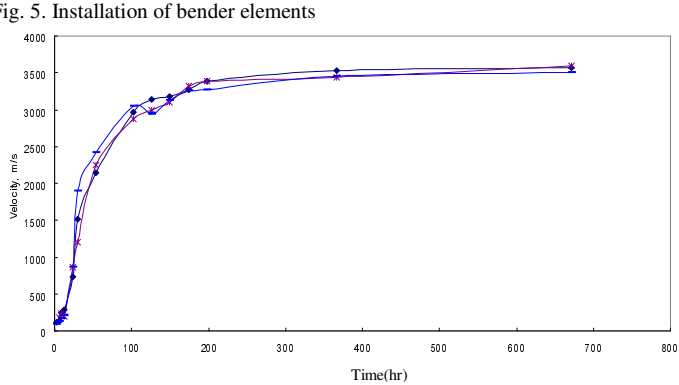

Fig. 6. Measured p-wave velocity during concrete curing

wedge were placed at the bottom center of the beam. The beam was loaded with two loading pistons generating the same force, as shown in Figure 7.

Figure 8(a) shows the velocity changes as the load increases and crack develops. The first crack between the actuators and receivers were detected at the load level of 32.5 kN. At the initiation of cracking, P-wave velocity dropped abruptly and it is due to the fact that the propagation ray path circumventing cracks between the actuator and the receiver becomes longer as the crack develops. However, as the load increases after crack initiation, the P-wave velocity decreases gradually. It may be due to the fact that new cracks develop rather than the depth of the first crack gets deeper as the load increases. Figure 8(b) shows the relationship between the P-wave velocity and the measured crack depth. From the comparison of the P-wave velocity between each sensor (① ⇒ ①′, ① ⇒②′, ③ ⇒③′), the pattern of the stiffness decrement can be correlated with the geometry of cracks.

Fig. 7. Loading of test beam

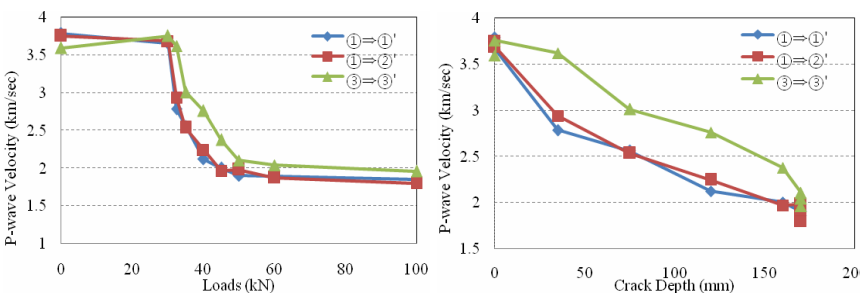

(a) (b)

Fig. 8. Stiffness Decrement with Increment of Loading and Cracking

5. Conclusions

Bender elements, used to measure stiffness of granular materials, have been modified to be applied to concrete. To verify the applicability to concrete material, bender elements were buried at three different locations in a concrete beam and p-wave measurements were carried out during concrete curing and as cracks developed under load increment. Following conclusions can be made from the study:

- The most suitable form of bender elements is the one with the polyester material as the compressive layer of the sensors. The modified bender elements work well and accurately measure the P-wave velocity in the plaster and concrete.
- The tests during concrete curing show that the bender elements can measure the stiffness during hardening of concrete and results are agreed with other measurements.
- P-wave velocity dropped abruptly at the initiation of cracking and was decreased as gradually as cracks progressed. The results indicate the pattern of the stiffness decrement can be correlated with the geometry of cracks.

Further study and tests are required to improve the reliability of the bender elements and to implement them to larger and longer structures

Acknowledgments

This work is a part of a research project supported by Samsung Corporation. The authors wish to express their gratitude for the financial support.

References

1. Y.J. Mok, J.W. Jung, and M.J. Han, “Implementation of Bender Elements to In-situ Measurements of Stiffness of Soft Soil,” *Journal of the Korean Geotechnical Society(written in Korean)*, Vol. 22(11): 37-45 (2006).
2. M.J. Jung, “Shear Wave Velocity Measurements of Normally Consolidated Kaolinite Using Bender Elements.” Master Thesis, University of Texas at Austin (2005).
3. Mehta, P.K. and Monteiro, P.J.M, Concrete-Microsturcture, Properties, and Materials, McGraw Hill (2006)

A FRAMEWORK FOR NONDESTRUCTIVE EVALUATION METHODS ACCOUNTING FOR UNCERTAINTY OF MODEL AND AGING EFFECT OF CONCRETE[†]

KEE JEUNG HONG[†]

Civil & Environmental Engineering, Kookmin University
Seoul, Korea

JEE SANG KIM[‡]

Civil & Environmental Engineering, Seokyeong University
Seoul, Korea

As concrete ages, the surrounding environment is expected to have growing influences on the concrete. As all the impacts of the environment cannot be considered in the strength-estimating equation of a nondestructive concrete test, the increase in concrete age leads to growing uncertainty in the strength-estimating equation. Therefore, the variation of the model error in the equation increases. It is necessary to verify those impacts before considering them in the strength-estimating equation so as to build a more accurate reliability model for structural performance evaluation. This paper examines the existing strength-estimating statistical models for concrete, and suggests a new framework for these strength-estimating statistical models to properly reflect the model uncertainty due to aging of the concrete. This new framework lay the foundation for more accurate structural performance evaluation.

1. Introduction

It is necessary to assess the safety of structures and predict their remaining spans in order to maintain and manage concrete structures. Based on the assessing results, a decision can be made on the repair, reinforcement and removal of the structures. With demand and interest for the structural performance evaluation on the rise, the need for an appropriate reliability model for accurate performance assessment is also growing [1]. It is needed to consider the probability of uncertainty arising from material strength and load condition in order to build a proper reliability model. In an effort to establish a statistical

[*] This work is supported by Korea Ministry of Construction and Transportation (MOCT) via the Infrastructures Assessment Research Center

[†] Email: kjhong@kookmin.ac.kr

[‡] Email: zskim@skuniv.ac.kr

model that can reflect the uncertainty of the strength-estimating statistical model used in conducting a concrete nondestructive test, this paper examined the previous strength-estimating statistical models and seeks to find out a model that can improve the existing ones.

As domestic strength-estimating equations suggested to estimate the concrete strength with a nondestructive test have yet to be verified, equations suggested by Japan are widely used in Korea. Depending on how to consider the impacts of concrete age, the strength-estimating equations can be broken down into three forms: 1) basic form, 2) form using age compensation coefficient 3) form using age as a variable of a statistical model. The first form takes into account only rebound number and ultrasonic velocity without considering the age. The second form was built to consider the change in strength based on the age by multiplying the basic form by age compensation coefficient. The third form uses the age as a variable of regression model without using age compensation coefficient.

Generally, with the concrete age rising, the environment is expected to have growing influences on concrete. As all the impacts of the environment can't be considered in the strength-estimating equation of a nondestructive test, the increase in concrete age leads to heightened uncertainty in the strength-estimating equation. It means that an increase in the concrete age results in increased variation of probability distribution. As the abovementioned strength-estimating equations do not consider the change in probability distribution according to the age, improving the existing equations is expected to help to assess the their performance and predict the span of concrete structures more accurately.

2. Existing Form of Strength-Estimating Statistical Model in Nondestructive Concrete Tests

To find out an improved framework of strength-estimating statistical models for nondestructive concrete tests aimed at assessing performance of concrete structures more precisely, this paper seeks to review the existing forms of the models and improve them by dealing with the shortcomings in accounting for the model uncertainty which varies along time.

2.1. *Basic Form*

Nondestructive tests of concrete include Schmidt hammer test, ultrasonic pulse velocity method and a method combining these two tests. This section explains the existing forms of the statistical models by using Schmidt hammer test as an

example. The strength-estimating statistical model of Schmidt hammer test is as follows:

$$f'_c = a_0 + a_1 R + \sigma\varepsilon \tag{1}$$

In the model, f'_c means the estimated concrete strength, R means the rebound number, and a_i are coefficients obtained from regression analysis. If ε is defined as a random error with standard normal distribution, σ becomes a standard error that shows the degree of distribution of statistical data. As the number of statistical data increases, it approaches the standard deviation of the model error. As the basic form does not consider the impacts of age, one of the important factors in estimating the concrete strength, modified forms like the following were suggested by many researchers.

2.2. *Form Using Age Compensation Coefficient*

As the basic form is not accurate in estimating concrete strength according to concrete age, the estimated strength is compensated by considering the impacts of concrete age. Estimated strength can be compensated according to the age by multiplying the concrete strength estimated in the basic form by the age compensation coefficient. In the case of Schmidt hammer test, the compensated concrete strength is obtained as following.

$$f'_c = \alpha(t,R) \times (a_0 + a_1 R) + \sigma\varepsilon \tag{2}$$

In this equation, f'_c is the estimated concrete strength compensated according to the concrete age, and $\alpha(t,R)$ is the age compensation coefficient. The age compensation coefficient $\alpha(t,R)$ is obtained by comparing the concrete strengths estimated by Eq. (1) and the corresponding real strengths, and conducting regression analysis with a nonlinear regression function of the concrete age t and the rebound number R [2].

2.3. *Form Using Age as an Explanatory Variable*

The impacts of concrete age can be considered like in Eq. (3) by adding the concrete age as an explanatory variable to a linear statistical model, instead of using the age compensation coefficient [3].

$$f'_c = a_0 + a_1 R + a_2 t + \sigma\varepsilon \tag{3}$$

In Eq. (3), the rebound number R and the concrete age t are used as explanatory variables, but a more accurate statistical model can be built by adding more explanatory functions such as $\log(t)$, $1/t$, $t \times R$ and R/t etc. The

form using age compensation coefficient (Eq. (2)) can be expressed when several nonlinear explanatory functions are added to a linear statistical model (Eq. (3)).

3. Improved Form of Strength-Estimating Statistical Model in Nondestructive Concrete Tests

The increase in concrete age leads to a growing influence of the environment on the concrete strength. However, this growing influence of the environment on the concrete strength is not yet considered in the existing strength-estimating models. For instance, as the concrete ages after concrete casting, carbonation and evaporation on the concrete surface greatly affects the rebound number [4]. And increasing concrete age helps to decrease gel water inside the concrete, ultimately reducing the ultrasonic pulse velocity [5]. Even though these impacts affect the nondestructive tests that use the rebound number and the ultrasonic pulse velocity, these impacts are not closely related with the concrete strength. Therefore, a rise in concrete age helps to increase the error of the existing models that estimates the concrete strength by the rebound number and the ultrasonic pulse velocity. This means that the model error σ in a strength-estimating model like Eqs. (2) and (3) increases according to the concrete age.

Since the model error of a strength-estimating statistical model significantly depends on the concrete age, the standard deviation or probability distribution of the model error can be defined as a function of the concrete age $\sigma(t)$. It is inevitable to properly consider the change in probability distribution of the model error according to the concrete age in order to predict the remaining lifespan and assess the performance of concrete structures in a more safe and accurate way. There have been many attempts to more precisely represent the mean value of concrete strength with a statistical model, but there have been no efforts to precisely indicate the probability distribution of the model error in a strength-estimating equation changing according to the concrete age. This paper suggests the standard form of a strength-estimating statistical model like Eq. (4) as a framework for study aimed at properly defining the probability distribution of the model error changing according to the concrete age in a strength-estimating model.

$$f'_c = \sum_i a_i(t) \cdot f_i(R,t) + \sigma(t)\varepsilon \tag{4}$$

In the equation, f'_c is estimated strength according to the concrete age, $a_i(t)$ are coefficients obtained from the regression analysis of the test data at a specific concrete age t, f_i are explanatory functions of the rebound number R and the

concrete age t, $\sigma(t)$ is a standard deviation of the model error that changes according to the concrete age, and ε is a random error with a standard normal distribution assuming that the model error has a normal probability distribution. $a_i(t)$ and $\sigma(t)$ can be defined by regression analysis of the statistical data in each concrete age and expressing them by fitting functions of the concrete age.

The framework shown in Eq. (4) is only for the Schmidt hammer test using rebound numbers. The framework can be easily applied to the ultrasonic pulse velocity method simply by replacing the rebound number R with the ultrasonic pulse velocity V_p in the explanatory functions in Eq. (4). In general, the framework applied to the combined method using both the Schmidt hammer test and the ultrasonic pulse method is as following

$$f'_c = \sum_i a_i(t) \cdot f_i(R, V_p, t) + \sigma(t)\varepsilon \tag{5}$$

4. Conclusion and Future Study Plan

Concrete strength-estimating equations by a nondestructive test used in Korea are mostly equations suggested by Japan. When the Japanese equations are used in estimating the strength of Korean concrete, there is expected to be an error in the estimation. Against this backdrop, the need for a strength-estimating equation tailored to Korean concrete has emerged, and many of Korean researchers suggested concrete strength-estimating equations by accumulating test materials on Korean concrete. Most of them have tried to represent the mean value of real concrete strength with a strength-estimating statistical model, and there has been a lack of efforts to properly represent the change in probability distribution of real strength according to the concrete age. This paper suggests a strength-estimating statistical model like Eq. (5) to make sure that the probability distribution of real strength according to the concrete age could be properly reflected in the estimation, which lays the foundation for accurate prediction of remaining lifespan of concrete structures and assessing their performance.

In an effort to build a strength-estimating equation for Korean concrete tailored to the suggested statistical model, authors has collected the data of tests previously conducted by other researchers, and plans to make use of data accumulated by Korean Infrastructure Safety & Technology Corporation. Comparing strength-estimating statistical models suggested in this paper with existing nondestructive test equations is expected to help build a more reliable strength-estimating equation.

Acknowledgments

This study has been a part of a research project supported by Korea Ministry of Construction and Transportation (MOCT) via the Infrastructures Assessment Research Center. The authors wish to express their gratitude for the financial support that made this study possible.

References

1. J.S. Kim, K.M. Lee, Y.W. Choi and E.I. Yang, "A comparison of the material property prescriptions in various concrete structure design codes," *Conference of Korea Concrete Institute.* Daegu, Korea, Spring 2007 (2007).
2. M.S. Kim, Y.H. Yoon, J.K. Kim, Y.W. Kwon and S.S. Lee, "Estimation of aging effects on determination of compressive strength of concrete by non-destructive tests," *Journal of the Korea Concrete Institute.* **Vol. 14, No. 5,** pp. 782~788 (2002).
3. C.K. Han and B.S. Lee, "Application of non-destructive testing of the concrete using aggregate produced in Cheju with Schmidt hammer," *Journal of the Architectural Institute of Korea.* **Vol. 18, No. 3,** pp. 91~98 (2002).
4. Y.W. Kwon, "Surface hardness test for concrete," *Magazine of the Korea Concrete Institute.* **Vol. 10, No. 2,** pp. 20~26 (1998).
5. S.S. Oh, S.K. Koh, S.H. Kim, C.H. Cho and J.S. Kim, "An experimental study on the cancellation effect of ultrasonic pulse velocity and rebound values in relation to the estimation of concrete strength," *Journal of the Architectural Institute of Korea.* **Vol. 12, No. 11,** pp. 201~210 (1996).

A STUDY OF THE STRUCTURAL INTERNAL ASSESSMENT OF CONCRETE SLAB USING THE GROUND PENETRATING RADAR EXPLORATION*

SEONG UK, HONG

Department of Architectural Engineering, Hanyang University,1271 Sa 3-dong Ansan-Si,425-791, R.O. Korea

YOUNG SANG, CHO

Department of Architectural Engineering, Hanyang University,1271 Sa 3-dong Ansan-Si,425-791, R.O. Korea

Ground Penetrating Radar (GPR) is a powerful tool with a wide range of applications in the nondestructive testing of concrete. It's useful for the detection of different materials embedded in a concrete, nondestructively. The purpose of this study is to detect a reinforced bar and PVC pipe embedded inside concrete and to determine the different depth using GPR. Concrete specimens used for this study has a 10mm diameter PVC pipe and 100-200mm depth and it's dimensions are 1000(L)x1000mm(W)x200mm(D) and 1200mm(L)x1200mm(W)x200mm(D). The advantages and limitations of GPR in these applications for concrete are also discussed.

1. Introduction

1.1. *Research Background*

Nowadays, nondestructive testing is widely used for safety assessment of concrete structures in relation to their maintenance, management and repair, and it has received much attention for quality and safety assurance of concrete structures and more efficient remodeling. Of these, Ground Penetrating Radar (GPR) exploration is a nondestructive testing method by using principles of radar that physical properties of electromagnetic wave emitted from the inside of material is reflected against the boundary of a different material and by applying geophysical exploration.[1] That is, after emitting electromagnetic waves into a structure or the ground instead of into the air, when waves reflecting off buried materials such as reflectors is received, time and speed of electromagnetic waves are used to reveal structure of a material.[2]

* This work is supported by the Korea Institute of Construction & Transportation Technology Evaluation and Planning (03 Sanhakyeon A10-05).

1.2. *Research Objectives*

This research aims to review theories of GPR exploration method; to find out propagation velocity and dielectric constant of concrete with test exploration on concrete slab specimen; to analyze the properties of waves regarding two flaw detection, thickness change and different material; and to present basic data for structural internal assessment of concrete structures. Also, the study is to increase reliability of the results of internal assessment in order to increase applicability of GPR exploration.

2. Theoretical Review

2.1. *Principles of GPR Exploration*

GPR Exploration is a method to apply observation radar to underground exploration. This is a kind of geophysical exploration with which high-frequency electromagnetic waves are emitted into the inside of host material via transmit antenna in contact with the ground, and the reflected waves hit off a buried material inside host material are converted to pulse voltage at receive antenna and reaction images are shown on the monitor in order to analyze findings of exploration(Figure 1).

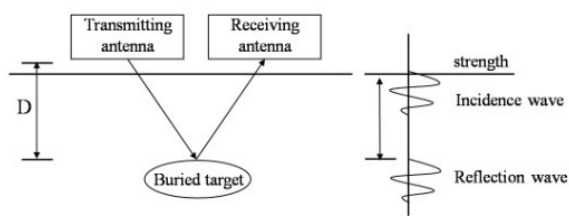

Fig. 1. Principle of GPR Exploration

2.2. *Electromagnetic Properties of Concrete*

Materials that have no conductibility and magnetism, such as concrete, are called dielectric materials. Since dielectric materials have almost 0 conductivity and permeability of general materials is mostly 1, electromagnetic properties of concrete are prescribed with permittivity and expressed as follows.[3]

$$\epsilon = \epsilon' - j\epsilon'' \tag{1}$$

ϵ' : Dielectric constant

ϵ'' : Loss factor

j : $\sqrt{-1}$

Permittivity is expressed with complex numbers, and relative permittivity which is a ratio of air to permittivity is usually used. Relative permittivity is also expressed with complex numbers and dielectric constant which is real value is used. In general, permittivity, relative permittivity, and dielectric constant are all used for the same meaning. When frequency of antenna is 1GHz, dielectric constant and loss factor of concrete is shown in Table 1.[4]

Table 1. Dielectric Constant and Loss Factor of Concrete

Material	Dielectric constant	Loss factor
Concrete (wet)	9 ~ 14	0.7 ~ 1.7
Concrete (dry)	4 ~ 8	0.03 ~ 0.1

2.3. Velocity of Electromagnetic Waves

Inside a dielectric material, velocity of electromagnetic wave is determined by dielectric constant.[5]

$$v = \frac{c}{\sqrt{\epsilon'}} \text{ [m/s]} \tag{2}$$

v : Velocity of electromagnetic wave inside material
c : Velocity of electromagnetic wave under vacuum (3×10^8) m/s

Also, propagation distance inside a material can be calculated with propagation velocity and time and propagation time is for roundtrip so a half of its value is used.(12)

$$\mathbf{S} = v \times t = \frac{c}{\sqrt{\epsilon'}} \times \frac{\Delta t}{2} \text{ [m]} \tag{3}$$

Δt : Estimated roundtrip time (ns)

3. Experiment Set-up

3.1. *Specimens*

Concrete slab specimens used in this experimental exploration had 30MPa of compressive strength and their sizes were 1200mm x 1200mm x 200mm and 1000mm x 1000mm x 200mm (Figure 2). In order to increase applicability of safety diagnosis, internal buried materials of general concrete was designated as flaw detection.

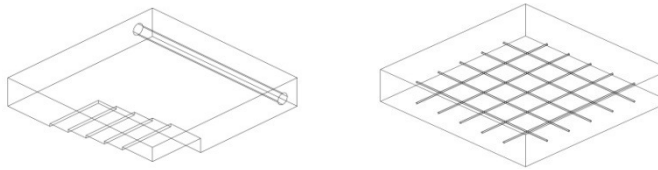

(a) (b)

Fig. 2. Perspective Projection of Specimens (a) Specimen 1 (b) Specimen 2

3.2. *Equipments*

The equipment used in experiment was SIR-2 System made by the U.S. Geophysical Survey System. An antenna can choose frequencies from 100MHz to 2.5GHz according to exploration situation, and because portable battery is used, there is no constraint on space.

4. Analysis of Experiment Results

4.1. *Propagation Velocity and Dielectric Constant of Concrete*

Through oscilloscope analysis of the obtained data, reflection time of upper and lower surfaces and thickness of material were used to reorganize Formulas (2) and (3) to obtain Formula (4), and propagation velocity and dielectric constant of material can be obtained with Formula (4).

$$v = S \times \frac{2}{\Delta t}, \quad \in = \left(\frac{c}{v} \right)^2 \tag{4}$$

According to oscilloscope analysis (Figure 3) of parts composes of pure concrete, it was found that propagation time Specimen 1 was 9.61ns and that of Specimen 2 was 11.66ns. Propagation speed and dielectric constant for each specimen is summarized in Table 2.

Table 2. Propagation Speed and Dielectric Constant of Each Specimen

	Specimen 1	Specimen 2
Upper Surface Arrival Time (ns)	0.11	0.28
Lower Surface Arrival Time (ns)	4.45	5.06
Propagation Time (ns)	4.34	4.78
Thickness (d)	0.21	0.21
Propagation Velocity (m/ns)	0.097	0.088
Dielectric Constant ( )	9.61	11.66

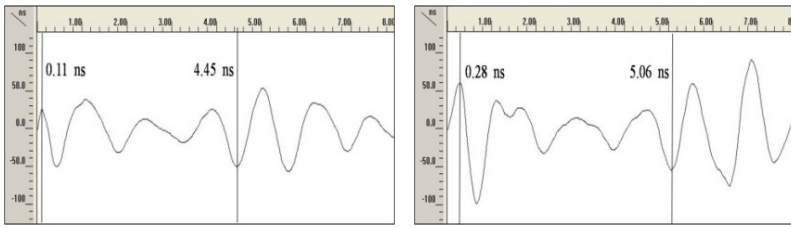

(a) Specimen 1 (b) Specimen 2

Fig. 3. Oscilloscope Analysis for Measuring Dielectric Constants

4.2. *Estimating of Flaw detection position*

Propagation time of each flaw detection and dielectric constant of host material were applied to Formula (5) in order to estimate positions and they are shown in Table 3. When error in construction is considered with the maximum difference between the estimated position and actual position, 14.2mm, it is possible to find almost accurate positions.

$$S = \frac{\Delta t}{2} \times v \tag{5}$$

4.3. *Data Analysis*

The final objective of GPR exploration is to find out the location, type, and depth of reflectors inside the material that is an object of survey and to make cross sectional images of internal structures to visualize them. By applying dielectric constants of host materials, cross sectional views of internal structure could be changed from time-distance area to depth-distance area. With data processing and position estimation, accurate positions of buried materials and analysis of reflection strength are used for general understanding of the types of buried materials.(Figure 4)

Table 3. Estimating of flaw detection position

Flaw detection	Propagation Time (ns)	Propagation Velocity (m/ns)	Measured position (mm)	Actual position (mm)
Thickness 100mm	2.63	0.097	114.2	100
Thickness 120mm	2.60	0.097	125.8	120
Thickness 140mm	3.15	0.097	152.4	140
Thickness 160mm	3.29	0.097	159.2	160
Thickness 180mm	3.51	0.097	169.8	180
Thickness 200mm	4.34	0.097	210.0	210
PVC Pipe	1.29	0.088	56.8	60
Reinforced Bar	2.09	0.088	91.8	100

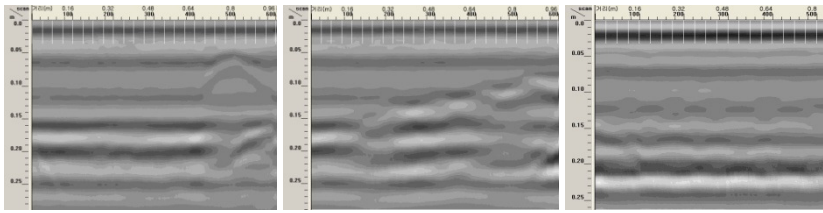

(a) (b) (c)

Fig. 4. Final Sectional Images (a) Vertical Cross-Sectional Image of PVC Pipe (b) Cross-Sectional Image of Thickness Change (c) Cross-Sectional Image of Reinforced Bar

5. Conclusions

In this study, based on review of exploration theories and existing research analysis, specimens were fabricated and tested to increase applicability of GPR exploration in internal diagnosis of concrete slab, and the following conclusions were obtained.

1. Materials with no conductivity and magnetism like concrete are called dielectric material. Electromagnetic properties of dielectric materials are prescribed with dielectric constant, and according to oscilloscope analysis, dielectric constants of Specimens 1 and 2 are 9.61 and 11.66, respectively.
2. Thickness and positions of PVC pipe and reinforced bar, which are flaw detection, were measured to have 5.95% of error on average. Considering error during construction, it is suggested that dielectric constant of materials were rather accurately measured.
3. The GPR exploration includes many variables related to survey materials, but it is limited because not all variables are known. Therefore, when research is conducted to reveal this limitation and to further increase technological reliability, applicability will be increased as GPR exploration is a very effective non-destructive method for safety diagnosis of structure.

References

1. Vincenzo Barrilea, Raffaele Pucinotti ; Application of radar technology to reinforced concrete structures a case study, NDT & E International 38, pp596-604 (2005).
2. Francesco Soldovieria, Raffaele Persicoa, Erica Utsib, Vincent Utsi ; The application of inverse scattering techniques with ground penetrating radar to the problem of rebar location in concrete,NDT & E International 39, pp602-607 (2006).
3. Rhim, H. C. and Buyukozturk, O. ; “Electromagnetic properties of concrete at micro-wave frequency range”, ACI Materials Journal, Vol 95, No.3, 1998, 262(10).
4. Daniels, D. J. ; Surface Penetrating Radar, The Institute of Electrical Engineers 300, (1996).

5. Cheng, D. K ; Field and Wave Electromagnetics, Addison-Wesley Pub. Co., Massachusetts 703,(1989)

REMOTE MEASUREMENT OF PIPE WALL THINNING BY MICROWAVES

YANG JU[†]

Department of Mechanical Science and Engineering, Nagoya University
Furo-cho, Chikusa-ku, Nagoya 464-8603, Japan

A method which can inspect a pipe in a large scale and measure the wall thinning remotely was demonstrated. A copper pipe having 17 mm inner diameter, 1 mm wall thickness, and 900 mm length was measured. The wall thinning having the value from 10% to 80% of the wall thickness was detected significantly. By building up a resonance for the microwave signal propagated in the pipe, it is possible to determine the wall thinning using the measured resonance frequency.

1. Introduction

Wall thinning is one of the most serious defects in the pipes used in chemical and power plants. Detection and evaluation of the wall thinning of pipes are very important issues for the prediction of lifetime of the pipes in order to avoid severe accidents. Recently, many nondestructive testing techniques, such as X-ray [1], Ultrasonic [2],[3], acoustic emission [4] and so on, have been used for the measurement of pipe wall thinning. However, those methods have to move the sensor in order to find the area where the wall thinning occurred. It takes a lot of time and labor. In this paper, a novel method to measure the wall thinning by microwaves is demonstrated. This method employs a microwave signal to propagate in the pipe, where the pipe is considered as a circular waveguide. Therefore the wall thinning changes the wavelength, thereby changing the resonance frequency, of the microwave signal in the pipe. Consequently, it is possible to inspect a great large scale of pipes and to measure the wall thinning remotely in a real time.

2. Experimental Approach

A network analyzer is used as the source to generate the microwave signal and also as the receiver to measure the signal collected from the investigated pipe.

[†]ju@mech.nagoya-u.ac.jp

Fig. 1. Conception diagram of the microwave signal propagating in the pipe

The microwave signal is fed into the pipe through a coaxial line sensor at one end of the pipe and is drawn out at the same end by another coaxial line sensor. As shown in Fig. 1, the signal in the pipe is separated into two signal components. One goes to the receiving sensor directly without propagating along the pipe. Another propagates along the pipe and then arrives at the same receiving sensor after reflected from another end of the pipe. At the receiving sensor, a resonance is built up by the two signal components, and the resonance frequency depends on the inner diameter of the pipe. To consider the pipe to be a circular waveguide, the wavelength of the microwave signal propagating in the pipe can be written as

$$\lambda_g = \frac{1}{\sqrt{\mu\varepsilon f^2 - (\frac{1.841}{\pi d})^2}} \tag{1}$$

where λ_g is the wavelength of the microwave signal in the pipe, f the frequency, d the inner diameter of the pipe, μ and ε the permeability and permittivity of the medium in the pipe.

Normally, μ and ε can be consider to be constants, therefore, λ_g is a function of f and d. At some area of the pipe, if d is increased due to the thickness reduction, while at the same place, λ_g will decrease for any frequency which allows the microwave signal to propagate in the pipe. It is means that to build up a resonance for the pipe containing the wall thinning, a microwave signal having larger wavelength in the pipe is required. Therefore, the resonance frequency will be decreased due to the thickness reduction. By sweeping the frequency, the shift of the resonance frequency due to the thickness reduction can be measured. Therefore, the value of the wall thinning can be determined by the measured resonance frequency.

Fig. 2 shows the photograph of the radiating and receiving coaxial line sensors connected at one end of the pipe. In this study, a copper pipe having 17 mm inner diameter, 1 mm wall thickness (t), and 900 mm length was used. To introduce different wall thinning at another end of the pipe, 5 copper joints having 17 mm length (wall thinning area) and the value of the thickness reduction from 10% to 80% of the wall thickness of the pipe were used

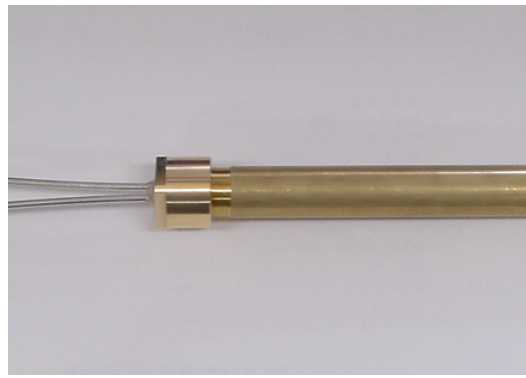

Fig. 2. Photograph of the connection of the coaxial line sensors with the pipe

Fig. 3. Photograph of the terminated pipe by a joint and the cap

Fig. 4. Photograph of the joints and the cap used to terminated the pipe

Table 1. Conditions for introducing the wall thinning

Joint	Inner diameter (mm)	Length (mm)	Value of the wall thinning (%*t*)
1	17.2	17	10
2	17.4	17	20
3	17.8	17	40
4	18.2	17	60
5	18.6	17	80

(see Table 1). A cap was used to terminate the joint as shown in Fig. 3. Therefore, the physical length of the microwave signal propagated in the pipe is 917 mm. Fig. 4 shows the photograph of the joints and the cap.

3. Results and Discussion

Fig. 5 shows the measured amplitude of the microwave signal received from the pipe by sweeping the frequency from 47.39 to 47.49 GHz, in the case that the pipe was open ended. In other words, there are no joint and cap to be connected to the end of the pipe. Therefore, almost no microwave signal which propagates along the pipe was reflected and arrived at the receiving sensor. Consequently, there is no resonance phenomenon to be observed. The amplitude of measured microwave signal indicates the value of the signal transmitted from the radiating sensor to the receiving one directly, without propagating along the pipe. Fig. 6 shows the measured amplitude of the microwave signal verses the swept frequency, in the case that the pipe was terminated by a joint and the cap. As shown in Fig, 6, the resonance was built up and the resonance frequency can be determined. It is also observed that with the increase of the wall thinning, the resonance frequency becomes lower. In Fig. 7, the relationship between the wall thinning and the resonance frequency (minimum) is shown, by which the thickness reduction can be determined precisely by the measured resonance frequency.

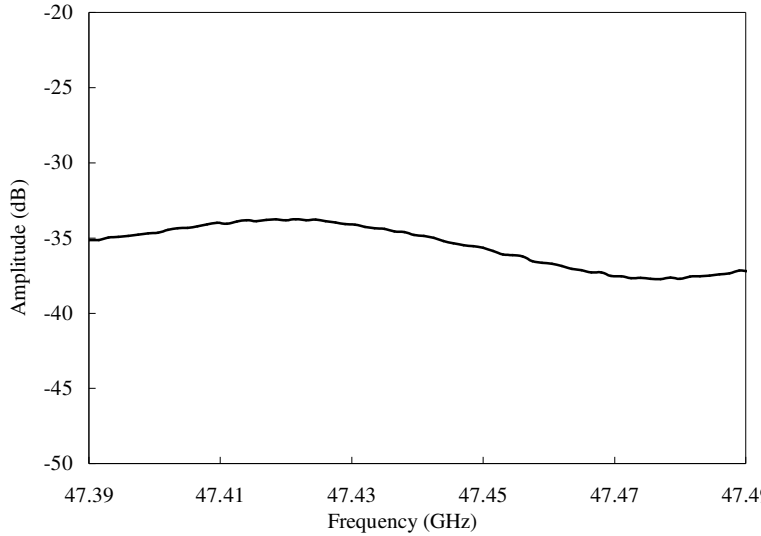

Fig. 5. Measured amplitude of the microwave signal received from the pipe by sweeping the frequency for the open ended pipe

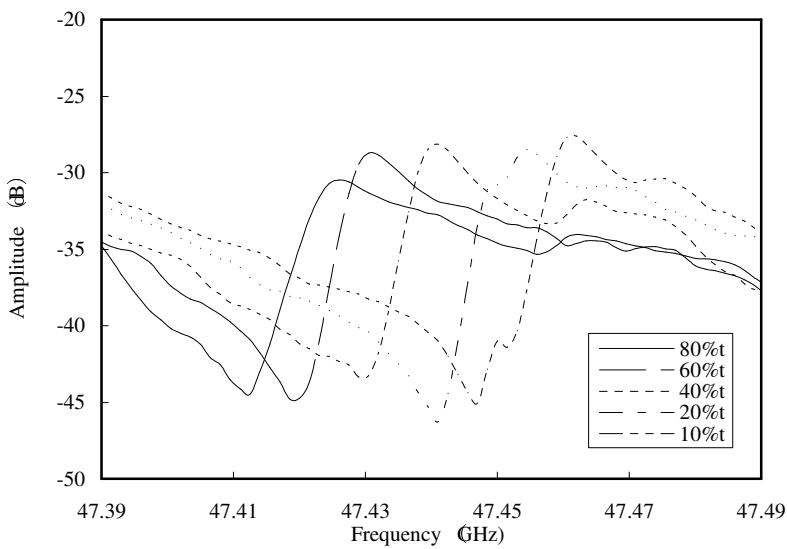

Fig. 6. Measured amplitude of the received microwave signal by sweeping the frequency for different wall thinning

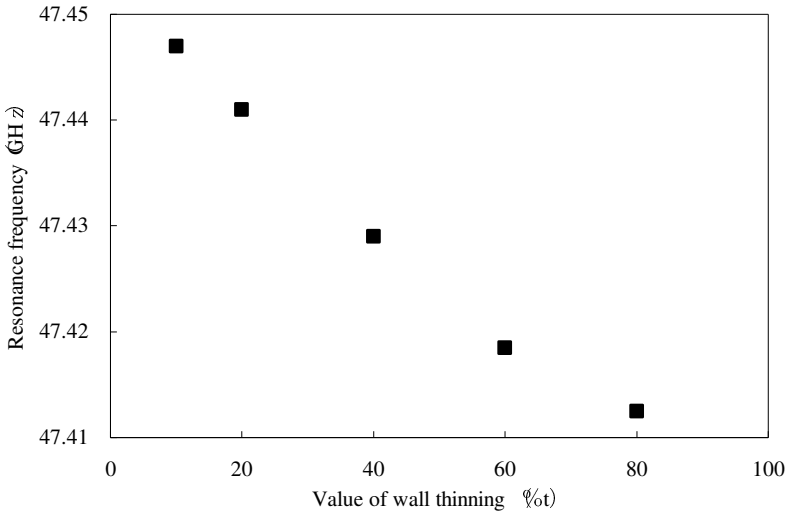

Fig. 7. Relationship between the resonance frequency and the value of wall thinning

4. Conclusion

Wall thinning having the value from 10% to 80% of the wall thickness of the pipe were detected successfully. The method to build up a resonance in the pipe is proved to be a significant means to measure the wall thinning precisely. Utilizing the propagation of microwave signal in the pipe, it is possible to inspect a pipe in a large scale and to determine the wall thinning remotely.

Acknowledgments

This work was partly supported by the Japan Society for the Promotion of Science under Grant-in-Aid for Scientific Research (A) 17206011.

References

1. G. Kajiwara, *Journ. Test. and Eval.* **33**, 295 (2005).
2. K. R. Leonard, and M. Hinders, *Ultrason.* **43**, 574 (2005).
3. Y. Cho, W. D. Oh, and J. H. Lee, *Key Eng. Mat.* **321-323,** 795 (2006).
4. K. W. Nam, and S. H. Ahn, *Key Eng. Mat.* **270-273,** 461 (2004).

3-DIMENSIONAL QUANTITATIVE MEASUREMENT OF A GEOMETRIC ANOMALY IN STEAM GENERATOR TUBES USING A DIAGNOSTIC EDDY CURRENT PROBE (D-PROBE)

DEOK HYUN LEE

Nuclear Material Research Center, Korea Atomic Energy Research Institute, Dukjin Dong 150, Yuseong Gu, Daejon, 305-353, Korea

MYUNG SIK CHOI

Nuclear Material Research Center, Korea Atomic Energy Research Institute, Dukjin Dong 150, Yuseong Gu, Daejon, 305-353, Korea

DO HAENG HUR

Nuclear Material Research Center, Korea Atomic Energy Research Institute, Dukjin Dong 150, Yuseong Gu, Daejon, 305-353, Korea

JUNG HO HAN

Nuclear Material Research Center, Korea Atomic Energy Research Institute, Dukjin Dong 150, Yuseong Gu, Daejon, 305-353, Korea

MYUNG HO SONG

Department of Metal and Material, Korea Institute of Nuclear Safety, Kusong Dong 19, Yuseong Gu, Daejon, 305-338, Korea

Occurrences of a stress corrosion cracking in the steam generator tubes of nuclear power plants are closely related to the residual stress existing on the region of a geometric change, that is, expansion transition, u-bend, ding, dent, bulge, etc. Therefore, information on the location, type and quantitative size of a geometric anomaly existing in a tube is a prerequisite to the activity of a non destructive inspection for an alert detection of an earlier crack and the prediction of a further crack evolution. In this paper, a newly developed eddy current probe, which has been equipped with the simultaneous dual functions of a crack detection and a 3-dimensional quantitative profile measurement, is introduced. The proof of the probe performance including the accuracy of the profile measurement and the applicability of the probe to a plant inspection is provided through the setting-up of a calibration procedure, and a comparison of the quantitatively measured data with those from the laser profilometry for the steam generator tube samples with geometric anomalies of various types and sizes.

1. Introduction

A geometric anomaly existing in steam generator tubes can affect the integrity of operating nuclear power plants. For example, many steam generator tube rupture events are directly related to a manufacturing or operation induced geometric anomaly such as an ovalization, denting and a bulge [1,2]. Moreover, a degradation such as a primary water stress corrosion cracking and a secondary side stress corrosion cracking, generally observed in the region of an expansion, u-bend, dent and an over expansion in the steam generator tubes of commercial power plants, are also from the residual tensile stress caused by a geometric transition. Therefore, information on the location, type and quantitative size of a geometric anomaly existing in a tube is a prerequisite for the activity of a non destructive inspection for the alert detection of a crack at an early stage and the prediction of a further crack evolution.

Conventional methods of an eddy current profilometry for measuring geometric changes can be categorized by using a bobbin coil probe and a multi-coil array probe. Bobbin coil probe profilometry has a merit of using a high test frequency of over 500 kHz in order to obtain a pure lift-off signal from a tube's inner surface, but the profile data is two-dimensional, that is, the average value of the diameter over a circumference is presented along the tube length and thus, information about a radial change along the circumference can not be provided. For the multi-coil array probe profilometry, the profile data is sensitive to the noise signal from a tube's wall or outer surface because the mid range of the test frequency, around 400 kHz, should be applied so that the field of view in an eddy current from each coil covers the entire circumferential area, and the difference in the coil impedance among the coil units may result in an uncertainty of the measured profile data, even though it has a merit of measuring a radial change along the circumference of a tube.

In order to overcome the technical limits of the conventional methods described above, a new eddy current probe, which has been equipped with the simultaneous dual functions of a crack detection and a 3-dimensional quantitative profile measurement, has been developed. The scope of this paper is mainly focused on evaluating the accuracy of a 3-dimensional profile measurement to provide proof for the applicability of the newly developed eddy current probe to a plant inspection.

2. Experimental

2.1. *Diagnostic Eddy Current Probe (D-probe)*

D-Probe is a brand-new, rotary type eddy current coil probe, developed by Korea Atomic Energy Research Institute (KAERI) [3]. It is designated as a D(diagnostic)-Probe for its break-through function of a diagnosis. The probe body is equipped with both a surface riding coil for a crack detection and sizing, and a non-surface riding coil for a profile measurement. Therefore, it has the simultaneous dual functions of a crack detection and a sizing, and a 3-dimenstional quantitative profile measurement with a single pass of a probe movement into the steam generator tubes. By comparing the eddy current data from the crack with those from the geometric changes, the relationship between the degradation and geometric changes can be revealed. Also, it supplies information on a tube location at which a cracking is most probable and thus, an earlier detection of a crack and a resultant increase in the possibility of a detection can be expected. Moreover, a management strategy based upon a quantitative size of geometric changes can be applied to the operating nuclear power plants, by establishing the role of geometric changes on a cracking.

Fig. 1 shows the prototype D-probe, manufactured by Zetec Inc. according to the technical design by KAERI. The prototype D-probe has three eddy current coil units(two surface riding type for crack detection and one none-surface riding type for profile measurement), which are located at a circumference of the probe body. Compared to the other recently developed multi-coil array probes such as an intelligent probe or x-probe [4], the D-probe has an advantage of measuring pure geometric changes in a tube's inner surface, by excluding the noise from a tube's outside, by the use of an exclusive eddy current coil for a profile measurement optimized at a high test frequency of 700kHz. The probe was designed to be compatible with commercial eddy current test equipment. In this work, the eddy current data was obtained using the Zetec MIZ-70 digital data acquisition system, and the conditions of the sampling rate, probe pulling speed, and probe rotating rate were adjusted so that each data set could be obtained at distance intervals of less than 1mm in both the axial and the circumferential directions of a tube.

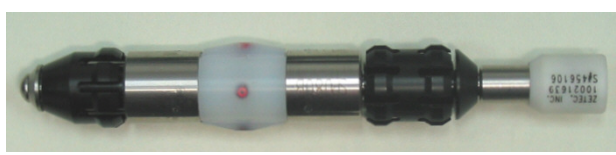

Fig. 1. Photograph of a prototype D-probe.

2.2. *Calibration Standard Tube and Tube Samples with Geometric Anomalies*

In order to set up the calibration procedure for converting the value of the eddy current signal from the D-probe to the value of a radius, a calibration standard tube containing 5 segments of uniform radial changes ranging from –0.35mm to +0.35mm was manufactured. Also, tube samples with various geometric anomalies of a local dent and expansion were used to compare the accuracy of the profile measurement by the D-probe with those by the laser profilometry.

2.3. *Laser 3-D Profile Measurement*

Among the existing technology for measuring the profile of a tube inside, a laser profilometry is regarded as the most advanced and precise one with the highest resolution. Therefore, a laser profilometry was applied to measure the real size of the expansion/dents in the standard tube used for the calibration of the D-probe profile signal, and the geometric anomalies of the tube samples. The sizes of the geometric anomalies of the tube samples measured by the laser profilometry were counted as the reference standards for a comparison with those from the D-probe. LTC LP-2000 profilometry system, used for the measurement, has a rotary laser sensor with a spot size of 0.13mm and a resolution of 0.013mm. The data was obtained at intervals of 1 degree in the circumferential direction and 0.4mm in the axial direction of a tube.

3. Results and Discussion

3.1. *Setup of the Calibration Procedure*

The relationship between the values of the eddy current signal from the D-probe and the values of the radius from the laser profilometry, obtained by using the calibration standard tube with 5 segments of radial changes, is shown in Fig. 2. The decrease and increase of the radius value from the nominal tube radius (8.44mm) are characterized by a dent and expansion, respectively. In order to obtain an equation for the optimal calibration, mathematical fitting methods were applied and it was found that the 2nd , 3rd and 4th order polynomial curves fitted well, as shown in Fig. 2. Compared to the 2nd order polynomial curve, a better fit was observed for both the 3rd and 4th order curves without any difference between the two. Thus, it can be concluded that the use of the 3rd order polynomial equation, fitted by 4 data points from a standard tube containing one segment of an expansion and two segments of dents, is the most effective calibration procedure.

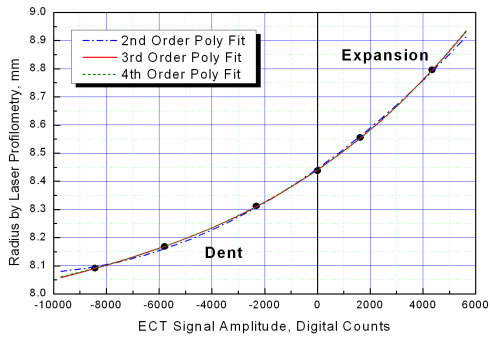

Fig. 2. Relationship between the eddy current signal amplitude from D-probe and the radius values from laser profilometry, measured by using the calibration standard tube.

3.2. *3-Dimensional Quantitative Measurement of Geometric Anomalies using D-Probe*

In order to examine the accuracy of the quantitative profile measurement using the D-probe, the results were compared with those from the laser profilometry for sample tubes with various geometric anomalies. For the calibration of the D-probe data, the optimized procedure using the 3-rd order polynomial equation, described in section 3.1, was applied.

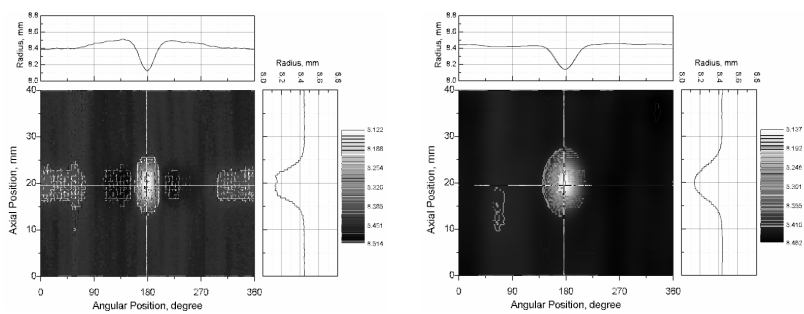

(a) (b)

Fig. 3. Radius distribution of the tube sample with single spot dent, measured by (a) laser and (b) D-probe.

Fig. 3 shows the distribution of the radius values measured along the angular and the axial directrions of the tube sample with a single spot dent, by the laser(Fig.3-a) and the D-probe(3-b). Almost the same results were obtained and the maximum value of the dent evaluated in the radial direction was 0.35mm in both figures. The size of a dent was evaluated to be 0.08mm for an identical tube sample by the bobbin coil probe profilometry, which greatly underestimated the

real size of a dent because the average value of the diameter over a circumference was reflected.

The results from the eccentrically expanded tube sample, made by the explosive expansion method, are shown in Fig. 4. The radius values measured in the expansion transition region of the tube were plotted on a polar coordinate. The same results are observed for the radius measurement by the laser(Fig. 4-a) and the D-probe(Fig. 4-b). The magnitudes of radial expansion are not uniform along the circumferential direction, and the maximum value of the eccentric expansion in the radial direction is evaluated to be 0.35mm in both figures. The bobbin coil probe profilometry for an identical tube sample could not detect the eccentric expansion shape and only showed a diametral expansion of 0.34mm.

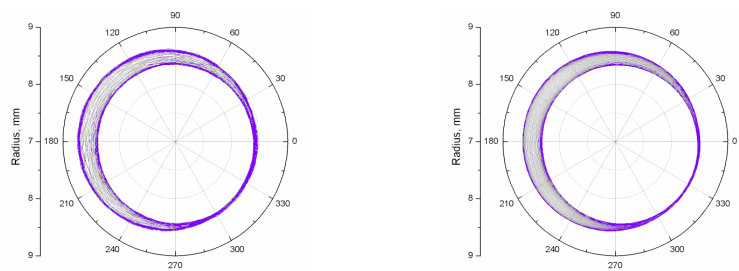

(a) (b)

Fig. 4. Radius distribution of the tube sample with eccentric expansion, measured by (a) laser and (b) D-probe

4. Conclusion

A new eddy current probe for a 3-dimensional quantitative measurement of geometric changes and a simultaneous detection of defects in steam generator tubes has been developed. Through the development and application of an optimized calibration procedure, it was proven that the quantitative measuring accuracy of the geometric changes by using the D-probe were comparable to that by a laser profilometry.

References

1. NUREG/CR-6345, Steam Generator Tube Failures, (1996).
2. H.J. Kim *et al*, Root Cause Analysis and Measures for the Steam Generator Tube Rupture Incident in Ulchin Unit 4, KINS, (2003).
3. D.H. Lee *et al*, Korea Patent No. 562358, KAERI/KHNP, (2006).
4. J. Kang, X-probe Experience at Diablo Canyon, *22nd EPRI SG NDE Workshop*, Hilton Head, USA, (2003).

METHODOLOGY FOR DETECTING FAILED FUEL ASSEMBLY IN A LIQUID METAL REACTOR

SEUNG-HWAN SEONG[†]

Fast Reactor Development Group, Korea Atomic Energy Research Institute
Daedeokdaero 1045, Yuseong-gu, Daejeon 305-353, Korea

SEOP HUR, JAE-CHANGE PARK, SEONG-O KIM

Fast Reactor Development Group, Korea Atomic Energy Research Institute
Daedeokdaero 1045, Yuseong-gu, Daejeon 305-353, Korea

When the fuel assemblies in a liquid metal reactor are failed, the safety and operability of that reactor will be threatened. The early detection of the failed fuel assembly during a normal operation is an important issue for a liquid metal reactor. The gaseous isotopes of fission fragments and the gaseous precursors of delayed neutron are confined in the fuel assemblies and are not released into primary coolant when the integrity of the fuel assembly is maintained. If a fuel assembly is failed, they are released into the primary coolant through the failed location. So, the existence of gaseous isotopes and delayed neutrons in a primary coolant can provide some information on the fuel assembly failure. These gaseous isotopes in the primary coolant are diffused into the cover gas region between the hot pool and the reactor head and the precursors of the delayed neutrons are dissolved in the primary coolant and circulated the reactor along the coolant. For detecting the isotopes in the cover gas region, we adopted the HPGe (High purity Germanium) gamma-ray detector on the reactor head and it was found to have a sufficient resolution to identify the gamma spectrum of the specific gaseous isotopes of fission fragments like xenon and krypton. The fission chambers for detecting the delayed neutron in the primary coolant were adopted and installed in the intermediate heat exchanger. The fission chambers are not sensitive to background noises such as the high energy gamma ray and alpha particles in a reactor and can be manufactured with a small size. After measuring the gaseous isotopes of fission fragments in cover gas and the delayed neutrons in primary coolant, we can identify a failure of the fuel assembly in a liquid metal reactor by evaluating whether those levels are beyond the predefined thresholds which will be determined from the detailed plant design data.

1. Introduction

In a liquid metal reactor, to keep the integrity of the fuel assembly is very important to assure the safety and the operational performance of that reactor. If the fuel assembly fails to keep the integrity, the gaseous radioactive materials in

[†] Seung-Hwan Seong: Tel. 82-42-868-8244, fax. 82-42-861-7697, e-mail: shseong@kaeri.re.kr

the gap fuel rods would be released into the primary coolant and the leakage probability of the isotopes to the atmosphere would be increased. The existence of specific radioactive materials in the primary coolant can provide some information to us about the failure of the fuel assembly. Otherwise, the detection of the failed fuel assembly during a normal operation can be possible if we monitor existence of some particular radioactive materials which should be generated from only fission reactions in the fuel assembly. The representative isotopes from the fission reactions are precursors like Br-87, I-137 etc and gaseous unstable isotopes of fission fragments such as the xenon (Xe) and krypton (Kr), which does not exist in natural atmosphere and only are generated by fission reactions in the reactor. A precursor is defined as a material which can produce delayed neutrons by nuclear reactions.

They are confined in the gap of fuel assemblies and are not released into primary coolant when the integrity of the fuel assembly is maintained. If the fuel assembly fails to maintain its integrity, then the gaseous precursors and gaseous isotopes are dissolved in the primary coolant and circulate along the primary heat transfer loop. Finally, the delayed neutrons are generated from the precursors in the primary heat transfer loop. Also, the gaseous isotopes of the fission fragments are released first into the primary coolant and then finally diffused into cover gas region. So, if the specific gamma energy of the isotopes is detected in the cover gas region, we can identify the fuel assembly failures.

First, for detecting the delayed neutron in the coolant, some fission chambers in the primary coolant will be adopted among several neutron measurement instruments and installed within the free space of the intermediate heat exchangers. A fission chamber is less sensitive to background noises such as the high energy gamma ray and alpha particles in the reactor or primary coolant, and it can be manufactured with a small size. In addition, to monitor the gamma energy in the cover gas region, we will use a diffusion-typed HPGe gamma detector on the reactor head, which can discriminate the specific gaseous isotopes of fission fragments with other gamma sources thanks to its high resolution.

After measuring the delayed neutrons in the primary coolant and the specific gamma energy in the cover gas region, we can identify the failure of the fuel assembly in a liquid metal reactor if those levels are beyond the predefined thresholds which will be determined from the detailed plant design data.

2. Characteristics of Radioactivity from Failed Fuel Assembly in a Reactor

2.1. *Delayed Neutron Behaviors in a Reactor*

The delayed neutrons in a core have been born from the radioactive decay of the precursors generated from fission reactions. The representative nuclides of the gaseous precursors are Br-87, Br-88, I-137, I-138 and so on. Their half-life is 55.60, 16.29, 24.5 and 6.49 sec, respectively. The circulation time of the primary coolant is evaluated to be about 30 sec. By considering its half-life and the circulation time of the primary coolant, Br-87 and I-137 should be chosen as target precursors to detect the fuel of the fuel assemblies.

The release rate is dependent on the failure size and the pressure difference between the gas pressure in the fuel rods and the pressure of the primary coolant in the core. [2][3] The exact pressure difference is varied according to the operational conditions and the characteristics of the manufactured fuel assembly and will be determined after the detailed design of the fuel assembly.

2.2. *Gaseous Isotopes Behaviors in a Reactor*

When the gaseous isotopes of fission fragments which are not in a natural atmosphere are released into the primary coolant, they first circulate by the flow of the primary coolant, and then are diffused into the cover gas region. There are Xe-131m, Xe-133, Xe-135, Xe-138, Kr-85m, Kr-87 and Kr-88 as representative gaseous isotopes only generated the fission reaction in the reactor. Table 1 shows the half-life, specific decay energy of gamma rays and the typical concentrations of the representative gaseous isotopes of fission fragments in the fuel rod of the 600MW-electric reactor.

Table 1. Characteristics of the representative gaseous isotopes in the reactor

nuclide	Half-life	Decay energy (keV)	Concentration (Ci/cm3)
Xe-131m	11.9 Day	163.93	0.1
Xe-133	5.24 Day	80.997	14.2
Xe-135	9.14 Hr	407.99	15.3
Xe-138	14.1 Min	325.3	10.1
Kr-85m	4.48 Hr	304.87	1.32
Kr-87	76.3 Min	2011.88	2.22
Kr-88	2.84 Hr	2029.84	3.09

As shown in table 1, the half-life is enough for gaseous isotopes to be detected by the gamma energy detector installed on the reactor head. In order to calculate the concentration in cover gas region, we will evaluate the transfer time and mechanism from failed fuel assemblies to the detector through an analysis of the circulating coolant flow and diffusion from the coolant to the cover gas region.

3. Characteristics of the Detectors [4][5]

3.1. *Detectors for the Delayed Neutron in a Reactor*

There are some types of neutron detector widely used in nuclear field such as BF-3, LF-6, He-3 counter using neutron reaction and fission chamber using fission reaction. The target precursors have the decay characteristics as below.

- Br-87 → Kr-86 + β + neutron (1.337MeV)
- I-137 → Xe-137 + β + neutron (1.850MeV)

The counters using neutron reaction are suitable to the thermal neutrons which have about energy of 0.025eV. However, fission chamber can be used for various neutron energies, which is dependent on the coating material in the detector. The U-238 coated fission chamber should be efficient to the high energy neutron with a few MeV thanks to its cross section for fission reaction. So, we think the fission chamber detector can be used for measuring the delayed neutrons in the coolant. The fission chamber measures the delayed neutron, which are based on the small fission reaction in the detector. In addition, it can be used in a high energy gamma-ray background and it has a high efficiency to detect neutrons with a small size because the energy peak of the fission reaction is very high (~167MeV). Figure 2 shows typical energy spectrum of fission reaction. We suggest that the fission chamber be most effective to detect the delayed neutron in the coolant from the failure of fuels in the reactor.

3.2. *Detectors for the Gaseous Isotopes in a Reactor*

For monitoring the gaseous isotopes, we will install a diffusion-typed HPGe (High purity Germanium) gamma detector on the reactor head. Contrary to other gamma detectors, it can discriminate the specific isotopes and eliminate the back ground noises which come from any other radioactive materials thanks to its superior energy resolution. For example, the HPGe gives a FWHM(full width at half maximum)≈ 1.9keV, while the Na(Tl) gives FWHM≈ 70keV for Co-60. [4] Figure 2 shows its capability for energy resolution comparing with the conventional scintillation detectors. Although the HPGe detector needs to be

cooled when in use, it has powerful resolution to identify the specific isotopes which have energy band from 3keV to 1MeV. Therefore, we should adopt the HPGe detectors for detecting specific isotopes of gaseous fission fragments due to its resolution to discriminate the specific isotopes. The HPGe detector cannot be easily mounted in the primary loop due to its integrity and requirements for cooling. However, it can be installed on the reactor head and we focused on the gaseous isotopes which can diffuse into the cover gas.

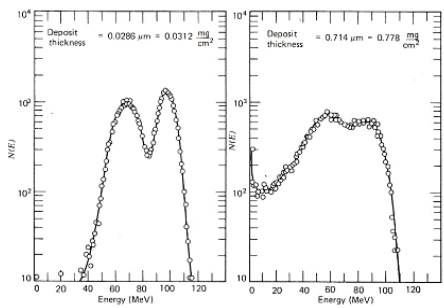

Fig. 1. Typical energy spectrum of fission reaction

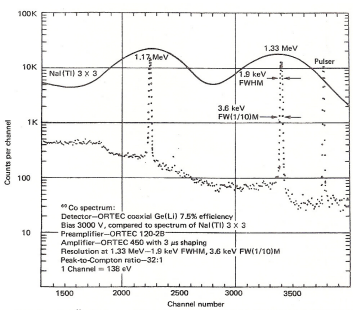

Fig. 2. Characteristics of HPGe detectors

4. Conclusions

We have developed the concept of an on-line detection methodology for fuel assembly failures in a liquid metal reactor. The gaseous isotopes of fission fragments in the cover gas and the delayed neutron in the primary coolant can provide information about the failures of fuel assembly. We suggest that the diffusion-type HPGe gamma detector for the gaseous isotopes of fission fragments and fission chambers for the delayed neutron be adopted. The HPGe detector can be mounted on the reactor head with cryostat cooling equipment and fission chambers can be installed in the intermediate heat exchanger (IHX) considering the detection efficiency and the reduction of background noises.

The detection rate of the delayed neutron in the primary coolant and the specific gamma energy of the gaseous isotopes in the cover gas are dependent on the concentrations of the precursors, the isotopes dissolved in the coolant, the location of the failed fuel and the failure size. The threshold of the detection rate will be determined through the hydraulic mockup test of primary coolant and by a consideration of the decay constants and the background noises in the primary coolant later. At present, we assume that 4 fission chambers will be installed in both intermediate heat exchangers and 4 HPGe detectors will be mounted on equidistantly the reactor head as shown Figure 3.

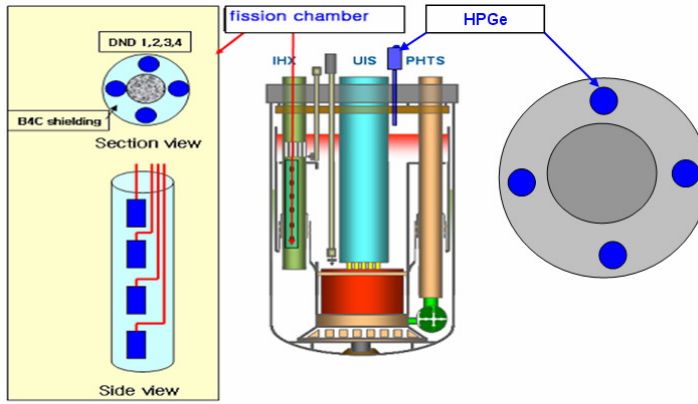

Fig. 3. Schematic location of detectors

Acknowledgments

This study has been carried out under the Nuclear R&D Program by MOST in Korea.

References

1. A.E. Walter and A.B. Reynolds, Fast Breeder Reactors, Pergamon Press (1981).
2. M.S.Kim et al, Investigation of Possibility for Failed Fuel Detection by Using the Neutron Measurement in Primary Cooling Circuit of HANARO, KAERI/TR-1608/2000.
3. Ayazuddin, et al, Fuel-Failure Detection System for Pakistan Research Reactor-1, Annals of Nuclear Energy, Vol 24, No. 15, pp 1213-1222 (1997).
4. N. Tsoulfanidis, Measurement and Detection of Radiation, Hemisphere Publishing Co. (1983).
5. G.F. Knoll, Radiation Detection and Measurements, John Willy & Sons Co. (1989).

DEVELOPMENT OF MAGNETIC PHASE DETECTION SENSOR FOR THE STEAM GENERATOR TUBE IN NUCLEAR POWER PLANTS

DERAC SON †

Physics, Hannam University, 133 Ojeong-dong, Daedeuk-gu Daejeon, Korea

WON IK JOUNG

Physics, Hannam University 133 Ojeong-dong, Daedeuk-gu Daejeon, Korea

DUCK-GUN PARK

Nuclear Mater. Devel. Center, KAERI, P.O.Box 105 Yuseong, Daejeon 305-600, Korea

KWON SANG RYU

Div. of Metrology for Quality Life, KRISS, P.O.Box 102 Yuseong, Daejeon 305-600, Korea

A new eddy current testing probe to separate the eddy current signal distortion due to permeability variation clusters and ordinary defects created in steam generator tubes has been developed. The signal processing circuits were inserted in the probe in order to increase the signal noise ratio and for the digital signal transmission. The new probe can measure and separate the magnetic phase which is created in the steam generator tubes by operating environment of nuclear power plant. Furthermore the new eddy current testing probe can measure the defects so rapidly as bobbin probe, and enhances the testing speed as well as reliability of the defect detection of steam generator tubes.

1. Introduction

Steam generator tube (SGT) in nuclear power plant is a boundary between primary side and secondary side, whose integrity is one of the most critical factors to nuclear safety. The SGT are continuously exposed to harsh environmental conditions including high temperatures, pressures, fluid flow rates and material interactions resulting in various types of degradation mechanism such as mechanical wear between tube and tube support plates, outer diameter

†

stress corrosion cracking (ODSCC), pitting, volumetric changes, primary water stress corrosion cracking (PWSCC), and inter granular attack (IGA) [1]. Multi-frequency eddy current inspection techniques are currently among the most widespread techniques for the rapid inspection of SG tubing in the nuclear power industry [2]. Although the eddy current technique(ECT) is adopted widespread in the nuclear industry, it has the limitation to size the flaw accurately because the eddy current measure the impedance signified by the conductivity change associated with the volumetric change of flaws, where the permeability of flaw is considered unity. The EC test currently applied in the nonferrous materials having relative permeability 1 such as Inconel alloy because the magnetic permeability of magnetic materials severely limits the depth of penetration of induced eddy currents. Furthermore, the small magnetic phase having permeability variation inherent in SGT can cause spurious ECT results [3]. It is well known that some part of SGT change as a magnetic phase known as permeability variation clusters (PVC) under the conditions of high pressure and temperature which is the operating environments of nuclear power plant. The relative permeability of the magnetic phase is greater than 1 and a number of ferromagnetic phases, a value of several thousand could be reached. Internal stresses caused by drawing, straightening, and similar working of the material, can give rise to severe fluctuations in the permeability. These fluctuations would always cause interference with the test signals. In order to eliminate this interference effect during testing, the ferromagnetic test piece is magnetized by a suitable device such as magnetized ECT probe. The relative permeability will approach unity by a suitable device. The magnetic properties of the ferromagnetic test piece become similar to those of a non ferromagnetic material and thus, the interference from permeability fluctuation is eliminated [4]. Recently, to eliminate ECT signal fluctuation, the magnetized probe with the built-in permanent magnet is being used in the SGT inspection, because a strong magnetic field of this probe reduces the variation of magnetic permeability, which improves S/N ratio. If we can separate magnetic phase selectively from the flaws using magnetic sensor, the reliability of ECT in SGT inspection will be greatly enhanced. This paper shows the possibility that the permeability sensor can be applied to detect the magnetic phase in the steam generator tubes and to measure them quantitatively.

1.1. *The principle of magnetic phase detection sensor*

The measuring principal of magnetic phase in Inconel alloy is based on the measuring magnetic flux density of sample, it composed of U-shape yoke wound

magnetizing coil and *B*-sensing coil, and *H*-sensing coil as shown in figure 1 (a). The appearance of magnetic phase in the Inconel alloy results in a change of magnetic flux density of the B-searching coil. The variation of flux density due to magnetic phase can be obtained by measuring the applied field by H-searching coil and induced flux by B-coil. In this testing, the magnetizing coil is generally close to the test sample so as to minimize the lift-off. So that as shown in figure 1 (a), the magnetic flux line that it creates affects the sample. The constructed probe shown in figure 1 (b) consists of a exciting coil and a magnetic field sensor, a SiFe yoke with two solenoids: the driving coil and the pick-up coil. This probe detects the voltage variation and phase shift induced by the magnetic field caused by the presence of the magnetic phase in the structure under test.

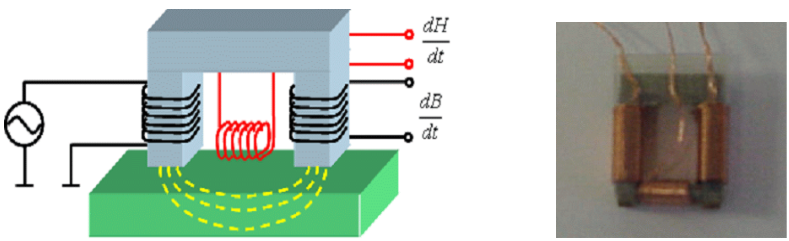

Fig. 1 (a) Structure of the sensor for magnetic phase detection, and (b) Photography of the sensor.

The measurement system was constructed by using a waveform generator to excite the coil with a sinusoidal current and a lock-in amplifier to detect vector component of magnetic flux. The new test probe and block diagram of the measuring system are shown in figure 2. The probe for measuring the flaws and magnetic phase in the SGT is constructed as the size of eddy current test, therefore the new probe pass through the 7/8" SGT tube having the size of 19.69 mm ID. The electronic circuits for magnetizing the sensor, measuring the induced voltage by magnetic phase are inserted in the probe. The induced voltages are converted as digital signal by 4-channel 16 bit analog digital converter (ADC) circuits, and the 8bit microcontroller 89C4501 embedded in the probe. The digital signals are transmitted in the personal computer through the RS232C interface.

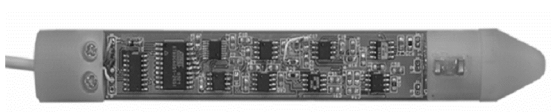

(a)

Fig. 2 (a) A new eddy current test probe and (b) Block diagram of the measuring system.

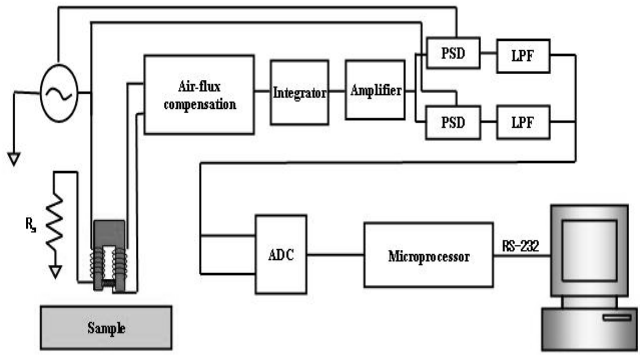

(b)

Fig. 2 *Continued.*

2. Results and discussions

In order to investigate the performance of the magnetic phase detection sensor, Inconel 600 plate specimen containing various artificial slots and magnetic phase was used in this experiment. The detecting capability of magnetic phase is investigated using the developed sensor and plate type specimen, and the results were applied in the manufacture of bobbin type probe for the detection of the SGT. Figure 3 shows the experimental results obtained by analyzing the Inconel plate containing artificial flaws and magnetic phase with permeability detection probe. In this figure, A2 is the EDM slot with the width of 0.127, length of 4.013 and the depth of 0.229 mm. The flaws B2 and C2 have the same area but depths are 0.457 and 0.686 mm, respectively. In D2 and E2 positions, the slice of ferromagnetic materials having the size of 0.15x1.6x0.2 mm and the permeability of 510 and 780 were inserted in the Inconel plate, respectively. The measurements have been carried out at a frequency of 10 kHz. The lift-off was varied from 0.25 to 0.75 mm. In this experiment, with the permeability measurement based system we can detect the different size of crack and magnetic phase. The induced voltages are proportional to the sizes of artificial cracks, and the y-component signal is reversed in the ferromagnetic fragments.

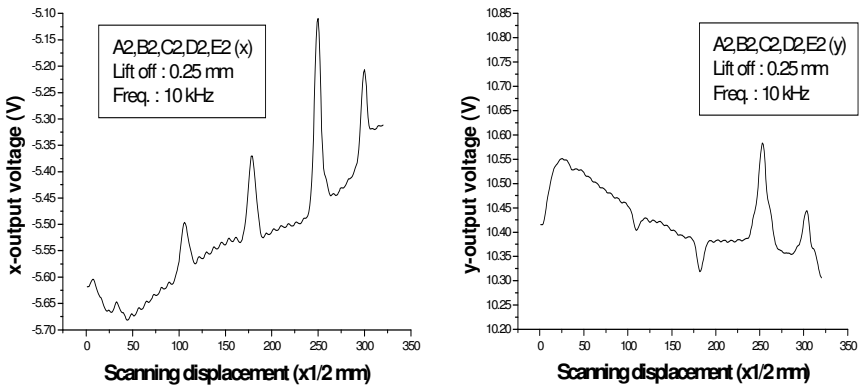

Fig. 3 Experimental results on the Inconel 600 plate having the artificial flaws (A2, B2, C2) and ferromagnetic phase (D2, E2).

Figure 4 shows the experimental results obtained by analyzing the Inconel tube containing artificial flaws and magnetic phase with permeability detection probe. The sample have EDM slot with the width of 0.5 mm, length of 10 mm and the depth from 0.254 mm to through hole as shown in Table 1. The ferromagnetic phases were inserted in the sample position 4, 6, and 8 to simulate the PVC effects. In this experiment, with the permeability measurement based system we can detect the different size of crack and magnetic phase. The induced voltages are proportional to the sizes of artificial cracks, and the signal phase is reversed in the ferromagnetic fragments.

Table 1.Dimensions of the artificial flaws and ferromagnetic phases as the sample positions in Inconel 600 tube.

Sample position	Width (mm)	Length (mm)	Depth (mm)
1	0.5	10	0.254
2	0.5	10	0.508
3	0.5	10	0.762
4	0.5	10	0.762
5	0.5	10	1.016
6	0.5	10	1.016
7	0.5	10	Hole
8	0.5	10	Insert

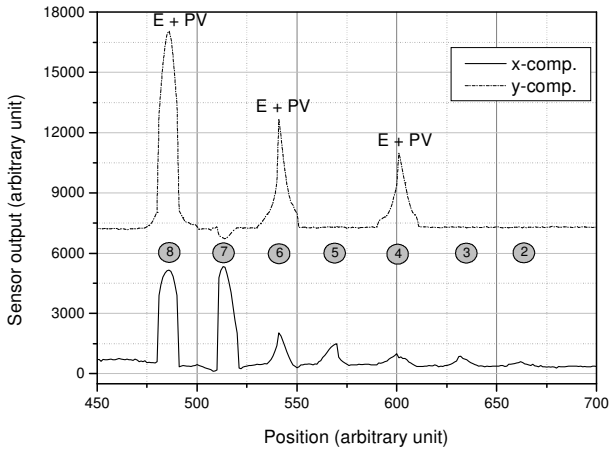

Fig. 4 The change of magnetic flux density in the artificial flaws and magnetic phase.

3. Conclusion

To eliminate the ECT signal distortion due to permeability variation clusters (PVC) in the SGT, probe with magnetic field biased by permanent magnet has been used in the SGT inspection but ferromagnetic phases of PVC's are not saturated by the built-in permanent magnetic of probe, S/N ratio becomes decreases. In this work, new technology based on the magnetic permeability measurement has been introduced. Using the developed sensor we could distinguish cracks and magnetic phases created in the SGT selectively.

References

1. P. Xiang, S. Ramakrishnan, X.Cai, P. Ramhalli, R. Polikar, S.S. Udpa, L. Udpa, Int. J. Appl. Electromagnetics and Mechanics. 12 (2000)151-164.
2. Avanindra, Multifrequency eddy current signal analysis, Master Thesis, Iowa State University, 1997.
3. V.S. Cecco, Eddy Current Manual, Ontario, Chalk River national Laboratories, 1983.
4. S. Chikazumi, « Physics of Magnetism » John Wiley & Sons, New York, 1964.

STUDY ON A NEUTRON FLUX DETECTION AND ITS DIGITAL SIGNAL PROCESSING FOR NUCLEAR REACTORS

SEOP HUR, JAE-CHANG PARK

I&C/HF Research Center, Korea Atomic Energy Research Institute, 150 Ducjin-dong, Yuseong-gu, Deajeon, 305-600, Korea

BUNG-HO KIM, SEUNG-HWAN SEONG

SFR Development Group, Korea Atomic Energy Research Institute, 150 Ducjin-dong, Yuseong-gu, Deajeon, 305-600, Korea

SANG-JUNG LEE

Department of Electronic Engineering, Chungnam National University,220, Goong-dong, Yuseong-gu, Daejeon, Korea

This study was aimed at developing a method for detecting a neutron flux and for simulating the digitized signal processing circuits of a wide-range neutron flux monitoring system for a nuclear reactor. The conventional analog neutron flux monitoring system has the shortcomings which are a non-linearity of the measurement values, a transmission error due to signal distortion, and environmental uncertainties due to the temperature fluctuation. The digitalized signal processing method for a neutron flux monitoring system has been developed by establishing a mathematical model for the measurement channel. The output pulse shape and resolving time of the system were determined by the bilinear transformation, and these parameters were verified by a simulation. It is noted that the sampling frequency of the digital system for detection of the mean-square voltage mode is 15 MHz.

1. Introduction

The objective of a neutron flux monitoring system is to provide indications and electrical signals proportional to a reactor power for a reactor control and protection. This system meets its objective by means of a neutron measuring instrumentation comprised of detectors and signal processing equipment which provides indications and signals for conditions of a reactor shutdown, startup and full power operation.[1]

Conventionally, the neutron detectors of loop-type reactors have been located at outside a reactor vessel because of an in-sufficient neutron leakage to sense a neutron flux and a very little variance of the measurement sensitivity against a

coolant temperature fluctuation. A neutron flux monitoring system, which is implemented by complicated analog logic circuits including a linear amplifier and summer, logarithmic circuits, differential circuits (rate of change circuits), mean square voltage circuits, and bi-stable trip circuits, etc., consists of a startup channel, control channel and a safety channel.[1,2] Such an analog system has shortcomings which are a non-linearity of the measurement values, a transmission error due to a signal distortion, and environmental uncertainties due to the temperature fluctuation.

This paper describes a digitalized signal processing method for neutron flux monitoring system developed by establishing a mathematical model for a measurement channel. The output pulse shape and resolving time of the system are determined by a bilinear transformation, and these parameters are verified by MATLAB simulation.

2. Configuration of Digital Neutron Flux Monitoring System

2.1. *Conventional Systems*

The neutron flux monitoring system consists of two startup channels, two control channels and four safety channels. Typically, the safety channels are provided to monitor the ex-core neutron flux over the range of a source power to full power of the nuclear reactor. Two startup channels provide source level range neutron flux information to a reactor operator. Two control channels provide neutron flux information, in the power operating range, to the reactor regulating system for use during automatic turbine load-following operations.

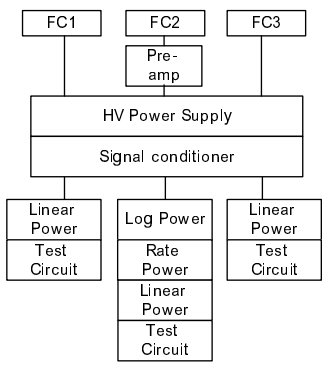

Fig. 1. Typical configuration of conventional neutron flux monitoring system (One channel of safety channels).

There are three kinds of neutron detectors, a fission chamber for the safety channels, a BF_3 proportional counter for the startup channels, and a ionization chamber for the control channels. [1]

Fig. 1 typically shows the analog type of a safety channel for a neutron flux monitoring system. The detector assembly provided for each safety channel consists of three identical fission chambers. The use of three sub-channel detectors in this arrangement permits a measurement of the axial power shape during a power operation. The center fission chamber is also utilized as a wide range detector. The signal processing circuitry of the wide range detection is a

complicated analog system which includes a counting circuitry, mean square voltage (MSV) circuitry, logarithmic circuits, etc.

2.2. *Proposed Digital System*

The digitalized signal processing module for a neutron flux monitoring system has been proposed as shown the Fig. 2. The digital signal processing module consists of a controller, a high speed A/D converter and calculator, a pulse counter, a low speed A/D converter and a field network card. The function and its correspondence with the conventional analog system of each digital component are shown in the Table 1. The digital component except for the high speed A/D and calculator is analogous to a conventional digital component. The high speed A/D and calculator has the special functions which perform a dedicated calculation such as a root mean square, logarithmic and differential calculation. The reason for the use of this component for a dedicated calculation is to achieve the high speed calculation to meet the A/D conversion rate. The A/D conversion rate of the high speed A/D and calculator has been established as 15 MHz. (See chapter 3).

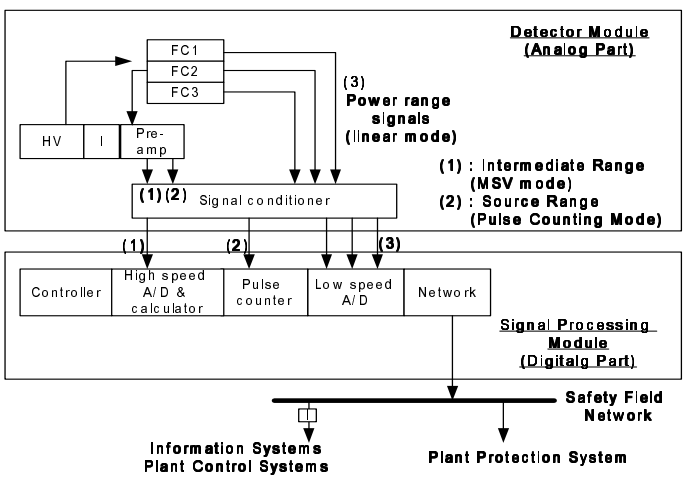

Fig. 2. The schematics of the proposed digital neutron flux monitoring system.

3. Discrete Modeling of the Neutron Flux Monitoring

3.1. *System Analysis*

The system modeling of a detector module had been established by L.M. Johnson et.al [3] using the following assumptions:

Table 1. The functions and correspondences with the analog circuits of the digital component of a proposed digital neutron monitoring system.

Digital Comp.	Function	Correspondence with Analog Circuits	Remarks
Controller	- Signal Integ.	- Average/calibrate linear power	
	- Calibration	- Count Sum	
	- Test logic	- Cross over detector	
	- Device control	- Log power calculate/sum	
		- Test circuits	
High speed	- A/D	- MSV mode	FPGA
A/D Converter	- RMS calculation	- RMS	based
& Calculator	- Logarithmic cal.	- Logarithmic circuit	
	- Differential cal.	- Rate of power	
Pulse Counter	- Pulse counting	- Discriminator	FPGA
		- Digital pulse counter	based
Low speed	- A/D	- Linear mode	FPGA
A/D Converter			based
Network Card	- Data trans.	- Hard-wired signal trans.	

1. The detector can be represented as a current source with a internal capacitance.
2. The input impedance of a cable is the same as those of the capacitance paralleling connected to the pre-amplifier.
3. Input impedance of the pre-amplifier is greater than the cable impedance.
4. The input impedance of the pre-amplifier can be expressed as a resistance, has a clipping time constant τ_1 and a delay time constant τ_2, and its output impedance is sufficiently small.

Fig. 3 represents the equivalent circuit of the detector, cable and pre-amplifier. The transfer function of the pre-amplifier can be expressed by equation (1), and the input voltage of the pre-amplifier due to the current impulse response at time t=0 can be expressed by equation (2), where K is the gain, ω_1 is $1/\tau_1$, ω_2 is $1/\tau_2$, q is the electric charge (C_0R_0), ω_0 is $1/\tau_0$.

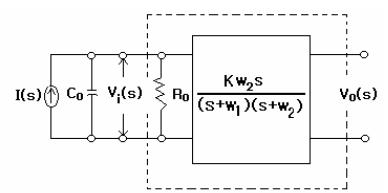

Fig. 3. Typical equivalent circuit of the neutron detector, cable and pre-amplifier.

$$G(s) = \frac{K\omega_2 s}{(s+\omega_1)+(s+\omega_2)} \tag{1}$$

$$V_i(s) = \frac{q}{C_0(s+\omega_0)} \tag{2}$$

The output of the pre-amplifier due to a single current impulse input at time t=0 is expressed by equation (3) and its time response is expressed by equation (4).

$$V_0(s) = \frac{qK\omega_2 s}{C_0(s+\omega_0)(s+\omega_1)(s+\omega_2)} \tag{3}$$

$$Vo(t) = qR0K\omega 2\left\{\frac{\omega_2 e^{-\omega_2 t}}{(1-\omega_2/\omega_0)(\omega_2-\omega_1)} - \frac{\omega_1 e^{-\omega_1 t}}{(1-\omega_1/\omega_0)(\omega_2-\omega_1)} - \frac{e^{-\omega_0 t}}{(1-\omega_1/\omega_0)(1-\omega_2/\omega_0)}\right\} \quad (4)$$

$(\omega_0 \neq \omega_1 \neq \omega_2)$

3.2. *Discrete Neutron Flux Monitoring*

Let $G_c(s)$ be a transfer function of a continuous time system. From equation (3) $G_c(s)$ is expressed by equation (5).

$$G_c(s) = \frac{K\omega_2 s}{C_0(s+\omega_0)(s+\omega_1)(s+\omega_2)} \quad (5)$$

By using a bilinear transform equation (5) can be transferred to a discrete time transfer function as equation (6).

$$G(z) = \frac{K\omega_2 \frac{2(z-1)}{T(z+1)}}{C_0\left\{(\frac{2(z-1)}{T(z+1)}+\omega_0)(\frac{2(z-1)}{T(z+1)}+\omega_1)(\frac{2(z-1)}{T(z+1)}+\omega_2)\right\}}$$

$$= \frac{K\omega_2}{C_0}\left[\frac{T}{2}(z+1)\right]^2 \frac{(z-1)}{\left\{(1+\frac{\omega_0 T}{2})z-(1-\frac{\omega_0 T}{2})\right\}\left\{(1+\frac{\omega_1 T}{2})z-(1-\frac{\omega_1 T}{2})\right\}\left\{(1+\frac{\omega_2 T}{2})z-(1-\frac{\omega_2 T}{2})\right\}} \quad (6)$$

Equation (6) is a discrete time modeling result using the continuous time model (equation (3)) of the pre-amplifier output. If equation (3) is stable, equation (6) is also stable.

To verify the proposed discrete time modeling, a simulation is performed by using following system parameters in the case of a long cable between the detector and the pre-amplifier;

$\omega_1 = 1.41\times10^5 rad/\sec$, $\omega_2 = 3.14\times10^6 rad/\sec$, $\omega_0 = 3.00\times10^5 rad/\sec$

$C_0 = 655pF$, $R_0 = 5.1k\Omega$, $K = 178$

$\bar{q}_n = 1.4\times10^{-13} Coulombs/\ pulse$

The output of the pre-amplifier is shown in the Fig. 4. The sampling frequency of the high speed A/D converter and calculator can be set at 15 MHz which is 1/5 times that of the fastest time constant of the system.[4, 5]

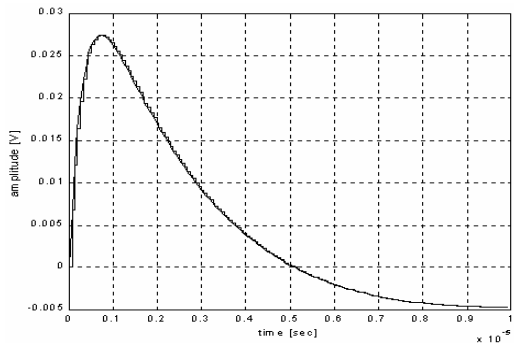

Fig. 4. The simulation results of the pre-amplifier output (for long cable).

4. Conclusion

The digitalized signal processing method for the neutron flux monitoring system has been developed by establishing of mathematical model for a measurement channel. A digital signal processing module has been proposed to enhance the system reliability. The high speed A/D and calculator have the special functions which perform a dedicated calculation such as a root mean square, logarithmic and a differential calculation. To provide the design requirements for the proposed system, a discrete modeling and simulation have been performed. It is noted that the sampling frequency of digital system for detection of the mean-square voltage mode is 15 MHz.

Acknowledgments

This study has been carried out under the Nuclear R&D Program supported by the Ministry of Science and Technology, Republic of Korea.

References

1. "Operation-Maintenance Instruction for Ex-Core Neutrin Flux Monitoring System Yonggwang 3& 4, Vol. I. II, WestingHouse (1994).
2. S. Hur, "Instrumentation Technique Analysis of SMART", KAERI-TR-1028/98, Korea Atomic Energy Research Institute (1998).
3. L.M. Johnson and C.H. Meijer, "A two-range system for ex-core neutron flux monitoring", IEEE Nuclear Power Systems Symposium-San Francisco, California, pp.1~8, Oct. 29~31 (1969).
4. R.A. DuBridge, "Campbell theorem-System concepts and results", IEEE Transaction on Nuclear Science, Feb., pp.241~246 (1967).
5. David A. Gwinn and William M. Trenholm, "A log N and period amplifier utilizing statistical fluctuation signals form neutron detector", IEEE Transaction on Nuclear Science, April, pp.1~9 (1963).

DEVELOPMENT OF AN UNDERWATER UT INSPECTION SYSTEM FOR REACTOR WELDING AREAS*

YOO-RARK CHOI†
ACMD, KAERI, P.O.Box 105
Yuseong Daejeon Korea

JAE-CHEOL LEE
ACMD, KAERI, P.O.Box 105
Yuseong Daejeon Korea

A reactor is a pressurized core safety instrument in a NPP(Nuclear Power Plant). It is made of carbon steel and its inner surface is covered with stainless steel. Its body consists of three cylinders and they are welded to each other. There are several holes for inlets and outlets in the reactor body. The welding areas are vulnerable points for a reactor. The inspection of a rector welding areas is one of the most important maintenance procedures during a NPP overhaul period. We developed a underwater reactor welding area UT(Ultra-sonic Test) inspection system for a pre-service. The main components of the inspection system are an underwater inspection robot, a laser positioner, a UT analysis system and a main control system. We executed an underwater UT inspection for the Ulchin unit 6 at Doosan Heavy Industries with the developed inspection system.

Keywords: Reactor; Safety; Welding; Underwater; Ultra-sonic; Robot.

1. Introduction

KAERI(Korea Atomic Energy Research Institute) had developed KSNP(Korea Standard Nuclear Power Plant) since 1984. It was designed to generate 100MKw electric power. The first KSNP was Ulchin Unit 3 constructed by Kepco(Korea Electric Power Corporation) in 1998. Korea has 6 KSNPs now.

These NPPs have pressurized water reactors. It must stand a 150~160 air pressure and 300 degrees centigrade heat. If there are some defects in the reactor, these conditions may cause serious accidents such as a loss of national electric power and human lives.

* This work is supported by MOST.

The reactor is made of carbon steel. It consists of a head, a body and a bottom head. There are welding areas on the body and bottom head. These welding areas are the weak points of the pressurized water reactor.

The regular maintenance procedures for the nuclear power plant safety instruments are executed during the overhaul period every fourteen months in a KSNP. The duration of an overhaul is 3 weeks. The reactor inspection is executed based on an international standard code such as the ASME(American Society of Mechanical Engineers) code. The UT inspection method is adapted for a reactor welding area inspection. It must be executed in radioactive water because contaminated water can not be moved to other place. It takes a long time to execute this inspection by the traditional equipment. We developed an automated and compact inspection system for the KSNP reactor welding areas to improve this problem.

2. Inspection Method for a Korean Standard Reactor

The height of the Korean Standard Reactor is about 11M. Its weight is 300t. The thickness of its body is about 28Cm. The reactor body and bottom head have 4 welding areas. It has 6 welded nozzles, 4 for inlets and 2 for outlets.

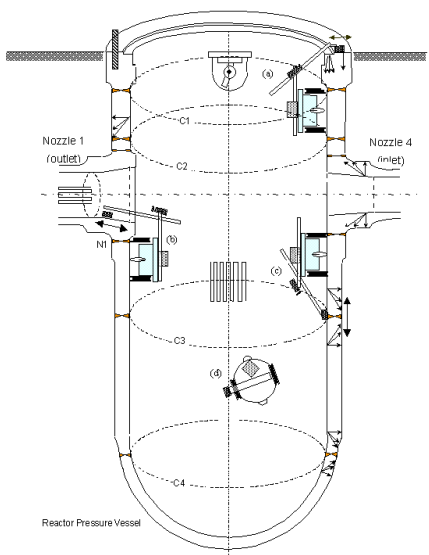

Fig. 1. Inspection of a Korean Standard Reactor

The reactor inspection is executed on C1~C4 and 6 nozzles. Figure 1 describes the inspection areas and inspection schemes for the underwater robot and table 1 explains the welding areas[1].

Table 1. Welding area

C1	Between Flange and Upper Shell
C2	Between Upper Shell and Middle Shell
C3	Between Middle Shell and Lower Shell
C4	Between Lower Shell and Bottom Head
Nozzle	Between Nozzle and Middle Shell Between Nozzle and Nozzle Pipe

There are two kinds of inspections methods. One is circumferencial inspection and the other is nozzle inspection[1].

Table 2. Inspection items of Korea Standard Reactor

Symbol	Scanning direction		UT probe		Robot Posture
			Probe	Angle	
Circumferencial Shell weld					
C1	DN	Flange		10.5°, 4.0°, -2.5°	(a)
	UP			0°,45°,60°, Slic	(c)
	CW			0°,45°,60°, Slic	(c)
	CCW			0°,45°,60°, Slic	(c)
C2	“				(c)
C3	“				(c)
C4	“				(d)
Nozzle(inlet : 0°,60°,180°, 240°)					
NI	Inside	Bore		5°, 45°	(b)
	Outside	Shell		0°,45°,60°, Slic	(b)
	CW	Shell		0°,45°,60°, Slic	(b)
	CCW	Shell		0°,45°,60°, Slic	(b)
NI-IRS	CW			Slic	(b)
	CCW			Slic	(b)
Nozzle(outlet : 120°, 300°)					
NO	Inside	Bore		0°, 45°	(b)
	Outside	Shell		0°,45°,60°, Slic	(b)
	CW	Shell		0°,45°,60°, Slic	(b)
	CCW	Shell		0°,45°,60°, Slic	(b)
NO-IRS	CW			Slic	(b)
	CCW			Slic	(b)

3. Design of the Inspection System

3.1. *Specification*

The inspection design specifications[2];

1. Inspection robot: It works underwater. It has four magnetic wheels. It moves along the reactor wall using these wheels. It has a 6-axis manipulator for an UT scanning and a PSD(Position Sensitive light Detector) for a position recognition. Computerized processors are built in to it.
2. Laser positioner: It is installed at the center of a reactor flange. It drives the inspection robot using a laser beam. The PSD on the robot recognizes its laser. A computerized processor is built in to it.
3. UT analysis system: It is a data acquisition and analysis system. It is a real-time system based on lynx OS. It has a 5Mbyte/sec UT data acquisition capability.
4. Main control system: It controls the inspection robot, laser positioner and UT analysis system based on a network. It generates the robot's moving path and generates a set of commands for the whole inspection procedures.

The inner surface of the reactor is covered with stainless steel. The thickness of the stainless steel is about 1Cm. The inspection robot has four magnetic wheels for moving on the reactor wall. Two of them are connected to the harmonic motors and the othersa are attached to the cast. The coordination of the robot is determined by its PSD and the laser positioner. Built-in processors in the robot control its posture and manipulator's movement. When the robot is ready to start an inspection, it send a trigger signal for a data acquisition to the UT analysis system. All of the inspection procedures are controlled automatically by the main control system[1].

3.2. *Design*

We needed a 6-axis manipulator and a LVDT(Linear Variable Differential Transmitter) to scan the reactor wall. The posture of the robot manipulator during an UT inspection is illustrated in figure 2.

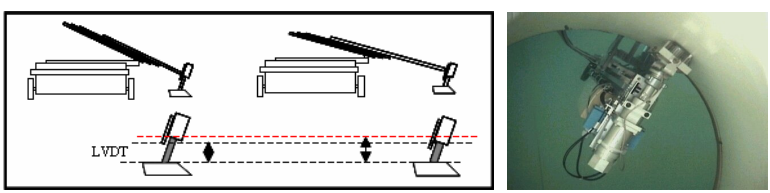

Fig. 2. LVDT movement

When the robot stretches the manipulator, the height of the LVDT is controlled by the controller that is installed in the built-in processor. Stress of the LVDT is fixed during a scanning. This operation can't be controlled by the main control system. The robot controls the angle of the manipulator by itself.[2]

The functions of the robot controller are;

- Communicate with the Main control system.
- Motor control(1 PSD and 6-axis manipulator) and laser recognition.
- LVDT control and generate a trigger signal to the UT analysis system.

Figure 3 shows the architecture of the robot controller.

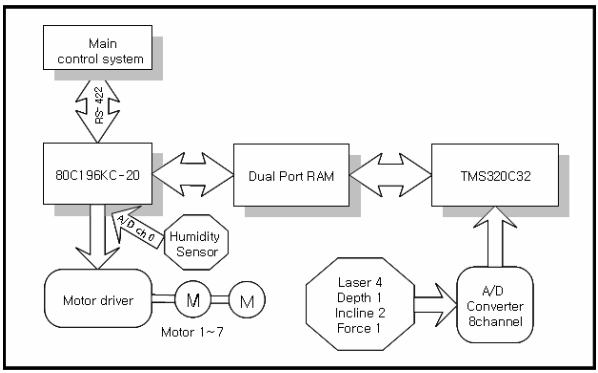

Fig. 3. Architecture of the robot controller

The functions of the main control system(MCS) are;

- Communicate with the laser positioner, the UT analysis system and the Robot. And control them.
- Generate a set of inspection commands and process them automatically based on an inspection error self-recovery algorithm.
- Show the inspection situation in 2-D graphics.

Figure 4 shows the SW architecture of the main control system.

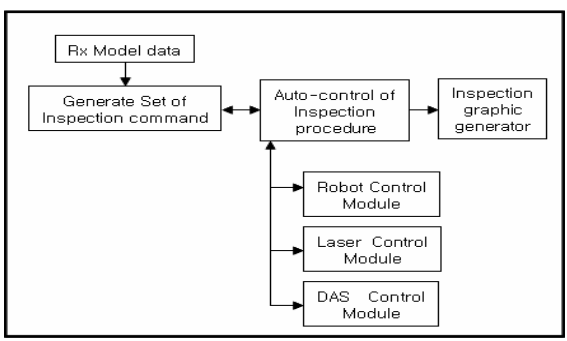

Fig. 4. SW architecture of the main control system

4. Experimental Overview of the Inspection System

Weight of the inspection robot is 45kg. Total weight of the inspection system is 130kg. When we execute an inspection in a KSNP, it only takes 2 hours for the system's installation.

The reactor UT inspection system that we developed is shown in the left side of Figure 5. The right side shows an experimental overview of the Ulchin unit 6 inspection at Doosan Heavy Industries.

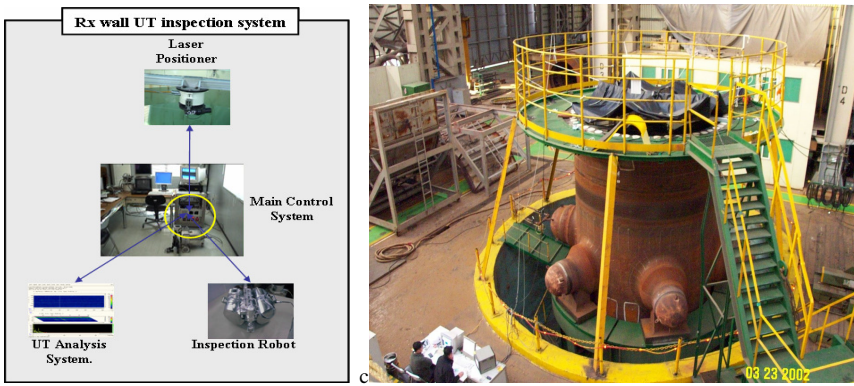

Fig. 5. Experimental overview

Figure 6 shows the laser positioner on the Ulchin unit 6 reactor and one of the UT analysis graphic results for it. The UT analysis system generates an A·B·C-scan display. The results of the inspection for the Ulchin unit 6 were verified by KAITEC.

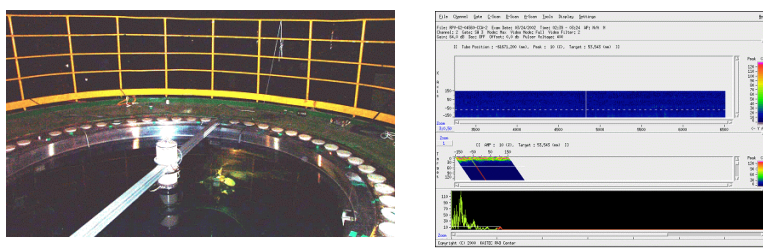

Fig. 6. Laser positioner and UT analysis graphic interface

Acknowledgments

This work is supported by the Nuclear Academic Research Program of the Ministry of Science and Technology(MOST).

References

1. J. H. Kim, J. C. Lee, Y. R. Choi, Development of an automatic reactor inspection system, KAERI/RR-2239/01, 2002.
2. J. H. Kim, J. C. Lee, Y. R. Choi, Development of a remote inspection system for NSSS components, KAERI/TR-2711/2004, 2004.

DEVELOPMENT OF 3D IMAGE PROCESSING SOFTWARE FOR UT-NDE OF STEAM GENERATOR OF NUCLEAR POWER PLANT*

MYUNGWOO NAM†

Digital electro-design, Hyejeon College, San 16, Namjang-ri, Hongsung-eup, Hongsung-gun, Choongnam, 350-702, Republic of Korea

YOUNGSEOCK LEE

Digital Broadcasting & Electronics Eng., Chungwoon Univ., San 29, Namjang-ri, Hongsung-eup, Hongsung-gun, Choongnam, 350-701, Republic of Korea

CHISEUNG PARK

Plant Safety Diagnosis Group, Korea Advanced Inspection Tech. Inc., 461-61, Jeonmin-dong, Yuseong-gu, Daejeon, 305-811, Republic of Korea

OK-YUL YANG

Healthcare & Medical Information, Hyejeon College, San 16, Namjang-ri, Hongsung-eup, Hongsung-gun, Choongnam, 350-702, Republic of Korea

This paper describes a development of UT-NDE software to analyze steam generator of nuclear power plant. The developed software includes classical analysis method such as A, B, C and D-scan images. And it can analyze the detected internal cracks using 3D image processing method. To do such, we obtain raw data from specimens of real pipeline of power plants, and get the envelope signal using Hilbert transform from obtained ultrasonic 1-dimensional data. The 3D image provides useful information on the location, shape and size of cracks, even if there is no special 2D image analysis technique. The results of applications showed that the developed software provided accurate images of cracks on various specimens.

1. Introduction

The equipments of power plants and chemical plants will be degraded by increasing use time and it is phenomenon that mechanical properties of material are weakening happens. Therefore these equipments necessarily need accurate evaluation. But it has various difficulties as like time restriction, economical

problem and so on, because of obtaining specimens which is not damaged from equipments in working plants. By these reason, the high precision nondestructive evaluation (NDE) is much used that is not necessary to inflict damage on equipments and can be monitoring the damage degree correctly. Among them, the ultrasonic method is considered to be the most suitable in aspect of cost-effectiveness, precision and workability in a radioactive environment[1].

This paper is about developing software which can analyze and evaluate for ultrasonic NDE. The developed software can display not only 1-dimensional A-SCAN image but also 2-dimensional B, C and D-SCAN images obtained from processing A-SCAN data, and calculate the crack area. And also, the simple and intuitional analyses of specimens are available, because of being possible to show the size and location of internal crack using 3D image. Additionally, to improve the accuracy of various analyses of specimens, many useful functions are programmed.

2. The Software functions

When an ultrasonic wave encounters an internal reflector, several interactions take place between it and wave. These interactions result in a complex phenomenon based on crack geometry, frequency and angle incidence of the wave among other variables as in Figure 1. The obtained ultrasonic signal patterns contaminated with speckle noises, system noises and so on[2].

So the observer who measures size, depth and shape of crack, has confusion for decision of crack or non-crack. In order to clear decision of existence of crack, observer requires more information about status of crack. From this point of view, various scan types are developed such as A, B, C and D-SCAN. The structures of scan views are shown in Figure 2.

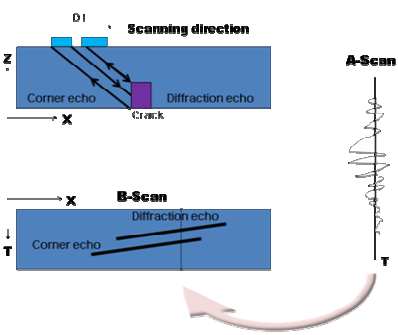

Fig. 2. Structure of A, B, C and D-SCAN.

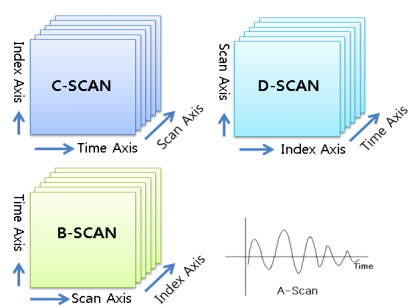

Fig. 1. Schematic diagram of ultrasonic NDE.

The developed software was designed by discussing with engineers in ultrasonic evaluation fields and has useful functions like as Table 1.

Table 1. The software functions of each scan views.

	A-SCAN	B-SCAN	C-SCAN	D-SCAN
Max Value	○	○	×	○
FFT	○	×	×	×
Crack Area	×	○	×	×
Gate	○	○	×	○
Length	○	○	○	○
3D	×	○	×	×

3. 3D image processing method

3.1. *Ultrasonic measurement method*

In this paper, we used a raw data obtained from specimens which is real pipeline of nuclear power plants. The 15MHz transducer frequency is used and the reflection signals are sampled by 100Msps ADC. Next, those are passed to 0.25MHz HPF and saved to PC through the selected channel among 8 channels. In saving process, only data within range set by operator will be saved and be displayed to A-SCAN view. Also among them, the maximum values of Gate area set by operator will be displayed in C-SCAN view. Figure 3 shows the schematic diagram of the ultrasonic measurement system used.

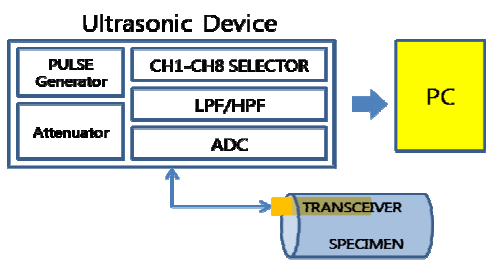

Fig. 3. Schematic diagram of the ultrasonic measurement system

3.2. *Crack area calculation (CAC)*

In order to calculate the crack area, we have to analyze the C-SCAN and B-SCAN data and decide the most proper scan view. And the CAC can be

obtained from the decided A-SCAN and B-SCAN data, after processing them using LPF, power spectrum and differential. The CAC algorithm is shown below.

Goal. Calculate the crack area of 2-dimensions

Step 1. Select the best image of C-SCAN and B-SCAN
Step 2. Compute new A-SCAN data of the first point of the scan axis using the inputted threshold value
Step 3. Pass them to LPF
Step 4. Get the maximum value of envelopes separated by zero
Step 5. Repeat step2 - step4 from second point to last point of the scan axis.

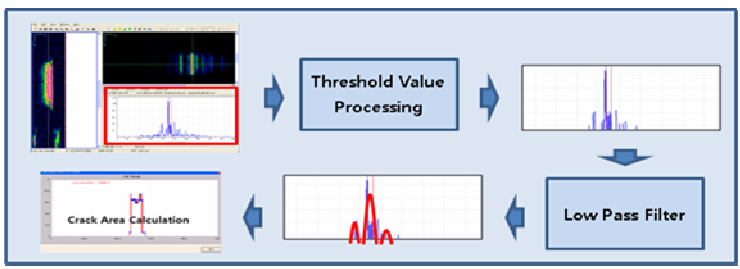

Fig. 4. Block diagram of the CAC algorithm

3.3. *3D image creation*

The developed software provides 3D image which can help 2D image analysis of cracks. The data of using 3D image processing are obtained from transceiver which consists of various angle sensors. From the obtained data, the location and

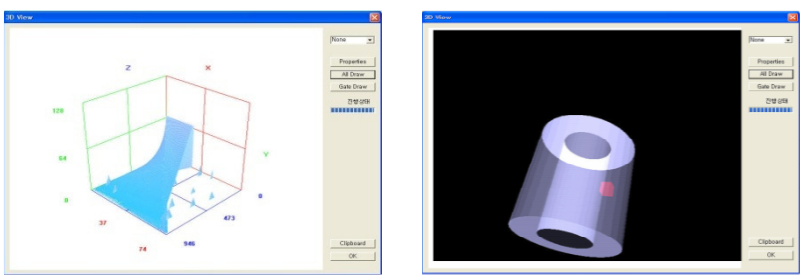

(a) Surface image of the B-SCAN (b) Rough 3D images of crack

Fig. 5. 3D images of the developed software

vertical length and horizontal length are calculated and 3D image is created by using them. The Figure 5 shows the 3D images of crack. Especially, the Figure 5 (b) is made by using straight beam data of ultrasonic and crack area data from angle beam[3][4].

4. Result and discussion

The various functions of the developed software are showed in Figure 6. The results obtained by using them are in good agreement with the specimen containing cracks with known dimensions. The developed software will be upgraded and modified continuously through the various cracks and environments.

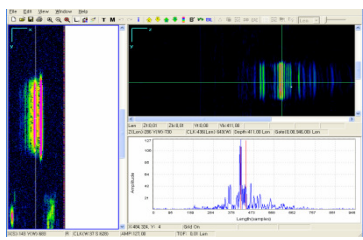

(a) The normal view

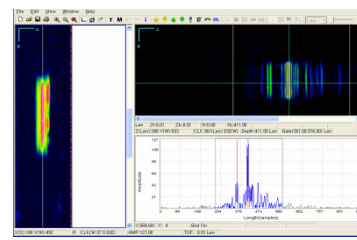

(b) The Gate change

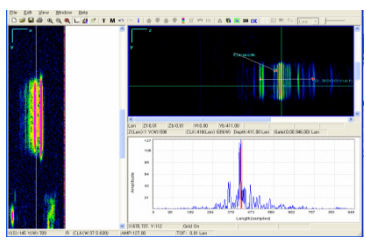

(c) Annotation and measurement

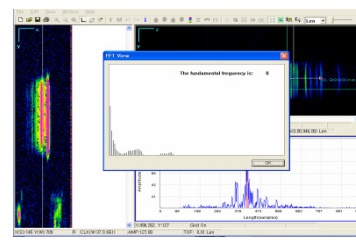

(d) FFT of the A-SCAN data

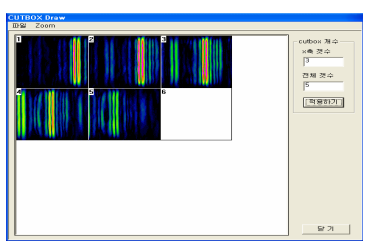

(e) The display of the Cutbox

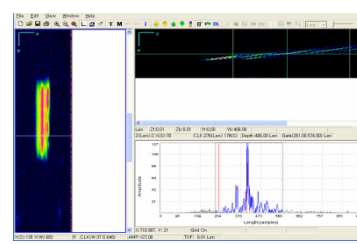

(f) The display of the D-SCAN (B′-SCAN)

Fig. 6. The various functions of the developed software

5. Conclusions

The ultrasonic NDE software is developed for analyzing steam generator of nuclear power plant. The developed software includes classical analysis method such as A, B, C, D-SCAN images and useful functions for obtaining the information of shape, depth, size and position of cracks. Following are the summaries of this study:

- For calculating the crack area, the CAC algorithm is proposed and programmed by VC++ 6.0 in Windows XP.
- For the analysis of crack, 3D image which has rough shape and size of crack is displayed and we obtained a good agreement with comparing the original crack of specimen with known dimensions.
- In the future, we will make specimens which have various shape and size of cracks and upgrade the developed software about the problems which could happen in them.

Acknowledgments

This work is supported by Hyejeon College Research Fund in 2007.

References

1. K.N. Park, C.M. Sim, C.O. Choi and C.H. Lee, *Measurement of Shape in the Radioactive Area by Ultrasonic Wave Sensor*, *KSME* Vol.16, p.927-934 (2002)
2. Youngseock Lee, C .S. Park and S. J. Kim, *3D imaging technique for shape estimation of flaw in UT-NDE*, *Mater. Sci. Forum*, p.270-273 (2004).
3. N.Y. Chung, S.I. Park, M.D. Lee and C.H. Park, *Ultrasonic Detection of Interface Crack in Adhesively Bonded DCB Joints, Automotive Tec.* Vol.3, p.157-163 (2002)
4. Richard S. Wright, Benjamin Lipchak et al, *OpenGL Super Bible*, Third Edition (2005)

CHARACTERISTICS OF PHASED ARRAY UT CTACK EVALUATION WITH THE NUMBER OF ACTIVE ELEMENT AND SCAN ANGLE CHANGES

YONGSANG, CHO[†]

NDE Center, Nuclear Power Lab. Korea electric power research Institute, Munji-Dong 103-16, Yuseong-Ku, Daejeon-City, 305-380, south Korea

JAEHOON, KIM

Mechanical design dept., Chungnam National University, Kung-Dong 220, Yuseong-Ku, Daejeon-City, 305-389, south Korea

Conventional ultrasonic test has some difficulties to detect crack or inspect material especially in the case of complex-shaped components in industrial fields. Phased array UT system and its application methods for complex shaped components will be a good alternative method which can overcome present UT weakness. This study was aimed at developing a new method for finding the crack on material or material structures, and especially for determining the crack length without moving transducer. Especially ultrasonic phased array with electronic scan technique was used in carrying out both sizing and detect ability of crack as scan angles changes. The response of ultrasonic phased array was analyzed to obtain the special method of determining crack length without moving the transducer and detect-ability of crack minimal length and depth from the material. The result showed crack length determining by phased array UT is very real method which has its accuracy and verify the effectiveness of method compared to a conventional crack length determining method

1. Introduction

1.1. *Basic concept of (phased array) triangle method*

The most outstanding characteristics of phased array UT is it has a possibility of the inspection or crack evaluation without moving search unit and even can shows the result as two dimensional state. The purpose of this study is to compare the accuracy of the crack length with a phased array UT triangle method to a conventional crack length determination. In this study, we explain the strategy used when crack evaluation by triangle method to small cracks. A very important feature of phased array systems is the ability to generate numerous incident angles in the material to be tested. When the shear wave by

[†] Work partially supported by grant 2-4570.5 of the Swiss National Science Foundation.

phased arrays propagate in the materials, it also has a certain electronic sweep range of angles by program or inspector's intention as well as its incident angle due to different sound velocity of materials of wedge or inspected materials. As well as phased array UT, the ultrasonic wave into the materials also have a certain range of beam sweep area and focusing area. When the ultrasonic wave induced by phased array go to the materials, if there is a crack in materials, the wave reflected in the front of crack and returns the phased array elements. So the same reasons and case of crack existence, it can be calculated easily the crack length and it can be noticed it's locations and even shapes. In the case of shear waves, if we know the real beam propagation distance and the angles between wave reflection start and stop which is easily seen in phased array signal screen or phased array UT display program. By this method, it is easy to detect the crack length and crack shape or its locations. Figure 1(a) shows the representative crack signals of the test specimens it's detection and it's evaluation signs of test specimens of artificial cracks expressed in figure 2. To evaluate crack length by phased array UT, it can be used by the sector scan method which has oblique way itself, and by check the sector scan angle of crack length which already known, by this method it can be measure the crack length by its angle of ultrasonic beam spread as the mode of ultrasound are changed. Fig 1(b) shows the schematic diagram of the crack length measuring method by the phased array triangular technique which has scan angle due to crack length as the beam propagating distance is change and also mode of ultrasound is changed. The length of crack by this triangle method is determined with the following formula.

$$L = 2S * \mathrm{Tan}\theta \quad \text{----------} \quad (1)$$

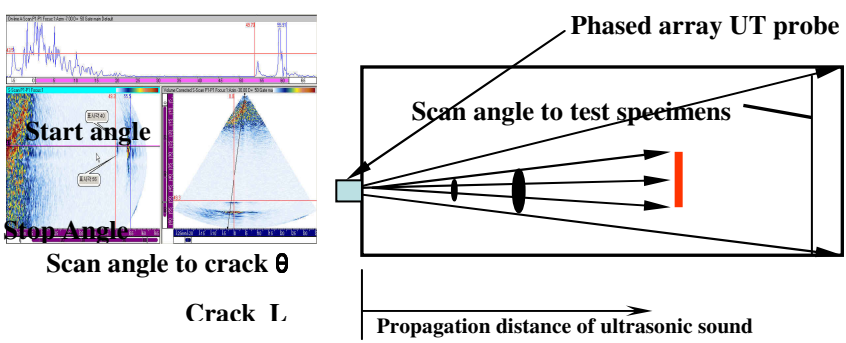

Fig. 1(a, b) Triangle method for crack evaluation by phased array UT

Test Equipment and Method

1.2. *Phased array UT equipments*

The ultrasonic phased array system used for this latest research was the FOCUS which has a special function that could be connected to phased array capability. As shown table 1 presents the specifications of the probe and the wedge was used to eliminate the effect of the dead zone for the emission delays. Phased Array UT System, and high performance computer have realized to develop automated data acquisition, maintaining data, analysis and 3-dimensional image processing, that consist of 128 elements in a specific transducer which is designed to different angles of incidence by different delay times between the array elements.

Table. 1 Probe Specifications

Probe Dimensions	18 X 14 X 23 mm
Frequency	10MHz
Number of element	32 elements
Type of Probe	Linear
Wedge angle	0°(LW) 31°(SW), 53.46°(Sf W)
Wedge material	Plexi glass
Beam Velocity	3200 m/s, Shear wave, Surface wave

1.3. *Test specimens*

The materials of the test specimens for this study of crack length determination and calibration for test equipment is carbon steel. The detailed scale of the test specimen is shown Figure 3. For quantative evaluation of crack length accuracy, reference block which has artificial crack has been used for detection of phased array UT signals and it's characteristics. In case of the crack evaluation test specimens the artificial crack is made by electro cathode machine to give the accuracy of the crack length.

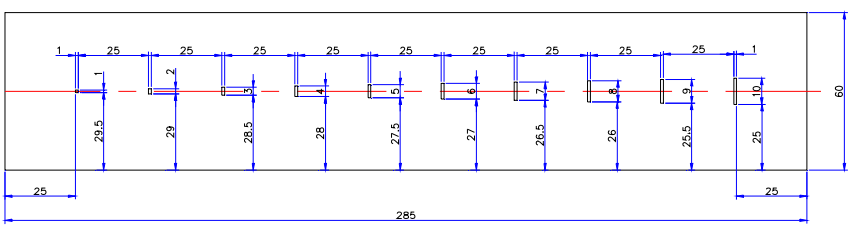

Fig. 2. Drawing of test specimens for crack length determination(mm)

1.4. *Test method*

To compare the conventional crack evaluation method and new technique by characteristics of phased array UT, the test specimens was designed for its real length and shape as shown in fig 2, for this test specimen we could compare on the same crack length by surface wave and longitudinal, and shear waves, respectively. The characteristics of crack is totally depend on its location and orientation, and length, in several cases we could determine the crack length and its size which seen on the monitor of phased array UT signal display.

2. Test results and considerations

2.1. *Characteristic of small crack length evaluation method*

To check the accuracy of crack length evaluation by the new method (triangle method) with electronic scanning angle changes basis on phased array UT, We compare the results of crack length evaluation by equation 1 to real artificial flaw length with changing electronic scanning angles, respectively. Table 2 shows the result of the crack length evaluation by triangle method for artificial crack length 1-5mm according to electronic scanning angle changes 1 to 5 degree with 8 active elements(32 active elements).

Table 2. Comparison of crack length by electronic scan angle with 8(32) elements

Crack length(mm) Scan angle(°)	1	2	3	4	5
1	1.03(1.02)	2.05(2.04)	3.07(3.06)	4.09(4.07)	5.11(5.08)
2	1.04(1.02)	2.07(2.06)	3.09(3.08)	4.12(4.09)	5.13(5.09)
3	1.06(1.02)	2.09(2.07)	3.14(3.11)	4.14(4.13)	5.18(5.11)
4	1.09(1.02)	2.11(2.08)	3.17(3.12)	4.17(4.16)	5.22(5.13)
5	1.09(1.02)	2.12(2.09)	3.19(3.15)	4.19(4.18)	5.28(5.16)

Figure 3 shows a trend of the small crack evaluation result changes according to electronic scanning angle variation of reflected from artificial flaws.

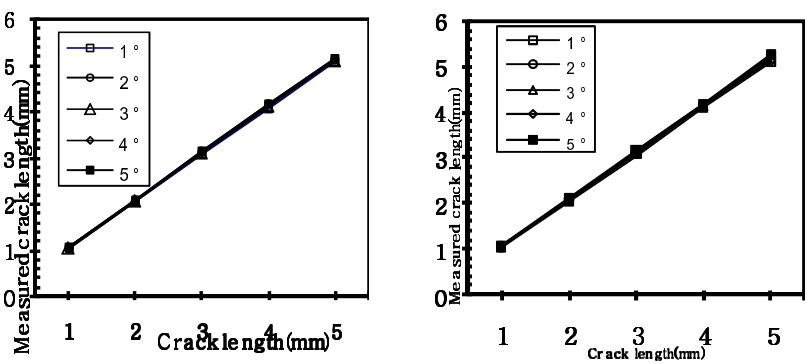

Fig. 3. Crack length evaluation by electronic scan angle changes with 8 and 32 active elements.

On Fig. 3(a, b) we can find the trend that the magnitude of crack length oversize by triangle method increase to artificial crack length increases, while the magnitude of crack length oversize decrease the electronic scanning angle

decrease and the number of active elements increase. Namely, the crack length evaluation by triangle method is more accurate as small electronic scanning angle and much more active elements.

This is the result that the decrease of returned beam angle loss from crack by electronic scanning angle decrease itself in case of small crack length. So, the crack length evaluation method by phased array UT characteristics is more accurate in small crack length and if crack length is large it should be increase the active element number or reduce the scanning angle by adjusting the beam propagating distance. According to this experiment results, the electronic scanning angle should be within 20 degree in general crack length evaluation and to get accuracy of 5% error ratio, the electronic scanning angle should be reduced within 10 degrees. Table 3 shows the result comparison of test for the error percentage of small crack length evaluation by scan angle and number of active elements changes for the same artificial crack lengths.

Figure 5 shows the error percentage of small crack length evaluation by scan angle and number of active elements changes with each variation. On Figure 5, we can find that the best method for small crack evaluation by phased array UT is in case of the smallest electronic scanning angle and the much active elements. In case of 32 active element, the error percentage of crack length evaluation is remain constant the crack length reach up to 5mm. So, we know that this is a main factor for accuracy issue of crack length evaluation.

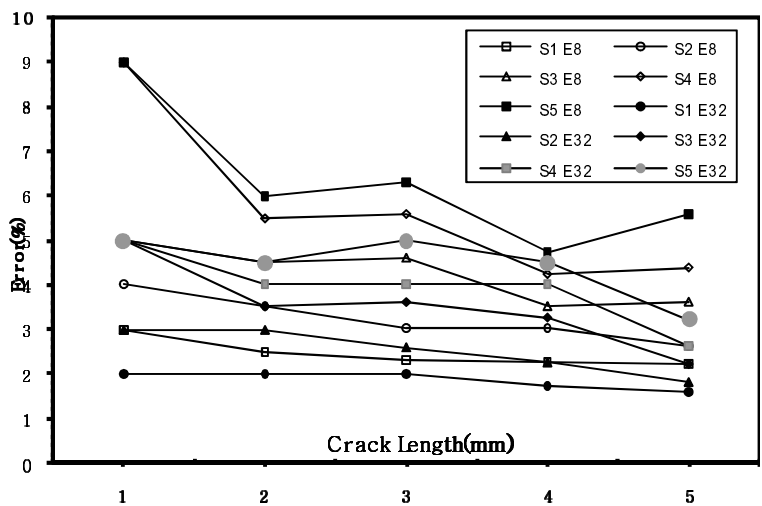

Fig. 4. The error percentage of crack length evaluation by scan angle and element changes

When the all modes of waves induced by phased array UT propagate and meets the crack, they reflected and returns to the phased array elements. By this method, it is very easy to detect the crack and evaluate the crack length.

3. Conclusion

According to the result of test and experiments, The crack evaluation with Ultrasonic phased array system provided improvement are as follows:
The relationship between the distance of ultrasonic beam propagation and the angle of which the crack meets, it can be simply calculated by triangle method and will be a good and new technology for easy crack length evaluations.
And we could have the conclusions of which can evaluate crack length not measuring the moving search units with scales but only to see the start and stop angle of the crack on phased array UT signal screens. The results showed that the newly developed method for crack length determination is a very effective method whose accuracy and verified effectiveness is comparable to conventional crack length determining method.
As the results of whole test and experiments for the all of the artificial cracks which is 1mm to 10mm on the surface of test specimens shown in fig. 2, the accuracy of crack length evaluation result by phased array UT is higher as the electronic scan angle decrease and as the number of active element increase. When the active element are little in a phased array probe, UT signal amplitude did not have big relations to focal depth changes, and when the active element are much in phased array probe, the influence of signal amplitude become smaller by ultrasonic scan angle changes, we should reduce the electronic scan angle with a deep focal depth to get accurate crack evaluation results. The crack evaluation technique by phased array triangle method has much benefits, when we evaluate small crack in complex shaped material or equipments, and the accuracy result of crack evaluation is within 10 % with a 20° scan angle scanning, and is within 5% with a 10° scan angle scanning.

References

[1] H.J. Shin, and S.J. Song, “Nondestructive Inspection of Steel Structure using Phased Array Ultrasonic Technique”, Journal of the Korean Society for Nondestructive Testing, Vol. 20, No. 6, pp.538-544, 2000.
[2] H. Presson and P. Sabourin, “Inspection of Turbine Disk Blade attachment Guide”, EPRI TR-104026, Vol. 1, September, 1994.
[3] Y.S. Cho, “A study of crack evaluation technique by a triangle method of the phased array UT”, Ph. D. Thesis, Graduate School of Chungnam National University, pp.1-156, 2004.

[4] Y.S. Cho, JH. Kim, “A study on the characteristics of surface wave induced by phased array UT”, the 11th Asia pacific conference on nondestructive testing, Jeju Island, 2003.11.5
[5] M. Goto, S. Nagai, K. Uchida, “Automated Phased Array UT System for Turbine Blade Inspection”, Proceedings of 10th. International Conference on NDE in the Nuclear Industry by ASM, 1986.
[6] B. D. Steinberg, Principles of Aperture and Array System Design. New York: Wiley, 1976.
[7] M. Soumekh, “Fourier array imaging”, Prentice-Hall, Inc., 1994.
[8] Wustenberg, H., et al.: Ultrasonic phased arrays for non destructive inspection of forgings, in *Mat. Eval*., June 1993, pp. 669
[9] Schenk, G., Erhardt, A, Hauser,T.: Development of two advanced ultrasonic inspection systems with phased arrays, in ASNT Fall Conf, Seattle 1996, pp.218-220.
[10] Y.S. Cho, and J.H. Kim, “A study on a Crack Evaluation Technique for Turbine Blade Root using Phased Array Ultrasonics”, Journal of Korean Society for Nondestructive Testing, Vol. 24, No. 2, pp.151-157, 2004.
[11] M.H. Park, “Ultrasonic Flaw Sizing Technique”, Journal of the Korean Society for Nondestructive Testing, Vol. 19, No. 6, pp.448-453, 1999.
[12] F. Lyle, and H. Burghard, “Steam Turbine Disc Cracking Experience”, EPRI Report NP-2429, Vol. 2, Project 1398-5, June, 1982.
[13] G. Brekow, “Ultrasonic Inspection at Complicated Geometries of Pressure Vessels with Phased Array Probes”, in 10th International Conference on NDE in the Nuclear and PV Industries, pp.423-429, 1990.
[14] M. Goto and Y. Matsunaga, “Application of portable phased array UT System”, 14th WCNDT, New Delhi, pp.415-422, 1996.
[15] Y.S. Cho, and J.H. Kim, “Evaluation of the Surface Crack by a Large Aperture Ultrasonic Probe”, Journal of Korean Society for Nondestructive Testing, Vol. 24, No. 2, pp.180-185, 2004.
[16] Y.S. Cho, and J.H. Kim, “A study on a Crack Evaluation Techique for Turbine Blade Root using Phased Array Ultrasonics”, Journal of Korean Society for Nondestructive Testing, Vol. 24, No. 2, pp.151-157, 2004.
[17] D.M. Suh and W.W. Kim, “A New Ultrasonic Technique for Detection and sizing of Small Cracks in Studs and Bolts”, Journal of Nondestructive Evaluation, Vol. 14, No. 4, pp.201-206, 1995.
[18] L. Nottingham, K. Solomon, and H. Presson, “Phased Array Ultrasonic Approach to Turbine Blade Attachment Inspection”, in 2th Int. Conf. on NDE in the Nuclear and P. Industries, Philadelphia, pp.493-497, 1992.

DEVELOPMENT OF WATER ABSORPTION TEST EQUIPMENT FOR GENERATOR STATOR WINDINGS IN POWER PLANT*

YONG-CHAE BAE†

Hydro & Fossil Power Generation Lab., Korea Electric Power Research Institute, 103-16 Munji-dong Yusung-gu, Daejeon, 305-380, Korea

HEE-SOO KIM, DOO-YOUNG LEE

Hydro & Fossil Power Generation Lab., Korea Electric Power Research Institute, 103-16 Munji-dong Yusung-gu, Daejeon, 305-380, Korea

The mechanical integrity of generator stator windings is one of the critical point because the electric power is generated and conducted to power system through these windings. De-mineralized water is used to cool stator bars during the normal operation of generator in large power plants because the water cooled method has highest cooling efficiency. Recently, in contrast, the critical accidents such as insulation breakdown are reported in the water-cooled generators in the world. One of the major causes of these accidents occurred many times recently is water leak and absorption of stator windings.

The new test equipment for water absorption in the insulation of stator winding is developed in this study. This paper describes water absorption mechanism of stator windings, the detection method of water absorption, and new equipment of water absorption test for stator windings. It is also provided the implication of the equipment to actual power plant. It is expected to improve the reliability of the predictive diagnosis for the generator stator winding failure due to water absorption in power plant with new developed equipment.

1. Introduction

To cool down the heat emitted from generator winding during its operation, a majority of generators use de-mineralized water characterized by high cooling efficiency. Contrary to such the excellent cooling efficiency, however, the damaged insulations attributed to the frequent leakage or absorption of cooling water in the generator stator winding lead to highly time- and cost-consuming efforts as well as to service deterioration due to unexpected forced outage of generator. Accordingly, if any moisture resulting from leaking cooling water of

* This work is supported by KEPCO, and Ministry of Commerce, Industry & Energy

.

generator stator winding exists within the ground wall insulation, it is required to replace the old winding with new one to prevent its secondary effects. According to a GE's report, it was found that about 57% of the generator stator windings tested by itself were affected by either leakage or absorption, and thus, the company recommends that in the event of winding absorption, the affected winding should be replaced with new one within one year [1]. In this context, there have been a great deal of concern, in Korea and other countries, in the techniques of diagnosing cooling water leakage and absorption in generator stator windings for the purpose of reducing the frequency of unexpected plant outages and the resulting costs. Although major generator manufactures such as GE, Westinghouse and Toshiba have employed both commercially available LCR meters and their own probes to detect and diagnose the presence of any absorption in generator stator windings, it is difficult to apply them to the practices in actual plants because of the poor precision and reproductibility of measurements. For the reason, KEPRI develop Gen-SWAD (Generator Stator Water Absorption Detector) and diagnostic techniques for generator stator windings, apply for its patent and use actively it in the practice.

2. Structure of Generator Stator

A generator consists largely of rotor, stator, stator frame, and bushing. Fig. 1 shows a 500MW-capacity standard thermal power generator stator which is mostly commonly used in the domestic power plants. Fig. 2 shows the inside of stator winding in which there are a number of cooling water flow passages intended to cool down the heat emitted from the internal copper conductors during operation. The outside is enclosed by mica-epoxy insulating material. The volume of cooling water supplied by the stator cooling water pump flows into the stator winding clip, and runs along the cooling water flow passages and finally cools down the windings.

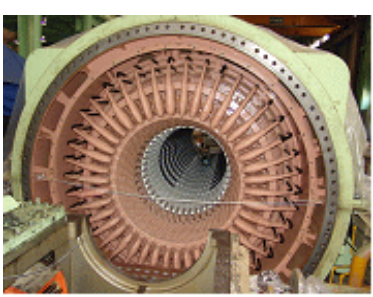

Fig. 1. Generator Stator

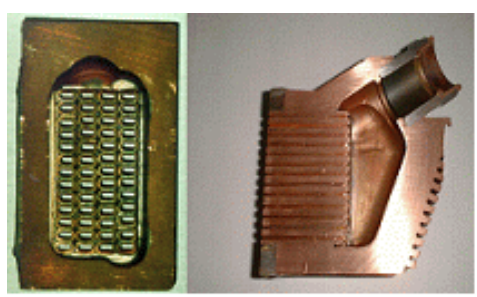

Fig. 2. Inside of Generator Stator Winding

3. Mechanism of Cooling Water Absorption [2, 3]

The major causes of water leakage and absorption in the generator stator winding are divided largely into twos: corrosion and vibration. As shown in Fig. 3, the cooling water flowing from the cooling water header is exposed to the brazing-alloy surface in the clip at the tip of strand. At this time, BCu_3P and cooling water become thermodynamically unstable resulting in crevice corrosion. and are decomposed into hydrogen and phosphorus. The resultant phosphoric acids phosphorylate the cooling water in the pores, facilitating corrosion and making the pores larger. In the event that due to brazing unit attacked by corrosion, the larger pores come in contact with any copper strands, phosphoric acids generated at the time of corrosion in the brazing unit trigger corrosion in the copper conductors faster than in the brazing unit. The initial path formed in this way is enlarged as a flow passage for cooling water leakage and absorption, as the insulators are delaminated owing to vibrations of the generator stator winding.

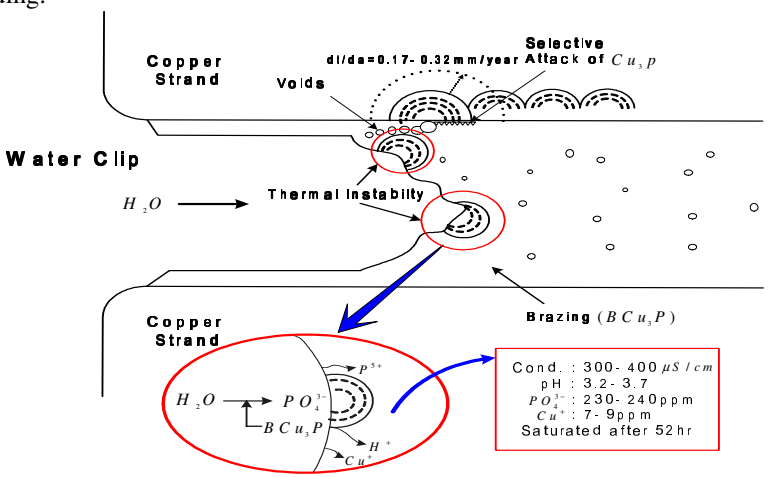

Fig. 3. Mechanism for initial water leakage / absorption path formation for stator winding

4. Development of Gen-SWAD

4.1. *Configuration and Features*

As shown in Fig. 4, the Gen-SWAD(Generator Stator Water Absorption Detector) developed to determine whether generator stator winding insulators absorb water, is composed of a measuring instrument and a sensor. Regarding its measuring principles, the detector measures any oscillation frequency drifts of RC oscillation circuit depending on capacitance variations of the insulator

between the probe and copper conductor, and converts the measurements into capacitance values. For the capacitance meter, the oscillation frequency and converted signal depending on capacitance variations between the sensor and ground are output as given in Fig. 5. The meter not only measures capacitance but also has simplified diagnostic function. Thus, any winding exceeding the given tolerable limit is followed up with diagnostic results displayed shortly after measuring the capacitance of stator winding.

Fig. 4. Gen-SWAD

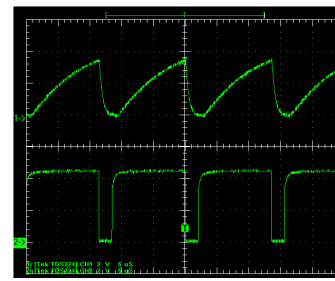

Fig. 5. Reference oscillatory & output signal

For the sensor, a guide was installed to minimize any errors caused by pressure applied when measuring the capacitance of winding, shielded to minimize ambient noises and designed to measure even curved surfaces of winding. In addition, so as to select optimal sensor surface, capacitance of three types (silver foil, copper foil, coating film) was measured depending on thickness variations. In result, it was revealed that there was difference in capacitance depending on the type of sensor and the thickness of insulator specimen, as shown in Fig. 6. The results of calculation and measurement with the dielectric constant are illustrated in Fig. 7 and the sensor using coating film was the most agreeable.

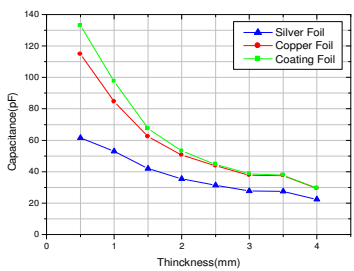

Fig. 6. Measured capacitance by sensor type

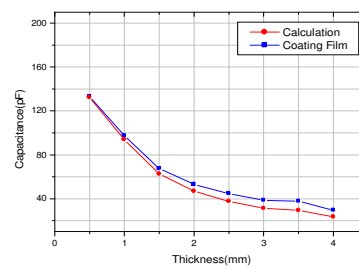

Fig. 7. Dielectric constant with specimen

4.2. *Verification*

An attempt was made to verify the reliability of the developed Gen-SWAD on the basis of the standard condenser after developing it. It was found that the measurements made by Gen-SWAD agree with those by the standard condenser very well in the target range from 0 to 100 pF. Additionally, as a result of requesting an authorized national standard agency to certify it, its reliability was verified that its error rate was within 0.8% in the range of 0~100 pF.

5. Water Absorption Test Algorithm and Diagnostic Tools

This non-destructive electrical test is based upon the fact that there is significant difference in dielectric constant between stator winding insulator(4) and water(80). So if any winding insulator absorbs water, the measured capacitance will increase. However, as the measurements are highly sensitive to sensor sensitivity, the surface conditions of stator winding, careful attention should be paid when carrying out this test. Fig. 8 shows a part of the algorithm proposed to determine an optimal value and the absorption testing procedures intended to minimize measurement errors. To diagnose water absorption in the insulation accurately, a capacitance diagram and two additional stochastic methods - a normal probability plot and a box plot - were suggested [3].

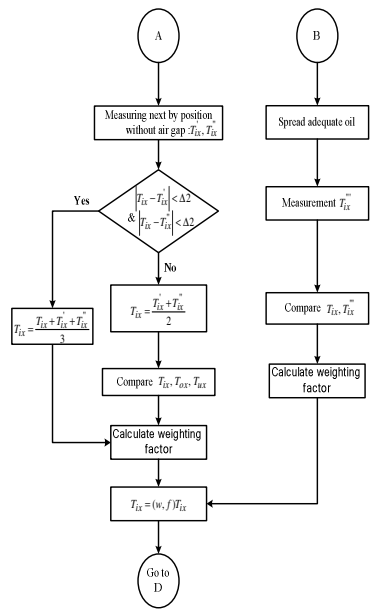

Fig. 8. Algorithm for water absorption test

6. Case of In-plant Application

An absorption test on generator stator winding in an actual plant ‘A’ was conducted with the developed equipment. The target generator is aged 15 years with 500MW of capacity. As a result of performing an absorption test on its stator winding during the period of regular checkup, it was diagnosed that winding No.3 and No.2 at the sides of exciter and turbine, respectively absorbed water as shown in Fig. 9. In the case of winding No.3, all of the upper, internal and external parts of the top bar exceeded 4σ in the capacitance diagram, and also the tolerable limits specified in the normal probability plot and box plot.

Accordingly, as a result of disassembling the insulator of generator stator winding, water leakage was confirmed as shown in Fig. 10. And, the possible accidents during operation were successfully prevented by implementing preventive maintenance by VPI (vacuum pressure impregnation) method at sites.

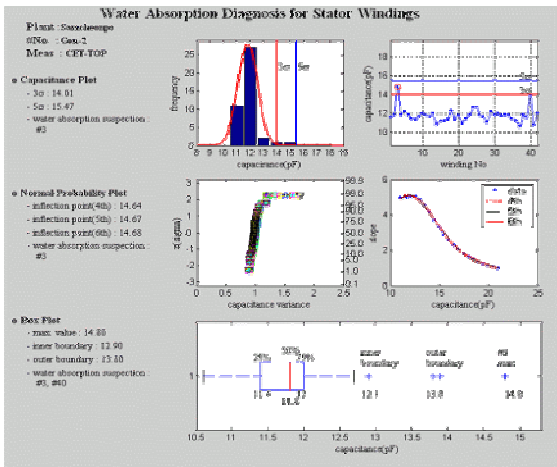

Fig. 9. Result of the water absorption test

Fig.10. Water leak and repair

7. Conclusion

1> As a result of verifying measurement data obtained from Gen-SWAD, very satisfactory results were seen with the error rate within 1%.

2> Gen-SWAD was designed to enable to make measurement even in bent sites and to ensure consistent results regardless of different measuring pressures of individual testing operators. And for probe, capacitance measurements agreed best with calculated results as with flexible coating film.

3> To improve the reliability of absorption test and diagnostics, new test algorithm and stochastic diagnostic techniques are suggested.

4> In the actual field application, it was verified that Gen-SWAD is very good device to diagnose the state of water absorption for generator stator windings.

References

1. GE, *Generator Stator Leaks,* **TIL-1098-3R2,** (1995).
2. EPRI, *Preventing leakage in the strand to clip connections of water cooled generator stator windings.* **EPRI TR-107681**, (1996).
3. Bae Y.C., et al., Development of Diagnosis System for Water Leak and Absorption at Generator Stator Winding. **KEPRI TR-019**, (2006).

ASSESSMENT OF FLUID LEAK FOR POWER PLANT VALVE USING PB-FREE ACOUSTIC EMISSION SENSOR

SANG-GUK LEE AND SUNG-KEUN PARK

Korea Electric Power Research Institute, 103-16 Munji-Dong, Yusung-Gu, Daejeon, 305-380, Korea

In this paper, valve leak tests were performed at various conditions to compare and analyze leak sensibility for both general piezoelectric acoustic emission sensors (PZT) and Pb-Free performance using an AE leak diagnosis system. AE signal voltage and FFT spectrum were measured during valve leak test for simulating power plant valve leak. AE signal voltage, FFT spectrum were recorded and analyzed from various valve operating conditions using both PZT and Pb-free piezoelectric acoustic emission sensor. From experimental results, it was suggested that valve leak assessment using the Pb-free AE sensor was feasible. The results of this study are utilized to select the type of sensors, the frequency band for filtering and thereby to improve the signal-to-noise ratio for leak diagnosis and monitoring of valves in power plant. And also, the outcome of this study can be definitely applied as a means of the diagnosis or monitoring system for energy saving and prevention of accident for power plant valve.

1. Introduction

A lot of valves are used in the power plant. The operation safety test and the valve inside leak detection are implemented on the valve which has a great impact on the safe operation of the plant [1]. While input and output pressure measurement using a pressure gauge, temperature change and the humidity measurement, and pressure-resistant test are used for the valve leak detection, there are many problems such as the difficulty of the real time measurement at the minute leak situation, complexity of the pressure gauge correction and the process of the pressure measurement, and the reliability of the measured value. Therefore, it is necessary to develop the valve leak detection system using the acoustic emission (AE) method which is fast and accurate, and allows the real time measurement and evaluation of the minute leak situation. The valve leak detection method using the AE method is a convenient way to detect the sound of the leak outside the valve in case of existing leak inside of the valve, and the research is in progress recently to apply the method to the power plant valve [2]. AE implies the transient elastic wave phenomena which come from the local

energy source in the material, and the AE sensor is mostly made by piezoelectric ceramics as a sensing device which transforms the elastic wave into electric signal [3]. In this study, the possibility of the application of the AE sensor using environment friendly lead free piezoelectric ceramics was investigated for the detection of the power plant valve leak.

2. Experimental Procedure

2.1. *Test Valves*

A test valve is 2 inch gate valve operated by motor as condition of high temperature and high differential pressure to feed condensing water of steam exhausted from turbine system in secondary system of nuclear power plant. The differential pressures across the valve were in the range of about 2~10 bar. Table 1 is a specification of the test valve.

Table 1. Specifications of the test valve.

Specification	
Valve Type	Motor Operated Gate Valve
Valve Name	PWR High-temp. Turbine Steam Exhaust
Valve Size(inch)	Valve
Max. Pressure(LB)	2
Operating Pressure(bar)	900
Operating	12.5
Temperature(°C)	310
Fluid	Steam
Valve Material	A217WC9

2.2. *Experimental Method*

Piezoelectric characteristics of the piezoelectric ceramics is the most important factor which affects the frequency characteristics and sensitivity of AE sensor. The specimens were manufactured using a conventional mixed oxide process. The lead free piezoelectric ceramics compositions used in this study was $[Li_{0.04}(Na_yK_{1-y})_{0.96}](Nb_{0.86}Ta_{0.1}Sb_{0.04})O_3$+ 0.1wt%$K_2CO_3$ (y = 0.40, 0.44, 0.48, 0.54, 0.58) and the composition of PZT was EC-65. Lead free powders were

sintered at 1080 ℃ for 2h and PZT powders were sintered at 1150 ℃ for 1.5h. To investigate the piezoelectric characteristics, specimens were measured according to IRE standard. Two kinds of AE sensors were fabricated with lead free and PZT ceramics in Langevin type structure with air backing. Figure 1 shows the valve leak test apparatus. N_2 gas was pressured and passed through the valve, and released in the air. Acoustic sound was assured at the valve sheet and detected by two kinds of AE sensor. Output response was amplified by preamplifier to 20 dB. The leak status was simulated by the crack at the valve disk in which the crack was made by 3.0 mm thick. The pressure of the valve entrance was varied 2, 6, 10 bar.

Figure 2 shows simple sensitivity measurement system [5] of AE sensor using transient elastic measurement method (ASTM E1106-86) [6]. A sharp pencil lead was used as the elastic source and the transfer material was the forged steel which has less attenuation and dispersion, and the size of that was 50cmΦx5cm. AE sensor was attached at the transfer material 10cm beside the elastic source by glycerin couplant. When indentor was dropped slowly and cut the sharp pencil lead, the cutting sound is the elastic source, and the cutting force was recoded by load cell indicator.

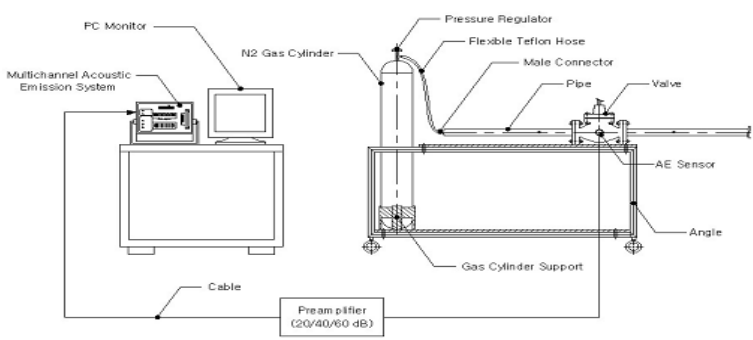

Fig. 1. Experimental apparatus of the valve leak test.

3. Results and Discussion

Table 1 shows the physical properties of the lead free $[Li_{0.04}(Na_{0.54}K_{0.46})_{0.96}](Nb_{0.86}Ta_{0.1}Sb_{0.04})O_3$ +0.1wt%K_2CO_3 specimens according to Na/K ratio[7]. In the case of 54/46, piezoelectric characteristics of that were as follows; electro-mechanical coupling factor, kp is 0.49 and piezoelectric constant is d_{33}=

300[pC/N] and g_{33}=27.20[mV·m/N], respectively. On the other hand, piezoelectric characteristics of PZT(EC-65) were as follows; kp=0.62, d_{33}=380[pC/N], g_{33}=25.0[mV·m/N]. From these results, piezoelectric characteristics of the lead free specimens were lower than that of PZT. Table 2 shows piezoelectric properties of PZT AE sensor and lead free AE sensor, and effective electro-mechanical coupling factor, k_{eff} of PZT AE sensor was 0.25 and k_{eff} of lead free AE sensor was 0.21.

Figure 2 shows sensitivity waveform processed from theoretical velocity of elastic source and voltage response of AE sensor by MATLAB program. At Figure 2(a), peak sensitivity frequency and sensitivity of PZT AE sensor were 29.4 kHz, 69.3 dB, respectively. At Figure 2(b), peak sensitivity frequency and sensitivity of the lead free AE sensor were 29.4 kHz, 66.3 dB, respectively. The peak sensitivity frequency of PZT and lead free AE sensor were same, since peak sensitivity frequency of AE sensor was determined by the ceramic size. The sensitivity of lead free AE sensor was lower than that of PZT by 3 dB and this was similar to k_{eff} of AE sensor at Table 2.

Table 1. Physical properties of specimens according to Na/K ratio.

Na/K ratio	Density [g/cm^3]	kp	Qm	Dielectric constant	d_{33} [pC/N]	g_{33} [mV·m/N]
40/60	4.69	0.445	46.05	1346.97	264	21.79
44/56	4.69	0.468	51.82	1264.83	275	24.37
48/52	4.67	0.490	53.31	1238.79	292	26.55
54/46	4.60	0.490	54.76	1237.00	300	27.20
58/42	4.55	0.474	63.39	1102.66	295	30.27

Table 2. Piezoelectric properties of AE sensor.

AE sensor	Fr[kHz]	Fa[kHz]	Δf[kHz]	keff
PZT	105.78	109.18	3.40	0.25
Lead free	158.32	161.80	3.48	0.21

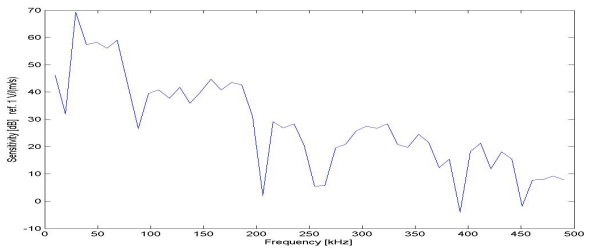

(a) PZT

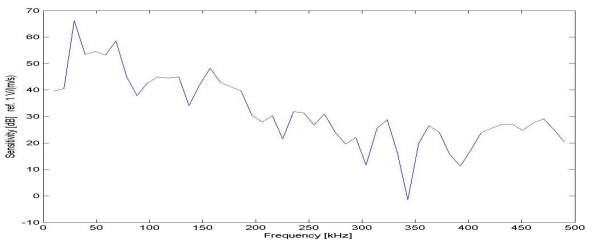

(b) Pb-Free

Fig. 2. Sensitivity waveform of AE sensor.

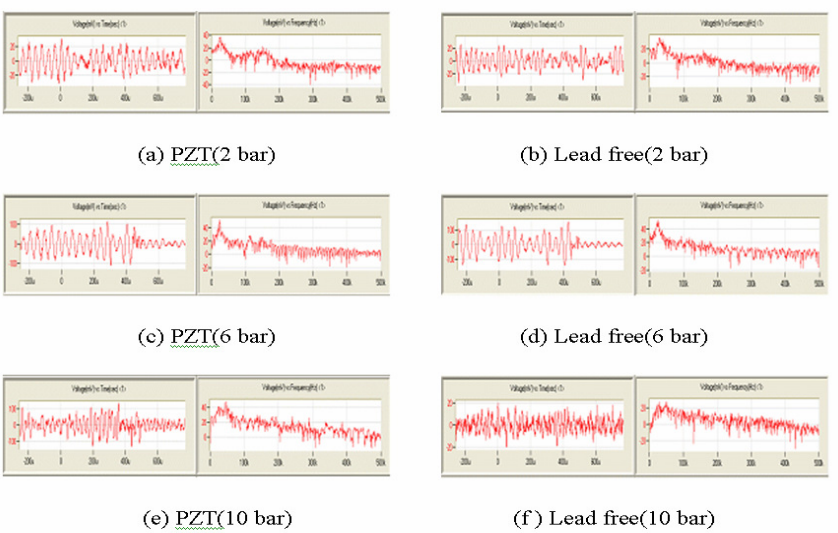

(a) PZT(2 bar) (b) Lead free(2 bar)

(c) PZT(6 bar) (d) Lead free(6 bar)

(e) PZT(10 bar) (f) Lead free(10 bar)

Fig. 3. Voltage and FFT waveform of the leak detection test.

Figure 3 shows the voltage waveform and the FFT frequency response waveform detected at the 3.0 mm cracked valve disk. There were typical continuous type voltage signals by the flux leak at the power plant valve. The peak frequency was 25 kHz between 2 and 6 bar and increased to 50 kHz at 10 bar. From the results, it was concluded that the peak frequency was proportional to the pressure. The voltage amplitude of Y axis was about 40 mV and wasn't changed. The voltage waveform and FFT frequency waveform of PZT AE sensor were similar to those of the lead free AE sensor.

4. Summary

In this study, the lead free $[Li_{0.04}(Na_{0.54}K_{0.46})_{0.96}](Nb_{0.86}Ta_{0.1}Sb_{0.04})O_3$+0.1 wt% K_2CO_3 piezoelectric ceramics and PZT were manufactured, and Langevin type with air backing AE sensors were fabricated with them. Piezoelectric and sensitivity characteristics of them were measured, and the leak detection at the cracked valve was tested with AE sensor. The results obtained from the experiments are as follows. Piezoelectric characteristics kp, d_{33} and g_{33} of lead free $[Li_{0.04}(Na_{0.54}K_{0.46})_{0.96}\ (Nb_{0.86}Ta_{0.1}Sb_{0.04})]O_3$ + 0.1wt%K_2CO_3 piezoelectric ceramics were 0.49, 300 pC/N, 27.02 mV·m/N, respectively. Sensitivity of PZT and the lead free AE sensor were 69.3 dB and 66.3 dB, respectively, and the peak sensitivity frequency of them was 29.4 kHz. From the leak detection test, the peak frequency of PZT and lead free AE sensor were 25 kHz between 2 and 6 bar and increased to 50 kHz at 10 bar. The voltage amplitude of them was about 40 mV and wasn't changed. Therefore, it was concluded that lead free AE sensor can substitute for PZT AE sensor for the leak detection at the power plant valve.

References

1. W. F. Hartman, *EPRI NP-1313*, 1 (1980).
2. J. W. Allen, W.F. Hartman, and J. C. Robinson, *EPRINP-2444*, 22 (1988).
3. ASTM E610-89a, *Standard Terminology Relating to Acoustic Emission.*
4. T.M. Proctor, *J. Acoustic Soc. Am.* **71**, 1163 (1982).
5. Y. Kim, D. Yoon, S. Lee, H. Kim, *Korean Applied Physics* **3**, 374 (1990).
6. ASTM E1106-86, *Standard Method for Primary Calibration of AE sensor.*
7. K. Lee, J. Yoo, J. Hong, S. Lee, Y. Kim and H. Jeong, *J. Korean Institute of Electrical and Electronic Material Engineers* **20-1**, 275 (2007).

LEAK DIAGNOSIS OF CONTROL VALVES FOR POWER PLANTS USING MULTI-MEASURING METHODS

SANG-GUK LEE, JONG-HYUCK PARK

Korea Electric Power Research Institute, 103-16 Munji-Dong, Yusung-Gu Daejeon, Korea

YOUNG-BUM KIM

System D&D Co., 13-9-4 Taprip-Dong, Yusung-Gu, Daejeon, Korea

Condition based maintenance for prevention diagnosis of important equipment related to safety or accident in power plant is essential by using the suitable method based on local condition. This study is to estimate the feasibility of multi-measuring method using three different methods, acoustic emission(AE) method, thermal image measurement and temperature difference Δ T measurement, applicable to valve leak diagnosis for the internal leak from power plant control valves. From the experimental results, it was suggested that data obtained from the multi-measuring method could be correlated for monitoring of valve leak.

1. Introduction

In this study, leak tests for a 50.8 mm globe steam valve using three different leak paths, two different pressures and various leak rates were performed in order to analyze AE properties, thermal image and temperature variation when leaks arise in valve seat. As a result of leak test for specimens simulated valve seat, we conformed that AE amplitude increased in proportion to the increase of leak rate, and leak rates were plotted versus peak frequencies recorded within a fixed narrow frequency bands on each spectrum plot. The resulting plots of leak rate versus peak frequency and amplitude were the primary basis for determining the feasibility of quantifying leak acoustically. And also, variations of thermal image following to leak conditions were observed clearly. The large amount of data attained also allowed a favorable investigation of the effects of various different leak paths, leak rates and pressure differentials using multi-measuring method.

2. Experimental Procedure

2.1. *Test Valve*

A test valve is the main steam dump globe valve of 50.8 mm nominal size operated by air pressure and operated as condition of high temperature(290 °C) and high differential pressure(76 bar). These valves are operated to pass condensed water generated from turbine to condenser system in secondary system of nuclear power plant.

2.2. *Experimental Method*

Figure 1 shows a high temperature and pressure fluid leak test loop. Leak tests were performed on a globe valve attached test loop system in operating using portable AE leak detector, temperature measuring system and thermal image measuring system. All tests were performed as condition of operating valve in actual power plant. Infrared thermometer emitted regular infrared wavelengths was used for the temperature difference measuring in valve. Measuring range of the infrared thermometer is from -30 to 900 °C and it has resolution up to 0.1 °C and accuracy of ± 2 °C or ± 0.75 % of reading. In order to raise reliability of the measurement, temperature sensors were located on pipeline and valve at a distance of the length in proportion to pipeline diameter (D). Using temperature sensor of locations showed in Figure 2, temperature difference(ΔT) was measured. In Figure 2, 2D, 3D and 4D mean positions corresponded to 2, 3 and 4 times of length of pipeline diameter to the fluid inlet direction from the center line of valve body 1 and 2, and also 2D-1, 3D-1 and 4D-1 mean positions corresponded to 2, 3 and 4 times of length of pipeline diameter to the fluid outlet direction, respectively.

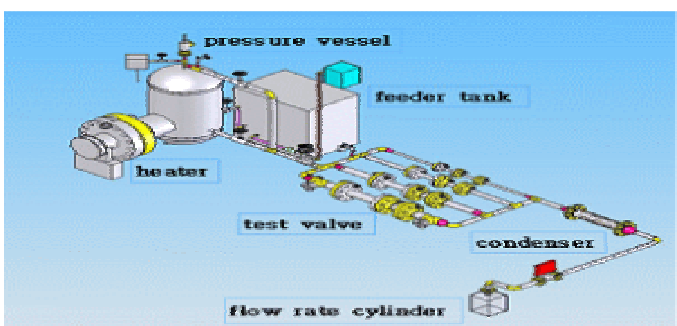

Fig. 1. High temperature fluid loop system.

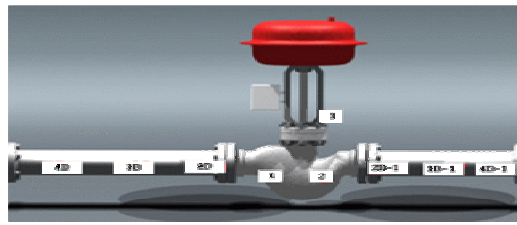

Fig. 2. Point of ΔT leak monitoring.

AE signal radiated from the leak in valves is detected using AE sensor detected on valve outside. The output signals from the sensor were fed into a portable AE leak detector. Table 1 shows specifications of AE measuring instrument.

Table 1. Specifications of AE measuring instrument.

Measuring instrument	Type and specifications
AE Sensor	Resonance frequency : 143 ㎑
Pre-amplifier	Frequency band : 20 ㎑~2 ㎒
	Gain : 20, 40, 60dB selectable
Local processor	Frequency range : 1~400 ㎑
	Main gain : 20 dB

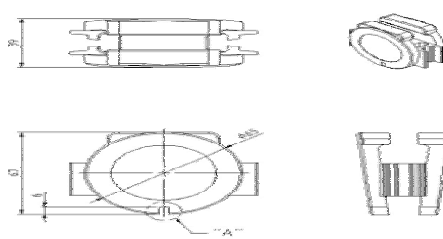

Fig. 3. Shape of valve disc and seat.

A simulated valve leak test for leak conditions on the valve seat side were performed by changing crack depth in valve disc, leak rate was regulated by changing the inlet pressure considering that leak rate varies by both a leak type and differential pressure worked in disc between inlet and outlet in valve. Valve inlet pressures were varied by two types of 20 and 40 bar, and crack on the disc was manufactured to crack of V-notch type in the direction of seat(“A” in Figure 3) using a cutting bite. Crack depths of V-notch type were varied to 0.5, 1.0 and

5.0 mm. Figure 3 shows disc and seat type of test valve and position of notch manufactured. Measuring range of the thermal image camera is from -40 to 2,000 °C and it has resolution up to 0.03 °C and accuracy of ± 2 °C or ± 2 % of reading.

3. Results and Discussion

3.1. *AE Measurement*

Figure 4 shows voltage and FFT frequency waveform obtained from AE measurement using piezoelectric acoustic emission sensor for steam valve leak test according to valve inlet pressures and leak conditions in the case of disc crack size of 0.5 mm. From the voltage waveform versus time elapsed in Figure 4(a)~4(d), it can be seen that continuous type signals show representatively. From the FFT waveform versus time elapsed in Figure 4, it can be seen that peak frequencies for all pressure conditions show in about around 25 kHz regardless of pressure increase. And also, it was conformed that all peak frequencies in case of leak conditions were moved in higher band than 25 kHz peak frequency band showed in case of not leaking, and that the voltage amplitude increased linearly in proportion to the increase of leak rate(In Figure 4, the voltage amplitude increased from 40 mV to 60 mV).

3.2. *Temperature Difference Measurement*

Surface temperatures on the test valve body and pipelines were measured both in the position of equivalent to length of 2, 3 and 4 times of pipeline diameter in the fluid inlet direction centering around valve body, and in the position of equivalent to length of 2, 3 and 4 times of pipeline diameter in the fluid outlet direction centering around valve body, respectively. Results of these measurements show in Table 2. From the twice measuring results obtained at both the number 1 and number 2 position on the valve body for “A” valve, it can be seen that the temperature(133.8 °C) of the number 2 in outlet side is higher than one(110.2 °C) of the number 1 in inlet side at first measurement, and temperature(101.9 °C) of the number 1 in inlet side are higher than one(82.1 °C) of the number 2 in outlet side at second measurement. And also, it can be seen that the temperature(99.6 °C) of the number 3 in inlet side of flange is higher than one(54.8 °C) of outlet side. From these results, we are conformed that temperature differences due to the irregular fluctuation of high temperature fluids, and fluid moving varies continuously, and these irregular temperature distribution same as results of temperature measurement for valve operating in actual power plant. Therefore, it is suggested that multi-measuring methods must be applied in addition to temperature difference measurement method

considering that single method by temperature difference measurement appears complex results.

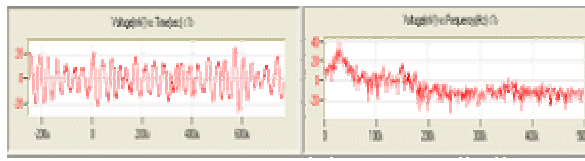

(a) 20 bar no leak

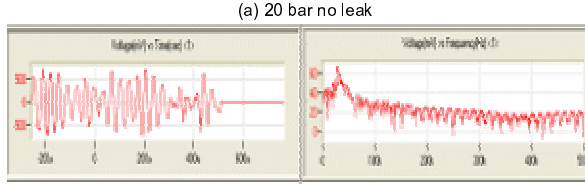

(b) 40 bar no leak

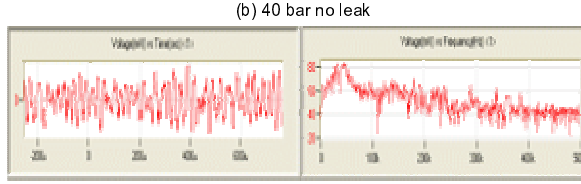

(c) 5.0 mm, 20 bar leak

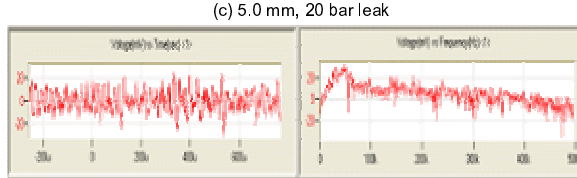

(d) 5.0 mm, 40 bar leak

Fig. 4. Voltage and FFT waveform analysis.

3.3. *Thermal Image Measurement*

Figure 5 shows a representative thermal image taken for thermal distribution measurement of "A" valve using a thermal image camera. It can be seen that there is no leak symptom in "A" valve at present because of valve closing. Besides, we conformed that the part sensing as high temperatures might be measured from other valves and temperature of surrounding facilities by both the heat conduction and radiation reaction. The reason for leak existence in valve "A" from AE measurement due to acoustic signal emitted from vibration owing to by passing of fluids and other equipment. Thus, these measuring uncertainties should be eliminated by multi-measuring methods through the precise analysis performance.

Table 2. Temperature difference measurement result of target components.

Valve	Temperature(□)					
	1	2	3	2D	3D	4D
				2D-1	3D-1	4D-1
A	110.2	133.8	99.6 54.8	52.7 52.1	48.8 48.7	48.6 48.5
	101.9	82.1	155.6 50.2	57.3 53.0	52.6 43.5	60.6 46.6
B	162.3	68.6	43.6 41.9	50.0 49.2	65.3 44.7	57.9 50.5
	158.3	63.8	43.2 44.8	48.6 47.0	42.3 39.2	41.0 39.3
C	49.0	58.6	42.6 41.6	45.1 42.0	44.7 40.1	47.6 42.0
	43.4	49.0	43.9 42.9	44.1 41.0	42.1 42.1	41.5 41.5

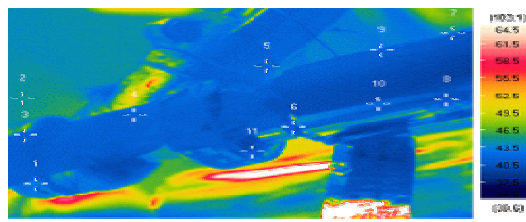

Fig. 5. Thermal image of valve “A”.

4. Summary

Measuring uncertainties should be eliminated by multi-measuring methods through the precise analysis performance, above all, it is recommended that the preceding of understanding and analyzing for valve system in actual power plant is essential and database should be established finally through a repeated in-situ valve leak test. From experimental results in this study, it was suggested that data obtained from these results could be applied hereafter for judgment for the leak existence and prevention of fluids leak loss in power valves.

References

1. J. W. Allen et al., *EPRI Report*, **NP-2444**, 22 (1988).
2. Kitazima A., *CREIPI Report*, **No. 277059**, 21 (1988).
3. Kitazima, A., *CREIPI Report*, **No. 285089**, 1 (1986).
4. Kumagai, H. et al., *CREIPI Report*, **No. T87112**, 1 (1988).
5. Hartman, W. F., *EPRI Report*, **NP-1313**, 1 (1980).

EFFECTS OF MAGNETIC PHASE ON THE ECT SIGNAL IN THE SG TUBES*

DUCK-GUN PARK†

Korea Atomic Energy Research Institute 150 Deokjin-dong Yuseong-gu, Daejeon 305-353, Korea

KWON-SANG RYU

Korea Research Institute of Standards and Science 102 Yuseong Daejoen 305-600, Korea

DERAC SON

Hannam University 133 Ojeong-dong Daedeuk-gu Daejeon 306-791, Korea

YONG-MOO CHEONG

Korea Atomic Energy Research Institute 150 Deokjin-dong Yuseong-gu, Daejeon 305-353, Korea

The magnetic phase created in the Inconel alloy , which is called as PVC (permeability variation clusters) results in a eddy current test(ECT) signal distortion during the inspection of steam generator (SG) of nuclear power plant (NPP). The effects of magnetic phase on ECT signals were analyzed using the inspection of data of NPP. The hystersis loops of PVC which is extracted from retired SG tubes of Kori-1 NNP were measured. The tensile tests were performed to identify the mechanism of PVC creation. The coercivity of PVC is larger than 0.2kA/m, and hysteresis loop was appeared in the tensile tested specimen at 600 ^{o}C.

Keywords: Eddy current; permeability variation cluster; magnetic phase; steam generator tube; hysteresis loop.

1. Introduction

Multi-frequency eddy current inspection techniques are currently the most widespread techniques for the rapid inspection of SG tubing in the nuclear power industry [1] among other techniques. Although the EC technique is adopted

* This work is supported by etc, etc.
† Work partially supported by grant

widespread in the nuclear industry, it has the limitation like size the flaw accurately because the eddy current signal behavior depends on the total volume of flaw. Furthermore, permeability variation clusters (PVC) such as the build-up of magnetite (Fe_3O_4) and magnetic phase on the secondary side of the SG tubing has no direct effect on the tube integrity but it causes spurious EC test results [2]. The relative permeability of the PVC is greater than 1, and with a number of ferromagnetic metals, a value of several thousand can be reached. Internal stresses caused by drawing, straightening or similar works on the material, creates the magnetic phase in the SG tube, which can give rise to several fluctuations in the permeability [3]. These fluctuations would always cause interference with the test signals. Since the ferromagnetic test piece of PVC is saturated by a strong magnetic field, in order to eliminate this kind of interference effects during the testing, a suitable device such as magbias ECT probe is employed. Recently, to eliminate EC signal fluctuation, the magnetized probe with the built-in permanent magnet is being used in the SG tube inspection, because of strong magnetic field of this probe reduces the variation of magnetic permeability, which gains S/N ratio [4]. However, the magbias ECT probe could not saturate strong PVC having large permeability, and the strong magnetic field of magnetized ECT probe amplifies the ECT signal with noise by the interaction of magnetic filed of ECT probe and induced currents of probe coil. In this study, ECT data containing the PVC obtained from nuclear power plant was analyzed, and also the hysteresis loop of PVC which is extracted from retired Kori-1 SG were measured.

2. ECT signal fluctuation due to PVC (magnetic phase)

Fig. 1 shows inspection results by using the conventional probe and magbias probes. These signals are extracted from ECT data which is recorded as PVC signal by ECT examiner. The tubes were inspected by bobbin and MEPC probe with and without magnetized unit. The Fig.1 (a,b,c) represent the results of conventional bobbin and MRPC probe and Fig.1 (d,e,f) represent that of magbias probe. The MRPC probe consists of three types of coils: two pancake and a +point. The pancake coils consist of two different diameters: 2.0 mm and 2.9 mm. The larger diameter pancake coil is to improve penetration depth of the signal to outside surface. Field experience shows that pancake coil has better sensitive to volumetric defects whereas +point coil has better sensitivity to crack like defect [5]. Prior inspection of SG tube by bobbin probe indicates continuous distribution of PV signal up to 1 m (Fig.1(a)(d)). However the PVC signal was not eliminated by magbias probe as shown in the left side of Fig. 1 (d, e, f), and

the S/N ratio was reduced which is contrary to our expectation. The magnetized probe was introduced to saturate the ferromagnetic nature of PVC, but the saturation field depends on various factors such as demagnetization coefficient of the PVC. If the magnetic field of magnetized probe can not saturate the PVC, then the distortion of the ECT signals increases by the interaction of the magnetic filed of magbias probe and PVC, which results low S/N ratio. The noise level by the +point coil was significantly decreased by the use of magbias probe. The data of the inspected tube shows the indication of long and narrow axial defects in bobbin and MRPC data. However, reevaluated results by magnetized probe shows that the data obtained from pancake coil covered with noise like signal and the data from plus point coil shows sharp ridge of mountain. The peak distribution obtained from pancake coil considerably decreased and that from plus point coil disappeared by using the magnetized coil. The S/N ratio obtained from the bobbin and pancake of MRPC probe considerably decreased by using the magnbias probe, which suggests the flaw is constituted as a volumetric defect.

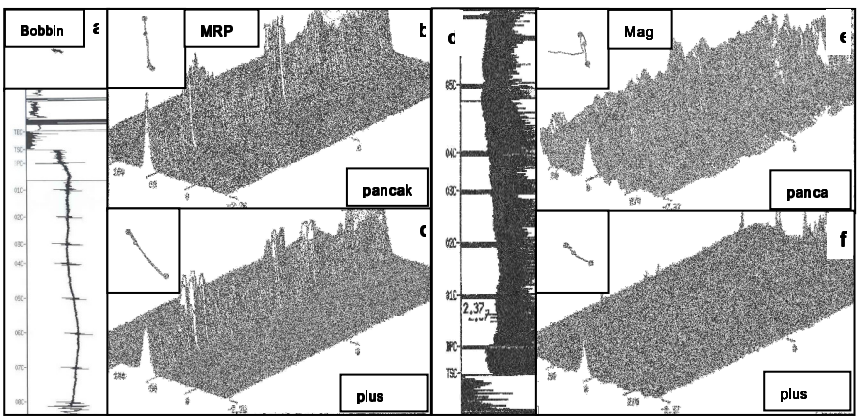

Fig. 1. The signal from (a) bobbin probe, (b) pancake coil (c) Plus point coil, and (d), (e), (f) represent the corresponding signals by magbias probe.

3. Experimental

The samples for PVC in SG tube were extracted from retired SGG tube of Kori-1 NPP in Korea. Fig. 2 shows a permanent magnet attached on the fragment of SG tube containing the PVC, which means that some parts of SG tube transformed as a ferromagnetic phase. In order to investigate the magnetic properties of this PVC, the fragment was machined as rectangular type of 2 x 2

mm samples for measuring hysteresis loop using VSM. To confirm the mechanism of ferromagnetic phase by deformation in Inconel (I600) alloy, the tensile tests were conducted in the room temperature and 600 ^{o}C. The deformed area of tensile tested specimen was cut as a slice with 2 mm length for VSM measurement, and deformation rate was measured at each slice.

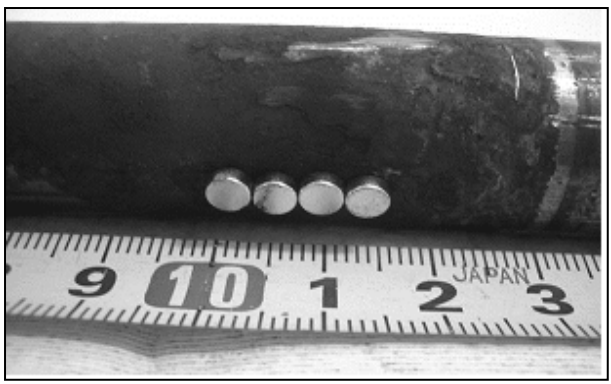

Fig. 2. The picture showing the substance of magnetic phase (PVC) in the SG tube. The sample was extracted from the retired SG tube of Kori-1 NPP.

4. Results and discussions

Fig. 3 shows the typical hysteresis loop of a fragment of PVC parts. The loop show different configuration for part by part of fragment. Although the sample is extracted from the same fragment, the magnetic moment and the coercivity shows different value with respect to sample position in the fragment. The onset of ferromagnetism in the high Cr and low Ni steels was associated with the formation of ferrite during sensitization [6]. However, in higher nickel contents alloy such as I600, no ferrite formed and sensitization occurred without an increase in magnetic induction [7]. For still higher Ni content alloys, Curie temperature decrease rapidly with an increase in Cr content [8,9]. Takahashi et al [2] proposed that the creation of ferromagnetic phase in I600 alloy is related with the decrease of Curie temperature by Cr depletion, however the permeability increase is less than 1.2 although the Cr content decreased from 17 to 14 wt% by depletion. These values are too small to form the hysteresis loop observed in Fig. 3. In order to identify the mechanism of ferromagnetic phase in the retired Kori-1 SG tube, the changes of hysteresis loop by deformation were investigated.

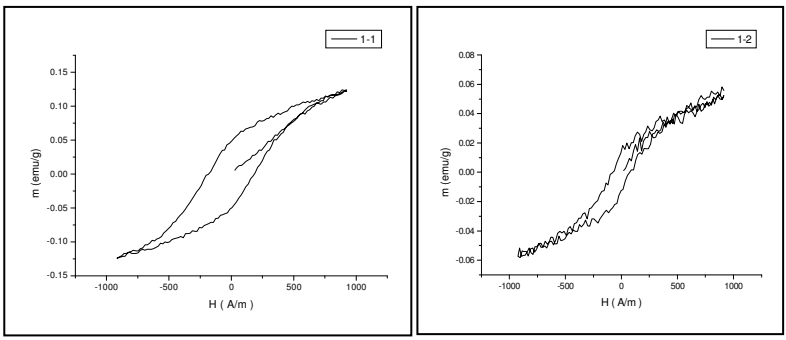

Fig. 3. The hystresis loop in the fragment of PVC parts of Kori-1 retired SG tube.

Fig. 4 show the change of hysteresis loop for the specimen which are deformed at room temperature and 600 °C. The hystereis was not appeared in the annealed specimen at high temperature and tensile specimen tested at room temperature, but it was appeared in the tensile specimen tested at high temperature. The hysteresis of the specimen in the Fig. 4(b) cannot be explained as a Cr depletion, because it was not appeared in the undeformed specimen at high temperature.

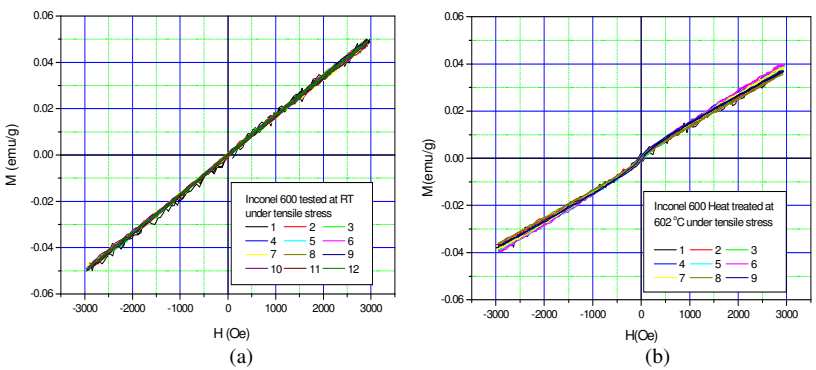

Fig. 4. The hysteresis loop of the tensile tested specimen at room temperature (a), and tensile tested at high temperature (b).

Therefore the magnetic phase can be created under the high temperature and pressure conditions, which is correspond to the stress corrosion cracking in the SG tube in the NPP [10].

5. Conclusion

The effects of magnetic phase on ECT signal were analyzed using the inspection data of NPP. The large coercivity and clear hystersis loops of PVC which is extracted from the retired SG tubes of Kori-1 NNP are cannot be explained as a decrease of Curie temperature by Cr depletion. The hysteresis loop which is observed in the tensile tested specimen at high temperature suggest that the magnetic phase created in the SG tube is related with stress corrosion cracking.

References

1. T. Sakamoto, et al., *Journal of the Japanese Society for Non-destructive Inspection.* **42**, No. 9 (1993).
2. Young H. Kim, S.-J. Song, J.-S. Heo, H.-B. Lee and M.-H. Song, *Key Engineering Materials.* **270-273**, 555 (2004).
3. S. Takahashi, Y.Sato, Y. Kamada, T. Abe, *J. Magn. Magn. Mater.* **269**, 139 (2004).
4. Subng-Chul Song, Yun-Tai Lee, Hee-Sung Jung, Young-Kil Shin, *J. Kor. Soc. NDT.* **26 (3)**, 174 (2006).
5. Steam Generator Tube Failures" NUREG/CR-6365, April 1996, USNRC.
6. B. Strauss, H. Schotty, and J. Hinnueber, *Z. Anorg. Allg. Chem.* **18**, 309 (1930).
7. E.C. Bain, R.H. Aborn, and J.J. Rutherford: *Trans. ASM.* **21**, 481 (1933).
8. P. Chevenard: *C.R. Acad. Sci.* **198**, 1144 (1934).
9. L.R. Jackson and H.W. Russel: *Instruments.* **11**, 280 (1938).
10. S.M. Bruemmer, L.A. Charlot, and C.H. Henager, *Corrosion*, 782 (1988).

SG EDDY CURRENT ISSUES UPDATES IN KOREA*

SU JIN KIM

NTSC, Korea Plant Service & Engineering, 216 Kori Jangan-Eup, Kijang-Gun Busan, 619-711, Korea

KYUNG JOO KWON, JONGIN KO, SANGGOOK LEE, HWASIK DO

NTSC, Korea Plant Service & Engineering, 216 Kori Jangan-Eup, Kijang-Gun Busan, 619-711, Korea

Recently, 20 Power Plants are commercially operated in Korea and their electric capacity is expected to be over 40% of country demand. It may say that the efficiency of producing electricity depends on the integrity of steam generator as a one of the main component in NPP. There are various SG types such as KSNP, Δ 60, F-model, Framatome 51B and CANDU. Each SG has same role of generating steam but shows different degradation of tubing. It has required lots of efforts of minimizing unexpected shutdown of plant. To accomplish stable operation and economical success, the SGMP (Steam Generator Management Program) has executed since 2005. The SGMP produces overall guideline and procedure to maintain the tube integrity. It includes all about the role, period, responsibility, and technique & system of inspection to keep high efficiency of nuclear plant. Since 2001, SCC of tubing has been regarded as a main issue among tube degradation in Korea. However, SG tube degradation such as crack and wear has relieved due to preventive repair, it is still performing preventive action under reinforced basis. One of the threatening degradation of SG tube integrity is the Loose Part Wear from secondary side. Continuous concern for the SG tube integrity will be a main point of SGMP. Sludge management of secondary side is also performing for the integrity of the SG tubing. As sludge on the secondary side has recognized a one of the affective factor of degradation, it regards an essential point for the tube integrity. The UBIB inspection for the upper bundle of SG has performed several times in F-model. It shows situation of sludge accumulation in the inner bundle and helps decide upper bundle cleaning with the UBHC (Upper Bundle Hydraulic Cleaning). SGMP combined by new inspection technique brings us safe environment. Under the SGMP, integrated and systematic management for nuclear plant will be final goal for the future.

* This work is supported by NTSC, KPS.

1. Introduction

1.1. *Nuclear Power Plant in Korea*

Since Kori 1 had commercially operated, 29 years ago, new era was started in power generation. Nowadays, there are 20 operating units in Korea. They composed of 8 units of KSNP and 5 units of F-model, 4 units of CANDU, 2 units of Framatome 51B and a Δ 60 of replaced SG in Kori 1. Up to 40% of domestic electric demand is charged by nuclear plants. After Yonggwang 3, CE System 80 down scale is called Korea Standard Nuclear Plant (KSNP). All under construction plants shin Kori and shin Wolsung adopted KSNP type. Various plant types led to various degradation on SG tubing because of their different design. Lots of tube degradation have identified so far. Also lots of efforts that prevents forced shutdown caused by tube degradation has performed together. Operation history showed tube degradation that has each own. It is important that exact diagnosis of degradation from Eddy Current Testing takes proper repair on SG.

2. Experience

2.1. *KSNP Experience*

The first unit of KSNP was Yonggwang 3 in 1985. It was 4th nuclear plant and first CE system 80 scale-down in Korea. After that, 7 more units have commercially operated as KSNP. Yonggwang unit 3,4,5,6 and Ulchin unit 3,4,5,6 represent as KSNP. It is basically composed of 2-loop system. Each SG has 8,214 U-bend tubes that have alloy 600 heat treated mill annealed except Ulchin 5&6. Ulchin 5&6 have recently operated and they have 8,340 tubes of each SG due to new tubing material as Alloy 690.

Common degradation of KSNP was known Fretting Wear and SCC. Wear on batwing areas & vertical strip areas are common problem throughout all CE types. It showed early outages but it has not led to forced shutdown. Wear was diagnosis by the Bobbin inspection. Most interesting degradation is SCC on TTS. Expansion transition area on top tube sheet is usually known as highly affective area due to residual stress. In case of KSNP, circumferential ODSCC & PWSCC were main degradation on TTS area. Therefore, inspection plan of RPC include 100% of TTS hotleg side. By the Notice 2004-13, inspection area established from +5” to -3”on TTS. Every outage shows numbers of SCC in KSNP. Sleeve

Table 1. KSNP SG Description

Unit	YONGGWANG				ULCHIN			
	3	4	5	6	3	4	5	6
Comm. Operation	Mar. 1995	Jan. 1996	May 2002	Dec. 2002	Aug. 1998	Dec. 1999	Jul. 2004	Feb. 2005
Tubing	600MA	600MA	600MA	600MA	600MA	600MA	690TT	690TT
Tubes	8,214	8,214	8,214	8,214	8,214	8,214	8,340	8,340
Operating Temp.	614° F	614° F	619° F	619° F	619° F	619° F	621° F	621° F
Internal Structure	Egg Crate	Egg Crate	Egg Crate	Egg Crate	Egg Crate	Egg Crate	Egg Crate	Egg Crate

tube installed as repair for SCC. Small number of stabilizer also performed for early repair. So far, over 800 sleeve tubes were installed in each YG 3&4. They are included repair and preventive sleeves. After first SCC reported, up to 300 tubes have selected as preventive sleeves. As a result, SCC has reported a few tubes during outage.

2.2. *Westinghouse F-model Experience*

Kori 2,3,4 & Yonggwang 1,2 are operating F-model in Korea. Westinghouse F-model has 3-loop design and 5,626 tubes each SG. Tubing material is alloy 600TT. Common degradation mechanism is AVB wear and SCC on Top Tube Sheet. Degradation Assessment Report shows that only SCC on TTS is categorized as an active degradation mechanism, because the growth of AVB wear has relieved. However, large distribution of plug was AVB wear. Several issues of F-model are known as SCC on TTS in YG1&2, Kori 3 and RCS leakage due to Loose Part Wear in YG 2. SCC and leakage because of Loose Part Wear has not reported yet so far. It reflects that proper inspection method and range brings stable operation of SG. There are new issues on F-model. One of the issues is Bobbin offset voltage diagnosis. As same units in Seabrook and Braidwood 2, Bobbin inspection detected ODSCC at hotleg and coldleg TSP. It caused by improper heat treatment. As a result of Bobbin offset voltage diagnosis, residual stress was very high for those tubes. According to this case, 413 tubes were monitored for ODSCC. The other issue is TSP Quatrefoil Blockage Diagnosis. SG level oscillation has reported in Kori 4. It may cause

forced shutdown of plant. Root cause is that secondary side flow blocked by sludge in the quatrefoil. Eddy current testing is limited to secondary side. General indication of tube can be found by Eddy current testing, but it may not give any information that sludge does not contact to tube. Visual inspection in the secondary side is accurate method, but this has limitation to inspection. It does not cover whole range of SG tubes. Aspect of blockage can show through the sampling of RPC inspection. UBIB (Upper Bundle In Bundle) inspection is performed with basis of RPC sampling result. Sequentially, Upper bundle cleaning system is performed to eliminate sludge blockage in the TSP quatrefoil. KULAN (KPS Upper bundle LANcing system) was performed in YG 1&2. That is mutual aid both primary and secondary management in SG.

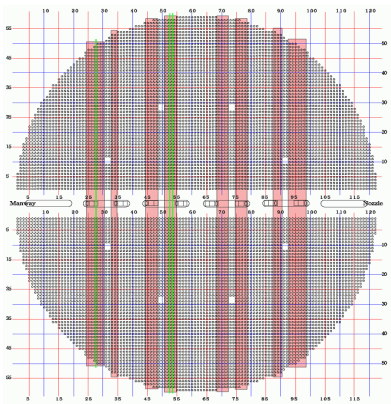

Fig. 1. RPC, UBIB and KULAN inspection area in Yonggwang

Table 2. F-model SG Description

Unit	KORI			YONGGWANG	
	KR2	KR3	KR4	YG1	YG2
Comm. Operation	Jul. 1983	Sep. 1985	Apr. 1986	Aug. 1986	Jun. 1987
Tubing	600TT	600TT	600TT	600TT	600TT
Tubes	5,626	5,626	5,626	5,626	5,626
Internal Structure	6AVB Quatrefoil	6AVB Quatrefoil	6AVB Quatrefoil	6AVB Quatrefoil	6AVB Quatrefoil

2.3. *Framatome 51B and CANDU Experience*

The first Framatome 51B was Ulchin 1 in 1998. One year later, Ulchin 2 was commercially operated. These units were French design. These were also similar to Westinghouse 51series. Main degradation mechanism is PWSCC on TTS. Expansion transition was treated by mechanical rolling, named Kiss Roll. PWSCC can be found all expansion transition area in hotleg side. It gradually spread out coldleg side. Since 1999, sleeves had performed as a repair. There was ARC to select tubes for repair. Alternative Repair Criteria has considered several conditions such as growth rate, length and voltage of PWSCC. Recent issue was the tube leakage in French EDF Cruas 4. Root cause was circumferential crack upper area of 8th TSP on Row8 Column47. There were no support structures to maintain tubes and suspect condition with local thermo hydraulic condition due to deposit on broached upper tsp. Because Cruas4 has same design to Ulchin units, Inspection area was expanded to cover under row10 and upper tsp. So far any degradation was not found in Ulchin 1&2. However, risk area was set to each SG and 58 tubes were performed as preventive plugging with removable plugs in hotleg side and sentinel plugs in coldleg side. Leakage monitoring was also added. All Ulchin units finished these preventive repairs in 2007.

Table 3.Framatome 51B and CANDU SG Description

Unit	ULCHIN		WOLSUNG			
	1	2	1	2	3	4
Comm. Operation	Sep. 1988	Sep. 1989	Apr. 1983	Jul. 1997	Jul. 1998	Oct. 1999
Tubing	600TT	600TT	Alloy800	Alloy800	Alloy800	Alloy800
Tubes	3,330	3,330	3,558	3,530	3,530	3,530
Loops	3	3	4	4	4	4
Internal Structure	4AVB	4AVB	6AVB	6AVB	6AVB	6AVB

Especially, these 4 Wolsung units were adopted PHWR from CANDU. Inspection scope shows less inspection than other PWRs because degradation has not detected so far. Therefore the Notice 2004-13 was required 50% Bobbin inspection and 20% RPC inspection on TTS. Main reason of no degradation on tube cab be explained that tubing material have much resistant to crack and lower operating temperature.

3. Summary

In 30 years, lots of trials and errors have shown nuclear history. In the past, many cases of the forced shutdown came from tube failure in the steam generator. Steam generator has the biggest heat transfer area in the nuclear plant. RCS leakage in steam generator is one of the most issues in the inside and outside of the country. Among many types of steam generator, KSNP, F-model, 51B and CANDU in Korea, new technology of primary and secondary side in steam generator has greatly produced to maintain tube integrity. As a 6^{th} big nuclear generation country in the world, it was necessary to have systematic steam generator maintenance, so the SGMP was rising. Under the SGMP, nuclear generation shows not only high economical efficiency but also preventing air pollution. It is highly necessary to maintain stable and safe operation on the plant for the public benefit.

References

1. YG 1,2,3&4 Eddy Current Testing Final Report, KPS (2007).
2. KR 2,3&4 Eddy Current Testing Final Report, KPS (2006).
3. UC 1,2,3&4 Eddy Current Testing Final Report, KPS (2007).
4. WS 1,2,3&4 Eddy Current Testing Final Report, KPS (2006).
5. UBIB & Upper Bundle Cleaning Final Result Report in YG1, KPS (2007).
6. Degradation Assessment Report, KR3&4 KHNP(2007), YG1,2,3,4,5&6 KHNP (2007), UC1,2,3,4,5&6 KHNP(2007), WS1&2 KHNP (2007).

APPLICATION OF DIGITAL RADIOGRAPHY INSPECTION FOR PIPE WELDMENTS IN THE POWER PLANTS

Sang-Ki Park*, Byung-Chul Park, Doo-Song Gil, Yeon-Sik Ahn
Yong-Sang Cho

Power Generation Laboratory, Korea Electric Power Research Institute
103-16 Munji-dong, Yusong-gu, Daejeon 305-380, Korea
**skpak@kepri.re.kr*

Since Power Plant has tens of thousands welded parts in its structures, the quality on the welded parts are always a key factor for ensuring the reliability of the structures. Film based Radiography Test (hereinafter called "FRT") is a generally accepted solution in inspecting the welded structure. However, the RT demands complex workflow, high cost, hazardous waste disposal, and etc…. In an effort to get over such shortcomings from FRT and present alternative inspection tools, this study was intended to evaluate a Digital Radiography Test (hereinafter called "DRT"). In this study, the evaluation were focused on if a DRT is applicable to the inspection of Welded structure in Power Plants, and what benefits can be generated in a use of DRT.

Keywords: Digital Radiography; Radiography Testing; Welding Inspection; Non Destructive Testing; CMOS Flat Panel Detector.

1. Introduction

The defects on the weldment in Power Plants are so critical that any failure of these components caused by such defects can lead to major shutdown and may even injure power plant personnel. To prevent such failures, plant engineers should implement quality assurance on welded parts periodically.
For more than several decades, FRT has been used as primary quality assurance tool in the construction or maintenance of welded components and assemblies. Unfortunately, FRT remains of less cost-effective and environmentally hazardous tool. The image medium (film) is a silver based technology that can only be used once. FRT requires photographic development that is both time consuming and involves the use of hazardous chemicals that must be discarded.
In contrast, DRT reduce exposure and processing times dramatically, lower recurring cost (no film or chemicals), and no chemical waste; all attributes that significantly cut costs. In addition, unlike film images, digital images can be enhanced for improved defect detection. Interpretation of inspection results can be fully automated in the most cases. In addition, digitized data can be shared

with on a real time basis through communication cable between the remote locations.[1]

2. Method of Digital Flat-panel Technology

Digital RT works in the following process; (i) X-rays strike a scintillation layer firstly, (ii) this layer emits photons in direct proportion to the energy of the X-rays striking it, then, (iii) the photons are picked up by the underlying a-Si or CMOS photo-diode matrix, which converts them to an electric charge, finally this charge is then converted to a digital value for each pixel. Because of the intermediate step of converting X-rays to light via the scintillation layer, this is called an indirect-imaging method.[2]

3. Characteristic Feature of Different Digital Flat Panels

3.1. *Amorphous Selenium and Amorphous Silicon*

These devices consist of very fine two dimensional array of thin film semiconductor based detectors referred to as pixels. Each pixel collects stores charge when exposed to X-rays. The primary difference between the two detectors is the way in which each collects the charge values. In a-Si devices, the charge at each pixel is indirectly produced by the combination of scintillation phosphor screen illuminated by X-ray beam and the light converted to charge by a photodiode. For a-Se detectors, no scintillator is required since the selenium layer converts the X-ray photons directly into electrical charge.

3.2. *Complementary Metal Oxide Silicon (CMOS)*

CMOS is a widely used type of semiconductor. In a **CMOS** sensor, each pixel has its own charge-to-voltage conversion, and the sensor often also includes amplifiers, noise-correction, and digitization circuits, so that the chip outputs digital bits. CMOS detectors have more advantages over Amorphous Silicon Detectors or Amorphous Selenium in durability, spatial resolution, temperature range, fill factor, sensitivity, off-axis detection, less image blooming, simple calibration, and cost.[3]

3.3. *Charged Coupled Device (CCD)*

In a **CCD** sensor, every pixel's charge is transferred through a very limited number of output nodes (often just one) to be converted to voltage, buffered, and sent off-chip as an analog signal. All of the pixel can be devoted to light capture, and the output's uniformity (a key factor in image quality) is high.

4. Digital Radiography Testing on Welded Parts

This testing is intended to compare the digital flat panel image with film image for evaluating the digital flat panel image resolution.

4.1. *Testing System*

The digital images on the welded parts were achieved by using computerized 12 X 14 inch and 83 μm pixel CMOS Flat Panel Detector.

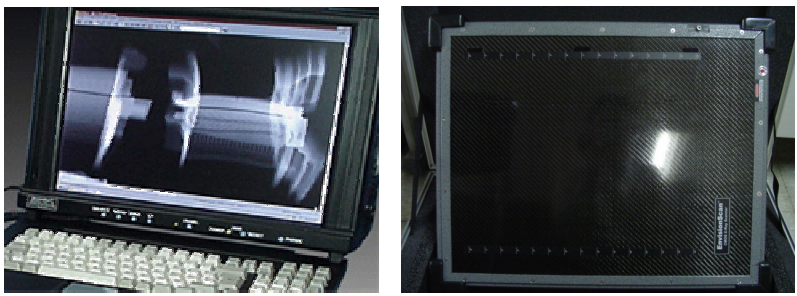

Fig. 1. Used Digital Radiography Imaging System

4.2. *Weld Specimen*

Specimen is fabricated by using TIG welding method**.** In the welded part of reheat steam pipe, Linear flaws of 1mm, 2mm, and 3mm in depth and 1mm, 2mm, 3mm, 5mm, 10mm in length are fabricated with electric discharge machining. In addition, in the welded part of boiler tube, micro linear flaws of 1mm, 2mm, and 3mm in length with 0.1mm in width, 0.2mm in depth and are made and circular flaws of 1mm, 2mm, 3mm in depth with 1mm and 2mm flat bottom drill.

Table 1. Specifications of Flaw Specimen

Specimen	Material	Specifications (OD X Thickness/mm)	Welding
Reheat pipe	A335-P12	¢ 710 X t 20	TIG
Superheater tube	TP-347H-T11	¢ 51 X t 8	TIG
Reheat Tube	2.25Cr1Mo	¢ 61 X t 6	TIG
Plate welding	Steel	t 10~15	Arc

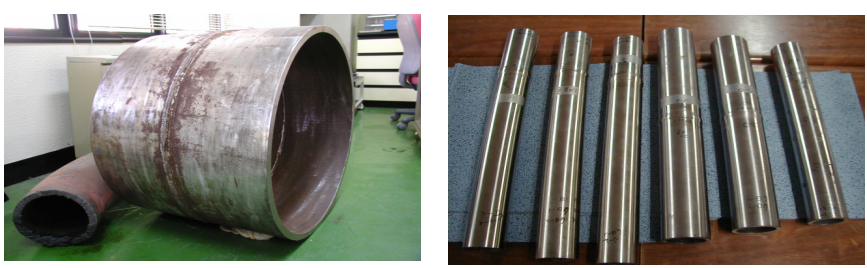

Fig. 2. Specimens for Digital Flat Panel Image Testing

5. Radiography Testing

5.1. *Assessment on the Detected Defect*

As a result of imaging flaw specimen with Image Quality Indicator (IQI) and Line Pair Gauge, Digital Flat Panel can resolve 6.3 Line Pairs/mm verifying 83 μm of pixel size.

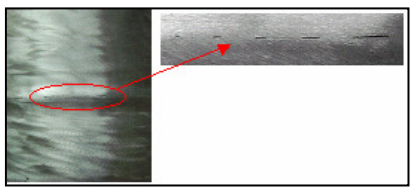

Fig. 3. Defect Image Enhancement

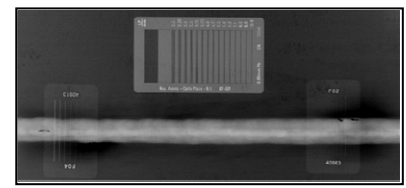

Fig. 4. Digital X-ray image on the welded part

One or two more lines of image quality indicator was/were detected in the digital images compared to in film images. With image enhancement, reconstruction and computer aided image analysis, flat panel detector enables to improve the detection capability. [4] In digital X-ray inspection for array defects for the welded specimen of reheat pipes and boiler tube specimen, all defections were successfully detected. Image enlargement make it possible to detect micro flaw of 0.5mm length x 0.5mm in depth.

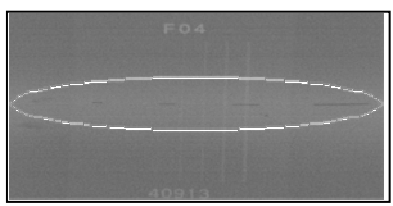

Fig. 6-a. 1mm depth linear flaw of reheat pipe.

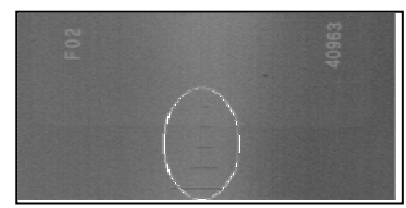

Fig. 6-b. 2mm depth linear flaw of reheat pipe.

Fig. 7. Digital X-ray image for Boiler Tube

To gain film images, high quality film (type 1) is used. Focusing to film distance (FFD) is set up with 650mm to protect image degradation. As a result of an analysis on the film image, 1mm depth flaw is not detectable, but 2mm and 3mm depth flaws are detected for reheat welding specimen.

In boiler tube inspection, tiny 0.5mm linear flaw can not be detectable. However, 1mm and 2mm OD size circular flaws can be detected in the range of 1mm, 2mm, and 3mm in depth respectively.

5.2. *Discrimination Rate with Image Quality Indicator*

Image quality indictor presents that digital X-ray image offers better quality than film image. The detailed each rate is shown in Table 2.

Table 2. Discrimination Rate

Specimen	Thickness (㎜)	Digital X-ray image		X-ray film image	
		Line Diameter (㎜)	Rate (%)	Line Diameter (㎜)	Rate (%)
Reheat Pipe	20	0.20	1.0	0.20	1.0
Superheat Tube	8	0.125	0.8	0.16	1.0
Reheat Tube	6	0.125	1.0	0.16	1.3
Welded plate	10	0.125	1.3	0.16	1.6
Welded plate	15	0.16	1.1	0.20	1.3

6. Conclusion

This digital imaging ability, along with appreciable economic and environmental advantages, has led to the use of this technology by many industries including Power Plants.

Based on testing result, it is established that digital flat panel detector provides highly reliable image in detecting defects. In addition, it enables to detect micro defect, which is not applicable in X-ray film inspection, with image manipulation like histogram adjustment, image enhancement, and etc.

It is demanded to take digital x-ray detectors out of the lab and into industry which may bring cost reduction and quality upgrade in inspection. Industry also demands the continuous development on digital radiography system and application for a widely use.

References

[1] W.P. HOSCH, C. FINK, Radiation Dose Reduction Chest Radiography Flat Panel Amorphous Silicon Detector, Clinical Radiology, 2002, pp 902-907.

[2] Evalluation of new Digital Detectors for High Resolution Radiography Kaftandjian INSA-CNDRI Laboratory France.

[3] Radiographic Inspection of Welding by Digital Sensors. H.Thiele, RADIS GmbH Germany.
[4] John Pursley Envision Product ix-pect Software Scanning Images Manual 2004, 15-22.

EVALUATION OF RESIDUAL STRESS FOR BOILER WELDS IN THERMAL POWER PLANT BY NONDESTRUCTIVE METHOD

KEUN BONG YOO

KPREA ELECTRIC POWER RESEARCH INSTITUTE, 103-16 MUNJI-DONG, YUSEONG-GU, DAEJEON, KOREA

JAE HOON KIM

CHUNGNAM NATIONAL UNIVERSITY, 220 GUNG-DONG, YUSEONG-GU, DAEJEON, KOREA

In the fossil power plant, the reliability of the components which consisted of the many welded parts depends on the quality of welding. The residual stress is occurred by the heat flux of high temperature during weld process. This decreases the mechanical properties as the strength of fatigue and fracture or occurs the stress relaxation cracking and fatigue fracture. Especially, the accidents due to the residual stress occurred at the weld parts of high-temperature and high-pressure pipes and tubes. So the residual stress of the welded part in the recently constructed power plants is more important. The aim of this study is the measurement of the residual stress using the x-ray diffraction and indentation method which are more accurate and applicable than other methods. Also we examine the site application of this nondestructive method in maintenance and construction of power plant.

1. Introduction

Residual stress induced during a welding process is known to have a great effect on the fatigue strength of materials. If the residual stress is higher than the yield strength, cracks and defects around welds can cause failures of the whole facility. If residual stress are evaluated exactly, and thus the part are replaced in right time, financial losses and the spreading of accident can be reduced. Figure 1 shows the crack generated by residual stress in boiler tube[1]. In order to evaluate the residual stress, fracture tests are required. However it is very hard to obtain test specimens from the site. So the evaluation of residual stress by a non-destructive method is preferred, though researches on this area are insufficient.

In this study, we measure residual stress values using the x-ray diffraction and indentation technique. Materials are A335 P92 and A213 T23 steel. Also we

examine the site application of these nondestructive methods to boiler welds in power plant.

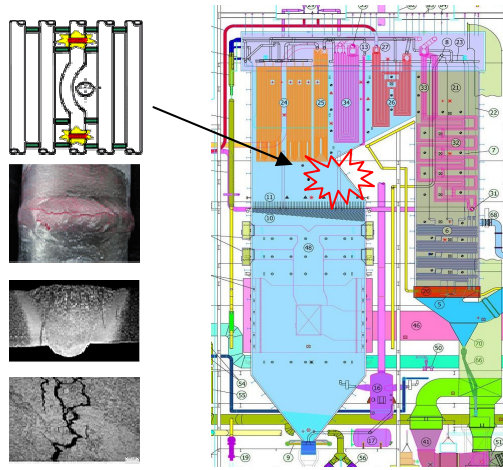

Fig. 1. The Crack of Water Wall Tube in 500MW Ultra Super Critical Boiler[1]

2. Experimental Details

2.1. *Materials & Specimens*

Materials used for this study are A335 P92 and A213 T23 steel for the use of high temperature pipe and tube on super critical condition. P92 steel can be used instead of 2.25Cr-1Mo steel, because of their oxidation and corrosion resistance at high temperature (above 590℃), and they can be overcome the weakness of 2.25Cr-1Mo steels such as high thermal extension coefficient, and low thermal conduction. The chemical composition and mechanical properties are shown in Table1, 2 respectively. The schematic view of the specimen is shown in Fig. 1, 2.

Table 1 Chemical compositions of P92 and T23 steel

Material	C	Si	Mn	P	S	Ni	Cr	Mo	W	V	Nb	B	N	Al
P92	0.10	0.22	0.48	0.017	0.006	0.18	9.11	0.47	1.71	0.18	0.056	0.003	0.041	
T23	0.08	0.28	0.46	0.012	0.006		2.02	0.17	1.54	0.22	0.061			0.012

Table 2 Mechanical properties P92 and T23 steel

Material	TS (MPa)	YS (MPa)	EL (%)
P92	674	506	23.6
T23	576	456	24.8

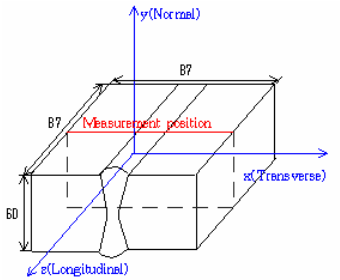

Fig. 2, Schematic view of pipe specimen

Fig. 3. Schematic view of tube specimen

2.2. *Measurement of Residual Stress*

2.2.1. *Measurement of Residual Stress using X-ray Diffraction*

X-ray diffraction method for the measurement of residual stress is based on the calculation of the distance(d) of the deformed lattice planes in the material. Namely, the mechanical deformation causes a change in the spacing of the lattice planes. The diffraction angle(2θ) illuminated on the surface of the material changes according to this deformation, and thus the residual stress is measured by a non-destructive method from this change using equation(1). The depth of X-ray penetration varies with types of targets used, and is typically about 10 ㎛. [2]. X-ray diffraction tests were conducted using portable equipment. Residual stress was measured using the multiple sin2ψ method. The five ψ tilting angles, 0°, 20.7°, 30°, 37.8° and 45°, were used for the measurements.

- Characteristic X-ray: Cr-Kα
- Diffraction plane: (211)
- Tube voltage: 30kV
- Tube current: 10mA
- Scanning speed: 2deg. /min
- Time constant: 3sec

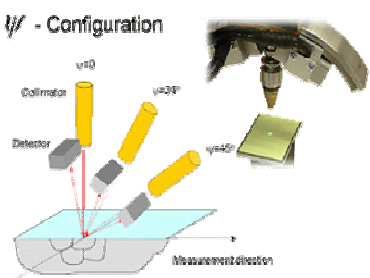

Fig. 4. Measurement principle of residual stress using x-ray diffraction technique[3]

$$\sigma_\varphi = \frac{E}{(1+\nu)\sin^2\psi}\left(\frac{d-d_n}{d_n}\right) \quad (1)$$

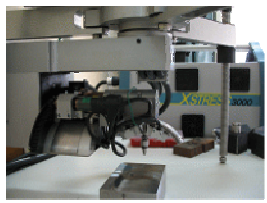

Fig. 5. Measurement of residual stress using portable x-ray diffraction equipment

2.2.2. *Measurement of Residual Stress using Indentation*

The change in indentation deformation caused by the residual stress was identified in the indentation loading curve in figure. 6. The applied load in the tensile-stressed state is lower than that in the stress-free state for the same maximum indentation depth. In other words, the maximum indentation depth desired is reached at a smaller indentation load in a tensile-stress state because a residual-stress–induced normal load acts as an additive load to the applied load. Therefore, the residual stress can be evaluated by analyzing the residual-stress–induced normal load. The indentation load and maximum depth for the tensile-stress state(LT, ht) are equivalent to those in the relaxed state(L0, ht). Indentation arrays using Vickers indenter were made on the polished surface. Maximum load and loading-unloading speed were 70 kgf and 0.5 mm/min, respectively[4].

$$L_0 = L_T + L_{res} \quad (2)$$

$$\sigma_{res} = C\, L_{res}/A^0_C \quad (3)$$

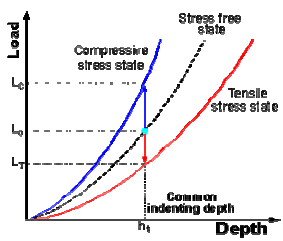

Fig. 6. Variation of indentation load-depth curve with stress

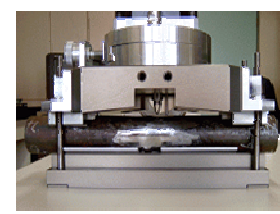

Fig. 7. Measurement of residual stress using indentation equipment

3. Result and Discussion

3.1. *Evaluation of Residual Stress*

Residual stress values by indentation method correspond to the values by saw cutting method[5]. In order to examine the relaxation effect of residual stress after post weld heat treatment, PWHT was performed. PWHT condition is 760°C, 2.5hours and air cooling. Figure 8 shows the residual stress values

obtained by x - ray diffraction technique before/after PWHT in P92 pipe steel. Residual stress relaxed considerably and effectively after PWHT. Figure 9 shows the residual stress values obtained by x - ray diffraction and indentation technique after PWHT in P92 pipe steel. Residual stress relaxed considerably and effectively after PWHT. Residual stresses obtained by two methods correspond considerably.

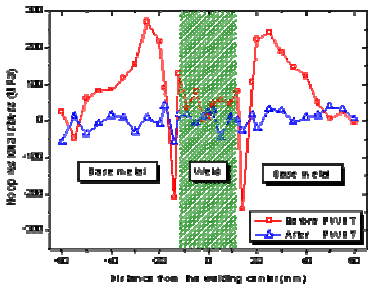

Fig. 8. Residual stress values of P92 steel obtained by x - ray diffraction technique before/after PWHT

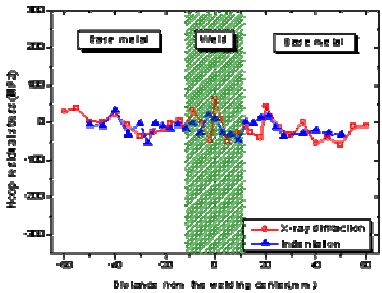

Fig. 9. Comparison of residual stress values in P92 steel obtained by x - ray diffraction and indentation technique after PWHT

Also, Figure 10, 11 show the residual stress values obtained by x - ray diffraction and indentation technique before/after PWHT in P92 and T23 steel respectively. Tendency of residual stress is very similar in P92 steel

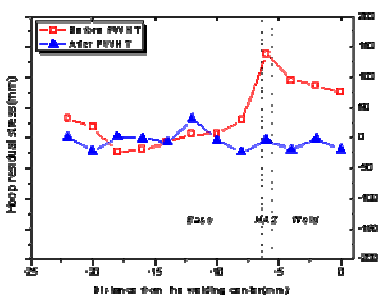

Fig. 10. Residual stress values of T23 steel obtained by x - ray diffraction technique before/after PWHT

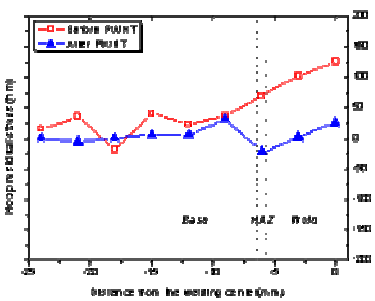

Fig. 11. Residual stress values of T23 steel obtained by indentation technique before/after PWHT

3.2. *Examine the Site Application*

The feature measuring residual stress to main steam pipe in power plant is shown in Figure 12, 13. X-ray diffraction and indentation equipment are very applicable to pipe line. Also, figure 14 shows the application feasibility of these methods to boiler tube.

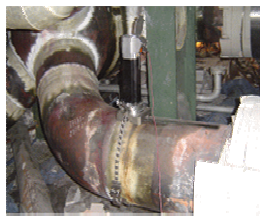

Fig. 12. Residual stress measurement of steam pipe by indentation

Fig. 13. Residual stress measurement of steam pipe by x-ray diffraction

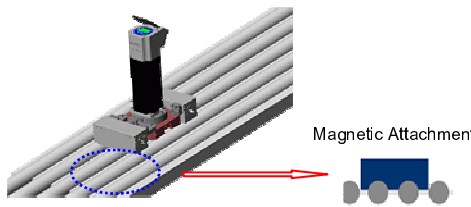

Fig. 14. Schemetic view of residual stress measurement of boiler tube in power plant by indentation equipment

4. Summary

The residual stress which was occurred during weld process was relaxed by post weld heat treatment and residual stress values which were obtained by x-ray diffraction correspond closely to the values by indentation, which corresponds with saw cutting method. Also, portable indentation and x-ray diffraction equipment are very applicable to steam pipe and boiler tube in power plant. So, residual stress measurement using these nondestructive methods and post weld heat treatment can prevent to failure by residual stress in maintenance and construction of power plant.

References

1. J. C. Jang, TM.C97GS01.S2007, KEPRI(2007)
2. Paul S. Prevery, Metals Handbook vol. 10, Lambda, In
3. K. B. Yoo, TM.00GE08.P2004.343, KEPRI(2004)
4. Y. Choi, and D. I. Kwon, Key Engineering Materials, Vol 297-300, pp. 2122-2127(2005)
5. S. K. Park, TR.01GS06.S2002.462, KEPRI(2002)

ULTRASONIC SIGNAL PROCESSING ALGORITHM FOR DETECTING THE KEYWAY CRACKS ON TURBINE ROTOR DISK

SEUNG IL CHO[1], JONG KYU LEE[1†], UN HAK SEONG[2], WON CHAN SEO[3], JONG O LEE[4], YOUNG HO SON[4] AND SUNG SOO JUNG[5]

[1] *Department of Physics, Pukyong National University, 599-1 Daeyeon-Dong Nam-Gu, Busan, 608-737, Korea*

[2] *R&D Center, Doosan Heavy Industries & Construction Co., Ltd, 555 Gwigok-Dong Changwon, Gyongnam, 641-792, Korea*

[3] *Materials Processing Engineering, Pukyong National University, 599-1 Daeyeon-Dong Nam-Gu, Busan, 608-737, Korea*

[4] *Authorized Nuclear Inspection Group, Korea Institute of Materials Science, 66 Sangnam-Dong Changwon, Gyongnam, 641-831, Korea*

[5] *Mechanical Metrology Group, Korea Research Institute of Standard and Science, P.O.Box 102 Yuseong, Daejon, 305-340, Korea*

An ultrasonic signal processing algorithm was developed to evaluate cracks generated around the keyway of a turbine rotor disk. The developed algorithm was composed of three processing steps; pre-processing, detection of the crack candidate region and classification of the crack region. The B-scan images obtained from the ultrasonic scanning system contained the ultrasonic images of the keyway, back wall and cracks. In order to distinguish the ultrasonic images of the cracks from those of the keyway and back wall in the B-scan images, the ultrasonic images of the cracks should be extracted from the obtained ultrasonic images by comparing the ultrasonic images without cracks. The ultrasonic images of the cracks were processed by the binary, dilation, segmentation, template matching and subtraction. Therefore, the cracks generated around the keyway of the turbine rotor disk could be detected more exactly by the ultrasonic images processed with the developed algorithm.

1. Introduction

A turbine of the nuclear and fossil power plants is more loaded according to increasing the number of start-up and stop operations and is subjected to stress, temperature, erosion, corrosion, and vibration which are main cause of cracking [1, 2]. Cracks have been found in all area, including disk rims, disk external surfaces, disk internal bore and keyway surfaces etc., mostly they are concentrated on the keyway. Cracking in turbine components is commonly caused by a combination of stress and corrosion. Stress corrosion cracking may

† Corresponding author: jklee@pknu.ac.kr.

occur singly (usually at a stress riser such as a keyway) or in clusters of many fine cracks [3 - 5].

The magnetic particle method has been principally used for the detection of cracks on the turbine disk, but it is impossible to access hub and keyway surface before disk was detached from rotor so that the ultrasonic method was used as a nondestructive examination. In conventional ultrasonic techniques to detect and evaluate cracks, reflective methods are unsuitable for sizing due to the variables affecting the amplitude of reflected energy such as crack transparency, orientation and general crack morphology [3, 6, 7]. In order to detect and evaluate cracks by using ultrasonic technique, the process of extracting the crack signals distinguished from geometrical indications is required, and the real situation is that the examiner directly performs this processing of extraction. In case of very complicated geometry such as the keyway of turbine rotor disk, a great amount of skill and knowledge are required to evaluate cracks. The abilities of crack detection depend on the expertness and experience of examiner.

In this study, an ultrasonic signal processing algorithm was developed to apply detecting more quantitatively the cracks generated around the keyway of a turbine rotor disk.

2. Experimental

2.1. *Specimens*

The simulated specimens of a turbine rotor disk used in this study were shown in Figure 1. A keyway that is the same size (φ = 19.05 mm) of the keyway of a real turbine was fabricated in an acrylic resin. The artificial cracks having 1 mm in width and 2 mm in length were machined on the point P of the curved surface on both sides from the top of the keyway with the angles of 30°, 45° and 90°. The identification of the simulated specimens, the angles and lengths of the cracks and the thicknesses of the specimens were shown in Table 1.

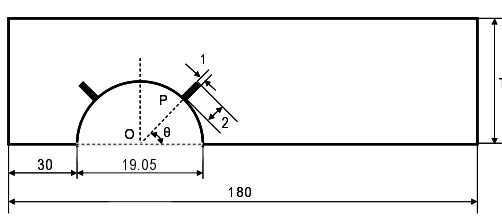

Fig. 1. Shape of the simulated specimen and cracks.

Table 1. Description of the simulated specimens.

Identification	Crack angle (degree)	Crack length(mm)	Thickness of specimen(mm)
S0	No crack	No crack	34.0
S30	30	2	34.8
S45	45	2	34.3
S90	90	2	34.1

2.2. *Experimental Procedure*

Figure 2 shows schematic diagrams of experimental set-up for generation of ultrasonic pulse, acquisition, display, and signal processing. Ultrasonic pulse-echo contact method was conducted to detect the artificial cracks in the simulated specimens. An ultrasonic transducer having 0.375 in. in diameter of element with center frequency of 5 MHz was used. Ultrasonic defect detector (USD 15, Krautkramer) which is able to generate impulse type waveform was used as pulser and receiver. Received ultrasonic analogue data (RF signal) were sent to digital oscilloscope (TDS 410A, Tektronix) in order to convert them digitally with sampling rate of 10 ns and the data were stored with 0.5 mm in scan index. The obtained data were used as input data of the developed ultrasonic signal processing algorithm and were evaluated, and then the final images containing the information on the cracks were presented on the monitor.

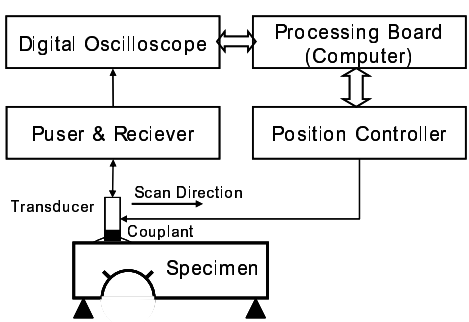

Fig. 2. Schematic diagram of ultrasonic signal processing system for crack detection.

3. Results and Discussions

3.1. *Ultrasonic signal processing algorithm*

An ultrasonic signal processing algorithm was composed of three processing steps, i.e., pre-processing, detection of the crack candidate region and classification of the crack region in order to obtain the ultrasonic images of the

cracks. In the pre-processing step, the ultrasonic reflected signals containing the scanning positions, time of flight and amplitudes were compared between cracks and no crack on the keyway to determine the features of the reflected signals. To eliminate the noises of the input data and to divide the peak amplitude of the reflected signal according to the propagation path, 40 points adjacent averaging was conducted. The B-scan images obtained from the pre-processed signals include not only the ultrasonic images of cracks but also those of the keyway and back wall, so it is necessary to develop a method to extract the cracked area from the B-scan images. In order to detect the crack candidate region by comparing the ultrasonic images of the keyway and back wall without crack, the algorithm which processed the images by the binarization, dilation, segmentation, template matching and subtraction was made up. In the final step, because the crack candidate region that was detected through the processes of subtraction and so on, contained also non-crack region, the feature values of the cracked area such as the conditions of the position, area and shape were estimated and then the final images that contained only the information on the crack region could be obtained.

3.2. *Classification of the crack region*

There were not only the crack regions, but also the noise region including the boundaries of the keyway and back wall detected in the crack candidate region obtained from previous stage. In order to attain only the crack region among these crack candidate regions, the feature values for the crack region were established. The conditions of feature values that could be a crack region were defined as shown in Table 2. The feature value of the condition of position could erase the crack candidate regions detected from the region below the back wall region. The feature value of the condition of area classified the crack regions in case that the areas of each crack candidate region were equal and greater than 1/5 of the crack area obtained from the specimen S90 that the angle of crack is 90°. The feature value of the condition of shape classified non crack regions in case that the ratio of horizontal length to vertical length of the crack candidate region was less than 0.25 or greater than 4.0.

Table 2. Conditions of the feature values for classification of the crack region.

	Threshold Conditions
Position	Erase : over than scanning depth of backwall (130 mm)
Area	Accept : over than threshold. (30 ≒ 1/5 X scanned area of crack)
Shape	Accept : $0.25 \leq V/H \leq 4.0$ (H : horizontal -length, V : vertical length)

Figure 3 shows the images that the regions without the crack below the back wall were erased by applying the feature value of the condition of position. It was found that 7, 5 and 5 crack candidate regions for the specimens of S30, S45 and S90, respectively remained.

After applying the conditions of position, area and shape in Table 2, the number of crack regions became 2, 2 and 1, respectively and three feature values for each region classified as the crack region were shown in Table 3. As shown in Figure 4, the cracks existed in each specimen could be detected exactly. Therefore it was found that the ultrasonic signal processing algorithm developed in this study could extract the crack regions only.

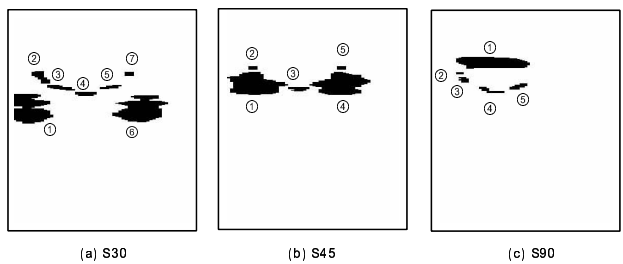

Fig. 3. The images after applying the condition of position.

Table 3. Results of classifying the feature values of the crack region.

	S30		S45		S90
	①	⑥	①	④	①
Position (mm)	64.2 ~ 123.4		64.8 ~ 95.6		47.1 ~ 87.5
Area (mm^2)	171	183	171	164	165
Shape	0.7	0.4	0.3	0.3	0.3
Result of Classification	Crack Region		Crack Region		Crack Region

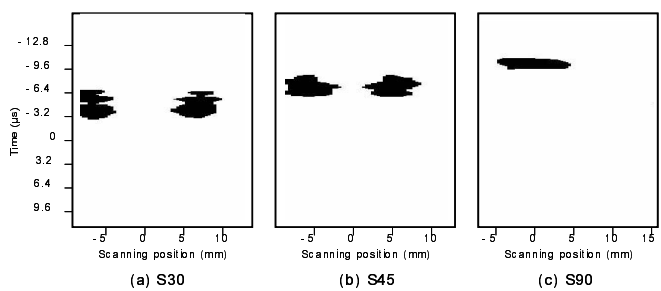

Fig. 4. Resulting images of final crack region.

4. Conclusions

In this study the ultrasonic signal processing algorithm was developed to detect cracks generated around the keyway of the turbine rotor disk. The developed algorithm was composed of three processing steps; pre-processing, detection of the crack candidate region and classification of the crack region. The B-scan images obtained from the ultrasonic scanning system were processed by the binarization, dilation, segmentation, template matching and subtraction. Only the crack regions could be extracted from the B-scan images by using this developed algorithm. Therefore, it was confirmed that the developed algorithm could be useful tool to detect the cracks on the keyway of turbine rotor disk.

References

1. M. Koike, F. Takahashi, S. Kajiyama, H. Chiba and Y. Yoshida, *Proceedings of the 13th International Conference on NDE in the Nuclear and Pressure Vessel Industries* 463 (1995).
2. G. P. Singh, R. A. Cervantes, R. L. Spinks, *Material Evaluation* 41, 1511 (1983).
3. John R Lilly, *EPRI turbine/generator workshop, 3rd* (1993).
4. F. F. Lyle, Jr. and H. C. Burghard, Jr., *EPRI Report NP-2429, 2, Project 1398-5* (June, 1982).
5. P. K. Nair, F. F. Lyle, Jr., J. E. Buckingham, H. G. Pennick, *EPRI Report Np-6444, 1, Project 1929-16, 2518-1* (July, 1989).
6. K. Date, H. Shmada and N. Ikenaga, *NDT International* 315 (December, 1982).
7. D. K. Mak, *Ultrasonics* 223 (September, 1985).

EXPERIMENTAL APPROACH FOR WATER DISCHARGE CHARACTERISTICS OF PEMFC BY USING NEUTRON IMAGING TECHNIQUE AT NRF, HANARO

TAEJOO KIM, JONGROK KIM, MOOHWAN KIM

Dept. of Mechanical Engineering, Pohang University of Science and Technology, San 31, Pohang, Kyoungbuk 790-784,Republic of Korea

CHEULMUU SIM

Korea Atomic Energy Research Institute 150, Deokjin-dong, Yuseong-gu, Daejeon, 305-353, Republic of Korea

An investigation into the water discharge characteristics of Polymer Electrolyte Membrane Fuel Cells(PEMFC) is carried out by using Neutron Radiography Facility (NRF) at HANARO. The feasibility test apparatus was composed of a distilled water supply line, a compressed air supply line, heating systems and single PEMFC which was a 1-parallel serpentine type with a 100 cm^2 active area. Heating method is suitable to remove the water at MEA for low water case. But it is difficult to remove the whole water at channel for much water case

1. Introduction

The polymer electrolyte membrane fuel cell (PEMFC) is one of the most promising candidates for automotive applications due to its high energy conversion efficiency and absence of chemical pollution. PEMFC usually uses hydrogen and oxygen as fuel in order to generate electricity, and heat and water are generated as byproducts during that procedure. These byproducts create several problems coupled with fluid flow, heat, and mass transfer processes. Moreover, water more seriously affects the efficiency of the PEMFC system since the proton conductivity of the membrane is highly influenced by the water content. If the water content at the membrane and channel is too low, the conductivity of proton is decreased and the efficiency is dropped. Conversely, too much water content causes flooding at the channel. The flooding impedes gas flow and also reduces the efficiency [1-4].

Management of such a system must be considered during a design process, and researchers must have an understanding of the water dynamics within a system. After Satija et al. [5], several researchers and organizations have developed a

high level of expertise for neutron imaging technique. However, most previous researches using the neutron imaging technique have been related with the performance of fuel cells. Since an auto-vehicle can be run in sub-zero temperature conditions, there must be a phase change at PEMFC. Especially the freezing of water at the MEA and channel means damage to fuel cells. Therefore water at the fuel cell, regardless of its position, must be removed as soon as possible. But there have been few studies on the water discharge characteristics at PEMFC until now and furthermore no criteria. In the present study heating method was used for the investigation of the water removal efficiency in PEMFC by using the Neutron Radiography Facility (NRF) at HANARO.

2. Experimental Setup and Neutron Image Technique System

2.1. *Experimental apparatus*

Since the objective of the present study was only an investigation for a water discharge behavior at PEMFC, the actual situation could be simulated by using a feasibility test apparatus. It consists of three parts; a distilled water supply loop, a compressed air loop, heating system and unit PEMFC. Figure 1-a) shows a schematic diagram of the feasibility test apparatus.

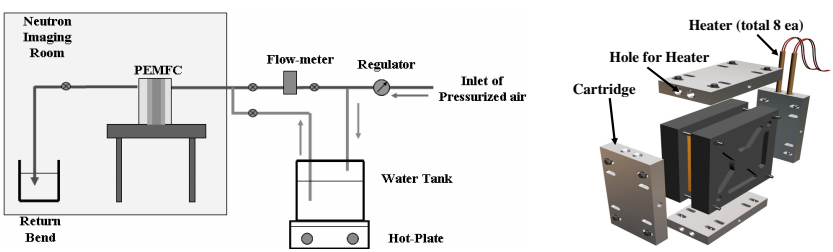

a) b)

Fig. 1. a) Schematic diagram of the test apparatus and b) heating system.

The water generated during an operation of the PEMFC usually exists at the cathode side, and distilled water is supplied into the cathode side only by using compressed air and a water tank system. Because the PEMFC is opaque, it is difficult to know how much water exists in the cathode channel. So water is supplied for about ten minutes into the cathode channel by using compressed air. The valve located at the outlet of the PEMFC is closed in order to entrap the water in the cathode channel. The compressed air is supplied again for about 2 minutes, and then it is stopped. Afterwards, the valve at the outlet of the PEMFC

is opened. Finally the neutron images were taken under different discharging methods.

Heating method was used to investigate the water discharge characteristics. The heating system as shown in Figure 1-b) consists of 8 heaters and 4 cartridges, which are independently controlled to create different temperature conditions of PEMFC.

The 1-parallel serpentine type sketched in Figure 2 has been chosen. The anode and cathode flow field channels each form a serpentine pattern across the active area of the 100 cm^2 fuel cell. The anode and cathode flow field utilizes a 1-channel, 67 pass with a channel width and depth of 1 mm and gap width of 0.5 mm. The flow field used for anode and cathode are symmetric.

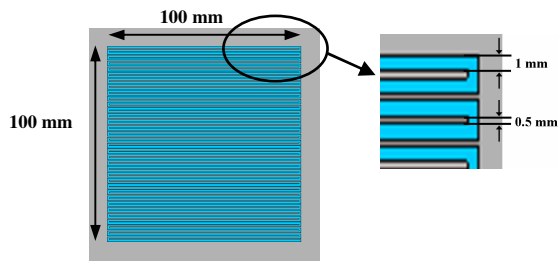

Fig. 2. Schematic diagram of flow field geometry: 1 parallel serpentine.

2.2. *Neutron imaging facility and image process*

All experiments described above were performed at the neutron radiography facility (NRF) at HANARO, KAERI. The NRF provides two measurement positions with different neutron intensities (from 5×10^6 to 1×10^7 n/cm^2s) and collimation ratios (from 200 to 270). The detecting system of this study consists of a neutron-sensitive scintillator fabricated by the Applied Scintillation Technologies and CCD camera with 1340×1300 pixels housed in a light tight box. The neutron beam is converted into light by the scintillator. The light is reflected by a mirror and then measured by the CCD camera with f 1.4, 85 mm Nikon lens system. Image processing is required in order to quantify the water contents although the raw neutron image can be used for non-destructive test. Equation (1) is the ideal relationship between the neutron beam and attenuation due to the materials.

$$\Phi = \Phi_o e^{-\sum_i \mu_i t_i} \tag{1}$$

Φ is the neutron beam flux in front of the scintillator and Φ_o is the uninterrupted neutron beam flux upstream of PEMFC. The exponent accounts for an

attenuating due to all materials, i, within the beam path; μ is the linear attenuation coefficient of the thermal neutron, and t is the thickness of the element in the beam path. The linear attenuation coefficient is found by a calibration or from the literature. The exponent contains a sum consisting of the t products for all the materials. Division of an image of an operating fuel cell (***wet*** image) by an image of a non-operating fuel cell (***dry*** image) results in subtraction of the exponents and isolation of the change in water content.

3. Calibration for Linear Attenuation Coefficient of Water

The linear attenuation coefficient of water must be known to calculate a water thickness as described 2.2. Because usually the linear attenuation coefficient depends on the neutron beam spectrum, this value is different under neutron sources. To avoid an uncertainty, the linear attenuation coefficient for water at NRF was measured by using reference device with 10 water steps. The value of the linear attenuation coefficient at NRF is determined to be 0.3029 mm^{-1} by using this device.

4. Results and Discussion

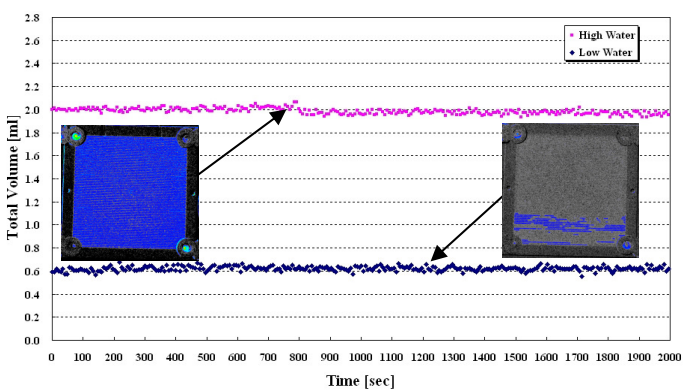

Fig. 3. Water contents variation and water distribution images at much water case and low water case.

In Figure 3, water distribution images are shown without water discharging methods at different water contents in order to check on the reliability of the neutron imaging technique. Although there are several unexpected data points, the overall water quantity of both cases is almost constant. The mean water content of both cases is 1.985 and 0.622 ml, respectively. Although it is difficult to discriminate the water at MEA for the high water case, it is easy to determine the water position and distribution for the low water case. Moreover, the

quantification is reliable. These results show why the neutron imaging technique is suitable for studying PEMFC.

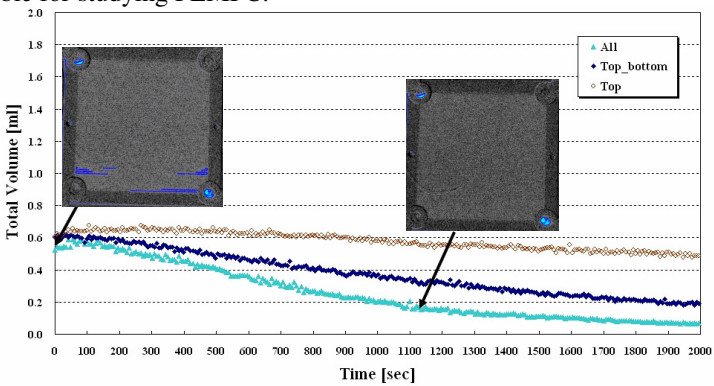

Fig. 4. Water contents variation according to the heating method only at starting position and after 1134 sec.

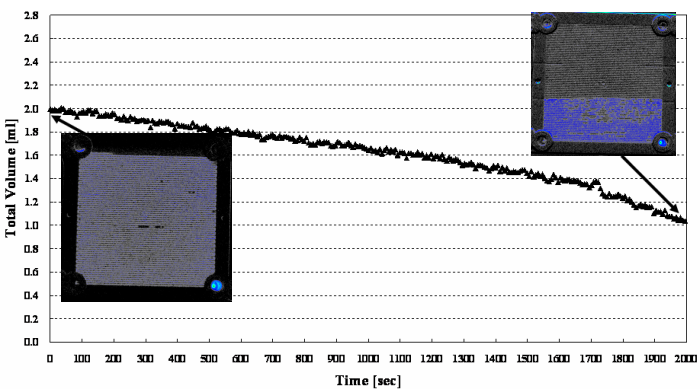

Fig. 5. Water contents variation according to the heating method only with full water at starting position, and after 2000 sec.

The water removal characteristics were investigated under heating method at the highest neutron flux position of the NRF. Although there is a little water at several channels and the MEA as shown at Figure 4, the water at cathode channel is removed and water only remains at MEA after heater is operating. Because it is difficult to control the water level into cathode channel, the initial water level is different according to the test conditions. Regardless the initial states, however, the water removal characteristics are different according to the heating positions. When only the top heater is operated, the water at the channel and MEA is slowly removed. But when all the heaters are heating, the removal efficiency is sharply increased and water only exists at MEA.

By the way, when the water fully occupies the whole cathode channel, the situation is changed as shown in Figure 5. Although all the heaters are operated, the water isn't removed at the cathode channel and the MEA. From these results, the heating method is only powerful to remove the water at MEA.

5. Conclusions

This present study has demonstrated that the neutron imaging technique at the NRF, HANARO is well suited for PEMFC research, especially water distribution and accumulation. Although the whole water at PEM fuel cell can't be removed during test time, the heating method is appropriate to discharge the water at the MEA. Since the neutron imaging technique is able to check on water distribution and fraction in PEMFC, it can give a help to improve the schemes of water management and efficiency.

Acknowledgments

This research has been by the Global Project Partnership, the Ministry of Science and Technology, Korea.

References

1. J. Larminie, A. Dicks, Fuel Cell Systems Explained, second ed., Wiley, West Sussex, 2003, p. 70.
2. G.A. Eisman, The application of Dow Chemical's perfluorinated membranes in proton exchange membrane fuel cells, J. Power Sources 29 (3–4) 389–398 (1990).
3. R. Baldwin, M. Pham, A. Leonida, J. McElroy, T. Nalette, Hydrogen–oxygen proton–exchange membrane fuel cells and electrolyzers, in: NASA Conference Publication 3056: Space Electrochemical Research and Technology (SERT), pp. 127–134 (1989).
4. D.J. Ludlowa, C.M. Calebrese, S.H. Yu, C.S. Dannehy, D.L. Jacobson, D.S. Hussey, M. Arif, M.K. Jensen, G.A. Eisman, PEM fuel cell membrane hydration measurement by neutron imaging, J. Power Sources, **162**, 271-278 (2006).
5. R. Satija, D.L. Jacobson, M. Arif, S.A. Werner, "In situ neutron imaging technique for evaluation of water management systems in operating PEM fuel cells", J. Power Sources, **129**, 238, (2004).

OPTIMAL DESIGN OF AN ULTRASONIC ARRAY SENSOR FOR NDE APPLICATIONS

HOEYONG KIM AND YONGRAE ROH

School of Mechanical Engineering, Kyungpook National University
Sankyukdong 1370, Bukgu, Daegu 702-701, Korea

The performance of an ultrasonic array sensor is determined by the properties of its constituent materials and the effects of many structural parameters. In this study, with the finite element method, the structure of an ultrasonic array sensor was optimized to achieve the highest sensitivity while satisfying such requirements as fractional bandwidth, center frequency and -20dB ring-down time. The optimization was carried out with the SQP-PD method for a target function composed of the ultrasonic array sensor performance. The optimized ultrasonic array sensor satisfied all the required specifications for NDE applications.

1. Introduction

Nowadays, the ultrasonic linear array sensor is gaining more and more importance in nondestructive evaluations (NDE) and in clinical communities for its multi-channel inspection, beam steering and dynamic focusing capability. The performance of an ultrasonic NDE system is heavily dependent on the ultrasonic sensor, thus there is a great need to improve the sensor's performance. However, most of the conventional linear array sensors have been designed with a simple equivalent circuit method and through trial and error [1]. In this study, a new design method was developed that can optimize the sensor's performance by considering all the cross-coupled effects of the structural variables of the sensor. The sensor performances considered were sensitivity, center frequency, fractional bandwidth, and -20dB ring-down time. Firstly, through finite element analyses (FEA), the variation of the performance factors was analyzed in relation to the structural variables. Then, the optimal structure of the sensor was determined to achieve the highest sensitivity while satisfying given constraints on center frequency, fractional bandwidth and ring-down time through the minimization of a target function. The optimization was carried out with the Sequential Quadratic Programming Method of Phenichny and Danilin (SQP-PD) method. The design technique was applied to a sample sensor to verify the validity of the method.

2. Linear array sensor

Figure 1 is a schematic structure of the linear array sensor under study. The sensor is composed of an acoustic lens, two matching layers, a piezoceramic layer and a backing material. The matching layers and the piezoceramic layer are divided by kerfs to form an array. The kerfs also work as insulation barriers to prevent interference between adjacent piezoceramic elements.

Table 1 shows the target performances of the linear array sensor, which need to be achieved through the optimal design in this work. The sensitivity and -20dB ring-down time are estimated from a temporal impulse response while the center frequency and fractional bandwidth are estimated from the frequency response of the transducer. The sensitivity is the ratio of the transmitted signal amplitude to the received signal amplitude as defined in Eq. (1)

$$Sensitivity[dB] = \frac{V_{pp}}{V_0} \tag{1}$$

(V_0: Peak voltage of transmitted signal, V_{pp}: peak voltage of received signal)

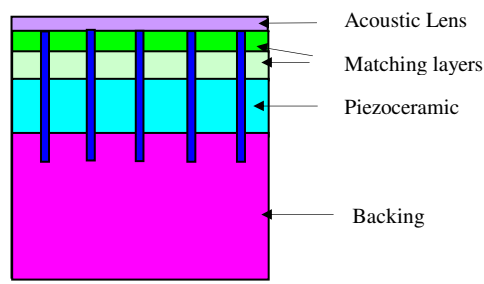

Fig. 1. Basic model of the linear ultrasonic array sensor.

Table 1. The target specifications of the ultrasonic array sensor.

Performance parameter	Specification
Sensitivity	-56.6 dB
Center frequency	3.5 ± 0.15 MHz
Fractional bandwidth	60 %
-20dB ring-down time	1.2 μs

3. Finite element modeling and analysis

The modeling and analysis were carried out with a commercial FEA package, PZFlex®. Figure 2 is the FEA model, and Table 2 shows the properties of the materials constituting the sensor. The initial geometry of the sensor is shown in Table 3 which indicates the actual dimensions of a typical ultrasonic linear sensor on the market. Table 4 lists the structural variables whose optimal values are to be determined within each variation range. The variation ranges were selected through rigorous preliminary calculations of the sensor's performance [5]. The preliminary results also revealed that the four variables in the Tables dominate the transducer's performance. The purpose of this study is to determine the optimal structure of the linear sensor that can provide the highest sensitivity while satisfying the other specifications in Table 1. The design scheme should reflect not only the individual but also all the cross-coupled effects of the structural variables.

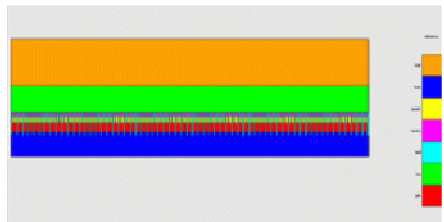

Fig. 2. Finite element model of the ultrasonic array sensor.

Table 2. Properties of the constituent materials of the sensor.

	Density	Longitudinal wave velocity	Shear wave velocity	Longitudinal attenuation	Shear wave attenuation
Acoustic lens	1125 kg/m^3	2418 m/s	1209 m/s	1.26 dB/mm	5.04 dB/mm
1st matching layer	3386 kg/m^3	2451 m/s	1225 m/s	1.0 dB/mm	4.0 dB/mm
2nd matching layer	1159 kg/m^3	2589 m/s	1295 m/s	0.93 dB/mm	3.72 dB/mm
Piezoceramic	7800 kg/m^3	4500 m/s	PZT-5H		
Backing	1260 kg/m^3	2393 m/s	1443 m/s	3.78 dB/mm	16.21 dB/mm

Table 3. Basic geometry of the ultrasonic array sensor.

Thickness of the Lens	1250 μm
Thickness of the 1st matching layer	300 μm
Thickness of the 2nd matching layer	170 μm
Thickness of PZT	460 μm
Thickness of the Backing	1000 μm
Pitch	260 μm
Kerf width	50 μm

Table 4. Variation ranges of the structural variables of the ultrasonic array sensor.

Structural variables	Variation range (μm)
Thickness of the 1st matching layer (x_1)	280 ~ 320
Thickness of the 2nd matching layer (x_2)	150 ~ 190
Kerf width (x_3)	45 ~ 55
Pitch (x_4)	190 ~ 330

4. Formulation of the performance parameters

Through the FE analyses with the model in Fig. 2, the variation of the performance parameters in Table 1 was analyzed in relation to the structural variables. 17 different combinations of the structural variables were analyzed to find the trend of the variation. Further, the design method of 2^n experiments was employed to efficiently select the representative performance of the sensor, where n is the number of the structural variables [2]. Table 4 shows the normalization factors established for each of the structural variables. Hence, with the normalization factors of ±0.5 and ±1, $2\times2^4 = 32$ more combinations were analyzed.

Then, the functional forms of the center frequency, sensitivity, fractional bandwidth and -20dB ring-down time were derived in relation to the four structural variables. The formulation of the performance parameters was carried out through multiple regression analysis of the FEA results. A second-order multiple regression model was utilized as shown in Eq. (2).

$$\begin{aligned} y = {} & a_1 x_1^2 + \cdots + a_4 x_4^2 + b_1 x_1 + \cdots + b_4 x_4 + c_1 x_1 x_2 + \cdots \\ & + c_6 x_3 x_4 + d_1 x_1 x_2 x_3 + \cdots + d_4 x_2 x_3 x_4 + e_1 x_1 x_2 x_3 x_4 + e_2 \end{aligned} \tag{2}$$

where, a_1~a_4, b_1~b_4, c_1~c_6, d_1~d_4 and e_1~e_2 are the 20 regression coefficients. The statistical analysis was made using the commercial software SAS. [3]

Table 5. Normalization factors of the structural variables.

Normalization factor	x_1	x_2	x_3	x_4
-1	280	150	45	190
-0.5	290	160	47.5	225
0	300	170	50	260
0.5	310	180	52.5	295
1	320	190	55	330

5. Optimal design

For the design of a linear array sensor that has the highest sensitivity while satisfying the other specifications in Table 1, we established a target function like Eq. (3) was established with the constraints in Eq. (4). The optimal design therefore means finding the combination of the structural variables that minimizes the target function while satisfying the three constraints in Eq. (4).

$$\text{Target function} \quad \frac{1}{sensitivit\ y} \tag{3}$$

$$\begin{aligned} \text{Subject to} \quad & 3.35\,MHz \le f_c \le 3.65 \\ & \text{Fractional bandwidth} \ge 60\% \\ & \text{-20dB ring-down time} \le 1.2\mu s \end{aligned} \tag{4}$$

For the minimization, the SQP-PD method was used because of its high convergence rate among various kinds of constrained optimization methods [4]. Figure 3 shows the characteristics of the sensor with the optimized structure. Table 6 shows the numerical result of the optimization, where the dimensions indicate the internal geometry of the optimized sensor. As evidenced in the table, the optimized sensor can provide a much higher sensitivity than required while also satisfying the specifications of the other performance parameters. These results confirm the validity of the design method developed in this work.

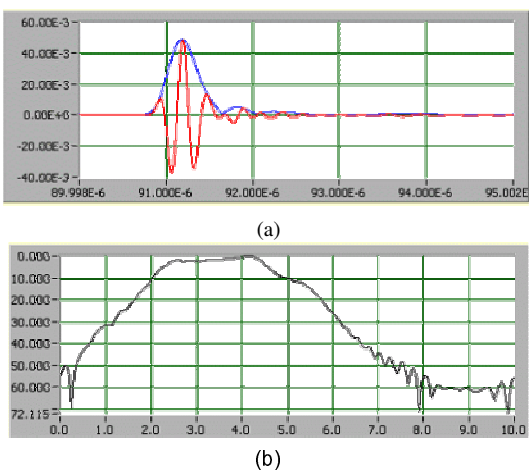

Fig. 3. The FEA result of the optimal sensor: (a) Time domain, (b) Frequency domain.

Table 6. Result of the optimization and optimized performance of the sensor.

Structural variables and performance	Optimized value	Normalization factor
x_1 (μm)	311.27	0.564
x_2 (μm)	155.52	-0.724
x_3 (μm)	46.16	-0.768
x_4 (μm)	316.48	0.807
Sensitivity(dB)	-50.686	-
Center frequency (MHz)	3.44	-
Fractional bandwidth (%)	69.97	-
-20dB ring-down time(μs)	0.765	-

6. Conclusions

The structure of an ultrasonic linear array sensor was designed to achieve the highest sensitivity at a given center frequency while providing a wide enough bandwidth and a short enough ring-down time. The finite element method was utilized to analyze the performances of a linear array sensor. The design process consisted of the formulation of the sensor's performance in relation to the structural variables of the sensor through the statistical multiple regression analysis of the FEA results and the optimization with the SQP-PD method of a target function. The optimization led to a sensor of much higher sensitivity while satisfying all the specifications on the other performance parameters. The design technique developed in this work is so general that it can also be applied to any other type of acoustic transducers.

References

1. J. C. Debus and J. N. Decarpigny, *Springer-Verlag, Orlando*, 1992.
2. R. O. Kuehl, *Design of experiments: Statistical principles of research design and analysis* (Duxbury Press, New York, 2000).
3. SAS Institute Inc., *Strategic Application Software* (Cary, New York, 2007).
4. D. A. Pierre, *Optimization theory with applications* (Dover Publications, New York, 1986).
5. K. J. Kang and Y. R. Roh, *J. Aco. Soc. Ame.* **114** 1454 (2003).

DESIGN OF SPECIAL SHOES WITH A POSITION CONTROL DEVICE FOR WATER LEVEL GAUGING IN A BELLOWS TUBE*

KIL-MO KOO, CHUL-HA SONG, YUN-SIK KIM†

Department of Thermal-Hydrauric Safety Research Center, KAERI, 150 Dukjin-dong, Yuseong, Daejeon, 305-353, Korea

YONG-MOO CHEONG

Department of Material Safety Research Center, KAERI, 150 Dukjin-dong, Yuseong, Daejeon, 305-353, Korea

IN-CHEOL LIM

Department of Hanaro Safety Control Center, KAERI, 150 Dukjin-dong, Yuseong, Daejeon, 305-353, Korea

CHI-SEONG PARK

Facilities of Safety Dignosis Group, KAETIC Inc, 461-61 Jeonmin-dong, Yuseong, Daejeon, 305-811, Korea

In this experiment, a residual water level measurement in a bellows tube was obtained by using an immersion ultrasonic technique and a special UT shoes with a position control device. So, we need a position control device for an accurate measurement. This device was designed and fabricated for a convenient control in an immersion tank, which has a combination of a sensor shoes and a position control device. The shoes were made by Lusite material which had the same shape as the bellows tube and the immersion transducers were controlled by a 3-axis position control device, which can be operated within a moving distance as small as 0.5mm, and then it is import to the center line from down position of the tube, and we also need to guide for UT shoe's device which was fabricated as the same radius of the bellows shape like a twin blade. Certain specialized applications such as an underwater testing require a long cable between the transducer and the ultrasonic gauging target in an immersion water tank.

* This work is supported by etc, etc.

† Work supported by the Korean Ministry of Science and Technology.

1. Introduction

A pulse-echo ultrasonic thickness gauge determines the thickness of a part or structure by accurately measuring the time required for a short ultrasonic pulse generated by a transducer. The ultrasonic pulse travels through the thickness of a material, then finally it is reflected by the back or inside surface, and it can be returned to the transducer. In most applications this time interval is only a few microseconds or less. The measured two-way transit time is divided by two to account for the down-and-back travel path, and then multiplied by the velocity of the sound in a test material[1-2].This UT system was designed and fabricated for a convenient control in a water tank, which has a combination of a sensor and a position control function. The shoes are specially made with Lusite material which has the same shape as the bellows tube and then the immersion transducers are controlled by a 3-axis position control system, and it can be operated within a moving distance as small as 0.5mm. Certain specialized applications such as an underwater testing require a long cable between the transducer and the ultrasonic gauging target in an immersion tank.

2. Measurement Modes and Frequency

The methods for making ultrasonic measurements of a thickness may be classified according to the type of transducer used to make the measurement, or they may be classified by the choice of the echoes used to determine the ultrasonic pulse transit time through a test piece. If we classify the measurement method by the transducer type, we find three basic classifications used in a precision thickness measurement such as the direct contact transducers, delay line transducers, and immersion transducers. It may be employed only when clean multiple back-wall echoes appear, which typically limits its use to materials of a relatively low attenuation and high acoustic impedance such as fine-grained metals, glass, and ceramics. In this experiment, we used Mode 2 and Mode 3 as the two kinds of immersion transducers which have a frequency of 15 MHz and 25 MHz. There are two kinds of transducers according to the water thickness. In this case, an enhanced S/N ratio is obtained from the 25 MHz frequency transducer more so than from the 15 MHz frequency transducer, because of the resolution of the transducer with a wide band frequency, and then we can obtain the frequency domain from the each time domain signal by the FFT function. It is also possible to analyze the signal patterns and obtain some information by the frequency domain. In order to obtain clean multiple echoes for a water thickness measurement, a focused immersion transducer should be operated at a considerably shorter distance than the focal length of 2 inch.

2.1. *Ultrasonic Measurement Methods*

In order to obtain clean multiple echoes for a thickness measurement, a focused immersion transducer should be operated at a considerably shorter distance than that of the focal length[3]. If it is operated at or near the focal length, intermediate shear mode echoes usually occur. (Note that this is a problem only in Mode 3 measurements; in Mode 2 nothing following the first back-wall echo is of interest.) Similar effects can occur in some cases where sharply radiused targets cause a refraction and/or mode conversion of beam components arriving at other than a normal incidence[4]. In general, it is often advisable to experiment with different combinations of a focus and water path to determine what produces the cleanest multiple echoes in a given measurement application. In this experiment, residual water level measurement in a bellow tube is obtained by using the immersion ultrasonic technique and a special UT probe attachment.

2.2. *The Immersion Ultrasonic Position Control System*

The immersion ultrasonic measurement & the position system are controlled by a 3-axis position control system, and it can be operated within a moving distance as small as 0.5mm using by a manual method. An ultrasonic module assembly, available in different frequencies and sensing ranges, easily plugs into the system, thus optimizing the sensing range for a specific application and allowing an easy and inexpensive modification of the system for other requirements. The shoes are made with Lusite material which has the same shape as the bellows tube and then the immersion transducers are controlled by the 3-axis position control system, and it can be operated within a moving distance as small as 0.5mm. The scanner which means the 3-axis position control system is used to carry out an ultrasonic immersion testing of the centered bellows tube. The scanning distance has a 50mm x 70mm x 60mm range. The scanning is done by providing the following ranges to move the probe. To enhance the contact efficiency of the transducer, transducer shoes in the shape of the outside of the bellows tube were designed, and the applied design recommends the following requirements of the shoes.

2.3. *Procedure for the Measurement*

In this experiment, as the procedures for the water level measurement, the first one and the second one are the reference glass tubes from which we could obtain the reference information for the real level thickness data. The dimensions of the first reference glass tube were 65.3mm in diameter and 2mm in thickness, when the water level was defined as 47.9mm and 50mm. The measured signals were obtained from the first reference glass tube. In the case of using the 25 MHz transducer, S/N ratio has been enhanced more so than that for the 15 MHz transducer. As a result, it is able to measure a reliable signal at the 25 MHz

frequency because of a signal which can be classified by the glass thickness signal and the measured water level signal between the initial echo and the first echo. (a) (b)

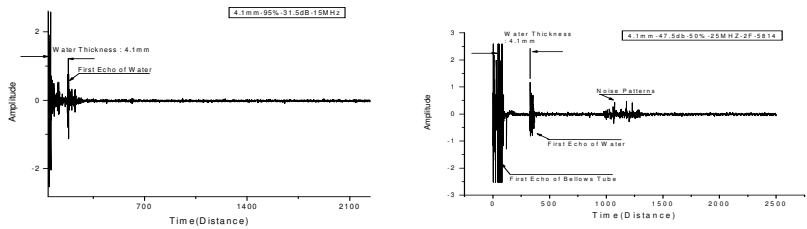

Fig. 1(a) Signal for the 4.1mm water thickness measured from the bellows tube. (at the 15 MHz transducer)

Fig. 1(b) Signal for the 4.1mm water thickness measured from the bellows tube. (at the 25 MHz transducer)

(a) (b)

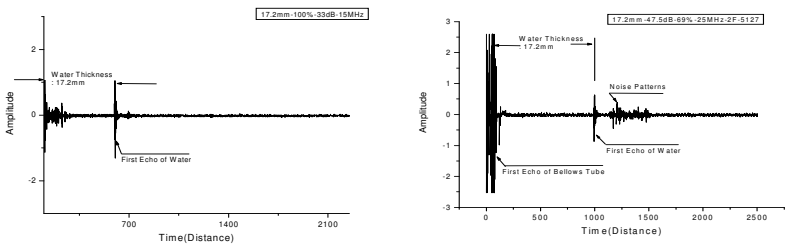

Fig. 2(a) Signal for the 17.2mm water thickness measured from the bellows tube. (at the 15 MHz transducer)

Fig. 2(b) Signal for the17.2mm water thickness measured from the bellows tube. (at the 25 MHz transducer)

The bellows tube in the water tank was attached by a supporter at both sides. The dimensions of the bellows tube were each 250mm, and 280mm in diameter and the thickness could be ignored because of a very thin thickness, when the measuring a water level is defined as 3.7mm, 4.1mm, 7.1mm, 17.2mm, 27.2mm, 37.2mm and 48mm in thickness. The reference signals were obtained from the first reference glass tube and then we are able to obtain the water thickness signals from the second bellows tube. Figure 1(a) shows a signal for the 4.1mm water thickness measured from the bellows tube by the 15 MHz transducer. Figure 1(b) shows a signal for the 4.1mm water thickness measured from the bellows tube by the 25 MHz transducer. Figure 2(a) shows the measured signal from the bellows tube with a 17.2mm thickness by the 15 MHz transducer. Fig. 2(b) shows a measured signal from the bellows tube with a 17.2mm thickness by the 25 MHz transducer.

(a) (b)

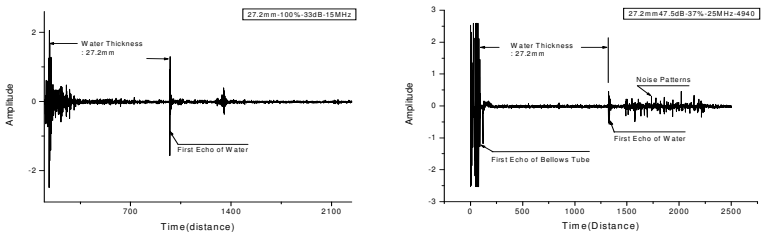

Fig. 3(a) Signal for the 27.2mm water thickness measured from the bellows tube. (at the 15 MHz transducer)
Fig. 3(b) Signal for the 27.2mm water thickness measured from the bellows tube. (at the 25 MHz transducer)

(a) (b)

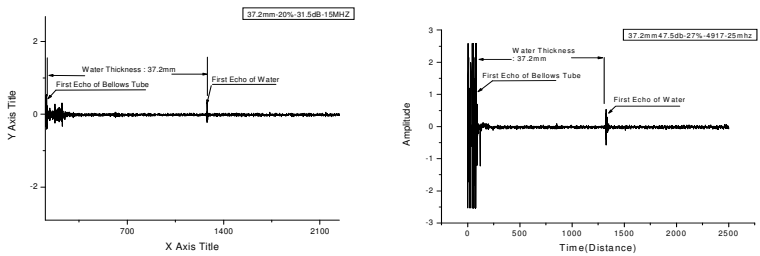

Fig. 4(a) Signal for the 37.2mm water thickness measured from the bellows tube. (at the 15 MHz transducer)
Fig. 4(b) Signal for the 37.2mm water thickness measured from the bellows tube. (at the 25 MHz transducer)

Figure 3(a) shows the measured signal from the bellows tube with a 27.2mm thickness by the 15 MHz transducer. Figure 3(b) shows the measured signal from the bellows tube with a 27.2mm thickness by the 25MHz transducer. Figure 4(a) shows the measured signal from the bellows tube with a 37.2mm thickness by the 15 MHz transducer. Figure 4(b) shows the measured signal from the bellows tube with a 37.2mm thickness by the 25 transducer. In all the cases, when using the 25 MHz transducer, the S/N ratio was enhanced more so than that of the 15 MHz transducer. But in the case of the 25 MHz transducer, uncertain noise patterns appeared from the back scattering region. As a result, it is possible to obtain a reliable signal at the 25 MHz frequency because of a signal which can be classified by the glass thickness signal and the measured water level signal between the initial echo and the first echo. In the case of 15 MHz frequency domain, main frequency domain was shifted at 11.5 MHz, side lobes were located over 15 Mhz-25 MHz. In case of 25 MHz frequency domain, main

frequency domain was shifted at 30 MHz, side lobes were located over 40 Mhz-65 MHz.

3. Conclusions

By using an immersion ultrasonic inspection, the developed system was aimed at measuring the water level in a bellows tube. In this experiment, as the procedure for the water level measurement, we obtained reference information from a reference glass tube. The dimensions of the first reference glass tube were 65.3mm in diameter and 0.4mm thick, when the water level was defined as a 47.9mm thickness with 15 MHz, and an 18mm thickness with 20 MHz. The resulting signals were obtained from the first reference glass tube by using the Mode 1 method. Using this reference data, 18mm thickness was determined as the water level in the reference tube whose diameter was 185mm and thickness was 0.4mm. Because the resulting measured data was comparable with the real data for the bellows tube, the error rate was ignorable. For a water thickness measurement in the bellows, we could measure from 4.1mm, 17.2mm, 27.2mm, 37.2mm in water thickness at each 15 MHz, 25 MHz transducer for the bellows tube. The resulting signals were obtained from the bellows tube by using the Mode 2 method.

References

1. K. M. Koo, S.B. Kim, I. C. Im, C. M. Sim, Y. M. Jeong and C. S. Park, "*Water Thickness Gaging in a Bellows Tube using the Special UT Shoes & an Immersion Ultrasonic System*", Key Engineering Materials Vols. 321-323, pp. 468-471, (Aug. 2006).
2. K. M. Koo, S.B. Kim, I. C. Im, C. M. Sim, Y. M. Jeong and C. S. Park, "*Using the Special UT Shoes & Immersion Inspection Method, Thickness measurement for residual Water in the Mock bellows Tube*", Abstract of Proceeding of the ANDE, pp. 214, (Nov. 2005).
3. K. M. Koo, S.B. Kim, I. C. Im, H. Y. Kang, K. O. Chang, and S. L. Lee, "*Using the Immersion Inspection Method, a System Development of Water Thickness Gaging in the bellows Tube*", Proceeding of the ASK, Vol. 24, No. 2(s), pp. 301-304, (Nov. 2005).
4. K. M. Koo, J. H. Kim, S.B. Kim, H. D. Kim, and D. Y. Ko, "*Ultrasonic Thermometry System for Measuring Very High Temperatures Using High Resolution Signal Processing*", Proceeding of the ICEIC 2000, pp. 229-232, (Aug. 2000).

A STUDY ON INHALATION FORCE IMPROVEMENTS OF VENTILATION HOOD TO REMOVE A HARMFUL MATERIAL

HO DONG YANG

Department of Precision Mechanical Engineering, Chosun University, 375 Seosuk-dong, Dong-gu, Gwangju 501-759, South Korea

YOOL KWON OH

Department of Mechatronics Engineering, Chosun University, 375 Seosuk-dong, Dong-gu, Gwangju 501-759, South Korea (corresponding author)

This study reports on the inhalation force improvements of hood attached a new device named "gas guidance device" in order to remove a harmful material. In this study, the numerical analysis is applied to analyze the flow velocity profile at the hood inlet and around the hood after the gas guidance device was installed. Also, the flow velocity on each position inside and around the hood was experimentally measured using the anemometer under the same condition as that of numerical analysis. And, the optimum shape of gas guidance device which is suitable for hood shape derived from the numerical and experimental result. The numerical and experimental results revealed that the effect of the optimum shaped gas guidance device (width (b) = 125 mm, X : Y = 4 : 6) confirmed that the capture velocity of the hood was higher for the hood with the gas guidance device and for the one without it. In the end, when the gas guidance device was installed inside the hood, the inhalation force was improved around the hood inlet in comparison to the hood without the gas guidance device.

1. Introduction

In general, there are basic means of protecting the workers from harmful factors such as substitution of raw materials, process change, airtight isolation and local exhaust [1]. The most convenient way to improve the working condition is to install the ventilation system. In the industrial fields, the ventilation systems are classified into general ventilation and local exhaust and depending on whether a fan is used or not, the general ventilation is classified into forced ventilation and natural ventilation [2]. When the work is characterized by high mobility or the entire work site is a source of pollution, general ventilation should be provided. On the other hand, local exhaust ventilates harmful substances directly from the pollution source. Therefore, it is possible to produce satisfactory results in improving the working conditions even with a small flow and thus it is most widely used as an engineering means of improvement [3]. In this study, among

various design factors of the hood, one of local exhaust ventilation systems, the mobility around and inside the hood is analyzed to improve the capture velocity of the hood, using the numerical analysis commercial code. The result of the numerical analysis is verified through the comparison with the result experimentally measured with the anemometer. Especially, by installing a new device named “gas guidance device” inside the hood, the hood that can improve the capture velocity at its tip is selected. Also, in order to identify the optimum shape of the gas guidance device, numerical analyses and experiments are performed under various conditions and their results are presented.

2. Numerical and Experimental Studies

2.1. *Numerical and Experimental Model*

As the model for the numerical analysis and experiment of this study, hoods that had been actually installed and used in the field of manufacturing were used. Figure 1 (a) shows the schematic of the gas guidance device installed inside the hood, where the shape of the gas guidance device is expressed with width (b), top length (X) and bottom length (Y). Figure 1 (b) shows 2-D analysis model in which 5 flow velocity measurement points are selected on the position 50mm away from the hood inlet in order to evaluate the effect of the gas guidance device on the hood performance and to derive the optimum hood shape.

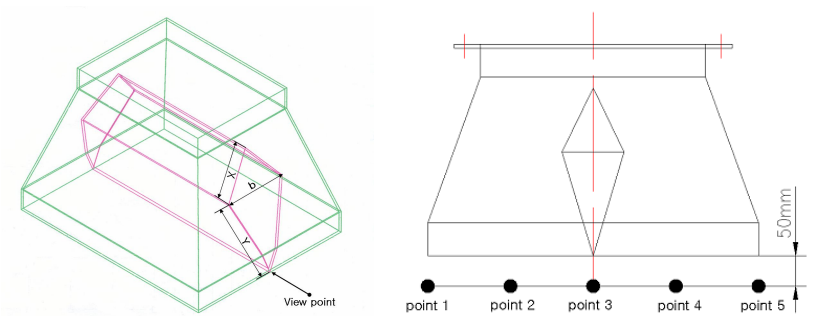

(a) 3-D hood attached gas guidance device (b) 2-D analysis model of 5 measurement points

Fig. 1. Schematic diagram of hood attached gas guidance device and test section.

2.2. *Numerical and Experimental Methods*

In this study, the thermal fluid commercial code “Phoenics 3.1” used for the numerical analysis. In order to evaluate the effect of the gas guidance device on the hood performance and to derive the optimum shape of the gas guidance

device, two experiment conditions were set for this study. First, to evaluate the effect of the gas guidance device on the hood performance, the hoods installed and being used in the field of manufacturing were selected as the analysis models. They were numerically analyzed and experimentally studied for those with the gas guidance device and those without the gas guidance device, respectively. The first experimental condition is shown in Table 1. Second, in order to derive the optimum shape of the gas guidance device according to the hood size, the flow rate and pipe diameter of the duct were set respectively to 12 m/sec and Ø 240 mm which were the rate and size actually used at the places of business. With changing the shape of the gas guidance device according to the hood size under the condition shown in Table 2, the hood performance was numerically analyzed and the optimum shape was determined based on the analysis result. The optimum shape determined in this way was actually installed to the hood and the flow rate on each point was measured using the hot-wire type airflow meter. Especially, in consideration of the fact that a variety of hood shapes are in use, lengths of the gas guidance device (X and Y) were set proportionally to its width (b), which are shown in Table 2.

Table 1. Experimental condition - 1

Gas Guidance Device (GGD)	Flow velocity of duct	Size of duct	Width (b)	Length (X)	Length (Y)
With GGD	6.85m/sec	Ø 400	-	-	-
Without GGD	6.85m/sec	Ø 400	400	250	350

Table 2. Experimental condition - 2

Unit: mm

Case	Case A (b = 125)		Case A (b = 125)		Case C (b = 175)	
Rate	X	Y	X	Y	X	Y
5 : 5	177	177	177	177	177	177
4.5 : 5.5	160	195	160	195	160	195
4 : 6	142	213	142	213	142	213
3.5 : 6.5	124	230	124	230	124	230
3 : 7	106	248	106	248	106	248

3. Results and Discussion

3.1. *Performance Evaluation for Gas Guidance Device*

In order to evaluate the effect of the gas guidance device installed inside the hood on the suction performance of the hood, the numerical analysis and the actual measurements were carried out under the conditions shown in Table 1. Figure 2 visually shows the flow velocity profiles generated at the inlet and

inside of the hood with the gas guidance device and of the one without it, which were obtained through the numerical analysis. As shown in Fig. 2, the flow velocity, which was low (expressed in white) at both ends of the hood when the gas guidance device was not installed, appeared to increase when the gas guidance device was installed.

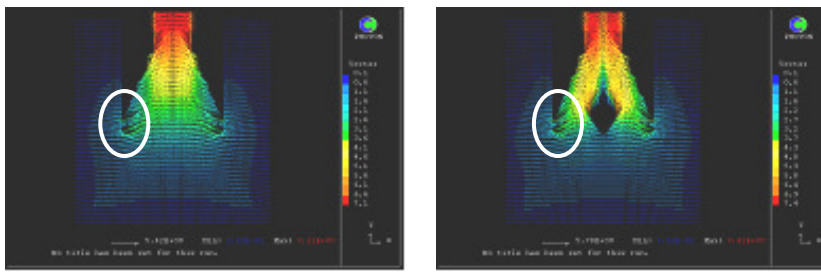

(a) Without the gas guidance device (b) With the gas guidance device

Fig. 2. Visualization of flow velocity inside the hood.

The result of calculation through numerical analyses for each position and that of experimental measurements are summarized in Table 3. Both the numerical analysis and the experimental measurement showed that the flow velocity increased when the gas guidance device was installed. In other words, when the gas guidance device was installed inside the hood, the inhalation force of the hood at its inlet and around it was improved, compared to when it was not installed.

Table 3. Numerical and Experimental results of flow velocity

Unit: m/sec

Result		Point 1	Point 2	Point 3	Point 4	Point 5
Without GGD	Num.	2.912	2.989	3.142	3.005	2.891
	Exp.	2.500	2.200	2.700	2.300	2.500
With GGD	Num.	3.618	3.515	3.401	3.527	3.609
	Exp.	3.000	2.900	2.800	3.100	3.000

3.2. *Selection of Optimum Shape for Gas Guidance Device*

Table 4 shows the results of the numerical analysis for each condition presented in Table 2 to derive the optimum shape of the gas guidance device. According to the results of the numerical analyses, when the flow velocity was measured for each X : Y ratio of the gas guidance devices whose widths were 125 mm, 150 mm and 175 mm respectively, the flow rate of the gas guidance device whose width was 125 mm was relatively higher than others at the X : Y ratio of 4 : 6.

For the gas guidance devices whose widths were 150 mm and 175 mm, the flow velocity appeared to be high when the X : Y ratio was 4 : 6, the same as the gas guidance device whose width was 125 mm.

Figure 3 visually shows the results of the flow simulation when the widths of the gas guidance devices were 125 mm, 150 mm and 175 mm and their X : Y ratios were 4 : 6. The result of the numerical analysis shows that the flow velocity was relatively high at the tips of both ends of the hood inlet and between the hood and the gas guidance device when the width was 150 mm or 175 mm.

Table 4. Numerical result of flow velocity by the measurement conditions

Unit: m/sec

Rate		Point 1	Point 2	Point 3	Point 4	Point 5
b = 125	5 : 5	1.208	1.379	1.208	1.380	1.207
	4.5 : 5.5	1.207	1.391	1.269	1.394	1.209
	4 : 6	1.213	1.396	1.275	1.399	1.212
	3.5 : 6.5	1.207	1.392	1.271	1.390	1.206
	3 : 7	1.205	1.406	1.321	1.403	1.204
b = 150	5 : 5	1.208	1.356	1.209	1.355	1.207
	4.5 : 5.5	1.207	1.368	1.235	1.368	1.208
	4 : 6	1.211	1.389	1.253	1.377	1.210
	3.5 : 6.5	1.207	1.384	1.260	1.383	1.207
	3 : 7	1.207	1.396	1.281	1.396	1.208
b = 175	5 : 5	1.209	1.330	1.173	1.299	1.208
	4.5 : 5.5	1.205	1.342	1.193	1.340	1.205
	4 : 6	1.213	1.363	1.216	1.361	1.211
	3.5 : 6.5	1.206	1.366	1.237	1.367	1.205
	3 : 7	1.206	1.338	1.255	1.336	1.214

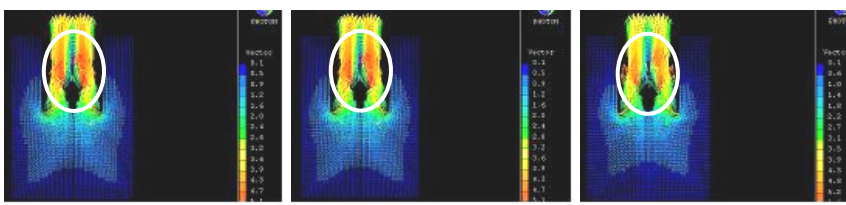

(a) b = 125 mm (b) b = 150 mm (c) b = 175 mm

Fig. 3. Visualization results of flow velocity in cases of width (b) and X : Y = 4 : 6.

However, taking into consideration that the vortex formed at the tip of the gas guidance device was larger for the gas guidance devices whose widths were 150 mm and 175 mm than for the one whose width was 125 mm, the gas guidance device whose width was 125 mm and X : Y ratio was 4 : 6 was selected as the optimum shape gas guidance device.

From this result, the numerical analysis results and the experimental measurement results for the hoods with and without the gas guidance device are

compared in Table 5. The comparison shown in Table 5 reveals that the capture velocity of the hood with the gas guidance device was relatively higher than that of the hood without gas guidance device, which means that when the gas guidance device was installed inside the hood, the inhalation force of the hood around its inlet was improved rather than when the gas guidance device was not installed.

Table 5. Numerical and experimental results of flow velocity, b = 125, X : Y = 4 : 6

Unit: m/sec

Result		Point 1	Point 2	Point 3	Point 4	Point 5
Without GGD	Num.	1.152	1.353	1.254	1.350	1.160
	Exp.	1.010	1.210	1.140	1.220	1.020
With GGD	Num.	1.213	1.396	1.275	1.399	1.212
	Exp.	1.130	1.290	1.170	1.270	1.120

4. Conclusion

1. As a result of the numerical analysis for deriving the optimum shape of the gas guidance device, it was shown that the inhalation force improvements of the hood measured at the hood inlet was improved when the width (b) of the gas guidance device was 125 mm, 150 mm or 175 mm and its X : Y ratio was 4 : 6.

2. However, when the width (b) of the gas guidance device was 150 mm or 175 mm, a larger vortex was formed at the inner side of the hood inlet than the one formed when the width (b) was 125 mm. Therefore, the gas guidance device whose width (b) was 125 mm and X : Y ratio was 4 : 6 was determined as the optimum shape.

3. The numerical analysis and the experimental measurement for evaluating the effect of the optimum shaped gas guidance device (width (b) = 125 mm, X : Y = 4 : 6) also confirmed that the capture velocity of the hood was higher for the hood with the gas guidance device and for the one without it.

4. In conclusion, when the gas guidance device was installed inside the hood, the inhalation performance was improved around the hood inlet in comparison to the hood without the gas guidance device.

References

1. T. I. Ohm and D. S. Jang, *J. of KIIS.* **10(1)**, 64 (1995).
2. H. J. Bae, W. H. Yang, J. O. Kim and B. S. Son, *J. of Sanitation.* **18(3)**, 27 (2005).
3. B. G, Chu, C. Kim, J. O. Choi and S. Y. Yoo, *J. of KIIS.* **15(1)**, 72 (2000).

ACOUSTIC NONLINEARITY OF ZIRONIUM ALLOY BY A RESONANT ULTRASOUND SPECTROSCOPY

YONG-MOO CHEONG AND YOUNG-SUK KIM

Nuclear Materials Research Center, Korea Atomic Energy Research Institute, Daeduk-daero 1045, Yusong-gu, Daejeon, 305-353, Korea

Zirconium alloys are used for many applications in nuclear components, such as the pressure tube material in a pressurized heavy water reactor, nuclear fuel cladding, etc. One of the problems during the operation of a nuclear reactor is a degradation of the zirconium alloys, which is believed to be a change of their microstructures due to a high dose of neutron irradiation and an increase of the hydrogen concentration. The resonant ultrasound spectroscopy (RUS) technique was originally developed for the determination of accurate dynamic elastic constants. More recently the deviation of the resonant frequency was correlated to the hydrogen concentration in a Zr-2.5Nb alloy. This paper investigates an acoustic nonlinearity of zirconium alloy by RUS technique, which can possibly be correlated to the microscopic degradation of an alloy. A shift of the resonant frequencies was observed by an excitation voltage and this fact was correlated to the nonlinear elastic behaviors of an alloy. The shift of the resonant frequencies was discussed on the basis of the nonlinearity parameter.

1. Introduction

Nonlinear acoustic material responses can be correlated to material damage or degradation. Recent nonlinear acoustics based methods offer a promising means for an NDE because of their sensitivity in comparison with linear methods (velocity, attenuation)[1].

Theoretically materials or defects must be mechanically soft to induce a nonlinear response. For instance, a crack will induce elastic nonlinear response, but a void will not. Thus these methods provide a means to distinguish between a crack and other damage in the presence of voids or other features that may be related to damage. The first applications of a nonlinear response for a material characterization employed measurements of the second harmonic generated by the nonlinear distortion of a sinusoidal acoustic wave propagating in a medium with damage.

Zirconium alloys are used for many applications in nuclear components, such as the pressure tube material in a pressurized heavy water reactor, nuclear fuel cladding, etc. One of the problems during the operation of a nuclear reactor is a degradation of the zirconium alloys, which is believed to be a change of their

microstructures due to a high dose of neutron irradiation and an increase of the hydrogen concentration. Therefore a non-destructive characterization of a material degradation is one of the important issues and needs to be addressed. The resonant ultrasound spectroscopy(RUS) technique was originally developed for the determination of accurate dynamic elastic constants. The dynamic elastic constants of Zr-2.5Nb alloy have been measured with a temperature range of 25°C~500°C[2-3].

In this paper, we first report on the results of an acoustic nonlinearity of a zirconium material by the RUS technique, which can possibly be correlated to the microscopic degradation of an alloy. A shift of the resonant frequencies was observed by an excitation voltage and this fact was correlated to the nonlinear elastic behaviors of an alloy. The shift of the resonant frequencies was discussed on the basis of the nonlinearity parameter.

2. Measurement of nonlinear parameter by RUS

RUS method was developed for a determination of an elastic constant of a material. Typical RUS can measure 30 ~ 50 resonance frequencies in a specimen based on various vibration modes and orders. The excitation voltage to a piezoelectric transducer can be controlled and the voltage can be correlated to the peak strain in a resonance system.

Nonlinear Resonant ultrasound spectroscopy(NRUS) is based on the measurement of a resonant frequency shift and a material damping as a function of the resonant peak amplitude for one or several resonance peaks[4]. This method is an extension of a linear resonant ultrasound spectroscopy that is widely used in industrial NDE[5]. In this type of measurement, the change of the resonant frequency of a mode with a driving voltage is a measure of an acoustic velocity and a change of the elastic modulus. In other words, the acoustic velocity in a simple long bar driven at the fundamental mode can be expressed as:

$$v = f_r \lambda = 2 f_r L = \sqrt{K / \rho} \tag{1}$$

where f_r is the resonance frequency of the fundamental mode, λ is the wavelength, L is the bar length, K is the modulus and ρ is the density. The equation becomes more complicated for sample geometries.

In addition to classical Lanau and Lifschitz theory[6] nonlinear responses may be physically explained at different scales by dislocations, rupture, recovery, porosity, opening/closing of micro-cracks, etc. As a result, these materials exhibit hysteresis in their pressure-strain response, the phenomenon of slow

dynamics. A nonlinear and hysteretic modulus in the stress-strain relationship in one dimension can be written as[1]

$$M(\varepsilon,\dot{\varepsilon}) = M_0(1-\beta\varepsilon-\delta\varepsilon^2-\cdots-\alpha(\Delta\varepsilon+sign(\dot{\varepsilon})\varepsilon)), \quad (2)$$

where M_0 is the linear modulus, ε is the strain, $\dot{\varepsilon}$ the strain rate, β and δ the second and third order nonlinearities, α being the nonlinearity hysteretic parameter, $\Delta\varepsilon$ the average strain amplitude, and the sign function equals +1 if the strain rate is positive and -1 if negative.

This model predicts a softening or hardening of a material with an increasing driving amplitude depending on the sign of β, δ and α. If the net effect is negative, the resonant frequency decreases as a function of the wave amplitude. At large strain amplitude levels in these materials, much empirical evidence suggests that the nonlinear hysteretic behavior proportional to α dominates [7], and the first order approximation gives

$$\frac{f_0-f}{f} \approx \alpha\Delta\varepsilon, \quad (2)$$

where f_0 is the linear resonant frequency and f the resonant frequency for an increasing driving amplitude. The evaluation of this linear (slope α) relative frequency shift dependency with a strain amplitude is the basis of NRUS.

3. Experimental consideration

Nuclear grade Zr-2.5Nb pressure tube materials are used as specimens. In order to determine the effect of the hydrogen concentration, the Zr-2.5Nb specimens were charged with hydrogen by an electrolytic method in accordance with our procedures for a characterization of the Zr-2.5Nb pressure tube[8]**.** Vacuum annealing was conducted to homogenize the hydrogen within the specimens at temperatures above terminal solid solubility for dissolution(TSSD)[9]. Hydrogen concentration in the specimen was determined by a chemical analysis.

Rectangular parallelepiped specimen was machined accurately, with dimensions of 2.5 mm X 3.0 mm X 3.5 mm. The initial 30 resonance frequencies are located in the range of 200-600 kHz. Among those resonance peaks, we selected two resonance modes, the (4, 3) shear vibration mode and the (5, 2) volumetric dilatation mode. Detail investigation of these two resonance modes were carried out by increasing the driving voltage by 0.1 volt to a maximum of 1.0 volt.

Considering the piezoelectric constant of an exciting transducer, PZT-5A as $374\times10^{-12}m/V$ and an elastic modulus, $E_{PZT-5A}=8.2\times10^{10}N/m^2=82Gpa$, a surface displacement can be estimated as $(374\times10^{-12}m/V)\times(1V)=0.374nm$ for

the case of a RUS driving voltage of 1 Volt [5]. Assuming the Q factor of the transducer as 5000, the peak displacement of the transducer can be calculated as $(3.74\times10^{-12}m/V)\times Q^{1/2}\cong 26.4nm$, and converted to a peak strain of the transducer as $\varepsilon\cong10^{-5}$. Therefore the peak stress to the transducer is $\sigma=(8.2\times10^{10}N/m^2)(10^{-5})=0.82MPa$. When we assume the contact area at the specimen corner as $10^{-10}m^2$, the force at the specimen corner is $F=(0.82\times10^{6}N/m^2)(10^{-10}m^2)=8.2\times10^{-5}N$. Stress at the specimen corner can be calculated as 0.82 MPa and the strain as 8.2×10^{-6} .

4. Results and discussion

Fig. 1 shows the resonance peak of the (4, 3) shear mode of the Zr-2.5 Nb RUS specimen. As the driving voltage increases from 0.1 Volt to 1.0 Volt, the resonance frequency decreases. This fact can be a potential parameter to characterize a microscopic variation of a zirconium material. The frequency shift can be a function of the driving voltage or the square of the peak strain, as shown

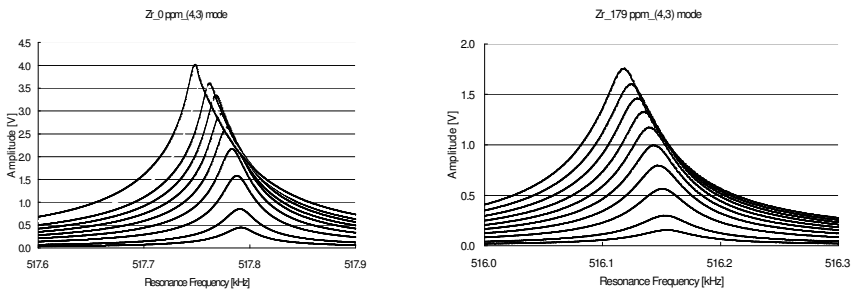

(a) No hydrogen (b) [H] = 179 ppm

Fig. 1. Resonance response of the (4,3) shear mode in the Zr-2.5Nb materials.

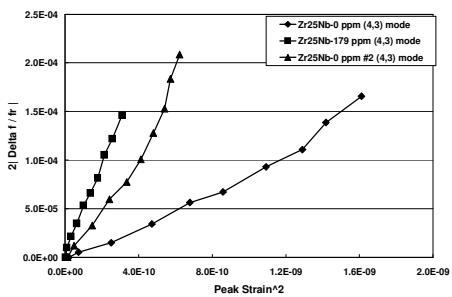

Fig. 2. Nonlinearity of Zr-2.5Nb material as a function of hydrogen concentration, (4,3) shear mode.

in Fig. 2. We can distinguish a difference of the slope of Δf between the specimen with no hydrogen and hydrogen concentration of 177 ppm.
Fig. 3 shows similar resonance peaks, but with the (5, 2) volumetric dilatation mode. The amount of frequency shifts are plotted with the square of the peak strain, as shown in Fig. 4. This dilatation mode is better to distinguish a difference between the specimen with no hydrogen and the one with hydrogen concentration of 177 ppm. The Zr-2.5Nb specimen with no hydrogen shows higher slope compared to the specimen with hydrogen of 177 ppm.

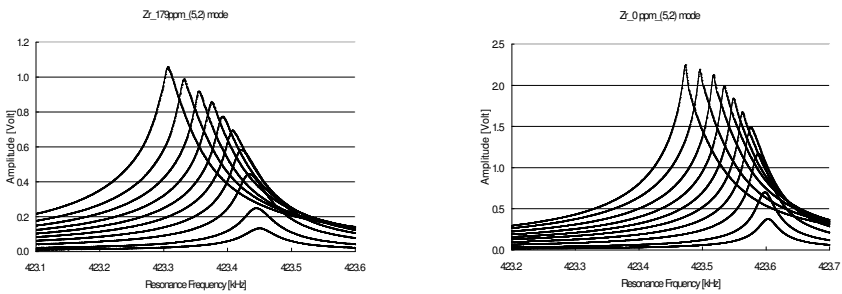

(a) No hydrogen (b) [H] = 179 ppm

Fig. 3. Resonance response of a (5,2) volumetric dilatation mode in a Zr-2.5Nb materials.

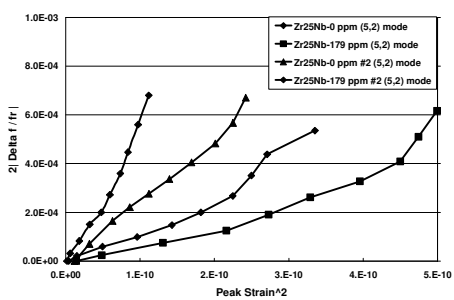

Fig. 4. Nonlinearity of Zr-2.5Nb material as a function of hydrogen concentration, (5,2) volumetric dilatation vibration mode.

The NRUS results are similar to other results from a damaged steel[4]. The slope of the shift of the resonance frequency can be related to α, the nonlinear hysteretic parameter. It is not clear why the high hydrogen concentration shows a lower slope of Δf. The phenomenon of the frequency change can be correlated to the change of elastic constants. It means that the elastic constant is changed, as the force to the specimen increases. If the specimen has a higher hydrogen concentration, the elastic constant would increase. Our observation reveals a lower slope of Δf for a specimen with a hydrogen concentration of 179 ppm. It

is not clear why this lower slope is observed in the hydrided zirconium alloy. More comprehensive experimental data is required for a clearer explanation.

5. Conclusion

Acoustic nonlinearity of a zirconium alloy has been investigated with the RUS method. A shift of the resonance frequencies depending on the driving voltage was observed. The slope of Δf can be distinguished between the specimen with hydrogen and the one with no hydrogen. It is not clear why a lower slope is observed in the hydrided zirconium alloy. More comprehensive experimental data is required for a clearer explanation.

Acknowledgments

This work was supported by the research project on the Development of Advance Diagnostic Techniques for Micro-materials Degradation and Damage as a part of Long-Term Nuclear R&D Program supported by the Ministry of Science and Technology, Korea.

References

1. C. Payan, V. Garnier, J. Moysan and P. A. Johnson, J. Acoust. Soc. Am. 121 (4) (2007).
2. Y. M. Cheong, S. S. Kim and Y. S. Kim, *J. Nucl. Mater*., 303, 83 (2002).
3. Y. M. Cheong, S. C. Kwon and H. K. Jung, *J. Mater. Sci.,* 35, 1195 (2000).
4. P. A. Johnson and A. Sutin, *Rev. Quan. Nondestructive Evaluation* **24**, 377 (2005).
5. A. M. Migliori and J. Sarrao, *Resonant Ultrasound Spectroscopy*, John Wiley (1997).
6. L. D. Landau and E. M. Lifshitz, *Theory of Elasticity*, Pergamon Press, New York (1959).
7. K. Van Den Abeele, J. Carmeliet, J. TenCate and P. A. Johnson, *Res. Nondestruct. Eval.* 12, 31 (2000).
8. Y. S. Kim and et al., *KAERI/TR-1329/99*, Korea Atomic Energy Research Institute (1999).
9. Y. M. Cheong and et al., *J. Korean Nucl. Soc.*, 33 192 (2001).

EXPERIMENTAL STUDY ON NONLINEAR ACOUSTIC PROPERTIES OF CONTACTING SOLID INTERFACES

JIN-YEON KIM

Woodruff School of Mechanical Engineering, Georgia Institute of Technology
Atlanta, Georgia 30322-0355, USA

ARTURO BALTAZAR

Robotics and Advanced Manufacturing Program
CINVESTAV-Saltillo, Ramos Arizpe, Coah, 25900, México

JUN-SHIN LEE

Nuclear Power Research Laboratory, Korea Electric Power Company
Daejeon 305-380, Korea

Experimental study on hysteretic nonlinear acoustic properties of a contacting interface between two aluminum blocks is presented. Two findings are: first, the acoustic nonlinearity of an elastoplastic interface is weaker during unloading phase as opposed to other existing results; second, in the certain range of contact pressure during unloading, the elastoplastic model fails to predict the nonlinear acoustic behavior of the interface, possibly due to the adhesive force that comes into play at this level of load.

1. Introduction

The inspection of components that contain fatigue cracks and imperfect interfaces is an important issue in the nondestructive evaluation (NDE) of materials. Recent incidents at nuclear power plants in the US and other countries, in which severe corrosion fatigue cracks were found in the reactor and the steel domes that were nearly breached, raise questions about aging nuclear plants, whether they are being inspected closely enough and the current inspection techniques are well suited to detect these environmental fatigue cracks. One of the technical issues involved in the inspection of environmental cracks and imperfect bonds is the random nature of their interfaces, which can substantially reduce the sensitivity of the ultrasonic signals and thus the reliability of a conducted ultrasonic inspection. Therefore, it is of fundamental importance to understand interactions of probing ultrasonic waves with the imperfect interfaces. Currently, there is a need for a combined experimental and

theoretical study to answer unresolved physical issues in this area of research. The objective of this paper is to conduct measurements of the harmonic generation from a contacting interface and to compare the experimental results with those from the recent theory [1].

2. Experiment

Ultrasonic measurements were performed on an interface formed between two Al 6061-T6 blocks pressed together in a load frame as shown in Fig. 1. Contacting surfaces were polished with a #1000 sand paper to remove any machining texture and rms roughness of both surfaces (σ_1=σ_2) were measured to be about 0.8 μm. Maximum load on the apparent nominal contact area of 5.0 cm^2 was about 50 kN, producing a compressive stress of 100 MPa. A narrow band ultrasonic transducer (lithium-niobate single crystal, 1/2 inch in diameter) with a 5 MHz center frequency and a broad band transducer (Panametrics V111, 1/2 inch in diameter) with a 10 MHz center frequency were used as a transmitter and a receiver, respectively. A digital high pass filter (HPF) was incorporated to remove low frequencies from the received signals.

During loading and unloading, ultrasonic linear reflection and nonlinear transmission measurements were performed with a load step between 5-10 MPa (a precise control of the load was not possible). At every loading step, reflected 5 MHz and 10 MHz tone burst signals (50 cycles) were measured independently from both sides and recorded; then, transmitted 5 MHz tone burst signals were measured. To maintain sufficient signal-to-noise ratio in the transmitted signals, amplifier gain was adjusted in the range of 20-40 dB above the level of the linear reflection measurements. A typical diffraction correction was made.

A calibration of the receiving transducer [2] was performed to compensate different frequency responses of the receiver at 5 and 10 MHz. This is needed to compare measured results for the nonlinear transmission to theoretical ones. In most of the existing works, however, the non-flat frequency response of receiving transducers was not calibrated. Moreover, piezo-ceramic (e.g. PZT) transducers that are inherently nonlinear were often used as transmitters. An application of high voltage inputs is needed especially when the amplitude of transmitted signals is low (at low pressures). Unwanted nonlinearity produced by the piezo-ceramic transducers will be added to the nonlinearity of the interface that is intended to solely be measured. Therefore, a comparison of measured nonlinearity parameters with theoretical ones can be meaningless if these are not properly taken care of. We used the single crystal transducer ($LiNbO_3$) to avoid this problem.

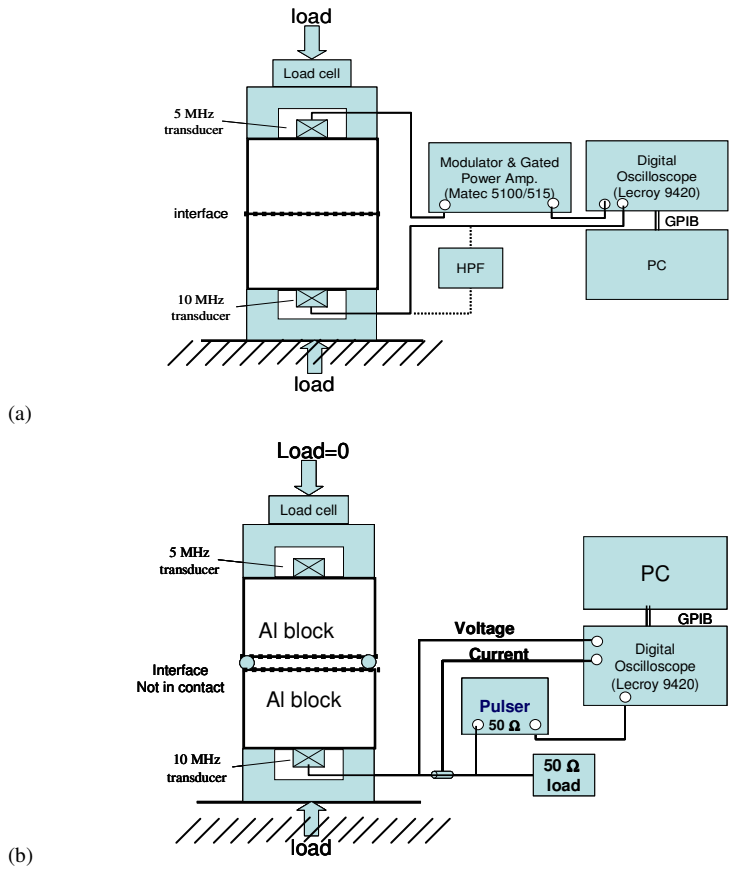

Fig. 1. A diagram of the measurement setups. (a) Setup for linear reflection and nonlinear transmission; (b) setup for calibration of receiving transducer.

3. Results and discussion

In Fig. 2, measured and theoretical reflection coefficients are shown. Note that this is not a comparison of independent theoretical results to experimental ones. First, three interface parameters (σ=1.2 μm; ξ=15.6 μm; α=0.62) are obtained by fitting the measured reflection coefficients (at 5 and 10 MHz) with the present theoretical model. Unlike the previous work [3,4], the fitting parameters are obtained with reflection coefficients rather than the interfacial stiffness since they are related by a simple algebraic expression. From the reconstructed surface parameters, linear and nonlinear interfacial stiffnesses (K_1 and K_2), which are

used to produce theoretical curves, are calculated using the model developed [1,3,4] as a function of the pressure applied.

The elastoplastic hysteresis is seen clearly in the reflection coefficients. Acoustic waves respond sensitively to the deformation state of the interface. Due to the increased area of contact, the transmission coefficient during unloading is higher than that during loading. The imperfectness of the interface is naturally more impedimental to the waves at higher frequencies, the result of which appears as higher reflection and lower transmission at 10 MHz than those at 5 MHz. It is also observed that this measurement is more stable at 5 MHz than 10 MHz. A systematic error that appears at pressures above 50 MPa is thought to be due to a slight loss of a perfect parallelism at higher loads. Experimental and theoretical linear acoustic interfacial stiffness K_1 of this interface are shown in Fig. 3. The systematic error in the reflection coefficients appears amplified in this figure. Nonetheless, the fitting seems to be still reasonable. The interfacial stiffness exhibits the usual hysteresis - stiffness during unloading is higher than when loading due to blunting of asperities.

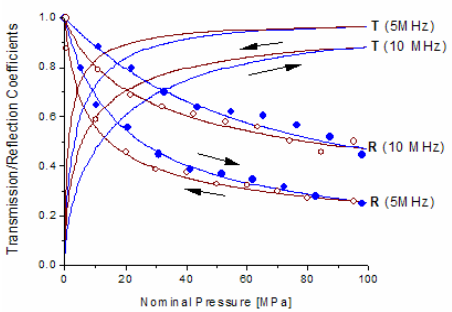

Fig. 2. Measured reflection coefficients of the interface at 5 MHz and 10 MHz. Theoretical reflection coefficient curves are obtained using the fit parameters of the interface: σ=1.2 μm; ξ=15.6 μm; α=0.62.

In Fig. 4, measured acoustic nonlinearity of the interface in A_2/A_1 is shown together with the theoretically predicted result. The nonlinearity is higher at low pressures as in other published results, and drops significantly at a pressure near zero. The strong nonlinearity due to clapping motions was not observed at the level of acoustic amplitudes that we applied. The theoretical nonlinearity increases indefinitely as the contact pressure decreases because the model assumes that two surfaces are always in contact even at an infinitesimally small contact pressure. At small contact pressure, the interface will be very flexible leading to high amplitude (thus more nonlinear) of oscillation of interfacial opening displacement. In reality, two surfaces can separate and be in clapping motions at an acoustic pressure higher than the static contact pressure, which is

another mode of nonlinear hysteretic motion [5]. The nonlinearity due to the clapping motion has been observed to be a maximum also at a low pressure. The nonlinearity is observed to not be continuous at the maximum load when unloading starts commonly in our theoretical and experimental results. It is interesting to note that the acoustic nonlinearity is lower during unloading than during loading. This is because two rough surfaces during unloading are better matched or more tightly locked to each other than during loading due to further plastic deformation (for example, from 80 MPa to 10 MPa, if the nonliearities at 80 MPa are compared). However, this increases significantly when the pressure decreases to near zero. This is in general the result of the fact that the interface is smoother now due to plastic deformation during loading period and the smoother interface is more nonlinear at small contact pressures. It is noted that these trends are similar to those in the work of Barnard et al. [6] but these are quite different from many experimental results reported so far. In the present experimental results, nonlinearity measured during unloading in the load range 50-20 MPa deviates from theoretical ones. The reason behind needs to be further investigated, but it may be partly due to the adhesive force [7] between two surfaces which is known to be more influential in the unloading process. In this range of load, a number of asperities located deep in the surface profile are unloaded but still are stuck together due to the adhesive force, producing higher interfacial stiffness than that predicted elastoplastically. On the contrary, in the range of load 100-50 MPa, two surfaces are tightly locked and thus the elastoplastic contact force is dominant. These clearly need further studies by incorporating the effects of the adhesive force into the present model.

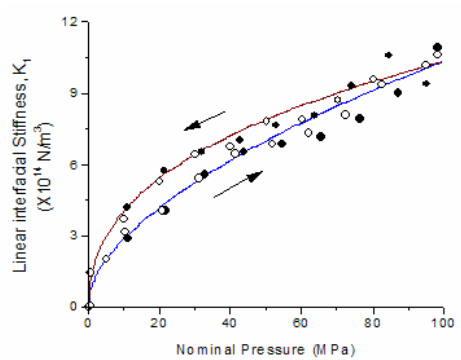

Fig. 3. Measured linear interfacial stiffness K_1 and the theoretical one calculated using the parameters obtained from reflection coefficients in Fig. 2. Open circles: 5MHz; Closed circles: 10 MHz.

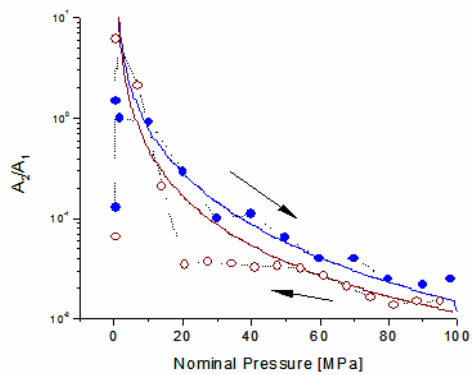

Fig. 4. Nonlinearity of interface in A_2/A_1 measured and predicted during loading and unloading.

4. Conclusion

Comparisons with ultrasonic experimental results show that our earlier model captures the essential features of physical behaviors of the interface during loading and unloading cycles. Improved conformity caused by the elastoplastic blunting of asperities affects the nonlinearity during unloading period differently depending on the level of applied pressure: the nonlinearity is lower for most of unloading period, while it is significantly high at very low pressures. An intermediate range of load (during unloading) in which the theoretical model does not seem to fully predict experimental results is observed. The effect of adhesion, which may be responsible for this, needs to be investigated. Important aspects in the nonlinear acoustic measurement are pointed out, which have not been taken into account in most of the existing experimental work. The present model can be useful for modeling nonlinear and hysteretic behaviors of imperfect interfaces and cracks and their ultrasonic nondestructive evaluation based on measuring these phenomena.

References

1. J.-Y. Kim and J.-S. Lee, J. Appl. Phys. **101**, 043501 (2007).
2. G. E. Dace, R. B. Thompson, and O. Buck, Review of Progress in Quantitative Nondestructive Evaluation, edited by D. O. Thompson and D. E. Chimenti (Plenum, New York) Vol. **11**, 2069-2076 (1992).
3. J.-Y. Kim, A. Baltazar, J.-W. Hu, S.I. Rokhlin, Int. J. Solids Struct. **43**, 6436 (2006).
4. J.-Y. Kim, A. Baltazar, and S. Rokhlin, J. Mech. Phys. Solids **52**, 1911 (2004).
5. I. Y. Solodov, A. F. Asainov, and K. S. Len, Ultrasonics **36**, 91 (1993).
6. D. Barnard, G. Dace, D. Rhbein, O. Buck, J. NDE. 16, 77 (1997).
7. V. Aleshin and K. Van Den Abeele, J. Mech. Phys. Solids **53**, 795 (2005).

A STUDY ON THE ANALYSIS OF O-RING UNDER UNIFORM SQUEEZE RATE AND INTERNAL PRESSURE BY PHOTOELASTIC EXPERIMENTAL HYBRID METHOD

O-SUNG KWON, JAISUG HAWONG, JEONGBWAN NAM, SONGLING HAN

School of Mechanical Engineering, Yeungnam University
Gyeongsan, Republic of Korea

SUNGHAN PARK

Research 4 Team, Agency for Defense Development
Daejeon, Republic of Korea

There are three kinds of loading conditions applied to O-ring, the first loading conditions are case which the uniform squeeze rates are applied to the upper portion and the lower portion of O-ring. The second loading conditions are case which uniform squeeze rates are applied to the upper portion and the lower portion of O-ring and another squeeze rates are applied to the front portion of O-ring. The third loading conditions are case which the uniform squeeze rates are applied to the upper portion and the lower portion of O-ring, another squeeze rates are applied to the front portion of O-ring and internal pressures are applied to another front portion of O-ring. In this research, The new photoelastic experimental hybrid method is developed. It's validity is certified. The stress of O-ring under the third loading conditions is analyzed by the new photoelastic experimental hybrid method developed in this research. The internal pressures applied to the O-ring are 0.98MPa, 1.96MPa, 2.94MPa and 3.92MPa.

1. Introduction

Rubber O-ring has been used as packing element for high pressure vessels, oil-pressure parts, air-plane parts and nuclear generator parts etc.. Stress distributions of O-ring under the third loading conditions are very complicated. Therefore stress distributions of O-ring under the third loading conditions have not been studied until now. Stresses of O-ring are analyed by many researchers[1,2,3], stresses of O-ring under the first loading condition or the second loading condition are studied by authors[4]. Stresses of O-ring under the third loading condition have not been studied untill now. The main purpose of this research is to develop the new photoelastic experimental hybrid method to apply the stress analysis of O-ring under the third loading conditions.

2. Basic Theory and Experiment

Eq. (1) is stress components using Muskhelishvili complex function and Airy stress function.

$$\sigma_x = Re\left[2\phi'(z) - \bar{z}\phi''(z) - \Psi'(z)\right] \qquad (1)$$
$$\sigma_y = Re\left[2\phi'(z) + \bar{z}\phi''(z) + \Psi'(z)\right] \quad \tau_{xy} = Im\left[\bar{z}\phi''(z) + \Psi'(z)\right]$$

Loading conditions to study in this research, that is, restrain conditions for the contact between O-ring and cylinder condition is the same as shown in Figure 1.

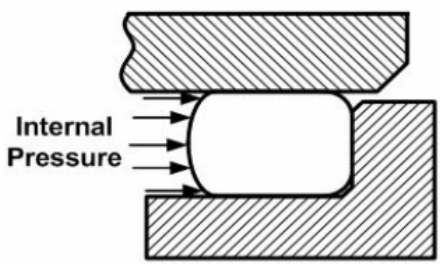

Fig. 1. Restrain conditions for the contact between O-ring and cylinder.

Loading condition of Figure 1. is contact problem. In general, contact problem is half-plane problem. Therefore eqt(2) is established in contact problems[6].

As stress functions ϕ (z) and Ψ (z) are analytic function, ϕ (z) and Ψ (z) can be expressed by power series as Eq.(4).

$$\Psi(z) = -\phi(z) - \overline{\phi(\bar{z})} - z\phi'(z) \qquad (2)$$

$$\phi(z) = \sum_{n=0}^{N} C_n z^{\frac{n}{2}}, \qquad \Psi(z) = \sum_{n=0}^{N} D_n z^{\frac{n}{2}} \qquad (3)$$

Using the relative equation between the coefficients of two stress function $\phi(z)$ and $\psi(z)$, stress components represented by only one coefficient of complex variable are obtained. Substituting the obtained stress components for stress optic law and substituting the experimental data for stress optic law.

And then applying the procedures of the conventional photoelastic experimental hybrid method[4] to the stress optic law with experimental data and stress components obtained in above. Stress components are obtained. These procedures are called the new photoelastic experimental hybrid method.

To study the contact stress of O-ring using photoelastic experiment, specimen of O-ring should be made of polymer, which has photoelastic properties.

In this research, epoxy resin is used as model material. Cross-sectional diameter of O-ring is *6.98±0.15mm*, internal diameter of O-ring is *121.5±0.94mm*. Specimen O-ring used in this research is made from the specimen molding processes developed in this research[4]. Loading device used in this research is loading device designed by authors[4].

3. Experimental Results and Discussions

When the internal pressures 0.98 MPa, 1.96 MPa, 2.94 MPa and 3.92 MPa are respectively applied to O-ring with uniform squeeze rate 20%. Isochromatic fringe patterns of the O-ring under 20% squeeze rate and with internal pressure are almost uniform with arbitrary position. Therefore the isochromatic fringe patterns of arbitrary position of O-ring are shown in Figure 2.

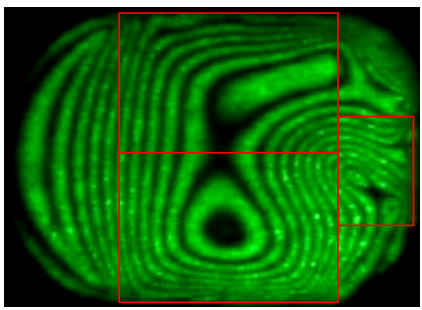

P_i=2.94MPa

Fig. 2. Isochromatic fringe pattern of slices of the stress frozen O-ring under 20% squeeze rate and with internal pressure.

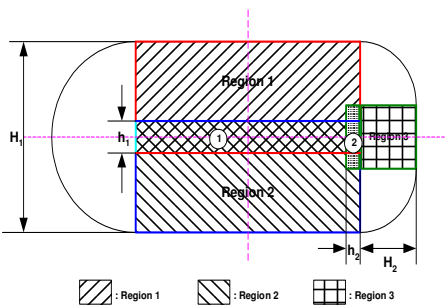

Fig. 3. Regions which photoelastic isochromatic data are measured.

Isochromatic fringe patterns of O-ring uniform squeeze rate 20% are changed according to the variations of internal pressures. Specially isochromatic fringe patterns in the right side of O-ring is completely different according to the variations of internal pressure. Figure 3 shows the regions which photoelastic isochromatic data are measured. Experimental data measured on upper contact region 1(= Retion 1), on the lower contact region 2(= Region 2) and on the front contact region 3(= Region 3) in Figure 3 are respectively used on the obtainment of stress components of three regions

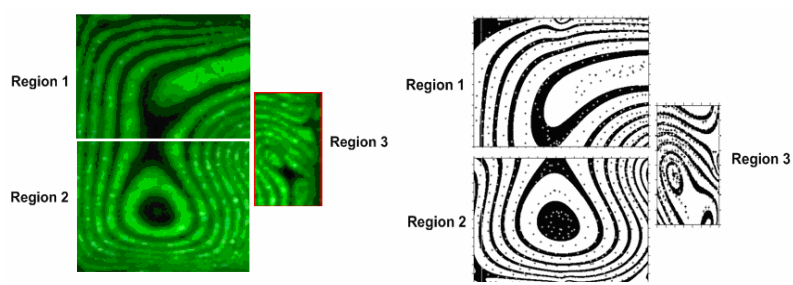

(a) Actual isochromatics (b) Plotted isochromatics

Fig. 4. Actual photoelastic fringe patterns and plotted photoelastic fringe patterns from the photoelastic experimental hybrid method (squeeze rate: 20%, pressure: 2.94MPa)

Figure(a) and Figure(b) in Figure 4. are respectively actual isochromatics in Region 1, Region 2 and Region 3 and plotted isochromatics in Region 1, Region 2 and Region 3 from new photoelastic experimental hybrid method when squeeze rate of O-ring is 20% and internal pressure applied to O-ring is 2.94Mpa. "+" symbols in Figure. 8 indicates the measured positions. All experimental data are measured on the centerline of each black band and each white band. As shown in Figure 8, actual isochromatic fringe pattern is almost identical to plotted isochromatic fringe pattern. All "+" symbols are located on the centerline of black band and white band. These results mean that the new experimental hybrid method developed in this research is effective.

In this research contact stress σ_x, σ_y and τ_{xy} and internal stress σ_x, σ_y and τ_{xy} in the upper contact region, in the lower contact region and in the front contact region of O-ring uniform squeeze rate 20% are analyzed with the internal pressure.

Figure 5. shows contact stress distributions σ_y of upper side of O-ring under 20% squeeze rate with contact length and with internal pressures.

Distributions of σ_y are almost symmetric about the center of contact line. Position of maximum σ_y are moved to the left side from the center of contact line, that is, to the applying derection of internal pressure is greater than 1.96MPa.

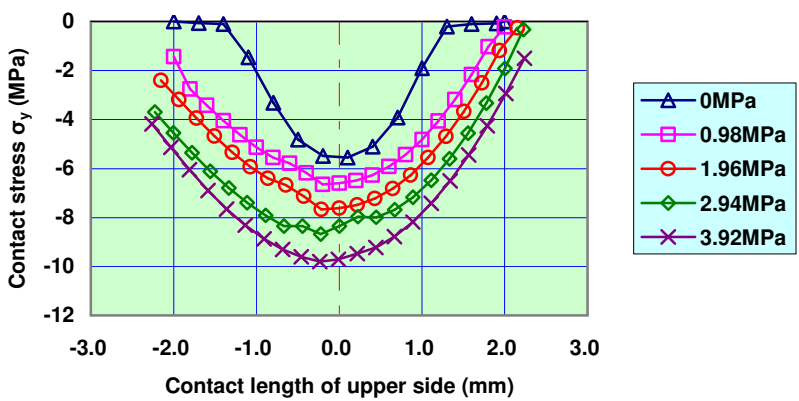

Fig. 5. Contact stress distributions σ_y's of upper side of O-ring under 20% squeeze rate with contact lengths and with internal pressures.

Positions which maximum σ_y's are occurred are the center of contact line when internal pressure is less than 1.96MPa. Stress distributions and maximum

positions of lower side of O-ring with internal pressures are very similar to those of upper side of O-ring with internal pressures. Contact stress distribution patterns of σ_y are almost uniform with contact length. But the positions, which the maximums of contact stress σ_y are occurred, are little by little moved to the side of internal cylinder corner with the increment of pressure.

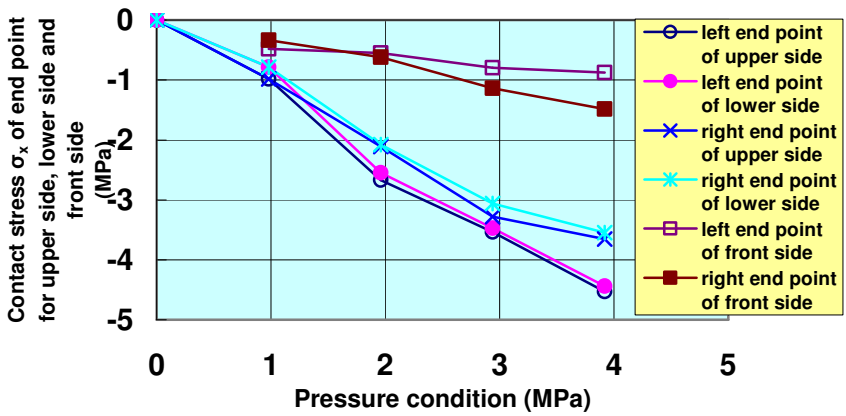

Fig. 6. Relationship between internal pressure and contact stress σ_x of end point for upper side, lower side and front side of O-ring under uniform squeeze rate

Figure 6. shows relationship between internal pressure and contact stress σ_x of end point for upper side, lower side and font side of O-ring under uniform squeeze rate.

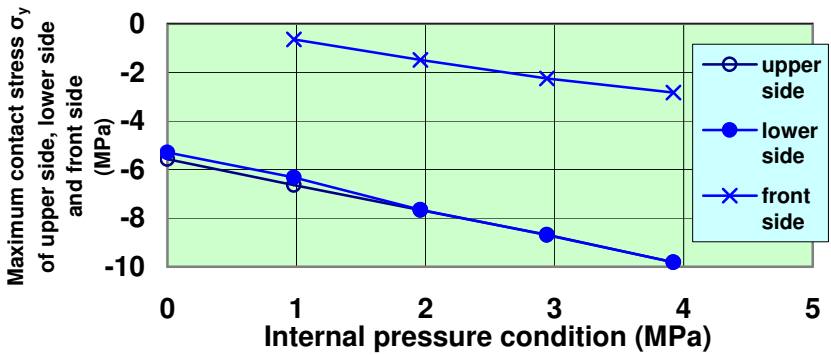

Fig. 7. Relationship between internal pressure and maximum contact stress σ_y for upper side, lower side and front side of O-ring under 20%squeeze rate.

Magnitudes and distributions in the contact stress σ_y of end point for upper side, lower side and front side are very similar to those in the contact stress σ_x of end point of upper side, lower side and front side.

Figure 7. shows the relationship between internal pressure and maximum contact stress σ_y in upper side lower side and front side of O-ring under 20% squeeze rate.

Maximum contact stress σ_y 's of upper side are very similar to those of lower side. Maximum contact stress σ_y 's of front side are much less than those of lower side. Maximums contact stress σ_x 's of upper side, of lower side and of front side are respectively very similar to maximums of contact stress σ_y of upper side, of lower side and of front side.

4. Conclusions

The following conclusions are obtained through the experimental results and discussions when uniform squeeze rate of O-ring is 20% and internal pressures applied to O-ring are respectively 0.98MPa, 1.96MPa, 2.94MPa, 3.92MPa.

1. Photoelastic experimental hybrid method for contact problem without external traction free boundary condition or internal traction free boundary condition is developed. It's validity is certified.
2. Contact stresses and internal stresses of O-ring under uniform squeeze rate (about 20%) and internal pressure are analyed by the photoelastic experimental hybrid method for contact problem.
3. Absolute value maximums of σ_x on the upper side or on the lower side are between 6MPa and 9MPa when internal pressures are varied between 0 MPa and 4 MPa. Absolute value maximums of σ_y on the upper side or on the lower side are between 6 MPa and 10 MPa when internal pressures are varied between 0 MPa and 4 MPa. Absolute value maximums of τ_{xy} are between 1.25 MPa and 2.4 MPa when internal pressure are changed between 0 MPa and 4 MPa.

References

1. A.F George, A. Strozzi, and J. I. Rich, *Tribol. Int. Wear* **237-247**, 1987.
2. E. Dragoni and A. Strozzi, *Elsevier Sequoia. Wear* **130**, . **41-51** 1989.
3. A. Karaszkiewicz*, Ind. Eng. Chem. Res. 29* **,** *Wear* **2134-2137**, 1990.
4. Jeonghwan Nam1, Jaisug Hawong1, Osung Kwon2, Songling Han2, Gun Kwon2, *ATEM'07 Lett. Wear* **OS16-2-4**, 2007.
5. Muskhelishvili, *N.I. Groningen*, Netherlands, 1963.
6. D. A. Hills, D.Nowell and A. Sackfield, 1993.

QUANTITATIVE MAGNETIC IMAGING USING MAGNETO-OPTICAL METHOD

TAKAYUKI ISHIBASHI

Department of Materials Science and Technology, Nagaoka University of Technology, 1603-1 Kamitomiokamachi, Nagaoka, Niigata 940-2188, Japan
t_bashi@mst.nagaokaut.ac.jp

KATSUAKI SATO

Graduate School of Engineering, Tokyo University of Agriculture and Technology, 2-24-16 Nakacho, Koganei, Tokyo 184-8588, Japan
satokats@cc.tuat.ac.jp

A magneto-optical (MO) microscope that uses the polarization modulation method was developed for quantitative MO imaging. In addition, Bi substitute yttrium iron garnet films prepared by a metal organic decomposition method were combined with the MO microscope to visualize magnetic flux strayed from a sample. Quantitative images of magnetic flux strayed from patterned superconducting thin films were measured, and images of current distribution were also deduced from the MO image.

Keywords: Magneto-optical microscope; magneto-optical effect; garnet.

1. Introduction

Magnetic imaging technique utilizing magneto-optical (MO) effect has been attracting attentions because it has several advantages compared with recently developed magnetic microscopes such as a magnetic force microscope, a SQUID microscope etc. In this technique, magnetic signal is transferred into an MO indicator film and is read out as MO signal measured by means of an optical method. Therefore, it allows us a faster measurement and to build a low temperature system easily. This is a reason why MO imaging has widely been used for research of superconductors.[1,2] However, a conventional MO imaging technique has drawbacks such as difficulty in quantitative evaluation of the MO signal. In order to achieve the quantitative evaluation in the magnetic imaging, we developed an MO microscope utilizing a polarization modulation method.[3] Quantitative MO values, Faraday rotation and Faraday ellipticity, are obtained from three kinds of optical images taken with linearly-polarized (LP) light, right circularly-polarized (RCP) light and left circularly-polarized (LPC) light

produced by a hand made liquid crystal polarization modulator. A stray magnetic field from a sample is transferred into the MO indicator film and visualized as a quantitative MO image. Values of magnetic flux can be determined by using a property of MO indicator film used for the measurement. As an MO indicator film, we also developed high quality Bi substituted yttrium iron garnet films with in-plan magnetization by using a metal organic decomposition (MOD) method.[4] An MO indicator film with a thickness of 400 nm and saturation magnetic field of 1 kOe was used in this experiment. Combining the MO microscope with this MO indicator film, magnetic sensitivity of < 1 mT and spatial resolution of < 1 μm were achieved.

2. MO microscope using polarization modulation technique

Figure 1 shows an optical setup for the MO microscope used in this experiment. In order to utilize the optical modulation method with a polarizer, a liquid crystal modulator (LCM) and an analyzer were installed with an optical axis of π/4, 0 and 0, respectively. An objective lenses with a long working distance (Mitsutoyo G Plan APO ×10, ×50) were employed. Digital images of 640 × 480 pixels are taken by a high speed CCD camera (Hamamatsu, C9300-201) with a 12-bit A-D converter, which can directly transfer 160 digital images/sec to RAM in the computer. A halogen lump was used as a light source, and a wavelength of 500 nm was selected by using interference filters for the experiment. A blue light emitted diode (LED) with a wavelength of 530 nm is also available as a light source for this experiment.

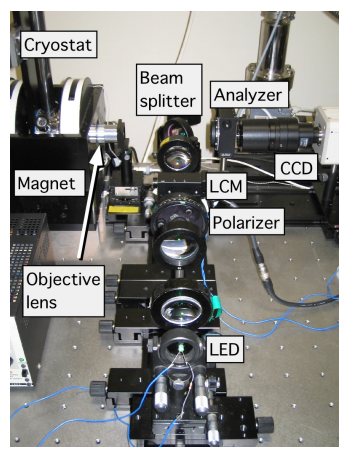

Fig. 1. A picture of low temperature MO microscope using polarization modulation technique.

We prepared an LCM employing a commercially available liquid crystal (ZLI-4792) and ITO-coated glass plates. The retardation was varied by an application of AC voltage of 0 - 10 V with a frequency of approximately 100 Hz to the LCM in this experiment. Images of Faraday rotation θ_F and Faraday ellipticity η_F can be calculated from three images taken with three different optical polarization states. MO values of each pixel are obtained from equations,

$$\theta_F \approx \frac{1}{2}\left\{\frac{2I_{LP}-(I_{RCP}+I_{LCP})}{(1-\eta_F{}^2)(I_{RCP}+I_{LCP})}\right\}, \tag{1}$$

$$\eta_F \approx \frac{1}{2}\left(\frac{I_{LCP}-I_{RCP}}{I_{LCP}+I_{RCP}}\right), \tag{2}$$

where I_{LP}, I_{RCP} and I_{LCP} are intensities at the detector obtained with LP, RCP and LCP, respectively. In order to obtain MO images, three polarization images for LCP, LP and RCP are sequentially measured by applying AC voltages to the LCM. Those images are captured with a delay time of 200 ms after each voltages corresponding to LCP, LP and RCP are applied, and are immediately transferred to the memory on the computer. MO images for rotation and ellipticity are constructed with MO values obtained for each pixel by using equation (1) and (2). In this experiment, although the delay time of 200 ms was required to measure images, we consider that the delay will be shortened as small as 10 ms by using other fast response LCM devices.

3. MO indicator films

Bi substitute iron garnet, $Y_2BiFe_5O_{12}$, films were prepare by a MOD method. MOD solution used in this experiment, which is consisting of solutions made from Bi, Y and Fe carboxylates with desired chemical composition for $Y_2BiFe_5O_{12}$ (Bi:YIG), was made by Kojundo Chemical Laboratory Ltd. The total concentration of carboxylates in those MOD solutions was fixed at 3%. These solutions were spin-coated on the gadolinium gallium garnet, $Gd_3Ga_5O_{12}$, (111) substrates in a 2 step process: 500 rpm for 5 s and 3000 rpm for 30 s, followed by drying at 150ºC for 2 - 60 min using a hot-plate. In order to decompose organic materials and to obtain amorphous oxide films, samples were pre-annealed at 450ºC for 15 min. These processes, i.e. spin-coating, drying, and pre-annealing, were repeated to obtain designed thickness. The thickness of

films obtained in the present study was 400 nm. Finally, the precursor films were annealed for crystallization in a furnace at 650ºC for 2 hour. All thermal treatments were performed in air. Detail of garnet films by the MOD method have been described in Ref.[2]. Pt mirror layer with a thickness of 100 nm was deposited on the garnet film by a magnetron sputtering method in order to obtain high reflectivity and to avoid scattering of the light due to the pattern fabricated on the sample.

Figure 2 shows a magnetic field dependence of Faraday rotation of $Y_2BiFe_5O_{12}$ film with a mirror layer measured by the MO microscope from substrate side with a light of 500nm in wavelength. It shows that the film has an easy-axis of magnetization in plane direction and reaches a saturation value at the magnetic field of approximately 1 kOe. Value of magnetic flux for each pixel in an MO image can be calculated by using a relation in Fig.2.

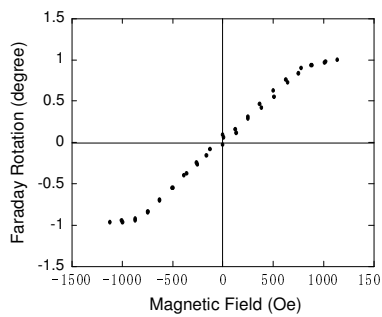

Fig. 2. Magnetic field dependence of Faraday rotation of Bi:YIG film measured at a wavelength of 500 nm.

4. Magnetic imaging of superconducting sample

MO images of superconducting MgB_2 film was measured by the MO microscope using the Bi:YIG film directly put on the sample placed in a cryostat with an electro-magnet. MgB_2 film grown by a molecular beam epitaxy method[5] was patterned into circular shape with a diameter of 500 μm and a thickness of 100 nm. MO images were measured at 3.9 K with different magnetic fields after zero-field cooling.

Figure 3 shows an optical image of the MgB_2 pattern and an MO image of a remanent state after application of magnetic field of 735 Oe. A magnetic flux gradient is clearly observed. As described above, the contrast in the image is showing an amount of magnetic flux. In addition, a current distribution can be calculated from the MO image taking account for the Biot-Savart law. Figure 4

shows a current flow image calculated using the convolution theorem[6], where color lines indicate current flow and density of lines corresponds to current density. The current density was also deduced to be as high as 6×10^7 A/cm^2. This value is consistent with a result measure by electrical measurement.

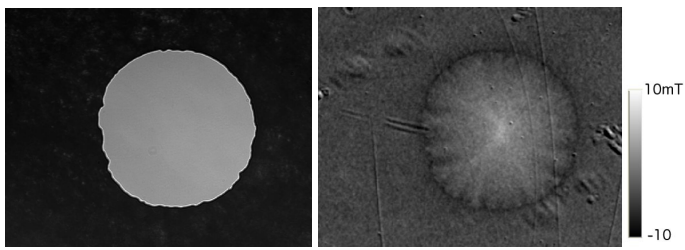

Fig. 3. (a) an optical image and (b) an MO image of MgB_2 circle pattern with a diameter of 500 μm.

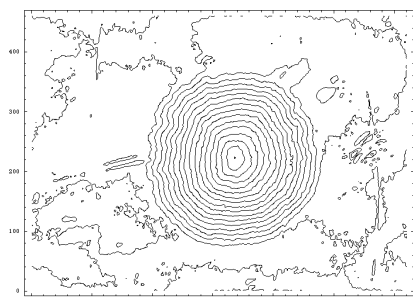

Fig. 4. Current flow image of MgB_2 circle pattern deduced from MO image in Fig.5(b).

5. Summary

Quantitative magnetic imaging by the MO imaging technique using the polarization modulation technique combined with MO indicator films was developed. This technique allows us quantitative and nondestructive measurements for magnetic stray field as well as current distribution in the samples. Evaluations of the stray field and the current distribution in the patterned MgB_2 were demonstrated

Acknowledgments

This work has been supported in part by the Grant-in-Aid for Scientific Research (No.16360003) from the Japan Society for Promotion of Science. We thank Dr. H. Shibata of NTT basic Research Laboratory and Prof. M. Naito of Tokyo Univ. of Agriculture and Technology for providing MgB_2 samples. We also thank Prof. T. H. Johansen and Dr. J. I. Vestgården of Univ. of Oslo for the calculation of current images.

References

1. T. H. Johansen and D. V. Shantsev, Magneto-Optical Imaging, Nato Science Series II Mathematics, Physics and Chemistry, Kluwer Academic Pub., 2004.
2. P. E. Goa, H. Hauglin, Å. A. F. Olsen, M. Baziljevich, and T. H. Johansen, Rev. Sci. Instr., **74**, 141 (2003).
3. T. Ishibashi, A. Mizusawa, M. Nagai, S. Shimizu, K.Sato, N. Togashi, T. Mogi, M. Houchido, H. Sano, and K. Kuriyama, , J. Appl. Phys., **97**, 013516 (2005).
4. T. Ishibashi, Z. Kuang, S. Yufune, T. Kawata, M. Oda, T. Tani, Y. Iimura, Y. Konishi, K. Akahane, X. R. Zhao, T. Hasegawa, and K. Sato, J. Appl. Phys., **100**, 093903 (2006).
5. K. Ueda and N. Naito, J. Appl. Phys. **93**, 2113 (2003).
6. Ch. Jooss, R. Warthmann, A. Forkl and H. Kronmüller, Physica C **299**, 215 (1998).

MEASUREMENT OF MODULATION TRANSFER FUNCTION OF AN OPTICAL SYSTEM BY USING SKEW RAY TRACING*

TE-TAN LIAO
Department of Mechanical Engineering, Far East University
No.49, Chung Hua Road, Hsin-Shih, Tainan, Taiwan

JING-FUNG LIN
Department of Computer Application Engineering, Far East University
No.49, Chung Hua Road, Hsin-Shih, Tainan, Taiwan

CHIA-HUNG LU
Department of Electrical Engineering, ROC Military Academy
No.1,Wei-Wu Road, Fengshan, Kaohsiung, Taiwan

The resolution and performance of an optical system can be characterized by a quantity known as the modulation transfer function (MTF), which is a measurement of an optical system's ability to transfer contrast from the specimen to the intermediate image plane at a specific resolution. Accordingly, this study employs skew ray tracing based on a 4×4 homogeneous coordinate transformation matrix and Snell's law to develop a detailed methodology for determining the spot diagram on the image plane when light rays pass through the optical system. And the authors present measurements of the MTF of an optical system by using the spot diagram on the image plane. The validity of the proposed methodology is verified using a symmetrical optical system.

1. Introduction

The determination of the modulation transfer function (MTF) enables the image quality of a system to be evaluated and characterizes the spatial-frequency response of an imaging system [1]. The MTF of an optical system is an accepted way of describing its optical properties. Its convenience results from the simple conversion of the convolution operation in the image space to multiplication in the spatial frequency domain. Describing a system by its MTF is most useful when the optics are complicated, in which case it gives a good measure of the spatial resolution attainable, and deviations of the measured MTF from a desired

* This work is supported by the National Science Council of Taiwan under grant NSC95-2221-E-269-013 is gratefully acknowledged.

MTF can easily be quantified. The MTF measures the frequency response of an optical system, and over the years a variety of techniques have been developed. The most common technique can be divided into four categories: the sine-wave method [2], the bar-target method [3], the edge-gradient method [4] and a series-expansion method [5].

As a light ray passes though an optical system, the light path can be determined by applying a ray tracing technique, in which the optical laws of reflection or refraction are applied at each boundary encountered by the light ray. The light rays in an optical system may be axial, meridional or skew rays. Axial rays and meridional rays can be traced using relatively simple trigonometric formulae, or even graphically if a very low level of precision is adequate. However, skew rays, which represent the most general type of ray, are far more difficult to trace. Nonetheless, without tracing their paths, it is impossible to accurately model optical systems or to evaluate their performance.

The transformation of a vector in 3-space to a homogeneous coordinate representation involves the addition of an extra coordinate (i.e. a scale factor) to each vector such that the vector retains the same meaning if each of its components, including the scale factor, is multiplied by a constant [6]. In the analysis presented in this paper, the position vector in 3-space is written in the form of a column matrix ${}^{j}P_i = [P_{ix} \quad P_{iy} \quad P_{iz} \quad 1]^T$, in which the pre-superscript "j" of the leading symbol, ${}^{j}P_i$, indicates that the vector is referred with respect to the coordinate frame $(xyz)_j$. Given a point ${}^{j}P_i$, its transformation ${}^{k}P_i$ is represented by the matrix product ${}^{k}P_i = {}^{k}A_j \, {}^{j}P_i$, where ${}^{k}A_j$ is a 4×4 matrix defining the position and orientation (referred to hereafter as the configuration) of a frame $(xyz)_j$ with respect to another frame $(xyz)_k$. The same notation rules are also applied to the unit directional vector ${}^{j}\ell_i = [\ell_{ix} \quad \ell_{iy} \quad \ell_{iz} \quad 0]^T$. Note that for vectors referred to the world frame $(xyz)_0$, the pre-superscript "0" is omitted for reasons of convenience. You can delete our sample text and replace it with the text of your own contribution to the proceedings. However we recommend that you keep an initial version of this file for reference.

2. Spot Diagram of Optical System by Skew Ray Tracing

A ray tracing technique can be used to determine the paths followed by the skew rays as they undergo successive reflection and refraction operations at the various optical surfaces they encounter as they travel through the system. The configuration of the world frame $(xyz)_0$ with respect to the boundary coordinate frame $(xyz)_i$ is given by

$$ {}^{i}A_0 = A_{i0} = \begin{bmatrix} I_{ix} & J_{ix} & K_{ix} & t_{ix} \\ I_{iy} & J_{iy} & K_{iy} & t_{iy} \\ I_{iz} & J_{iz} & K_{iz} & t_{iz} \\ 0 & 0 & 0 & 1 \end{bmatrix}. \tag{1} $$

Fig. 1 shows the general case where a light ray originating at point $P_{i-1}=[P_{i-1x} \;\; P_{i-1y} \;\; P_{i-1z} \;\; 1]^T$ and directed along a unit directional vector $\ell_{i-1}=[\ell_{i-1x} \;\; \ell_{i-1y} \;\; \ell_{i-1z} \;\; 0]^T$ is reflected / refracted at an optical medium boundary surface, ${}^{i}r_i$. The incident point P_i, refracted ray ℓ_i, and reflected ray $\underline{\ell}_i$ are given by the following formulae [7]:

$$ P_i = [P_{i-1x} + \ell_{i-1x}\lambda_i \quad P_{i-1y} + \ell_{i-1y}\lambda_i \quad P_{i-1z} + \ell_{i-1z}\lambda_i \quad 1]^T , \tag{2} $$

$$ \ell_i = \begin{bmatrix} \ell_{ix} \\ \ell_{iy} \\ \ell_{iz} \\ 0 \end{bmatrix} = \begin{bmatrix} -n_{ix}\sqrt{1-N_i^2+(N_iC\theta_i)^2}+N_i(\ell_{i-1x}+n_{ix}C\theta_i) \\ -n_{iy}\sqrt{1-N_i^2+(N_iC\theta_i)^2}+N_i(\ell_{i-1y}+n_{iy}C\theta_i) \\ -n_{iz}\sqrt{1-N_i^2+(N_iC\theta_i)^2}+N_i(\ell_{i-1z}+n_{iz}C\theta_i) \\ 0 \end{bmatrix}, \tag{3} $$

$$ \underline{\ell}_i = \begin{bmatrix} \underline{\ell}_{ix} \\ \underline{\ell}_{iy} \\ \underline{\ell}_{iz} \\ 0 \end{bmatrix} = \begin{bmatrix} \ell_{i-1x}+2n_{ix}C\theta_i \\ \ell_{i-1y}+2n_{iy}C\theta_i \\ \ell_{i-1z}+2n_{iz}C\theta_i \\ 0 \end{bmatrix}, \tag{4} $$

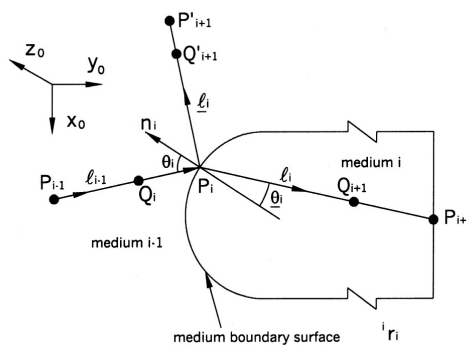

Fig. 1. Skew ray tracing at medium boundary surface ${}^{i}r_i$

where λ_i is the magnitude of vector $P_{i-1}P_i$, $N_i = \xi_{\text{medium},i-1}/\xi_{\text{medium},i}$ is the relative refractive index of medium i-1 with respect to medium i, and θ_i is the incident angle. Following reflection / refraction at the boundary surface, the light ray

proceeds along its new path with point P_i as its new point of origin and ℓ_i ($\underline{\ell}_i$) as its new unit directional vector(s).

Without loss of generality, the following analysis traces a light ray originating at $P_{i-1} = [P_{i-1x} \quad P_{i-1y} \quad P_{i-1z} \quad 1]^T$ and having a unit directional vector of $\ell_{i-1} = [\ell_{i-1x} \quad \ell_{i-1y} \quad \ell_{i-1z} \quad 0]^T$ $(i = 1,2,3,....,n-1)$ which is refracted / reflected at an optical boundary surface ${}^i r_i$. To trace the path of the light ray as it travels through the optical system, it is first necessary to label the individual boundary surfaces within the system sequentially from 1 to n, where n is the total number of boundary surfaces in the system. Any ray can then be traced via the application of a conventional skew ray tracing algorithm at each boundary surface $i = 1, i = 2, i = 3,....$n-1. The point of input ray path to the system's sensor plane r_n is given by

$$P_n = [P_{n-1x} + \ell_{n-1x}\lambda \quad P_{n-1y} + \ell_{n-1y}\lambda \quad P_{n-1z} + \ell_{n-1z}\lambda \quad 1]^T \ . \tag{5}$$

In Eq. (5), P_n is referred to the world frame $(xyz)_0$. Its expression with respect to the sensor frame $(xyz)_n$ is given by ${}^nQ_n = A_{n0}Q_n$, in which

$$A_{n0} = \begin{bmatrix} 1 & 0 & 0 & t_{nx} \\ 0 & 1 & 0 & t_{ny} \\ 0 & 0 & 1 & t_{nz} \\ 0 & 0 & 0 & 1 \end{bmatrix} \tag{6}$$

is the configuration of the world frame $(xyz)_0$ with respect to the sensor frame $(xyz)_n$. The parameter $\lambda = \lambda_n$ can then be obtained as

$$\lambda_n = \frac{-(P_{n-1z} + t_{nz})}{\ell_{n-1z}} \ . \tag{7}$$

The sensor readings $[{}^nP_{nx} \quad {}^nP_{ny}]^T$ of the system are given by

$$\begin{bmatrix} {}^nP_{nx} \\ {}^nP_{ny} \end{bmatrix} = \begin{bmatrix} P_{n-1x} + \ell_{n-1x}\lambda_n + t_{nx} \\ P_{n-1y} + \ell_{n-1y}\lambda_n + t_{ny} \end{bmatrix}. \tag{8}$$

Equation (8) provides the basis for determining the sensor readings $[{}^nP_{nx} \quad {}^nP_{ny}]^T$ using a ray tracing approach. And the spot diagram of the object on the image plane can be obtained.

3. Measurement of MTF by Using Skew Ray Tracing

Fig. 2 is the optical system for the measurement of MTF by simulation in this paper. The parameters of this optical system are: numerical aperture (NA) being -0.045, f-number 11.1, effective focal length (EFL) 99.99mm, back focal length (BFL) 179.375mm and object distance (OD) 179.38mm. The constructional parameters of lenses are listed in table 1.

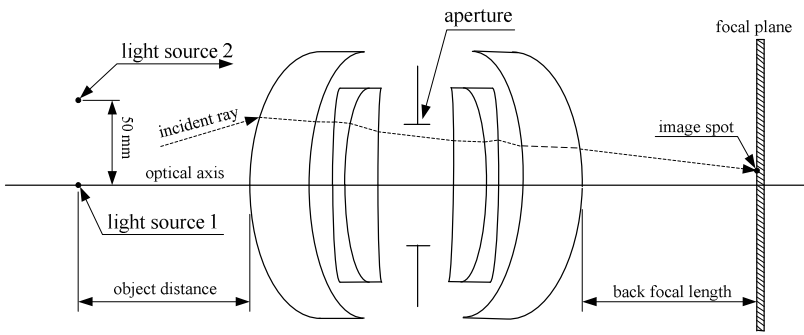

Fig. 2. The optical system for the measurement of MTF

Table 1 The data of lens in the symmetrical optical system (unit: mm)

Boundary i	Radius (mm)	Thickness (mm)	Refractive index ξ_i	Boundary i	Radius (mm)	Thickness (mm)	Refractive index ξ_i
1	21.907	9.020	1.658	8	-74.290	4.097	1.611
2	19.003	1.950	1	9	-14.402	0.180	1
3	42.090	1.096	1.589	10	-13.928	1.096	1.589
4	13.928	0.180	1	11	-42.090	1.950	1
5	14.402	4.097	1.611	13	-19.003	9.020	1.658
6	74.290	3.812	1	13	-21.907	179.375	1
7	---	3.812	1				

In this study, two cases of light source position are studied. The first case considered the light source being in the optical axis (light source 1 in Fig. 2) while the second considered the source 50 mm off the axis (light source 2 in Fig. 2). The OD was 179.38 mm and the radius of the aperture 4.5mm for both studies. The aperture was firstly divided in a grid shape with each side of the aperture being divided into forty equal parts. Light rays are emitted from the light source with different incident angle. The light ray that passed through the mesh point was selected to simulate ray tracing, and there were 1576 light rays traced. Then the spot diagram of the light rays on the focal plane of the optical system was obtained, thus the MTF of the optical system was measured.

Fig. 3(a) is the curve of the MTF value for case 1 study and it can be seen that the spatial-frequency is 127 cycle/mm. Fig. 3(b) is the curve of the MTF

value for case 2. Obviously, the MTF curve decreases rapidly and has a serious perturbation under far from optical axis. There is no obvious spatial-frequency.

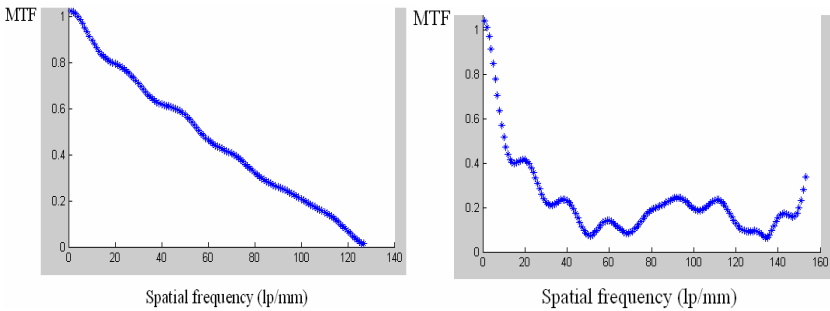

(a) (b)

Fig. 3. The MTF of the optical system (a) light source is in the optical axis (light source 1); (b) light source is 50 mm off the optical axis (light source 2)

4. Conclusion

In this paper the spot diagram on the focal plane of an optical system is obtained by using skew ray tracing. The MTF value of optical system based on the luminous intensity distribution which is computed from a spot diagram is calculated. Two important topics are addressed in this study. First, the spot diagram obtained by using ray tracing of point light source is bigger than that obtained from diffraction limit. The MTF curve is lower and has comparatively lower analytical ability. Second, the MTF curve calculated for off-axis light source decreases and then slightly increase. There is no obvious spatial-frequency.

References

1. S. K. Park, R. Schowengerdt and M. Kaczynski, Appl. Opt., **23**, 2572(1984).
2. S. Inoue, N. Tsumura and Y. Miyake, J. Imaging Sci. Technol. **41**, 657(1997).
3. G. D. Boreman and S. Yang, Appl. Opt., **34**, 8050(1995).
4. R. Barakat, J. Opt. Soc. Am., 55, 1217(1965).
5. Geoffrey L. Rogers, Appl. Opt., 37, 7235(1998).
6. R. P. Paul, Robot Manipulators-Mathematics, Programming and Control, MIT press, Cambridge, MA (1982).
7. Psang Dain Lin and Te-Tan Liao, Trans. of the ASME J. of Dyn. Sys., Measur., and Con., **126**, March, 102(2004).

DIGITAL SPECKLE PATTERN INTERFEROMETER TO MEASURE THE DEFORMATION DISTRIBUTIONS OF A TENSILE SPECIMEN*

SEUNG-KYU PARK†, SUNG-HOON BAIK, HYUNG-KI CHA

Quantum Optics Research Center, Korea Atomic Energy Research Institute, Daedeokdaero 1045, Yusong-gu, Daejeon, 305-353, Rep. of Korea

YOUNG-SUK KIM, YONG-MOO CHEONG

Nuclear Materials Research Center, Korea Atomic Energy Research Institute, Daedeokdaero 1045, Yusong-gu, Daejeon, 305-353, Rep. of Korea

HYUN-KYU JUNG

Nuclear Robotics Lab., Korea Atomic Energy Research Institute, Daedeokdaero 1045, Yusong-gu, Daejeon, 305-353, Rep. of Korea

We have fabricated a digital speckle pattern interferometer to measure the deformation distributions of a tensile specimen. The configured system acquires the phase information of the deformed area for a specimen through capturing its phase shifted laser interference images. To obtain a precise phase image, a spike-noise removing filter is applied to a phase map image. This filter is designed to remove an isolated spike-noise without damaging the phase wrapping area. A fast path independent unwrapping algorithm based on the discrete cosine transform is adopted to obtain unwrapped phase. The fabricated digital speckle pattern interferometer to measure the deformation distributions of a specimen with experimental results is described in this paper.

1. Introduction

Laser nondestructive testing (NDT) techniques using an optical interferometer have emerged as valuable measuring and testing tools for many industrial applications [1]. This non-contact optical method is a full-field measurement technique with a high accuracy and high inspection speed [2]. This system provides strain distributions with an exact stress point and discontinuities without scanning a component. In recent years, a digital electronic speckle

* This work has been carried out under the nuclear R&D Program organized by MOST of Rep. of Korea.

pattern interferometer (ESPI) has evolved with the development of electronic and optical techniques [1].

In this paper, an ESPI is fabricated on a movable table for measuring the deformation distributions of a sample. Phase information of the deformed area is extracted through an unwrapping of a phase map acquired by capturing the phase shifted images. A spike-noise removing filter is designed and applied to a phase map image that removes an isolated impulse noise. This filter improves the extracting efficiency of the phase information around the wrapping area. A fast unwrapping algorithm based on the discrete cosine transform (DCT) is adopted. This algorithm is efficient for obtaining unwrapped phase information of a tensile specimen which is smoothly deformed. In this paper, the hardware and software configurations of the fabricated ESPI to measure the deformation distributions of a specimen with experimental results are described.

2. Configuration of an electronic speckle pattern interferometer

The block diagram of a fabricated ESPI is shown in Fig. 1. The ESPI can measure a change of deformation in the in-plane or out-of-plane direction of a specimen by controlling the SW block. Fig. 2 shows a Zr-2.5Nb tensile specimen for experiments. This specimen is come from a transverse section of a pressure tube used in a CANDU type nuclear power plant. The ESPI is configured on an movable optical table by using optical components with a CW laser (532 nm, Samba-150, Cobolt), a PZT actuator (P-841.10, PI) with a controller (E-662, PI), a CCD camera (TM-7CN, PULNIX) with a image capturing board (Meteor2/4-Matrox) and a control computer.

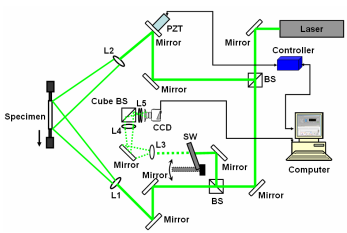

Fig. 1 Block diagram of ESPI

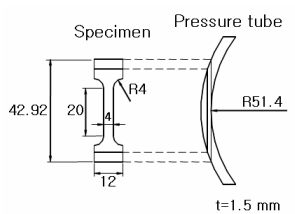

Fig. 2 Dimension of a specimen

Each laser beam is projected onto the surface of a specimen after passing it through a beam expander. The computer acquires a digital object image by using a CCD camera. To measure precise deformation, the 4 phase maps algorithm is adopted because it is robust for noises. Equation (1) shows 4 phase shifted images (I_1, I_2, I_3, I_4) with each step of 90 degrees [3].

$$
\begin{aligned}
I_1(x,y) &= I_{dc} + I_{ac}\cos[\phi(x,y)] \quad \phi(t) = 0 \\
I_2(x,y) &= I_{dc} + I_{ac}\cos[\phi(x,y)] \quad \phi(t) = \frac{\pi}{2} \\
I_3(x,y) &= I_{dc} + I_{ac}\cos[\phi(x,y)] \quad \phi(t) = 3\pi \\
I_4(x,y) &= I_{dc} + I_{ac}\cos[\phi(x,y)] \quad \phi(t) = \frac{3\pi}{2}
\end{aligned} \tag{1}
$$

The notation of I(x, y) is the intensity value at one position of (x, y) on a captured CCD image. The pixel intensities of I_{dc} and I_{ac} are the background DC intensity and modulation AC intensity values, respectively. Φ is the phase shifting value which is changed by a PZT actuator attached to a mirror [3].

The wrapped phase map of φ_d for a deformed area can be acquired by subtracting the φ_a from φ_b according to equation (2),

$$\phi_d = \phi_a - \phi_b \tag{2}$$

Here, the φ_a are φ_b are the phase maps before and after deformations, respectively.

The phase maps of φ_a and φ_b can be calculated by using 4 phase shifted images according to equation (3)

$$\phi(x,y) = \tan^{-1}\left(\frac{I_2(x,y) - I_4(x,y)}{I_1(x,y) - I_3(x,y)}\right) \tag{3}$$

3. Signal processing flowchart for an electronic speckle pattern interferometer with experiments

The signal flowchart to measure the 3D deformation is shown in Fig. 3. A ∏-shift filter is applied to a raw wrapped phase map which is extracted according to equation (2). Here, a median filter is used to reduce the speckle noises. The out-of-plane deformation of a steel plate is produced by slightly pushing a stick on to the backside of a sample. The measured deformation for the out-of-plane direction of a sample is shown in Fig. 4 which is a raw phase map. Fig. 5 shows the phase wrapping positions. As shown in Fig. 5, there are many phase wrappings in one range from 0 to 2∏ and at the positions of the speckle noises. If there is a rough surface change or noise around a wrapping position, then it could possibly produce other unwanted phase wrappings. Also, the noises are spread over the whole area. So, a median filter is applied to reduce the speckle noises during a processing of the ∏-shift filter. If a smoothing filter is applied to the wrapped phase, then the filter damages the phase information near the wrapping positions. This damage can cause large errors during unwrapping procedures. So, we adopted the ∏-shift filter which selects the filtered data from ∏/2 to 3∏/2 from the original phase map and selects other data from 0 to ∏/2

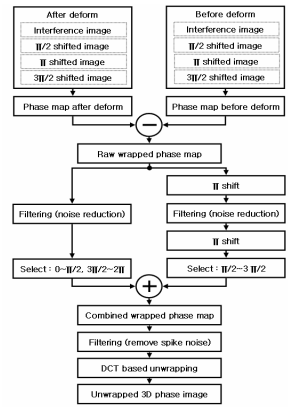

Fig. 3 Signal flowchart of ESPI

and from 3∏/2 to 2∏ from the ∏-shifted phase map which is already filtered by the ∏-shifted phase map as shown in Fig. 3. This ∏-shift filter efficiently maintains the wrapping positions without any damage during signal filtering.

A combined wrapping phase map is acquired by applying the ∏-shift filter where a median filter with a 7x7 window is used. Figs. 6(a) and Fig. 6(b) are the unwrapped 3D phase image and its pseudo-color display by using the path independent unwrapping algorithm based on DCT [4]. Here, we can see some spike-noises near the wrapping positions.

So, a filter is designed to remove these spike-noises. This filter replaces the spike noise value near a wrapping position with an average value of a searching window according to equation (4).

$$\text{If } |I_c - I_{\min}| > I_{th} \text{ and } |I_c - I_{\max}| > I_{th} \text{ then set } I_c \text{ to } I_{avg} \qquad (4)$$

Here, I_c is the intensity value of the checking pixel and I_{th} is a user set threshold value. The notations of I_{min}, I_{max} and I_{avg} are the minimum, maximum and average intensity values in the search window of a n x n pixel size except for the intensity value of I_c at the center position.

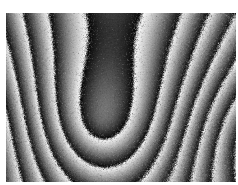

Fig. 4 Acquired raw phase map

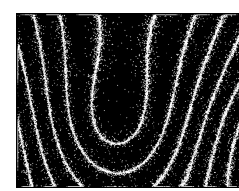

Fig. 5 Phase wrapping positions

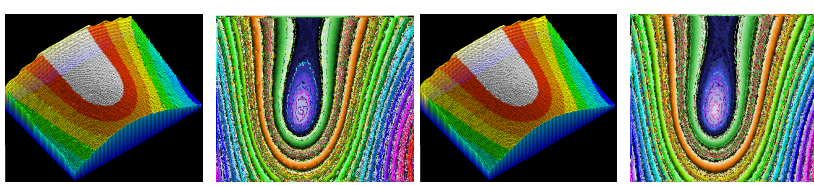

(a) (b) (c) (d)

Fig. 6 Unwrapped 3D phase image and its pseudo-color display

Figs. 6(c) and 6(d) show the unwrapped 3D phase image and its pseudo-color display after applying the designed removing filter for the spike noises. We can see that these spike noises are effectively reduced by the filter.

Fig. 7 shows the measured wrapping phase map for the deformation in the in-plane direction of the tensile specimen of Fig. 2 in the elastic and plastic regions. The experiment for measuring the deformation distributions is carried out without any vibration isolation. So, the fringe pattern is wobbled even at a steady state. A new reference phase map should be created periodically because the correlation for two projecting laser beams is often broken during a tensile testing. So, the deformation area of 4 mm x 20 mm of a specimen is measured periodically with a displacement step of 10 to 20 μm. As shown in Fig. 7, we could observe the deformation changes and the breaking point with an increasing load.

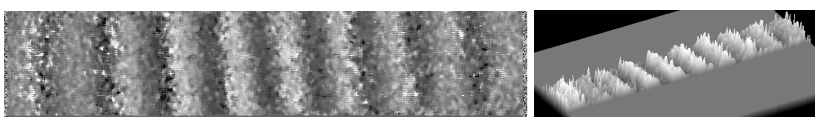

(a) Load: 2.000KN, strain: 0.0430~0.0558 mm

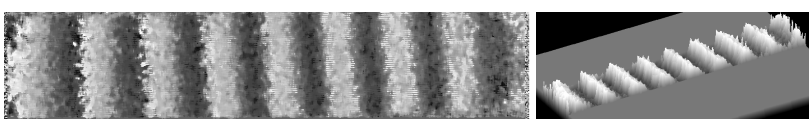

(b) Load: 2.970KN, strain: 0.1039~0.1199 mm

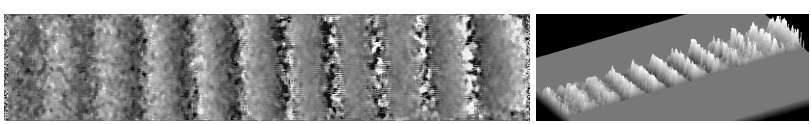

(c) Load: 4.680KN, strain: 0. 2573~0.2766 mm

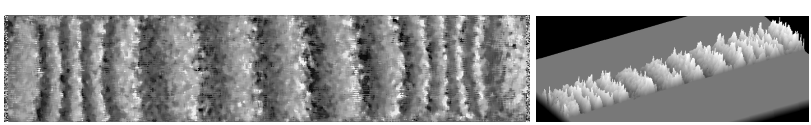

(d) Load: 4.692KN, strain: 0.3763~0.3891 mm

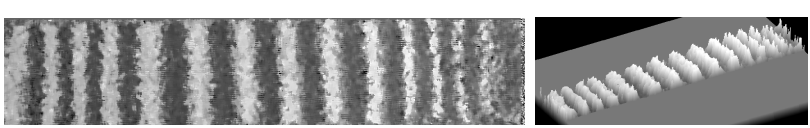

(e) Load: 4.655KN, strain: 0.4534~0.4695 mm

Fig. 7 Measured phase map and its 3D display

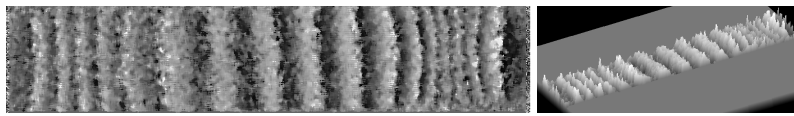

(f) Load: 4.680KN, strain: 0.5145~0.5370 mm

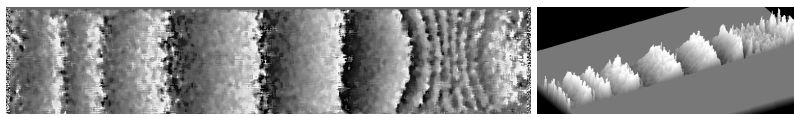

(g) Load: 4.616KN, strain: 0.6173~0.6334 mm

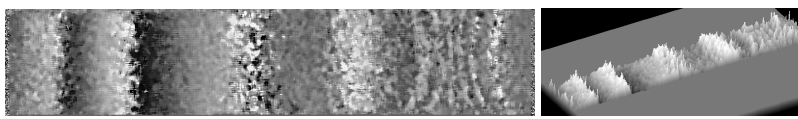

(h) Load: 4.577KN, strain: 0.6945~0.7106 mm

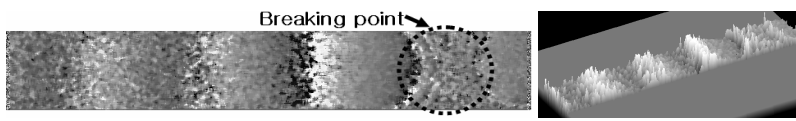

(i) Load: 4.300KN, strain: 0.8454~0.8582 mm

Fig. 7 Continued

4. Conclusions

An electronic speckle pattern interferometer is established to measure the deformation distributions of a tensile specimen. The 冂-shift filter with a median filter generates a reliable phase map. A filter is designed to reduce the effect of spike noise on the 冂-shift filtered phase map. This filter helped to effectively produce an unwrapped 3D phase image from a wrapped phase map. A path independent unwrapping algorithm based on DCT with the designed spike noise removing filter effectively produced an unwrapped 3D phase image with high speed. As for the experimental results, we confirmed that the ESPI system is a valuable tool for measuring the deformation changes during a tensile testing.

References

1. Andreas Ettemeyer, *American Soc. For NDT*, July (2006).
2. Yang L and A. Ettemeyer, *Optical Engineering,* **Vol. 42**, 1257 (2003).
3. S. H. Baik, S. K. Park and C. J. Kim, *Optics Comm.,* **Vol. 192**, 205 (2001).
4. D. C. Ghiglia and M. D. Pritt, *2D Phase Unwrapping,* A Willey-InterSci. Pub., 178 (1998).

MEASUREMENT OF THE CONCENTRATION OF GLUCOSE BY A CIRCULAR POLARISCOPE WITH ELECTRO-OPTIC MODULATION*

Jing-Fung Lin†

Department of Computer Application Engineering, Far East University, No. 49, Chung-Hua Rd., Hsin-Shih Township, Tainan County 744, Taiwan

Te-Tan Liao Chih-Chao Chang

Graduate School of Mechanical Engineering, Far East University, No. 49, Chung-Hua Rd., Hsin-Shih Township, Tainan County 744, Taiwan

In this paper, we presented a circular polariscope with electro-optic modulation and used the phase-lock technique for measuring the optical rotation angle that corresponds with the concentration of glucose. The validity of the proposed design is demonstrated by the measurement of rotation angle of the chiral medium such as a half-wave plate and the glucose solutions. The average relative error in rotation angle level of 0.00378 degrees has been obtained for a solid half-wave plate, with a correlation coefficient of 0.999995 indicates a good linear response. Moreover, the standard deviation in rotation angle level of 0.00654 degrees has been obtained for glucose solutions with concentrations ranging from 0-1.2 g/dl in 0.2 g/dl increments, with a correlation coefficient 0.99860 between the reference and the measured values. The developed system is capable of measuring minimum glucose concentration of 0.2 g/dl. Compared to its conventional counterparts, the proposed measurement system has advantages of a simpler structure, fewer optical elements, tunable heterodyne frequency, and easy signal processing. The dynamic range of the optical rotation angle is -90 degrees to 90 degrees, and the direction of polarization rotation can be determined explicitly. The developed apparatus could be an alternative in the glucose measurement systems.

1. Introduction

When linear polarized light passes through chiral (optically active) materials such as glucose solutions, its plane of polarization may rotate. This phenomenon is referred to as optical rotation (or circular birefringence) and is a result of the asymmetric structure of the chiral material. Obtaining accurate measurements of the rotation angles of optically active materials is a key concern in the optics

* This work is supported by Far East University.

† Work partially supported by the National Science Council of Taiwan, Republic of China, under contract number 95-2622-E-269–028-CC3.

field and this measurement process is an essential task in many research and drug discovery fields.

In the past, the linearly-polarized light source used to conduct polarimetric glucose sensing was generally modulated using either a Pockels cell or a Faraday rotator [1-2]. For example, Cameron *et al.* [2] designed a digital closed-loop processing system for polarimetric glucose sensing in which Faraday rotators were employed to carry out both modulation and compensation. In 1997, Chou *et al.* [3] proposed an amplitude-sensitive optical heterodyne polarimeter in which the optical rotation angle of glucose solutions was derived from the amplitude of the signal produced by the lock-in amplifier. Oakberg [4] developed a polarimeter for measuring optical rotation based upon a linear polariscope modulated by a photoelastic modulator. The optical rotation of the sample of interest was determined using an intensity-ratio technique. However, the dynamic range of the system was limited to just 90°.

Instead of using some forms of intensity-signal-based approach outlined above, various true-phase measurement systems have also been proposed [5-7]. For example, Lin *et al.* [6] presented a heterodyne Mach-Zehnder interferometer capable of measuring the optical rotation angles of chiral media with a resolution of approximately 6×10^{-5} degrees. However, the signal-processing algorithm was rather complex. In 2006, Lo and Yu [8] developed a polarimetric glucose sensor in which the azimuth of the linearly-polarized light source was modulated using a liquid-crystal modulator driven by a sinusoidal waveform and the resulting signal was processed using a novel demodulation algorithm.

The current study develops an electro-optically modulated circular polariscope for glucose sensing applications in which the optical rotation angle of the sample is measured using a phase-lock technique and the corresponding glucose concentration is then proportionally extracted.

2. Methodology

2.1. *Optical Configuration*

Figure 1 presents a schematic illustration of the proposed common-path circular polariscope. As shown in Fig. 1, a He-Ne laser beam of wavelength 632.8 nm is passed through a polarizer and enters an electro-optic (EO) modulator (Conoptics Inc., Model 370) driven by a saw-tooth waveform signal. The light beam then passes through a quarter-wave plate (Q_1), the sample of interest, a second quarter-wave plate (Q_2), and finally an analyzer. The intensity of the light emerging from the analyzer is detected using a photodetector (NEW

FOCUS, Model 1801 DC-version type). The phase of this signal is extracted using a lock-in amplifier (Stanford Research System, Model SR830).

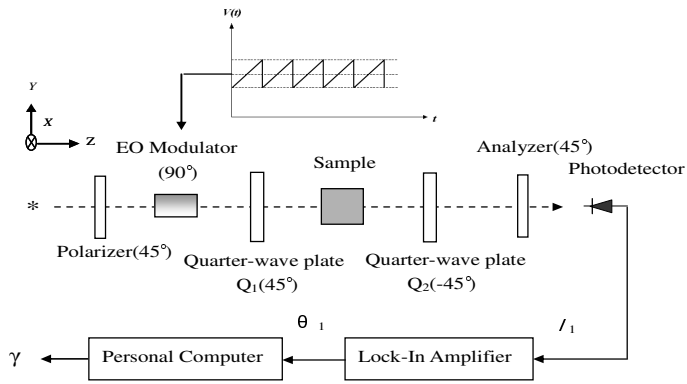

Fig. 1. Schematic illustration of electro-optically modulated circular polariscope for optical rotation angle measurement.

2.2. *Principle*

According to the Jones matrix formalism, the vector of the electric field emerging from the optical configuration shown in Fig. 1 has the form

$$E_{out} = A(45^\circ).Q_2(-45^\circ)S(\gamma).Q_1(45^\circ).EO(90^\circ,\omega t).P(45^\circ).E_{in}$$
$$= \begin{bmatrix} \frac{1}{2} & \frac{1}{2} \\ \frac{1}{2} & \frac{1}{2} \end{bmatrix} \begin{bmatrix} \frac{1-i}{2} & \frac{-1-i}{2} \\ \frac{-1-i}{2} & \frac{1-i}{2} \end{bmatrix} \begin{bmatrix} \cos\gamma & \sin\gamma \\ \sin\gamma & -\cos\gamma \end{bmatrix} \begin{bmatrix} \frac{1-i}{2} & \frac{1+i}{2} \\ \frac{1+i}{2} & \frac{1-i}{2} \end{bmatrix} \begin{bmatrix} e^{-i\frac{\omega t}{2}} & 0 \\ 0 & e^{i\frac{\omega t}{2}} \end{bmatrix} \begin{bmatrix} \frac{1}{2} & \frac{1}{2} \\ \frac{1}{2} & \frac{1}{2} \end{bmatrix} \begin{bmatrix} 0 \\ E_0 \end{bmatrix} e^{j\omega_0 t}, \quad (1)$$

where E_0 is the amplitude of the incident electric field, $A(45^\circ)$ and $P(45^\circ)$ represents the Jones matrix of the analyzer (polarizer) when set at 45° to the *x*-axis respectively. $Q_1(45^\circ)$ and $Q_2(-45^\circ)$ denote the Jones matrix of the two quarter-wave plates, Q_1 and Q_2, when set with its fast axis at $\pm 45^\circ$ to the *x*-axis respectively. $S(\gamma)$ is the Jones matrix of the chiral medium. Additionally, $EO(90^\circ,\omega t)$ denotes the Jones matrix of the EO modulator driven by a saw-tooth voltage waveform with a frequency ω and orientated such that its fast axis is parallel to the y-axis.

The intensity of the transmitted light, I_1, can be expressed as

$$\begin{aligned} I_1 &= I_{dc}(1-\cos(\omega t - 2\gamma)) \\ &= I_{dc} - R_1\cos(\omega t - \theta_1)\,, \end{aligned} \quad (2)$$

where the phase term θ_1 of the output intensity I_1 can be measured by locking the AC component of I_1 at the reference frequency ω using a lock-in amplifier. Consequently, the rotation angle of the chiral sample γ can be determined from

$$\gamma = \frac{\theta_1}{2}. \tag{3}$$

3. Experimental Results

After conducting the calibration and fine-tuning procedures, the tuning parameters for the EO modulator were found to be a 100 V dc-bias voltage of controller and a 1 kHz saw-tooth signal with a dc-offset voltage of 0.44 V and an AC amplitude of 1.25 V. The time constant of the lock-in amplifier was 1 second and its voltage sensitivity was 500 mV. The verification experiment was performed using a half-wave plate (Casix Inc., WPF1225-633- $\lambda/2$) as a sample, the rotation angle was measured as the principal angle of the half-plate was rotated through a full 180° in increments of 5°. As results illustrated in Figure 2, the correlation coefficient of 0.999995 confirms that the system has an excellent linear response. Moreover, the average relative error is determined to be just 0.00378°.

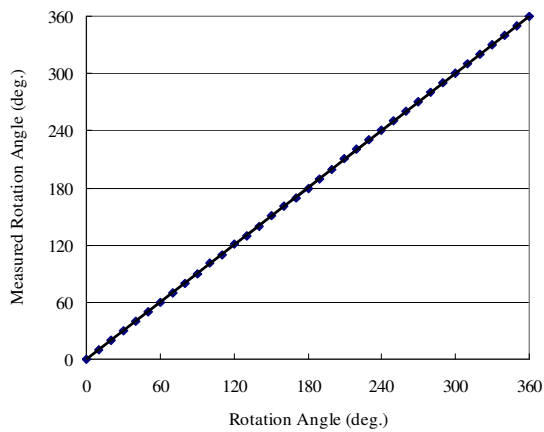

Fig. 2. Variation of measured rotational angle (sample: half-wave plate).

Having verified the performance of the metrology system, it was employed to measure the optical rotation angles of glucose samples with known concentrations. The samples were prepared from a 60-mg/ml stock glucose solution produced by dissolving 6.00 g of D-glucose (Merck Ltd) in a total volume of 100 ml of de-ionized water. Individual glucose samples with concentrations ranging from 0~1.2 g/dl in increments of 0.2 g/dl were then

prepared by diluting and injected into 50-mm long cells. From inspection of Figure 3, the correlation coefficient is found to be 0.99860 between the rotation angle and the glucose concentration at a temperature of $22^{\circ}C$, while the standard deviation is just 0.00654°.

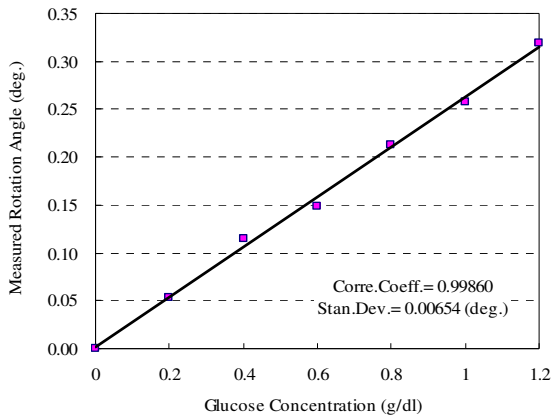

Fig. 3. Variation of rotation angle with glucose concentration (sample: glucose solution).

To verify the repeatability, a glucose sample with a concentration of 0.2 g/dl was measured 10 times. As illustrated in Figure 4, a standard deviation of 0.0032° and the average value of 0.0518° are observed, which leads to a 1σ value of ~6.3 % of the average. Therefore, the proposed setup has the ability to perform precise measurements of the rotation angle. Compared with the value of 0.0527° in reference [9], the average relative error is just 1.7 %.

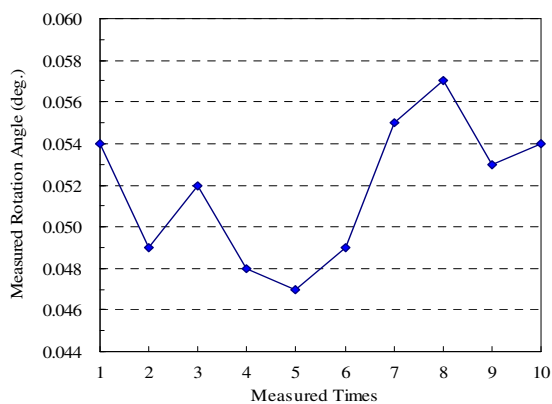

Fig. 4. Measurement repeatability test (sample: glucose solution with concentration of 0.2 g/dl).

4. Discussions and Conclusions

This study has developed an electro-optically modulated circular polariscope based on a phase-lock technique for measuring the optical rotation angle and the corresponding concentrations of glucose samples. In a verification experiment using a half-wave plate, the correlation coefficient between the measured and reference value of rotation angle was determined to be 0.999995, thus demonstrating the excellent linear response of the system. Moreover, the average relative error in the measured rotation angle was found to be just 0.00378°. For glucose samples with concentrations ranging from 0 ~ 1.2 g/dl, the correlation coefficient between the rotation angle and glucose concentration was found to be 0.99860, while the standard deviation of the measurement is just 0.00654°.

Compared to others, the proposed system has the advantages of a simpler structure, a tunable heterodyne frequency, and a straightforward signal processing scheme. Furthermore, the system has a common-path configuration and therefore has improved stability. In conclusion, the proposed metrology system provides a highly-precise, non–invasive means of measuring glucose samples with concentrations as low as 0.2 g/dl, and the dynamic range of optical rotation angle measurement is -90° to $+90^\circ$.

Acknowledgments

This research was partially supported by the National Science Council of Taiwan, Republic of China, under contract number 95-2622-E-269 –028-CC3.

References

1. T. W. King, G. L. Cóte, R. McNichols and M. J. Goetz, *Opt. Eng*. **33**, 2746 (1994).
2. B. D. Cameron and G. L. Cóte, *IEEE Trans. Biomed. Eng*. **44**, 1221 (1997).
3. C. Chou, Y. C. Huang, C. M. Feng and M. Chang, *Jpn. J. Appl. Phys*. **36**, 356 (1997).
4. T. C. Oakberg, www.hindsinstruments.com.
5. C. M. Feng, Y. C. Huang, J. G. Chang, M. Chang and C. Chou, *Opt. Commun*. **141**, 314 (1997).
6. J. Y. Lin, K. H. Chen and D.C. Su, *Opt. Commun*. **238**, 113 (2004).
7. C. Chou, W. C. Kuo, T. S. Hsieh and H. K. Teng, *Opt. Commun*. **230**, 259 (2004).
8. Y. L. Lo and T. C. Yu, *Opt. Commun*. **259**, 40 (2006).
9. B. Wang, *Proc. SPIE.* **355**, 294 (1998).

FABRICATION AND CHARACTERIZATION OF PRISMATIC BAND FILTER GRADIENT RUGATE POROUS SILICON

JIHOON KIM

Department of Chemistry, Chosun University, 375 Seosuk-dong, Dong-gu, Gwangju 501-759, Korea

SEUNGHYUN JANG

Department of Chemistry, Chosun University, 375 Seosuk-dong, Dong-gu, Gwangju 501-759, Korea

YOUNGDAE KOH

Department of Chemistry, Chosun University, 375 Seosuk-dong, Dong-gu, Gwangju 501-759, Korea

HONGLAE SOHN*

Corresponding author, Department of Chemistry, Chosun University, 375 Seosuk-dong, Dong-gu, Gwangju 501-759, Korea

Band filter gradient (BFG) rugate porous silicon (PSi) was generated by an electrochemical etching of silicon wafer through an asymmetric electrode configuration in aqueous ethanolic HF solution. BFG rugate PSi prepared from anisotropic etching conditions displayed the reflection band whose reflection maximum varied spatially across the PSi. BFG rugate PSi displayed a prismatic reflection due to the disproportion of current from the position of cathode across the silicon wafer. In this work, we have developed a method to create planar gradient refractive index in Si substrate. Reflection peak of BFG rugate PSi was shifted to shorter wavelength and its pore sizes and film thickness were decreased across the silicon wafer.

Keywords: Rugate porous silicon; asymmetric; band filter; gradient.

1. Introduction

The development of a new technology to build one-dimensional photonic structures is of great interest because they are too complex to fabricate by using conventional lithographic methods. PSi is an attractive material for photonic applications due to its high surface area, open pore structure, and optical signal transduction capability. A variety of passive devices, such as mirrors,[1] filters,[2] and microcavities,[3,4] has already been employed by using PSi which is based on

a relatively simple electrochemical etching process. The first reports giving details of a new form of silicon appeared in 1956 when Uhlir described a study of the electropolishing of silicon in hydrofluoric acid.[5] Research on PSi has been increased significantly since the discovery of efficient visible luminescence of PSi by Canham suggesting the possibility of silicon based light sources.[6]

One-dimensional photonic crystals of PSi have also found application in chemical detection,[7,8] remote sensing,[9] and biomolecular screening.[10] PSi is a nano-crystalline material that is generated by etching of bulk crystalline silicon in aqueous hydrofluoric acid (HF).[11] Molpology and optical properties of PSi are dependent on HF concentration, dopant type, density in the Si substrate, and applied current density.[12,13] Porous silicons containing gradient refractive index have been recently developted.[14,15] The direction of the refractive index gradient is perpendicular to the optical. Here we report the optical characteristics and morphology of BFG rugate PSi whose appearance is prismatic due to gradient refractive index. This is achieved by various porosity and depth of PSi during the electrochemical fabrication process.

2. Experimental Methods

2.1. *Preparation of ruagte PSi using asymmetric electrode configuration*

BFG rugate PSi dielectric mirror was prepared by using electrochemical etching of silicon wafer (boron doped, polished on the (100) face, resistivity of 0.8-1.2 mΩ -cm, Siltronix, Inc.), and using a computer-generated periodic sine wave current. The etching solution consists of a 1:3 by volume mixture of absolute ethanol (ACS reagent, Aldrich Chemicals) and aqueous 48% hydrofluoric acid (ACS reagent, Aldrich Chemicals). Etching is carried out in a Teflon cell by using a two-electrode configuration with Pt needle counter electrode. BFG rugate PSi containing a distribution of pore sizes and film thickness was prepared by using the asymmetric electrode configuration as shown in Fig. 1.

2.2. *Instrumentation and data acquisition*

The anodization current was supplied by Keithley 2420 high-precision constant current source which is controlled by a computer to allow the formation of PSi multilayers. Optical reflectivity spectra were measured using a tungsten-halogen lamp and an Ocean Optics S2000 CCD spectrometer fitted with a fiber optic input. The reflected light collection end of the fiber optic was positioned at the focal plane of the optical microscope. Scanning electron microscope (SEM)

images were obtained by a cold field emission scanning electron microscope (FE-SEM, S-4700, Hitachi).

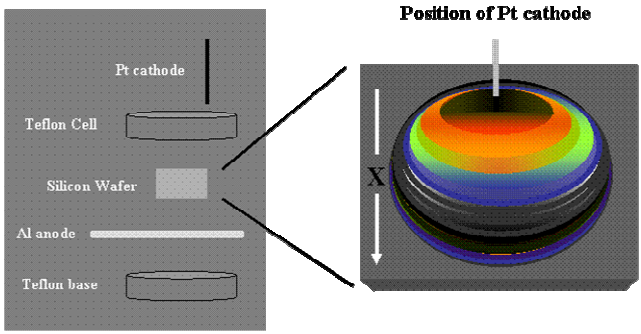

Fig. 1. Schematic diagram of the electrochemical cell and electrode arrangement used to generate pore gradients.

3. Results and Disussion

BFG rugate PSi has been generated by an electrochemical etching of silicon wafer using an asymmetric electrode configuration in aqueous ethanolic HF solution. BFG PSi prepared by using anisotropic etching conditions displays the anisotropic reflection bands whose reflection maximum varied spatially across the porous silicon. The waveform used in the present work, which is represented by Equation 1.

$$y_i = A_i[\sin(k_i t)] + B \tag{1}$$

Where y_i represents a temporal sine wave of amplitude, A_i; frequency, k_i; time, t; applied current density, B. The values of k_i are from 0.39 Hz. The values of A_i and B are 11.55 and 63.05 mA with 205 repeats.

To have anisotropic distribution of pore sizes and film thickness in PSi, Pt needle electrode is placed at the side of etching cell and Al plate electrode is located at the back side of the silicon wafer as shown in Fig. 1. With this asymmetric electrode arrangement, the porosity and the thickness of the film at any point depend on the magnitude of the etching current flowing through that point. The current at any point of silicon wafer depends on the resistance of the Si wafer between the electrolyte on one side and the Al plate electrode on the back side and varies as a function of distance from the Pt counter electrode due

to solution resistance. Since the geometry is asymmetric, the current density decreases as the distance from the counter electrode increases. The asymmetric electrode configuration provides a current density gradient across the wafer that result in a distinct variation in the morphology of the pores and produces a BFG PSi lens showing asymmetric Newton's ring. Photograph and reflection spectra of BFG rugate PSi are shown in Fig 2. The reflection spectra of BFG rugate PSi are recorded by moving every 2 mm from the position closest to the Pt counter electrode on the silicon surface.

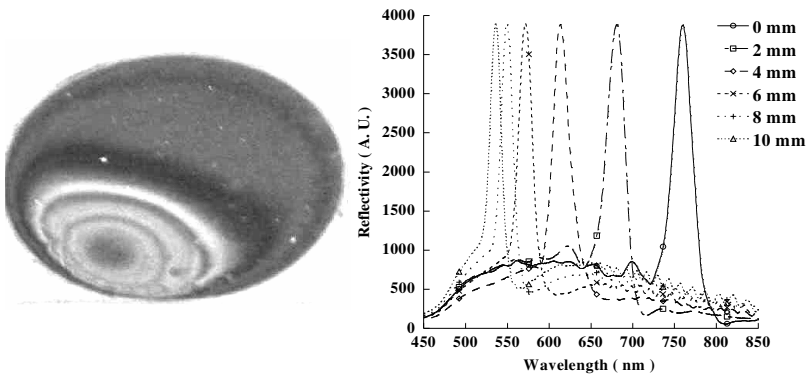

Fig. 2. Photograph and reflection spectra of BFG rugate PSi. The value position used refers to the distance from the position closest to the Pt counter electrode across the silicon wafer.

Changes of reflective maxima and FWHM are summarized in Table 1. The reflection wavelength shifts exponentially to shorter wavelengths and full-width at half-maximum (FWHM) is narrower across the silicon wafer. The BFG rugate PSi displays a prismatic appearance due to the continuously changing refractive index distribution.

Table 1. Data analysis of BFG rugate PSi about the position of electrode.

X (mm)	λ (nm)	Δλ (nm)	FWHM (nm)
0	759	0	28.78
2	680	79	27.67
4	612	68	25.15
6	569	43	23.37
8	548	21	19.89
10	535	13	18.25

The cross-section and surface SEM image of BFG rugate PSi are shown in Fig. 3. The film thickness of BFG rugate PSi becomes shorter as the distance from the position of Pt counter electrode increases.

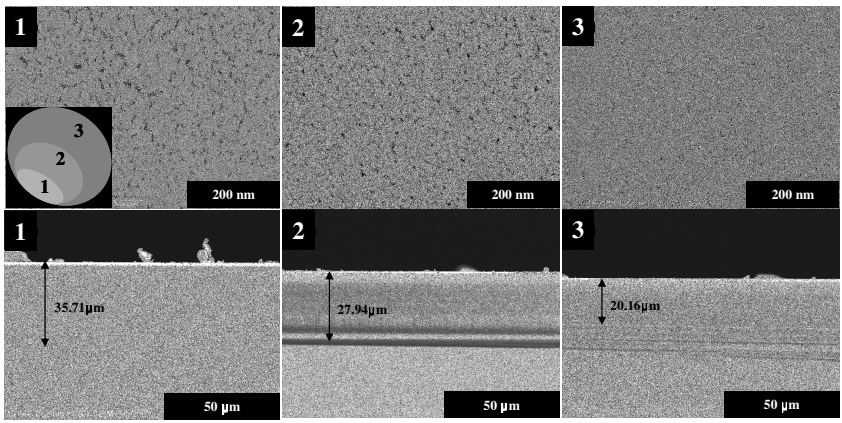

Fig. 3. The surface and cross-section SEM images of BFG rugate PSi. 0 mm (1), 5 mm (2), and 10 mm (3) refer to the distance from the position closest to the Pt counter electrode across the silicon wafer.

Profilometry measurements shown in Fig. 4 reveal that the thickness of the PSi layer varies as a function of distance from the counter electrode. BFG rugate PSi is thickest at the point directly under the counter electrode, consistent with that being the position of highest current density.

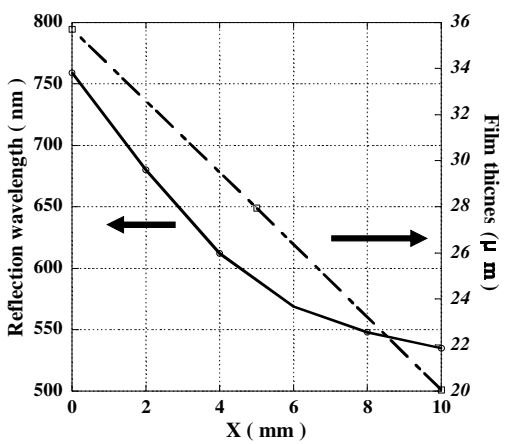

Fig. 4. Profile of the change of reflection wavelength and film thickness of BFG rugate PSi as a function of x represented to the distance from the position closest to the Pt counter electrode across the silicon wafer.

4. Conclusions

BFG rugate PSi was prepared that contain a controlled distribution of pore sizes and film thickness using anisotropic etching conditions. In this work, BFG rugate PSi displays a prismatic appearance due to the uneven distribution of current across the silicon wafer during the etching. The reflectivity of BFG rugate PSi is shifted to shorter wavelengths and its bandwidth and film thickness become narrower and shorter across the wafer from the position of electrode. This might be a demonstration for the fabrication of specific reflectors or filters.

References

1. W. H. Zheng, P. J. Reece, B. Q. Sun, and M. Gal, *Appl. Phys. Lett.* **84**, 3519 (2004).
2. M. G. Berger, F. Arens-Fischer, M. Thönissen, M. Krüger, S. Billat, H. Lüth, S. Hilbrich, W. Theiβ, and P. Grosse, *Thin Solid Films* **297**, 237 (1997).
3. S. Chan and P. M. Fauchet, *Opt. Mater.***17**, 31 (2001).
4. M. Ghulinyan, C. J. Oton, G. Bonetti, Z. Gaburro, and L. Pavesi, *J. Appl. Phys.* **93**, 9724 (2003).
5. A. Uhlir, *Bell System Tech.* **35**, 333 (1956).
6. L. T. Canham, *Appl. Phys. Lett.* **57**, 1046 (1990).
7. H. Sohn, S. Létant, M. J. Sailor, and W. C. Trogler, *J. Am. Chem. Soc.* **122**, 5399 (2000).
8. J. Gao, T. Cao, Y. Y. Li, and M. J. Sailor *Langmuir* **18**, 2229 (2002).
9. T. A. Schmedake, F. Cunin, J. R. Link, and M. J. Sailor, *Adv. Mater.* **14**, 1270 (2002).
10. F. Cunin, T. A. Schmedake, J. R. Link, Y. Y. Li, J. Koh, S. N. Bhatia, and M. J. Sailor, *Nature Mater.* **1**, 39 (2002).
11. H. Foll, J. Carstensen, M. Christophersen, and G. Hasse, *Phys. Status Solidi A* **182**, 7 (2000).
12. K. -P. S. Dancil, D. P. Greiner, and M. J. Sailor, *J. Am. Chem. Soc.* **121**, 7925 (1999).
13. S. Chan, P. M. Fauchet, Y. Li, L. J. Rothberh, and B. L. Miller, *Phys. Status Solidi A* **182**, 541 (2000).
14. S. Ilyas and M. Gal, *Appl. Phys. Lett.* **89**, 211123 (2006).
15. B. E. Collins, K. -P. S. Dancil, G. Abbi, and M. J. Sailor, *Adv. Funct. Mater.* **12**, 187 (2002).

ANALYSIS OF CHEMICALLY INDUCED RESIDUAL STRESS IN POLYMERIC THIN FILM USING CURVATURE MEASUREMENT METHOD

SANG SOON LEE AND IN WOOK JEON

Korea University of Technology and Education School of Mechatronics Engineering
P.O.Box 55, Chonan, Chungnam, 330-600, South Korea

MI HIE YI

Korea Research Institute of Chemical Technology, Polymeric Nanomaterials Lab.
South Korea

This paper deals with the chemically induced residual stress in an epoxy film deposited on Si wafer due to the volumetric shrinkage in cross-linking resins during polymerization. The curvature measurement method and the boundary element method (BEM) are employed to investigate the residual stresses. The film/wafer system is assumed to be linearly elastic. The normal stress across thickness of the thin film is estimated from wafer curvature measurements. The boundary element method is employed to investigate the whole stresses in the film. The singular stress is observed near the interface corner. Such residual stresses are large enough to initiate interface delamination to relieve the residual stresses.

1. Introduction

Polymeric films such as an epoxy are widely used in electronic industry as adhesive layers. During the curing procedure, the epoxy undergoes polymerization. Polymeric films deposited on a substrate can be subjected to residual stresses due to the volumetric shrinkage in cross-linking resins during polymerization. The deformation of the film is constrained by the substrate, and hence residual stresses are built up in the film**.** Such chemically induced residual stresses can play a very important role during subsequent loading of the film/substrate system. Such residual stresses may cause premature failure upon external loading.

Residual stresses in bi-material systems have received much attention. Stoney[1] observed that a metal film deposited on a thick substrate was in a state of tension or compression when no external loads were applied to the system and that it would consequently deform the substrate so as to bend it. He suggested a simple analysis to relate the stress in the film to the amount of bending in the substrate. Timoshenko [2] derived thermoelastic solutions for curvature and

stress development in a bimetallic strip as a function of temperature change, for arbitrary variation in the relative thickness and elastic properties of the two films in the strip. Freund [3] presented certain conditions governing the onset of plastic deformation with arbitrary combinations.

The change in substrate curvature induced during curing processes provides valuable insight into the development of residual stress in the thin film. Methods to measure changes in substrate curvature during stress development in a thin film can be broadly classified into the following groups: mechanical methods, capacitance methods, x-ray diffraction methods, and optical methods. All these techniques, with the exception of x-ray diffraction, have the common feature that they provide a measure of the out-of-plane deflection of the curved film-substrate system. The optical method for measuring substrate curvature is generally convenient for in-situ measurement of film deposition stress, provided that optical access is provided to the substrate and that the specimen is mounted in a manner that facilitates unconstrained curvature evolution in one direction. One of the most common optical methods of estimating thin film stress, particularly for films deposited on Si wafer used in microelectronics, involves the reflection of a laser beam from substrate; this technique is simply referred to as the wafer curvature measurement method. Details of methods for curvature measurement can be found in Freund and Suresh [4].

In this study, the chemically induced residual stress in an epoxy film deposited on Si wafer due to the volumetric shrinkage in cross-linking resins during polymerization is investigated. The film/wafer system is assumed to be linearly elastic. The curvature measurement method and the boundary element method (BEM) are employed to investigate the residual stresses.

2. Boundary Element Analysis

An epoxy film deposited on an infinitely thick substrate is shown in Fig.1(a). Due to symmetry, only one half of the film needs to be modeled. Fig. 1(b) represents the two-dimensional plane strain model for analysis of the interface stresses between the film and the substrate.

During the polymerization, the epoxy film shrinks due to chemical reaction, i.e. cross-linking of material. In view of the small thickness of the film used in practice it is permissible to employ the assumption that the chemical reaction, i.e. cross-linking, takes place uniformly throughout the epoxy film. Under the assumption of uniform cross-linking of epoxy during the cure, the chemical shrinkage is equivalent to increasing the tractions by $\gamma(t) n_j$ [5] where

$$\gamma(t) = 3K \varepsilon_c H(t) \tag{1}$$

Here, ε_c is the strain due to chemical shrinkage; K is the bulk modulus; n_j are the components of the unit outward normal to the boundary

surface; $H(t)$ represents Heaviside unit step function. The boundary integral equations without any other body forces are written as follows[5]:

for thin film,

$$c_{ij}^{f}(\mathbf{x})u_j^{f}(\mathbf{x}) + \int_{S^f} u_j^{f}(\mathbf{x}')T_{ij}^{f}(\mathbf{x},\mathbf{x}')dS^{f}(\mathbf{x}')$$

$$= \int_{S^f} t_j^{f}(\mathbf{x}')U_{ij}^{f}(\mathbf{x},\mathbf{x}')dS^{f}(\mathbf{x}') + \int_{S^f} \gamma^{f} n_j U_{ij}^{f}(\mathbf{x},\mathbf{x}')dS^{f}(\mathbf{x}') \quad (2)$$

for substrate,

$$c_{ij}^{s}(\mathbf{x})u_j^{s}(\mathbf{x}) + \int_{S^s} u_j^{s}(\mathbf{x}')T_{ij}^{s}(\mathbf{x},\mathbf{x}')dS^{s}(\mathbf{x}') = \int_{S^s} t_j^{s}(\mathbf{x}')U_{ij}^{s}(\mathbf{x},\mathbf{x}')dS^{s}(\mathbf{x}') \quad (3)$$

where superscripts f and s represent the thin film zone and substrate zone. u_j and t_j represent displacement and traction, and S is the boundary of the given domain. $c_{ij}(\mathbf{y})$ is dependent only upon the local geometry of the boundary. For $\mathbf{y}$ on a smooth surface, the free term $c_{ij}(\mathbf{y})$ is simply a diagonal matrix $0.5\delta_{ij}$. The fundamental solutions, $U_{ij}(\mathbf{x},\mathbf{x}')$ and $T_{ij}(\mathbf{x},\mathbf{x}')$, are Kelvin's fundamental solutions of linear elasticity. Solving Eqs. 2 and 3 under boundary conditions leads to determination of all boundary displacements and tractions of the film/substrate system.

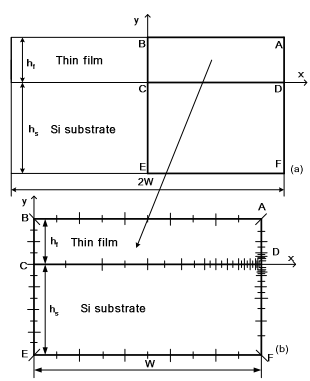

Fig. 1. Boundary element analysis model.

3. Experimental Procedure

Epoxy resin is coated on p-type silicon wafer with 3 inch diameter and 380 μm thickness. The coated epoxy is soft cured at the room temperature. Residual stresses originate during the film formation and curing processes as a result of solvent evaporation and the cross-linking of thermosetting films. The change in substrate curvature induced during curing processes provides valuable insight into the development of residual stress in the epoxy film.

Details of the fundamentals of curvature measurement method can be found in Pan and Blech[6], Volkert [7], and Shull and Spaepen[8]: however, a brief review of such process is in order. The curvature measurement method is based on the principle that a laser beam reflected on a curved surface depends on the orientation of the surface. The substrate is fixed at one point such that its position and orientation there are known. Then, a laser beam incident on the substrate surface is scanned along a straight line, and the angular deflection of the reflected beam from the incident is measured as a function of distance from a reference point. The scanning mirror arrangement utilizes mirrors and laser to scan a single laser beam along the specimen surface. The deflection of the scanned beam is monitored through a position-sensitive detector. Referring to the geometric relations shown in Fig. 2, the law of deflection yields the radius of curvature in terms of Δx , Δd , and L as follows:

$$R = \frac{2\Delta x L}{\Delta d - \Delta x} \tag{4}$$

in which the translation of laser beam in $x-$direction, Δx , is assumed to be very small enough to have $\Delta x = R\theta$.

Residual stress in thin film deposited on a substrate can be obtained by Stoney's formula as follows:

$$\sigma_f = \frac{E_s h_s^2}{6(1-\nu_s)R h_f} \tag{5}$$

where subscripts s and f represent the substrate and the film, respectively, E_s and ν_s are Young's modulus and Poisson's ratio of the substrate, respectively. h_s and h_f represent the substrate thickness and film thickness, respectively.

Stress distribution across thickness of the film is shown in Fig. 3. The residual normal stress across thickness of the film is less than 1 MPa , which is relatively small. In order to investigate the whole stresses in the film, the boundary element method is employed.

4. Numerical Results

The film/substrate system is assumed to be cured at the room temperature. The boundary element discretization is shown in Fig.1. The refined mesh was used near the interface corner. Quadratic shape functions were used to describe both the geometry and functional variations. Residual stress profiles were plotted along interface to investigate the nature of stresses. Fig. 4 shows the distribution of normal stress σ_{yy} and shear stress τ_{xy} on the interface. Large gradients are

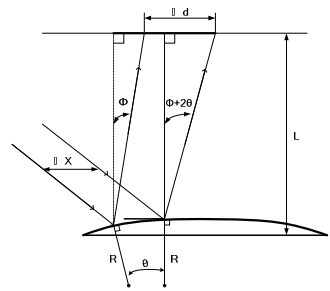

Fig. 2. Schematic illustration of laser beams reflected on a specimen surface.

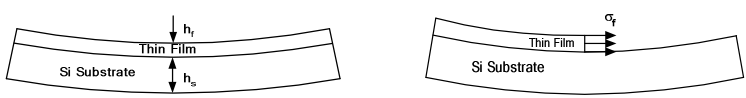

Fig. 3. Normal stress across thickness of the film.

observed in the vicinity of the free surface. Such residual stress may cause interface delamination in the absence of applied external loads.

5. Conclusions

The chemically induced residual stresses in an epoxy film deposited on Si wafer have been investigated. Such residual stresses originate during the film formation and curing processes as a result of solvent evaporation and the cross-linking of thermosetting films. The film/wafer system has been assumed to be linearly elastic. The curvature measurement method and the boundary element method (BEM) have been employed to investigate the residual stresses. Epoxy resin has been coated on p-type silicon wafer with 3 inch diameter and 380 μm thickness. The coated epoxy has been soft cured at the room temperature. The normal stress across thickness of the thin film has been estimated from wafer curvature measurements to be less than 1 MPa . The boundary element method has been employed to investigate the whole stresses in the film. The singular stress has

been observed near the interface corner. Such residual stresses are large enough to initiate interface delamination to relieve the residual stresses. In this study, an epoxy material has been selected as being a technical interest. This method, however, can be extended to other types of polymeric materials.

Acknowledgments

This work has been supported by KESRI(R-2005-B-124), which is funded by MOCIE(Ministry of commerce, industry and energy).

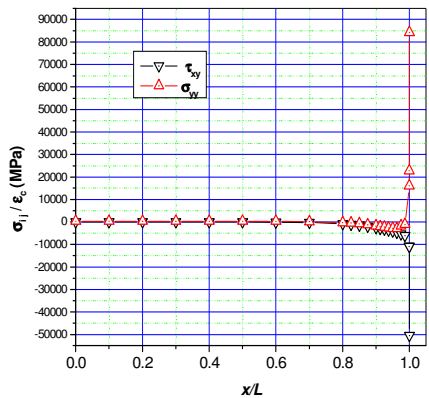

Fig. 4. Chemically induced residual stress distribution along the interface of the film.

References

1. G.G. Stoney: Proc. of the Royal Society(London), A82(1909), p.172.
2. S.P. Timoshenko: J. of the Optical Society of America, 11, 233(1925).
3. L.B. Freund: J. the Mechanics and Physics of Solids, 48, 1159(2000).
4. L.B. Freund and S. Suresh: Thin Film Materials (Cambridge, 2003).
5. S.S. Lee and R.A. Westmann: Int. J. Num. Meth. Engr.,38, 607(1995).
6. J.T. Pan and I.A. Blech: J. of Applied Physics, 55, 2874(1984).
7. C.A. Volkert: J. Applied Physics, 70 (1991).
8. A.L. Shull and F. Spaepen: J. Applied Physics, 80 (1996).

FATIGUE LIFE EVALUATION FOR THE FLOOR SYSTEM OF A STEEL RAILWAY BRIDGE

DONG-HO CHOI

Department of Civil Engineering, Hanyang University, Seongdong-gu Seoul, 133-791, Korea

HANG-YONG CHOI

Structure Division, Seoyeong Engineering Co., Ltd., Seocho-gu Seoul, 137-739, Korea

HOON YOO

Department of Civil Engineering, Hanyang University, Seongdong-gu Seoul, 133-791, Korea

JOUNG-SUN LEE

Department of Civil Engineering, Hanyang University, Seongdong-gu Seoul, 133-791, Korea

SEOK-KYUN PARK

Department of Civil Engineering, Daejeon University, Dong-gu Daejeon, 300-716, Korea

The coped stringers of this study cracked 94% in 13 years after opened. The connections of floor-beam and stringer were designed as a hinge with sharply notched cope on the web of stringers. Evaluation of the fatigue stresses, prediction of the fatigue life, and analysis for two repair methods at the crack details are presented. Fatigue loads are obtained by loading conditions, such as traffic schedules, passenger numbers and train coincidental placements on both tracks. Fatigue crack growth analysis is carried through the equivalent stress range obtained from a time history analysis. The results show that the maximum fatigue stress range of the repaired stringer may go down to that of infinite fatigue life.

1. Introduction

Some of the floor systems of railway bridges have no deck and ballast, while those of highway bridges have concrete decks. Due to the weight of the concrete deck, the members of railway bridges inherently carry less dead load than those of highway bridges. Therefore, the members of railway bridges are much vulnerable to fatigue crack than highway bridges [1,2].

The bridge, showed in Fig. 1 is Dangsan Bridge of Subway Line 2 over the Han River in Seoul, Korea. The bridge was 3 span continuous Pratt half through truss open deck steel structure. The connections of floor-beam and stringer were designed as a hinge with sharply notched cope on the web of stringers. Fatigue cracks were found on 94% upper coped section of stringers.

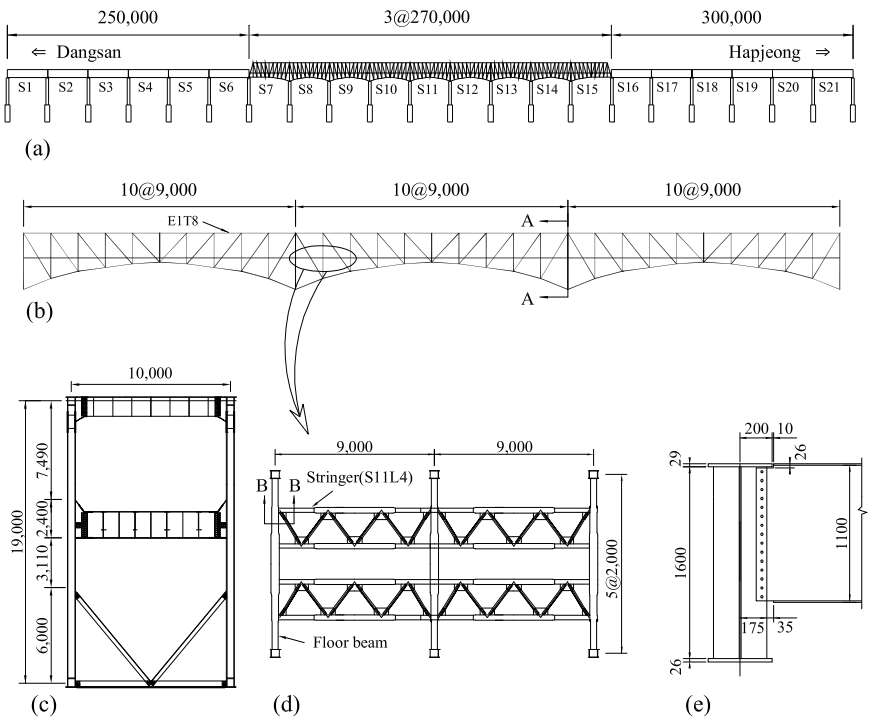

Fig. 1. Bridge profile (unit: mm): (a) overall profile; (b) main span(S10,S11,S12); (c) section A-A; (d) floor system; (e) section B-B.

2. Fatigue Loading

The fatigue life can be estimated based on the stress ranges obtained from the time history analysis of traveling subway trains. A train consists of 6 cars from May 1984 to December 1990 and 10 cars from January 1991 to December 1996. The live load of passengers is defined as the ratio of the number of on-board passengers to the regular passenger number(160 persons). The train weight and the passenger volume during the service life are provided in [3].

The total weight of the traveling trains can be obtained simply by adding the passenger weight to that of the train self-weight. All of mean train weight in each time is calculated by a cubic root mean method for reasonable fatigue loading. The number of traveling frequency during bridge's service life is tabulated in Table 1. The applied load cycles to calculate the fatigue loading are assumed to equal to the number of traveling frequency. The calculated fatigue loading was about 51% of the design loading.

Table 1. Number of the traveling frequency for one direction during bridge's service.

Trains	Operating duration	Frequency (day)	Operating duration(month)	Number of the traveling frequency	
6 cars	1984. 5.~1986. 2.	302	20	551,150	2,777,284
	1986. 2.~1986. 9.	393	7	251,028	
	1986. 9.~1989. 4.	390	31	1,103,213	
	1989. 4.~1991. 9.	455	21	891,893	
10 cars	1991. 9.~1992. 1.	535	13	1,057,739	5,839,095
	1992. 1.~1992. 9.	507	7	539,744	
	1992. 9.~1992.12.	489	3	223,106	
	1992.12.~1993. 8.	484	3	220,825	
	1993. 8.~1993.10.	489	7	520,591	
	1993.10.~1994. 3.	504	5	383,250	
	1994. 3.~1994.12.	535	9	732,281	
	1994.12.~1995. 1.	569	2	173,070	
	1995. 1.~1995. 3.	563	2	171,245	
	1995. 3.~1996.12.	569	21	1,817,244	
Total			151		8,616,379

Fatigue loading obtained by the cubic root mean method is summarized by

$$\left[\sum(Frequency \times Vehicle\ Loading^3)/Total\ Frequency\right]^{1/3} = 52.77\,\mathrm{kN}. \quad (1)$$

3. Time History Analysis

Dynamic tests have been conducted on the three-span continuous Pratt truss at normal operating speed, 80km/hr. Fig. 2 shows the results of stress time histories obtained from the field measurement and the FE analysis for the truss E1T8. Wheel load was directly applied on the stringer according to AREA [4] distribution for tie design. The connection of truss member has been analyzed with two types, fixed and pinned connection. The stress time history of fixed connection provided much better results than that of pinned connection although it produced a little higher than that of measured data in the field.

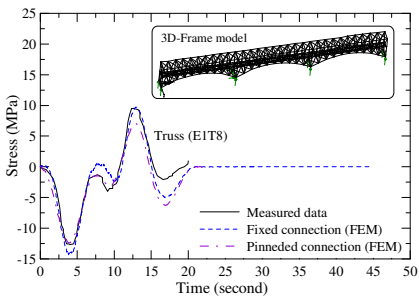

Fig. 2. Comparison field measurement with time history analysis for the truss E1T8.

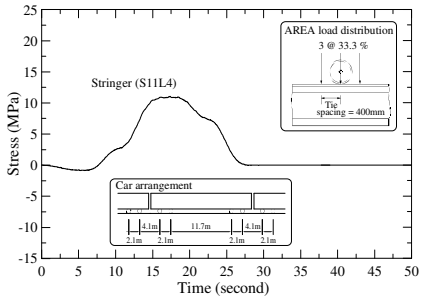

Fig. 3. Stress time history for the coped stringer S11L4.

The time history analysis for the stringer of the floor system was conducted on the coped stringer S11L4 which developed the maximum stress. Fig. 3 shows the stress time history of the stringer obtained from the FE analysis with the calculated fatigue loading. The equivalent stress range was evaluated from the root mean cube(RMC) stress range providing correlation with Miner's cumulative damage rule. The equivalent constant amplitude stress range for the coped stringer was 12.40MPa.

4. Fatigue Life Evaluation

4.1. *Fatigue Crack Growth Analysis*

Fatigue crack growth is expressed by the stress intensity factor(SIF) range ΔK and crack growth rate da/dN in the form [5]

$$da/dN = C(\Delta K)^m , \tag{2}$$

where material constants $C = 1.5\times10^{-11}$ and $m = 2.75$ as given in the JSSC fatigue design recommendations for steel structures [6].

The stress intensity factor range is given by [7]

$$\Delta K = F(a)\Delta\sigma\sqrt{\pi a} = F_e F_s F_w F_g \Delta\sigma\sqrt{\pi a} \ . \tag{3}$$

where the correction factor F_e=1.0, F_s=1.2 for the edge crack. The correction factor for stress gradient F_g was determined by repeating the integration of the stresses obtained from LUSAS [8] as shown in Fig. 4.

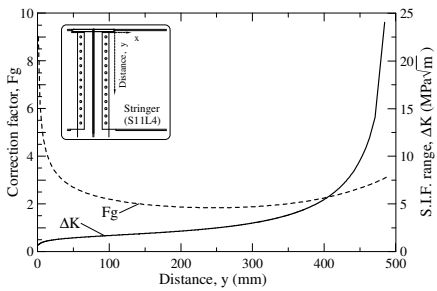

Fig. 4. Stress gradient factor and SIF range for the coped stringer S11L4.

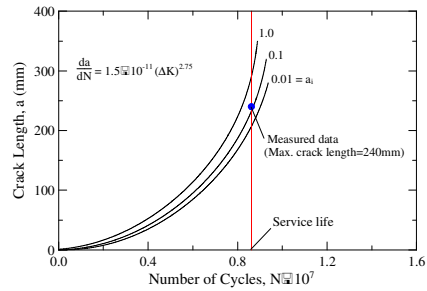

Fig. 5. Comparison of measured data and predicted crack growth curves.

Fig. 5 compares the measured data and predicted crack growth curves for the coped stringer S11L4. The maximum crack length of the coped stringer was 240mm after approximately 13 years of the service life. The effect of the initial crack length a_i on fatigue life was evaluated by varying the initial crack lengths. The fatigue life decreases as the initial crack length increases. The results of fatigue crack growth analysis using a_i=0.1mm was in good agreement with the measured data.

4.2. *Retrofitting Fatigue Crack*

The fatigue crack initiated at the corner of the coped stringer(S11L4) web and propagated downward. Fig. 6 shows the repair methods of the fatigue crack. The first method(Repair method I) is to drill a hole of *d*=20mm at the crack tip and the second method(Repair method II) is to drill a hole of *d*=20mm at the crack tip and then bolt a new plate to make moment connection.

Fig. 7 shows the predicted crack growth curves for two repair methods. The initial crack length used was 0.1mm. The fatigue life after the repair by the method I increased about 20% as much as the fatigue life of NO repair. The maximum fatigue stress range after the repair with the method II decreased by 45% and went down to the level where crack would not be expected to reinitiate. Retrofitting the bridge by employing the repair methods would control the fatigue propagation at stringer to floor-beam connections.

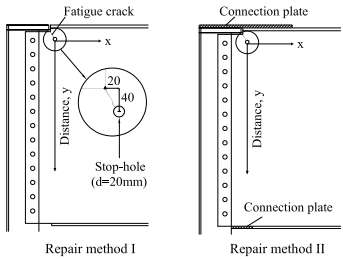

Fig. 6. Retrofitting the fatigue crack by two repair methods of stop-hole and connection plates.

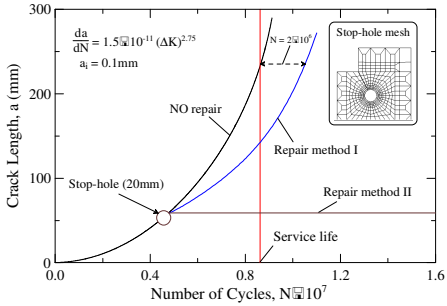

Fig. 7. Predicted crack growth curves for two repair methods.

5. Conclusion

Evaluation of the fatigue stresses, prediction of the fatigue life and analysis for repair methods at the crack details are presented. Fatigue crack growth analysis is carried through the equivalent stress range obtained from a time history analysis. The conclusions are as follows:

1) The stress time history of fixed connection provided much better results than that of pinned connection although it produced a little higher than that of measured data in the field.
2) The results of fatigue crack growth analysis are in good agreement with the measured data.
3) The fatigue stress range after the repair with the method II decreased to the level where crack would not be expected to reinitiate.

References

1. S. Kato, O. Yoshikawa, H. Terada and Y. Matsumoto, *Proc. of JSCE Struc. Engrg./Earthquake Engrg*. **2**(2), 455-472 (1985).
2. W. John, J.W. Fisher, T. Ben and D. Wang, *FHWA-RD*, 89-169 (1990).
3. S.H. Kim, S.W. Lee and H.S. Mha, *Engrg. Struct*. **23**, 1203-1211 (2001).
4. Manual for Railway Engineering, *AREA* (1994).
5. P.C. Paris and F. Erdogan, *J. Basic Eng*. **85**, 528-538 (1963).
6. Fatigue Design Recommendations for Steel Structures, *JSSC* (1993).
7. P. Albrecht and K. Yamada, *Proc. ASCE* **103**(ST2), 377-389 (1977).
8. LUSAS User's Manual - Version 13.6, *U.K. FEA Ltd*. (2004).

STRESS INTENSITY FACTOR CALCULATION ON CRITICAL POINTS OF RAILWAY BOGIE FRAME*

HYUNKYU JUN†

Korea Railroad Research Institute
Uiwang, Gyeonggi, 437-757, Korea

A stress intensity factor, SIF calculation method on a cracked railway bogie frame incorporating sub-modeling method was presented. For this purpose, a 3D FE model of railway bogie frame was built and performed structure analyses following UIC code. The locations of high stressed points were compared with the physical crack locations which were found at the railway bogies frame which had over 20 years of commercial line operation history. Base on the structure analyses results, we created a three dimensional crack on the railway bogie frame and applied two analysis methods to calculate the SIF. First, we created a sub-model and calculated the SIF by using the displacement field calculated from structure analysis. Second, we created a full FE model which was meshed from the geometry model of bogie frame and calculated the SIF directly. The proposed sub-modeling method to calculate the SIF was verified by comparing the analysis results. The analysis results showed a reasonable correlation.

1. Introduction

Railway vehicles, operated in urban area, run under very severe operating conditions of tight curves and frequent accelerating and braking. They induce high dynamic stresses and lead to the initiation of fatigue cracks on railway bogie frame. And eventually cause failure of railway vehicle. Railway bogie is the most important component to maintain running stability of railway vehicle. Although, the strength of a railway bogie is analyzed and proved to be safe in the design stage, the lifetime of railway bogie could be significantly reduced by the creation of crack during operation. But, most of researches on the prediction of lifetime of railway bogie have been focused on the crack initiation life.

On the recent close examination did in Korea on the railway vehicles which had more than 20 years of operation history in commercial line, several cracks were found in critical areas of bogie frame. Most of them were very short, but some of them were not. Therefore, to assure integrity for whole life cycle,

* This work is supported by Korea Research Council of Public Science & Technology

researches on the crack propagation in railway bogie frame and its effects on the lifetime and stability of railway bogie are highly necessary.

Fatigue lifetime analysis procedure on a railway bogie frame due to periodic in-service load was established well. Goo[1] suggested the lifetime assessment procedures of a bogie. He introduced a fatigue strength estimation procedure based on the modified Goodman diagram and evaluated the lifetime of bogie based on a cumulative damage rule. Yoon[2] also performed structural analysis on the bogie which is planned to use in Kwangju line railway vehicle in Korea and proved the structural safety of the bogie following UIC 615-4[3], JIS E 4207[4] and 4208[5].

But on the other hand, researches on crack propagation lifetime prediction on bogie frame were hardly to find. The FE models for structure analysis were often constructed by engineers to verify the safety of structure. But the FE models for crack evaluation were seldom constructed. Therefore it is very hard to construct a FE model for crack evaluation, if we do not have a geometry model, such as 3D cad model, of a structure. Therefore, a SIF calculation method needs to be developed even though we only have FE model for structure analysis.

In this paper, we suggest a procedure for calculating the SIF with FE model for structure analysis by incorporating sub-modeling method. For this purpose, we created a 3D FE model of railway bogie frame for structure analysis as a global model and created a crack model as a sub-model. And we calculated the SIF and verified the procedure by comparing the SIFs from sub-modeling method and those of full FE model, constructed from a geometry model.

2. Stress Intensity Factor Calculation Procedure

2.1. *SIF Calculation Procedure*

Figure 1 shows the procedure to calculate SIF of crack by incorporating sub-modeling method. Since the sub-modeling method use displacement field of global model at boundary, it is important to locate exact crack location and make a crack in the model by dividing element of global model. To calculate SIF of cracked structure, we performed stress analysis on global model and found a critical location. Then we made a crack at the location and recalculated displacement field around the crack. Finally by importing the displacement field around crack, we could calculate J-contour integral on the crack. The results were verified by checking the stress field of global model and those of sub-model at boundary.

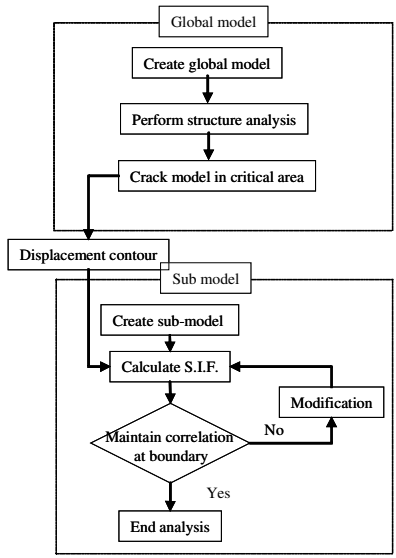

Fig. 1. Stress intensity factor calculation procedure by incorporating sub-modeling method

2.2. *Center Cracked Plate in Tension*

To verify the SIF calculation procedure, the SIF of a center cracked plate in tension load was calculated. Figure 2(a) shows geometry of a center cracked plate model under remote tension load. Figure 2(b) is a global model to calculate displacement field. Figure 2(c) is a sub-model to calculate SIF. The SIF of the plate can be calculated theoretically using Eq. (1).

$$K_I = \sigma\sqrt{\pi a}\cdot f(2a/W) \tag{1}$$

$$\xi = 2a/W$$
$$f(\xi) = \sqrt{\sec(\pi\cdot\xi/2)} \text{ or}$$
$$= (1-0.025\xi^2+0.06\xi^4)\sqrt{\sec(\pi\cdot\xi/2)} \text{ or}$$
$$= (1-0.5\xi+0.370\xi^2-0.044\xi^3)/\sqrt{1-\xi}$$

The magnitude of crack length, *2a* was assigned as 6 mm and the width and height of plate was both 100 mm. The remote tension stress was assigned as 20 MPa. The elastic modulus of material was 207 GPa and Poisson's ratio was 0.3. The sub-model was created around the crack area which width and height were both 20mm as shown in Figure 2(c). To calculate the SIF, 5 *J*-contour paths

around the crack tip were created and commercial stress analysis software, ABAQUS ver. 6.7 was used. The SIF of the plate by Eq. (1) was calculated as 61.53 $MPa\sqrt{m}$ and that of finite element was 61.44 $MPa\sqrt{m}$. The difference of results between analytical method and sub-modeling method was 0.2% only.

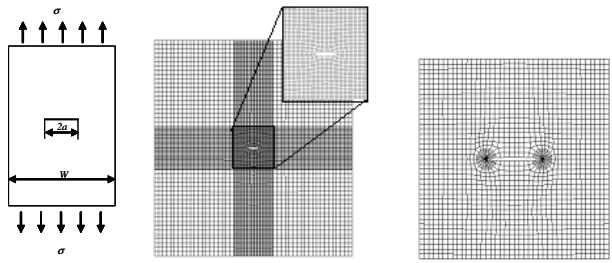

(a) Center cracked plate (b) Global model (c) Sub-model

Fig. 2. Finite element analysis on a center cracked plate using sub-modeling method

3. Bogie Frame Analysis

Since the sub-modeling procedure for calculating SIF of a cracked structure was verified, we applied the procedure in calculating the SIF of cracked railway bogie. The analysis model implemented in this research is the bogies which had over 20 years of commercial line operation history. Based on the close examinations of railway bogie, we could assure the size of crack and location near the critical area of railway bogie. Figure 3 shows critical areas of bogie. The point is the welding spot to connect a side frame and a transom. Based on the results of close examinations, we modeled a 100mm vertical through-wall crack at red marked point.

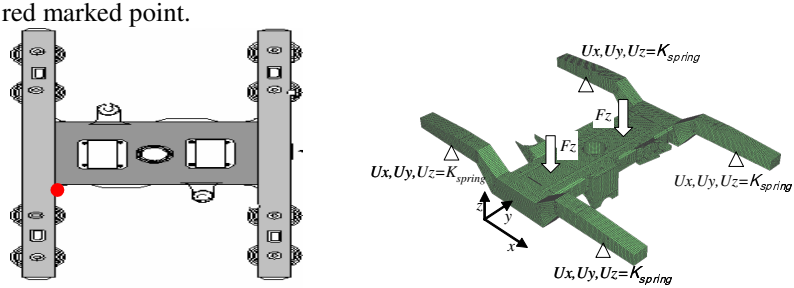

(a) Crack location (b) Loading and boundary condition

Fig. 3. FE analysis condition of railway bogie frame

Figure 3(b) shows the loading and boundary condition of FE analysis model. The model was constructed with 8 node shell element. Total numbers of element are 49,701 and those of node are 46,959. The load per bogie, F_z was calculated as

Eq. (2). The pure weight of each passenger car, W_t was defined as 41.5 ton and the passenger load, W_p was defined as 30 ton. The weight of a bogie is 14.0 ton and the weight under the secondary spring, W_u was defined as 6.5 ton. The applied load per bogie was calculated from the following equation.

$$F_z = (W_t + W_p - W_u)/2/2 \tag{2}$$

Displacement field around the crack location was obtained by performing structure analysis. And the results were imported to the sub-model to calculate the SIF. To model a crack at the critical area of bogie, we made finer meshes near critical area as shown in Figure 4(a) and modeled a crack by detaching nodes at crack face. We obtained the displacement field of cracked railway bogie by re-performing stress analysis. The field was imported to the sub-model as shown in Figure 4(b) and finally the SIF of cracked bogie could be calculated.

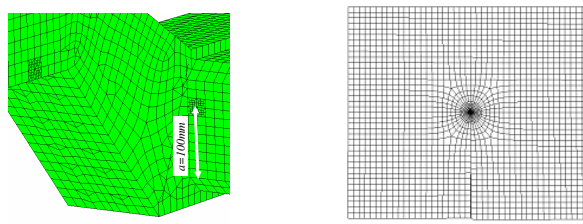

(a) Global model (b) Sub-model

Fig. 4. FE model for applying sub-modeling method

Figure 5 is the full FE model, constructed to verify the sub-modeling method. To construct the model, we made a geometry model of railway bogie frame as shown in Figure 5(a) and meshed a FE model which included the same crack as shown in Figure 5(b). The analysis condition was the same as the sub-modeling method.

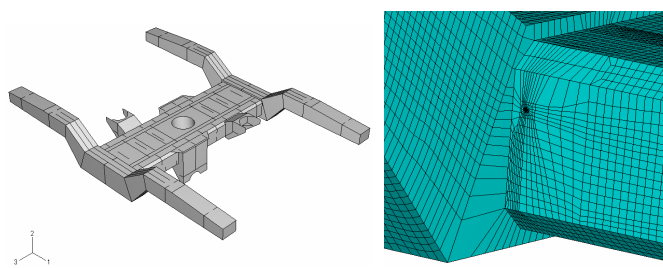

(a) Geometry model (b) FE model with crack

Fig. 5. FE model for calculating SIF generated from the geometry model of bogie frame

Figure 6 is the comparison of SIF calculation results by varying the crack length as 25mm, 50mm, 77mm, 90mm, 95mm and 100mm. The hollow marks represent the SIFs calculated by applying the sub-modeling method and the solid marks represent those of full modeling method. The averaged difference between SIF from the sub-model and the full model was around 7% and the results showed a reasonable correlation.

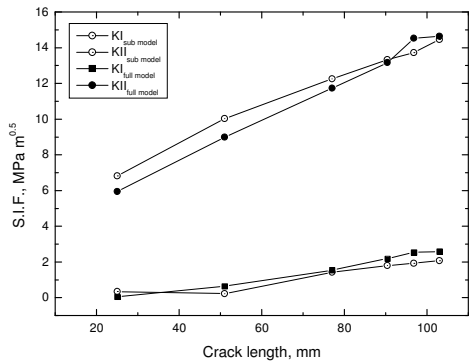

Fig. 6. Comparison of the SIFs calculated by sub-modeling method and full FE modeling method

4. Conclusion & Discussion

Building a cracked FE model is a very hard and tedious work, especially if there aren't any geometry models such as a 3D cad model. In this study, we proposed a sub-modeling method to calculate the SIF from the FE model for structure analysis without creating a crack model. The proposed method showed a reasonable correlation compared to the results from the full FE model.

The displacement field around crack front is very important to determine the accuracy of analysis result. But sometimes the region is not wide enough due to geometry limitation and it can cause error in calculating the displacement field. Therefore it is necessary to consider wider region as boundary if possible.

References

1. B.C. Goo, *Proceedings on Cumulative Fatigue Damage*, 130 (2003).
2. C.H. Yoon, W.K. Kim and J.G. Kim, *Key Engineering Materials*, **326**, 1087 (2006).
3. UIC, *UIC CODE 615-4* (2003).
4. JARI/JSA, *JIS E 4207* (2004).
5. JARI/JSA, *Japanese Industrial Standards Committee, JIS E 4208* (2004).
6. H. Nakamoto, H. Homma, S.Suzuki and S.Kusutani, *Transaction of JSCES, Paper No. 20040007* (2004).

A STUDY ON PARTIAL SIDE WEARS FOR THE BRAKE SYSTEM OF RAILWAY VEHICLES*

JOON HO SONG, SEUNG HYUN YOO, DAE JIN OH, DHANESHWAR MISHRA

Mechanical Engineering, Ajou University, 209 East-Hall WonChun-dong PalDal-gu, Suwon 442-749, Korea

DONG HYUN JO

R&D Department, Yujin Machinery LTD., Wonsi-Dong Ansan, Korea 425-852

The HSR-350x (high-speed rail 350x), also known as Korean G-7, is the experimental high speed train which was developed independently by G-7 R&D Project. The G-7 is now being investigated for its performance and tested at the high speed line. Partial side wear occurred in proposed braking system more than in KTX (Korean Train Express) according to experiment. In this study, comparison between KTX, KTX-II and G7 models of caliper unit of brake system has been done using FEM. The factor of generated partial side wear was investigated by comparing with results. Suitability of the caliper unit with KTX-II would be verified.

1. Introduction

To verify the durability and reliability of the caliper unit that play important roles as the brake on G7, which is a test vehicle of the Korean high-speed railway, a friction braking experiment was implemented. In this experiment, partial side wear appears to occur more than the preexisting high speed railway KTX. A finite element analysis was conducted in this research on the caliper units of the preexisting KTX, test vehicle G7, and the high-speed railway of the next generation, KTX-Ⅱ. The relevance of the caliper unit that is to be applied to KTX-Ⅱ was verified by comparing and analyzing the results.[1]

2. Finite element analysis

2.1. *Geometry*

The caliper, which is utilized as the friction-braking device of Korean high-speed railway, is made up of many parts, as shown in Fig 1. The braking force

* This work is supported by Yujin Machinery LTD.

passes the lever and pad holder and goes on to the brake pad. It causes friction with the disc, and thus triggers a brake. The three kinds of calipers used in this research are similar in shape, but it was modeled in regard to the difference of lever proportion and stud location.[2][3]

2.2. *FE modeling*

Hyper-mesh and ABAQUS(V6.5). were used for modeling and analysis, respectively. The elements used in analysis were C3D10 (10-node quadratic tetrahedron), C3D4 (4-node linear tetrahedron), R3D3 (3-node 3-D rigid triangular facet), etc. The two pins were designed with R3D3 so that the pad holder and the lever could be connected movable. [4][5]

2.3. *Boundary conditions and loads*

As shown in Fig. 1, the brake disc has been entirely fixed, and then the central pin has been restrained except for the rotation in the x-axis direction in this analysis. The brake cylinder output value was applied to the pin at the end of the lever for analysis. The disc was rotated counter-clockwise in the direction of the z-axis for the analysis including the disc rotation.

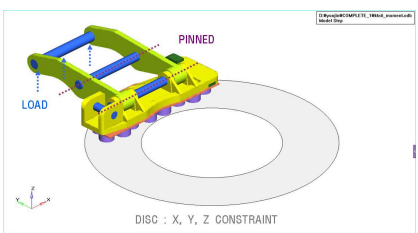

Fig. 1. Geometry

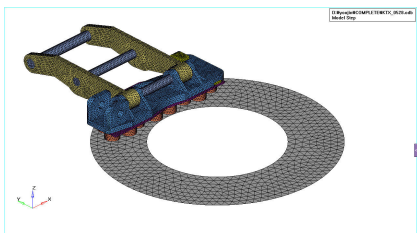

Fig. 2. FE model

3. Results

3.1. *Method*

The wear rate (δ) of the pad is proportionate to the friction and the friction is proportionate to the vertical force (stud contact normal force) of the friction surface. Thus, the wear rate of each stud depends on the contact normal force.

$$\delta \propto \mu N \rightarrow \delta \propto N$$

Therefore the partial side wear on the pad can be indirectly estimated by examining the distribution of contact normal force on the stud. The values in this analysis are the contact normal force of the stud on each pad. The cause and tendency of the partial side wear is understood through observing the distribution of 18 contact normal force values. The analysis method is to observe the change

of the stud contact normal force by applying various factors that are expected to influence the partial side wear. The contact normal force per stud is the value of contact pressure distribution of each stud integrated by the area. The measurement unit of the contact normal force is Newton (N), and there is a single value for each stud.

3.2. *Effect on disc rotation*

To examine the factors of partial side wear according to braking speed, the disc was rotated counter-clockwise in the direction of the z-axis (Fig 1). The rotation speed was 60.387rad/s and 181.16rad/s respectively, and the cylinder pressure was 4.3bar.

When the disc is rotated, the contact pressure distribution tends to center more on the rotation direction, than when the disc is not in motion. Therefore, disc rotation is considered as a factor of partial side wear. However as shown in Fig 3, the contact normal force distribution is not affected by the rotation speed.

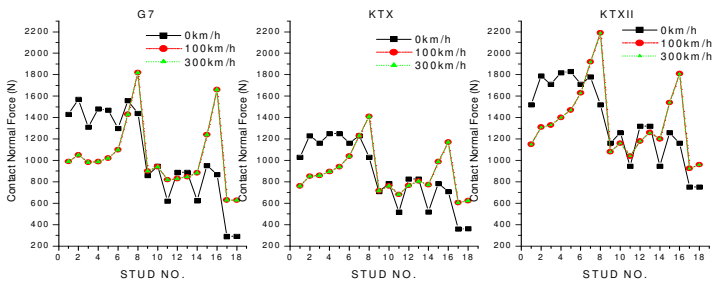

Fig. 3. Contact normal force according to braking speed

3.3. *Effect on increased braking cylinder output*

The stud contact normal force distribution was examined in proportion to the total normal force and braking cylinder output normal force. The output values used are the following.

Table 1. Braking cylinder output

	Step1[1bar]	Step2[2bar]	Step3[3bar]	Step4[4.3bar]
KTX	2.4 kN	6.5 kN	10.5 kN	14.5 kN
KTXII	3.3 kN	8.3 kN	13.3 kN	18.2 kN
G7	1.7 kN	4.8 kN	8.0 kN	11.2 kN

The disc was analyzed in two ways: when it is not in motion, and when it is rotating at the speed of 300km/h. The partial side wear of the railway pad is generating in the direction of the disc radius. Therefore as shown in Fig 4, the pad needs to be divided into three parts and the average of the stud contact

normal force needs to be measured at each section. Also, out of the three averages, the ratio of the maximum (A) and the minimum (C) were measured and compared with.

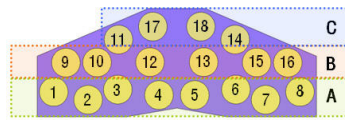

Fig. 4. Divided three parts

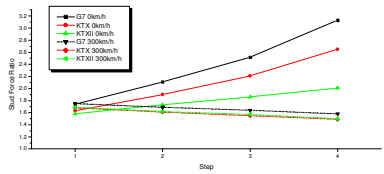

Fig. 5. Contact normal force

Under the premise that the pad wear rate (δ) and contact normal force are proportionate, the ratio of contact normal force is an invariable number that can estimate the relative difference in wear rate. As shown in Fig 5, the difference of the ratio of contact normal force is severe between the immobile disc and the rotating one. In the comparison of the contact normal force ratio, a mobile analysis in regard to the disc's rotation is essential because the abrasion of a pad cannot occur in an immobile state.

In a mobile analysis, the contact normal force ratio is reduced up to 10% in every model, as the cylinder output increases. Due to this fact, it is safe to conclude that changes according to cylinder output are small. The difference in the ratio for each model is also around 6% (Fig. 6-8).

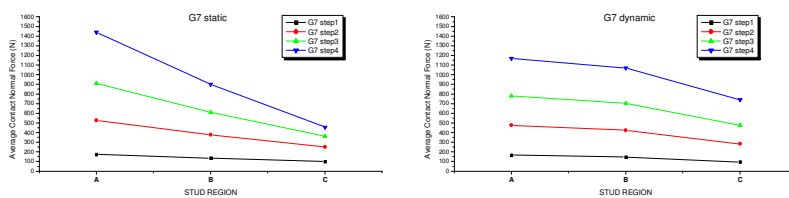

Fig. 6. Stud contact normal force (G7, braking speed = 0, 300km/h)

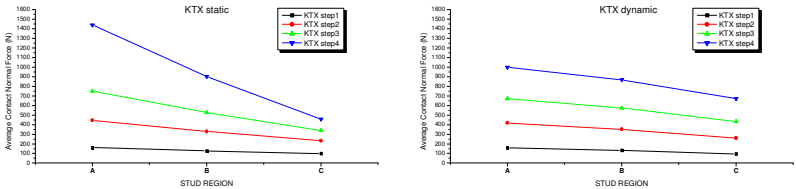

Fig. 7. Stud contact normal force (KTX, braking speed = 0, 300km/h)

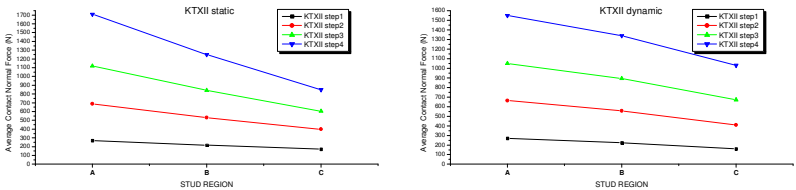

Fig. 8. Stud contact normal force (KTXII, braking speed = 0, 300km/h)

3.4. *Comparison with each models in same force condition*

The distribution of the stud contact normal force was examined when the same amount of total contact normal force was applied to each model. In a total of 4 steps, contact normal force was applied to the pad (Table 2). The cylinder output value was also adjusted so that the same amount of contact normal force was applied to each model.

Table 2. Contact normal force applied to the pad

step1	step2	step3	step4
2.5 kN	7.3 kN	12.0 kN	16.8 kN

The disc was analyzed in two situations: when it is immobile, and when it is rotating at the speed of 300km/h.

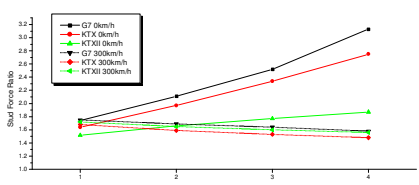

Fig. 9. Contact normal force ratio

As shown in Fig. 9, the ratio decreases up to 12% as the contact normal force increases on the pad. However, this is considered small. The ratio difference for each model is around 7%.

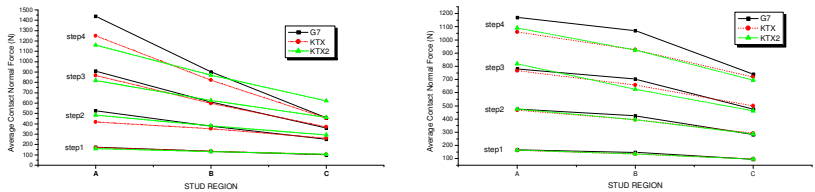

Fig. 9. Stud contact normal force (braking speed = 0, 300km/h)

4. Conclusions

The results from this analysis for the expected factors that influence partial side wear on brake pads can be summarized as follows.

As shown in Fig 3.4, the partial side wear ratio for each model when the same contact normal force is applied increases in the order of KTXⅡ < KTX < G7. As the contact normal force increases, the difference between the models also increases. The maximum difference reached 170% when the cylinder pressure was 4.3 bars. However, the order of the partial side wear ratio is KTX < KTXⅡ < G7 in regard of rotation as shown in 3.2. Contrary to the immobile models, the difference reduced greatly to 5%. Furthermore, there was no change in the distribution of the stud contact normal force, according to brake speed. Thus, there was also no change in the partial side wear ratio.

The partial side wear ratio increased as the total contact normal force of the pad elevated from the brake cylinder output value differences as shown in 3.3. The incremental amounts were in the order of KTXⅡ < KTX < G7. For G7, which had the biggest incremental amount, the partial side wear ratio was 170% at 4.3 bars, compared with the ratio at 1 bar. Also, the partial side wear ratio in rotation increased as the total contact normal force increased. However, the difference was small at about 10%. All the models did not show a significant change in the partial side wear ratio according to the total contact normal force.

As a result of the implementation of finite element analysis on the partial side wear of KTX, G7, and KTXⅡ caliper units, the adequacy of the caliper units that will be used on KTXⅡ could be verified.

References

1. S. W. Kim, Y. G. Kim, C. K. Park, T. W. Park, A Study on the Measurement of Disc-Pad Friction Coefficient for HSR-350x, *Korean Society for Railway*, Vol. 9 (2006), p. 677~681

2. N. K. Kim, J. P. Kang, FEM Analysis of Caliper Housing Cut Inside Upper Face for Unbalance Wear Prevention of Disk Brake Pad, *Journal of The Korean Society of Manufacturing Technology*, Vol. 1 (2002), p. 89~100
3. K. Y. Kim, S. H. Kim, Y. S. Kim, B. J. Lee, S. W. Kim, Development of the Sintered Friction Material for the High Speed Railway, *Korean Society for Railway*, Vol. 1 (2004), p. 163~169
4. ABAQUS User's Manual, *Hibbitt, Karlsson & Sorensen*, Inc., (2004)
5. X. Loranga, F. Foy-Margiocchib,_, Q.S. Nguyena, P.E. Gautierb, TGV disc brake squeal, *Journal of Sound and Vibration*, Vol. 293 (2006), p. 735–746

SENSITIVITY FOR INTERNAL AND SURFACE DEFECTS OF RAILWAY WHEEL USING INDUCED CURRENT FOCUSING POTENTIAL DROP*

SEOK JIN, KWON†

Railway System Research Department, Korea Railroad Research Institute, 360-1 Woulam-dong, Uiwang-City, Kyounggido, 437-757, Korea

DONG HYUNG, LEE

Railway System Research Department, Korea Railroad Research Institute, 360-1 Woulam-dong, Uiwang-City, Kyounggido, 437-757, Korea

JUNG WON, SEO

Railway System Research Department, Korea Railroad Research Institute, 360-1 Woulam-dong, Uiwang-City, Kyounggido, 437-757, Korea

The damaged railway wheel in running would cause a poor ride comfort, a rise in the maintenance cost and even a fracture of the wheel, which then leads to a tremendous social and economical cost. It is important to detect defect of internal and surface in railway wheel. Recently, many searchers have actively tried to improve precision for defect detection of railway wheel. However, it is very difficult to find the internal defects in wheel. In the present paper, the new NDT method is applied to the detection of surface and internal defects for railway wheels. To detect the defects for railway wheels, the sensor for new NDT is optimized and the tests are carried out with respect to 8 internal defects each other. The result shows that the internal crack depth of 1 mm from wheel surface could be detected by using new NDT method.

1. Introduction

The fatigue cracks are initiated in railway wheel tread which suffer from rolling contact fatigue damage [1]. Fatigue failures are much more than violent wear and may cause a part of the wheel to break off, leading to damage to the rail and to train suspensions and bearings and may even cause derailment. Although the wheel materials are considerably improved, the damages of the railway wheels have continuously occurred. If the inspection interval of the wheel could be extended by high quality NDT, the maintenance costs for railway

* This work is supported by Ministry of Construction and Transportation of Korea

†

wheel would decrease significantly. Rainner et al. [2] reported on ultrasonic testing and eddy current inspection for inner detection of wheel. However, these methods are difficult to find the sub-surface crack. Kendserian et al. [3] have researched the defect inspection of railway wheel using LAHUT (Laser-Air Hybrid UT). The method has an advantage which a defect of wheel surface can be scanned in railway depot but it is not unavailable in an inspection of internal defects. Therefore, it is necessary to develop a non-destructive technique that is superior to conventional NDT techniques in order to ensure the safety of railway wheel. The induced current focusing potential drop technique (ICFPD) is a new non-destructive testing technique that can detect cracks in railway wheels by applying on electro-magnetic field and potential measurement [4]. In the present paper, the detection sensitivity of the surface and internal defect of railway wheel by using ICFPD are evaluated.

2. Defects in railway wheel

Fatigue cracks are initiated in wheel tread, rim and flange that suffer from rolling contact fatigue damage. The actual fatigue cracks of wheel tread are occurred from the wheel tread surface and at 3 mm from the inner of the wheel tread surface in the radial direction [5]. Generally, the fatigue cracks of railway wheel have initiated at a depth of 10~25 mm and at a depth of some 3~5 mm below the wheel tread. The crack propagation at an almost constant depth below the wheel tread corresponding to the depth of initiation. The face of the crack that initiates in the wheel is almost perpendicular to the longitudinal axis. In order to detect cracks in wheel tread, new NDT sensors must be located at positions apart from the crack. In order to detect the crack in railway wheel, the pick-up pins must be positioned at a certain distance from the crack. Therefore, the pick-up pins and induction wire must be rearranged to a direction of parallel to the location of crack initiation.

3. Experimental procedures

3.1. *Test specimens*

The railway wheel used for this test was the rolling contact fatigue specimen and had artificial flaws 0.5, 1.0, 1.5, and 2.0 mm depth. The ICFPD sensors with 5 mm pick-up distance(i) and induction wires 40 mm length can detect cracks in the radial direction. Figure 1 show the artificial crack size used in the tests. The tests are carried out with respect to 4 surface defects and 3 inner defects each other. The geometries of the surface defects are used semi-elliptic crack which initiated in railway wheel.

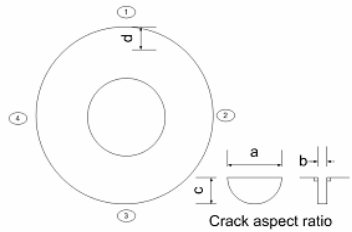

defect / position	surface defect(mm)		inner defect(mm)	
	depth(c)	length(a)	distance(d)	diameter(ϕ)
①	2.0	8.0	0.3	1.5
②	1.5	6.0	0.5	
③	1.0	4.0	0.7	
④	0.5	2.0	1.0	

Fig. 1. Artificial crack sizes for test

3.2. *Measuring system*

Figure 2 shows the measuring system used in the tests. The measuring system consists of the measuring sensor, a jig for controlling the contact force between the pick-up pins and the rail, a device for measuring potential drops. The measuring system for crack detection for railway wheel can easily measure azimuthal direction of the crack by installing casters underneath the railway wheel and indicating the rotation angle on an attached graduator. Also, the measuring system can be moved to the axial direction and constantly sustained the contact force between the pick-up pins and the wheel tread. The scanning for defects of specimen was performed in the azimuthal directions of railway wheel. The scanning interval is 5mm and the potential drops had been measured with respect to unknown defect position.

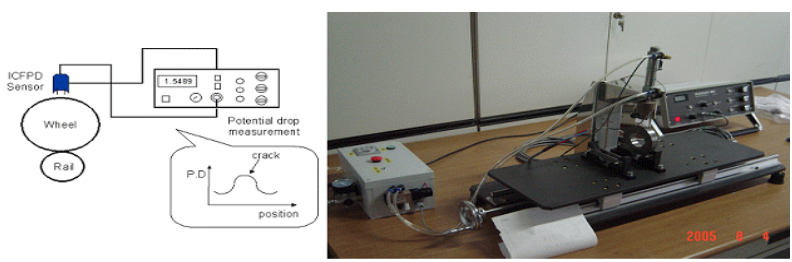

Fig. 2. Measuring system

4. Experimental results &discussions

4.1. *Surface defects*

The variations of potential drops in accordance with the difference of crack depth with respect to the surface defect of wheel are shown in Figure 3 and

Figure 4. The cracks in the railway wheel were inspected in the azimuthal direction. As can be seen from Figure 3, the potential drop for the sensor with a 10 mm distance between pick-up pins increased remarkably at 0 mm distance which defect is existed and decreased at other locations. It is thought that pick-up pins distance close together can scan regions of high current density, which is the sensor with pick-up pins close together can measure the potential drops more sensitivity. It was shown the potential drop increased remarkably at the crack location. It is clear, therefore, that cracks can be detected at crack depth of 0.5mm. In case of ICFPD technique, the variations of potential drops without defect are not appeared and the variations of potential drops with defect are considerably occurred as can be seen from Figure 4.

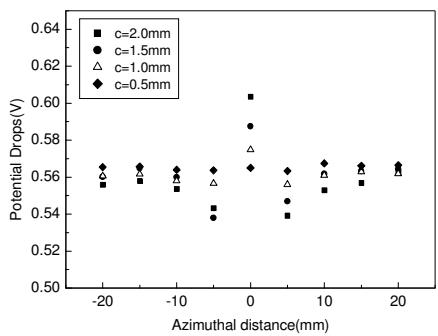

Fig. 3. Variations of P.D at pick up pin=5mm

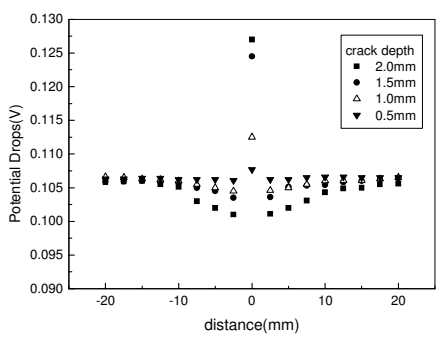

Fig. 4. Variations of P.D pick up pin=5mm

The variation of potential drop by pick up interval 5 mm is shown in Figure 4. As can be seen from Figure 3 and Figure 4, 0.5 mm defect can be detected. As can be seen from Figure 4, crack detection with a pick up interval 5 mm demonstrated good results. Totally, Induced current in surface of a specimen flows in the opposite direction of the current in an induction wire. Lorenz forces create on attraction force because the induced currents that are distributed underneath the induction wire all flow in the same direction. As shown in Figure 6, a part of the induced current around the induction wire is attracted to the region of high current density and the current density around the induction wire decreases. According to this mechanism, it is suggested that the potential drops decrease as the induction wire is close to the discontinuity.

4.2. *Internal defects*

Figure 5 and Figure 6 show the variation of the potential drop with respect to internal defect, it can be seen that a variation of the potential drop occurred at the location of the 1.0 mm from wheel surface. There was a distinct variation of potential drop that occurred with respect to the 2 mm crack at 1.0 mm wheel surface, as shown in Figure 6. The results show that for the railway wheel with fatigue cracks, 0.5 ~ 2.0 mm deep crack can be clearly detected at a wheel surface and inner crack. Furthermore, this result shows that the accuracy of the crack detection of the newly suggested ICFPD technique is superior to UT, which could only detect the 3 mm deep crack in railway wheelset. As can be seen from Figure 5 and Figure 6, it is evident that the newly suggested ICFPD technique can detect cracks in a railway wheel.

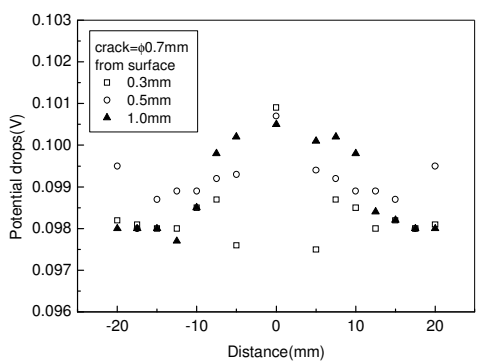

Fig. 5. Variations of P.D at crack=0.7mm

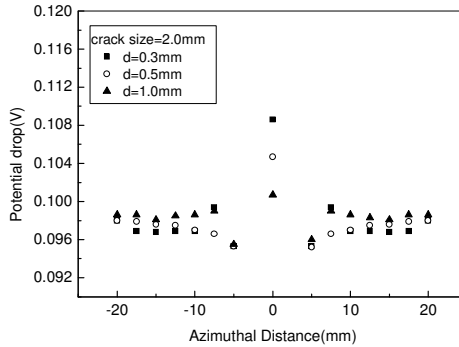

Fig. 6. Variations of P.D crack=2.0mm

5. Conclusion

The surface and internal defect of railway wheel are evaluated by using ICFPD. Obtained results are summarized as follow.

(1) The newly suggested ICFPD technique can detect cracks from 0.5 mm to 2.0 mm deep in a surface of railway wheel.
(2) The internal defects can detect the crack of 2 mm at 1 mm apart from the surface of wheel tread.

From the above results, the ICFPD technique is useful for detecting the cracks that initiated in railway wheels. In future works, the detection sensitivity in accordance with the crack size and surface distance from wheel tread will conduct.

References

1. A. Ekberg, J. Marais, Pro. Inst. Mech. Eng. Part F., Vol. 214, (2000).
2. V. Esslinger, R. Kieselbach, R. Koller, B. Weisse, Eng. Fail. Anal., Vol. 11, (2004).
3. P. Rainer, A. Erhard, H.-J. Montag, H.M. Thomas, NDT & E inter, Vol. 37, (2004).
4. S. Kenderian, D. Cerniglia, B. B.Djordjeve, G. Garcia, 16th WC NDT, (2004).
5. Seok-Jin Kwon, Jung-Won Seo, Dong-Hyung Lee, Chan-Woo Lee, 2nd JSME/ASME ICMP, (2005).

THE EFFECT OF THE EVOLUTION OF CONTACT SURFACE PROFILE ON FATIGUE CRACK NUCLEATION SITE IN PRESS-FITTED SHAFT

DONG-HYONG LEE, SEOK-JIN KWON

Railway System and Safety Research Department, Korea Railroad Research Institute, Wolam 374-1, Uiwang, Kyonggi, 437-050, Korea

JAE-BOONG CHOI, YOUNG-JIN KIM

School of Mechanical Engineering, Sungkyunkwan University, Jangan-gu, Suwon, Kyonggi, 440-746, Korea

The objective of the present paper is to evaluate the effect of the evolution of contact surface profile by fretting wear on fatigue life of press-fitted shaft by means of an analytical method based on experimental data. A finite element analysis was performed to analyze the stress states of press-fitted shaft, considering the worn surface profiles of shaft. The evolutions of contact stress and fatigue crack nucleation site as wearing of contact surface were evaluated by finite element analysis and fretting fatigue damage parameter (FFDP). It is found that the stress concentration of contact edge in press-fitted shaft decreases rapidly at the initial stage of total fatigue life, and its location shifts from the contact edge to the inside with increasing number of fatigue cycles. Thus the change of crack nucleation position in press-fitted shaft is mainly caused by stress change of contact edge due to the evolution of contact surface profile by fretting wear.

1. Introduction

Because axles are one of the most critical components in railway vehicles for safety and reliability, there have been many studies on fatigue strength and maintenance methods to prevent axle's failure [1, 2]. However, a small number of axle failures still occur in practice [1, 3]. There should be many reasons, but the dominant cause is that the fretting which occurs in press fits involves with various phenomena at the same time, and there are still lacks of understanding on the characteristics of fretting damage [1, 2].

Thus, the present study mainly focuses on the effect of the evolution of contact surface profile by fretting wear on contact variables of press-fitted shaft through the analytical method based on the experimental data. The effect of fretting wear on contact stress and fretting damage of press-fitted shaft are evaluated applying finite element method and fretting fatigue damage

parameter(FFDP), considering the worn contact profiles of shaft. The effects of the evolution of surface profile on fretting damage of press-fitted shaft are discussed.

2. Analysis

2.1. *Finite element modeling*

In order to calculate a stress distribution of press-fitted and loaded condition before and after fretting wear, a commercial FE code ABAQUS [4] which is widely used in the non-linear numerical analysis was used. The press-fitted specimen was modeled using asymmetric-axisymmetric element (CAXA4R4) and the details of modeling method refer to authors' previous report [5]. The noticeable features of the analysis are described briefly below.

The surface of the shaft is defined as axisymmetric slide line contact elements (ISL21A) as slave surface and the contact surface of the boss is defined as slide line as master surface. Because the contact stresses and strains are greatly changed at the contact edge and the micro-slip exists in local area, a fine mesh with an element width 0.015mm was used near the contact edge. The tolerance of press-fitted specimens was adopted interference condition as same as specimens used in the experiment. The friction coefficient μ is applied as 0.6 to analyze frictional behavior of press-fitted contact region. A Lagrange multiplier formulation is used for the resolution of the stick/slip behavior between two contact surfaces.

2.2. *Contact stress analysis*

The surface profiles from contact edge to 1mm inside of press-fitted assemblies were considered in finite element analysis because there is no change of surface profile more than 1mm inside of contact edge from experimental observations. Only the surface profiles of shaft were reflected in stress analysis because the change of contact surface profile is rarely happened to the surface of boss. The worn surface profiles from experiment were applied as fitted curve to remove irregular shape by wear particle in FE model. Fig. 1 shows an example of comparison between measured surface profiles (dotted lines in Fig. 1) and fitted surface profiles (solid lines in Fig. 1) that are applied in analysis, which represent well the evolution of wear characteristics of contact edge according to the fatigue cycles. The analysis was carried out to 25% fatigue cycles of total fatigue life to evaluate variations of contact stress by fretting wear to the early stage of life.

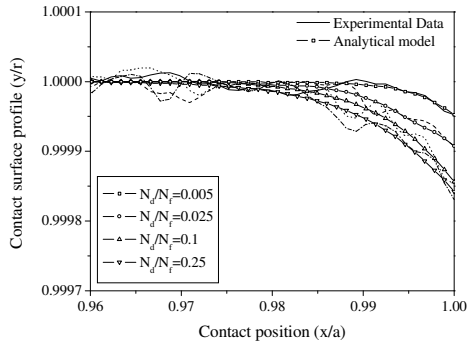

Fig. 1. Contact surface profile measured and adopted in FE analysis.

2.3. *Stress concentration and fretting damage*

The evolutions of stress concentration based on the result of stress analysis with finite element method are calculated considering the worn contact surface profiles which are obtained from experiment [6]. The contact edge of shaft shows a multiaxial state of stresses when a bending load is subjected. Therefore, equivalent stress amplitude $\sigma_{eq,a}$, according to the von Mises theory, was calculated using the amplitude of principal stresses $\sigma_{1,a}$, $\sigma_{2,a}$ and $\sigma_{3,a}$ at contact interface as follows:

$$\sigma_{eq,a} = \frac{1}{\sqrt{2}}\sqrt{(\sigma_{1,a}-\sigma_{2,a})^2+(\sigma_{2,a}-\sigma_{3,a})^2+(\sigma_{3,a}-\sigma_{1,a})^2} \tag{1}$$

Elastic stress concentration factor K_t is defined as the ratio of equivalent stress amplitude $\sigma_{eq,a}$ to nominal bending stress $\sigma_{no\min al}$ as follows:

$$K_t = \sigma_{eq,a} / \sigma_{no\min al} \tag{2}$$

Fretting Fatigue Damage Parameter (FFDP) was calculated to evaluate the effect of fretting wear on the variation of crack initiation site. Ruiz et al. [7] proposed FFDP which is based on frictional work in contact interface, and FFDP is applicable only to the fretting fatigue condition. FFDP was formulated by combining the effects of the surface tangential stress σ_T, the surface shear stress τ and the slip δ at the contact interface. This parameter is as follows:

$$FFDF = \sigma_T \tau \delta \tag{3}$$

It has been reported in the literature [8] that this parameter could predict the location of crack initiation in fretting fatigue environment.

3. Result and discussion

3.1. *Evolution of contact stress*

Fig. 2 shows the variation of equivalent stress amplitude of the contact surface with an increase of fatigue cycle number under loading condition of 180MPa. In this figure, a horizontal axis is shown by dividing contact length (a=14.5mm) and the position of x/a=1 is indicated the contact edge and a vertical axis is represented by dividing contact pressure by nominal contact pressure (p_n).

The stress amplitude is maximum in the contact edge at the initial contact condition, however, as the fretting wear is proceeded, the maximum stress amplitude is rapidly reduced at early stage of total fatigue life. The position of maximum bending stress amplitude is moved from contact edge to the inner side of contact edge after 10% of total fatigue life. The evolution of shear stress has same tendency with the variation of equivalent stress amplitude.

Fig. 3 shows the change of maximum equivalent stress amplitude with loading condition and fatigue cycle number. The maximum stress amplitude increases with an increase of bending load. As the fretting wear is progressed, a maximum equivalent stress amplitude decreases rapidly under all loading condition at the initial stage of total fatigue life, and thereafter it remained nearly constant. This indicates that the fretting wear influences greatly on contact stress only during the initial stage of life.

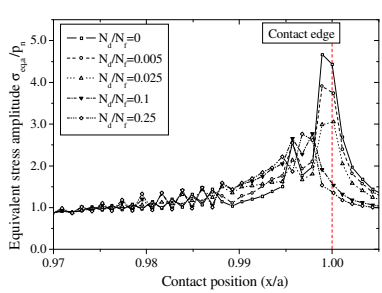

Fig. 2. Equivalent stress distributions at the bending stress amplitude of 180MPa.

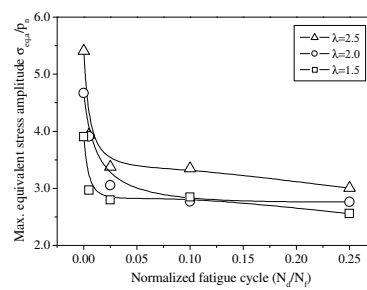

Fig. 3. Normalized maximum equivalent stress variation with fatigue cycle.

3.2. *Evolution of fatigue damage*

The stress concentration factor of press-fitted shaft shows the biggest value at the state of without fretting wear. The stress concentration factor decreased rapidly with increasing fatigue cycle up to 2.5% cycles of total fatigue life, but after 2.5% cycles of total fatigue life (N_d/N_f =0.025) there was little variation in the stress concentration factor as same as the change of maximum equivalent stress amplitude.

Fig. 4 shows the variation of FFDP with an increase of fretting wear cycle number under bending load condition of 180MPa. The maximum value of FFDP at the initial contact condition is at the contact edge. However, as the fretting wear is proceeded, the maximum value of FFDP is rapidly reduced at early stage of total fatigue life and the position of maximum value is moved from contact edge to the inner side of contact edge. At the 10% fretting wear cycles of total fatigue life, the maximum value of FFDP is at the position of x/a=0.996 (the inner position of 0.05mm from contact edge). From the fact that the position of maximum value of equivalent stresses amplitude and FFDP is shifted from the contact edge to the inside because of fretting wear with increasing number of fatigue cycles, it can be concluded that the variation of contact stress due to fretting wear is the main cause of multiple crack nucleation in contact surface.

Additionally, it can be concluded that fretting wear mitigates high stress concentration in contact edge of press fits at the early stage of fatigue life. Although there are some uncertain factors to estimate the lives of press-fitted parts, it is obvious that fretting wear makes modification of contact profile and thus the condition of fatigue life estimation is varied by fretting wear.

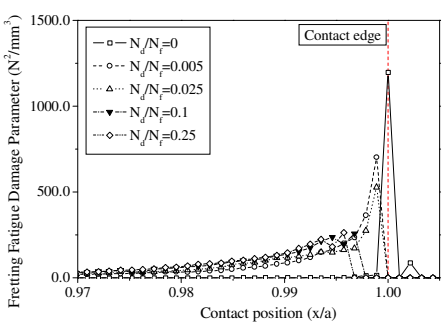

Fig. 4. Fretting fatigue damage parameter at bending stress amplitude of 180MPa.

Therefore, it is clear that fretting wear has an important influence on the fatigue life prediction in the press-fitted structures.

4. Conclusion

The effects of the fretting wear on contact variable caused by fretting in press-fitted shaft were investigated by analytical methods based on experimental data.

When a bending load is applied on the press-fitted structures, the contact stresses and strain are redistributed because the wear at the contact edge modify the initial contact edge profiles. Therefore, the variation of contact stress due to fretting wear is the main cause of multiple crack nucleations in contact surface. And the fretting wear mitigates high stress concentration in contact edge of press fits at the early stage of fatigue life. Therefore, the fatigue crack nucleation and propagation process is strongly related to the evolution of surface profile by fretting wear because the profile change due to fretting wear makes the modification of high contact stress at the contact edge.

References

1. R. A. Smith and S. Hillmansen (2004), *Proc. Instn Mech. Engrs. Part F: J. Rail and Rapid Transit*, 218, 4, pp. 267-278.
2. K. Hirakawa and M. Kubota (2001), *Proc. Inst. Mech. Engrs.*, 215, Part F, pp. 73-82.
3. C. Lonsdale and D. Stone (2004), *Proc. Instn Mech. Engrs Part F, J. Rail and Rapid Transit*, Vol. 218, No. 4, pp. 293-298.
4. ABAQUS user's and theory manual (2003), Version 6.4, Hibbit, Karlson & Sorensen, Inc.
5. D. H. Lee, S. J. Kwon, J. B. Choi and Y. J. Kim (2006), *9th International Fatigue Congress*, CD rom.
6. D. H. Lee, S. J. Kwon, J. B. Choi and Y. J. Kim (2006), *Key Engineering Materials*, Vols. 326-328 (2006) pp. 1071-1074.
7. C. Ruiz, P. H. B. Boddington, and K.C.Chen (1984), *Experimental Mechanics,* Vol. 24, No. 3, pp. 208-217.
8. D. Nowell and D. A. Hills (1990), *Wear*, Vol. 136, pp. 329-343.

THE INFLUENCES OF THE WHEEL PROFILES ON THE WHEEL WEAR AND VIBRATIONAL CHARACTERISTICS OF THE PASSENGER CARS RUNNING ON THE KYEONGBU LINE*

CHAN WOO, LEE†

Railway System Research Department, Korea Railroad Research Institute, 360-1 Woulam-dong, Uiwang-City, Kyounggido, 437-757, Korea

JAE CHUL, KIM

Railway System Research Department, Korea Railroad Research Institute, 360-1 Woulam-dong, Uiwang-City, Kyounggido, 437-757, Korea

Wheels of the railway vehicle play the important role for driving train through wheel-rail interaction. Especially wheel profile is one of the most important design factors to rule the running stability and safety of train. Accordingly maintenance of wheel like wheel profile control is also very important for securing safety and stability of train operation. This study presents the wheel wear measurement results of KTX running on the Kyeongbu line. The train set included two different cars which have different shape of wheel profile including KORAIL profile currently used in KTX. Train set was operated on Seoul-Pusan line with fixed train set formation for commercial service. Wheel wear measurements were performed periodically. We can find the influence of wheel profile on the wheel wear of the train running on the operating line through the measurement results.

1. Introduction

The Korea Train Express (KTX), started its revenue services since April 2004 have brought a radical change in lives of Koreans, consists of 20cars for 1 set. The technical requirements of these high speed trains are being proved through design, manufacture and performance test based on the wheel-rail contract condition. But there is a little difference in operation-environment and railroad-conditions for a high speed train between Korea and France. Currently, KTX is designed to operate in existing railroads as well as new high speed railroads. For that, wheels for a high speed train for both of new high speed railroads & old existing railroads and examination for the interface problems, which can be occurred with old existing railroads, are needed.[1] Especially for KTX, train-

* This work is supported by Korea Railroad Corporation

†

rail interface examination in new high speed railroads is almost completed in test track. Service routes of KTX consists of new high speed railroads and old existing railroads, but suitability test of the train-rail interface cannot be conducted in current conditions on the operating railroads although it is important and necessary. Therefore, for the inspection of train-safety while operating KTX in Kyeongbu Line between Busan and Seoul, the effect on operation by wheel wear profile of a train is studied by examining the wear properties of KTX train wheel profile, 1/40 wheel profile(power cars) and 1/20 wheel profile(passenger cars).

2. On-line Test

2.1. *Test Line and Procedure*

The total Korean high-speed line, 412km double track, consists of 112km (27%) of at-grade sections, 109km (27%) of viaducts and 191km (46%) of tunnels. However, KTX rails have no joints, and thus produce less noise and vibration despite the significantly greater speed of operation. Special welding technique is available 300m long rails for KTX line. The individual rails were then connected together to create a continuously welded track. Besides, KTX trains are designed with wheels installed between the compartments rather than below each compartment, which significantly lowers the degree of noise and vibration caused by the wheels. A lot of vehicle types such as KTX train No. 4, No. 9, No. 11, No. 19, No. 22 and No. 29 are selected and tested in Kyeongbu Line between Busan and Seoul. Two different shapes of wheels are attached to 1/40 wheel profile(power cars, GV40) and 1/20 wheel profile(passenger cars, XP55) of each vehicle to observe wheel wear property. Original profile of each wheel is compared and shown in Fig. 1.

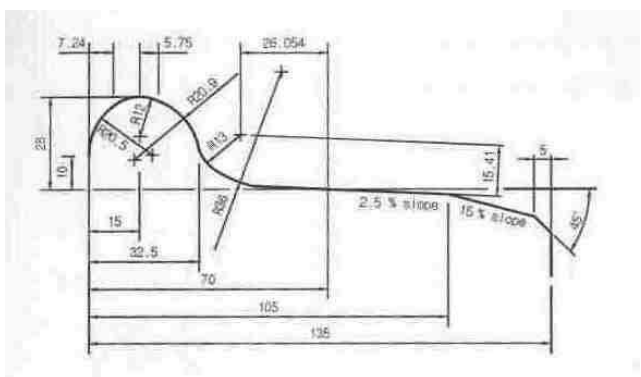

(a) GV - 40

Fig. 1. Wheel tread profile of KTX train

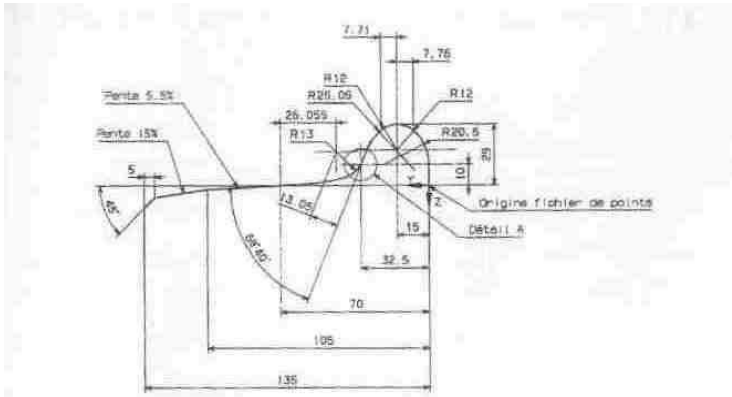

(b) XP –55

Fig. 1. Continued

For a testing period (2004. 1.1 – 2005. 8. 31), wheel wear status is tracked down and investigated on travel up to more than 550,000Km that is the standard distance covered for inspection after profiling of each wheel. During testing period, wheel profile & wear amount is periodically measured by Miniprof system.

2.2. *The Type of Test Car*

The car type arrangement and car number of KTX train are shown in Fig. 2.

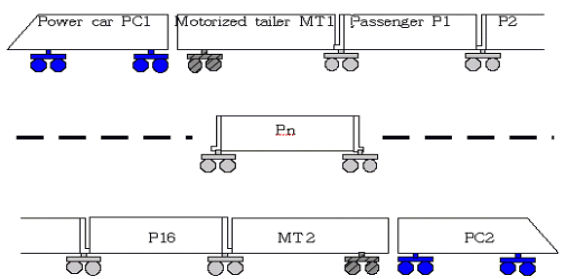

Fig. 2. KTX train arrangement

3. Results and Discussion

3.1. *Wear Rate*

Fig. 2 shows KTX truck description that is used in the test. KTX truck like figure has coil spring as primary suspension and air bag spring as secondary

suspension. The measurement is for thickness(Sd), gradient(qR) and height(Sh) of wheel flange, which is used as a criterion of inspection. Fig. 3 shows a standard parameter, used for inspection of wheel wear amount and Table.1 shows an initial profile dimension of three different profiles used in the test.

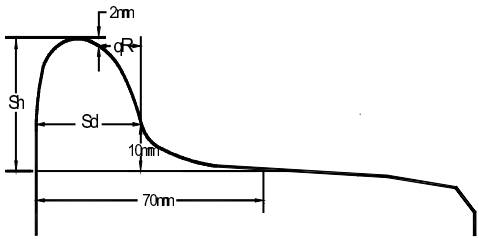

Table 1 Initial profile dimension(unit:mm)

Type	New Wheel	
	KTX 1/20	KTX 1/40
Sd(mm)	32.03	32.50
Sh(mm)	29.03	28.07
qR(mm)	10.78	10.93

Fig. 3. Criteria of Sd(flange thickness),qR(flange gradient) Sh(flange height)

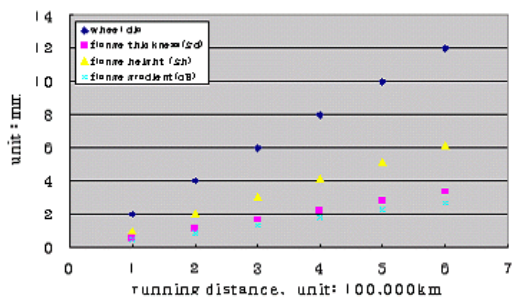

Fig. 4. Wear per mileage at power cars

Fig. 4~5 and table 2 shows wear rate per unit distance of all 6 different KTX trains after running test with trains that have two different wheel profiles. Fig. 4~5 shows that KTX 1/40 wheel has the better wear rate for thickness of wheel flange, then KTX 1/20 wheel, and 1/20 wheel was even getting thicker instead by having minus(-) value. For 1/20 wheel, thickness and gradient of wheel flange even get increased due to the lowered base surface by wear of tread surface when getting the wheel profile through measurement following the criteria of Fig. 3. In other words, wear rate around tread surface area is bigger than around wheel flange area. From wear rate for the height of wheel flange in Fig. 4~5, 1/20 wheel has a little higher wear rate. Fig. 4~5 show that wear rate

of gradient of wheel flange has a similar phase to that of thickness of wheel flange. Table 2 show the wheel wear quantity for each 6 test trains. Compared to KTX 1/40 wheel, KTX 1/20 wheel has avg. 2.04 times higher wear rate.

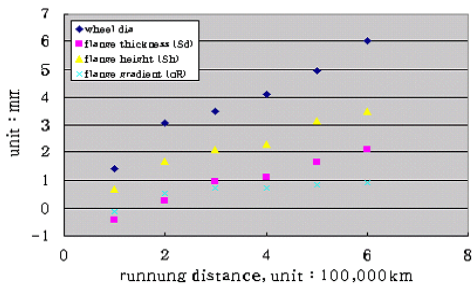

Fig. 5. Wear per mileage at passenger cars

Table 2 Wheel wear quantity

Test train No.	Running distance(km)	Wear quantity (per 100,000km)	
		Power cars	Passenger cars
4	572,000	4.86	2.10
9	590,000	4.88	2.90
11	582,000	4.19	2.63
19	560,000	4.47	2.09
22	648,000	5.85	2.54
29	655,000	4.58	1.86

3.3. *Vibration Characteristics*

Wheel profile relates to operation-safety and stability of a train.[2] As wear proceeds, equivalent conicity of wheel tread surface increases, and the increased conicity causes unstable operation of a train in a certain speed. To investigate the influence of wheel profile on vibrational characteristics, running test was conducted at the initial stage of the wear test. The locations of measurement in the train with 20cars for KTX train No. 11 was shown in Fig. 2. Acceleration was measured in the test train car P1. Carbody lateral acceleration was filtered with 2Hz filter for low frequency characteristics and transferred to RMS to compare the magnitude by dB. Table 3 shows lateral acceleration measured on the line between Seoul – Dongdaegu.

Table 3 Measured vibration level (V = 300±2.5km/h)

Test Section		2004. 4		2005. 10	
		Side wall	Bottom	Side wall	Bottom
Up	Open field	119.8	111.1	119.3dB	110.7dB
	Slab tunnel	124.8	112.0	124.5dB	111.1dB
	Ballasted tunnel	122.8	112.4	122.6dB	112.3dB
Down	Open field	120.2	111.2	121.3dB	110.8dB
	Slab tunnel	126.8	110.3	126.5dB	110.2dB
	Ballasted tunnel	123.8	111.9	123.4dB	112.2dB

Table 3 shows that lateral vibration is a few higher in the case of 2004 April test than 2005 October test. Also, the wheel attrition quality which it follows in mileage increase of the vehicle to vehicle vibrating quality effect is not big is a possibility of knowing.

4. Conclusion

Running test is conducted on the KTX train in Kyeong-Bu Line between Seoul and Busan by attaching 1/40 wheel profile(power cars, GV40) and 1/20 wheel profile(passenger cars, XP55); as results, effect of wheel profile on wheel wear and carbody vibration can be analyzed. Below results are obtained from the test.

1. KTX 1/40 wheel has the better wear rate for thickness of wheel flange, then KTX 1/20 wheel.
2. Compared to KTX 1/40 wheel, KTX 1/20 wheel has avg. 2.04 times higher wear rate.
3. The wheel attrition quality which it follows in mileage increase of the vehicle to vehicle vibrating quality effect is not big is a possibility of knowing.

References

1. Bubyoung Kang, Hisung Lee: Study on wheel wearcharacteristics of high speed train running on the conventional line, *Proceedings of Korean Society for Railway Autumn conference*, pp. 120-125 (2000).
2. Aea Technology: Introduction to railway vehicle dynamics - Ch9 wheel and rail profiles, Vampire Seminar (2002).

EVALUATION OF STRENGTH FOR BOGIE FRAME OF RAILWAY FREIGHT CAR THROUGH FINITE ELEMENT ANALYSIS

YOUNG-SAM, HAM

Railway System Research Department, Korea Railroad Research Institute, #360-1, Woram-dong, Uiwang-si, Gyeonggi-do, 437-757, KOREA

Bogie is the connection device between carbody and wheel in railway vehicles. It is the core part that exert a important effect on the riding quality and running safety. A static and dynamic load have acted on it complexly. When the bogie is designed, a finite element method, static load test, fatigue test, running test should be considered. A welded structure type bogie was developed for high speed freight car. But some bogie frames have the problems in end beam. There were some cracks in end beams. The crack situation of the end beam have a bad effect on the brake system. In that case, the cars would be in danger of derailment. This report shows the cause of end beam crack, improvement method. In order to clear the crack cause, many tests were tried. The test result concludes that the crack cause of the end beam is not the brake load but the vibration at the main line running on the track. It is estimated that the improved car which end beam was reinforced was safe enough within permitted life of the car. On the basis of the results, the existing end beam was improved. In this paper, through finite element analysis, examined structural strength of end beam. The safe of the improved end beam was proved by main line test on the track. The operation of freight car have no problems any more.

1. Introduction

The freight car is not formed by bogie type but car-body type. So the forms of cars are to be mixed each other in one formation of the cars. There are two types bogie. One is cast iron type, the other is welded type bogie. The maximum speed of the cast iron type bogie limited to 90 km/h. The maximum speed of the welded type bogie limited to 110 km/h. So, if one cast iron bogie was to be formed in one formation of the cars, the whole maximum speed limited to 90 km/h. For the solution of this problem, the speed- up research of the cast iron bogie is on progress. Because the KTX opened in 2004, the freight car also needs fast transportation speed. For the speed-up of the freight car, a welded type bogie was developed in 1993 year, and practically used in 1999 year.

Some bogie frames were manufactured in 1999, 2000 year, a fatal problem was occurred. The cracked end beam among them have discovered in 2002,

2003 year. The crack of the end beam could be a bad effect on brake system. In that case, the cars would be in danger of derailment.

To clear the cause of crack, a research of covering the whole field of welded type bogie frame was started. First of all, FEM was performed to the existing bogie frame which end beam was cracked and the improved bogie frame which end beam was reinforced. Their results were compared to each other. In the basis of FEM results, the stress concentration positions were founded. Many strain gauges were attached on them for static load test. The total eight types test methods were acted on the basis of JIS E 4208 (Load test methods of bogie for railway vehicle).

2. Crack of the End Beam

Bogie is the connection device between car-body and wheel in railway vehicles. It is the core part that exert a important effect on the passenger safety and running safety. Bogie largely consists of bogie frame, suspension, brake, wheel-set. Some bogie frames of high speed railway freight car have the problem. Those end beams were cracked. The crack situation of the end beam have a bad effect on brake system. In that case, the cars would be in danger of derailment. Fig. 1, 2 shows the crack position.

Fig. 1 Crack of end beam

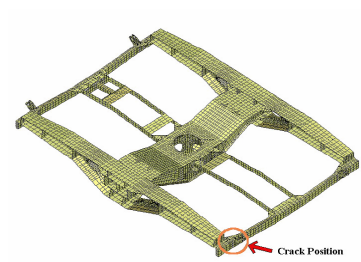

Fig. 2 Position of crack

3. Finite Element Analysis

3.1. *Weight condition*

Table 1. Calculated weight of bogie frame

Type	Calculated weight(kg)
Tare weight	22,000
Maximum load	53,000
Unsprung mass	4,530
Vertical static load per bogie	35,235

Vertical static load per bogie = (Tare weight + Maximum load - Unsprung mass)/2. Load conditions for analysis is referred to JIS 4207, JIS 4208. Total eight analysis conditions for analysis the bogie frame is used such as table 2.

Table 2. Load condition for analysis

No.	Load condition	Load(kg)	Remark
1	Vertical direction	49,329	Dynamic load(1.4g)
2	Front-rear direction	10,571	0.3g(max)
3	Lateral direction	14,094	0.4g(max)
4	Brake(per pad)	797.8	μ=0.3
5	Brake parts load * Parts weight = 531 kg	4,779	(1-10)g(max)
6		5,841	(1+10)g(max)
7		1,593	3g(max)
8		2,124	4g(max)

3.2. *Analysis results*

FEM is accomplished for the end beam which shape is changed about two type. And it's result is compared to conventional type. Model 1 shows that the end beam is mounted to the down of side frame such as fig. 3. Model 2 shows that the end beam is mounted to the end of side frame such as fig. 4. Model 3 is conventional end beam type such at fig. 5. NISA Ⅱ software is used for analysis. Full model for the bogie frame is accomplished by use the shell element. Material mark of end beam is SS400.

Analysis results, model 2 is the best, model 1 is the second, model 3 is the third. Namely, model 2 is more than safe other ones.

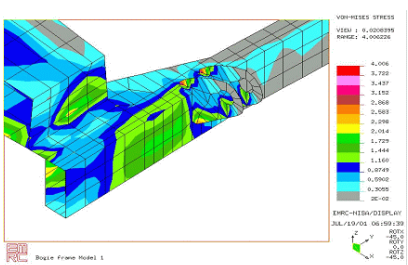

Fig. 3 Result of brake load of model 1

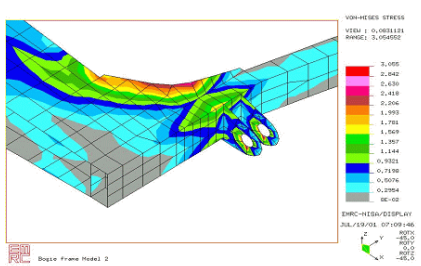

Fig. 4 Result of brake load of model 2

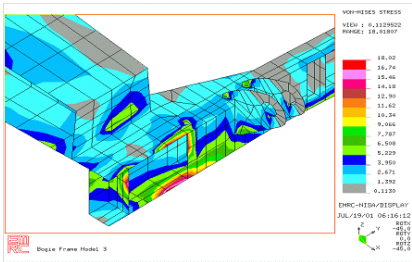

Fig. 5 Result of brake load of model 3

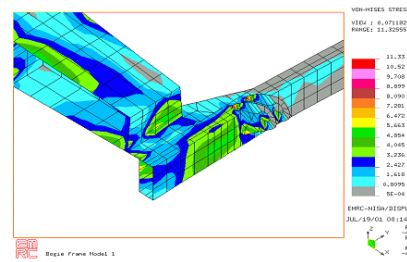

Fig. 6 Result of parts load of model 1

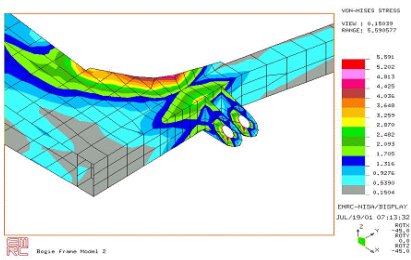

Fig. 7 Result of parts load of model 2

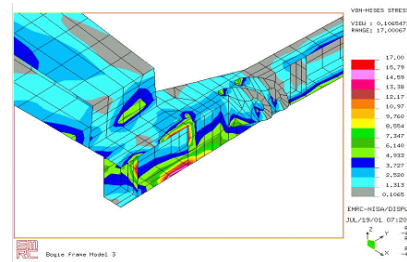

Fig. 8 Result of parts load of model 3

4. Static Load Test for Bogie Frame

A static load test was performed for bogie frame. It was based on the result of FEM. The method of static load test was based identical to FEM conditions. The most severe load conditions were adopted. Fig. 9 shows that the vertical load test and brake parts load test.

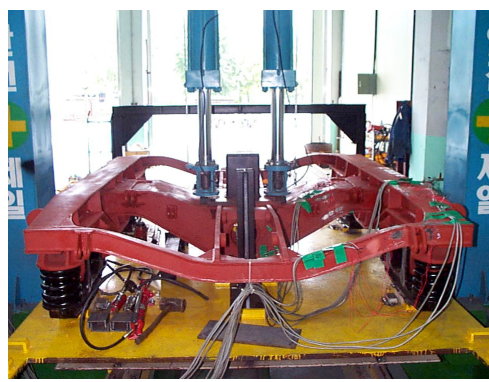

Fig. 9 Vertical static load test

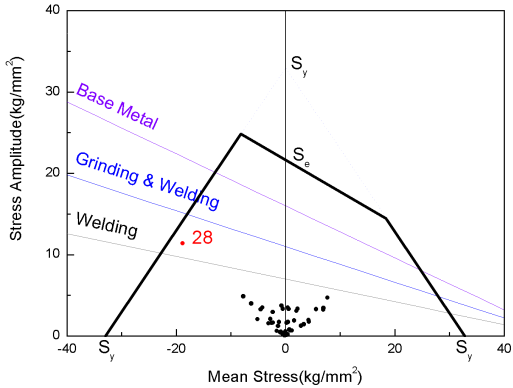

Fig. 10 Stress limit 1(0.531 ton)

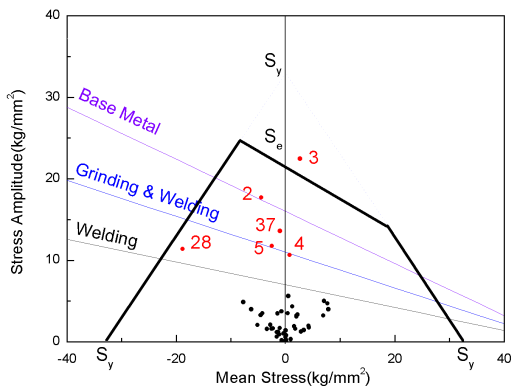

Fig. 11 Stress limit 2 (5.31 ton)

Fig. 10 shows the stress limit figure in case that the break parts load applied to eight hanger bracket(0.531ton). Fig. 11 showed the stress limit figure in case that all break parts load applied to one hanger bracket(5.31ton).

We tested that the brake parts load applied to eight hanger bracket individually. Also, we tested that all brake parts load applied to one hanger bracket. In each case, the combined stress was calculated. These results compared to stress limit figure each other in fig 10, 11. In case that the brake parts load applied to eight hanger bracket, maximum stress was occurred in the original bracket of the bolster inner stiffener. The occurrence stress type was compression. It's value was within the fatigue limited.

In case that all brake parts load applied to one hanger bracket, the stress concentration was generated around the hanger bracket of end beam largely. The maximum stress exceed the fatigue limit in upper part of the side of hanger bracket. Actually, it is impossible that all brake parts load apply to one hanger bracket. So we could ignore the result.

5. Conclusion

We draw conclusion as follows

1) The largest factor which was influenced on the fatigue life of bogie was not the brake load at running.

2) When existing car and improvement car was compared each other about the occurred stress which was not changed, the stress of improvement car occurred largely. It was concluded that the cause was maybe the huge lateral stiffness.

3) The most weak position of the end beam of the existing end beam was the center of the end beam. It's position was supported by frame at the outside position of hanger bracket. It was concluded that the fatigue life was not satisfied with standard life.

4) Twist stress occurred in end beam of the improved end beam. And the most weak position was the outside-lower part(welded position) of hanger bracket. It was estimated that there are no fracture danger within fatigue life about the standard life 25 years.

References

1. Korea Railroad Research Institute: *Design Optimization Study on Bogie Mechanism*, Research report, pp. II-151～II-155(2001).
2. Young-Sam Ham, Heung-Chai Chung, Woo-Jin Chung, *Strength Evaluation of Swing Motion Bogie by Finite Element Analysis*, Key Engineering Materials, pp. 1153-1158, Vols. 270-273(2004).
3. Young-Sam Ham, Jai-Sung Hong, Taek-Yul Oh, Young Nam Paik, *Development of a Torsion-free Brake Shoe Holder Hanger for the Bogie of Railway Freight Car*, Key Engineering Materials, pp. 316-321, Vols. 297-300(2005).

MEASUREMENT OF THE LATERAL DISPLACEMENT OF THE WHEEL-RAIL BASED ON THE VISION SENSOR

MIN-SOO KIM, WON-HEE YOU

Korea Railroad Research Institute, #360-1, Woram-dong
Uiwang-si, Gyeonggi-do, 437-757, KOREA

This paper describes the design and implement of a real-time vision system for active steering of a railway vehicle to detect a lateral displacement between wheel and rail. Active steering bogie of railway vehicles has proven its ability to bridge the gap between stability and curve friendliness. This system consists of one actuator, a controller, and sensors to detect lateral displacement, track disturbance, and track curvature. The vision sensor is applied to digital image processing techniques for detecting wheel/rail displacement in active steering bogie in various dynamic environments. Running test results show that our vision based lateral displacement measurements are accurate in each sampling rate, and make it a sensor to be placed in the active steering control systems.

1. Introduction

Importance of computer based vision system has been increasing by a cheap, plenty of information source for control of rail vehicles. In this paper, we present the design and implementation of a real time vision system for a railway vehicle to measure its wheel/rail displacement. Our vision system use off-the-shelf hardware to perform image processing, that is, segmentation and labeling, edge detection, and feature extraction. The data output from cameras are generally analog and should be digitized by a frame-grabber device. The input picture of the wheel/rail passes to a feature extractor whose purpose is to reduce the data by measuring certain properties that distinguish pictures of wheel/rail. These pictures are then passed to a post processing that evaluates the evidence presented and calculates the wheel-rail displacement.

In urban transit systems, rail passenger vehicles are often required to negotiate tight curves. During curve negotiation, the wheelset of conventional vehicles generally misalign radically with the track increasing wheel/rail contact forces and resulting in increased wheel and rail wear, outbreak of squeal noise, fuel consumption, and risk of derailment. To alleviate these problems, modified suspension system designs, application for alternate wheel profiles, active and semi-active steering techniques have been proposed.

This paper is organized as the followings. Section 2 describes an image processing algorithm for measurement of lateral displacement. Section 3 contains the experiment results. The main conclusions are then summarized in section 4.

2. Image Processing for Measurement of Lateral Displacement

Our goal for image processing is to measure the wheel/rail displacement then uses its values as a sensor output in the active steering control system. We achieve this by thresholding the gray scale image to a binary image, segmenting the wheel/rail target out of the background, labeling those clusters, and finally detecting the displacement between wheel and rail. In order to simplify the image processing, the wheel/rail target must be easy to identify and segment from the image background, provide robust feature clusters, simplify feature labeling, and allow for an algorithm that can execute in real time using off-the-shelf hardware. Figure 1 shows a flow chart of the proposed image processing algorithm.

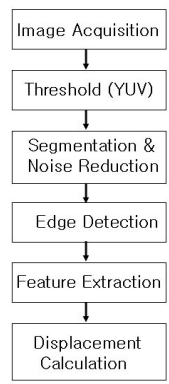

Fig. 1. A flow chart of the proposed image processing algorithm for wheel/rail displacement calculation.

2.1. *Threshold*

The threshold algorithm must produce a binary image so that the black and white regions of the wheel/rail target are preserved. During the development of the image processing algorithm, we explored various techniques for selecting a threshold from the image histogram. Lastly, we chose the following upper/lower boundary values for making binary images considering the robustness of light and shade variety as follows:

$$\begin{cases} (Y_{\min} \le Y \le Y_{\max}) \,\&\, (U_{\min} \le U \le U_{\max}) \,\&\, (V_{\min} \le V \le V_{\max}) \text{.....(white region)} \\ otherwise \text{.....(black region)} \end{cases}$$

where $Y_{\min}$ =60, $Y_{\max}$ =200, $U_{\min}$ =114, $U_{\max}$ =158, $V_{\min}$ =120, and $V_{\max}$ =140.

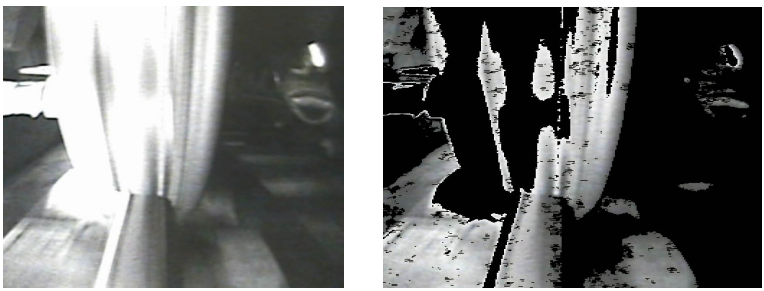

Fig. 2. Wheel/rail target image and its binary image through threshold.

2.2. *Segmentation and Labeling*

Given a binary image as shown in Figure 2, our segmentation stage must remove noises out of an initial binary image and then separate the wheel/rail target from the total image. We segment the wheel/rail target via two consecutive passes of a standard connected components labeling algorithm based on 4-onnectivity. A single pass of the components labeling algorithm numbers distinct regions of pixels such that any element of a group can reach any other element of the group through a sequence of 4-neighbors (pixels left, right, up, or down) in the group. The first pass of the labeling algorithm operates on the original binary image to determine the initial regions. The second pass of the labeling algorithm operates on a new binary image where we define the background as black and the wheel/ rail regions as white. We improve robustness to noise by ignoring all component regions with less than threshold number pixels (i.e. 50).

2.3. *Edge Detection*

Once we have segmented the wheel/rail target from the background, our next stage of processing is to detect edge detection. To avoid the computational cost of a general purpose corner detector, we employ an algorithm to specifically find displacement of the wheel/rail target of a contact region.

2.4. *Feature Extraction*

Our feature extraction algorithm consists of two steps: first, each contact point is uniquely identified based on calculation of cluster number, then the variation of the pixel number with in each cluster are computed. To identify the real size of the inter-pixel, we use the known information of rail width (i.e. 65[mm]) at contact point in the extracted wheel/rail image.

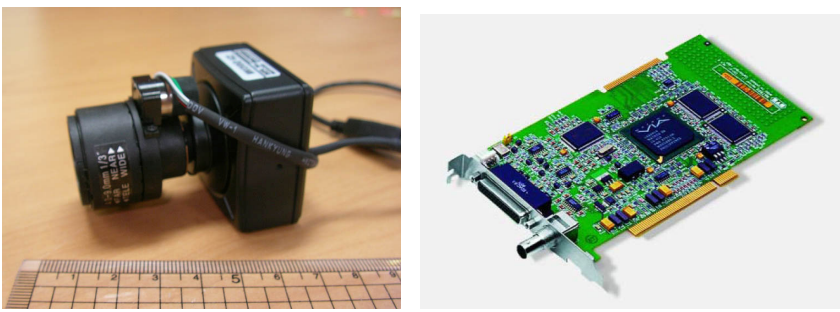

Fig. 3. CCD camera (MN1310VD) and Frame grabber (Matrox Meteor-II).

3. Experiment and its results

3.1. *Experiment Environments*

We capture color images from a small CCD camera in a running subway vehicle. For display and program execution, the image is stored in a buffer memory of the frame grabber at a resolution of 320×240 pixels at 30 frames/s to produce a visibly continuous display

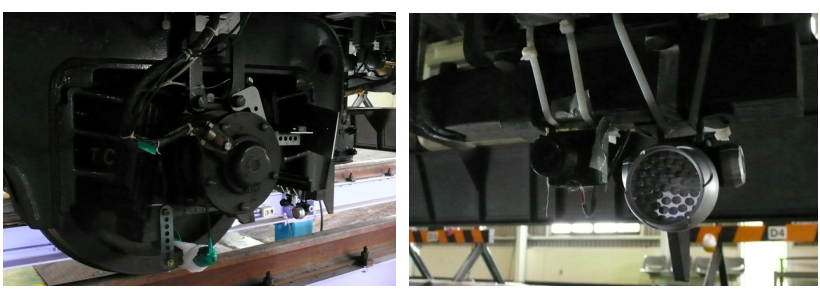

Fig. 4. Views of a wheel/rail mounted MN1310VD CCD camera and lighting equipment.

To reduce the cost of image processing, we convert a color image into a binary image by applying the min-max YUV threshold values to the total image

pixels. We then search the cluster of the contact regions of the wheel/rail image from the binary 320×240 image.

We develop and debug our vision algorithms using Visual C++ for execution on the vision computer. Figure 3 shows the CCD camera and the Matrox Meteor-II frame grabber. The camera system is set up and recorded under lighting configurations, as in Figure 4.

3.2. *Results*

An algorithm was developed that dynamically calculates the displacement between wheel and rail from running vehicle. Detection of wheel/rail displacement under the running subway vehicle requires artificial lighting because of dark underground environment. The installed CCD camera and lighting system on the bogie frame is shown in Figure 4. And Figure 5 shows the source image to be used in the proposed digital image processing.

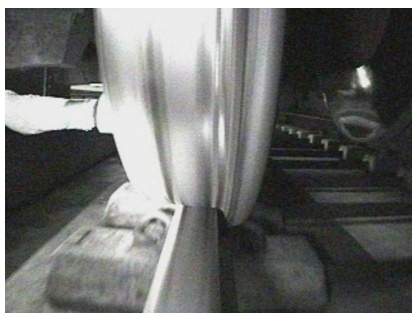

Fig. 5. Actual model image from a running vehicle.

Figure 6 shows examples of several different types of images representing displacements between wheel and rail under the running vehicle.

Fig. 6. Examples of various wheel/rail displacement images.

Figure 7 shows a binary image from source image and a reconstructed virtual wheel/rail shape image as a result of the image processing.

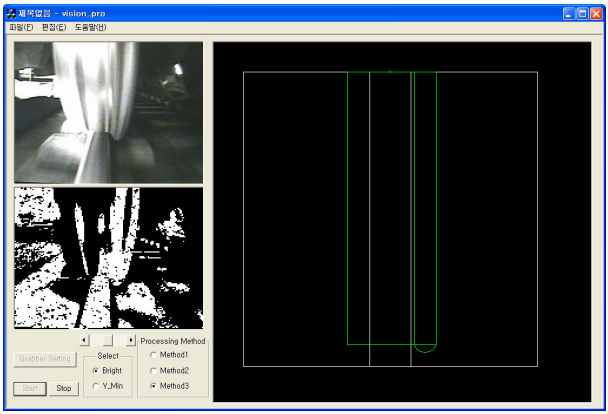

Fig. 7. Validation of algorithm performance on the model image.

4. Conclusion

This paper presents a vision sensor system designed for the measurement of the lateral displacement between wheel and rail for the active or semi-active steering techniques in the railway systems. In this case, the measurement must be carried out above the rail and without contact under the requirement of rolling stock limit for the active steering of the railway wheelset. That is the reason why we choose vision sensors instead of various sensing methods such as laser sensors and eddy current sensors.

References

1. V. K. Garg and R. V. Dukkipati, *Dynamics of Railway Vehicle Systems*, Academic press, (1994).
2. T. X. Mei. and T. M. Goodall, "Recent Development in Active Steering of Railway Vehicles," *Vehicle System Dynamics*, (2003).
3. Katsuya Tanfuji, "Active Steering of a Rail Vehicle with Two-Axle Bogies based on Wheelset Motion," *Vehicle System Dynamics*, (2003).
4. Yoshihiro Suda, Takefumi Miyamoto, "Active Controlled Rail Vehicles for Improved Curving Performance and Response to Track Irregularity," *Vehicle System Dynamics Supplement*, (2001).
5. Shen Shuiwen and T. X. Mei, "Active Steering of Railway Vehicles: A Feedforward Strategy," *European Control Conference*, (2003).
6. J. Pèrez and R. M. Goodall, "Control Strategies for Active Steering of Bogie-based Railway Vehicles," *Control Engineering Practice*, (2002).
7. R. C. Gonzalez, *Digital Image Processing*, Addison Wesley Publishing Company, (1992).

RELIABILITY ANALYSIS OF STATIC BEARING CAPACITY EVALUATION OF DRIVEN STEEL PIPE PILES USING MCS

JAE HYUN PARK

Senior Researcher, Geotechnical Engineering Research Department, Korea Institute of Construction Technology, 2311 Daehwa-dong, Ilsan-gu, Goyang-si, Gyeonggi-do, 411-712, Korea

JUNGWON HUH

Assistant Professor, Department of Civil and Environmental Engineering Chonnam National University, San 96-1 Dunduck-dong, Yeosu, Jeonnam 550-749, Korea

KYUNG JUN KIM

Eastern Regional Geotechnical Manager North Carolina Department of Transportation 6005 Atkins Farm Court, Raleigh, NC 27606, U.S.A.

JUHYUNG LEE

Researcher, Geotechnical Engineering Research Department, Korea Institute of Construction Technology, 2311 Daehwa-dong, Ilsan-gu, Goyang-si, 411-712, Korea

KISEOK KWAK

(Corresponding Author) Research Fellow, Geotechnical Engineering Research Department, Korea Institute of Construction Technology, 2311 Daehwa-dong, Ilsan-gu, Goyang-si, Gyeonggi-do, 411-712, Korea

As part of study to develop LRFD codes for foundation structures in Korea, reliability analyses of the two static bearing capacity analysis methods for driven steel pipe piles adopted in Korean Standards for Structure Foundations were performed using Monte Carlo Simulation method. A database of 58 static load tests on steel pipe piles were compiled from over 2,000 case histories collected from all around the country. The resistance bias factors were calculated by comparing the representative bearing capacities with the design values. Reliability of the current static design methods were evaluated separately for two different load test data sets based on the SPT N-value at the pile tip: N at tip<50 and N at tip≥50 for safety factors in the range of 3.0 to 5.0. The computed failure probabilities appear to be within a reasonable range; however, the large variation in the resistance bias factors undermines the reliability of the static methods.

1. Introduction

During the last two decades, structural and geotechnical engineering design in a number of countries including United States, Canada, and European Union has shifted from Allowable Strength Design (ASD) to Load and Resistance Factor Design (LRFD). It is important to incorporate local ASD experience and practice accumulated over many decades in developing LRFD codes in order to make them acceptable to the local engineering and construction communities. This can be achieved by selecting the target reliability indices for calibration of load and resistance factors based on reliability analysis of the current ASD practice.

This paper presents the reliability analysis of static bearing capacity design methods commonly used in Korea for driven steel pipe piles using Monte Carlo Simulation (MCS). This is a part of the research effort in Korea for LRFD implementation in geotechnical engineering.

2. Resistance Bias Factor

2.1. *Static Load Test Data*

Static load test reports, research papers and theses on driven steel pipe piles were collected from all around the country along with available records of design, construction, subsurface investigation, and laboratory testing. Even though a total of 2,000 static load test data were collected and reviewed, it was found that only 58 static load test data were found reliable and useful for this study. The diameter of the test piles was in the range of 406 ㎜ to 812 ㎜. Twenty of them were 5m to 10m long, 18 were 10m to 30m long, and the remaining 20 were 30m to 58m long. The static load test was performed using the loading procedures described in the ASTM Designation 1143. A majority of the selected load test data showed only total bearing capacity without a separate value of shaft or tip resistance because no load transfer readings along the pile shaft were made during the test. Hence, reliability analysis was performed only for total pile capacity.

There are several failure criteria available to estimate ultimate bearing capacity of a pile from the load-displacement curve. Six different failure criteria were employed in this study to estimate the pile's measured ultimate bearing capacity: Davisson[3], Shape of Curve[7], DeBeer[4], D=25.4mm, D=0.1B (where, D: pile top displacement and B: pile diameter or width), and ASCE 20-96[2].

The load-displacement curves of the 58 test piles were evaluated by the six failure criteria, and the results are summarized in Figure 1. D=0.1B criterion was

applicable to only 22 test data. Shape of Curve criterion is generally more subjective than ASCE 20-96, and Davisson criteria. ASCE 20-96 is not yet widely accepted in Korea. Davisson criterion was proven to perform the best in another research project[7]. Therefore, Davisson criterion was chosen to determine the ultimate capacity from the load test, which is called 'measured capacity'.

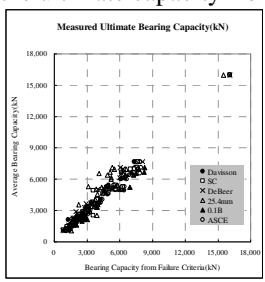

Fig. 1. Measured capacities of piles

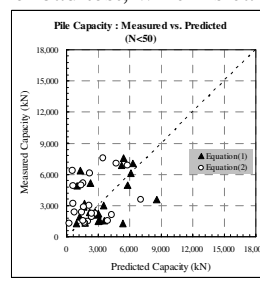

(a) N at tip < 50

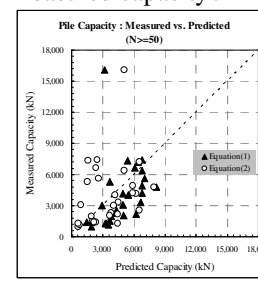

(b) N at tip ≥ 50

Fig. 2. Correlation between measured and predicted capacities

2.2. *Static Bearing Capacity Evaluation*

The Korean Design Standards for Foundation Structures[5] adopts two static bearing capacity analysis methods. These two methods were used to estimate the static ultimate capacity (Q_u) of the 58 test piles. The first method is expressed in the following formula.

$$Q_u = (\sigma_v' N_q + c N_c) A_p + \Sigma f_s A_s \quad (1)$$

where, σ_v' : effective overburden pressure at pile tip with the depth limit to 20B(B: pile diameter), N_q, N_c: bearing capacity factor, c : cohesion of soil, A_p : cross section area of pile assuming 100% plugging, f_s : unit frictional resistance along the shaft(= $K_s \overline{\sigma_v'} \tan\delta$ for cohesionless soils, and = αc_u for cohesive soils), $K_s = 1.4(1 - \sin\phi)$ and $\delta = 20$ degrees, $\overline{\sigma_v'}$: average effective overburden pressure along the shaft, α : adhesion factor, and c_u : undrained shear strength of soil, A_S : pile shaft surface area.

The second method is the empirical formula proposed by Meyerhof[6] as presented below.

$$Q_u = m N_p A_p + n N_s A_s \quad (2)$$

where, $m = 3 L_b/B \leq 30$ (L_b: pile embedment depth), N_p : average SPT N value (uncorrected) in the vicinity of pile tip, $mN_p \leq 1500$ metric tons/m^2, n=0.2, N_s : average SPT N-value (uncorrected) along pile shaft, $nN_s \leq 10$ metric tons/m^2.

Static bearing capacity of the 58 test piles was calculated by these two methods for the same pile size and length as used in the load test, and for the

subsurface conditions of the test site. SPT N-value 50 is widely regarded as the boundary between easy driving and hard driving in Korean pile driving practice. Thus, the data were sorted into two cases for reliability analysis: 1) SPT N-value at pile tip less than 50 (N<50), and 2) SPT N-value at pile tip equal to or more than 50 (N≥50). The computed static bearing capacities are called 'predicted capacity' and plotted in Figure 2 along with the measured bearing capacities by the Davisson criterion. As shown in Figure 2, it seems to be no good correlation between the measured capacity and the predicted capacity by either static analysis method.

2.3. *Resistance Bias Factor Statistics*

Resistance bias factor is defined as the ratio of the measured ultimate bearing capacity over the predicted ultimate bearing capacity. The resistance bias factor accounts for all of the uncertainties from various sources of errors such as model uncertainty, spatial variability of the soil parameters, load test error, soil sampling and testing error, and so on. The statistics of resistance bias factors are computed to be used for reliability analysis and presented in Table 1. Distribution of these resistance bias factors is also examined and lognormal distribution is found to represent the bias factor distributions most closely.

Table 1. Statistics of resistance bias factors for reliability analysis

Resistance bias factor	N at tip < 50		N at tip ≥ 50	
(λ)	Equation(1)	Equation(2)	Equation(1)	Equation(2)
Mean	1.010	1.782	0.730	1.341
Standard Deviation	0.520	1.377	0.309	1.011
Coefficient of Variation	0.515	0.773	0.423	0.754

For SPT N-value at pile tip less than 50 case, equation (1) appears to predict the bearing capacity more closely to the measured capacity than equation (2). Equation (2) underestimates, in general, the bearing capacity in both cases, however, the conservatism in the method cannot be assured due to the large variation in the bias factors.

3. Reliability Analysis

Reliability of pile foundation design can be expressed in terms of probability of failure. Assume that there are two basic random variables, the load (Q) and the resistance (R). The limit state function can be defined as g(R, Q) = 0, which can be a linear or nonlinear function of R and Q. The probability of failure, P_f, can be expressed by the following equation.

$$p_f = \iint_{g<0} f_{R,Q}(r,q)\,drdq \tag{3}$$

in which, $f_{R,Q}(r,q)$ is the joint probability density function for the basic random variables R and Q. Since this integration is practically very difficult or impossible, analytical approximation or numerical simulation techniques are employed to compute failure probability. In this study, Monte Carlo Simulation(MCS) method was used to evaluate the reliability of the static bearing capacity design methods.

There are two sets of information that are required for reliability analysis of pile foundation design: statistics of load bias factors and statistics of resistance bias factors(see Table 1). The load bias factor is defined as the ratio of the observed actual load over the nominal load. This study employed the statistics of load bias factors used for the AASHTO LRFD Bridge Design Code[1] Strength Case I: dead load bias factor mean(λ_{QD}) = 1.05, dead load bias factor coefficient of variation (COV_{QD}) = 0.10, live load bias factor mean(λ_{QL}) = 1.15, and live load bias factor coefficient of variation (COV_{QL}) = 0.20. Distribution of both dead and live load bias factors was assumed to be lognormal. In the MCS analysis, the limit state function g(R, Q) was rewritten to a mechanically equivalent form as shown in Equation (4).

$$g = \{FS \times \lambda_R \times (QD / QL + 1)\} - \{\lambda_{QD} \times QD / QL + \lambda_{QL}\} \qquad (4)$$

A FORTRAN language based computer program was developed to facilitate the computation of the probability of failure. A million cycles of simulation were applied in the MCS analysis and the failure probabilities of the two static design methods in the two pile tip cases were calculated and tabulated in Table 2. Reliability of the static design methods for SPT N at pile tip less than 50 case seems to be within a reasonable range. The reliability indices for SPT N at pile tip equal to or more than 50 case are relatively small, but the difference is not significant for all factor of safety cases to propose different target reliability indices for calibration of load and resistance factors.

Table 2. Summary of reliability of analysis using MCS

Case / Factor of Safety	P_f for N at tip <50 case		P_f for N at tip ≥50 Case	
	Equation (1)	Equation (2)	Equation (1)	Equation (2)
3.0	0.03274	0.02446	0.06755	0.05420
3.5	0.01584	0.01426	0.03150	0.03353
4.0	0.00781	0.00856	0.01485	0.02143
4.5	0.00386	0.00532	0.00700	0.01399
5.0	0.00212	0.00337	0.00333	0.00934

4. Conclusions

This study presents the following findings and conclusions.

1. Reliability of the current static design methods were evaluated separately for two different load test data sets based on the SPT N-value at the pile tip: N at tip<50 and N at tip≥50. However, the differences in the reliability indices were not significant to recommend different target reliability indices for resistance factor calibration.
2. The computed failure probabilities appear to be within a reasonable range; however, the large variation in the resistance bias factors undermines the reliability of the static methods.
3. The predicted axial pile capacity was calculated by two static design methods and there is no good correlation between the measured capacity and the predicted capacity by both of the two methods.

Acknowledgments

This study was conducted under a research contract between the Korea Institute of Construction Technology (KICT) and the Ministry of Construction and Transportation (MOCT), Korea: supported by grant C105B1000014-07B010001110.

References

1. AASHTO, *LRFD Bridge Design Specifications*, American Association of State Highway and Transportation Officials, Third Edition, Washington, D.C., (2004).
2. American Society of Civil Engineers. *Standard Guidelines for the Design and Installation of Pile Foundations*, ASCE 20-96, ASCE, Reston, Virgiia, USA, (1997).
3. Davisson, M. High Capacity Piles, Proceedings, *Soil Mechanics Lecture Series on Innovations in Foundation Construction*, ASCE, Illinois Section, Chicago, IL, (1972), pp. 82-112.
4. DeBeer, E. Proefondervindellijke bijdrage tot de studie van het grandsdraagvermogen van zand onder funderinger op staal. English version, *Geotechnique*, Vol.20, No.4, (1970), pp. 387-411.
5. Korean Society of Geotechnical Engineers, *Design Standards for Foundation Structures*, Ministry of Construction and Transport, Seoul, Korea, (2003).
6. Meyerhof, G.G. Bearing Capacity and Settlement of Pile Foundations. *Journal of the Geotechnical Engineering Division*, ASCE, Vol. 102, No. GT3, (1976), pp. 197-228.
7. Paikowsky, S.G. *Load and Resistance Factor Design for Deep Foundations*, NCHRP Report 507, Transportation Research Board, Washington, D.C., (2004).

SAFETY ASSESSMENT OF SUBWAY ROLLING STOCKS USING NONDESTRUCTIVE EVALAUTION AND ENGINEERING ANALYSIS TECHNIQUES

JEONGGUK KIM†, JUNG-WON SEO, SUNG CHEOL YOON, SUNG-TAE KWON

Railroad Safety Research and Testing Center, Korea Railroad Research Institute, 360-1 Uiwang, Kyunggi, 437-757, Korea

In order to guarantee the performance and safety during the operation of subway rolling stocks, the safety assessment was performed with various types of engineering analysis techniques in terms of the understanding of the current wear status. The car body and bogies were characterized by the employment of nondestructive evaluation (NDE) techniques, corrosion testing, and three-dimensional dimension measurements. In braking system, degradation and performance tests were conducted, while the functional and degradation tests were performed on electrical system in order to identify the actual performance of the system. Moreover, stress and structural analyses using commercial finite element method (FEM) software provided important information on stress distribution and load transfer mechanisms, and also the FEM results were compared with NDE signatures. In this investigation, various advanced engineering analysis techniques for the safety analysis of subway rolling stocks have been introduced and the analysis results have been used to provide the critical information for the criteria of safety assessment.

1. Introduction

It is required to assess the current safety and/or deterioration conditions in subway vehicles including main components, such as carbody and bogies, as well as the whole systems in order to guarantee the running performance and safety issues during the operation of subway electric multiple units (EMUs), which have been used for over 20 years [1-3]. Also, according to Korean urban transit railway law [4,5], the precision diagnosis should be conducted for subway EMUs operated for over 25 years. The basic concept for the precision diagnosis of subway EMUs is to make sure the timely replacement opportunity in primary components/parts through the safety evaluation of the vehicle systems operated over 25 years, to avoid fatal disaster, and to save the expenses for maintenance and/or replacement [1-5].

Moreover, in order to validate the extension possibility of deteriorated subway vehicles for legal lifetime of 25 years, the current condition assessment,

† Corresponding Author: Jeongguk Kim, jkim@krri.re.kr

safety assessment, remaining lifetime evaluation, etc. need to be performed. Depending on the precision diagnosis results, the legal lifetime of subway rolling stocks could be extended up to 5 years. Figure 1 shows the working process of the precision diagnosis for metropolitan subway rolling stocks, and detailed inspection of rolling stocks is classified with 4 main parts of subway vehicle systems; carbody, bogie frames, braking systems, and electrical systems. Table 1 exhibits the detailed inspection items for each process. After general inspection of those main parts, in case of more detailed inspection is required, in-depth precision diagnosis, e.g., lifetime analysis, could be conducted as described in Korean Law [4,5].

Therefore, the main objectives for this investigation are to introduce and apply various types of engineering analysis tools and/or techniques for safety evaluation of subway rolling stocks, investigate the techniques on precise diagnosis of subway rolling stocks, and provide safety performance information of subway rolling stocks based on diagnosis results.

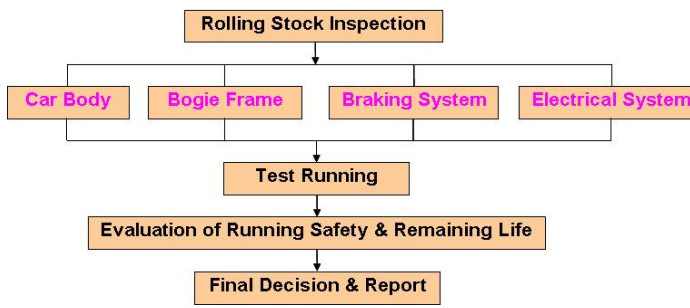

Fig. 1. A working process of the precision diagnosis for metropolitan subway rolling stocks

Table 1. Detailed inspection items for 4 primary parts

Components	Inspection Items
Car Body	1) 3-D Measurement 2) Surface Inspection - Visual Inspection/NDE (PT, MT) 3) Internal Flaw Inspection : Weldments Inspection 4) Corrosion Testing
Bogie	1) Exterior Visual Inspection (Deformation, Cracks) 2) 3-D Measurement 3) Weldments Inspection : MT, UT
Braking System	1) Leak Testing 2) Exterior Inspection 3) Corrosion Testing and Braking Performance Testing
Electrical System	1) Functional Testing 2) Insulation Resistance Measurement/Degradation Testing 3) Traction Motor Lifetime Estimation

2. Experimental Procedures and Results

2.1. *The Rolling Stocks, Car Body, and Bogie Frames*

The subway rolling stocks investigated in this study were manufactured in Korea, and currently available for the public transportation system in Korea. The subway rolling stocks should possess sufficient stiffness and strength for normal operation with maximum numbers of passengers, and they are composed of under frame, side frame, roof frame, and end frame. The current rolling stock systems for this investigation were composed of total 6 vehicles including 2 control cars, 2 motor cars, and 2 trailer cars.

Engineering analyses with several advanced analysis methods were employed for mainly car body analysis. All analyses were conducted on car body part as presented in Table 1, and the following advanced techniques were employed. Using the laser tracker, 3-D measurement of carbody dimension was performed to check out the dimension changes during the use of subway rolling stocks as shown in Figure 2. The camber, which is pre-stressed state with convex surface in under-frame part, horizontal and diagonal dimensions were measured and evaluated comparing with the design criteria. Not much change in dimension was observed except some carbody showed out of standard value in camber measurements, which present a serious defect in subway vehicles. Various types of NDE methods, such as magnetic particle testing (MT) and ultrasonic testing (UT), were used to inspect and/or detect in-service flaws at the components of rolling stocks as presented in Figure 3 [6,7]. Furthermore, internal flaw inspection, weldments inspection, and corrosion testing were conducted to identify the thickness change and defects in carbody. Although some defects in carbody were found in NDE inspection, but they were within an allowable range.

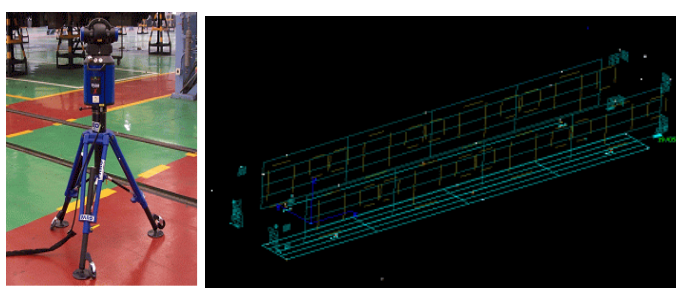

(a) (b)

Fig. 2. (a) A laser tracker for 3-D measurement, and (b) 3-D measurement of a carbody dimension

Like the carbody investigation, the similar approach was applied to the analysis of bogie frames. First, exterior visual inspection was conducted for checking out the deformation and visual cracks. Also, 3-D measurement was conducted. Since the bogie frames were composed of many weldments parts, the

MT and UT NDE analyses were performed. Through the weldments inspection using MT and UT, a large size crack of larger than 100 mm in length was found under part of bogie frame as shown in Figure 4.

(a) (b)

Fig. 3. (a) Magnetic particle testing for a bogie, and (b) ultrasonic inspection for a bogie

Fig. 4. A large size crack, approximately 100 mm, was found under part of bogie frame.

2.2. *Braking Systems and Electrical Systems*

In order to evaluate the current deterioration information of braking system, leak testing applying to the actual braking pressure, exterior inspection using an endoscope, and corrosion testing, and braking performance testing were performed. From the testing results, it was found that the function and performance of braking system were good due to periodical inspection, maintenance, and/or replacement. Also, the vibration characteristics were relatively good condition although the rolling stocks were deteriorated.

The electrical system inspection was conducted with insulation resistance measurement, degradation testing, and infrared image inspection. The electrical systems, such as wires, cables, and connecting parts, were checked out using the infrared image analysis. The thermographic diagnosis results after operation of the subway system showed an abnormal heating, a localized heating, at the connection areas of high-voltage cables. This is mainly due to the overall deterioration of cables and/or under deterioration. Figure 5 shows the infrared image showing thermal degradation at high-voltage cables.

Through the combination of these tests, the lifetime evaluation for electrical system was performed. For electrical system, the degradation and deterioration of high-voltage cables and devices were found due to long-term use. Therefore, the periodical precision inspection would be required in case of extended use.

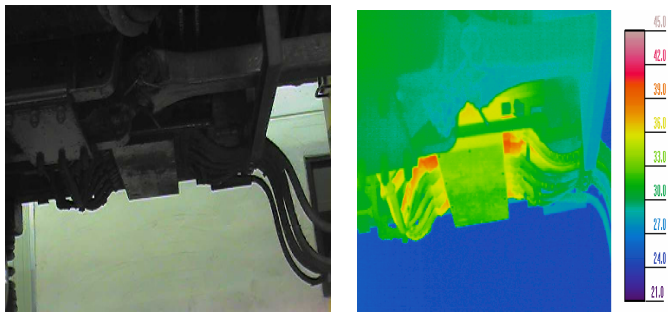

(a) Actual image (b) Infrared image

Fig. 5. Infrared image showing thermal degradation at high-voltage cables as compared with actual image for electrical cables

2.3. *Structural Analysis of Carbody and Bogie Frames*

The structural analyses of carbody and bogie frames using commercial FEM software (MSC Patran and Nastran 2003) were conducted to evaluate the lifetime of carbody and bogie frames. The shell elements were used in the most of elements in structural analysis. Figure 6 presents the structural analysis result for a bogie frame showing stress distributions. Based on the analysis results, the structural weak areas can be found. For carbody analysis, the highest stress was obtained at the side frame area under the vertical loading condition. From the bogie frame structural analysis, as shown in Figure 6, the highest stress concentration occurred at the intersection of bolster and frame, and the results showed a good agreement with NDE results for the bogie frame.

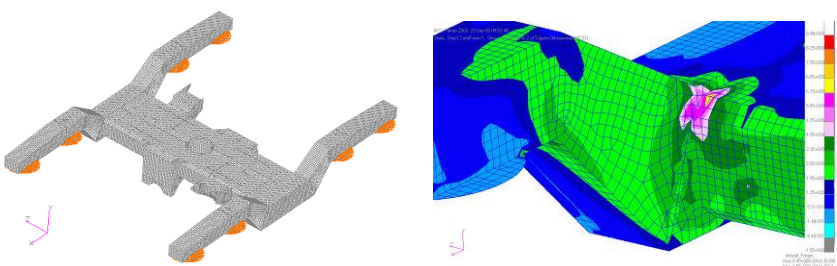

Fig. 6. The structural analysis results of (a) bogie frame model, and (b) the area at the intersection of side frame

3. Summary

In this investigation, the subway vehicles used for over twenty years were selected for the safety evaluation. Various advanced engineering analysis

techniques for the deterioration analysis of subway electric multiple units have been introduced and the results of the analysis have been used to provide the critical information for the criteria of reliability assessment. The current investigation leads to the following summary.

In the carbody investigation, the degree of corrosion was approximately 10%, and no eminent cracks were found. Therefore, overall exterior condition was good, but the serious deformation in terms of camber was found at the underframe of carbody from the results of 3-D measurement. Therefore, for the deformed rolling stocks in underframe, the extended use of the carbody should not be allowed. In the investigation of the bogies, weldments cracks were found at stress concentration area from the NDE analysis. Since the presence of serious defects in bogie parts, the overall inspection and repair are required for the current operation of subway systems. In braking system, the function and performance of braking system were good due to periodical inspection, maintenance, and replacement. Also, the vibration characteristics were relatively good condition although the rolling stocks were deteriorated. For electrical system, the degradation and deterioration of high-voltage cables and devices were found due to long term use. Therefore, the periodical precision inspection would be required in case of extended use.

Based on the above analysis results, the test running on commercial track is needed to evaluate the running performance related to safety issues.

References

1. J.D. Chung, J. Kim, and D.S. Bae, Key Engineering Materials, 297-300, 1876 (2005).
2. J. Kim, J.D. Chung, W.K. Kim, and Y.K. Hong, WCRR Proceedings (2006).
3. *Safety diagnosis of Seoul subway system,* Seoul Metropolitan Subway Corporation, (1995), in Korean.
4. The Performance Testing Guideline for EMUs, The Korean MOCT, (2002).
5. The Precision Diagnosis Guideline for EMUs, The Korean MOCT, (2002).
6. ASM Handbook, Nondestructive Evaluation and Quality Control, ASM International, (1992).
7. Nondestructive Testing Handbook, vol. 10, Nondestructive Testing Overview, ASNT, Inc., (1996).

FAILURE ANALYSIS OF INTEGRATED CIRCUITS BASED ON NONDESTRUCTIVE EVALUATION*

HYUNGJUN KIM, KEE-HONG UM, SEUNG-JUNG SHIN

Division of Information Technology, Hansei University
604-5 Dangjung-dong Gunpo-si Kyunggi-do, Korea

We propose failure analysis procedures for integrated circuits (IC) using nondestructive evaluation based digital image processing. Failure analysis is accomplished by performing the following two steps: DC characteristic measurement using a pin-to-pin V/I curve tracer, and non-destructive inspection using X-ray radiography and Scanning Acoustic Microscope (SAM) photography. The proposed failure analysis methods are applied to Power and AMP ICs in order to find the failure mode, mechanism, and root causes. We discovered that there are several main causes for each IC failure.

1. Introduction

Because the use of electronics has increased explosively in modern society, demand for integrated circuits used in electronic devices has also increased proportionally. The quality of manufactured electronic components is heavily dependent on ICs, thus must be guaranteed in order to improve quality [1]. Many new types of failures are continually being reported and the causes of these failures are not clearly defined or explained. Additional analysis of the physics of the failures is required in order to prevent the failures from reoccurring. Failure analysis based on failure physics is defined as a series of actions to remove the mechanism of the failure by discovering and analyzing the causes of failure which occurred as a result of faulty process and design, insufficient design tolerances, and inadequate circuit assembly. This new analysis method is expected to solve most of the undefined failures which have not been solved by existing analysis methods [2].

Product failure is known to occur in the whole development and manufacturing processes and throughout the life-cycle of the product. The results of analyzing the failures discovered during these processes are important for improving the quality and reliability of a product.

In this paper, we determine the failure mode and causes for failure by reviewing the expected failure mode in the IC. We present appropriate failure

* This work is supported by Hansei University.

analysis techniques and procedures, analyze the failures against the defective components and parts utilizing the failure analysis techniques discussed in this paper, and suggest methods to solve these issues.

2. Failure Analysis Techniques and Procedures

Figure 1 shows the cross section of a common IC. The die (chip) which processes electrical signals is bonded to the paddle by a silicon adhesive. The chip and lead frame which transmits the signal are connected via a gold wire. These components are safely protected by a molded compound package.

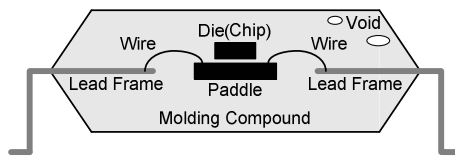

Fig. 1. The cross section of a common integrated circuit

2.1. *Failure Modes*

There are some common failure modes or mechanisms which may cause failures in ICs. The main causes of electronic damage are electrostatic discharge damage, latch up, and voltage punch-through. The main causes of wire or wire bond failure are excessive bonding pressure, thermal fatigue fracture after stress, and the fusing open of bond wires due to electronic overstress. Package failure is caused by delamination and voids. Main chip defects are caused by a fracture of the die due to mechanical or thermal stress.

The most often specified critical failure mechanisms occur when the IC is damaged and loses all functionality. However, weak EOS (Electrical Over Stress) or void causes occasional faulty operations by changing some electrical properties of the IC. The most frequent failure is the failure which results from EOS/ESD (Electrostatic Discharge). After reviewing recent technical trends, it was apparent that bonding depth, thickness of gate silicon dioxide film and transistor length have been considerably reduced because of IC downsizing [3]. As a result, the risk of failure resulting from ESD is increased and failures of diverse forms are frequently reported. The failure mechanisms specified above frequently cause defects in retail products used by consumers. In the following section, we will review possible failure mechanisms.

2.2. *Failure Analysis Procedures*

Detailed failure analysis procedures are as follows:

1. *Visual inspection* is conducted to observe the appearance of defective products and check if the IC is correctly installed, terminal is contaminated and parts are operating normally.
2. *Electrical property inspection* is conducted to check if there are any errors by comparing the pin-to-pin V/I curve of the defective product with a non-defective product using specialized equipment such as a curve tracer.
3. *Nondestructive inspection* is conducted using X-Ray inspection and SAM (Scanning Acoustic Microscope) to check the failure types of the product.
4. *Destructive inspection* is conducted to locate the defective component using a SEM(Scanning Electron Microscope) after decapsulation when the installed IC is shown to be defective.

2.3. *Applied Nondestructive Inspections*

We applied nondestructive failure analysis procedures for integrated circuits mainly using V/I curve tracer, X-ray radiography, and SAM [4,5]:

- *V/I curve tracer* is a device that will show you a device's voltage vs. current characteristics. With this you can see how the device under test will perform with respect to voltage and/or current.
- *X-ray radiography* is used for the inspection of encapsulated foreign material, internal opens and shorts, and changes in alignment due to the encapsulation process.
- *SAM* uses the absorption and reflection of ultrasonic waves in a sample. Typical applications for SAM include the evaluation of die-attach integrity, characterization of wire bonds, and identification of cracks in the die or molding compound.

3. Application of Failure Analysis Cases

We have clarified the failure mode and mechanisms of ICs by analyzing the failure against a properly functioning IC according to presented failure analysis procedures and methods.

3.1. *Failure Analysis of Power IC*

The Power IC, a 23-lead Single-In-Line (SIL) plastic power package, is used as the mode select switch of automobile. The results of measuring the pin-to-pin electrical property of the specimen using a curve tracer show that the curve of defective component is shifted when compared to a non-defective component.

Figure 2(a) clearly shows the measured results. If the parameter value of a defective component shifts more than 30% when compared with a non-defective component, it is evaluated as a failure in the V/I Characteristic curve. In the ESD test [6], we have reproduced the MM (Machine Model) test conducted when static electricity is discharged from an appliance to the product if the appliance comes in contact with the IC or surrounding components. We have tested static electricity resistance between GND-to-Pins through the ESD test and then applied static electricity to Pin 16 where the severe parametric shift occurs. The results of this test show that the failure, as with the V/I curve, occurred in the defective component is reproduced at a voltage of 4kV. Figure 2(b) shows the results of this test.

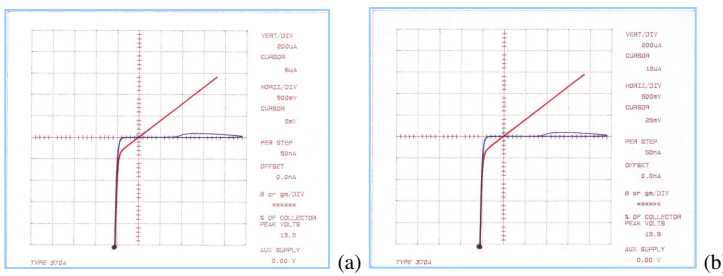

(a) (b)

Fig. 2. V/I curve, (a) defective item, (b) ESD test

Figure 3 shows the photos taken during X-Ray inspection and Figure 4 shows SEM results. The X-ray photos clearly show that many voids exist in both the defective component and the properly functioning component.

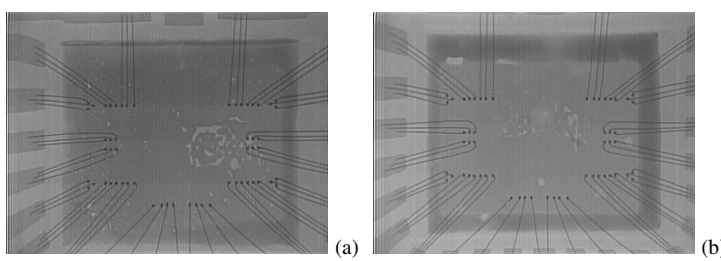

(a) (b)

Fig. 3. X-ray radiography, (a) defective item, (b) non-defective item

The results show that the main cause of Power IC failure is the over voltage caused by a surge instead of a defect. We decide that some complementary efforts such as adding the ESD/EOS bypass or a protective circuit are required to ensure final product quality.

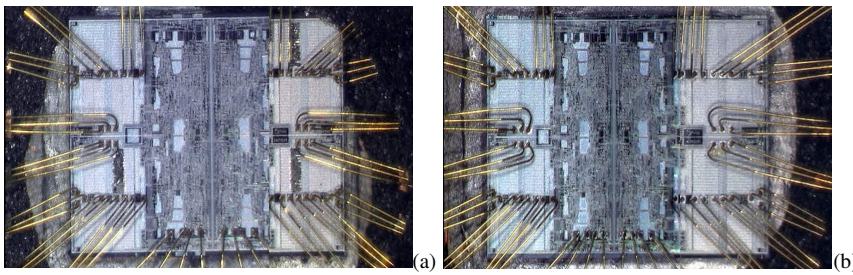

Fig. 4. SEM (Scanning Electron Microscope), (a) defective item, (b) non-defective item

3.2. *Failure Analysis of AMP ICs*

The Amp IC is a component used commonly in televisions which is designed to change an incoming small signal into a larger signal by amplifying the small signal to a specific gain. The results of the electrical property test conducted using the curve tracer show that defects such as open, short and change of parameter value are detected in many pins. We have analyzed the X-Ray photos to check for internal failures. The analyzed results show that many die attachment voids are found inside the defective specimen and Pin #1 and #2 gold wires are disconnected or cut. For the details, refer to Figure 5.

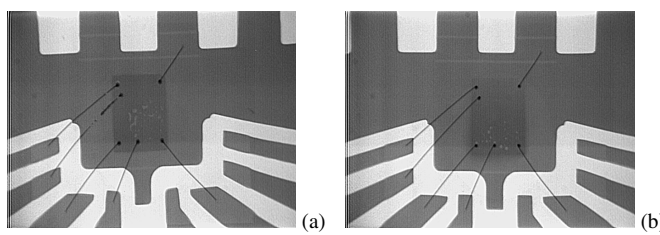

Fig. 5. X-ray radiography, (a) defective item, (b) non-defective item

The components were also analyzed using a SAM. As shown in Figure 6, the test results show that the color of the paddle and lead frame is changed into red in the unused components and defective ones. Failure analysis results show that the failure of the components are caused by the separation of paddle and lead frame due to faulty manufacturing. The chip was damaged due to the separation of the packaging. This separation was caused by a disruption in IC heat dissipation which in turn caused the IC to overheat. Packaging separation allows the penetration of moisture and thermal grease which also causes failure. The test results show that the power end and output end of Amp IC are damaged by over voltage or over current, so contingencies need to be implemented.

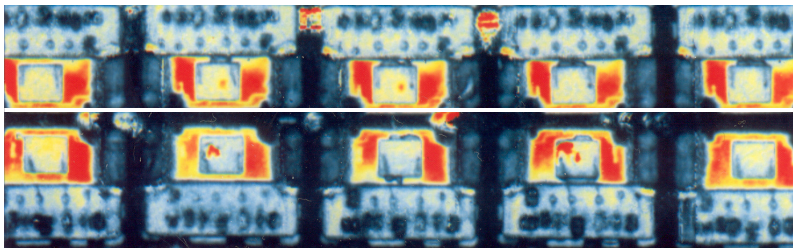

Fig. 6. SAM photography, (a) defective item, (b) non-defective item

4. Conclusions

Failure analysis is a series of actions performed in order to discover the failure mode/mechanism of ICs through failure analysis procedures and removing the causes of failure. Failure analysis is highlighted as an important element of reliability engineering. Failure analysis procedures are classified into visual, electrical property, nondestructive and destructive inspections. We are able to identify the failure mode/mechanisms by analyzing the failures against actual field defective specimens of Power ICs and AMP ICs according to analysis procedures. In this regard, we decide that the method of analyzing the failure of ICs according to the proposed procedures is useful and effective. Preliminary experimental results show that there are some typical failures depending on the type of IC and that we can avoid these types of failures by taking them into consideration during the design and manufacturing process.

References

1. C. Boit, Can failure analysis keep pace with IC technology development?, *Proc. of 7th Int. Symp. on the Failure Analysis of Integrated Circuits*, 9-14 (1999).
2. B. Michel, Failure analysis of automotive electronics and microsystems, *Technology, Law and Insurance*, **5**, 3 & 4, 179-181 (2000).
3. V. Lakshminarayanan, Failure analysis techniques for semiconductors and other devices, *RF Design,* **2**, 34~46 (2001).
4. P. L. Martin, *Electronic Failure Analysis Handbook*, McGraw-Hill Professional (1999).
5. Electronic Device Failure Analysis Society, *Microelectronics Failure Analysis*, ASM International (2004).
6. M. Ker, J. Peng, H. Jiang, ESD test methods on integrated circuits: an overview, *Proc. of 8th Int. Conf. on the Electronics, Circuits and Systems*, 1011-1044, 2 (2001).

AN ANALYSIS OF THE MAIN EFFECT FACTORS OF BRUSH WEAR FOR AUTOMOTIVE BLOWER MOTORS

WAE-GYEONG SHIN

School of Mechanical Engineering Yonsei University, 134 Shinchon-dong, Seodaemoon-Ku, Seoul 120-749 / Reliability Division, Korea Automotive Technology Institute, 74 Yongjung-Ri, Pungse-Myun, Chonan, Chungnam 330-912, South Korea

SOO-HONG LEE

School of Mechanical Engineering Yonsei University, 134 Shinchon-dong, Seodaemoon-Ku, Seoul 120-749, South Korea

YOUNG-SIK SONG

Reliability Division, Korea Automotive Technology Institute, 74 Yongjung-Ri, Pungse-Myun, Chonan, Chungnam 330-912, South Korea

As motors used for automobiles use battery-stored electricity, most motors are of the small-sized DC variety, of which typical failures are primarily classified into brush wear, coil burn-out, and bearing damage. From such failures, it is required to understand the failure mechanism due to the brush wear as it relates to the life of DC motors, as a result of the wearing defects. As the lifespan of DC motors is strongly associated with brush wear and as the effect factors of brush wear relate to several mixed actions, it is necessary to conduct research on the analysis of the effects of such wear processes. This study aims to analyze the main effect factors emerging from a brush wear test of the blower motor, a representative DC motor used in automobiles. The main effect factors of brush wear are associated with both mechanical wear and electrical wear. For examples, there are voltage, current, rotation speed, spring load, and temperature effects on the operational and environmental conditions. This study was intended to examine the effects of these major factors on brush wear through a brush-wearing test for each factor. With an adequate analysis of these effects, the extracted acceleration factors for DC motors may be applied to the development of an accelerated life test method for DC motors.

Keywords: Failure mechanism; brush wear; main effect factors; blower motor; accelerated life test; small DC motor.

1. Introduction

A life test may be conducted to determine reliability. However, because the product under study often has high reliability levels, it is difficult or even impossible to gain information about the product life within a reasonable time

period by the use of a general life test. Therefore, it is essential to introduce an accelerated test, which conducts a test under a poorer environment than normal conditions of use, in order to reduce the testing time[1],[2]. The automobile industry is also recognizing this trend. Recently, as the electronic controls of automobiles are increasing rapidly, the need for small motors for automobiles is becoming quite heightened, with brush-type DC motors primarily being used. The primary failure mechanism of brush-type DC motors is brush wear, and the life of a motor may be predicted by the degree of brush wear. In general, the electricity in a motor flows from an external circuit, passes through a brush, commutator, amature coil, and a brush on the other side, and then flows to an external circuit. This electricity flow drives the motor. Therefore, to design an accelerated life test under the conditions of use in the brush-type DC motor environment, we need to understand the brush wear mechanism and analyze the effect factors that facilitate brush wear.

This study attempted to conduct a brush wear test for a blower motor, a component of a blower that rotates a fan by a motor to the inside and outside of an automobile in order to supply air to the indoor and outdoor units of the automobile, as well as maintain appropriate air flow levels. The brush wear of a blower DC motor can be divided into mechanical wear by the contact of the commutator, and electrical wear. The effect factors of mechanical wear include spring load and rotation speed, while the effect factors of electrical wear include electric current and voltage. The effect factors of the environment of use include temperature and humidity[3],[4].

This study was intended to examine the effects of the major factors on brush wear through a brush-wear test for voltage, current, rotation speed, and temperature – all of which affect brush wear – among the elements of accelerated life test design in the user environment of a brush-type blower DC motor, and apply these derived factors to the design of an accelerated life test method for DC motors in the future.

2. Design of Brush wearing test for Blower DC motor

Considering the mechanical, electrical, and environmental effects of a brush-type DC motor, the major factors that affect brush wear caused by friction between the commutator and the brush can be summarized as voltage, current, temperature, rotation speed or frequency of use, (number of revolutions), and spring load[5]. Voltage and current are electrical effect factors, temperature an environmental effect factor, with frequency of use and spring load being mechanical effect factors. A test was conducted to examine the effects of these

factors on the brush wear of a blower motor under test conditions outlined in Table 1. The test level for each condition was determined on the basis of actual use. After 100 hours of each test, brush wear was measured. These brush wear quantities were measured and represented as wear rates. The wear rate is the reduced length of the brush (mm) against the circumference (sliding distance (mm)) of the commutator[6]. As shown in Figure 1, the equipment required for this test were a temperature chamber, power supply, and oscilloscope, employed to check changes in current.

Table 1. The test conditions of the main effect factors of brush wear for DC motor(each test time : during 100 hours)

Factors	Test Conditions	Test level
Voltage	13.5V, 14.8V, 16.2V	3
Current	20A, 22A, 24A	3
Temperature	25℃, 40℃, 50℃, 60℃	4
Rotation speed	500 rpm, 1000 rpm, 2000 rpm, 3000 rpm, 4000 rpm	5

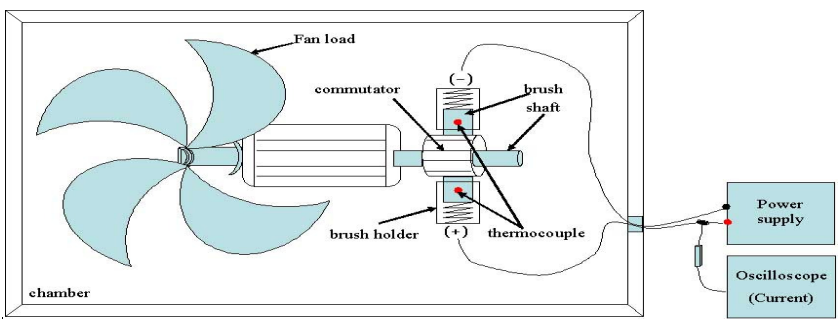

Fig. 1 The simplified schematic diagram for the measurement of the brush wear for voltage, current and temperature factors by using blower unit

3. Analysis of the Brush Wear Test

3.1. *Voltage Change Test*

We conducted a test with all the conditions of the DC motor identical, except voltage. The DC motor was operated continuously for 100 hours at each of the voltages of 13.5V(100%), 14.8V(110%), and 16.2V(120%). The current was maintained at a constant of 20A, and the load conditions were also kept identical. Figure 2 shows the brush wear rate for each voltage determined by measured brush wear after the voltage change test. As shown in this graph, as there was no change of brush wear when only voltage was changed, with other operating

conditions being identical to those in the test results, we may conclude that the voltage factor cannot cause brush wear independently. Under the actual usage conditions, however, the voltage factor adjusts the strength of the wind volume, and carries out its role because a change of voltage also changes other factors.

3.2. *Current Change Test*

We conducted a test with all the conditions of the DC motor identical, except current. The voltage of the test device was 13.5V and the system was operated for 100 hours continuously for each of 20A, 22A, and 24A. All other conditions were maintained identical.

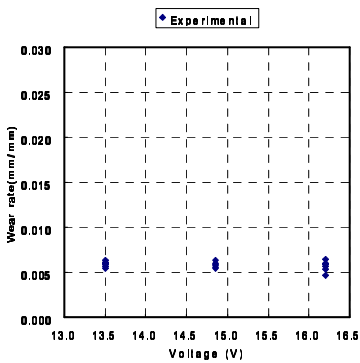

Fig. 2 Wear Rate(mm/mm) of brush as changing voltage by continuous operating DC motor for blower (operating time : 100 hrs)

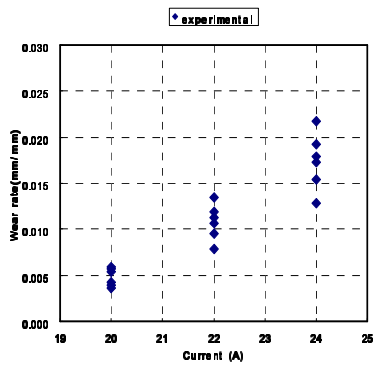

Fig. 3 Wear Rate(mm/mm) of brush as changing current by continuous operating DC motor for blower (operating time : 100 hrs)

Figure 3 shows the brush wear rate for each current determined by measured brush wear after the current change test. This figure shows that the change of brush wear according to current change, increases rapidly. The difference in wear rate is higher than that for voltage, which indicates that the effect on brush wear is large. The reason why brush wear increases with current flows is that the brush material deteriorates because of frictional heat at the point where the brush and the commutator make contact, and because of the heat generated by the arc.

3.3. *Temperature Change Test*

We conducted a test with all the conditions of the DC motor identical, except external temperature. The voltage was set to 13.5 V and the current to 20 A. The DC motor was operated for 100 hours continuously for each of the ambience temperatures of 25°C, 40°C, 50°C, and 60°C. All other conditions were maintained identical.

Figure 4 shows the brush wear rate for each temperature determined by measured brush wear after the ambience temperature change test. The higher the external environmental temperature, the higher the brush wear was found to be. From this, we may estimate that the surface temperature of the brush increases with the external temperature, which increases against the wear of the brush material caused by temperature deterioration.

3.4. *Rotation Speed Change Test*

We conducted a test to check the mechanical brush wear trend when no power was supplied to the DC motor. We measured brush wear when the number of revolutions was increased, by rotating the motor axis of the sample to conduct a test using a BLDC motor with a physical method. The rotation speeds of the motor were 500, 1000, 2000, 3000, and 4000 rpm, and the test time was 100 hours.

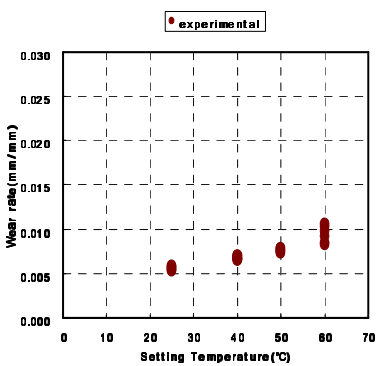

Fig. 4 Wear Rate (mm/mm) of brush as changing ambient temperature by continuous operating DC motor for blower (operating time : 100 hrs)

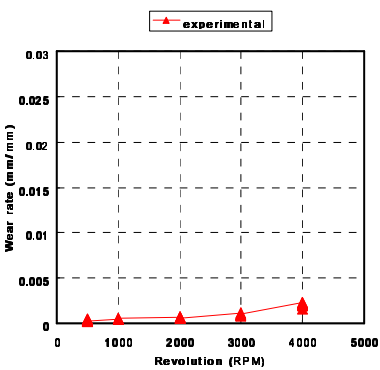

Fig. 5 Wear Rate(mm/mm) of brush as changing the revolution of the motor for mechanical motion by continuous operating DC motor for blower (operating time : 100 hrs)

Figure 5 shows the brush wear rate for each current determined by measured mechanical brush wear by the rotation speed of the motor. We can see that brush wear increased very slightly as the rotation speed increased. However, the increasing quantity was very small compared to other effect factors. This means that the electrical effect is higher than the mechanical effect on the brush wear of the motor. An increase of motor speed implies an increase in friction speed between the commutator and the brush. The higher the friction speed, the lower was the coefficient of friction, and the higher the mechanical wear. However, electrical wear is inversely proportional to friction speed. Mechanical wear increases as friction speed and the number of contact incidents increase, while

electrical wear is in inverse proportion to friction speed, because wear is generated by the self-heating of the current. Therefore, this test found that although brush wear increases along with rotation speed, it has a very small effect compared to the electrical effect factors.

4. Conclusion

This study conducted a brush wear test to derive the effect factors on brush wear, which is the primary failure mechanism of a DC motor, in order to design an accelerated life test for blower DC motors. We arrived at the following conclusions:

1. Although brush wear increased together with current, temperature, and rotation speed, the independent factor of voltage had no effect on brush wear.
2. The most important factor that facilitates brush wear is current, which increases wear because the brush material deteriorates due to friction heat at the contact point between the commutator and the brush, and due to the heat generated by the arc.
3. More brush wear is generated by electrical effects than by mechanical effects.

Therefore, we can see that the primary factor accelerating brush wear is current.

References

1. E.Rabinowicz, R.H.Mcentire, B.Shiralkar, “A technique for accelerated life testing”, Journal of engineering for industry, pp. 706~710, August (1970).
2. Milena Krasich, “Test design and acceleration for product lifetime reliability demonstration”, SAE technical paper series, 2004-01-1640.
3. V.P.Astrakhantsev, R.F.Bekishev, and G.A.Bokman, “Investigation of the characteristics of the sliding contact between a brush and a carbon-graphite commutator”, Elektrotehhnika, Vol. 50, No. 3, pp. 96~100(1979).
4. Takahiro UENO and Koichiro SAWA, “An influence of atmospheric humidity and temperature on brush wear of sliding contact”, IEICE TRANS. Electron, vol. E83-C, No. 9, September (2000).
5. B.S.Park, J.S.Ku, G.D.Kim, “Analysis of preponderant wear of earth brush for an Electrical multiple Units(EMUs)”, Korea society for railway, pp. 64~69(2005).
6. Nickolai K. Myshkin, Chung Kyun Kim and Mark I. Petrokovets, “Introduction to Tribology”, Cheong Moon Gak, pp. 99~102 (1997).

DESIGN & RELIABILITY OF AN OPTIMAL STRUCTURE USING NEURAL NETWORK

JONG-SHIN, LEE

Dept. of Computer Aided Mechanical Eng., Juseong College, San 4, Deokam-Ri, Naesu-Ep, Cheongwon-Gun, Chungbuk, Korea

This study estimated the optimized design specifications using neural network algorithm, and covered the methods by which the reliability of the estimated data was tested. Changes in stress and strain, when load changes, were collected in data by changing specifications of parts, and the date were used in neural network learning. Optimization of design was carried out by response surface methodology in varying conditions, and the result was compared with the estimation by neural network algorithm for the same condition to find out whether neural network learning can be used in design optimization. It was found, through comparison with FEM analysis, that optimization of design using neural network is possible and reliable.

1. Introduction

Recently the ways of production are becoming more of optimal amount of production system with a lot of items on production at the same time. Consumption patterns of products have also been changed greatly and the interval between fade-in and fade-out of product has been significantly shortened. As the life cycle of products gets shorter, the capability to develop products is becoming one of the major competitive edges. As development periods get shorter, lots of efforts are being centered on reliability-based design optimization. This study takes the mechanical stopper, which is used in mechanical appliances, as the model. Adjustment of design to different load condition is necessary for the mechanical stopper and design optimization was applied for parts which are sensitive to load condition and reliability was tested. For the study, response surface methodology, neural network learning and FEM analysis was applied. Variations in data of stress and strain were collected by variously changing load condition and size of parts. Based on the data, neural network learning was applied. Through neural network learning, time for design optimization can be shortened by estimating optimum sizes for any given condition of load, stress and strain, based on the collected data from various load conditions. Also reliability has been tested by comparing data from various load conditions and the results of response surface methodology and FEM analysis. To make use of

neural network algorithm, lots of data for learning are required. However, if neural network algorithm can be applied to design optimization, it can estimate optimal design parameters efficiently in response to changing design specifications. To reduce amount of data learning, this study kept abreast of finding major factors through analysis of variance [1][2][3].

2. Neural Network Learning

2.1. *Model Design*

Figure 1. shows the model which is applied in this study. When the force F is applied to the mechanical stopper, which is used in mechanical appliances, values of stress and strain are collected as the resulting data in accordance with the changes of width 1, width 2 and pitch so that the data can be used in neural network learning.

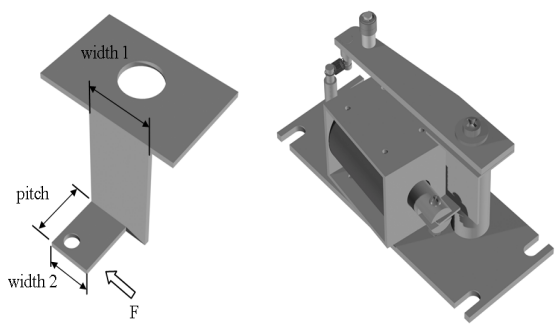

Fig. 1. Model for optimization.

2.2. *Structure of Neural Network*

Input data into the neural network are stress and strain. Output data are width 1, width 2 and pitch. Error backpropatation was used in neural network learning [4]. Error backpropagation used in this study is a kind of learning algorithm of guide which adjusts weight reversely and repeatedly so that the error between actual outputs and target outputs gets smaller, eventually minimizing sum-squared error. Rule of error backpropagation is also called generalized delta rule, devised by Rumelhart, which is one of the most well-known learning rules. Input layer is composed of three neurons, two hidden layers are composed of seven neurons and output layer is comprised of three

neurons. Figure 2. illustrates the structure of the neural network used in this study.

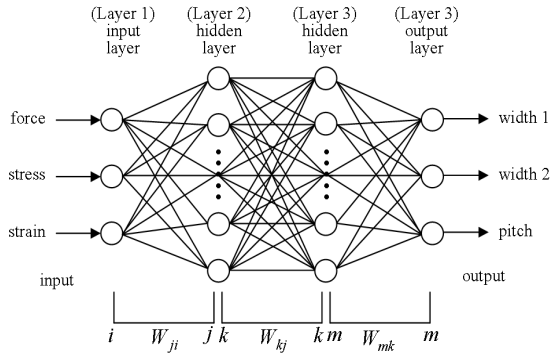

Fig. 2. Structure of the neural network.

2.3. *Neural Network Learning*

The pattern of learning neural network made 108 learning data for stress and strain neural network by various applying force in four levels and by applying width 1, width 2 and pitch in three levels respectively. Since we made use of this neural network learning to estimate optimal specifications of parts when applied forces vary, the input data shall be force, stress and strain and the output data shall be width 1, width 2 and pitch.

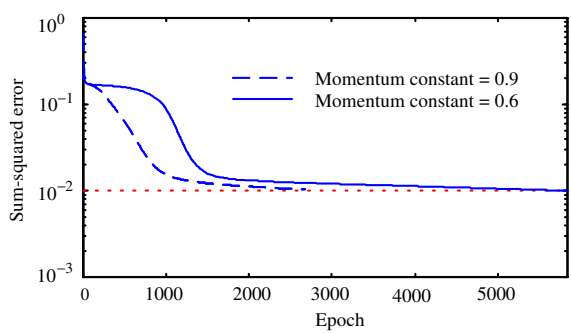

Fig. 3. Effect of the moment constant.

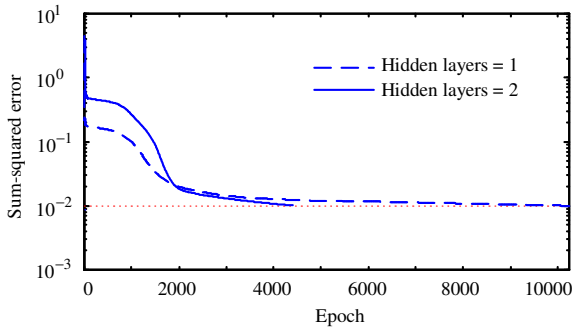

Fig. 4. Effect of the number of the hidden layers.

This neural network learning tested learning error by changing momentum constant, learning rate, number of hidden layers and weight. As a result of the learning, learning time and learning error could be reduced when momentum constant of 0.9, learning rate of 0.9, two hidden layers, and seven neurons in hidden layer was applied and it was an acceptable result. Figure 3. and Figure 4. shows the result of the simulation.

3. Optimization Using the RSM

To estimate the optimal specifications of parts for random force is applied, response surface methodology (RSM) was used [5]. The result of variance analysis of stress and strain showed that linear term, square term and interaction were all significant. Figure 5. shows the contour line of strain for pitch and width 1 and Figure 6. shows contour line of strain for pitch and width 2.

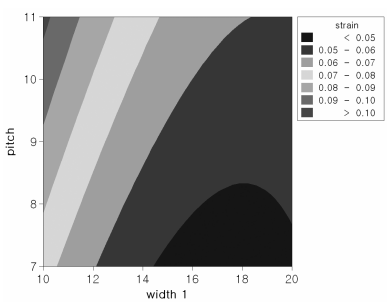

Fig. 5. Contour plot (strain, pitch, width 1).

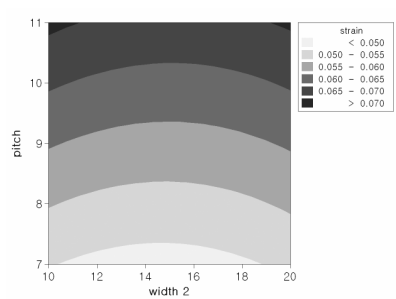

Fig. 6. Contour plot (strain, pitch, width 2).

As the response value shows in Figure 5., strain gets higher as pitch increases and width 1 decreases. Also Figure 6. shows that strain gets higher as pitch increases regardless of width 2. It means that width 2 within linear term has no influence on the change of strain. This study carried out optimization by finding out level of significance for each factor step by step. The condition for optimization was set to compare with the result of the neural network learning and the target value of stress was set as 40MPa and the strain was set as 70 ㎛ for force of 10.5N. The optimization was resulted in width 1=11.4mm, width 2=19.5mm and pitch = 7mm.

4. Finite Element Analysis

FEM analysis was carried out at the optimal condition, which has been resulted by response surface methodology, for the parts used in this study. ANSYS DesignSpace was used in FEM analysis of this study. Maximum stress and strain was interpreted at the condition where force of 10.5N is applied and width 1=11.4mm, width 2=19.5mm, pitch = 7mm. The interpretation resulted in the maximum stress of 38.8MPa and the maximum strain of 68 ㎛. Figure 7. and Figure 8. show the result of the interpretation.

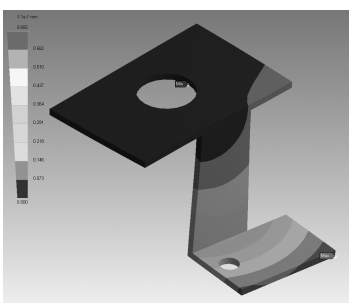

Fig. 7. Strain Contour.

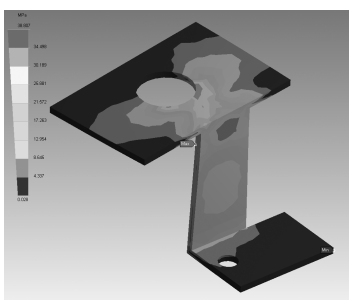

Fig. 8. Stress Contour.

5. Reliability Test

Lastly, for the purpose of reliability test, the estimations resulted by use of neural network algorithm, response surface methodology and FEM analysis were compared. Reliability test was carried out by comparing the actual data with the estimation using neural network algorithm while changing conditions variously. In this study, results were compared where force of 10.5N is applied and the target stress of 40MPa and strain of 70 ㎛ was set respectively. Estimations were resulted

in width 1 =12.2mm, width 2 = 18.2mm and pitch =7.5mm as a result of applying neural network algorithm. This result shows a maximum error of 7.1% with the actual results by FEM analysis and it is found that estimation using neural network can be relied upon.

6. Results

This study looked into the possibility of estimating optimized design specification using neural network learning in carrying out optimization design of mechanical parts. There is a problem of interpreting and modifying each time with the help of FEM analysis to find out optimized design specification when load changes. The purpose of this study lies in the test of how much the optimization design by neural network learning is reliable to resolve this kind of problem. As a result, it is concluded as follows:

1) For the model case of this study, it was found that the neural network can be used in the optimization design since there were approximately 7% of error between the estimation by use of neural network algorithm and the actual data.

2) For the case where optimization of parts specification is carried out while load condition changes after neural network learning is carried out through lots of data learning, neural network algorithm was at least found to be reliable.

Therefore, it was found that neural network algorithm can be used very effectively when optimization design is possible simply by changing parts specifications in accordance with product specifications.

References

1. Jasbir S. Arora, *Introduction To Optimum Design*, Mcgraw-Hill International Editions, (1994).
2. J.S. Siddal, 1983, Probabilistic Engineering Design, Marcel Dekker Inc.
3. S.S. Rao, *Reliability-Based Design*, McGraw Hill Inc (1992).
4. H. B. Demuth and M. H. Beale, *Neural Network Toolbox*, The MathWork, Miami (1997).
5. R. H. Myers, and D. C. Montgomery, *Response Surface Methodology: Process and Product Optimization Using Designed Experiment*, Jon Wiley & son, (1995).

COMPARISON OF THE MECHANICAL PROPERTIES OF LASER AND ARC WELDED 9CR-1MO STEEL

CHONG-IN OH †

Dept of Naval Architecture and Ocean Engineering, Chosun University, 375 Seosuk-dong Dong-gu, Gwangju 501-719, Korea

HAN-SUR BANG†

Division of Aerospace and Naval Architectural Engineering, Chosun University, Korea

HEE-SEON BANG

Division of Aerospace and Naval Architectural Engineering, Chosun University, Korea

MIN-SEONG GO

Project Planning Department, Hyundai Samho Heavy Industries CO. LTD, Korea

SEONG-JOO KIM

Senior Surveyor in Survey Team, Korea Register of Shipping, Korea

CHAN-SEUNG RO

Institute of Joining and Manufacturing, Chosun University, Korea

In this paper, comparison of mechanical features of the welded joint in 9Cr-1Mo steel welded by shielded metal arc welding (SMAW), and CO_2 laser welding using Numerical Analysis and Mechanical test, is presented more particularly. The result of residual stress and hardness analyses regarding each welding method shows that CO_2 laser had slightly higher value than SMAW. However, its difference was minute. Charpy impact test on specimens indicated that the impact absorbing energy of CO_2 laser was more than five times higher than SMAW. It has been observed that all specimens in both tensile test and bending test, were fractured in the base metal regardless of welding method

Keywords: 9Cr-1Mo steel; shielded metal arc welding; CO_2 laser welding; Numerical analysis; Mechanical property.

† Corresponding author E-mail : chong1015@hotmail.com
E-mail : hsbang@chosun.ac.kr

1. Introduction

The pressure vessel used for atomic power plant and petrochemical plant are subjected to harsh environments such as high temperature, high pressure, hydrogenous etc. 9Cr-1Mo steel known to be considerably superior for heat, pressure and corrosion resistance are used for manufacturing these structures. However, welding process generates deterioration of material and welding residual stresses caused by thermal cycles of heating and cooling, which reduce the stability in the weld. These effects are quite different according to the welding methods. Latest technical advance has made welding for thick plates capable by high output of laser welding equipment.

Therefore, in this present study, in order to confirm the possibility of applying the laser welding to heat and pressure resistance steel, low alloy 9Cr-1Mo steel was fabricated by SMAW and CO_2 laser welding, and the characteristic of welding heat distribution and residual stress in weldments of each welding process have been investigated and analyzed using the two dimensional heat conduction and elasto-plastic simulation. The strength of welded joints has been evaluated through the mechanical tests (hardness, low thermal toughness, bending and tensile). The mechanical phenomenon of thermal elasto-plastic behavior of laser welded joint has been characterized by means of two dimensional thermal elasto-plastic finite element analysis.

2. Method of experiments and finite element analysis

2.1. *Experiment conditions*

The chemical compositions and mechanical properties of the base metal are shown in Table 1 & 2. The principal dimension of specimens is 500(Length)× 300(Width)×16mm (Thickness). Considering heat input according to the welding process i.e. SMAW process with 10 passes with V-groove (60°) type and CO_2 laser welded joint with the full penetration 1 pass respectively. Table 3 & 4 shows the welding conditions of SMAW and CO_2 laser welded material. The hardness measurements with 1 Kg load. Bending and cryogenic toughness fracture test specimens were considered according to American Society for Testing and Materials (ASTM) and Korean Standard (KS)

2.2. *Finite element analysis*

Von-Mises condition based on the Linear Isotropic Hardening Rule is used as a yield function in the plastic region, with four-nodal iso-parametric element. The 2D finite element mesh view is as shown in Fig. 1 with 3069 nodes and 2944 elements and the boundary conditions for the stress analysis are as in Fig. 2. The work piece is initially at 20□. Convective flows in the weld pool, vaporization in

the keyhole and radiation heat transfer are not considered. The material is assumed to recover its mechanical stiffness below 750□. The temperature dependency of physical and mechanical properties of material is taken in account [1],[2]. To calculate heat input Q_{net} of each welding process, equation have been adopted from the established researches [3],[4].

3. Result of numerical analysis

Fig. 3 shows the thermal history of each welding process in the upper part of welds (Z=15mm). When thermal history and thermal gradient curves are examined; the local temperature in each of the welds reaches the melting point instantaneously and falls off rapidly. From the thermal history curves in each of the welds, it can be assumed that the heat generated by heat source in CO_2 laser welds dissipates at a faster rate to the area near the welds and the area affected by heat source is wider in SMAW joint than CO_2 laser welded joints. It is also assumed that the value of hardness in CO_2 laser welds is higher than SMAW.

Distribution of welding residual stresses is compared at upper line (Z=15.5mm) as shown in Fig. 4. Though slightly higher longitudinal welding residual stress (σ_x) is produced in the CO_2 laser welds, its distribution is narrow, uniform and symmetrical by the full penetration welding. But in the SMAW, the distribution of σ_x is wider and non-uniform due to the 10 passage laid along the different weld lines. In the case of SMAW, the stress component of thickness direction (σ_z) is less than other stress components. It can be assumed that restraint condition of thickness direction has a relation with aspect ratio of weld metal and cooling rates.

4. Result of experiments

4.1. *Hardness test of welded joint*

Distribution of hardness value in each welded joints are shown in Fig. 5. From the result of hardness measurement, the hardness of CO_2 laser weldment is little higher than that of SMAW. But the difference is negligible. And particularly the hardness distribution in CO_2 laser welding is much smaller than SMAW. This may be due to the narrow weld metal and HAZ.

4.2. *Bending and tensile test*

The main objective of this test was to determine the strength and weldability of each welding process. On close observation of the tested specimen in the tensile

test, rupture of all the specimens were in the region of base metal and in bending test no surface cracks were found.

4.3. *Low temperature fracture toughness of welded joint*

The test has been conducted at temperature of 0°C and -20°C and the tested specimen are shown in Table 5. The entire specimen showed a decrease in the absorbed energy of about 40~50% at -20°C. Also the impact absorbed energy of CO_2 laser welded joint was 5 times larger than SMAW case at 0°C. The reason for the larger absorbed energy in CO_2 laser welding than SMAW is due to the phenomenon that the fracture path deviated from deposited metal to base metal in CO_2 laser weld. (i.e. FPD: Fracture Path Deviation). This is considered as the characteristics of the laser welding that is caused by the narrow width of the deposited metal zone and HAZ.

5. List of tables

Table 1 Chemical Composition of used Material (%)

C	Si	Mn	P	S	Cr	Ni	Cu	Mo	V	Nb
0.085	0.150	0.379	0.080	0.097	9.376	0.17	0.020	0.911	0.008	0.001

Table 2 Mechanical Properties of used Material

Yield strength (MPa)	Tensile strength (MPa)	Elongation (%)	Reduction area (%)
500	670	30	59

Table 3 Welding condition of SMAW (Butt joint)

Pass	Current (A)	Volt (V)	Speed (cm/min)	Inter-pass Temp.(°C)
1	170	25	32.6	
2	170	25	32.0	
3	170	25	34.8	
4	170	25	32.9	175±10
5	170	25	38.7	AWS A5.5
6	170	25	32.9	E9016-B3
7	170	25	38.2	(163~191°C)
8	170	25	38.7	
9	170	25	37.6	
10	170	25	35.8	

Table 4 Welding condition of CO_2 Laser (Butt joint)

Type of Laser	Pulse-F CO_2 Laser (TRUMPF, 50,000 Hz)
Output power	12 kW
Travel speed	100 cm/min
Shield gas	He (15ℓ/min)

Table 5 Result of charpy impact test

SMAW		CO_2 laser	
0°C	-20°C	0°C	-20°C
64J	347J	38J	73J

6. List of figures

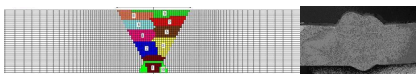

(a) SMAW (node :3069, element : 2944, 1.0 ㎜ × 1.0 ㎜) (b) CO_2 laser (node :3069, element : 2944, 1.0 ㎜ × 1.0 ㎜)

Fig. 1 Mesh Division & Cross Section according to welding process

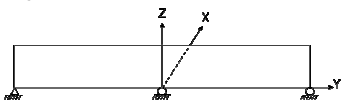

Fig. 2 Boundary condition for thermal elasto-plastic analysis

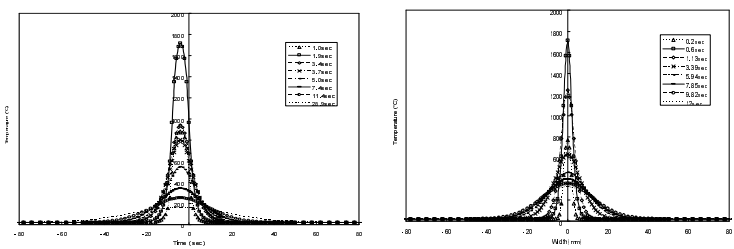

(a) SMAW (b) CO_2 laser

Fig. 3 Thermal history in welds (Z=15 ㎜)

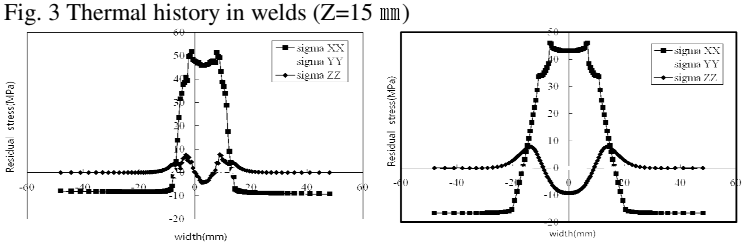

(a) SMAW (b) CO_2 laser

Fig. 4 Distribution of welding residual stress in welds (Z=15.5 ㎜)

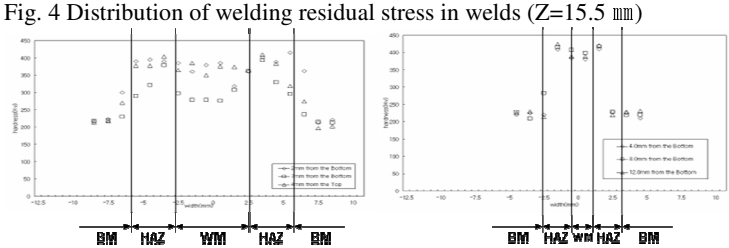

(a) SMAW (b) CO_2 laser

Fig. 5 Hardness distribution in each weld

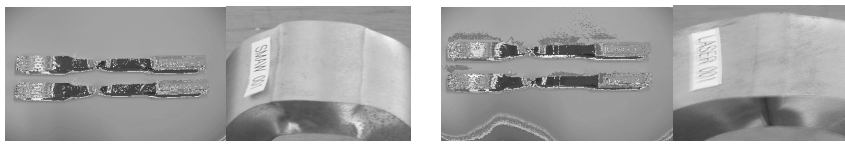

(a) SMAW (b) CO_2 laser

Fig. 6 Result of tensile and bending test in each weld

7. Conclusion

We reached the conclusions below

(1) Thermal history curve of each weld shows area affected by heat source in the order SMAW> CO_2 laser. From the result of residual stress analysis of each welding method, CO_2 laser has slightly higher value than SMAW but there is no much differences and also the residual stress distribution in CO_2 laser welding is much smaller than SMAW. The hardness of weldment using CO_2 laser is a little higher than that of SMAW. But its difference is negligible.

(2) Tensile test all specimens fractured in the base metal and in bending test all of them are without surface crack. The impact absorbing energy of CO_2 laser is found five times as large as the other two based on the Charpy impact test.

Based on the study Considering mechanical properties (residual stress distribution, bending test, low thermal toughness, hardness, microstructure etc.) in all their aspects with respect to each welding method, we confirm that it is more reasonable to choose the CO_2 laser welding in the fabrication of 9Cr-1Mo steel.

Acknowledgments

This study was supported by research funds from Chosun University, 2006.

References

1. E. A. Brandes and G. B. Brook, Smithells metal reference book, *Butterworth-Heinemann*, 7th ed., pp.14-27~14-41 (1992).
2. David R. Lide and H. P. R. Frederikse, CRC Handbook of Chemistry and Physics, *CRC press (National Institute of Standards and Technology),* 76th Edition, pp.12-176, 12-190 (1995-1996).
3. K. W. Carlson, The role of heat input in deep penetration laser welding, ICALEO, 49-57 (1985).
4. Koichi Masubuchi, Analysis of Welded Structures (Residual Stresses, Distortion, and their Consequences, Pergamon Press (1980).

ARTIFICIAL NEURAL NETWORK (ANN)-BASED RELIABILITY ANALYSIS OF A FIBER REINFORCED POLYMER (FRP) DECK

DONG HYAWN KIM

Department of Ocean System Engineering, Kunsan National University, Miryong, Kunsan, Jeonbuk, 573-701, Republic of Korea

DOO KIE KIM AND JINTAO CUI

Department of civil Engineering, Kunsan National University, Miryong, Kunsan, Jeonbuk, 573-701, Republic of Korea

In order to predict the failure probability of a complicated structure, the structure responses usually need to be estimated by a numerical procedure, such as finite element method. In this paper, an artificial neural network (ANN)-based reliability analysis is proposed. In this method, the relationship between the random variables (input) and structural responses is estimated using ANN models. ANN model is then connected to a reliability method, such as first order second moment (FOSM), or Monte Carlo simulation method (MCS), to predict the failure probability. The proposed method is demonstrated through application on a fiber reinforced polymer (FRP) deck. To reduce the computational effort required for reliability analysis, response surface method could be used. The obtained results show that the ANN-based reliability analysis method has comparative accuracy and efficiency.

1. Introduction

The use of Fiber Reinforced Polymer (FRP) as a primary structural material is increasing rapidly in the construction industry. FRP materials have considerable advantages in terms of weight, strength and corrosion resistance. They have been used for several decades in the aerospace, automobile and marine industries, where they have developed a good record of accomplishment in very adverse environmental conditions. Although FRP composites are increasingly being considered for use in civil engineering, their widespread use is constrained due to current consideration of higher initial cost, lack of comprehensive design approaches and guidelines, and the predominant use of a one-to-one replacement methodology that often restricts the full utilization of the characteristics of the material. The development of such new FRP composite bridge systems raises concerns related to the dynamic responses to traffic loads, mass and stiffness

characteristics, which are significantly different from those of conventional steel and structural concrete bridge structural components. However, there are few researches on the reliability analysis of the FRP material.

Structural reliability can be expressed by defining functional relations between strength (R) and load (L) parameters as follows,

$$M = R - L = g(X_1, X_2, ...X_n) \tag{1}$$

M is the limit state function and is sometimes referred to as safety margin or performance function. $X = (X_1, ..., X_i, ..., X_n)(i = 1, ..., n)$ denote n basic design random variables, g() denotes a function of all design variables. In general, the function g(X) can take any form provided that the failure of the structure is defined when $M \le 0$, and the survival of the structure is defined when $M > 0$.

For most practical structures (or system), the structural responses have to be calculated by a numerical procedure such as finite element analysis. This brings another level of complexity to reliability analysis because the limit state function g(X) is not available as an explicit, closed-form function of the input variables. Several computational approaches could be pursued for the reliability analysis of structures with implicit limit state functions. These can be divided into three categories, based on their essential philosophy: (1) Monte Carlo simulation (including efficient sampling methods and variance reduction techniques), (2) response surface approach, and (3) sensitivity-based analysis.

The inherent disadvantage of MCS is the tremendous computational effort for problems involving low probability of failure or problems that require a considerable amount of computation in each sampling cycle. To defeat this problem, numerous variance reduction techniques have been proposed, for example, importance sampling [1, 2], directional simulation [3], conditional expectation [4], and response surface method [5]. Shao and Murotsu [6, 7] developed a method to use ANN in reliability analysis. ANN is applied to approximate the limit state function and failure probability is then predicted by a reliability method, such as, FORM, SORM, and MCS in reliability analysis [8-12].

The aim of this paper is to develop a procedure in which ANN will be combined with some reliability methods so that the computational efficiency may be improved. Response surface method and an ANN model are used to approximate the limit state function so that the number of finite element runs can be dramatically reduced. Then connect the ANN model with both FORM and MCS.

2. Theory

2.1. *Reliability Analysis*

Reliability is defined as probability of safety of a system in a given environment and loading conditions and is assessed in terms of reliability index (β) values. For the estimation of reliability index, methods such as first order reliability method (FORM), second order reliability method (SORM), point estimate method (PEM), Monte Carlo simulation (MCS) are available in literature.

A reliability problem is normally formulated using a failure function, $g(X_1, X_2, ..., X_n)$, where $X_1, X_2, ..., X_n$ are random variables. Using Monte Carlo simulation technique, probability of failure can be computed for both explicit and implicit limit state functions. This method involves the generation of N random numbers of input soil parameters with given probabilistic characteristics. These N sample points for output response are used to obtain required sample statistics, which is incorporated in probabilistic calculations.

2.2. *Response Surface Method*

Response surface methodology (RSM) is a set of statistical techniques designed to find the optimized value of the response or to examine the relationship between experimental responses and variations in the values of input variables. It is also used to optimize response quantities, which are influenced by several independent variables, as it provides simple models of complicated processes.

Response surface method involves generation of polynomial equation using regression analysis and an approximate linear or non-linear functional relationship between dependent output y and input variables $(X_1, X_2, X_3, ...)$ is established. The following Eq. (2) shows second order regression model without interaction terms containing n input variables $X_1, X_2, ..., X_n$.

$$\bar{g}(X) = b_0 + \sum_{i=1}^{n} b_i X_i + \sum_{i=1}^{n} b_{ii} X_i^2 \tag{2}$$

Where $b_0, b_1, b_2, ...$ are regression coefficients.

2.3. *Artificial Neural Networks (ANN)*

Artificial neural networks (ANN) are relatively crude electronic models based on the neural structure of the brain. ANN has the capability of establishing a functional relationship between two data spaces during a learning process and reproduce/generalize these data during a recall process.

ANN is the most prevalent of the self-learning model of artificial neural networks. A simple architecture of ANN consists of an input layer, a hidden layer, an output layer, and connections between them (Figure 1). Sigmoid functions are utilized as non-linear activation functions for all layers.

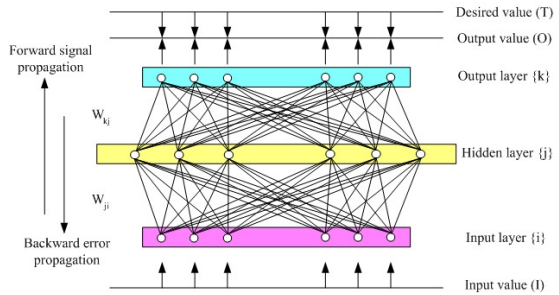

Fig. 1. Structure of back-propagation neural network

The corresponding architecture for back-propagation learning is incorporating both the forward and the backward phases of the computations involved in learning process. The learning mechanism of this back-propagation network is a generalized delta rule that performs a gradient descent on the error space to minimize the total error between the actual calculated values and the desired ones of an output layer during modification of connection strengths. In other words, a least mean square procedure is carried out which finds the values of the connecting weights that minimize the error function by using a gradient descent method.

Once the ANN model is created, it will be linked with a reliability method. For instance when FORM is linked with ANN, the main steps relating to linkage between ANN and reliability module for reliability analysis are : (1) set initial design point at the first iteration; (2) when a value of limit state function is required at the given design point, the trained ANN is called to provide the value of the limit state function; (3) repeat the calculation until it converges. Similarly, when MCS is linked with ANN, the main steps are: (1) randomly generate a set of values for all random variables; (2) when a value of limit state function is required at the randomly generated values of the variables, the trained ANN is called to provide the value of the limit state function; (3) repeat the calculation until the stop criteria is satisfied.

3. Example Study

3.1. *Definition of the Model*

A test model of a fiber reinforced polymer (FRP) composite deck that is adjoined by several FRP deck units as shown in Figure 2 is instrumented. The two longitudinal steel girders are supported by four base blocks at each end of the bottom flanges, in which the unsupported lengths are about a quarter of the steel girder lengths. The load with a magnitude of 50KN is exerted at the center area of the deck using two tires. The FE model in this analysis was developed based on best engineering judgment as shown in Figure 3.

Fig. 2. FRP Test Model

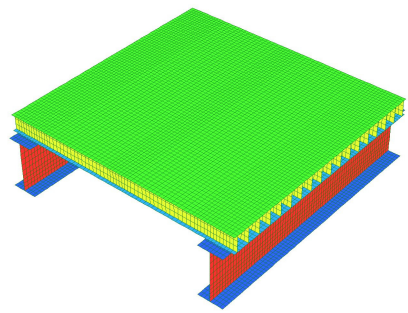

Fig. 3. Finite element model of the test FRP model

Here the limit state function was defined as the discrepancy of the allowable displacement from design codes and the maximum displacement from static analysis, which is a function of the stiffness. The stiffness of flanges and webs of the FRP deck was set to be random variables for the reliability analysis. Table 1 shows the probabilistic characteristics of the basic random variables of the composite plate by assumption.

Table 1 Probabilistic characteristics of the basic random variables

Basic design variable	Mean	Coefficient of variance COV	Standard deviation	Distribution type
TF_Ex	15.83Gpa	0.2	3.166	Normal
TF_Ey	14.86Gpa	0.2	2.972	Normal
W_Ex	17.61Gpa	0.2	3.522	Normal
W_Ey	14.27Gpa	0.2	2.854	Normal
BF_Ex	15.21Gpa	0.2	3.042	Normal
BF_Ey	15.80Gpa	0.2	3.160	Normal

3.2. *Results and Discussion*

Presented in Figures 4 and 5 are the probabilities of failures using MCS and FOSM, respectively. By using ANN, one can just prepare the training data of ANN and connect the developed ANN model with reliability methods (such as FORM and MCS). The process of ANN-based MCS satisfied the stop criteria after about 100,000 samples, while ANN-based FOSM took 7 iterations to converge. The values of safety index for MCS and FOSM are 3.402 and 3.313, respectively. One can see that the differences between them are very small that can be negligible. The results demonstrates that even though the limit state function is implicit, the ANN-based reliability method can accurately and efficiently estimate the probability of failure of structures.

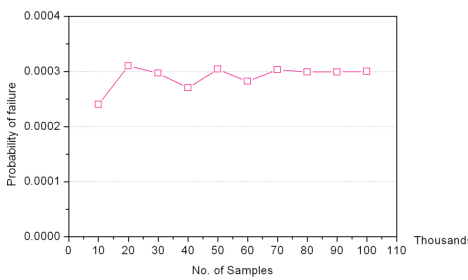

Fig. 4. Probability of failure for MCS

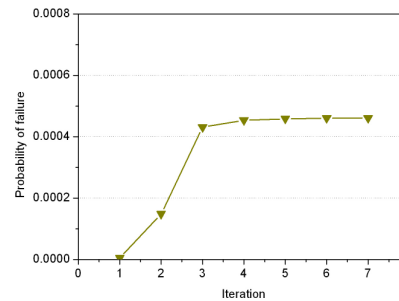

Fig. 5. Probability of failure for FOSM

4. Concluding Remarks

In order to reduce the computational effort required for reliability analysis of complicated structures to an acceptable level, several techniques, such as response surface method and artificial neural network, may be used in conjunction with the reliability method such as FORM and simulation techniques. In this paper, artificial neural network is applied to establish relation between input variables and important output parameters so that the limit state functions could be constructed based on ANN model. The developed ANN models are then successfully connected with reliability methods, Such as FORM and MCS, to predict the failure probability of structures. It is found that the ANN-based response surface method is more accurate and efficient than polynomial-based response surface method. It demonstrates that the ANN-based response surface method can be effective and efficient in reliability analysis, can be easily connected with other reliability methods.

References

1. Bucher C. Adaptive sampling-an iterative fast Monte Carlo procedure. Structural Safety, 5(2), 119-126, (1988).
2. Zheng Y, Fujimoto Y, Iwata M. An empirical fitting-adaptive approach to importance sampling in reliability analysis. Journal of Society of Naval Architects of Japan, 171, 433-441, (1991).
3. Bjerager P. Probability integration by directional simulation. Journal of Engineering Mechanics ASCE, 114(8), 185-302, (1988).
4. Ayyub B, Chia C. Generalized conditional expectation for structural reliability assessment. Structural Safety, 11, 131-146, (1992).
5. G.L. Sivakumar Babu, A. Srivastava. Reliability analysis of allowable pressure on shallow foundation using response surface method. Computers and Geotechnics, 34, 187-194, (2007).
6. Shao S, Murotsu Y. Structural reliability using a neural network. JSME. International Journal, 40(3), 242-246, (1997).
7. Murotsu Y, Shao S, Chiku N, Fujita K, Shinohara Y. Studies in assessment of structural reliability by response surface method and neural network, Reliability and Optimization of Structural System, B-12, 173-180, (1993).
8. Papadrakis M, Papadopoulos V, Lagaros N. Structural reliability analysis of elastic-plastic structures using neural networks and Monte Carlo simulation, Computer methods in applied mechanics and engineering, 136, 145-163, (1996).
9. Hurtado JE, Alvarez DA, Neural-network based reliability analysis: a comparative study. Computer Methods in Applied Mechanics and Engineering, 191, 113-132, (2001).
10. Deng J, Gu D, Li X, Yue Z. Structural reliability analysis for implicit performance functions using artificial neural network. Structural Safety, 27, 25-48, (2005).
11. Joao B. C., Joao R. de A., Jose M. D., and Pedro G. C. Structural reliability analysis using Monte Carlo simulation and neural networks, Advances in Engineering Software, (2007).
12. A. Hosni Elhewy, E. Mesbahi, Y. Pu. Reliability analysis of structures using neural network method. Probabilistic Engineering Mechanics, 21, 44-53, (2006).

MECHANICAL CHARACTERISTICS OF HYBRID WELDED JOINTS OF GALVANIZED STEEL

YEON HO KIM[*]

[*]*Graduate School, Department of Naval Architecture and Ocean Engineering*
Chosun University, Korea

HEE SEON BANG[**]

[**] *Department of Naval Architecture and Ocean Engineering*
Chosun University, Korea

SEONG JOO KIM[***]

[***]*Survey Team, Korea Register of Shipping, Korea*

HAN SUR BANG[****]

[****] *Department of Naval Architecture and Ocean Engineering*
Chosun University, Korea

Hybrid welding process has been taken as a technical attraction due to its superiorities such as deep penetration, gap bridging ability, high speed, and automation compared with other conventional methods. Galvanized steel is a promising material for long service life and superior corrosion resistance capability, namely, at least 3~6 times than that of Zn-coated steel. Therefore, this study has tried to prepare the hybrid welded (Pulsed Nd:YAG laser+TIG)Joints of galvanized steel as a new substitute process for conventional welding of lightweight parts.

Keywords: Hybrid Pulsed Nd:YAG laser +TIG; galvanized steel.

1. Introduction

Galvanized steel, widely used in the industry, are selected in this study for their high strength to weight and ratio combined excellent corrosion resistance and general good durability, low cost. For the reasons, Galvanized steel is an ideal material for a multitude of building applications and the industry The purpose of this study is to apply high speed hybrid welding process, for Galvanized steel that consist of Pulsed Nd:YAG Laser + TIG welding process, For this purpose, the

Corresponding Author [**] Tel. +82-62-230-7134, e-mail : hsbang@mail.chosun.ac.kr
[****] Tel. +82-62-230-7251, e-mail : banghs@mail.chosun.ac.kr

characteristics of process parameters(laser -arc distance, travel speed and output power of welding equipment, etc)are investigated for hybrid bead on plate and butt joint Relation between process parameter and geometric shape of bead is also investigated with the characteristics of metallurgical aspects of welds formed by hybrid welding. Reliability assessment and verification of the welding design and construction criteria for welds formed by hybrid welding are conducted through the experiment

1.1. Materials List

Chemical composition of galvanized steel has been given in Table 1~2. Thickness of sheet, used in experiment of Hybrid welding for Galvanized steel, is 0.8~1.2mm. And standard of sheet, is used in experiment, is 200 mm(L) x 100mm(w) x 1mm(t).

1.2. Experimental Set-up

A combined welding setup including a Pulsed ND:YAG Laser and TIG torch was developed, as shown in Fig1 Principle of experimental set-up focal angle of incident for Hybrid welding. The welding direction is Laser leading. Focal length is 112mm. Focused spot size of approximately 1mm diameter. The diameter of tungsten electrode was 1.0mm. The TIG torch was connected close to the Pulsed Nd:YAG laser focusing optic at an angle of about 40? Shielding gas was supplied through a TIG gas nozzle only. Experimental setup for Pulsed Nd:YAG laser, TIG and hybrid welding is shown in Fig 1 and the other parameters concerning the experimental setup are shown in table 3. In this study, for the initial test, the angle between hybrid head and flange was at angle of 40 degrees and incidence position was a contact line. The gap size was approximately zero with considering gap tolerance. Comparison between top-side, bottom-side, and cut section

1.3. Result and Discussion

In the case of TIG welding for Butt joints, welding speed about 40mm/s is quite good for making proper weld bead even if Pulsed Nd:YAG Laser welding has benefits for inducing good welds . TIG welding alone does not become the welding process here due to the lack of filler metal and high welding speed which is caused due to less heat input. It does not secure molten pool sufficient is caused by with the quick welding the nail printed style of writing There were two cases of hybrid welding like laser leading and TIG leading conditions. Many previous research reports, generally, mentioned that laser leading process causes good welds. Laser leading process has less contamination and spatter because laser induce plasma near the molten pool is effective in stabilizing the arc. In TIG leading case, occurrence of contamination and spatter were increased as compared

with laser leading condition. Moreover, it seems to be humping beads because welding speed was too fast with strong arc force and incomplete fusion. Figure 2. Bead shapes of butt joints by Hybrid welding process; No.1Pulsed Laser power is in 40mm/s welding speed, No.2, No.3, No.4, No.5. From the result of cross section, the all of specimen have not enough penetration. because TIG pulsing which occurs that the energy of heat input is only used for wire melting. Therefore, those specimens are hardly welded.

1.3.1. Hardness

A micro hardness measurement was made on transverse sections of the weld meltals in bead on plate welding specimen at condition No 1. A load of 10g and a spacing of 0.1mm and 0.1 mm between the indentations were used. From the test result of hardness shown in figure 5, hardness value of HAZ (heat affected zone) has the intermediate value between WM and BM (base metal) in general. it is known that strength of metal has the relation being proportional with the hardness value. Therefore, it can be estimated that the strength of WM and HAZ are reduced in the hybrid welds compared with the strength of BM.

1.3.2. Tensile strength

The tensile specimens were excised from each of the welded test plate transverse to the welding direction and tested according to the KS0801-5. The sub size specimen was used for the test. The reinforcement of the welded specimens was not removed to consider actual joint condition. From the test result of tensile strength shown in figure 4 Ultimate tensile strength of the parent material is about 400MPa. NO 1~3 specimens for tensile test have been failed in the basic metal. But No 4~5 specimens for tensile test have been failed in the weld metal

1.4. List of tables

Table 1. Chemical composition of specimen(wt %)

C	Si	Mn	P	S	Ni	Cr	Mo
0.06	**0.0244**	**0.225**	**0.0128**	**0.0167**	**0.0056**	**0.0192**	**0.0071**

Table 2. Mechanical property

Mechanical property		
YP(MPa)	TS(MPa)	EL(%)
235	**400**	**21**

Table 3. Range of welding parameters

Pulsed Nd:YAG Laser	TIG	Hybrid welding
Power = 400W ~600W Focal depth = 0mm Focal length = 112mm Shielding gas = 30L/min Ar(90%)/He(10%) Welding speed = 40~49mm/min	Tungsten electrode d=1mm TIG current = 100~500mmA Shielding gas = 30L/min Ar(90%)/He(10%) TIG torch angle = 40 degrees	Laser welding condition + TIG Condition Leading process : Laser leading Welding speed =40~49mm/min Distance between Laser + Tungsten electrode tip = 3mm Shielding gas = 30L/min Ar(90%)/He(10%)

Table 4. Range of welding parameters

Condition	Laser(Input)	Laser(output)		TIG	Speed
1	1.8kw	3.4J	511.3w	300mA	40mm/s
2	1.7kw	3.2J	483.0w	300mA	40mm/s
3	1.6kw	3.0J	456.2w	300mA	40mm/s
4	1.5kw	2.8J	430.2w	300mA	40mm/s
5	1.4kw	2.6J	403.9w	300mA	40mm/s

1.5. List of figure

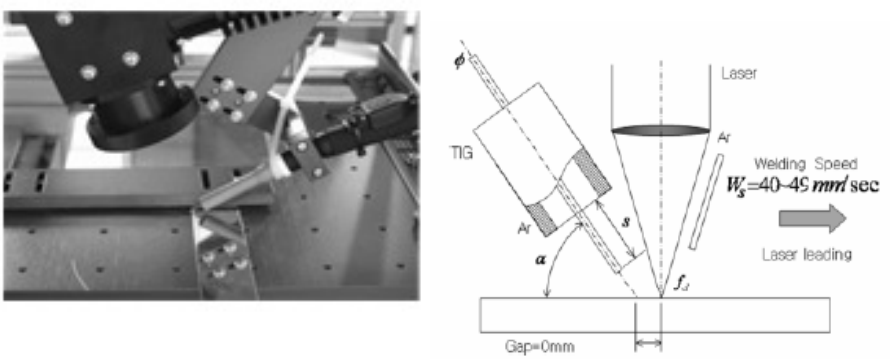

Fig.1. Principle of experimental set-up focal angel of incident for Hybrid welding

Fig. 2. Bead shapes of butt joints by Hybrid welding
Process; No.1, No.2, No.3, No.4, No.5 is pulsed Nd:YAG
Laser_TIC is in 40mm/s welding speed

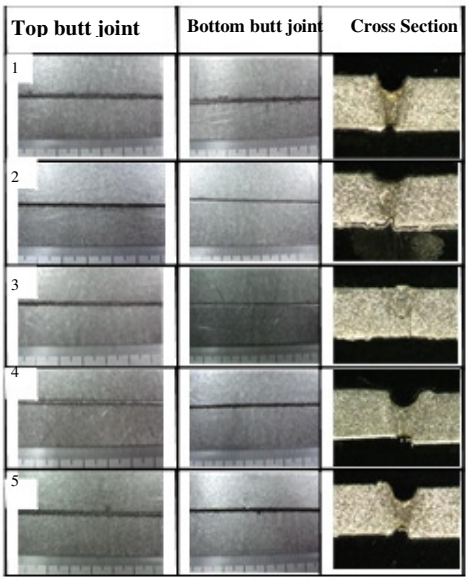

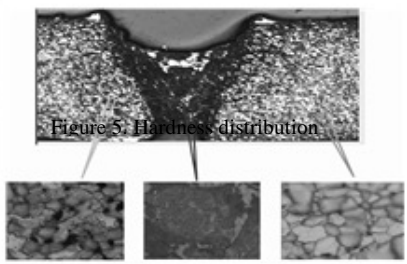

Fig. 3. Micro Structure

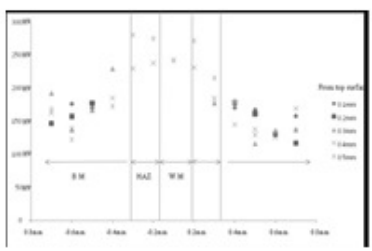

Fig. 5. Hardness distribution

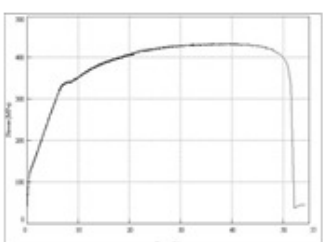

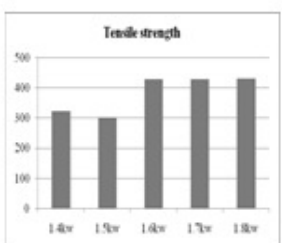

Fig. 4. Tensile strength

Conclusion

Pulsed Nd:YAG laser and TIG arc hybrid welding on Butt joints of 1mm Galvanized steel are considered as given in below steps. Fundamental welding phenomena of hybrid process using Pulsed Nd:YAG laser and TIG was investigated by the experiments. Mechanical and metallurgical characteristics of hybrid welds were also analyses and compared with other results in order to supply the fundamental information for the criteria of welding design and construction is compared with different welding speeds

1. Although the welding speed of laser is high enough to meet the productivity demand, in Butt joints case, quality is the problems.
2. Compared with laser welding and TIG, penetration depth in laser-arc hybrid welding is greatly increased due to improvement of laser beam absorption. Furthermore, laser beam produces a stabilized arc in hybrid welding.
3. In this study, the gap size is almost zero. So the laser leading condition for hybrid weld was recommended which usually make better welds than TIG leading condition.
4. TIG welding alone does not become the welding process here due to the lack of filler metal and high welding speed which is caused due to less heat input

Acknowledgments

This study was supported (in part) by research funds from Chosun University, 2006

References

1. S. Kaierle, K. Bongard, M. Dahmen, R. Poprawe, “Innovative hybrid welding process in an industrial application”, ICALEO 00, section C, pp. 91~98
2. E. G. WEST, THE WELDING OF NON-FERROUS METALS, CHAPMAN & HALL LTD, 1951, pp. 129~254.
3. ASM International Handbook Committee, ASM Handbook, Volume 6 Welding, Brazing, and Soldering, pp. 537~540, ASM International 1993.
4. K. Behler, J. Berkmanns, A. Ehrhardt, W. Frohn. “Laser beam welding of low weight materials and structures.” Materials & Design, Vol. 18, Nos. 4/6, pp. 261~267, 1997.
5. WELDING HANDBOOK, Eighth Edition, Volume 3, MATERIALS AND APPLICATION PART 1, pp. 100~110, AMERICAN WELDING SOCIETY.
6. Ulrich Dilthey, “Laser Arc Hybrid Welding - an Overview.” International Institute of Welding, IIW-Doc. XII - 1710-02, pp. 243-248, Copenhagen 2002.

ANALYSIS OF ROUND ROBIN TEST FOR RELIABILITY EVALUATION ON ULTRASONIC THICKNESS MEASUREMENT OF WALL THINNED PIPE IN NUCLEAR POWER PLANT*

JOON-HYUN LEE

Graduate School of Mechanical Engineering, Pusan National University, San 30 Jangjeon-dong, Kumjeong-gu, Pusan, 609-735, KOREA

DAE-HOON LEE

Graduate School of Mechanical Engineering, Pusan National University, San 30 Jangjeon-dong, Kumjeong-gu Pusan, 609-735, KOREA

SUNG-HO LEE

Korea Electric Power Research Institute, Yuseong Daejeon, 305-380, KOREA

Wall thinning measurement of pipeline is carried out during every overhaul period to keep integrity in Nuclear Power Plants (NPPs). Therefore, the reliable inspection of thickness measurement is very important. The objective of this study is to evaluate confidence of conventional thickness measurement system by conducting Round Robin Test (RRT). Artificial corrosion flow of varying depths 20, 40, 60, 80% of nominal thickness were machined on 19 types of artificial mock-up specimen with 2, 4, 6, 8 or 12 inch nominal diameter for all types of pipe, elbow, tee and reducer. To compare with artificial mock-up specimen, 4 types of field specimens with natural corrosion used in NPPs were prepared. The RRT was preformed by 4 teams consisting of 3 member per team from 3 certified inspection companies. One team is consist of ordinary inspectors and others are consisting of normal inspectors. 23 specimens with different size and shape of pipe were used according to standard practice in RRT. For analysis of accuracy and precision, bias and repeatability and reproducibility can be estimated from RRT results. Gage R&R was introduced for six sigma level. Confidence intervals of thickness measurement system were obtained by analyzing bias.

* This work is supported by KEPRI.

1. Introduction

Local wall thinning of pipes used in nuclear power plants (NPPs) is the major cause of accidents in the nuclear power plant (NPP). Therefore, the prevention of these accidents has necessitated reliable non-destructive inspection methods. The conventional inspection of wall thinning in the pipeline of NPPs was carried out by ultrasonic testing. In overhaul, the ultrasonic thickness measurement is performed selectively for the pipelines of NPP. This selection is based on criteria such as temperature, pressure, enthalpy, power level, water chemistry, and component geometry, etc. Subsequently, the selective data for each component of the pipeline is stored and analyzed in the computer S/W of CHECWORKS for maintenance and conservation. The CHECWORKS code is used as a tool for making a diagnosis of the wear level of plant. This enables the prediction of the degree of wall thinning and the remaining service life on components. The CHECWORKS program uses the results from the ultrasonic thickness measurement as one of the important factors in the process of analysis that predicts the remaining service life of the NPP. Therefore, if the thickness of the pipe measured by the inspector is in any way different from the real thickness of the pipe, serious problems can arise in terms of the integrity of the nuclear power plant. To solve this problem, it is important to verify the expertise of the inspector. In this study, a round robin test (RRT) was performed so as to evaluate the reliability of the data obtained from the ultrasonic thickness measurement.

2. Experimental set-up and analysis

2.1. *Round Robin Test (RRT)*

The objective of this test is to verify the reliability of the thickness measurement by evaluating critical factors that may influence the results. In order to meet this objective, the standard practice of NPPs is used in RRT, and each process of RRT is established in consideration of various factors.

2.1.1. *Specimens*

Artificial corrosion flaw of varying depths, from 20 to 80% nominal thickness, were machined on specimens with 2, 4, 6, 8 or 12-inch nominal diameter for all types of pipe, elbow, tee, and reducer respectively. In addition, in order to compare with the artificial mock-up specimens, 4 types of field specimens that are used in NPPs were prepared for the test. The full grids of the mock-up

specimens were marked according to standard practice. Artificial FAC were fabricated on the inner side of the mock-up specimen by the Eq. (1) as shown below.

$$L = 4\sqrt{Rt}$$
$$W = \pi R \times 0.25 \quad (1)$$

All of the specimens using the Round Robin Test are 23 sets. The diameter, nominal thickness and defect number of each part are shown in Table 1

Table 1. Specimens of Round Robin Test

Type		Nominal thickness (mm)	Flaw	Type		Nominal thickness (mm)	Flaw
2”	Pipe	3.91	7	8”	Pipe	8.18	7
	Elbow	3.91	2		Elbow	8.18	2
	Tee	3.91	3		Tee	8.18	3
	Reducer	3.91	2		Reducer	8.18	2
4”	Pipe	6.02	7	12”	Pipe	9.52	7
	Elbow	6.02	2		Elbow	9.52	2
	Tee	6.02	3		Tee	9.52	3
	Reducer	6.02	2		Reducer	-	-
6”	Pipe	7.11	7	16” Elbow		12.7	Natural
	Elbow	7.11	2	3.5” Elbow		5.49	Natural
	Tee	7.11	3	3.5 Tee		5.49	Natural
	Reducer	7.11	2	16” Expander		30.96	Natural

2.1.2. *Experimental method*

4 teams, from 3 inspection companies, performed the RRT. Each team in the experiment consisted of 3 members as shown in Table 2. 9. Groups 1, 2, and 3 participants were general inspectors, while in Group 4, 3 expert inspectors over ASNT level II participated. Each inspector measured all the mock-up specimens that had an artificial or natural wall thinned defect, using a thickness gage and probe.

Table 2. Inspector of Round Robin Test

Group	Company	Experience (year)	Level	Group	Company	Experience (year)	Level
1	A	5~10	II	3	C	5~10	II
		5~10	II			5~10	II
		5~10	II			5~10	II
2	B	10~15	II	4	D	10~15	III
		10~15	III			10~15	II
		10~15	II			10~15	II

Expert inspectors are permanently employed in NPPs to periodically inspect the thickness of pipes, while general inspectors are employed to inspect the thickness of pipelines only for overhaul periods in NPPs. After the inspectors mastered the thickness measurement standard practice, all of the specimens of the RRT were measured again 3 times.

2.2. *Gage R&R analysis*

Measurement system errors consist of repeatability and reproducibility. Repeatability error refers to a measurement variation by one inspector with the same gage. Repeatability errors include measurement direction, position variations etc. Reproducibility errors consist of variation depending on the expertness, measurement methods etc., of each inspector. The sum of the repeatability and reproducibility is called the Gage R&R value.

3. Experimental result

In this study, the data measured from the RRT was analyzed using the Gage R&R method. Tables 3 and 4 show the results of the Gage R&R analysis of ultrasonic thickness measurement data for specimens measured by 3 expert inspectors and 9 general inspectors. The gage R&R method was applied to the analysis of the repeatability and reproducibility error in terms of the shape and diameter of the mock-up specimen and the expertness of the inspectors.

Table 3. Gage R&R analysis of expert inspectors

Diameter (inch)	Pipe (mm)	Elbow (mm)	Tee (mm)	Reducer (mm)
2	0.10 (2.6%)	0.11 (2.8%)	0.19 (3.6%)	0.16 (2.6%)
3.5	-	0.11 (1.9%)	0.15 (2.6%)	-
4	0.11 (1.8%)	0.09 (1.5%)	0.18 (2.2%)	0.19 (2.4%)
6	0.10 (1.4%)	0.16 (2.3%)	0.17 (1.8%)	0.24 (2.9%)
8	0.14 (1.5%)	0.17 (2.1%)	0.16 (1.6%)	0.23 (2.2%)
12	0.14 (1.5%)	0.13 (1.4%)	0.14 (1.2%)	-
16	-	0.11 (0.9%)	-	0.37 (1.2%)

Table 4. Gage R&R analysis of general inspectors

Diameter (inch)	Pipe (mm)	Elbow (mm)	Tee (mm)	Reducer (mm)
2	0.21 (5.4%)	0.31 (7.9%)	0.31 (5.6%)	0.31 (5.0%)
3.5	-	0.37 (6.8%)	0.41 (7.5%)	-
4	0.17 (2.8%)	0.29 (4.7%)	0.28 (3.5%)	0.31 (3.9%)
6	0.16 (2.3%)	0.25 (3.5%)	0.25 (2.7%)	0.24 (2.9%)
8	0.16 (1.9%)	0.20 (2.4%)	0.22 (2.1%)	0.20 (2.0%)
12	0.17 (1.8%)	0.19 (2.1%)	0.19 (1.6%)	-
16	-	0.19 (1.5%)	-	0.70 (2.3%)

The analysis compared results from general inspectors and expert inspectors. The results show confidence internals of 31.6% in pipe, 42% in elbow, 32.7% in tee, and 43.9% in reducer and over 60% in 3.5-inch specimens.

Table 5. Gage R&R analysis in elbow

Diameter (inch)	Total (mm)	Intrados (mm)	Extrados (mm)
2	0.11(2.8%)	0.13(3.2%)	0.14(3.7%)
4	0.09(1.5%)	0.16(1.4%)	0.11(1.8%)
6	0.16(2.3%)	0.26(3.7%)	0.21(2.9%)
8	0.17(2.1%)	0.27(2.8%)	0.21(2.9%)
12	0.11(1.2%)	0.17(1.8%)	0.13(1.4%)
Average	0.13(1.9%)	0.15(2.2%)	0.14(2.1%)

Table 6. Gage R&R analysis of reducer

Diameter (inch)	Inlet (mm)	Middle (mm)	Outlet (mm)
2	0.18(3.4%)	0.17(2.7%)	0.15(2.1%)
4	0.08(1.1%)	0.16(2.0%)	0.09(1.0%)
6	0.13(1.7%)	0.37(3.9%)	0.11(1.1%)
8	0.25(2.7%)	0.21(2.1%)	0.13(1.2%)
Average	0.16(2.2%)	0.21(2.7%)	0.12(1.4%)

In order to acquire accurate confidence, mock-up specimens of the elbow and reducer were analyzed at intervals. . Tables 5 and 6 show confidence intervals of the intrados & extrados parts in the elbow and inlet, and of the outlet and middle parts in the reducer.

Tables 5 and 6 show that the intrados and extrados parts in the elbow and the middle part in the reducer have a higher error rate than other parts. This higher rate could be a consequence of the degree of difficulty in measuring the curved shapes of these parts.

4. Conclusion

The precision of the thickness measurement of wall-thinned pipe in NPPs was analyzed by RRT and Gage R&R analysis. Furthermore, the reliability of the UT inspection system was verified.

The results of the study show that accuracy is affected by the diameter and shape of the specimen. Accuracy is greater when the diameter is larger and the shape of the pipe is simple. . Results with the most accuracy occur when a pipe is straight, while results with the least accuracy occur in elbow and reducer pipes.

Using ultrasonic thickness data of verified confidence intervals will assist in judging the adequate time to replace the pipeline in NPPs. Analyzing reliability between general and expert inspectors will help to find error factors and improve reliability.

The results of this study can therefore be used to prepare standard practice for reliable thickness measurements in pipelines of NPPs. These results verified confidence intervals according to specimens and can improve the integrity of the CHECWORKS program.

Acknowledgments

This work was supported by Optimization of Thinned Pipe Management Program and Application project conducting by Korea Hydro & Nuclear Power Co. LTD and Korea Electric Power Research Institute.

References

1. P. G. Heasler, S.R. Doctor, NUREG/CR-5068 PNNL-10475 (2004).
2. Burdic, Richard K., and Larsen, Journal of Quality Technology, Vol. 29. (1998).
3. Smith, J. O. and Abel, J. S., IEEE Trans. Speech and Audio Proc., 7(6): 697-708 (1999).

BOUNDARY ELEMENT ANALYSIS OF OSMOTIC BLISTERING BEHAVIOR OF POLYMERIC COATING FILM

SANG SOON LEE

Korea University of Technology and Education School of Mechatronics Engineering
P.O.Box 55, Chonan, Chungnam, 330-600, South Korea

The osmotic blistering behavior of polymeric coating film which is in contact with an aqueous environment has been investigated. In this study, the coating film has been assumed to be linearly viscoelastic. Interfacial stresses induced in a laminate model consisting of the viscoelastic film and the elastic substrate as the film absorbs moisture from the ambient environment have been investigated using the time-domain boundary element method. The overall stress intensity factor for interfacial cracks subjected to a uniform osmotic pressure has been computed using the tractions at the crack tip node. The magnitude of stress intensity factors decreases with time due to viscoelastic relaxation, but remains constant at large times. The numerical procedure does not permit calculation of the limiting case for which the crack length vanishes.

1. Introduction

The adhesion of polymers to a variety of substrates is of great technological importance. Many polymers are widely used as coating films which are in contact with an aqueous environment[1-3]. The coating films are semi-permeable membranes, permeable to water, but impermeable to dissolved solids. Under such conditions, after water is absorbed by the film, it is subsequently transferred to the film/substrate interface. There it may come in contact with the soluble material on the substrate and leave the film to dissolve the material. Under fresh water conditions (distilled water or even high humidity), such interface dissolution creates a concentration gradient across the film, which here acts as a semi-permeable membrane. On the downstream side of the film where the solute is dissolved by water from the film, the solute concentration is much higher than the solute concentration at the external (or up-stream) face of the film. Under these conditions, water is drawn through the film towards the concentrated solute, under osmotic pressure. This transfer of water occurs because the water pressure and salt concentrations on either side of the membrane attempt to equilibrate. As solution concentration drops with additional migration of water, osmotic pressure becomes too great for the adhesive forces holding coating film to the substrate and results in interfacial cracks[4-6] or the localized delamination of film as a solution-filled blister.

This paper deals with the osmotic blistering behavior of polymeric coating film which is in contact with an aqueous environment. Polymeric films in general respond in a viscoelastic manner under loads and their time-dependent behavior is affected by moisture. In this study, the coating film is assumed to be linearly viscoelastic. The boundary element method[7-9] is employed to investigate the blistering behavior of the coating film.

2. Boundary Element Analysis

A viscoelastic thin film bonded to an elastic substrate is shown in Fig.1(a). The osmotic pressure becomes too great for the adhesive forces holding coating film to the substrate and results in the interfacial crack of film as a solution-filled blister. Due to symmetry, only one half of the layer needs to be modeled. Fig. 1(b) represents the two-dimensional plane strain model for analysis of the interfacial stresses between the film and the substrate.

The osmotic pressure is assumed to be uniform along the interfacial crack. It is further assumed that moisture effects are analogous to thermal effects. A uniform moisture change $\Delta mH(t)$ in the film is equivalent to increasing the tractions by $\gamma(t)n_j$ [10] where

$$\gamma(t) = 3K\beta\Delta mH(t) \tag{1}$$

Here, K is the bulk modulus; n_j are the components of the unit outward normal to the boundary surface; and β is the coefficient of hygral expansion of the viscoelastic film.

The boundary integral equations without any other body forces are written as follows [10]:

For viscoelastic thin film,

$$\begin{aligned}
&c_{ij}(\mathbf{y})u_j(\mathbf{y},\xi) \\
&+\int_S\left[u_j(\mathbf{y}',\xi)T_{ij}(\mathbf{y},\mathbf{y}';0+)+\int_{0+}^{\xi}u_j(\mathbf{y}',\xi-\xi')\frac{\partial T_{ij}(\mathbf{y},\mathbf{y}';\xi')}{\partial\xi'}d\xi'\right]dS(\mathbf{y}') \\
&=\int_S\left[t_j(\mathbf{y}',\xi)U_{ij}(\mathbf{y},\mathbf{y}';0+)+\int_{0+}^{\xi}t_j(\mathbf{y}',\xi-\xi')\frac{\partial U_{ij}(\mathbf{y},\mathbf{y}';\xi')}{\partial\xi'}d\xi'\right]dS(\mathbf{y}') \\
&+\int_S\left[\gamma(\xi)n_jU_{ij}^m(\mathbf{y},\mathbf{y}';0+)+\int_{0+}^{\xi}\gamma(\xi-\xi')n_j\frac{\partial U_{ij}(\mathbf{y},\mathbf{y}';\xi')}{\partial\xi'}d\xi'\right]dS(\mathbf{y}')
\end{aligned} \tag{2}$$

For elastic substrate

$$c_{ij}(\mathbf{y})u_j(\mathbf{y},\xi)+\int_S u_j(\mathbf{y}',\xi)T_{ij}(\mathbf{y},\mathbf{y}')dS(\mathbf{y}')$$

$$=\int_S t_j(\mathbf{y}',\xi)U_{ij}(\mathbf{y},\mathbf{y}')dS(\mathbf{y}')+\int_S \gamma(\xi)n_j U_{ij}(\mathbf{y},\mathbf{y}')dS(\mathbf{y}') \tag{3}$$

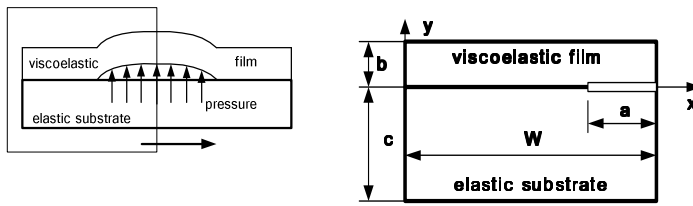

(a) (b)

Fig. 1. Interfacial crack of film as a solution-filled blister

where u_j and t_j represent displacement and traction, and S is the boundary of the given domain. $c_{ij}(\mathbf{y})$ is dependent only upon the local geometry of the boundary. For $\mathbf{y}$ on a smooth surface, the free term $c_{ij}(\mathbf{y})$ is simply a diagonal matrix $0.5\delta_{ij}$. The viscoelastic fundamental solutions, $U_{ij}(\mathbf{y},\mathbf{y}';\xi)$ and $T_{ij}(\mathbf{y},\mathbf{y}';\xi)$, can be obtained by applying the elastic-viscoelastic correspondence principle to Kelvin's fundamental solutions of linear elasticity.

In Eq. 2, ξ is the *reduced time* defined as follows:

$$\xi=\xi(t)=\int_0^t A_m\big(m(\lambda)\big)d\lambda \tag{4}$$

where A_m is the shift function, a function of moisture cycle. Under the constant moisture change $\Delta mH(t)$, the reduced time ξ of Eq. 4 becomes

$$\xi=A_m t \tag{5}$$

Eqs. 2 and 3 can be solved in a step by step fashion in time by using the modified Simpson's rule for the time integrals and employing the standard BEM for the surface integrals. Solving Eqs. 2 and 3 under boundary conditions leads to determination of all boundary displacements and tractions.

The following viscoelastic model for the film is in this study

$$E(t)=\frac{3200}{1+0.0336t^{0.19}}\quad \text{MPa} \tag{6}$$

$$K(t) = 3550 \quad \text{MPa} \quad (t : \min.) \tag{7}$$

where $E(t)$ is a tensile relaxation modulus, $K(t)$ is a bulk modulus.

3. Stress Intensity Factor for an Interfacial Crack

The stress field near an interface crack between linear elastic material and linear viscoelastic material in the Laplace transformed space are given as follows [6]:

$$\left[\overline{\sigma_{yy}}(r,\theta;s) + i\overline{\tau_{xy}}(r,\theta;s)\right]_{\theta=0} = \frac{\overline{K_1} + i\overline{K_2}}{\sqrt{2\pi r}} \exp\left[i\overline{\beta}(s)\ln\left(\frac{r}{d}\right)\right] \tag{8}$$

where

$$\overline{\beta}(s) = \frac{1}{2\pi}\ln[\overline{\gamma}(s)], \quad \gamma = \frac{\overline{\kappa_I}(s)\mu_{II} + s\overline{\mu_I}(s)}{\kappa_{II}\, s\overline{\mu_I}(s) + \mu_{II}} \tag{9}$$

$$\overline{\kappa_I}(s) = 3 - 4s\overline{\nu_I}(s), \quad \kappa_{II} = 3 - 4\nu_{II} \tag{10}$$

Here $\overline{\sigma_{yy}}(s)$ and $\overline{\tau_{xy}}(s)$ are the Laplace transformed viscoelastic stresses, $\overline{K_1}(s)$ and $\overline{K_2}(s)$ are the Laplace transformed stress intensity factors, and s is the transform variable. $\overline{\mu_I}(s)$ and $\overline{\nu_I}(s)$ are Laplace transforms of the shear relaxation modulus $\mu_I(t)$ and the viscoelastic Poisson's ratio $\nu_I(t)$.

As can be seen from Eq.8, the stresses exhibit an oscillating singularity. However, the maximum amplitude of these singular stresses is determined by the overall stress intensity factor as follows:

$$K_O(t) = \lim_{r\to 0}\sqrt{2\pi r}\sqrt{\left[\sigma_{yy}(r,0;t)\right]^2 + \left[\tau_{xy}(r,0;t)\right]^2} \tag{11}$$

The overall stress intensity factor $K_O(t)$ for the elastic-viscoelastic interface crack can be determined from the stresses near the crack tip using Eq. 11. It is well known that by using the quarter-point element for displacement fields and the traction singular quarter-point element for the traction field, the variation of the displacements and tractions along the crack tip element is of the correct order as those established in fracture mechanics theory [8,9]. The stress intensity factor can be expressed from Eq. 11 as

$$K_O(t) = \sqrt{2\pi L}\sqrt{\left[t_1^A(t)\right]^2 + \left[t_2^A(t)\right]^2} \tag{12}$$

where t_i^A denote the BEM computed traction on the traction singular crack tip element at the crack tip node and L is the length of the crack tip element.

The problem for interfacial cracks between the viscoelastic film and the elastic substrate subjected to a uniform pressure $PH(t)$ is solved. The analysis model is

shown in Fig.1. It is assumed that $(W-a)>9b$. The model has 38 boundary elements for $a/b=1.0$, 0.5 0.06 , 0.03 . Fig.3 shows the BEM results of $K_O(t)$ for crack lengths $a/b=1.0$, 0.5 0.06 , 0.03 , in which $K_O(t)$ for each crack length is relaxed with time. $K_O(t)$ is seen to decrease with decreasing crack size. The crack tip elements are used with small crack tip element to crack length ratios (L/a) to represent properly both the $\sqrt{r}$ displacement behavior and $1/\sqrt{r}$ traction behavior. As $a \to 0$ ($a/b<10^{-3}$), however, the boundary element procedure is inaccurate due to the instability of the crack tip elements to represent the stress singularity. This means that the numerical procedure does not permit calculation of the limiting case for which the crack length vanishes.

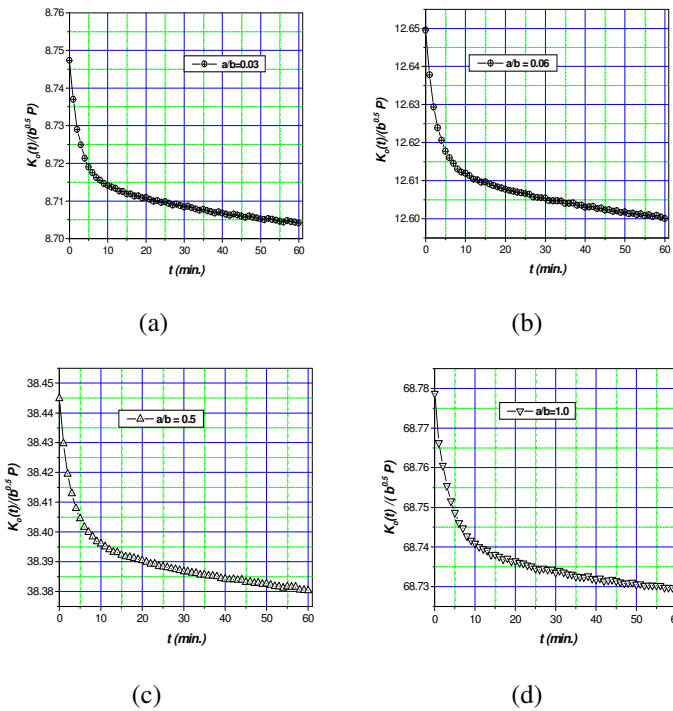

Fig. 2. Variation of overall stress intensity factors

4. Conclusions

The osmotic blistering behavior of polymeric coating film which is in contact with an aqueous environment has been investigated using the time-domain boundary element method. Polymeric films in general respond in a viscoelastic

manner under loads and their time-dependent behavior is affected by moisture. Therefore, a time-dependent stress analysis of the film has been performed to understand and predict failure in coating systems. In this study, the coating film has been assumed to be linearly viscoelastic.

The overall stress intensity factor for interfacial cracks between the viscoelastic film and the elastic substrate subjected to a uniform osmotic pressure has been computed using the tractions at the crack tip node. The magnitude of stress intensity factors decreases with time due to viscoelastic relaxation, but remains constant at large times. The numerical procedure does not permit calculation of the limiting case for which the crack length vanishes.

Acknowledgments

This work has been supported by KESRI(R-2005-B-124), which is funded by MOCIE(Ministry of commerce, industry and energy).

References

[1] D.G. Weldon, *Failure Analysis of Paints and Coatings*, John Wiley & Sons, Ltd. (2001)

[2] P.A.Schweitzer, *Paint and Coatings*, CRC Press (2006)

[3] C.H. Hare, *Paint Film Degradation*, SSPC(2001)

[4] M.L. Williams: *Bull. Seismological Society of America*, 49, 199(1959)

[5] A.H. England: *Journal of Applied Mechanics*, 32, 400(1965)

[6] J.R. Rice: *Journal of Applied Mechanics*, 55, 98(1988)

[7] R. Yuuki and S.B. Cho: *Engr. Fracture Mechanics*, 34, 179(1989)

[8] C.L. Tan and Y.L. Gao: *Engr. Fracture Mechanics*, Vol. 36, p.919(1990)

[9] S.T. Raveendra and P.K. Banerjee: *Engr. Frac. Mechanics*, 40, 89(1991)

[10] S.S. Lee and R.A. Westmann: *Int. J. Num. Methd in Engr.*, 38, 607(1995)

GEARBOX CONDITION MONITORING USING FEATURE SAMPLES AND PRINCIPAL COMPONENT ANALYSIS*

WEIHUA LI†, KANG DING, ZHIJIAN YANG

School of Automotive Engineering, South China University of Technology, 381WushanRoad, Guangzhou, 510640, China

This paper presents a study of feature samples selection and principal component analysis (FS-PCA) in gearbox condition monitoring and fault diagnosis. The key issues studied in this paper are nonlinear feature extraction, optimal feature samples selection, and diagnostic performance assessment. Firstly, the feature samples of gearbox vibration features are selected to construct the feature subspace by use of the integral operator gauss kernel function. Then PCA is used to classify three kinds of gearbox running conditions: normal, tooth crack and tooth broken. Experiment results indicate the effectiveness and efficiency of FS-PCA for gearbox condition monitoring and fault diagnosis, which can also be regarded as a new KPCA method.

1. Introduction

Diagnosis of actual faults related to gearbox is often performed through the interpretation of patterns in operating data or observed characteristics of currently known malfunctions. The advanced techniques for fault diagnosis range from expert diagnosis with the assistance of various instruments to statistic models. In more recent years, artificial intelligence (AI) has played an important role. The typical AI-based diagnostic techniques include *model-based methods*, *neural networks*, *fuzzy sets* and *support vector machine* [1-2]. It has been shown that SVM has two distinct features. First, it requires only small amount of training samples which is meaningful to machinery fault diagnosis. Second, it is easy to solve the nonlinear problem linearly by use of '*kernel tricks*'.

Kernel methods have recently gained wide attention and enabled new solutions and improved know ones in the field of communication, geophysics, biomedical, and text categorization etc.[3]. The main idea behind kernel methods is to map the input space into a convenient high dimensional feature space, where variables are nonlinearly related to the input space. In the feature space, one can solve the problem in a classical way. It is able to approximate almost

* This work is supported by grant 50605021 of National Natural Science Foundation of China.

† Corresponding author. Email: whlee@scut.edu.cn; weihualee@gmail.com

any nonlinear functions, and is possible to model the nonlinear dynamics of gearboxes using kernel methods when failures occurring. SVM, and KPCA (kernel principal component analysis) have found applications in machine fault diagnosis [2-4].

This paper investigates the use of FS-PCA as a powerful tool to select the feature samples and perform classification in the sub feature space for gearbox condition monitoring. It proceeds as follows. Section II presents the basics of Feature Samples Selection and PCA. Section III focuses on the gearbox experiments, and experiment datasets are also used for investigation of FS-PCA based fault classification method. The work is concluded in Section IV with an illustration of the proposed method to classify the data effectively in the goal of gearbox fault classification, and some perspectives are also introduced.

2. Feature Samples Selection and Principal Component Analysis

2.1. *Feature Samples Selection*

Consider the input space $\boldsymbol{X}$ contains of M condition samples, and every sample represents a feature vector of machine condition at that time. Suppose we map the data into a high dimensional space $\boldsymbol{F}$ by a possibly nonlinear map

$$[\mathbf{x}_1, \mathbf{x}_2, \cdots, \mathbf{x}_M] \xrightarrow{\varphi} [\varphi(\mathbf{x}_1), \varphi(\mathbf{x}_2), \cdots, \varphi(\mathbf{x}_M)] \tag{1}$$

These data can be represented in a subspace $\mathbf{F}_s$ of $\mathbf{F}$, and the dimension of this subspace is lower than M and equal to the ranks of kernel matrix $\mathbf{K}$. According to Baudat[5], the purpose of feature samples selection is to choose a basis of the subspace for expressing all the data as a linear combination of these selected samples in the transformed space $\mathbf{F}$, so that classical linear methods can be used to do classification or regression.

Let L be the number of feature vectors need to be selected ($L \le M$), the mapping of $\mathbf{x}_i$ simplified as $\boldsymbol{\varphi}_i$ ($i = 1, \cdots, M$), and the selected vectors noted as $\mathbf{x}_{S_j}$, its mapping as $\boldsymbol{\varphi}_{S_j}$ ($1 \le \mathrm{j} \le \mathrm{L}$), here '$S$' is used in subscripts to declare the selected feature vectors.

According to the definition of basis vector, for a given set of selected vectors $\mathbf{S} = \{\mathbf{x}_{s_1}, \mathbf{x}_{s_2}, \cdots, \mathbf{x}_{s_L}\}$, after mapping into subspace $\boldsymbol{F}_s$, the mapping of any vector $\mathbf{x}_i$ can be denoted as a linear combination of $\mathbf{S}$

$$\hat{\boldsymbol{\varphi}}_i = \sum_{j=1}^{L} \boldsymbol{a}_i^j \boldsymbol{\varphi}_{s_j} \tag{2}$$

where it can be formulated as a dot product

$$\hat{\boldsymbol{\varphi}}_i = \boldsymbol{\varphi}_S \cdot \boldsymbol{a}_i \tag{3}$$

where $\hat{\boldsymbol{\varphi}}_i$ is the mapping of $\mathbf{x}_i$ in subspace $\boldsymbol{F}_s$, $\boldsymbol{\varphi}_S = (\boldsymbol{\varphi}_{s_1}, \cdots, \boldsymbol{\varphi}_{s_L})$ is the matrix of selected samples into F and $\boldsymbol{a}_i = [\boldsymbol{a}_i^1, \boldsymbol{a}_i^2, ..., \boldsymbol{a}_i^L]^{\mathrm{T}}$ is coefficient vector that weighted this matrix.

For a given set **S**, the key is to find coefficients $\boldsymbol{a}_i$ in order to minimize the difference between $\hat{\boldsymbol{\varphi}}_i$ and $\boldsymbol{\varphi}_i$. Consider solving this problem in space $\boldsymbol{F}$, the normalized Euclidean distance can be given by the following ratio

$$\delta_i = \left\| \boldsymbol{\varphi}_i - \hat{\boldsymbol{\varphi}}_i \right\|^2 \Big/ \left\| \boldsymbol{\varphi}_i \right\|^2 \tag{4}$$

So, the minimum of Eq.(4) can be expressed with dot products and leads to

$$\min \delta_i = 1 - \frac{\mathbf{K}_{Si}{}^{\mathrm{T}} \mathbf{K}_{SS}^{-1} \mathbf{K}_{Si}}{\mathbf{K}_{ii}} \tag{5}$$

where $\mathbf{K}_{SS}$ is the matrix of dot products of the selected vectors, $\mathbf{K}_{SS} = (\mathbf{k}_{s_p s_q}) = \mathbf{K}(\boldsymbol{\varphi}_{s_p} \cdot \boldsymbol{\varphi}_{s_q})$ $(1 \le p \le L,\ 1 \le q \le L)$, $\mathbf{K}_{Si}$ is the vector of dot products between $\mathbf{x}_i$ and selected vector set **S**, $\mathbf{K}_{Si} = (\mathbf{k}_{s_p i}) = \mathbf{K}(\boldsymbol{\varphi}_{s_p} \cdot \boldsymbol{\varphi}_i)$ $(1 \bullet p \bullet L,\ \ 1 \bullet i \bullet M)$,and $\boldsymbol{K}_{ii}$ is the matrix of dot products of all condition samples, $\mathbf{K}_{ii} = (\mathbf{k}_{ii}) = \mathbf{K}(\boldsymbol{\varphi}_i \cdot \boldsymbol{\varphi}_i)$ $(i=1, \cdots, M)$

The problem now is to find the condition samples set **S** minimizing Eq.(5) over all samples $\mathbf{x}_i$

$$\min_S \left(\sum_{\mathbf{x}_i \in \boldsymbol{X}} \left(1 - \frac{\boldsymbol{K}_{Si}{}^{T} \boldsymbol{K}_{SS}^{-1} \boldsymbol{K}_{Si}}{\boldsymbol{K}_{ii}} \right) \right) \tag{6}$$

For solving this problem, the fitness function J_s is defined as

$$J_S = \frac{1}{M} \sum_{\mathbf{x}_i \in \boldsymbol{X}} \left(\frac{\boldsymbol{K}_{Si}{}^{T} \boldsymbol{K}_{SS}^{-1} \boldsymbol{K}_{Si}}{\boldsymbol{K}_{ii}} \right) \tag{7}$$

Obviously, Eq.(6) is equivalent to maximize Eq.(7), and note that for $\mathbf{x}_i \in \mathbf{S}$, Eq.(5) is 0. J_s can be used to descript the fitness of selected samples, the larger the value of J_s, the selected samples more representative, and the maximum of J_s is 1.

The selection algorithm is an iterative process, which is sequential forward selection: at each step looking for the sample that, when combined with the previously selected samples, maximize fitness function J_s. The algorithm stops when $\mathbf{K}_{SS}$ is no longer invertible, which means that **S** is a basis for expressing data in subspace $\boldsymbol{F}_s$. Besides, the stop criterion can also be that the fitness or the number of selected samples reaches a given value.

2.2. *Principal Component Analysis*

Principal Component Analysis is a technique to approximate an original data with lower dimensional feature vector. The basic concept behind PCA is to project the dataset onto a subspace of lower dimensionality. PCA achieves this

objective by explaining the variance of the original data matrix in terms of a new set of independent variables: the *principal components*. In this paper we will not discuss the mathematical details of PCA, and a complete treatment is given by J.E.Jackson [6].

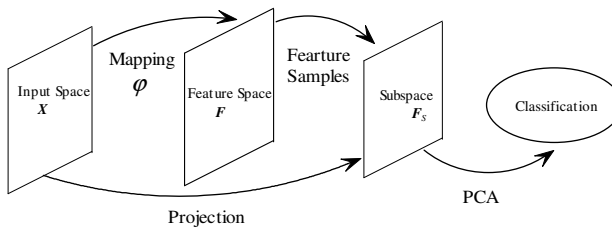

Fig. 1 Procedure of Feature Samples Selection and PCA

Kernel PCA is a nonlinear data analysis method, which transformed a nonlinear problem in input space into a linear one in high dimension space. By performing PCA on the high dimensional feature sets, the nonlinear principal components are obtained. In this paper, this method is modified to be a FS-PCA method, which is completed by two steps. First, we select the feature samples within all the input data, and construct the subspace of the high dimensional feature space F, then projecting all input data onto this subspace and applying PCA to classify different gearbox working conditions. The process of FS-PCA can be described in the Figure. 1.

3. Experiments Analysis

The experiments were conducted on an auto-gearbox, and the vibration signals were measured externally on the bearing case using an acceleration sensor and amplified by a charge amplifier. The total testing time of the gear fatigue experiments was up to 182 hours. During the testing process, the gearbox's running condition underwent three different stages naturally. At first, the gearbox's operating condition was normal. Then a crack in one tooth root arose and propagated gradually. Lastly one tooth of the meshing gear was broken and the testing experiment was terminated. The meshing frequency of the first gear-pair is 550Hz and that of the second gear-pair is 307Hz.

Typical raw signals of different conditions are displayed in Fig.2, which were measured at a constant sampling rate 12.5 KHz, (normal condition, tooth cracked condition, and tooth broken condition). Obviously there are distinct differences between the vibration signal of the gearbox with a broken tooth and those under the other two operating conditions, but it is very difficult to separate the signal under normal condition from that under tooth cracked condition.

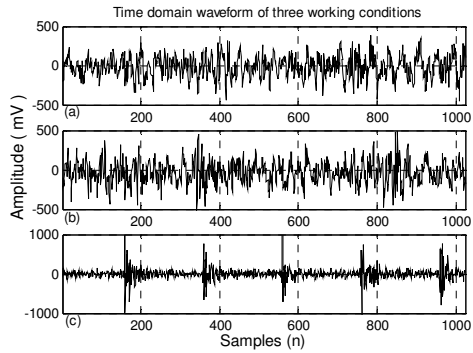

Fig. 2 Gearbox vibration signals of three conditions: (a) normal, (b) tooth cracked and (c) tooth broken

Many feature parameters have been defined in the pattern recognition field. Here only 11 time domain features, including *maximum value*, *minimum value*, *standard deviation*, *absolute mean value*, *crest factor*, *impulse factor*, *clearance factor*, *root mean square value*, *kurtosis*, *skewness and variance*, were used as raw feature sets for further analysis. These parameters are non-dimensional and are used to construct input space in this work.

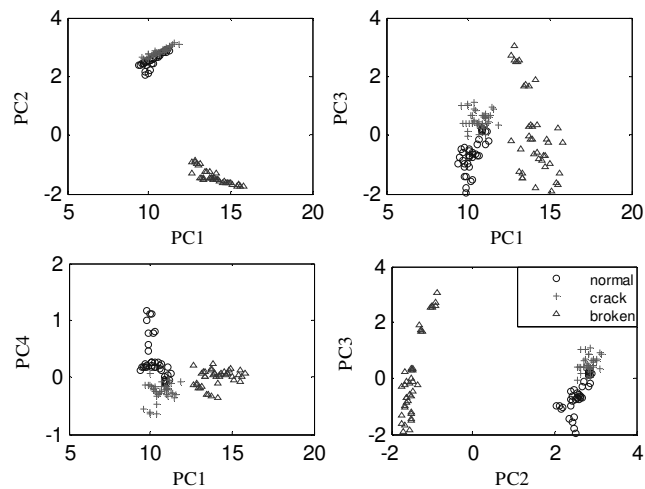

Fig. 3 Classification of Gearbox Running Conditions using unsupervised FS-PCA with a Gaussian kernel function $K(\mathbf{x},\mathbf{y}) = \exp\left(-\|\mathbf{x}-\mathbf{y}\|^2 / 0.3\right)$

There were 120 raw vibration signals, giving 40 datasets per condition and each having 1024 samples. Firstly, 11 features mentioned above of each raw signal were computed and normalized; in total 120 11-D raw feature data were obtained. Then selecting feature samples of these three conditions, the criterion of feature samples selection was that the number of samples reaches 60 or the

fitness value reaches 0.95. When 60 feature samples have been selected, the fitness value reached 0.841517. Therefore these 60 feature samples are used to construct the subspace for gear faults classification, and the result is shown in Figure.3.

All the elements of the principal component have the same sign, making it a weighted average of all the features. In the 2-D PC subspace, feature sets of gearbox conditions are classified into 3 clusters as shown in Fig.3, especially in the projection along with 'PC1-PC3' and 'PC1-PC4'. In the subspace, clusters are identified, and each cluster represents a particular condition. Such clusters provide the basis for a condition recognition method. When the gearbox continues to run in a normal condition, the feature points are bounded around its center with little fluctuation. However, while the local crack was beginning to develop on a single tooth, the new points moved away along directions of PC2, PC3, and PC4. The feature points appear to be consistent in the same region with a growing crack. With the crack propagating, the value of the first PC increases extremely and spreads to a much wider areas, which indicates that the tooth is broken.

4. Discussion

The feature samples selection algorithm captures the structures of the input data by approximating a basis of the subspace. After the samples selection and projection steps, many algorithms can be easily applied. Here PCA is investigated, and we have compared it with Kernel PCA and SVM. It can be seen that the result of unsupervised FS-PCA performed as well as those of supervised ones. The selected samples were sufficient to obtain high performance and reduce significantly the computation time, especially comparing with SVM, the number of feature samples is usually smaller than the number of support vectors. Limited by the length, the results of Kernel PCA and SVM are not shown in the paper.

Experiment results indicate that the proposed method is sensitive and is capable of detecting early machine failure such as gear crack. It has great potential for machine fault diagnosis in practice.

References

1. M A Awadallah and M M Morcos: *IEEE Trans. Energy Conversion* v18.245, 2003
2. M Ge, R Du, G Zhang and Y Xu: *Mech. Syst. Signal. Process.* v18.143, 2004
3. K.R. Muller, S. Mika, G. Rätsch.et al: *IEEE Trans. Neural Networks* v12.181, 2001
4. WH Li, K Ding, TL Shi and GL Liao: *Key Eng. Mater.* v321-323.1556, 2006
5. Baudat G and Anouar F, in: *Procs of Int. Joint Conf. NN*, Washington.DC. 2001
6. J.E.Jackson: *A User's Guide to Principal Components.* John Wiley&Sons, NY, 1991

AN ADAPTIVE FILTER FOR THE MINIMIZATION OF TRACKING ERROR IN A NON-MINIMUM PHASE BEAM WITH UNCERTAINTY

YOUNG-SUP LEE

Dept. of Multimedia Systems Eng., University of Incheon, Dohwa-dong 177, Nam-gu, Incheon, South Korea

This paper presents a methodology to design an adaptive feedforward controller which minimizes the tracking error at the tip of a flexible cantilever beam to follow a command signal. The beam is lightly damped and so the natural transient response is rather long, and also since the sensor and actuator are not collocated, the plant response is non-minimum phase. The adaptive controller is implemented in a digital finite impulse response (FIR) filter, it can be adapted to minimize the quadratic cost function using the filtered-reference least mean square (LMS) algorithm, which is particularly robust to changes in plant response. In computer simulation, the filtered-reference LMS adaptive filter could provide an excellent performance in tracking error minimization.

1. Introduction

A very lightly damped cantilever beam is considered and the objective is to eliminate its ringing motion after a sudden movement in order to follow a command position using a piezoceramic PZT (piezoelectric zirconate titanate) actuator. This is an approach for the tip position control in that the actuator is driven so that the beam tip follows a command signal. In practice, structural beams could be exposed to temperature fluctuations. Thus the need to ensure robust stability in the face of the uncertainty in temperature and load leads to some limitations in the performance of a smart beam. In order to overcome the inherent long transient response of such structures, a feedforward control strategy could be considered. The problem is made more difficult by the non-minimum phase behavior of the system response, caused by the non-collocation of sensor and actuator, and the dispersive property of flexible structures [1].

A digital FIR filter can be designed to minimize the mean-square tracking error [2]. It is, however, well known that the performance of any feedforward strategy is sensitive to changes in the response of the system under control. An alternative control strategy would be to use feedback control. Conventional analogue techniques, such as PID control, could be used, but the non-minimum

phase behavior limits the maximum control gains before there is a danger of instability, resulting in a rather long closed-loop transient response.

A new method of making the feedforward controller into a closed-loop system would be to make it adaptive, and one method of achieving this is mainly discussed. In this study, a pair of integrated PZT actuators is used, which provides many attractive features such as light weight, high sensitivity, large bandwidth and distributed properties, although only limited motion is possible.

2. Theoretical Considerations

An arrangement for the setpoint tracking problem using the filtered-reference LMS algorithm when independent reference signal is available is illustrated in Figure 1, where $G(z)$ is the physical plant which can be varied with temperature, $W(z)$ is an adaptive FIR control filter with I coefficients, $z^{-\Delta}$ is a modeling delay, although in this case $\Delta = 0$, $r(n)$ is a command signal, $d(n)$ is a desired signal, $y(n)$ is a plant output signal $\hat{v}(n)$ is an estimated filtered reference (command) signal and $e(n)$ is an error signal. The update equation of the practical form of the filtered-reference LMS algorithm is given by [3]

$$\mathbf{w}_{n+1} = \mathbf{w}_n + \alpha \hat{\mathbf{v}}(n) e(n)\,, \tag{1}$$

where α is a convergence coefficient, $\mathbf{w}$ is the vector of LMS adaptive filter coefficients and $\hat{v}(n)$ is the vector of past values of the filtered reference signal. The normal LMS algorithm limits the maximum convergence coefficient by [3]

$$\alpha_{\max} \approx 1 / IE[\hat{v}^2(n)]\,, \tag{2}$$

where I is the adaptive filter length. However, it is suggested that $\alpha_{\max}$ can be found empirically and it is approximately [4]

$$\alpha_{\max} \approx 1 / (I + \delta) E[\hat{v}^2(n)], \tag{3}$$

where δ is the overall delay in the secondary path in samples. The delay δ in the secondary path, which usually forms the most significant part of the system response, reduces $\alpha_{\max}$ in the filtered-reference algorithm. The condition for stability is that the real part of each of these eigenvalues must be positive [4], as

$$\mathrm{Re}[\mathrm{Eig}\{E(\hat{\mathbf{v}}(n)\mathbf{v}^T(n))\}] > 0. \tag{4}$$

Because the steady state value of the filter coefficients $\mathbf{w}_\infty$ is expressed [4] when the algorithm is stable with

$$\mathbf{w}_\infty = -[E(\hat{\mathbf{v}}(n)\mathbf{v}^T(n))]^{-1} E(\hat{\mathbf{v}}(n) d(n)). \tag{5}$$

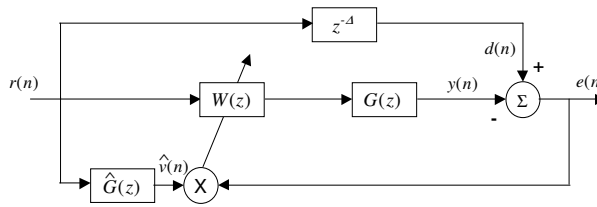

Fig. 1. Arrangement of the filtered-reference LMS algorithm.

The effect on the eigenvalue matrix $E(\hat{\mathbf{v}}(n)\mathbf{v}^T(n))$ of the differences between the responses of the physical plant and the plant model is not straightforward. It is also showed that a sufficient condition for convergence is that the ratio of transfer functions of $\hat{G}(z)/G(z)$, is strictly positive real (SPR) which represents that the stability of the algorithm is assured providing [4]

$$\mathrm{Re}[\hat{G}^*(e^{j\omega T})G(e^{j\omega T})] > 0 \qquad \text{for all } \omega T. \tag{6}$$

The algorithm can be more robust to the differences between the physical plant and the model by introducing a leakage term into the update equation as

$$\mathbf{w}_{n+1} = (1-\alpha\beta)\mathbf{w}_n + \alpha\hat{\mathbf{v}}(n)e(n), \tag{7}$$

which minimizes the modified cost function, and where β is an effort parameter.

3. Flexible Beam for Experiment

An experimental flexible beam was 800 * 20 * 1.5 mm and was constructed of aluminum strip, clamped at one end by a standing frame and free at the other, as shown in Figure 2(a). A pair of PZT actuators which were both 100 * 20 * 1 mm were bonded on either side of the beam [5]. The measured frequency response function of the sensor-actuator pair is plotted in Figure 2(b). For the detection of the beam tip motion, an inductive position sensor was used. The frequency range of interest was 0 - 100 Hz and the input signal to the PZT actuator was amplified to 100V by a PCB 790 series power amplifier.

4. Discussion with Experiment and Simulation

The effect of significant temperature changes, or uncertainty, in the plant on the stability and performance of the controller, temperature variation between -30 ^{o}C and 70 ^{o}C have been assessed in the plant model, while the nominal temperature was 20 ^{o}C. Temperature changes will cause changes in the value of piezoelectric constant d_{31} of the PZT 5H and of the beam length. The value of d_{31} is about 2.74×10^{-10} N/m^2 at the nominal temperature (20 ^{o}C), however it varies to about

3.20×10^{-10} N/m^2 at 70 ^{o}C and about 1.95×10^{-10} N/m^2 at -30 ^{o}C. Thus, experiment and simulation for the two different control strategies with a PID feedback controller and an adaptive feedforward controller using filtered-reference LMS algorithm are performed and discussed in detail.

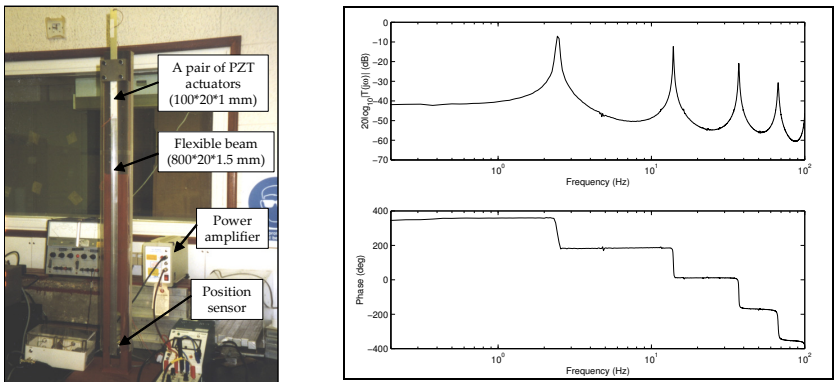

(a) (b)

Fig. 2. (a) Experimental setup and (b) measured frequency response of the test beam.

4.1. *PID Feedback Control*

In the PID feedback control, an analogue controller with three gain terms (K_P = 0.4, K_I = 1.6, K_D = 0.0004), which were manually tuned to give the fastest step response and adequate stability margins, was considered in actual control experiment. As shown in Figure 3, the PID control showed a very high gain margin due to the light damping and a phase margin of about 44 degrees. The stability was dominantly dependent on the open-loop behavior of the first resonance. The measured 95 % settling time in step response was about 67 seconds with the PID control. The closed-loop response of the PID feedback control was not significantly affected by these temperature changes of the beam.

4.2. *Adaptive Feedforward Control*

The Brownian noise was used for this simulation and did not give zero-mean inputs $d(n)$ and $\hat{v}(n)$ of the filtered-reference LMS algorithm. A very small convergence coefficient α was applied by assuming from Eq. (2)

$$\alpha_{\max} \approx \alpha_0 / IE[\hat{v}^2(n)] \tag{8}$$

with a value of $\alpha_0 = 10^{-5}$, which thus gave a slow convergence behavior as shown in Figure 4(a) because of the very large phase delay in the plant at the first resonance. The convergence coefficient α used was about 7.87×10^{-12} with

I = 200, $E[\hat{v}^2(n)] = 6.352\times10^3$. The average phase delay for an analogue plant was about 0.186 sec, however, it was about 0.200 sec for a digital plant $G(z)$.

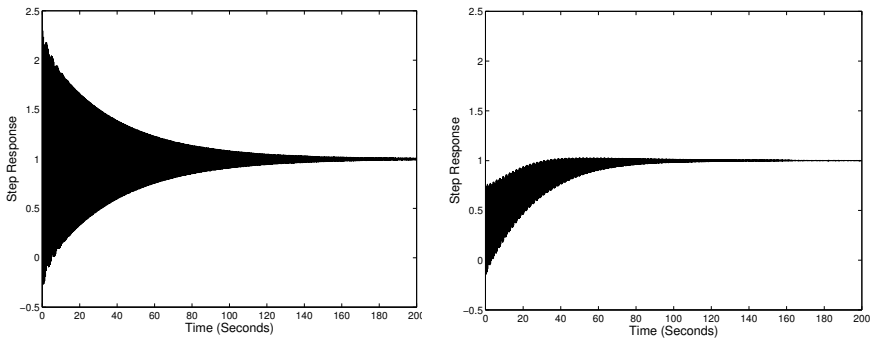

(a) (b)

Fig. 3. Measured step responses. (a) Before control. (b) After control with the PID controller.

The overall delay δ in $\alpha_{\max}$ for a delayed system as shown in Eq. (3) is then about 60 samples for a digital plant when the sampling frequency is 300 Hz. The response of the system is dominated by the sharp resonance at the first mode, and the overall delay could be expressed by the instantaneous phase delay $-\partial\varphi(\omega) / \partial\omega$ at $\omega = \omega_n$, which is proportional to $1/\zeta_n$, where ζ_n is the damping ratio of the nth resonant mode. For this case, the instantaneous phase delay at the first resonance is calculated with $\varphi(\omega_1)/\Delta\omega_1 = (93.4^{\circ} * \pi/180) / (0.01 \text{ Hz} * 2\pi) = 25.9$ [sec] for the small phase change $\Delta\varphi(\omega_1)$ [deg] due to a small frequency interval $\Delta\omega_1$ [rad/sec] read from the phase response plot. So the maximum convergence coefficient by Eq. (3) with this overall delay of $\delta = 7770$ samples is 1.98×10^{-8}.

It is also suggested an $\alpha_{\max}$ for a lightly-damped second-order system as [6]

$$\alpha_{\max} \approx \omega_n T \zeta_n. \tag{9}$$

For the experimental flexible beam system, ω_1 = 2.37 Hz, T = 1/300 sec, and ζ_1 = 0.0026 which gives $\alpha_{\max}$ = 2.054*10^{-5}. The above results for the estimation of $\alpha_{\max}$ for the flexible beam are summarized in Table 1. The learning curves for the system with three different temperatures of T = 20 ^{o}C, -30 ^{o}C and 70 ^{o}C are shown in Figure 4(a) and were not entirely finished by 15×10^6 iterations for the adaptation, because of the low value of α which caused slow convergence, and the MSE had reached only about –20 dB. Figure 4(b) illustrates the step responses after adaptation for 15×10^6 iterations for the three different plants. The settling times of the three step responses are similar as summarized in Table 1.

Table 1 Maximum convergence coefficients for the filtered-reference LMS algorithm.

Method	Formula for $\alpha_{\max}$	Remark	$\alpha_{\max}$
Computer simulation (empirical)	$\alpha_0 / IE[\hat{v}^2(n)]$	$\alpha_0 = 10^{-6}$	7.87×10^{-12}
Widrow and Sterns [3]	$1/IE[\hat{v}^2(n)]$	-	7.87×10^{-7}
Elliott [4]	$1/(I+\delta)E[\hat{v}^2(n)]$	Overall delay [samples] $\delta = -\varphi(\omega)/\omega \times f_s = 60$	6.06×10^{-7}
Reading from phase response	$1/(I+\delta)E[\hat{v}^2(n)]$	Instantaneous phase delay [samples] $\delta = -\Delta\varphi(\omega_1)/\Delta\omega_1 \times f_s = 7770$	1.98×10^{-8}
Morgan and Sanford [6]	$\alpha_{\max} \approx \omega_n T \zeta_n$	-	2.05×10^{-5}

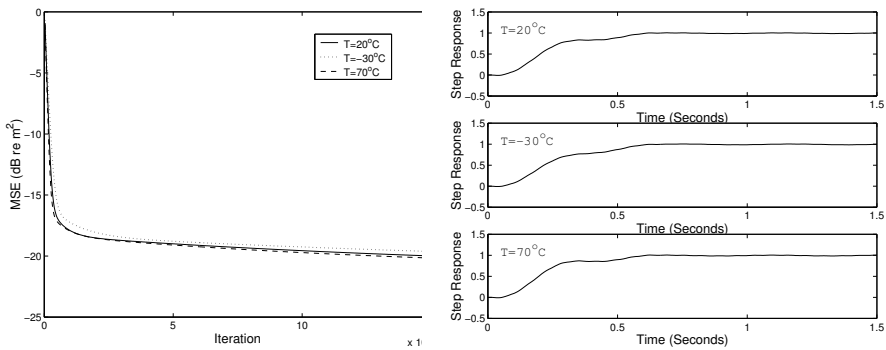

(a) (b)

Fig. 4. Adaptive control using the filtered-reference LMS algorithm. (a) Learning curves at T = 20°C, -30°C and 70°C. (b) Step responses after adaptation at T=20°C, -30°C and 70°C.

5. Conclusions

An adaptive filter using the filtered-reference LMS algorithm was considered to use as a position controller, however a long adaptation time was required to learn the behavior of a very lightly damped flexible beam. The control performance was much better than conventional PID feedback control.

References

1. R. L. Well *et al.*, *IEEE Cont. Sys. Mag.*, 9-15, (1990).
2. Y. S. Lee and S. J. Elliott, *MOVIC'98*, 769-774 (1998).
3. B. Widrow and S. D. Stearns, *Adapt. Sig. Processing*, Prentice-Hall (1985).
4. S. J. Elliott, *Sig. Processing for Active Control,* Academic Press (2001).
5. Morgan Matroc Inc., *Guide to Modern Piezoelectric Ceramics* (1993).
6. D. R. Morgan and C. Sanford, *IEEE Trans. on Sig. Processing*, **40**(**9**), 2341-2346 (1992).

A ROBUST ERROR-ADAPTIVE NLMS ALGORITHM FOR ECHO CANCELLATIONS

MIN-SOO KIM

Korea Railroad Research Institute, #360-1, Woram-dong
Uiwang-si, Gyeonggi-do, 437-757, KOREA

Echo canceller using adaptive filtering techniques has been used in various applications in solving communications system problems. This paper presents an optimal algorithm, the error-adaptive NLMS (Normalized Least Mean Square) algorithm, which is able to remove echo in communication environment by using adaptive parameter μ. This parameter μ is actively changing a step size to update weights by means of the magnitude of the moving average of the absolute error signals. The simulation results show that the echo cancellation performance of the proposed algorithm is much better than NLMS algorithm under the single-talk as well as the double-talk conditions.

1. Introduction

An Echo is a reflection of sound, where the transmitted voice signal gets reflected back due to unavoidable impedance mismatch and four-wire/two-wire conversion between the telephone and the communication network. Echo's severity depends on the round-trip time delay[1]. If the round-trip time delay is more that 30 ms, the echo becomes significant and it makes the normal conversation difficult. Due to the impedance mismatch between the hybrid and the telephone line some of the signal transmitted from one side returns and corrupts the signal, generating an echo that is very disconcerting in voice communications. To solve this problem the telephone companies employ a device called an Echo Canceller[2]~[4].

Talker echo occurs when a talker's speech energy, transmitted down the primary signal path, is coupled into the receive path from the far end. The talker then hears his/her own voice, delayed by the total echo path delay time. Talker echo is a direct result of the 2-wire to 4-wire conversion that takes place through hybrid transformers. Listener echo occurs at the far-end by circulating voice energy. This type of echo occurs when gain mismatches allow the energy returned from the listener echo path to be greater than the original energy, and when the waveforms are in-phase. Generally talker echo deteriorates the quality of the communication service seriously.

This paper is organized as follows. Section 2 discusses the echo canceller algorithm. Section 3 contains the simulation results. The main conclusions are then summarized in section 4.

2. Echo Canceller Algorithm

The echo cancellation block diagram is shown in Figure 1. The non-linear processor is used to remove residual echoes by injecting comfort noise. A low level of comfort noise is usually added during the silence periods as an audio-psychological comfort effect for the listener. The double-talk detector is used to sense the near-end and far end signal levels[4]. Once both activities are detected double-talk is declared and the adaptation of the echo canceller is stopped until the system is no longer in double-talk mode.

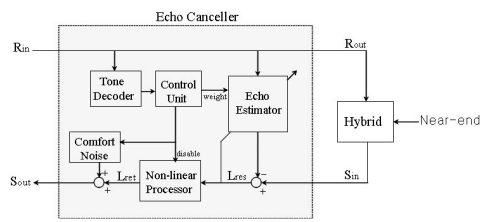

Fig. 1. Block diagram of echo canceller, where R_{in} stands for Receive-In Port, R_{out} for Receive-Out Port, S_{in} for Send-In Port and S_{out} for Send-Out Port as stated in ITU-T G165[5].

2.1. *LMS (Least Mean Square) Algorithm*

In adaptive filtering, the LMS algorithm is a very popular for its simplicity and predictable behavior, but the compromise must be made between the convergence speed and the steady-state error. This is because the LMS algorithm updates the adaptive filter coefficients with a term whose magnitude is proportional to the so-called step size μ. To obtain the fast convergence speed, μ has to be relatively large but using a large μ produces a large steady-state error. To solve this problem, many variable step size algorithms that try to achieve both the fast convergence speed and the small steady-steady error have been developed.

Let $\mathrm{x(n)}$ be the input samples for an unknown system H, which is modeled by the filter coefficient $\mathrm{a_k}$, $0 \le k \le N-1$.

$$H(z) = a_0 + a_1 z^{-1} + \cdots + a_{N-1} z^{-(N-1)} = \sum_{i=0}^{N-1} a_i z^{-i} \tag{1}$$

Then the differential equation of the output, $\mathrm{y(n)}$, is given by Eq. (2)

$$y(n) = a_0 x(n) + a_1 x(n-1) + \cdots + a_{N-1} x\big(n-(N-1)\big) \tag{2}$$

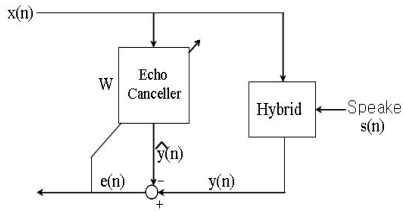

Fig. 2. Adaptive echo canceller, where $x(n)$ stands for Far-End signals, $s(n)$ for Near-End signals, $e(n)$ for error signals, and $y(n)$ for echo signals to be removed. In case of double-talk, $y(n)$ contains $s(n)$.

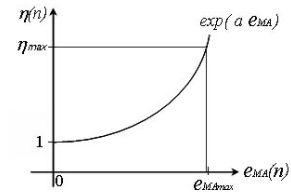

Fig. 3. Relation grape between $e_{MA}(n)$ and $\eta(n)$.

Figure 2 shows adaptive echo canceller. The error signal e(n) defines difference between echo signals y(n) and filter output signals $\hat{y}$(n)

$$\hat{y}(n) = X(n)^T W = W^T X(n) \tag{3}$$
$$e(n) = y(n) - \hat{y}(n) = y(n) - X(n)^T W \tag{4}$$

Each time as sample is received from the line, the following weight update procedure is executed and the corresponding values computed.

$$W(n+1) = W(n) + \mu_{LMS} e(n) X(n) \;\text{ where }\; 0 < \mu_{LMS} < \frac{2}{\lambda_{\max}} \tag{5}$$

where $\lambda_{\max}$ is the maximum value of correlation matrix R of input signal vector X(n). The input vector and weight vector are followings:

$$X(n) = \big[\, x(n) \;\; \text{x(n+1)} \;\cdots\; \text{x}\big(\text{n-(N-1)}\big) \,\big]^T \tag{6}$$
$$W(n) = \big[w_0(n) \;\; w_1(n) \;\cdots\; w_{N-1}(N) \big]^T \tag{7}$$

2.2. *NLMS (Normalized LMS) Algorithm*

The basic algorithms of the proposed NLMS and modified NLMS (M-LMNS) are shown in Eq. (8) and (9), respectively.

$$W(n+1) = W(n) + \mu_{NLMS} e(n) X(n) \;\text{ where }\; \mu_{NLMS} = \frac{\mu_{LMS}}{X^T(n) X(n)} \tag{8}$$

$$W(n+1) = W(n) + \mu_{MNLMS} e(n) X(n) \text{ where } \mu_{MNLMS} = \frac{\sigma_x^2(n)}{\sigma_x^2(n) + \sigma_s^2(n)} \mu_{NLMS} \quad (9)$$

where $\sigma_x^2(n)$ represents variance of input signal x(n) and $\sigma_s^2(n)$ is variance for near-end signals s(n).

2.3. *Error-Adaptive NLMS Algorithm*

The proposed algorithm has a good convergence in single-talk mode and makes a slow convergence in double-talk so as to increase performance of echo cancellation. For this variable step size, we use moving average of error signals as Eq. (10).

$$e_{MA}(n) = \frac{1}{K} \sum_{i=0}^{K-1} \left| e(n-i) \right| \quad (10)$$

Then, the adaptive coefficient μ_{EANLMS} can be determined as Eq. (11).

$$\mu_{EANLMS} = \begin{cases} \eta \mu_{NLMS} & \ldots \text{ single talk} \\ \eta \mu_{MNLMS} & \ldots \text{ double talk} \end{cases} \quad (11)$$

where η is calculated as Eq. (12) and its shape is shown in Figure 3.

$$\eta(n) = \exp\left(a e_{MA}(n) \right) \quad \text{where} \quad a = \frac{\ln(\eta_{\max})}{e_{MA_{\max}}} \quad (12)$$

Eq. (13) shows the basic algorithms of the proposed EA-NLMS.

$$\begin{aligned} \hat{y}(n) &= W^T(n) X(n) \\ e(n) &= y(n) - \hat{y}(n) \\ W(n+1) &= W(n) + \mu_{EANLMS} e(n) X(n) \end{aligned} \quad (13)$$

3. Simulation

3.1. *Simulation Environment*

To verify performance of the proposed algorithm efficiently, we use the far-end signals x(n) and the near-end signal s(n) as sinusoidal wave forms stated in ITU-T G168[6].

$$x(n) = x_1(n) + x_2(n) + x_3(n) + x_4(n) + x_5(n) = \sum_{i=1}^{5} a_i \sin\left(2\pi f_i \left(\frac{n}{F_s} - \tau \right) \right) \quad (14)$$

$$s(n) = s_1(n) + s_2(n) + s_3(n) + s_4(n) + s_5(n) = \sum_{i=1}^{5} b_i \sin\left(2\pi f_i \left(\frac{n}{F_s} - \tau \right) \right) \quad (15)$$

where a_i and b_i stand for the amplitude of the waves, f for frequency, F_s for sampling rate, and τ for time delay of echo path through hybrid.

For representing the attenuation of the hybrid, we define a quantities usually used to describe the characteristic of an Electrical Echo Canceller. It is the Echo Return Loss (ERL) defined as $ERL = 10\log_{10} E[x^2]/E[y^2]$ [dB].

Table 1. Parameter values for far-end signal and near-end signals. And 32 ms of echo path.

Far end signals				Near end signals			
a_1	1.0	f_1	300	b_1	1.0	f_1	400
a_2	0.8	f_2	900	b_2	0.8	f_2	1200
a_3	0.5	f_3	1500	b_3	0.5	f_3	2000
a_4	0.3	f_4	2100	b_4	0.3	f_4	2800
a_5	0.1	f_5	2700	b_5	0.1	f_5	3600

All this simulation was carried out by a sampling frequency 8kHz(F_s), 20 [dB] of echo path noise, and 32ms echo path time delay(τ). And the adaptive filter length K was chosen a 64 taps as same as the unknown system.

3.2. *Simulation Results*

Figure 4 shows the simulation results based on the NLMS and M-NLMS algorithm. The error signal e(n) (=y(n) -ŷ(n)) in case of single-talk mode(1~3000 sample) and e(n)-s(n) in case of double-talk mode(3001 ~ 8000 sample) are presented in Figure 4-(a). Figure 4-(b) shows the frequency spectrum of e(n) in single-talk mode between 1001 sample and 3000 sample and Figure 4-(c) represents the frequency spectrum of e(n)-s(n) in double-talk mode between 6001 sample and 8000 sample.

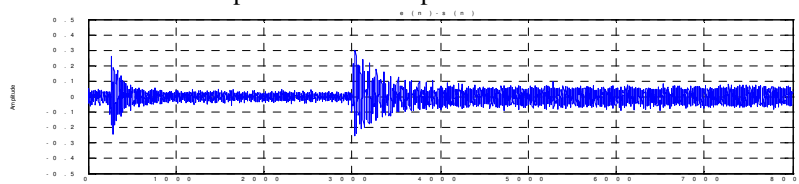

(a) Error signals

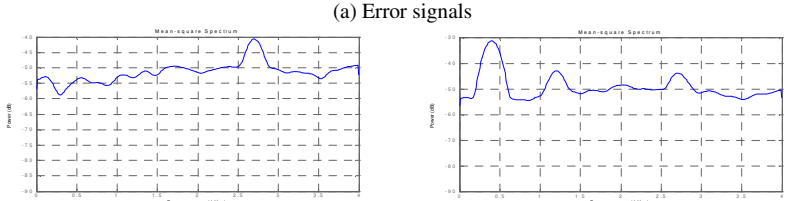

(b) Frequency spectrum (Single-talk) (c) Frequency spectrum (Double-talk)

Fig. 4. Error signal e(n)-s(n) and its spectrum in case of M-NLMS algorithm.

Figure 5 shows the simulation results using the proposed EA-NLMS. As a result, the proposed algorithm has a good echo cancellation in both situations using variable step size algorithm. As well-known, the computational complexity of this algorithm increase as a size of the unknown system is larger.

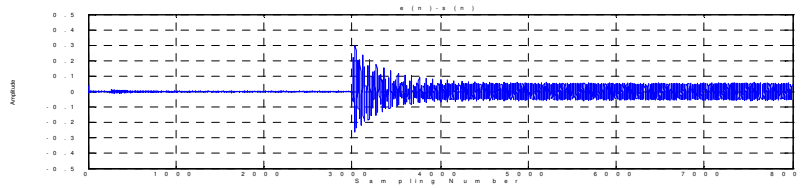

(a) Error signals

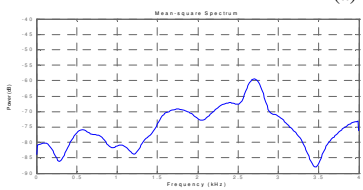

(b) Frequency spectrum (Single-talk)

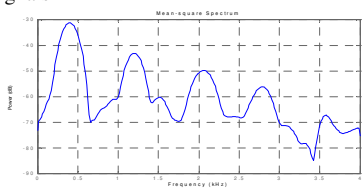

(c) Frequency spectrum (Double-talk)

Fig. 5. Error signal e(n)-s(n) and its spectrum in case of EA-NLMS algorithm.

4. Conclusion

This paper presents the error-adaptive NLMS (Normalized Least Mean Square) algorithm for the efficiently echo cancellation using adaptive parameter μ. This parameter μ is actively changing a step size to update weights by means of the magnitude of the moving average of the absolute error signals.

References

1. N. Benvenuo and G. Cherubini, *Algorithms for Communication Systems and their Applications*, WILEY, (2002).
2. Makino, Y. Kaneda, and N. Koizumi, "Exponentially weighted step-size NLMS adaptive Filter based on the Statistics of a Room Impulse Response," *IEEE Trans. Speech and Audio Processing*, **Vol. 1, No. 1**, pp. 101-108, Jan. (1993).
3. J. E. Greenberg, "Modified LMS Algorithms for Speech Processing with an Adaptive Noise Canceller", *IEEE Trans. on SAP*, **Vol. 6, No. 4**, pp. 338-351, July (1998).
4. De Courville, M. Duhamel, P., "Adaptive Filtering in Subbands using a Weighted Criterion," *IEEE Transactions on Signal Processing*, **Vol. 46, No. 9**, pp. 2359-2371, Sep (1998).
5. ITU-T Recommendation G.165.
6. ITU-T Recommendation G.168.

DEVELOPMENT OF A LATERAL MODE PIEZOELECTRIC OSCILLATOR SENSOR TO DETECT DAMAGES IN A STRUCTURE

YONGRAE ROH AND BYUNGSOO KIM

School of Mechanical Engineering, Kyungpook National University
Sankyukdong 1370, Bukgu, Daegu 702-701, Korea

This paper presents the feasibility of a lateral mode piezoelectric oscillator sensor to detect damages in civil infrastructures. The sensor is composed of an electronic feedback oscillator circuit and a piezoelectric lateral mode vibrator to be attached to a structure of interest. Damage to a structure causes a change in the impedance spectrum of the structure, which results in a corresponding change of the resonant frequency of the piezoelectric vibrator. The piezoceramic patch responds to this change of the frequency, and the oscillator circuit instantly detects and feeds back a new oscillation signal to the piezoceramic. Feasibility of the sensor was investigated through finite element analyses. Practical applicability of the sensor was verified with a sample aluminum plate where artificial cracks of different lengths and number were imposed in sequence. Validity of the measurement was confirmed through comparison with the results of finite element analyses of a plate with cracks.

1. Introduction

Recent research activities on structural health monitoring (SHM) led to the development of smart sensors and integrated sensing systems in the fields of mechanical, aeronautical and civil engineering [1, 2]. Structural health monitoring technology is essentially aimed at the development of autonomous systems for continuous monitoring and integrity assessment in structures with minimum labor involvement. Low-cost smart sensors are key ingredients for wide adoption of the structural health monitoring technique. In particular, the electro-mechanical impedance based technique, which uses smart piezoelectric ceramic (PZT) materials, has emerged as a powerful technique for SHM [3, 4]. This paper presents the feasibility of a piezoelectric oscillator sensor to detect the damages in civil infrastructures. The oscillator sensor is composed of an electronic feedback oscillator circuit and a piezoelectric lateral mode vibrator to be attached to a structure of interest. Damage to the structure causes a change of the impedance spectrum of the structure, which results in a corresponding change of the resonant frequency of the PZT patch. The oscillator sensor can

instantly detect the frequency change in a very simple manner. Feasibility of the piezoelectric oscillator sensor is verified in this work with a sample aluminum plate where artificial cracks of different depth are imposed in sequence. Validity of the measurement is confirmed through comparing the experimental data with the results of finite element analyses of a plate with cracks.

2. Finite Element Analysis

Influence of the damages on a simple structure was analyzed with the finite element method by a commercial package, ANSYS. Figure 1 is a sample model of the analyses, where artificial multiple cracks of different lengths are to be imposed on an aluminum plate. The model contains a small PZT patch attached to the aluminum plate as an SHM sensor. The sensor in this work utilized a lateral vibration mode of the PZT patch. Through the finite element analyses, the change of the lateral mode resonant frequency of the PZT sensor was investigated in relation to the crack geometry. Firstly, the change of the impedance spectrum of the plate was analyzed in relation to the number of cracks of a certain length and then similar analysis was performed in relation to the length of cracks. According to the results in Figs. 2 and 3, the resonant frequency of the PZT patch decreased in proportion to both the length and the number of cracks. After a certain threshold length, the resonant frequency showed almost linear decrease in proportion to the crack length. For a short crack, increase of the crack number did not have much influence on the resonant frequency of the PZT sensor. However, for a relatively longer crack, the number of cracks had significant influence on the impedance spectrum.

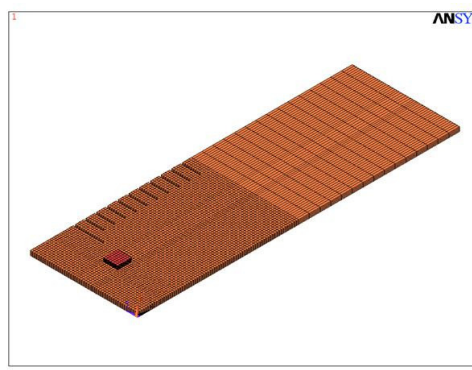

Fig. 1. Basic finite element analysis model.

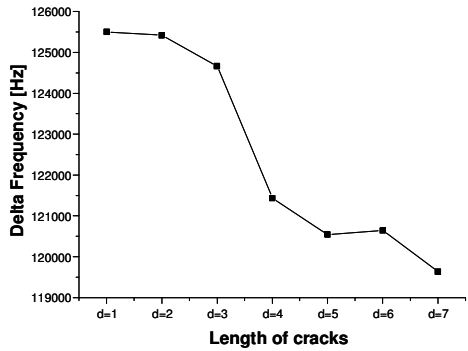

Fig. 2. Relationship between the resonant frequency of the PZT sensor and the crack length.

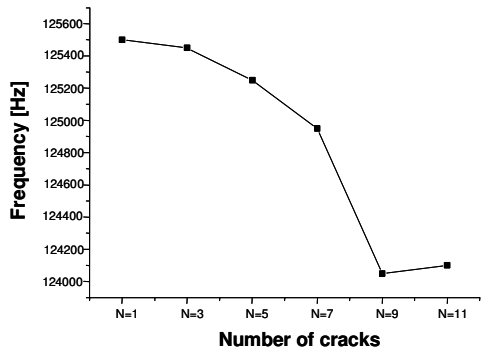

Fig. 3. Relationship between the resonant frequency of the PZT sensor and the number of cracks.

3. Piezoceramic Oscillator Sensor

Experimental oscillator sensor consisted of a feedback oscillation circuit and a piezoceramic element attached to the structure of interest as shown in Figs. 4 and 5. The oscillator circuit was tuned to a specific resonant frequency of the piezoceramic element and was used to feedback the resonant signal in response to the structural condition. Damage to the structure caused a change of the impedance spectrum of the structure, which led a corresponding change of the resonant frequency of the PZT patch. The sensor instantly detected the frequency change and oscillated at the new resonant frequency. Feasibility of the piezoelectric oscillator sensor was verified in this work with a sample aluminum plate where artificial cracks of different depth were imposed in sequence. Figure

6 displays a schematic diagram of a measurement setup with the PZT oscillator sensor. Figure 7 is a photograph of the experimental plate specimen with the PZT sensors attached. PZT is a typical piezoceramic generating electricity in response to an external force. However, the PZT is inherently also a pyroelectric material that generates electricity in response to environmental temperature changes. In use of the PZT as SHM sensors, the sensor signal is likely to be contaminated by this pyroelectricity. During the measurement, if the PZT sensor encounters a change of its environmental temperature, the sensor generates corresponding electricity, which will be confused with the real electric signals caused by structural damages. There must be a clever way to compensate for this pyroelectric contamination. For resolution, a dual sensor system was employed as shown in Fig. 6, which consisted of a reference sensor and a real sensor. The reference sensor was bonded to a small aluminum plate, and the small aluminum plate was exposed to the same environment as that for the big experimental plate specimen. The small aluminum plate with the reference sensor did not have any cracks and was stored close to the experimental specimen. The experimental specimen, thus the real sensor, was open to the effects of both the cracks and the environment while the reference plate, thus the reference sensor, was open to the effect of the environment only. Difference of the sensor signals reflected the effect of the cracks only. Figures 8 and 9 are results of the measurements with the PZT oscillator sensors. As expected from the finite element analysis results, the oscillator sensor showed changes in its oscillation frequency in proportion to the length and the number of the cracks. These results agreed well with the results of the finite element analysis, and confirmed the validity of the present piezoceramic oscillator sensor.

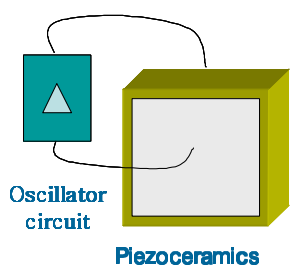

Fig. 4. Schematic structure of the piezoceramic oscillator sensor.

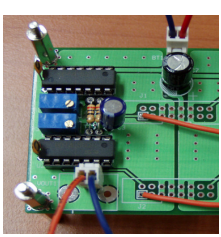

Fig. 5. Photograph of the oscillator circuit for the sensor.

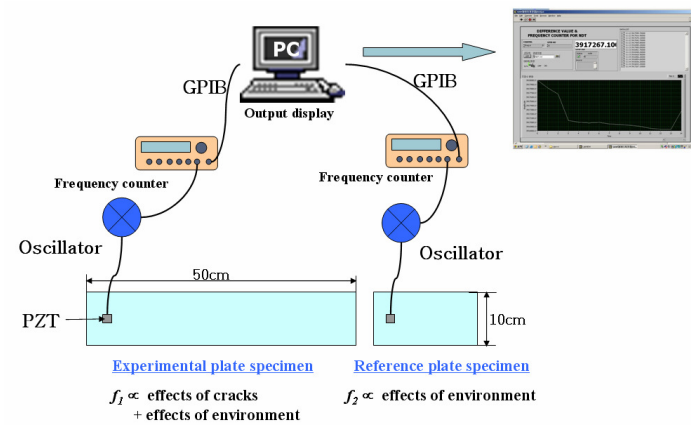

Fig. 6. Schematic diagram of the measurement setup.

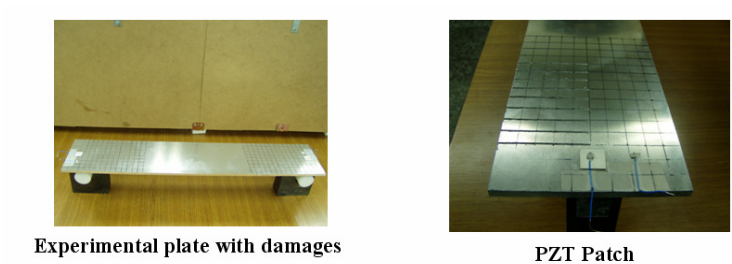

Fig. 7. Photograph of the experimental plate specimen.

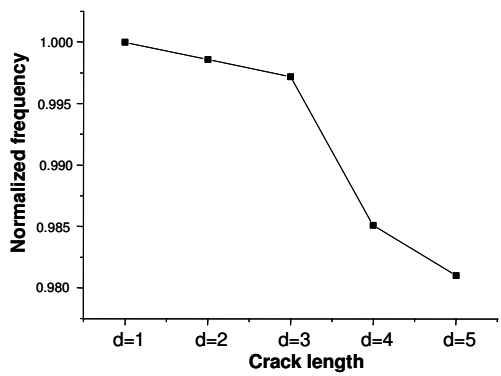

Fig. 8. Oscillation frequency vs. crack length on the plate.

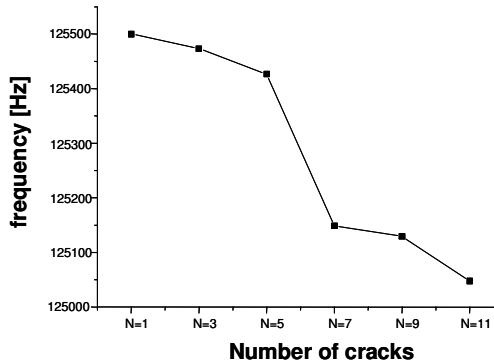

Fig. 9. Oscillation frequency vs. number of cracks on the plate.

4. Conclusions

The feasibility of the piezoelectric oscillator sensor was verified to detect the damages in civil infrastructures. The oscillator sensor was composed of an electronic feedback oscillator circuit and a piezoelectric lateral mode vibrator attached to the structure of interest. The oscillator sensors could instantly detect the resonant frequency change of the piezoelectric patch in response to the change in the length and the number of cracks in an experimental sample plate. Validity of the measurement was confirmed through comparing the experimental data with the results of the finite element analysis of the plate with cracks.

Acknowledgments

The study was supported by Smart Infra-Structure Technology Center (SISTeC) sponsored by Ministry of Science and Technology (MOST) and the Korea Science and Engineering Foundation (KOSEF). Their financial supports are greatly acknowledged.

References

1. K. K-H. Tseng and A. S. K. Naidu, *Smart Mater. Struct.* **11** 317 (2002).
2. W. T. Yeung and J. W. Smith, *Engineering Structures* **27** 685 (2005).
3. J. W. Ayres, F. Lalande, Z. Chaudhry and C. A. Rogers, *Smart Mater. Struct.* **7** 599 (1998).
4. S. H. Park, C. B. Yun and Y. R. Roh, *J. NDT&E Int.* **40** 71 (2007).

RETROFIT OF CONCRETE CYLINDERS BY STEEL JACKETS WITH LATERAL CONFINING STRESS*

EUNSOO CHOI †

Department of Civil Engineering, Hongik University, 72-1 Sangso Mapo, Seoul, 121-791, Korea

BAIK-SOON CHO

Department of Civil Engineering, Inje University, 607 Obang Gimhae, Gyeong nam, 621-749, Korea

YOUNG-SOO CHUNG

Department of Civil Engineering, Chungang University, 72-1 Naeri Daedeok Anseong, Gyeongi-do, 456-756, Korea

SUNG-CHUL CHO

Department of Civil Engineering, Hanyang University, 17 Haengdang Seongdong, Seoul, 133-791, Korea

This study introduced a new method to retrofit RC bridge columns with lap splice which do not have enough ductility during an earthquake. The new method used mechanical external pressure to attach split steel plated around RC columns. In this study, at first, 45 concrete cylinders were manufactured with varying the design compressive strength of 21, 27, and 35 MPa, and, then, the part of them was retrofitted with two split steel jackets under lateral confining pressure. The parameters in steel jacketing were the steel jacket's thickness and the existence of adhesive between steel and concrete surface. The effect of the new method was verified through comparing the results of the compressive tests for plain and retrofitted cylinders. The steel jacketing built following the new method showed good results of increasing the compressive strength and ductility of the jacketed cylinders with respect to the plain cylinders. The thicker steel jackets increased more compressive strength, and the ductility at failure depended on the welding quality on steel jackets. The adhesive between steel and concrete surface reduced the confining effect of the steel jackets. In the second experiments, a whole around steel jacket was used to wrap cylinders with lateral pressure. Also, a double-layered jacket of two steel jackets was introduced; a cylinder was jacketed by two steel plates one after another. The double-layered jackets showed the same performance as that of a steel jacket having

* This study has been supported by the KOSEF.

† (Korea Science and Engineering Foundation; Project No. R01200600010048020006).

the same thickness of the double-layered jacket. Therefore, this study showed that the multi-layered steel jacket is available in the new jacketing method.

1. Introduction

Recent earthquakes in urban areas, such as 1989 Loma Prieta and 1994 Northride in the United States, and 1995 Kobe in Japan, have induced damages to many reinforced concrete columns in bridges and buildings; which indicates that the reinforce concrete columns built before 1970s do not possess the adequate strength and deformation capacity and retrofits for them are required [1,2]. A lot of existing bridges were designed and constructed along with smaller seismic loads compared to that from the current design codes; which can lead to major damages or collapses of bridges due to an expected earthquake. Therefore, seismic retrofit techniques have been developed for the substandard RC columns.

Steel jackets were used in retrofitting of reinforced columns and were proved to be efficient to increase the strength and ductility of the columns with providing additional confinement and shear resistance [3]. However Lap splices were located in the plastic hinge region of most bridge piers that were constructed before the adoption of the seismic design provision of Korea Highway Design Specification on 1992. But sudden brittle failure of lap splices may occur under loading. This study introduces a new method to retrofit RC bridge columns with lap splice which do not have enough ductility during an earthquake. The new method use mechanical external pressure and steel plates around RC columns. In this study, 45 and 15 concrete cylinders, with time delays, are manufactured with varying their nominal strength of 21, 27, 35MPa and then, part of them are retrofitted with steel jackets undergoing lateral confining stress. The effect of the new method is verified through comparing the results of the compressive tests of the plain and retrofitted cylinders.

2. Concrete Cylinders and Two-Split Steel Jacketing

At first, 45 concrete cylinders of ϕ 150 mm x L300 mm were prepared with considering the compressive strength of 21, 27 and 35MPa. Next, two-split steel jackets were made with the thickness of 1.0 and 1.5 mm. The dimension of a steel jacket is 230 mm x 290 mm (BxH); the height of steel jackets is less than that of concrete cylinders, which guaranties that no compressive force is transferred through the steel jackets. The last factor in this study was the adhesive which located at between concrete and steel surface. As shown in Table 1, there were five kinds of specimens with combining the above three factors.

Table 1. Five kinds of specimens of concrete cylinders.

Case 1	Case 2	Case 3	Case 4	Case 5
Plain	1mm+adhesive	1mm	1.5mm+adhesive	1.5mm

The jacketing process is shown in Figure 1. As shown in ③ of Figure 1, the confining stress (or lateral pressure) was introduced by three clamps having two horseshoes to press steel jackets. The welding of the two-split jackets was performed under the confining stress. In the ⑥, a heating jacket was used to heat up the adhesive inside the jacket, and, then, the melted adhesive paste the steel jacket on concrete surface. The Polyurethane adhesive film is melted by heating for 5 minutes with 120℃. In the above jacketing procedure, the grouting, essential for the existing steel jacketing method, is not necessary.

① ② ③ ④ ⑤ ⑥

① Adhesive film; ② attaching two-split steel jackets; ③ introducing confining stress; ④ welding spit jackets; ⑤ point welded jacketed cylinder; ⑥ heating jacket

Fig. 1. Procedure of steel jacketing for concrete cylinders.

3. Compressive Tests and Results

The compressive tests of concrete cylinders were performed with a 2000 kN UTM. The axial deformation and force of each test were measured to construct a stress-strain curve from which the ultimate strength and the failure strain were estimated.

Figure 2 shows the stress-strain curves of the plain and the jacketed cylinders of 21 MPa design strength. Also, Table 2 shows the ultimate strengths and the failure strains of the tested cylinders. Most of all, it is found from the results that the steel jackets with or without the adhesive increase significantly the strengths and the failure strains of concrete cylinders. The introduced steel jacketing method does not use grouting but shows good performance as like the existing method.

The adhesive between steel and concrete surface puts the negative effect on increasing the strengths since the adhesive played a role as like a gap between the two surfaces; the adhesive is much softer than the two materials of steel and

concrete. In Table 2, the strengths with the adhesive are always less than those without the adhesive for varying the jacket's thickness and the concrete strength. As expected, the thicker jacket increases more the strength. The failure of the jacketed cylinders was observed on the welds of steel jackets. Figure 3 shows the failure mode of a jacketed cylinder.

Table 2. Measured compressive strength and failure strain of concrete cylinders.

Classification		Measurement data		Classification		Measurement data		Classification		Measurement data	
Case number		Strength	Strain x 10^{-2}	Case number		Strength	Strain x 10^{-2}	Case number		Strength	Strain x 10^{-2}
21MPa cylinder	[1]	34.59	0.494	27MPa cylinder	[1]	39.24	0.2960	35MPa cylinder	[1]	47.8	0.230
	[2]	39.4	2.559		[2]	42.22	2.501		[2]	47.53	1.720
	[3]	44.04	2.291		[3]	49.9	1.478		[3]	55.43	1.183
	[4]	52.78	2.398		[4]	56.26	1.477		[4]	63.28	3.207
	[5]	56.42	1.664		[5]	62.34	1.778		[5]	66.04	0.538

* [1] : Plain [2] : 1.0mm Steel jacketing + Polyurethane bonding [3] : 1.0mm Steel jacketing
[4] : 1.5mm Steel jacketing + Polyurethane bonding [5] : 1.5mm Steel jacketing

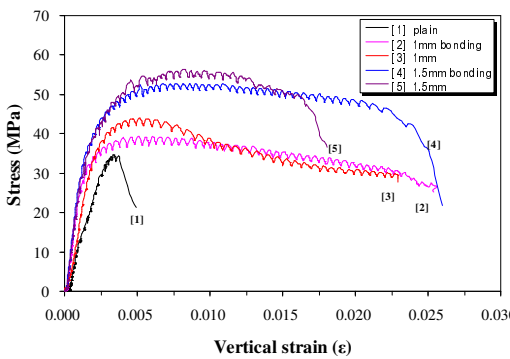

Fig. 2. Stress-strain curves for 21MPa concrete cylinders.

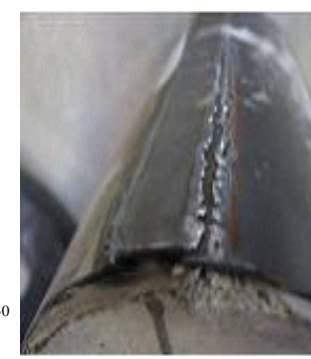

Fig. 3. Failure of a jacketed cylinder.

4. Whole Steel jackets for Concrete Cylinders

The second compressive tests were conducted to improve the welding condition of steel jackets and to check the availability of double or multiple jackets. For the first purpose, a whole steel jacket was used and the welded strip was reinforced with strips as shown in Figure 4.

(a) A whole jacket wraps around a cylinder and steel strips reinforce the welding line of the jacket.

(b) A double jacket and the weld between two jackets.

(a) (b)

Fig. 4. Whole steel jacketing method

In the second tests, the thicknesses of steel jackets were 1.0, 1.5, and 2.0 mm; the jacket of 2.0 mm thickness consists of the two 1.0 mm jackets, which is called a double jacket. Three specimens were prepared for each case. Figure 5 shows the stress-strain curves and Table 3 arranges the strength for each specimen.

Table 3. Strength of cylinders.

	Sp1 (MPa)	Sp2 (MPa)	Sp3 (MPa)	Avg (MPa)
Plain	26.0	27.5	-	26.8
1.0	38.5	40.0	38.0	38.8
1.5	45.6	44.6	43.0	44.4
2.0	48.6	50.5	50.2	49.8

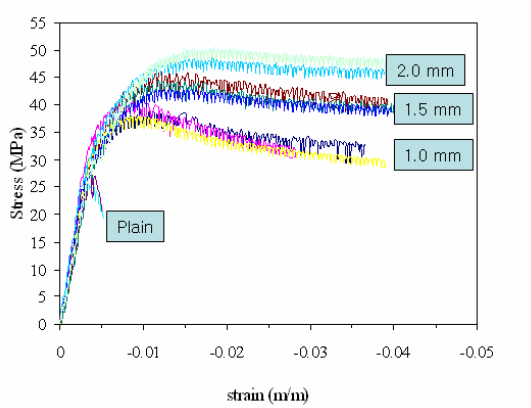

Fig. 5. Stress-strain curves of single or double jacket cylinders.

Figure 5 and Table 3 shows that the concrete strength and the jacket's thickness have a linear relationship; which means that the double jacket can show the same performance as a single jacket of the same thickness. In the second jacketing method, the failure at the welding line was not observed.

5. Conclusions

A new steel jacketing method without grouting was introduced in this study and its good performance was verified through the compressive tests of plain and jacketed concrete cylinders. The new method increased the strength and the failure strain of concrete cylinders. It is found that the adhesive put a negative effect on increasing the strength of cylinders. Also, the double or multiple jackets are available in this method. Since a thin and flexible plate is suitable to build a steel jacket, the multiple jackets is proper for large cross-section concrete columns.

Acknowledgments

This study has been supported by the KOSEF (Korea Science and Engineering Foundation; Project No. R0120060001004802006).

References

1. Buckle, I.G. (1994). "The Northridge, California earthquake of January 17, 1994: performance of highway bridge," Technical Report, NCEER-94-0008, National Center of Earthquake Engineering Research, State University of New York at Buffalo, NY.
2. Priestly, M.J.N. (1988). "Whittier narrow, California earthquake of October 1, 1987 – damage to the I-5/I-605 separator," Earthquake Spectra Journal; 4(2), pp.389-405.
3. Park, R. and Paulay, T., Reinforced Concrete Structures, John Wiley & Sons, New Zealand, 1975, pp. 17-30.

PIEZOELECTRIC SENSOR SELF DIAGNOSTICS USING A MODIFIED IMPEDANCE MODEL*

SEUNGHEE PARK, CHUNG-BANG YUN

Department of Civil and Environmental Engineering, KAIST
Daejeon, 305-701, South Korea

GYUHAE PARK, CHARLES R. FARRAR

Engineering Institute, Engineering Science & Applications Division, Los Alamos National Laboratory, Los Alamos, NM 87545, USA

The active sensing methods using piezoelectric materials have been extensively investigated for the efficient use in structural health monitoring (SHM) applications. Relying on high frequency structural excitations, the methods showed the extreme sensitivity to minor defects in a structure. Recently, a sensor self-diagnostic procedure, that performs in-situ monitoring of the operational status of piezoelectric active sensors and actuators in SHM applications, has been proposed. In this investigation, previously developed impedance models were revisited in order to investigate the effects of sensor and/or bonding defects on the admittance measurement. New parameters for sensor quality assessment of a PZT and coupling degradation effects between a PZT and bonding layer/host structure were incorporated into the traditional electro-mechanical impedance model for better estimation of the electro-mechanical impedance signatures and sensor diagnostics. The feasibility of the modified impedance model for sensor self-diagnosis using the admittance measurements was demonstrated by a series of parametric studies using a simple example of PZT-driven single degree of freedom spring-mass-damper system. This paper summarizes the description of the proposed modified electro-mechanical impedance model, parametric studies for impedance-based sensor diagnostics, and several issues for future investigation.

1. Introduction

The active sensing methods using piezoelectric (PZT) sensors are ones of the recent developments in the field of structural health monitoring (SHM). One critical aspect of the active sensing-based SHM technologies is that usually large numbers of distributed sensors are needed to perform the required monitoring process. In addition, the structures in question are usually subjected to various

* This work is supported by SISTeC sponsored by KOSEF and ISARC sponsored by MOCT.

external loading and environmental condition changes that may adversely affect the functionality of SHM sensors. The PZT sensor self-diagnostic and validation procedure is therefore critically important issue to successfully implement the SHM process. In addition, the integrity of bonding layer between a PZT sensor and a host structure should be maintained and monitored throughout their service lives. Park *et al*. (2006) [1] introduced a piezoelectric sensor-diagnostic procedure based on tracking the imaginary parts of the measured electrical admittance. Fig. 1 illustrates the measured admittances of free and surface bonded PZT patches. The PZT5A materials with dimensions of 20 x 20 x 0.25 mm were used. The admittances of free PZT patches were measured in the frequency range of 40-20,000 Hz using an impedance analyzer HP4294A. The PZT patches were then surface-mounted to a thick aluminum beam and plate using a super-glue to ensure a good bonding condition. The admittance measurements were then repeated. As can be seen in Fig. 1, the downward shifting effect of the bonding layer is remarkable. In addition, the figure demonstrates that bonding defects would cause au upward shift in the slop of the imaginary part of the measured admittances. Contrary to the bonding defects, sensor breakage would cause a downward shift in the slope of the imaginary part of the electrical admittance. Therefore, it is noted that the sensor functionality including the sensor breakage and the degradation of the bonding condition can be assessed by monitoring the imaginary part of the admittances. Actually, various models to carry out the dynamic analysis for the electromechanical impedance method have been developed so far. Typical examples include a single degree of freedom (SDOF)'s impedance-based model using spring-mass-damper (SMD) system (Liang *et al.*, 1996) [2] and a two DOFs' impedance-based model including a bonding layer between a PZT patch and a host structure (Xu and Liu, 2002) [3]. However, Liang *et al.* (1996) [2] did not take into account the effect of bonding layers between a PZT patch and a host structures on the dynamic interaction in the coupled electromechanical system. Xu and Liu (2002) [3] did not consider degradation of sensor quality due to aging effects and/or that of coupling effects due to bonding defect.

In this paper, a modified electromechanical impedance model that can be utilized for both functions of SHM and sensor diagnostics is studied. The key issue of this study is that the modified model would consider the following

factors: 1) sensor quality assessment and 2) coupling degradation effects between a PZT and bonding layer/host structure. As a result, a rigorous impedance model is established which considers the sensor quality assessment of a PZT and coupling degradation effects between a PZT and bonding layer/host structure for better estimation of the electro-mechanical impedance signatures and sensor diagnostics on the subsequent admittance measurements. Finally, the feasibility of the proposed model method is demonstrated by a series of parametric studies using a simple example of PZT-driven SDOF's SMD system.

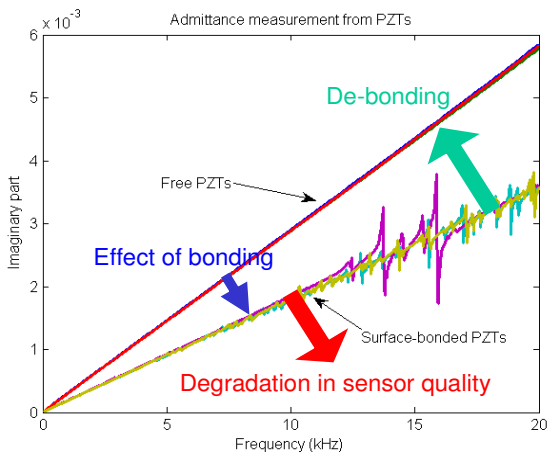

Fig. 1. Effects of sensors and boding defects on electromechanical admittance.

2. A Modified Electro-Mechanical Impedance Model for SHM and Sensor Diagnostics

When a PZT patch is surface-bonded to a host structure, Liang *et al.* (1996) [2] showed that the electrical admittance, $\mathrm{Y}(\omega)$, of the PZT patch is a combined function of the mechanical impedance of the host structure, $Z_s(\omega)$, and that of the PZT patch, $Z_a(\omega)$, which is given by

$$\mathrm{Y} = j\omega C\left(1-\kappa_{31}^2\frac{Z_s}{Z_s+Z_a}\right) \tag{1}$$

where $C\left(=\frac{wl}{h}\bar{\varepsilon}_{33}^{T}\right)$ is the capacitance of the PZT patch, and $\kappa_{31}^{2}\left(=\frac{d_{31}^{2}\bar{Y}^{E}}{\bar{\varepsilon}_{33}^{T}}\right)$ is the electromechanical coupling factor of the PZT patch: w, l, h are the width, length, and thickness of a PZT patch, $\bar{\varepsilon}_{33}^{T}=\varepsilon_{33}^{T}(1-\delta j)$ is the complex electric permittivity of a PZT patch at constant stress: δ denotes the dielectric loss factor of a PZT patch, d_{31} is the piezoelectric constant of a PZT patch, $\bar{Y}^{E}=Y^{E}(1+\eta j)$ is the Yong's modulus of a PZT patch at constant electric field: η denotes the mechanical loss factor of the PZT patch, and ω is the angular frequency.

However, equation (1) does not consider influences caused by the changes in sensor qualities and bonding layer's shear lag effect or coupling degradation effects. To solve this problem, a new 2D impedance model (Fig. 2) is proposed, that includes control parameters for sensor quality assessment and the coupling degradation effects between a PZT and bonding layer/host structure for better estimation of the electro-mechanical impedance signatures and sensor diagnostics on the subsequent admittance measurements as

$$\tilde{\mathrm{Y}}(\omega)=j\omega\tilde{C}\left(1-\tilde{\kappa}_{31}^{2}\frac{\xi\cdot Z_{s}(\omega)}{\xi\cdot Z_{s}(\omega)+Z_{a}(\omega)}\right) \tag{2}$$

where $\tilde{\mathrm{Y}}(\omega)$ is the resultant admittance; $\tilde{C}=a\cdot C$; a is a sensor quality index $(0\le a\le 1)$; $a=0$ means a complete sensor failure-condition and $a=1$ means a perfectly good condition; $\tilde{\kappa}_{31}^{2}=b\cdot\kappa_{31}^{2}$; b is a coupling degradation index $(0\le b\le 1)$; $b=0$ means a free-free condition of the PZT patch and $b=1$ means a perfect surface-bonded condition; $\xi(=1/(1+K_{s}/K_{b}))$ is the shear-lag coefficient of the bonding layer; K_{s} is a dynamic stiffness (or mechanical impedance $Z_{s}=K_{s}/j\omega$) of the host structure generalized by the PZT driving point; and K_{b} is a dynamic stiffness (or mechanical impedance $Z_{b}=K_{b}/j\omega$) of the bonding layer (Hixon (1998)[4]). The modified electromechanical impedance formulation, Equation (2) might be effectively utilized for both functions of SHM and sensor diagnostics on the subsequent admittance measurements. To demonstrate the feasibility of the proposed model equation, a series of parametric studies considering

continuous degradations of the sensor quality and coupling effects between a PZT and bonding layer/host structure are carried out on a simple PZT-driven SDOF's SMD system. The material properties and geometric sizes of the PZT patch are listed in Table 1. The SMD system for the host structure is set as follows: mass $m = 2\,\text{kg}$, damping constant $c = 125\,\text{N/ms}^{-1}$, and spring stiffness $k = 2.0\times10^{9}\,\text{N/m}$.

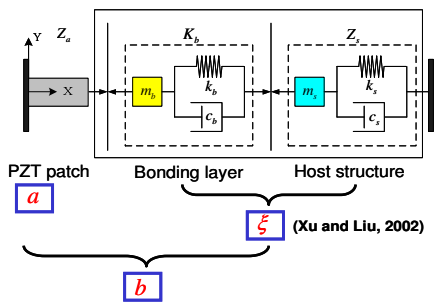

Fig. 2. A new 2D impedance model for both of SHM and sensor diagnosis.

Table 1. Material properties and geometric sizes of PZT patch

Y^E (N/m^2)	d_{31} (m/V)	ε_{33}^T (Farads/m)	δ	η	w (mm)	h (mm)	l (mm)
6.3×10^{10}	-1.66×10^{-10}	1.5×10^{-8}	0.005	0.001	25.4	0.254	25.4

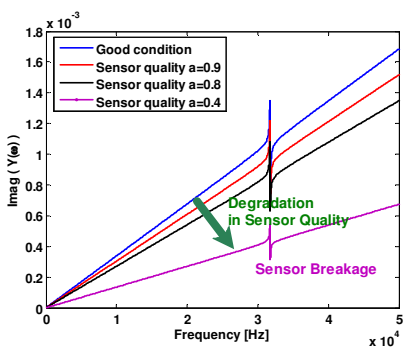

(a) Sensor quality assessment

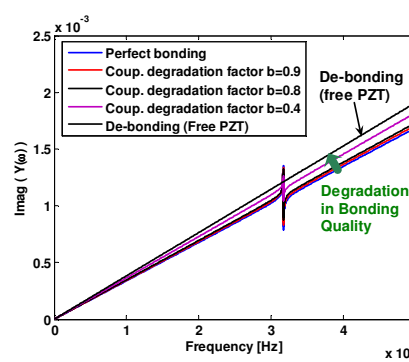

(b) Bonding degradation assessment

Fig. 3. PZT sensor self diagnostics using a modified impedance model.

The results are illustrated in Fig. 3. It was confirmed that the degradation of the sensor quality and/or bonding layer can be identified by monitoring the slope of the imaginary part of the electrical admittance. The degradation of sensor quality would cause a downward shift in the slope of the imaginary part of the electrical admittance. On the contrary, the bonding defects would cause an upward shift in the slope of the imaginary part of the admittance. This is well-consistent with the experimental results of Fig. 1. Herein, note damage in a host structure can be detected by looking at the changes in the amplitudes and resonant frequencies of the real part of the impedance signature.

3. Conclusions

A new electro-mechanical impedance model was formulated which can be effectively used for both functions of structural health monitoring and sensor diagnostics. New parameters for sensor quality assessment and coupling degradation effects between a PZT and bonding layer/host structure were incorporated into the traditional electro-mechanical impedance model. The feasibility of the modified model has been demonstrated throughout a series of parametric studies using a simple PZT-driven single degree of freedom spring-mass-damper system. It was observed that the results of the parametric studies showed a good consistency with previous experimental investigations. Conclusively, it was verified that the modified impedance model can be very effectively used for more reliable damage detection and sensor self-diagnostics on continuous long-term active sensing-based structural health monitoring.

Acknowledgments

This work was jointly supported by the SISTeC at KAIST sponsored by the Korea Science and Engineering Foundation, and the ISARC sponsored by Ministry of Construction and Transportation, Korea. This financial support is greatly appreciated.

References

1. G. Park, C.R. Farrar, A.C. Rutherford, and A.N. Robertson, *Journal of Vibration and Acoustics, AMSE* (2006).
2. L. Liang, F.P. Sun, and C.A. Rogers, *Smart Mat. and Str.* **5**, 171 (1996).
3. Y.G. Xu and G.R. Liu, *J. of Intelligent Mat. Sys. and Str.,* **13**, 389 (2002).
4. E.L. Hixon, *Shock and Vibration Handbook,* **10.1** (1998).

SMART PARTICLES CONTAINING MULTIPLE PHOTONIC BAND GAPS BASED ON RUGATE-STRUCTURED POROUS SILICON

SUNG JIN KIM

Department of Chemistry, Chosun University,375 seosuk-dong Dong-gu, Gwangju, 501-759, Korea

SEUNGHYUN JANG

Department of Chemistry, Chosun University, 375 seosuk-dong Dong-gu, Gwangju, 501-759, Korea

YOUNGDAE KOH

Department of Chemistry, Chosun University, 375 seosuk-dong Dong-gu, Gwangju, 501-759, Korea

JIHOON KIM

Department of Chemistry, Chosun University, 375 seosuk-dong Dong-gu , Gwangju, 501-759, Korea

CHEOLYOUNG PARK

Department of Chemistry, Chosun University, 375 seosuk-dong Dong-gu , Gwangju, 501-759, Korea

JAEHYUN PARK

Department of Chemistry, Chosun University, 375 seosuk-dong Dong-gu, Gwangju, 501-759, Korea

HONGLAE SOHN

Corresponding author, Department of Chemistry, Chosun University, 375 seosuk-dong Dong-gu, Gwangju, 501-759, Korea, hsohn@chosun.ac.kr

Photonic crystals containing multiple rugate structure are prepared by applying a composite waveform summed three computer-generated pseudo-sinusoidal current waveforms. They exhibit three sharp photonic band gaps in the optical reflectivity spectrum. Three types of rugate PSi prepared in this study. Typically etched PSi, oxidized PSi, and hydrosilylated PSi. The rugate PSi films have been removed from the

silicon substrate by applying a lift-off current and are then made into particles by ultrasono-method in an organic solution. The sensing experiments using these particles for organic solvents such as methanol and hexane have been achieved. Condensing of organic vapors in the pores increases the refractive indices of entire particle which results a red shift in the photonic peaks.

Keywords: Rugate porous silicon; sensing; organic vapors; encoding.

1. Introduction

The development of new technology, which can achieve at nanometer scale, to build such a device is of great interest. Porous silicon (PSi) is one of candidate because of the unique optical properties of a dielectric material with an effective refractive index, *n*, which depends directly on the porosity. PSi is also an attractive material due to its high surface area, convenient surface chemistry, and optical signal transduction capability.[1-7] Electrochemical etching offers the opportunity to modulate the porosity in depth and allows the fabrication of structures with any refractive index profile. When the current is gradually modulated, a smooth index profile of PSi is achieved, which generates the so-called rugate filters.[8] Rugate-structured PSi having the photonic structure of a rugate filter in which the refractive index varies sinusoidally has been recently developed by applying a computer-generated pseudo-sinusoidal current waveform. Chemical[9] and bio molecules[10] can be detected based on changes in the spectral interference pattern. In the present work, we report the detection of volatile organic molecules based on optical interferometer by using optically encoded particles containing multi-structured rugate PSi.

2. Experiment

2.1. *Preparation of PSi Samples*

Rugate PSi samples are prepared by an electrochemical etch of heavily doped p^{++}-type silicon wafers (boron doped, polished on the <100> face, resistivity of 0.8-1.2mΩ-㎝, Siltronix, Inc.). The etching solution consisted of a 3:1 volume mixture of aqueous 48% hydrofluoric acid (ACS reagent, Aldrich Chemicals) and absolute ethanol (ACS reagent, Aldrich Chemicals). Etching is carried out in a Teflon cell by using a two-electrode configuration with a Pt mesh counter electrode. A composite waveform summed three computer-generated pseudo-sinusoidal current waveforms varying between 39.95mA·cm^{-2} and 86.15mA·cm^{-2} (100 seconds periodicity, 20 repeats) is applied as an anodization current density. Each sine component varies from 0.32 ~ 0.28, 0.30 ~ 0.26, and

0.28 ~ 0.24Hz with a spacing of 0.02 Hz between each sine component. The anodization current was supplied by a Keithley 2420 high-precision constant current source which is controlled by a computer to allow the formation of PSi multilayers. To etch the required apodized sinusoidal index profile into Si, the etching current was computer controlled via the power supply (Keithley Source Meter 2420). Galvanostatic etching was performing in a dark room. All samples were then rinsed several times with ethanol and dried under argon atmosphere prior to use. Three types of rugate PSi are (1) typically etched rugate PSi chip and (2) decyl-derivatized rugate PSi ; freshly etched rugate PSi chip was placed in 50 mL of schlenk flask under argon atmosphere. After 20 mL of 1-decene was added, the reaction mixture was refluxed for 6 hr. Decyl-derivatized rugate PSi chip was washed several times with ethanol, acetone and dichloromethane and then dried under argon gas prior to use. (3) Oxidized rugate PSi ; rugate PSi was thermally oxidized by using a furnaces. The sample was heated at 300 ℃ for 3 hour in ambient air condition and then allowed to cool to room temperature. The resulting rugate PSi film has been obtained from the silicon substrate by an applying of electropolishing current at 450 $mA \cdot cm^{-2}$ for 1.5 min in a solution of 48% aqueous HF and ethanol (3:1 by volume), and then at 24 $mA \cdot cm^{-2}$ for 1.5 min in a solution of 48% aqueous HF and ethanol (1:15 by volume) to obtain a free-standing rugate PSi films. The freestanding films were then made into particles by ultrasono-method in ethanol solution.

2.2. *Spectral Measurements*

Samples were illuminated with a tungsten lamp, and the reflected light spectrum was measured using an Ocean Optics USB 2000 CCD spectrometer. Reflectance spectra of the samples were taken with Ocean Optics spectrometers in the range of 200-1100 nm. Scanning electron microscope (SEM) images were obtained by a cold field emission scanning electron microscope (FE-SEM, S-4700, Hitachi).

3. Result and Discussion

Photonic crystals containing the rugate structure result in a mirror with high reflectivity in a specific narrow spectral region and are prepared by applying a computer-generated pseudo-sinusoidal current waveform. The rugate PSi generated with this method exhibits a very sharp line in the optical reflectivity spectrum. Rugate filters possess a sinusoidally varying porosity gradient in the direction perpendicular to the plane of the filter. The waveform used in the this work involves an individual sine component, which is represented by Eq. 1.

$$Y_i = A_i \sin(k_i t) + B \tag{1}$$

Where yi represents a temporal sine wave of amplitude, A_i; frequency, k_i; time, t; applied current density, B. Triply encoded rugate structures can be etched on a silicon wafer. To generate triple rugate structure, three individual sine components are summed together to create a composite waveform as shown in Eq. 2.

$$Y_{comp} = A_1 \sin(k_1 t) + A_2 \sin(k_2 t) + A_3 \sin(k_3 t) + B \tag{2}$$

Eq. 2 can be converted to an analog current-time waveform to etch using a computer-controlled digital galvanostat. Reflectivity spectrum of triple rugate structured PSi displayed three peaks. After the generation of optically encoded rugate porous silicon, the resulting porous silicon films were removed from the silicon substrate by applying an electropolishing current to obtain a free-standing rugate film. A pulse of current is sufficient to undercut the porous silicon layer and to lift it completely from the Si substrate. These freestanding films are fractured into few decade nanometers to few micrometer-sized pieces in an ultrasonic bath.

SEM images of these particles are shown in Fig. 1. The surface image of smart particles indicates that the distribution of pore size is even and retains a good porosity with no destruction of porous structure during the ultrasonication. The pore size varies depending on the treatment of surface.

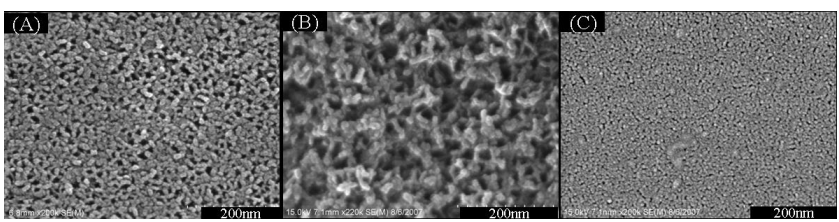

Fig. 1. SEM images of smart particles: (a) High resolution SEM image for the surface of the fresh smart particles, (b) oxidized smart particles, (c) hydrosilylated smart particles.

Triply encoded rugate PSi smart particles have been subjected to expose to the vapor of organics such as methanol and hexane. When these smart particles are exposed to the organic vapors, capillary condensation causes the reflection wavelength to shift to longer wavelengths as shown in Fig. 2.

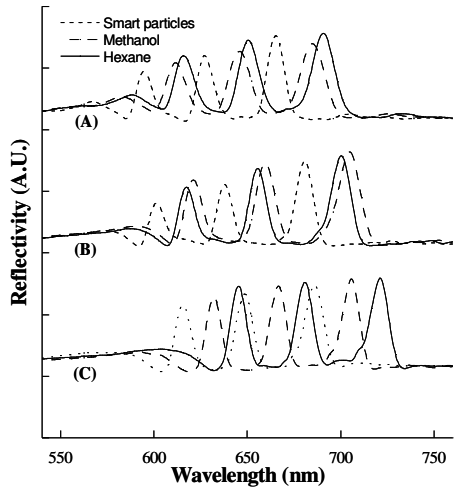

Fig. 2. Optical reflectivity spectra of fresh smart particles (a), oxidized smart particles (b), and hydrosilylated smart particles (c) under the exposure of organic vapors.

Such a large red shift is characteristic of an increase in the average refractive index of the multilayers, consistent with the replacement of a significant amount of empty pore volume with analyte.

Table 1. Red-shift of reflection maxima for the fresh smart particles under the exposure of organic vapors.

	peak 1	peak 2	peak 3
methanol	17 nm	19 nm	21 nm
hexane	21 nm	24 nm	27 nm

Table 2. Red-shift of reflection maxima for the oxidized smart particles under the exposure of organic vapors.

	peak 1	peak 2	peak 3
methanol	19 nm	22 nm	25 nm
hexane	16 nm	18 nm	20 nm

Table 3. Red-shift of reflection maxima for the hydrosilylated smart particles under the exposure of organic vapors.

	peak 1	peak 2	peak 3
methanol	11 nm	13 nm	15 nm
hexane	29 nm	32 nm	35 nm

The red-shifts of reflection maxima for the triple encoded rugate structured PSi under the exposure of organic vapors are summarized in Table 1, 2, and 3. Peak 1 represents the shortest reflection wavelength. Particles modified with decyl functionalities are hydrophobic materials and has a much greater affinity for hydrophobic versus hydrophilic analyte. Thus the particles exhibit the most red-shifted photonic feature for the hydrophobic hexane (ca. 29, 32, and 35 nm, 97 mmHg), but are quite insensitive to the methanol vapor (ca. 11, 13, and 15 nm, 97 mmHg) at a partial pressure comparable to that of hydrophobic analyte hexane. However particles modified with hydroxyl group have a greater affinity for hydrophilic analyte and thus display in reverse.

4. Conclusions

This work demonstrates the surface modification of optically encoded smart particles and their surface chemistry. The detection of organic vapors using surface-modified rugate PSi smart particles exhibits different responses depending on the surface modifications. In the present system, the possibility for multi-agent analysis can be readily achieved by chemical modification for the detection of broad range of organic analytes.

References

1. J. R. Link and M. J. Sailor, *Proc. Natl. Acad. Sci.* 10607 (2003).
2. R. Herino, *Short Run Press* London, 89, (1997).
3. V. S. –Y. Lin, K. Motesharei, K. –P. S. Dancil, M. J. Sailor, and M. R. Ghadiri, *Science* **278**, 840 (1997).
4. A. Janshoff, K. –P. S. Dancil, C. Steinem, D. P. Greiner, V. S. –Y. Lin, C. Gurtner, K. Motesharei, M. J. Sailor, and M. R. Ghadiri, *J. Am. Chem. Soc*. **120**, 12108 (1998).
5. K. –P. S. Dancil, D. P. Greiner, and M. J. Sailor, *J. Am. Chem. Soc*. **121,** 7925 (1999).
6. D. van Noort, S. Welin-Klinstrom, H. Arwin, S. Zangooie, I. Lundstrom, and C. –F. Mandnius, *Biosens. Bioelectro.* **13,** 439 (1998).
7. S. Chan, S. R. Horner, B. L. Miller, and P. M. Fauchet, *J. Am. Chem. Soc.* **123,** 11797 (2001).
8. B. E. Collins, K. –P. S. Dancil, G. Abbi, and M. J. Sailor, *Adv. Funct. Matter*. **12,** 187 (2002).
9. H. Sohn, S. Létant, M. J. Sailor, and W. C. Trogler, *J. Am. Chem. Soc.* **122**, 5399 (2000).
10. J. R. Dorvee, A. M. Derfus, S. N. Bhatia, and M. J. Sailor, *Nat. Mater*. **3**, 896 (2004).

ACCURATE VIBRATION ANALYSIS OF *N*-SIDED POPLYGONAL MINDLIN PLATES WITH V-NOTCHES OR SHARP CRACKS*

JOO-WOO KIM

Department of Architectural Engineering, Semyung University, 579 Sinweol-dong Jecheon, Chungbuk 390-711, Korea

HIE-YOUNG JUNG

Department of Civil Engineering, University of Seoul, 90 Jeonnong-dong Seoul, 130-743, Korea

This paper provides first known flexural vibration data thick (Mindlin) *N*-sided polygonal plates having V-notches. A specific feature here is that the analysis explicitly considers the bending moment and shear force singularities occurring at the sharp corner of the V-notch during transverse vibratory motion. Based upon Mindlin plate theory, in which transverse shear deformation and rotary inertia effects are considered, the Ritz procedure is employed with a hybrid set of admissible functions assumed for the rotational and transverse vibratory displacements. This set includes: (i) a mathematically complete set of admissible algebraic-trigonometric polynomials which guarantee converges to exact frequencies as sufficient terms are retained; (ii) an admissible set of Mindlin *corner functions* which account for the bending moment and shear force singularities at the sharp corner of the V-notch. Extensive convergence studies summarized herein confirm that the Mindlin corner functions substantially enhance the convergence and accuracy of non-dimensional frequencies for the Mindlin polygonal plates having V-notch. Accurate frequencies are presented for notches for the spectrum of notch angles, notch depths and thickness ratios.

1. Introduction

Thick polygonal plates can be commonly found in civil, aerospace and ocean engineering systems, electronic and optical packages and machine components. Literature on the vibrations of the polygonal plates containing discontinuities, such as cracks or V-notches, is extremely limited or non-existent. One effort was reported by Liew, *et al*,[1] who studied free vibration of polygonal plates with reentrant corners, such as L-, T- and C-shaped planforms using the Ritz method. Recently, Kim, *et al*,[2] offered the natural frequencies and mode shapes of thin

* This work was supported by the Korea Science and Engineering Foundation (KOSEF) grant funded by the Korea government (No. R01-2006-000-10610-0)

polygonal plates with discontinuities using the classical plate theory in conjunction with the Ritz procedure.

The present work examines Mindlin *N*-sided polygonal plates including stress singularity effects at the vertex corner (see Fig. 1) for which no previously published vibration frequencies is known to exist. For a very small notch angle notch angle, $360^\circ - \alpha$ (say, one degree or less), sharp radial crack ensues. A single-field energy-based Ritz procedure is employed, which incorporates a complete set of admissible algebraic-trigonometric polynomials in conjunction with an admissible set of corner functions that exactly model the singular vibratory moments and transverse shear forces which exist along a re-entrant corners (i.e., $\alpha > 180^\circ$) of the V-notch.[3] The first set guarantees convergence to exact frequencies as sufficient terms are retained. The second set substantially accelerates the convergence of frequencies, which is demonstrated through a convergence study summarized herein

2. Methodology

Consider in Fig. 1 a completely free, thick notched *N*-sided polygonal plate having thickness *h* with polar coordinates (r, θ) at the middle surface. The vibratory rotations and a transverse displacement are assumed in terms of polar coordinates (r, θ) at the middle surface as

$$\phi_r = \Phi_r(r,\theta)\sin\omega t, \quad \phi_\theta = \Phi_\theta(r,\theta)\sin\omega t, \quad w_z = W_z(r,\theta)\sin\omega t, \tag{1}$$

where t is time and ω is the circular frequency of vibration. In using the Ritz method, one requires the maximum values of strain and kinetic energies, which occur during a cycle of vibratory motion. On the maximum energy equations, the limits of the integration are defined as $r(\theta)$, describing the *N*-sided polygonal circumferential boundary:

$$r(\theta) = \frac{\left| y_n - x_n \tan\eta_n \right|}{\sin\theta - \tan\eta_n \cos\theta} \qquad (-\pi \le \theta \le \pi), \tag{2}$$

where $n = 1, 2, \ldots, N$ ($N =$ number of sides). In the Eq. (2),

$$\begin{cases} \eta_1 = \beta + \dfrac{\pi}{2} \\ \eta_n = \eta_{n-1} + \beta \end{cases}, \quad \begin{cases} x_1 = a + c \\ x_n = x_{n-1} + L\cos\eta_{n-1} \end{cases}, \quad \begin{cases} y_1 = \dfrac{L}{2} - d \\ y_n = y_{n-1} + L\sin\eta_{n-1} \end{cases}, \tag{3}$$

in which $n = 2, \ldots, N$, $\beta = \dfrac{2\pi}{N}$, and $L = 2a\tan\dfrac{\beta}{2}$.

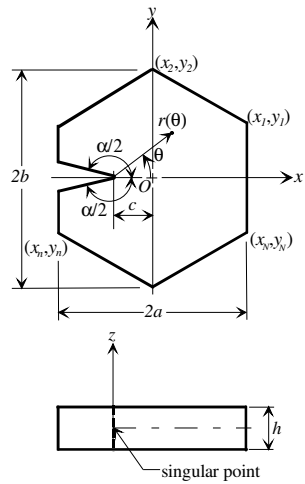

Fig. 1. Geometric description of *N*-sided polygonal plate with a V-notch

In the present Ritz approach, displacement trial functions are assumed as the sum of two finite sets:

$$\Phi_r = \Phi_r^p + \Phi_r^c, \qquad \Phi_\theta = \Phi_\theta^p + \Phi_\theta^c, \qquad W_z = W_z^p + W_z^c, \tag{4}$$

where Φ_r^p, Φ_θ^p, and W_z^p are usual algebraic-trigonometric polynomials and Φ_r^c, Φ_θ^c, and W_z^c are Mindlin corner functions. The polynomials should, in principle, yield accurate frequencies. However, the number of terms may be computationally prohibitive. This problem is alleviated by augmentation of the displacement polynomial trial set with admissible *corner functions*, which introduce the proper singular vibratory moments and shear forces at the vertex of the V-notch (Fig. 1). The set of corner functions is taken as, for the symmetric modes:

$$\Phi_r^c = \sum_{k=1}^{K_1} G_k r^{\lambda_k} \left[\zeta_k \cos(\lambda_k + 1)\theta - \gamma_k \cos(\lambda_k - 1)\theta\right],$$

$$\Phi_\theta^c = \sum_{k=1}^{K_2} G_k r^{\lambda_k} \left[-\zeta_k \sin(\lambda_k + 1)\theta + \gamma_k \sin(\lambda_k - 1)\theta\right], \tag{5}$$

$$W_z^c = \sum_{k=1}^{K_3} H_k r^{\hat{\lambda}_k + 1} \cos(\hat{\lambda}_k + 1)\theta,$$

with

$$\zeta_k = \frac{(\gamma_k + 1)(\lambda_k - 1)\sin(\lambda_k - 1)\alpha/2}{2\lambda_k \sin(\lambda_k - 1)\alpha/2}, \quad \text{where} \quad \gamma_k = \frac{\lambda_k(1+\nu) - 3 + \nu}{\lambda_k(1+\nu) + 3 - \nu}. \tag{6}$$

In Eqs. (7), the λ_k and $\hat{\lambda}_k$ are the roots of the characteristic equations

$$\sin \lambda_k \alpha = -\lambda_k \sin \alpha, \qquad \sin(\hat{\lambda}_k + 1)\alpha/2 = 0. \tag{7}$$

Similarly, the corner functions used for antisymmetirc modes are analogous to those defined for the symmetric ones in Eqs. (7), except the cosine functions are changed to sine functions, or vice versa. Some of the λ_k obtained from Eqs. (8) may be complex numbers, and thus result in complex corner functions. In such cases, both the real and imaginary parts are used as independent functions in the present Ritz procedure.

The free vibration problem is solved by substituting Eqs. (4) into the equations of maximum strain and kinetic energies and employing the frequency equations of the Ritz method. This results in a set of linear homogeneous algebraic equations involving the coefficients. The vanishing determinant of these equations yields a set of eigenvalues (natural frequencies), expressed in terms of the non-dimensional frequency parameter, $\omega a^2 \sqrt{\rho h / D}$ commonly used in the plate vibration literature.

3. Convergence Study and Frequency Results

Having outlined the Ritz procedure employed in the preceding sections, it is now appropriate to address the important question of the convergence accuracy of frequencies as sufficient numbers of displacement functions are retained. According to the number of sides (N) of the polygonal plates, they may be pentagonal, hexagonal, heptagonal, and octagonal shaped plates.

Here, as an example for the sake of brevity, convergence study is summarized in Table 1 for the completely free Mindlin hexagonal plates (i.e., $N = 6$) having 5° notch angle (i.e., $\alpha = 355^\circ$) and c/a = 0 in. This example is appropriately described as a thick plate (a/h = 10) with a sharp notch or radial crack. All of the frequency data discussed in the present section are for materials having shear correction factor κ^2 equal to $\pi^2/12$ and Poisson's ratio ν equal to 0.3. It can be seen in Table 1 that the fundamental frequency mode is an antisymmetric one. An upper bound convergence of frequencies to an inaccurate value of 4.674 is apparent, as the sizes of polynomial series are increased with no Mindlin corner functions. Adding five corner functions improves the convergence rate significantly. An examination of the next three rows of data reveals that an accurate value to four significant figures is 2.450. It should be

noted that there are three rigid body modes in the vibration of the completely free Mindlin hexagonal plate which are not shown in the table.

Table 1. Convergence of frequency parameters $\omega a^2(\rho/D)^{1/2}$ for a completely free thick hexagonal plate (N = 6) with a V-notch (α = 355^0, c/a = 0, a/h = 10)

Mode no. (symmetry class*)	No. of Corner Functions	Solution size of polynomials				
		21	22	23	24	25
1 (A)	0	4.676	4.676	4.675	4.675	4.674
	1	4.272	4.261	4.253	4.243	4.236
	5	2.465	2.462	2.459	2.457	2.454
	10	2.460	2.457	2.455	2.453	2.451
	20	2.453	2.451	2.450	2.450	2.450
2 (S)	0	4.715	4.714	4.713	4.712	4.711
	1	4.179	4.165	4.148	4.134	4.119
	5	3.834	3.833	3.831	3.831	3.830
	10	3.830	3.829	3.828	3.828	3.827
	20	3.829	3.829	3.828	3.827	3.826
3 (S)	0	7.865	7.864	7.862	7.861	7.859
	1	7.018	7.002	6.985	6.971	6.956
	5	6.674	6.674	6.672	6.672	6.670
	10	6.670	6.670	6.669	6.669	6.668
	20	6.670	6.670	6.669	6.668	6.668

*(S) symmetric mode; (A) antisymmetric mode

Table 2. Frequency parameters $\omega a^2(\rho/D)^{1/2}$ for completely free thick hexagonal plates (a/h = 10) with V-notches

a/h	Mode no.	c/a	α (degrees) 270	300	330	350	355	359
10	1	0.75	4.189*	4.610*	4.642*	4.605*	4.601*	4.601*
		0.5	3.023*	2.770	4.144*	4.531*	4.147*	3.191*
		0	4.189*	3.334*	2.700*	2.492*	2.450*	2.419*
		-0.5	4.395*	3.018*	2.518*	1.489*	1.432*	1.381*
	2	0.75	5.192	4.721	4.671	4.640	4.616	4.625
		0.5	4.988	3.026*	4.582	4.725	4.457	4.708
		0	5.192	4.758	4.218	3.906	3.828	3.761
		-0.5	5.641	4.606	4.485	3.079	2.959	2.873
	3	0.75	8.652	7.844	7.842	7.823	7.803	7.812
		0.5	6.091*	6.070*	7.553	7.886	7.571	6.298*
		0	8.652	7.277	6.771	6.691	6.669	6.654
		-0.5	10.75	8.390	7.115	6.247	6.198	6.158
20	1	0.75	4.661*	4.710*	4.666*	4.659*	4.658*	4.660*
		0.5	4.405*	3.210*	4.223*	4.226*	4.236*	3.221*
		0	4.294*	3.498*	2.777*	2.565*	2.523*	2.494*
		-0.5	4.466*	3.144*	1.896*	1.538*	1.473*	1.424*
	2	0.75	4.834	4.792	4.720	4.693	4.670	4.680
		0.5	5.041	4.824	4.643	4.553	4.519	4.755
		0	5.274	4.369	4.301	3.983	3.905	3.837
		-0.5	5.716	4.744	3.689	3.159	3.038	2.949
	3	0.75	7.946	7.953	7.922	7.909	7.889	7.900
		0.5	7.804	8.517	7.650	7.675	7.674	6.319*
		0	8.783	6.951	6.868	6.794	6.774	6.762*
		-0.5	10.94	8.514	6.640	6.328	6.279	6.239

*Antisymmetric modes in θ□

In Table 2, extensive convergence studies were performed to compile the least upper bound $\omega a^2\sqrt{\rho h/D}$ for the first three modes of hexagonal plates having V-notches with various α and *c*/*a* and two different thickness ratios (*a*/*h* = 10 and 20). Frequency data corresponding to the antisymmetric modes are indicated by an asterisk (*). It is seen in Table 2, regardless of thickness ratios, that for $\alpha \geq 330°$, the frequency values in the first three modes monotonically decrease with decreasing *c*/*a*. At $\alpha = 300°$, a reversal of the cited trends develops quite significantly. For instance, the fundamental values of $\omega a^2\sqrt{\rho h/D}$ in this case monotonically decrease with decreasing *c*/*a*, while some of the higher mode values of $\omega a^2\sqrt{\rho h/D}$ are increased with decreasing *c*/*a*. At small vertex angle ($\alpha = 270°$), a similar frequency increase with notch depth is observed in all modes except in the fundamental mode.

4. Concluding Remarks

Highly accurate frequencies and mode shapes for completely free thick polygonal plates with V-notches have been obtained using a Ritz procedure in conjunction with Mindlin plate theory. In this approximate procedure, the assumed displacements of the plate constitutes a hybrid set of complete algebraic-trigonometric polynomials along with Mindlin corner functions that account for singular bending moments and shear forces at the vertex of acute corner angles. The efficacy of such corner functions has been substantiated by a convergence study of non-dimensional frequencies.

Detailed numerical tables have been presented, showing the variations of non-dimensional frequencies with different geometric parameters. Some fundamental understanding of the effect of highly localized stresses on the plate dynamics can be obtained through careful examination of the frequency data offered herein. Most of all, the accurate vibration data presented here serves as benchmark values for comparison with data obtained using modern experimental and alternative theoretical approaches.

References

1. K.M. Liew, K.C. Huang and Y.K. Sum, *J. Sound and Vibration,* **183(2)**, 221-238 (1995).
2. J.W. Kim, H. Jung, D.W. Lee, and S.S. Lee, *Int. Sym. IASS-APCS 2006*, **DR33** (2006).
3. J.W. Kim, *Ph.D. Thesis, Georgia Institute of Tech.*, (1998).

ACTIVE STRUCTURAL CONTROL TECHNIQUE USING LATTICE PROBABILISTIC NEURAL NETWORK BASED ON LEARNING RULE

DONG HYAWN KIM

Department of Ocean System Engineering, Kunsan National University, Kunsan, Jeonbuk, 573-701, Republic of Korea

DOO KIE KIM, SEONG KYU CHANG AND CHARITO FE M. NOCETE

Department of Civil and Environment Engineering, Kunsan National University, Kunsan, Jeonbuk, 573-701, Republic of Korea

WOO SUN PARK

Costal and Harbor Engineering Research Center (KORDI), Ansan P.O. Box 29, Seoul 425-600, Republic of Korea

Active control of structures using lattice probabilistic neural network (LPNN) employing the gradient descent method (GDM) for learning to increase control capability is proposed. With the lattice pattern of the state vector used as the training data, LPNN calculates the control force using only the adjacent information of input, thus response is greatly faster. One-story building under California earthquake is used to train the LPNN. El Centro earthquake is used to verify the proposed method. In the results, although the structural response reduction is not so large, the effect of the learning methodology is effectively demonstrated the in the practical application.

1. Introduction

Recently, various active structural control algorithms [1-6] including probabilistic neural networks (PNN) [7] have been studied. PNN showed good control performance, but requires a big amount of computational efforts in calculating the control force in any instant of time. It calculates the hamming distances of invoked input from all patterns saved in the memory, and selects the most adjacent output pattern as the control force output. Increasing the training data also increases calculation time in proportion to the number of patterns.

Therefore, a new method called the lattice probabilistic neural network (LPNN) is used in this study. Unlike the conventional PNN with randomly distributed training patterns, LPNN uniformly distributes these patterns at the lattice points in state space. The position of invoked input can be known and the

output is obtained using only adjacent patterns, greatly reducing the calculation time. Moreover, LPNN control capability is increased by employing the gradient descent method (GDM) for learning.

LPNN is applied for the vibration control of one-story shear building and California earthquake is used to train the LPNN. El Centro earthquake is used to verify the proposed method. In practical application, although the structural response reduction is not so large, the effect of the learning methodology is effectively demonstrated for practical application.

2. Active Control Using LPNN

2.1. *Training pattern and control force*

The training pattern of the LPNN controller is composed of the lattice form of the control force ($f_{j,y}$) and the state vector (u, $\dot{u}$) as shown in Fig. 1. The state vector is the uniform interval between the maximum and the minimum of the optional structural response. The control force is calculated by the product of the control gain ($\mathbf{G}$) and the state vector (z) of the system, as in equation (1).

$$f_{j,y} = -\mathbf{G} \cdot z = -(\mathbf{R}^{-1} \cdot \mathbf{L}_e{}^T \cdot \mathbf{S}) \cdot z \qquad j,\ y = -3, \cdots, 3 \tag{1}$$

The solution of the Riccati equation ($\mathbf{S}$) is obtained as follows

$$\mathbf{A}^T\mathbf{S} + \mathbf{S}\mathbf{A} - \mathbf{S}\mathbf{L}_e\mathbf{R}^{-1}\mathbf{L}_e{}^T\mathbf{S} + \mathbf{Q} = 0 \tag{2}$$

where $\mathbf{Q}$ and $\mathbf{R}$ are referred to as weighting matrices.

In this paper, the maximum and the minimum of the optional structural responses are defined as $\pm 0.002m$ and $\pm 0.2m/\sec$, while uniform widths are $0.0001m$ and $0.01m/\sec$.

2.2. *Lattice probabilistic neural network*

Fig. 1 shows the structure of LPNN with two inputs and a single output at the k th time step, where the maximum and minimum of the state vectors are ± 3 and the uniform width is one. With training patterns uniformly distributed in state space, the position of any given input can then be easily known as follows

$$position = \left(\frac{u_k}{j} + \frac{s}{2}, \frac{\dot{u}_k}{y} + \frac{v}{2} \right) \tag{3}$$

where u_k and $\dot{u}_k$ are the displacement and velocity at the k th time step, respectively, j and y are uniform widths of the training pattern in state space,

s and v are the sizes of u_k and $\dot{u}_k$ axes, respectively. Adjacent patterns can be directly identified by the coordinates calculated using equations (4) - (7)

$$j_1 = ceil\left[\frac{u_k}{j} + \frac{s}{2}\right] \qquad j_2 = ceil\left[\frac{u_k}{j} + \frac{s}{2}\right] - 1 \qquad (4) - (5)$$

$$y_1 = ceil\left[\frac{\dot{u}_k}{y} + \frac{v}{2}\right] \qquad y_2 = ceil\left[\frac{\dot{u}_k}{y} + \frac{v}{2}\right] - 1 \qquad (6) - (7)$$

Here, $ceil(\cdot)$ means the smallest integer greater than the input value. Since the adjacent pattern is known, calculating hamming distances of all patterns, as done by PNN, is avoided.

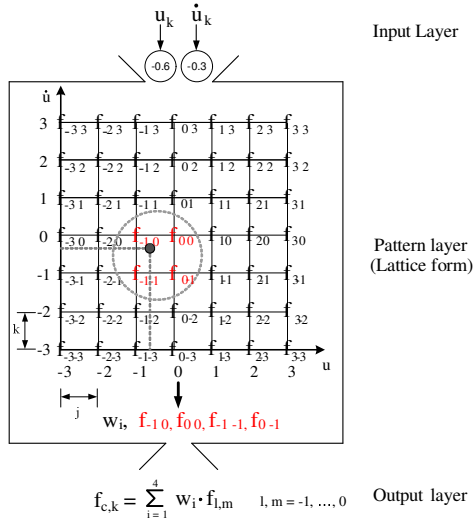

Fig. 1. Structure of LPNN

The distance between the input pattern (response of structure) and the training pattern (lattice type) for LPNN can be calculated by the equation below

$$dist_i = \sqrt{\sum (\mathbf{X} - \mathbf{Y})^2} \qquad i = 1, \cdots, 4 \qquad (8)$$

where $\mathbf{X}$ is the input pattern (u_k, $\dot{u}_k$) at the k th time step, and $\mathbf{Y}$ denotes four training patterns ($[u_l, \dot{u}_m]$) around the input pattern in Fig. 1. The calculated distance in the pattern layer is converted to the weighting as follows

$$w_i = \frac{pd_i}{sp}, \quad pd_i = \frac{(sd - dist_i)}{2} \qquad i = 1, \cdots, 4 \qquad (9)$$

where sd is the sum of the distances, pd_i is the participated rate of weighting of the training pattern, sp is the sum of pd_i, and w_i is the weighting of the training pattern corresponding to the distance. In the output layer, the control force ($f_{c,k}$) is calculated as the product of the weighting (w_i) and the control forces ($f_{l,m}$) corresponding to the training pattern as follows

$$f_{c,k} = \sum_{i=1}^{4} w_i \cdot f_{l,m} \qquad i = 1, \cdots, 4 \tag{10}$$

2.3. *Learning rule of LPNN (gradient descent method)*

A cost function composed of the state vector and control force is as follows

$$J_k = \sum_{k=0}^{N_f - 1} (z_{k+1}^T \, Q \, z_{k+1} + f_{c,k}^T \, R \, f_{c,k}) \tag{11}$$

where z_{k+1} is the structural response, $f_{c,k}$ is the control force, Q and R are the weighting matrices, N_f and k are the number of the sampling time and the sampling number, respectively. Learning rule for the LPNN is defined as

$$f_c^{new} = f_c^{old} + \Delta f_c \tag{12}$$

where f_c^{new} is the new training pattern with the control force, f_c^{old} is the old training pattern, Δf_c is the variation of control force. For optimal control force, gradient descent rule is applied to the cost function. The variation of the control force is expressed as

$$\Delta f_c = -\eta \frac{\partial J_k}{\partial f_{c,k}} = \eta \delta \tag{13}$$

where η is the learning rate and $f_{c,k}$ is the control force. δ is the partial differential of the cost function with respect to the control force as follows

$$\delta = \left(z_{k+1}^T \, Q \, \frac{\partial z_{k+1}}{\partial f_{c,k}} + f_{c,k}^T \, R \right) \tag{14}$$

The response sensitivity ($\frac{\partial z_{k+1}}{\partial f_{c,k}}$) in the above equation can be obtained through the sensitivity evaluation algorithm [4].

3. Practical Application

For application, a one-story shear building model with active tendon control system is considered where mass ($98kg$), damping ($50N\sec/m$) and stiffness ($6.84\times10^5 N/m$) values are set. California earthquake (1952, 0.152g) is used for training, while El Centro (1940, 0.341g) is used for testing. Fig. 2 shows the block diagram of the LPNN controller for the example building.

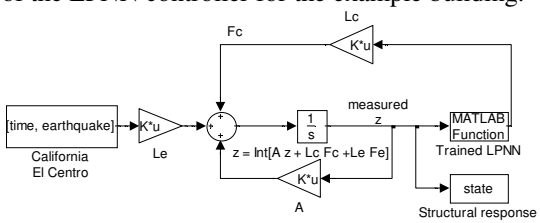

Fig. 2. Block diagram of LPNN controller

4. Control Results

In this section, the effect of the learning methodology is illustrated. Control results of training using the California earthquake before and after learning are shown in Fig. 3(a) and Fig. 3(b), respectively.

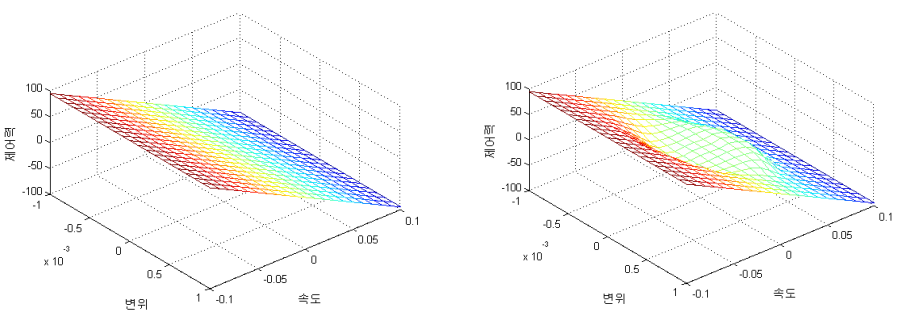

(a) before learning (b) after learning

Fig. 3. Comparison of the training pattern before and after learning

El Centro earthquake is used for testing, and the displacement and velocity responses of the roof before and after learning are shown in Fig. 4(a) and Fig. 4(b). Decreasing rate of responses after learning slightly increased from 59.64% to 61.96%.

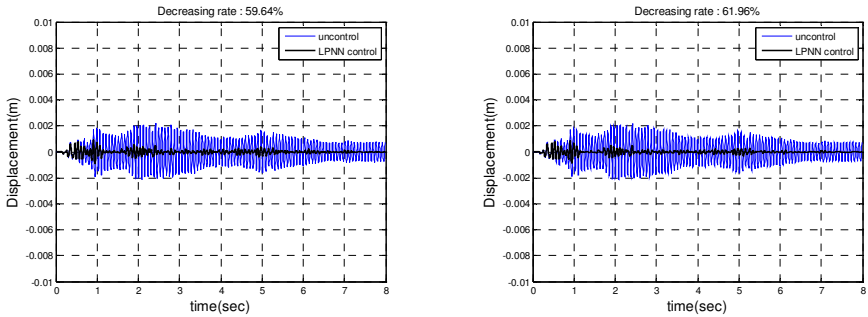

(a) before learning (b) after learning

Fig. 4. Comparison of the uncontrolled and controlled responses to El Centro earthquake before and after learning

5. Conclusion

LPNN is proposed in this study for the active control of structures under unknown earthquake loads. The control capability of LPNN is enhanced by employing a learning methodology using GDM. Results prove that decreasing rates of structural responses are slightly increased when learning is employed. Although the difference in the decreasing rate is not very large, the effect is successfully demonstrated.

Acknowledgments

This research was accomplished as a part of the project, Development of Intelligent Port and Logistics System for Super-Large Container Ships, sponsored by Ministry of Maritime Affairs and Fisheries (MOMAF) in Korea.

References

1. H.M. Chen, K.H. Tsai, G.Z. Qi, J.C.S. Yang, F. Amini, *J Comput Civil Eng*. **9,** 168 (1995).
2. J. Ghaboussi, A. Joghataie, *J Eng Mech.* **121**, 555 (1995).
3. K. Bani-Hani, J. Ghaboussi, *J Eng Mech.***124**, 319 (1998).
4. D.H. Kim, I.W. Lee, *Earthquake Engng Struc Dyn.* **30**, 1361 (2001).
5. A. Madan, *J sound and vibration.* **287**, 759 (2005).
6. D.H. Kim, J.W. Oh, I.W. Lee, *J Comput Civil Eng.* **16**, 291 (2002).
7. D.K. Kim, J.J. Lee, S.K. Chang, S.K. Chang, *In: The TRB 86th Annual Meeting. Compendium of papers (CD-ROM) .Washington DC*: (2007).
8. T.T. Soong, Active Structural Control: Theory and Practice. Longman Scientific and Technical (1990).
9. D.F. Specht, *Phys. Rev.* C52, 2072 (1995).

CORNER STRESS SINGULARITY EFFECTS ON THE VIBRATION OF SKEW PLATES HAVING V-NOTCHES OR SHARP CRACKS*

JOO-WOO KIM

Department of Architectural Engineering, Semyung University, 579 Sinweol-dong Jecheon, Chungbuk 390-711, Korea

HIE-YOUNG JUNG

Department of Civil Engineering, University of Seoul, 90 Jeonnong-dong Seoul, 130-743, Korea

An accurate method is presented for flexural vibrations of skew plates having V-notches. The prime focus here is that the analysis explicitly considers the bending stress singularities at re-entrant (i.e., exterior) corners. A single-field energy-based Ritz method is employed the dynamical energies derived from classical thin-plate theory. The transverse vibratory displacements of the V-notched or cracked skew plate is approximated as a hybrid series of (i) mathematically complete algebraic-trigonometric polynomials which guarantee convergence to exact frequencies as sufficient terms are retained, and (ii) corner functions which account for the bending moment singularities at the re-entrant vertex corner of the radial edges. Accurate frequencies are presented for the spectra of notch angles, notch depths, aspect ratios, and skewnesses.

1. Introduction

Skew plates are used in several practical structures, such as skew bridge or building decks, aircraft wings, ship hulls and vehicle bodies. A considerable quantity of natural frequency data for skew plates has been offered by a number of researches employing the Ritz, Galerkin, and other approximate procedure.[1,2,3]

However, literature on the vibrations of skew plates containing discontinuities, such as cracks or V-notches, is extremely limited or non-existent. The present work examines skew plates including stress singularity effects at the sharp vertex corner (see Fig. 1) for which no previously published vibration frequencies is known to exist. For very small notch angle, $360^\circ - \alpha$ (say, one degree or less), sharp crack ensues. A single-field Ritz procedure is employed, which incorporates a complete set of admissible algebraic-trigonometric

* This work was supported by the Korean Research Foundation, Award No. KRF-2005-041-D00851.

polynomials in conjunction with an admissible set of corner functions that explicitly model the flexural stress singularities which exist along a reentrant corners (i.e., $\alpha > 180^\circ$) of the V-notch.[4] The first set of polynomials guarantees convergence to exact frequencies as sufficient terms are retained. The second set of edge functions substantially accelerates the convergence of frequencies, which is demonstrated through extensive convergence studies herein. Accurate frequencies are presented for skew plates having various vertex angles, skewnesses and different aspect ratios *a*/*b* (see Fig. 1).

2. Methodology

Consider in Fig. 1 a completely free, isotropic skew plate having *a* and *b* with polar coordinates (r, θ) at the vertex of the V-notch. The location of the V-notch is defined by the horizontal and vertical distances *c* and *d*, respectively, as shown in Fig. 1. For the Ritz approach, the vibratory transverse displacement is assumed as

$$w(r,\theta,t) = W(r,\theta)\sin\omega t, \tag{1}$$

where ω and *t* denote the circular frequency of vibration and time, respectively. In the Ritz procedure, one requires the maximum values of strain and kinetic energies, which occur during a vibratory motion. On the maximum energy equations, the limits of the integration are defined as $r(\theta)$, defining the skewed circumferential boundary:

$$\begin{aligned} r(\theta) &= \frac{b-d}{\sin\theta} \quad (\theta_1 \le \theta < \theta_2), \quad r(\theta) = \frac{a-c-d/s_2}{\sin\theta/s_2 + (b\cos\theta)/a} \quad (\theta_2 \le \theta < \theta_3) \\ r(\theta) &= -\frac{b+d}{\sin\theta} \quad (\theta_3 \le \theta < \theta_4), \quad r(\theta) = \frac{a+c-d/s_1}{\sin\theta/s_1 + (b\cos\theta)/a} \quad (\theta_4 \le \theta < \theta_1) \end{aligned} \tag{2}$$

where

$$\begin{aligned} \theta_1 &= \tan^{-1}\left(\frac{b-d}{a+c-b/s_1}\right), \quad \theta_2 = -\tan^{-1}\left(\frac{b-d}{a-c-b/s_2}\right), \\ \theta_3 &= \tan^{-1}\left(\frac{b+d}{a-c+b/s_2}\right), \quad \theta_4 = -\tan^{-1}\left(\frac{b+d}{a+c+b/s_1}\right) \end{aligned} \tag{3}$$

and s_1 and s_2 are the slopes of the right and left side of the skew plate (see Fig. 1), respectively, by which skewness may be determined.

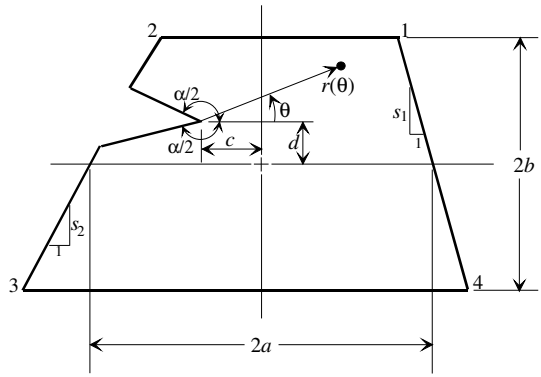

Fig. 1. Geometric description of a skew plate with a V-notch

In order to substantiate the singular behavior of the notched skew plate, displacement trial functions are assumed as the sum of two finite sets:

$$W = W_p + W_c\,, \tag{4}$$

where W_p are mathematically complete algebraic-trigonometric polynomials and W_c are corner functions, which account for singular stress behavior at vertex of the V-notch. The admissible displacement polynomials should theoretically yield accurate frequencies even for the skew plates having stress singularities. However, when a large size of polynomials is utilized, numerical ill-conditioning becomes an obstacle and prohibits one from achieving accurate solutions. This problem is alleviated by augmentation of the displacement polynomial trial set with admissible *corner functions*, which introduce the proper singular vibratory stresses along the vertex of a V-notch or sharp radial crack. The set of corner function is taken as

$$W_c = \sum_{k=1}^{K} C_k W_{c_k}^*\,, \tag{5}$$

where C_k are arbitrary coefficients, and $W_{c_k}^*$ are solutions of the fourth-order biharmonic, static equilibrium equation for bending of plates at acute corner angles:

$$\begin{aligned} W_{c_k}^*(r,\theta) = r^{\lambda_k+1}\big[&\cos(\lambda_k+1)\theta + \zeta_{1k}\cos(\lambda_k-1)\theta \\ &+ \zeta_{2k}\sin(\lambda_k+1)\theta + \zeta_{3k}\sin(\lambda_k-1)\theta\big], \end{aligned} \tag{6}$$

where

$$\zeta_{1k} = \frac{(1-\nu)(\lambda_k+1)}{-\lambda_k(1-\nu)+(3+\nu)},$$
$$\zeta_{2k} = \frac{[\lambda_k(1-\nu)+(3+\nu)][\cos(\lambda_k-1)\alpha-\cos(\lambda_k+1)\alpha]}{[-\lambda_k(1-\nu)+(3+\nu)]\cos(\lambda_k-1)\alpha+[\lambda_k(1-\nu)+(3+\nu)]\sin(\lambda_k+1)\alpha}, \quad (7)$$
$$\zeta_{3k} = -\frac{(1-\nu)(\lambda_k+1)[\cos(\lambda_k-1)\alpha-\cos(\lambda_k+1)\alpha]}{[-\lambda_k(1-\nu)+(3+\nu)]\cos(\lambda_k-1)\alpha+[\lambda_k(1-\nu)+(3+\nu)]\sin(\lambda_k+1)\alpha}.$$

In Eq. (8), the λ_k are the roots of the characteristic equation

$$\sin^2\lambda_k\alpha = \left(\frac{1-\nu}{3+\nu}\right)^2 \lambda_k^2 \sin^2\alpha. \quad (8)$$

Some of the λ_k obtained from equations (8) may be complex numbers, and thus, result in complex corner functions. In such cases, both the real and imaginary parts are used as independent functions in the present Ritz procedure.

The free vibration problem is solved by substituting Eqs. (4) into equations of strain and kinetic energies and using the frequency minimizing equations of the Ritz method. The roots of the vanishing determinant of these equations are a set of eigenvalues, which are expressed in terms of the non-dimensional frequency parameter $\omega a^2\sqrt{\rho/D}$ commonly used in the plate vibration literature.

3. Convergence Studies and Frequency Results

The Ritz formulation described in the previous section is now employed to obtain reasonably convergent frequency solutions as sufficient number of algebraic-trigonometric polynomials and corner functions are used. All of the results shown in this sections are for materials having a Poisson's ratio (ν) equal to 0.3.

Extensive convergence studies were performed to compile the least upper bound frequency parameters $\omega a^2\sqrt{\rho/D}$ for the first three modes of the skew plates with increasing vertex angles (decreasing notch angles), α (or $360^\circ-\alpha$) = 180°(180°), 270°(90°), 300°(60), 330°(30°), 350°(10°), 355°(5°), and 360°(0°) and with increasing notch depths c/a = 0.75, 0.5, 0, and −0.5. Depicted in Fig. 2 are four typical plate configurations which were analyzed to construct the summary of results in Tables 1 and 2, with different aspect ratios (*a*/*b*) as well as slopes (s_1 and s_2). All frequency results are converged to the four significant figures shown in Table 1 and 2. Hence, These tables provide a reasonably accurate database of frequencies for V-notched skew plates having

various aspect ratios notch angles and depths against which future results using experimental or other theoretical methods (such as finite element analysis) may be compared.

Table 1 Frequency parameters $\omega a^2(\rho/D)^{1/2}$ for completely free skew plates with V-notches ($b/a = 2$, $s_1 = 4$, $s_2 = 2$, $d = 0$)

Mode no.	c/a	α (degrees)						
		180	270	300	330	350	355	360
1	0.75	6.709	4.999	10.85	11.02	11.06	4.727	4.690
	0.5	8.509	6.258	10.33	10.92	10.14	4.844	4.463
	0	13.13	8.403	8.794	5.482	2.912	4.783	1.835
	-0.5	20.59	11.72	4.990	3.734	4.679	1.692	1.639
2	0.75	7.877	7.397	19.10	19.02	18.99	7.321	6.783
	0.5	9.875	7.585	19.05	18.86	17.19	7.248	6.516
	0	19.40	11.94	18.47	17.26	15.96	7.241	5.405
	-0.5	27.78	19.01	13.77	13.75	17.00	5.370	5.290
3	0.75	16.27	11.34	23.61	23.86	23.90	11.50	8.652
	0.5	19.55	13.79	22.82	23.48	19.31	12.02	9.722
	0	23.56	18.90	29.23	18.23	19.64	11.26	9.235
	-0.5	53.02	25.49	20.58	15.74	18.14	10.41	9.865

Table 2 Frequency parameters $\omega a^2(\rho/D)^{1/2}$ for completely free skew plates with V-notches ($b/a = 2$, $s_1 = -4$, $s_2 = 4$, $d = 0$)

a/b	Mode no.	c/a	□ (degrees)						
			180	270	300	330	350	355	360
1	1	0.75	15.04	13.51	13.47	5.159	13.53	13.36	13.27
		0.5	17.33	12.96	10.79	4.582	12.81	12.87	12.92
		0	20.64	12.43	10.27	8.783	8.467	8.846	8.899
		-0.5	21.38	15.11	8.926	4.582	6.062	5.938	5.904
	2	0.75	20.98	18.49	18.66	5.731	18.49	17.64	17.37
		0.5	21.68	18.50	17.81	5.661	18.58	18.53	18.47
		0	27.86	19.21	18.14	18.35	18.42	18.36	18.25
		-0.5	54.49	18.22	17.34	5.661	17.83	17.91	18.08
	3	0.75	28.13	21.08	21.48	11.89	21.63	20.52	20.10
		0.5	36.08	19.93	21.14	10.97	20.66	20.82	20.94
		0	53.27	25.97	19.82	18.78	20.08	20.76	21.62
		-0.5	57.10	33.64	21.42	10.97	20.18	20.85	21.08
2	1	0.75	6.710	5.552	5.394	5.072	5.262	5.264	5.263
		0.5	8.492	6.448	5.656	5.351	3.899	5.206	5.230
		0	13.18	8.528	5.788	3.580	3.047	3.132	3.095
		-0.5	20.64	11.82	6.980	2.702	1.966	1.881	1.815
	2	0.75	7.872	6.604	6.558	6.422	6.564	6.586	6.604
		0.5	9.868	6.970	6.198	6.002	5.546	6.083	6.044
		0	19.41	11.96	7.982	5.692	5.379	5.323	5.281
		-0.5	27.86	19.17	13.93	5.839	5.310	5.277	5.191
	3	0.75	16.33	13.58	13.13	9.600	13.46	13.64	13.77
		0.5	19.49	13.98	12.24	11.61	7.286	10.38	11.61
		0	23.63	18.51	13.87	11.35	9.709	9.707	9.698
		-0.5	53.27	25.51	18.22	10.54	10.08	10.11	8.189

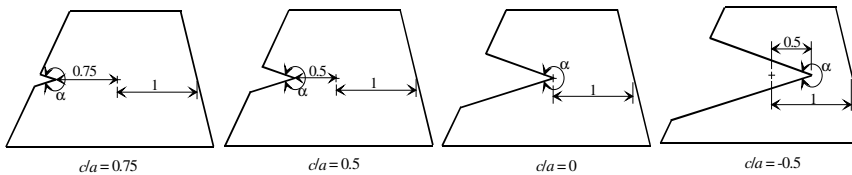

Fig. 2. V-notches with various depths

4. Concluding Remarks

A Ritz procedure in conjunction with classical thin-plate theory has been developed to obtain highly accurate frequencies for completely free skew plates having V-notches or sharp cracks. In this approximate procedure, the assumed transverse displacement of the plate consists of a hybrid set of complete algebraic-trigonometric polynomials along with corner functions that account for the proper singular bending moments at the vertex of acute corner angles. The modeling capability of such corner functions has been substantiated through supporting convergence studies of non-dimensional frequencies.

Detailed numerical tables have been presented, showing the variations of non-dimensional frequencies (accurate to four significant figures) with three geometric parameters; namely, notch angle, notch depths, skewneeses and aspect ratios. Some fundamental understanding of the effect of highly localized stresses on the notched or cracked skew plate dynamics can be obtained through careful examination of the frequency data offered herein.

References

1. A.W. Leissa, *Acoustical Society of America*, **NASA SP-16**, U.S. Government Printing Office, 1969, Reprinted (1993).
2. A.W. Leissa, *Shock and Vibration Digest*, **9(10),** 13-24 (1977).
3. A.W. Leissa, *Shock and Vibration Digest*, **13(9),** 11-22 (1981).
4. A.W. Leissa, O.G. McGee and C.S. Huang, *J. Applied Mechanics*, **60**, 134-139 (1993).

EFFECTS OF TIP MASS ON STABILITY OF ROTATING CANTILEVER PIPE CONVEYING FLUID WITH CRACK

IN-SOO SON[†], HAN-IK YOON, SANG-PIL LEE AND DONG-JIN KIM

School of Mechanical Engineering, Dong-eui University, 995 Eomgwangno, Busanjin-Gu, Busan, 614-714, Korea

In this paper, the dynamic stability of a rotating cantilever pipe conveying fluid with a crack and tip mass is investigated by numerical method. That is, the effects of the rotating angular velocity, the mass ratio, the crack and tip mass on the critical flow velocity for flutter instability of system are studied. The equations of motion of rotating pipe are derived by using the extended Hamilton's principle. The crack section of pipe is represented by a local flexibility matrix connecting two undamaged pipe segments. The crack is assumed to be in the first mode of fracture and always opened during the vibrations. Finally, the stability maps of the cracked rotating pipe system as a rotating angular velocity and a mass ratio β are presented.

1. Introduction

Rotating cantilever beams are found in several practical engineering examples such a turbine blades and aircraft rotary wings. A good structural model for the rotating flexible beam system is essentially important in many engineering applications such as aerospace, aviation and robotics. Since significant variations of modal characteristics result from rotational motion of the structures, they have been investigated by many researchers [1,2]. In addition, the dynamic stability of pipes conveying fluid has been studied for a long time [3]. It has established that a straight cantilevered pipe is stable for flow velocities less than a certain value, called the critical flow velocity. If such a pipe conveys fluid has the critical flow velocity it loses stability by flutter [4]. Recently, the vibration of a rotating cantilever pipe conveying fluid with a tip mass has been studied by numerous researchers [5,6]. Liu *et al*.[7] examined the suitability of using coupled response to detect damage in thin-walled tubular structures. Dado and Abuzeid [8] studied a modeling and analysis algorithm for cracked beams by considering the coupling between the bending and axial modes of vibration. However, other's researches did not study about the coupling effects of a tip mass, fluid flow, rotation and crack for stability analysis of pipe system. Therefore, in this paper,

[†] Work partially supported by grant 2-4570.5 of the Swiss National Science Foundation.

the effects of the mass ratio, the rotating angular velocity, a crack and tip mass on the stability and instability of pipe system are studied by numerical method.

2. Mathematical Model

Fig. 1(a) shows the schematic diagram of a rotating cantilever pipe conveying fluid with a tip mass and crack. Consider a cantilever pipe of a length L, which is fixed at point O of a rigid hub with a radius r. The hub is rotating about the axis of symmetry with a rotating angular velocity ω. P_0 and P are the positions of a generic point before and after deformation, respectively. When the point P_0 moves to the point P, using the Cartesian co-ordinates, the deformations of the pipe in the directions of $\mathbf{i}$ and $\mathbf{j}$ is generally described by the axial deformation y_1 and the lateral deformation y_2, respectively. In addition, s is the arc length stretch. m_t is a tip mass, U and x_c are the velocity of fluid flow and the position of a crack, respectively. Fig. 1(b) shows a circular hollow cross-section of the cracked section. θ_c and $2b$ are the crack depth and the length of a crack.

2.1. *Crack modeling*

The additional strain energy due to the crack can be considered in the form of a flexibility coefficient expressed in terms of the stress intensity factor, which can be derived by Castigliano's theorem in the linear elastic range. Therefore the local flexibility in the presence of the width $2b$ of a crack is defined by [7]

$$C_{ij} = \frac{\partial u_{ij}}{\partial P_j} = \frac{\partial^2}{\partial P_i \partial P_j}\left(\int_{-b}^{b}\int_{0}^{a_c} J \; dydz\right), \tag{1}$$

where P_i is the load in the same direction as the displacement and J is the strain energy density function [7]. The flexibility matrix can be obtained as

$$\begin{bmatrix} k_{11} & k_{12} \\ k_{21} & k_{22} \end{bmatrix} = \begin{bmatrix} C_{11} & C_{12} \\ C_{21} & C_{22} \end{bmatrix}^{-1} = \frac{1}{\Delta}\begin{bmatrix} C_{22} & -C_{12} \\ -C_{21} & C_{11} \end{bmatrix}, \tag{2}$$

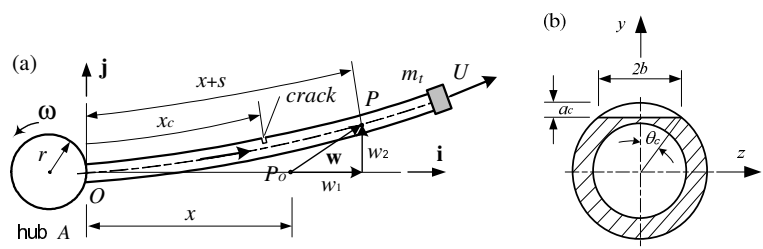

Fig. 1. (a) Mathematical model and (b) cross section of cracked pipe.

where $\Delta = C_{11}C_{22} - C_{12}C_{21}$. In this study, the coupling elements are ignored because the effect of coupling elements is very small [8]. Therefore, the crack stiffness used in this study are defined as

$$K_T \equiv k_{11} = C_{11}^{-1}, \qquad K_R \equiv k_{22} = C_{22}^{-1}, \tag{3}$$

where K_T , K_R denote the translated spring and the rotating spring coefficient.

2.2. *Dimensionless equation of motion*

In the present modeling method, a non-Cartesian variable s denoting the arc length stretch of the neutral axis is employed. In order to use the arc length stretch s instead of y_1, the geometric relation between the arc length stretch s and the Cartesian variables is given in reference [2].

For simplicity, the following dimensionless quantities are introduced:

$$\begin{aligned} &\xi = x/L, \quad \beta = M/(m+M), \quad u = UL\sqrt{M/(EI)}, \quad a = \theta_c/\pi, \\ &\Omega = \omega L^2\sqrt{(m+M)/EI}, \quad \mu = m_t/\left[(m+M)L\right], \quad \xi_c = x_c/L, \quad \bar{r} = r/L, \end{aligned} \tag{4}$$

where m , M are the mass of pipe and fluid per unit length. EI denotes the flexural rigidity of the pipe. The dimensionless quantities of s , y_2 are given by

$$v_k = \frac{s_k}{L} = \sum_{i=1}^{n} \phi_{ki}(\xi) q_{1i}(\tau), \qquad \eta_k = \frac{y_{2k}}{L} = \sum_{i=1}^{n} Y_{ki}(\xi) q_{2i}(\tau), \tag{5}$$

where k is the number of the segments due to the crack. In this study, we consider only the bending vibration. Therefore, the dimensionless equations of motion for bending vibration of the cracked pipe conveying fluid with a tip mass are obtained as follows:

(i) segment $1: 0 \le \xi \le \xi_c$,

$$\begin{aligned} &\ddot{\eta}_1(\xi,\tau) + 2u\sqrt{\beta}\dot{\eta}_1'(\xi,\tau) + u^2\eta_1''(\xi,\tau) + \eta_1^{iv}(\xi,\tau) \\ &-\Omega^2\eta_1(\xi,\tau) - \Omega^2\left[\bar{r}(1-\xi) + \frac{\left(1-\xi^2\right)}{2}\right]\eta_1''(\xi,\tau) + 2\Omega\dot{v}_1(\xi,\tau) = 0, \end{aligned} \tag{6a}$$

(ii) segment $2: \xi_c \le \xi \le 1$,

$$\begin{aligned} &\ddot{\eta}_2(\xi,\tau) + \mu\ddot{\eta}_2(1,\tau) + 2u\sqrt{\beta}\dot{\eta}_2'(\xi,\tau) + u^2\eta_2''(\xi,\tau) + \eta_2^{iv}(\xi,\tau) - \Omega^2\eta_2(\xi,\tau) \\ &-\Omega^2\left[\bar{r}(1-\xi) + \frac{\left(1-\xi^2\right)}{2}\right]\eta_2''(\xi,\tau) - \Omega_\mu^2\left[\eta_2(1,\tau) - \eta_2''(1,\tau)\right] + 2\Omega\dot{v}_2(\xi,\tau) = 0 \end{aligned} \tag{6b}$$

where ($\cdot$) denotes the dimensionless time derivative, and ( )' stands for partial differentiation with respect to ξ. The boundary conditions are obtained in Ref. [8]. By using the equations of motion, we can obtain the complex eigenvalue λ. The stability of the cracked pipe system consideration is determined by the sign of imaginary part of λ. As the flow velocity increases, the imaginary part of λ becomes negative, and the pipe system loses stability by buckling for Re(λ)=0 and by flutter for Re(λ) $\neq$ 0. If Im(λ)=0, it has the critical flow velocity u_{cr}.

3. Numerical Results and Discussion

In this study, the dynamic stability of a rotating cantilever pipe conveying fluid with crack is investigated. First of all, the accuracy of the present numerical results needs to be confirmed. Fig. 2 shows a comparison between present numerical results and data of Ref. [5] of two different tip mass cases(Ω =0). These results show that present results are a good agreement with the result of the reference.

Fig. 3 shows the effect of tip mass on critical flow velocity of cracked pipe. As the tip mass increases, the value of critical flow velocity of cracked pipe system is decreased. It is noted that one jumps take place in the critical velocity at $\beta \simeq 0.552$ and $\beta \simeq 0.781$ for two cases of μ =0 and 0.1, respectively. However, it has no phenomenon of jumps for the case μ =0.2. In this case, the flutter occurs only on the second mode for all β in the range of 0< β <1.

The critical flow velocity for flutter, u_{cr}, of a cracked pipe with a tip mass, as β is shown in Fig. 4. The tip mass and crack depth are 0.1 and 0.1, respectively. When the angular velocity is 1, it has just one jumps for the case of ξ_c =0.1. However, in the case of ξ_c =0.5, it is noted that two jumps take place in the critical velocity at $\beta \simeq 0.418$ and 0.860. In the case of ξ_c =0.5, the flutter occurs on the second mode in the ranges 0< β <0.388, on the third mode for

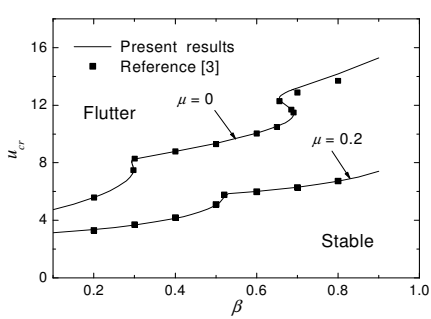

Fig. 2. Comparison of present numerical results with Ref. [3].

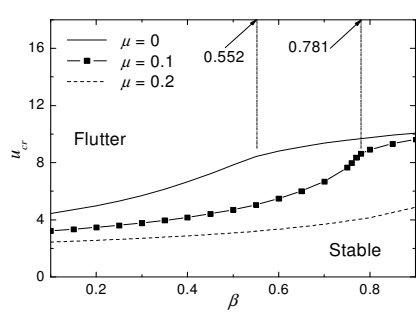

Fig. 3. Critical flow velocity of cracked pipe system($a = \xi_c$ =0.1, Ω =1).

β =0.388 ≤ β <0.838 and on the forth mode for β =0.838 ≤ β .

Fig. 5 shows the stability maps of cracked pipe with a tip mass, where μ =0.1 and Ω =3. In Fig. 5(a), the value of critical flow velocity of the case of a =0.1 is larger than the case of a =0.2 in the range β <0.480, however, in the range 0.480 ≤ β , the critical flow velocity of the case of a =0.1 is smaller than the case of a =0.2. In Fig. 5(b), the values of critical flow velocity of the case ξ_c = 0.3 are larger than the case of ξ_c =0.5. However, the value of critical flow velocity of the case ξ_c =0.3 is smaller than the case of ξ_c =0.5 in the specific ranges 0.380 ≤ β < 0.417 and 0.838 ≤ β .

Figs. 6(a), (b) for β =0.2 show that the stability map of cracked pipe according to the angular velocity of a pipe. Generally, when the tip mass and crack position are constant, as the crack depth increases, the region of stability is increased. That is, unstable region undergo right shift as the depth of crack increases. In Fig. 6(a), if the angular velocity is 15, the critical flow velocity of case a =0.2 is higher than the case of a =0.1 approximately 55%. In Fig. 6(b), the values of critical flow velocity of ξ_c =0.5 are larger than the case of ξ_c =0.1

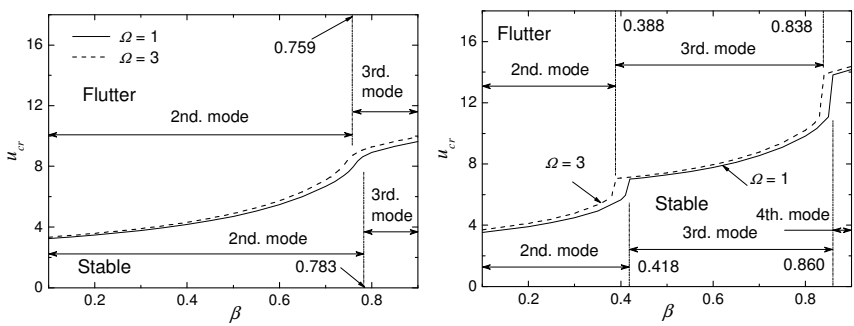

(a) ξ_c =0.1 (b) ξ_c =0.5

Fig. 4. Critical flow velocity of cracked pipe system(μ =0.1, a = 0.1).

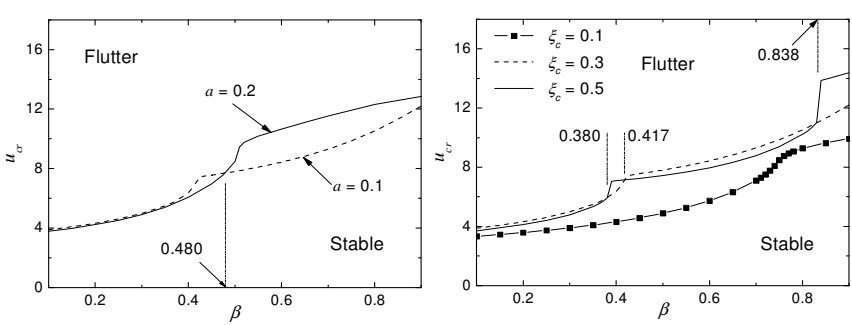

(a) ξ_c =0.3 (b) a =0.1

Fig. 5. Critical flow velocity of cracked pipe system(μ =0.1, Ω =3).

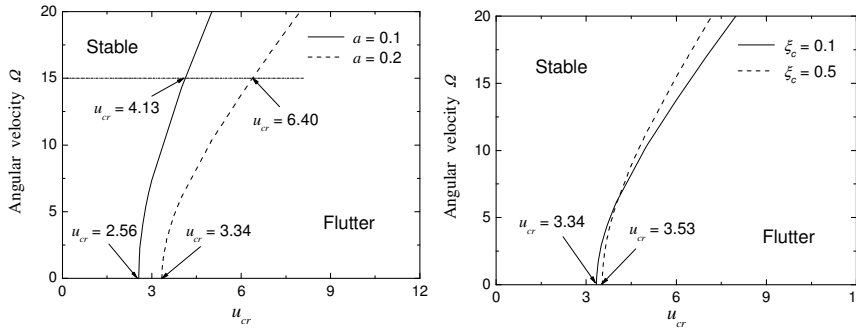

(a) ξ_c =0.1 (b) a =0.2

Fig. 6. Stability map of cracked rotating pipe system($\beta = \mu$ =0.2).

in the range Ω <6.43, however, in the range $6.43 \leq \Omega$, the result is quite the other way round.

4. Conclusions

In this paper, the effects of the mass ratio, the rotating angular velocity, a crack and the tip mass on the stability and instability of pipe system are studied by the numerical method. The cracked rotating cantilever pipe conveying fluid is modeled by the Euler-Bernoulli beam theory. The equation of motion of the system is derived by using extended Hamilton's principle. The crack is assumed to be in the first mode of fracture and always opened during the vibrations.

As the tip mass increases, the critical flow velocity u_{cr} becomes smaller. In the special case of μ =0.2, the flutter occurs only on the second mode of system. When the tip mass and crack is constant, the critical flow velocity for flutter is proportional to the rotating angular velocity of a pipe. The crack position is very important parameter because it has not consistent trend in the analysis of stability. It should be remarked that the above results are presented in dimensionless form, valid for arbitrary rotating pipe system with a tip mass and crack.

References

1. S. Hoa, *J. Sound Vib.* **67**, 369 (1979).
2. H. H. Yoo, R. R. Ryan and R. A. Scott, *J. Sound Vib.***181(2)**, 261 (1995).
3. M. P. Païdoussis, *Academic Press.* (1998).
4. T. B. Benjamin, *Proc. Royal Society*, **A261**, 261 (1961).
5. D. A. Panussis and A. D. Dimarogonas, *J. Fluids Struct*. **14(1)**, 1 (2000).
6. H. I. Yoon and I. S. Son, *Int. J. Mech. Sci*. **49(7)**, 878 (2007).
7. D. Liu, G. Gurgenci and M. Veide, *J. Sound Vib*. **261(1)**, 17 (2003).
8. M. H. F. Dado and O. Abuzeid, *J. Sound Vib*. **261(4)**, 675 (2003).